12th International Conference on

Steel Space & Composite Structures

Prague, Czech Republic
28–30 May 2014

Organised by:
Czech Technical University in Prague

Editors: **F. Wald and S.P. Chiew**

Proceedings of the 12th International Conference on

Steel, Space & Composite Structures

Prague, Czech Republic
28 – 30 May 2014

Edited by:

Frantisek WALD, Czech Technical University in Prague, Czech Republic
Sing-Ping CHIEW, Nanyang Technological University, Singapore

Organised by:

Czech Technical University in Prague

Supported by:

- Czech Constructional Steelwork Association
- Singapore Structural Steel Society
- Hong Kong Institute of Steel Construction

Managed by:

- CI-Premier Conference Organisation, Singapore

ISBN No. 978-981-09-0077-9

Conference Secretariat:

CI-PREMIER PTE LTD
150 Orchard Road #07-14
Orchard Plaza
Singapore 238841
Republic of Singapore
Tel: +65 67332922
E-Mail: ci-p@cipremier.com
Web: http://www.cipremier.com

PREFACE

The 12th international conference on **Steel Space & Composite Structures** is organized by The Czech Technical University in Prague and held in the beautiful city of Prague, Czech Republic on 28-30 May 2014. This successful international conference series on **Steel Space & Composite Structures** was initiated by the Singapore Structural Steel Society to mark its inception and formation in Singapore back in March 1984. Since then, the subsequent conferences have been held in various oversea venues, i.e. Jakarta, Indonesia (1985), Singapore (1987 & 1990), Jakarta, Indonesia (1994), Singapore (1999 & 2002), Kuala Lumpur, Malaysia (2006), Yantai & Beijing, China (2007), Gazimagusa, North Cyprus (2011) and Qingdao, China (2012).

Again, this 12th conference has been well received by researchers and practitioners in the field of steel space and composite structures and it provides a timely platform to bring together those who shared a common interest in the related subject areas to promote international communication of new ideas, developments and innovations. A total of 42 selected papers covering the latest development, innovation and research findings from 24 different countries were accepted for presentation after a careful review process. This includes the keynote conference plenary lecture and 10 keynote papers by renowned international experts in their respective fields, and 31 technical papers by some prominent researchers. New construction technologies and design concepts to achieve impressive architectural marvels and application of new products such as CFRP and high strength and high performance steel are some of the highlights among the contributed papers. Advancements in analytical methods including effects of fire, buckling, vibration and dynamic loads with the aim of improving productivity and novel application of steel and composite structures are also highlighted in the contributed papers.

We take this opportunity to express our sincere gratitude to all authors and contributors for preparing and sharing your latest research works with others, and for your expert input and unfailing support without which this conference would not have been possible. We also acknowledge the reviewers for their speedy review and the members of the conference advisory committee for their invaluable advice and guidance. We also like to record our appreciation to The Czech Technical University in Prague for hosting this 12th conference and to the Czech Constructional Steelwork Association, Singapore Structural Steel Society and Hong Kong Institute of Steel Construction for your wonderful support.

Finally, we thank the conference secretariat for taking care of the details and we also thank all conference participants and presenters for your excellent contributions to the conference. We wish all participants an enjoyable and memorable conference held for the first time in this beautiful city of Prague and we also wish everybody a very successful and convivial gathering and fellowship among like-minded friends and colleagues.

Frantisek WALD and Sing-Ping CHIEW
The 12th International Conference on Steel Space & Composite Structures
Prague, Czech Republic

12th International Conference on

STEEL, SPACE & COMPOSITE STRUCTURES

28-30 May 2014, Prague, Czech Republic

Conference Organising Committee

Conference SS14 Chairman
Prof Frantisek Wald, Czech Technical University in Prague, Czech Republic

Conference Series Chairman
A/Prof Sing-Ping Chiew, Nanyang Technological University, Singapore

Members
-Prof Yong-Bo Shao, Yantai University, China
-Er John S Y Tan, CI-Premier Pte Ltd (director)
-Ms Peggy L P Teo, CONLOG (secretariat)

Conference International Advisors

- Prof Robert Beale, Oxford Brookes University, United Kingdom
- Prof Mark A Bradford, The University of New South Wales, Australia
- Prof Murude Celikag, Eastern Mediterranean University, North Cyprus
- Prof Daniel Dan, Politehnica University of Timisoara, Romania
- Prof Hans De Backer Universiteit Gent, Belgium
- Prof Guo-Qiang Li, Tongji University, China
- Prof Hartmut Pasternak, Brandenburg University of Technology, Germany
- Prof Kang-Hai Tan, Nanyang Technological University, Singapore
- Prof Brian Uy, The University of New South Wales, Australia
- Prof Y C Wang, University of Manchester, United Kingdom
- Prof Eiki Yamaguchi, Kyushu Institute of Technology, Japan
- Prof Toshitaka Yamao, Kumamoto University, Japan

12th International Conference on

STEEL, SPACE & COMPOSITE STRUCTURES

28-30 May 2014, Prague, Czech Republic

TABLE OF CONTENTS

Conference Plenary Lecture

Keynote Papers

Technical Papers

Technical Papers

CONFERENCE PLENARY LECTURE

12th International Conference on
Steel, Space and Composite Structures
28-30 May 2014, Prague, Czech Republic

TENSIONED STEEL STRUCTURES - CASE STUDIES

Vladimír Janata*

*EXCON, a.s.
Sokolovská 187/203, 130 00 Praha 9, Czech Republic
e-mail: janata@excon.cz, webpage: http://www.excon.cz

Keywords: tensioned steel structure, prestressed tendon, strain gauge

Abstract. *The application of prestressed tendons in the global static schema of steel structures has an essential influence on their architectural expression. Slender tensioned steel structures are mostly cost effective (considering the ratio of weight and cost to load bearing capacity). The basic principles and special problems of tensioned structures are presented using several case studies of the structures designed by the author over the last ten years. Methods for tensioning and on-line measurements of the forces in the tendons (solid bars) and ropes are described here. Exact tensioning procedures designed to achieve the designed values of the prestressing and to minimize the time of erection on site are also presented.*

1 INTRODUCTION

The wider use of steel structures tensioned by prestressed tendons has been made possible by improvements in CAD and FEM methods, the accessibility of new materials, products and simple and exact methods of the prestressing and its measurement. Basic principles and objectives of prestressing can be characterised in the following points:

a) One of the basic objectives of the prestressing is to avoid the compressive forces in slender tendons at any load configuration. Prestressed tendons can be considered as compression members in a structural model in this case. The replacement of the compression members with prestressed tendons and using high-strength material can significantly reduce dead weight of the structure.
b) Structures can also be simply pre-deformed by prestressing in order to reduce deformations caused by applied loading or to modify the shape according to the designer's presumptions.
c) Internal forces in the structure can be positively re-distributed to counter the ones caused by loading, which enables reduction of the dimension of certain units of the structure.
d) Tensioning can reduce or eliminate the non-linear character of long tendons due to sag, or modify the dynamic characteristics of a structure.
e) Tensioning makes it possible to create new structural systems of an unusual appearance of structures.
f) Methods of tensioning should be simple, and measurement methods of forces in tendons should be reliable. Preferably, two independent methods are to be used.
g) Tensioning cannot usually be applied all at once in all tensioned units. The effect of the mutual interaction of successively prestressed tendons has to be taken into account.
h) Different statical models must be considered in various phases of erection and prestressing.

i) Thanks to advanced methods, the tensioning procedure can be optimized to reach the shortest way and best achievable accuracy.

2 CASE STUDIES

The following tensioned structures were designed and most of them built over the last ten years in the Czech Republic.

2.1 Sazka Arena (O_2 Arena) in Praha, prestressed space beam-string structure

The multipurpose Arena for 18,000 spectators was built for the Ice Hockey World Championships held in Praha in April 2004. In addition to various sports events, the arena is used for numerous other cultural and social events. The arena was completed in 16 months between September 2002 and its opening in March 2004. The roof is designed to withstand heavy asymmetrical loads by concert and theatre technology.

Figure 1: Roof of arena under construction

The roof of Sazka Arena (O2 Arena at present) in Praha [1] has the shape of a spherical cap spanning 135 m with a rise of 9 m (Fig. 1). The prestressed space beam-string structure consists of 36 radial truss girders with tie-rods connected to a central cylindrical truss. The structure was assembled on central falsework (Fig. 2).

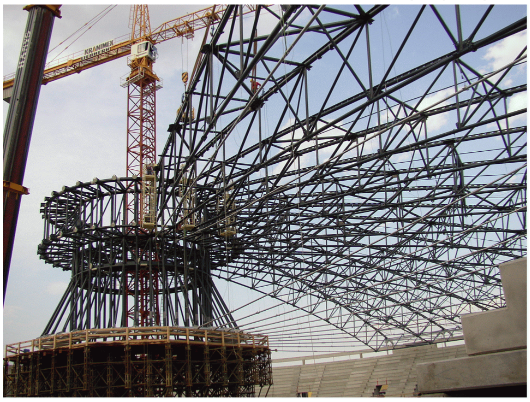

Figure 2: Structure on the falsework

Figure 3: Tensioning the bars using a hydraulic device

The all-welded central cylinder, weighing 170 tons and 18 m in diameter and with a height of 12.3 m, is hollow. It consists of three main horizontal circular trusses connected by 36 columns

and radial diagonal braces. The arched radial trusses with a structural height of 4 m are connected to the cylinder and supported by columns on the other side. The steel tendons are fabricated from European steel grade 460 with M100 rolled threads, and are anchored to the ends of the trusses on one side and to the central cylinder on the other side by forks and pins.
The tendons were tensioned according to the precise procedure using a hydraulic device (Fig. 3). The mutual interaction of the successively prestressed tendons was taken into account. The Specific aesthetic impression of the interior view is significant for the completed multifunctional arena (Fig. 4).

Figure 4: Sazka Arena (O_2 Arena), interior view

2.2 Arena in Chomutov, structure suspended on a main arch

The steel roof structure of ice-hockey arena in the Czech town of Chomutov (Fig. 5), finished in the year 2010, is suspended on a set of eleven twins of tensioned hangers anchored to main arch, situated above the longitudinal axis of the stadium. The main arch is the steel tube with a diameter of 1 m, a span of 120 m and a rise of 28 m. The suspended roof is the lattice structure curved in two directions. The tensioning of the hangers, carried out on completed structure, favourably redistributed internal forces in the arch and lattice trusses of the roof. Thus, a significant reduction of the dead load was achieved. The forces in the hangers were measured with strain gauges commonly with the frequency analysis method. Monitoring of the structure geometry was carried out simultaneously. The prestressing procedure was optimized using the linear programming method with boundary conditions.

Figure 5: Arena in Czech town of Chomutov


Figure 6, 7: Erection phases


Figure 8, 9: Interior view of the slender structure

Although the arena is cubature efficient, the high central clearance (Fig. 9) of the inner space creates room for alternative usage of the arena. The structure, the entire appearance and the utility of the structure met the architect's vision and investor's input. The solution designed is also economical from the perspective of acquisition costs and with regard to the minimization of heated space and facade surfaces and thus contributes significantly to lowering future operating costs and the protection of the environment.

2.3 Speed skating stadium

The roof of the speed skating stadium is suspended on two main arches. The experience from the Chomutov project was utilised. The stadium has not yet been built, but the concept was verified in design (Fig. 10, 11),

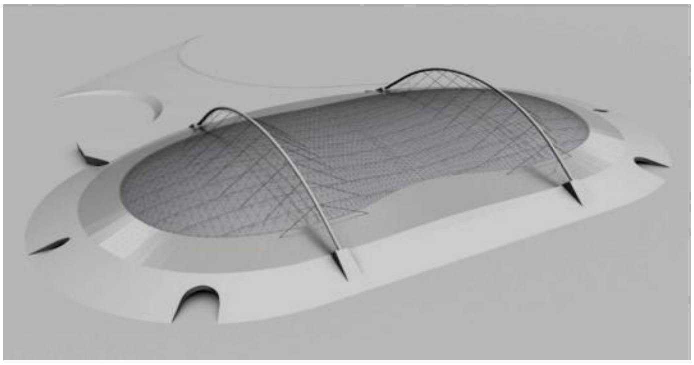


Figure 10, 11 The speed skating stadium

2.4 The hangar at Mošnov Airport, bowstring lattice girder with prestressed bottom chord

The hangar at Mošnov Airport is situated to the south Ostrava (Fig. 12) and has served for the medium maintenance of various types of aircrafts since January 2008. The main hangar hall has a rectangular ground plan 143.5 x 80 m. Along one of the 143.5 m sides of the hangar is an adjacent 5-storey service building. The minimum clear height of the hangar is 21 m. Prestressed tendons (Fig. 13) are used as the bottom chords (couple of tendons with M100 thread) of the bowstring lattice trusses spanning 143.5 m, as well as for the horizontal bracing of the hangar roof at the level of the top of the hangar door (bottom chord’s plane) and for the bracing of the hangar’s walls. The roof structure was assembled on the ground, including the roof cladding and technological equipment, and then lifted to their final position on top of the columns.

Figure 12: The Mošnov hangar

Figure 13, 14. Detail of bottom chord connection and cross bracing from prestressed tendons

Thanks to the original structural and erection solution, an average weight of the roof structure of 65 kg/m^2 was achieved. Approximately 25% of steelwork weight was saved and consequently the cost of steelwork was reduced compared to the originally designed standard beam solution.

Thanks to the assembly of the steel, structure of the roof, roof cladding and technology equipment on the ground, construction time was significantly shortened.

The whole process from conceptual design to detail design, fabrication and erection of steelwork took only 10 months.

2.5 The glassed-in atrium roof of ČSOB bank in Praha, beam – string girders

The structure of the glassed in atrium roof of a cylindrical shape (Fig. 15) is created by 7 beam-string girders with a 32 m span. The girder consists of an upper rigid beam, pinned verticals and down prestressed tendons. The structure is favourable due to simple fabrication and erection. The exact shape of the structure is easy to achieve by the manual prestressing (Fig. 16) of the tendons. Asymmetrical loads and uplift due to wind and buckling stability has to be carefully checked in this type of structure. This construction built in the year 2006 fulfilled the architect's dream of an "invisible" structure bearing the glassed in roof.

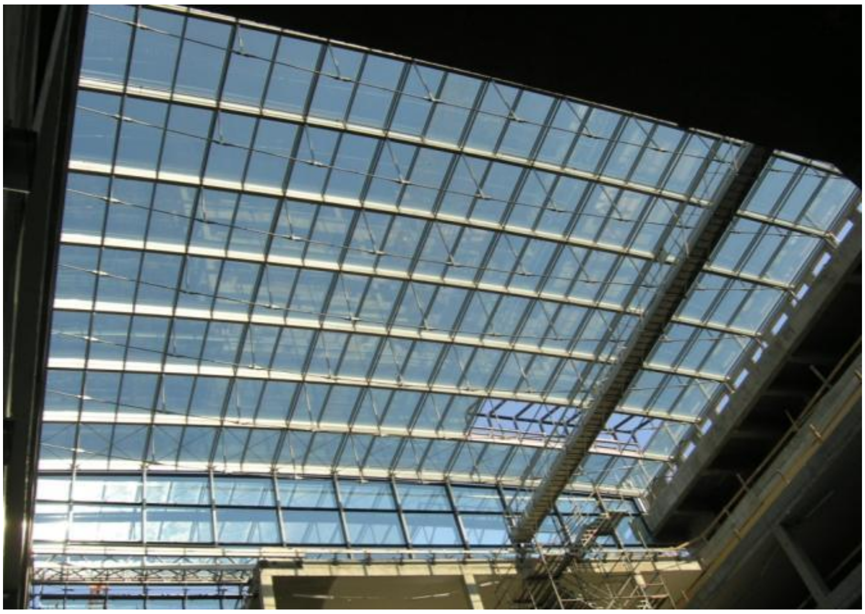

Figure 15, 16. Beam-string girders of the glassed-in atrium

2.6 Anti-noise tunnel supported with the network of tensioned bars

The anti-noise tunnel in the centre of the town of Hradec Králové (Fig. 17) was built on the existing bridge rising between two rows of blocks of flats. The steel glassed-in tunnel with a length of 180 m, a width of 20 m and a height of 6.7 m is anchored on new concrete columns and slabs situated outside the bridge, which is curved with a changing diameter. The central longitudinal beam of the steel structure is suspended on the prestressed network of 180 tendons anchored to columns with a height of 9 m which are part of the main cross frame (Fig. 18). The intermediate structure bearing the glass cladding consists of transverse ribs with a T profile and longitudinal grids. Erection was carried out without interrupting traffic, which was always diverted to one side of the road. The central beam was erected first on temporary supports followed by the part of the structure on the side without traffic.

Figure 17 Anti-noise tunnel

The problem of achieving the designed network's forces from the actual ones measured on site was solved with the matrix of mutual interference of individual tendons and with the tensioning procedure theoretically prepared in advance. Tensioning was carried out in three phases (approx. 70 tendons each).
The forces measured by strain gauges were available on-line to the designer leading the tensioning procedure, making it possible to modify the tensioning procedure on site. Finally, after finishing the structure, including the glass cladding, the forces in the network were monitored by the frequency analysis method; the forces will be checked as part of regular inspection and maintenance.

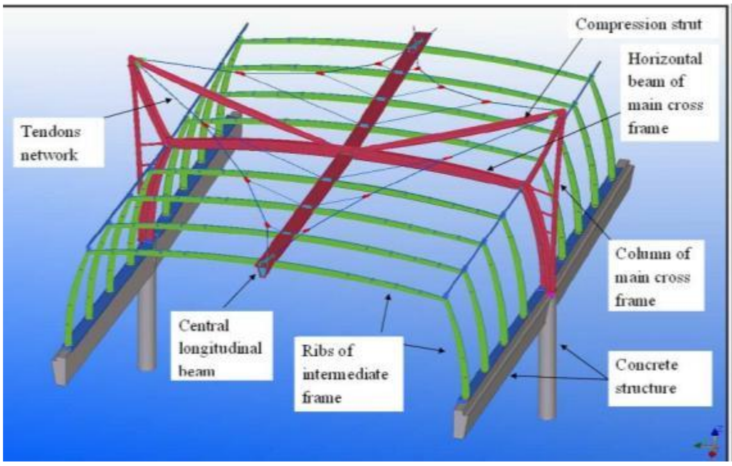

Figure 18. Disposition scheme of the tunnel

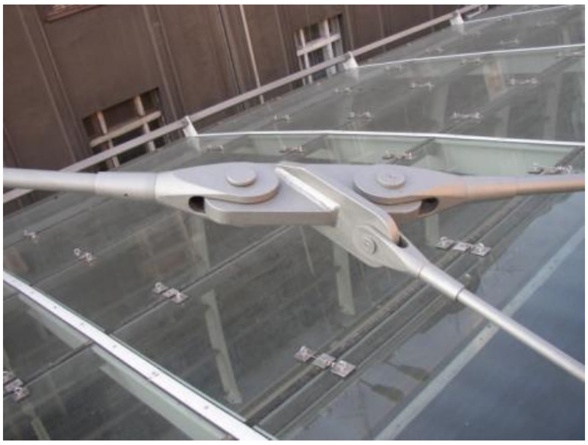

Figure 19, 20 Detail solution of the tendons network

2.7 Troja Bridge in Praha, the bowstring arch structure with a network of 200 tendons.

The new Praha bridge (Fig. 21) spanning the Vltava River for trams, cars in four traffic lanes and pedestrians between the districts of Troja and Holešovice is nearly finished. The deck is 36 m wide, including the walkways. The bridge of the main span 200.4 m in length is a simply supported bowstring-arch type bridge with two longitudinal prestressed steel-concrete chords and two twins of inclined network type webs. The arch body divides the transitional part into two sections called "legs". The tram rails are inside the arch between the arch legs, the roadways and walkways are on the cantilevers outside the arch.

The steel arch spanning 200.4 m with a rise of only 20 m has a flat pentagonal box cross section with varying width and height. The structural height of the box is only 1.3 m and is 7 m wide in the middle of the span. The upper and lower flange of the arch is made of plate 60 mm thick and side walls are from 50 mm plate. The lower flange is divided into two parts of a cylindrical shape connected to one other creating an arrow shape. Inside the pentagonal arch cross-section are another six longitudinal walls (webs). Four longitudinal walls with a thickness of 40 mm are welded with the connecting plates for hangers which pass through the lower flange (Fig. 22). There are transversal diaphragms with a thickness of 25 mm situated by 1.8m inside the arch sections. The legs of the arch have a tetragonal box cross-section. The "legs" are connected to the steel core of the arch tendons through four base sections filled with concrete.

Figure 21 Troja Bridge in Praha

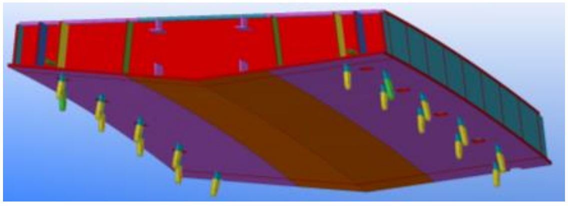

Figure 22, 23 Troja Bridge - steel arch body

There are 200 hangers (Fig. 24) fabricated from European steel grade 520 with dimensions of rolled thread M76 – M105 in the bridge network. Hangers are created by certified system consisting of solid bars with rolled threads, turnbuckles, forks, pins, and lock covers. The employed Macalloy system was successfully tested to withstand two million cycles of stress range 130 MPa. The turnbuckles were designed especially for this purpose. The material, dimension, internal shape and shape of thread were optimized to withstand heavy fatigue loading.

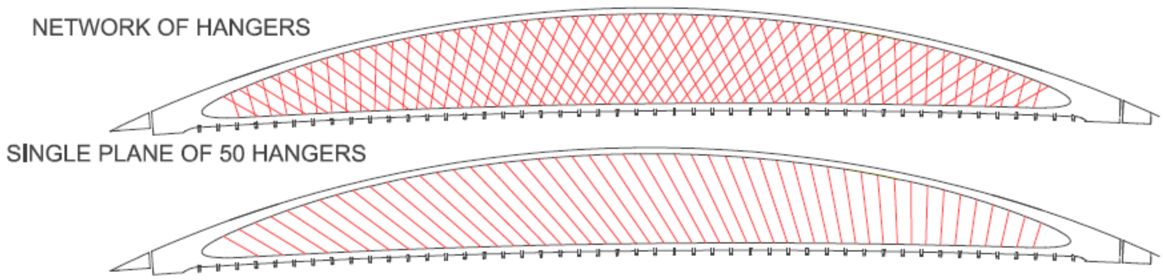

Figure 24 Troja Bridge, network of hangers in four planes

The steel chords with concrete transverse girders supported by temporary steel lattice structure were launched across the river over the temporary supports in the river. The concrete slab and steel chords were then cast on site. The steel structure of the arch was welded from transport parts into larger assemblies, transported to the deck, hoisted up to temporary supporting towers and welded to one piece. After releasing the arch from the temporary towers, the hangers were installed and tensioned. Finally the deck was released from the supports in the river and the temporary steel lattice structure was removed. The prestressing of the concrete slab and chords was carried out in three phases during the construction process. The steel walkway construction was then fixed to the deck.

Figure 25 Troja Bridge, deck on the temporary supports, installation of the hangers

Tensioning of the hangers is realized mostly by the dead weight of the structure released from the temporary supports in the river. The hangers were installed on the supported deck after releasing the arch from the erection towers (Fig. 25). The main reason of hanger tensioning during the installation was to ensure their linear behaviour during releasing the structure from the supports in river. Tensioning of the hangers near the ends of the arch is higher to ensure favourable redistribution of internal forces in the arch acting against the ones originating from the release of the arch from the supports. Installation and tensioning of the hangers was carried out in six phases (Fig. 26) according to a prestressing procedure elaborated in advance in order to minimize the repeated adjustment of previously finished phases.

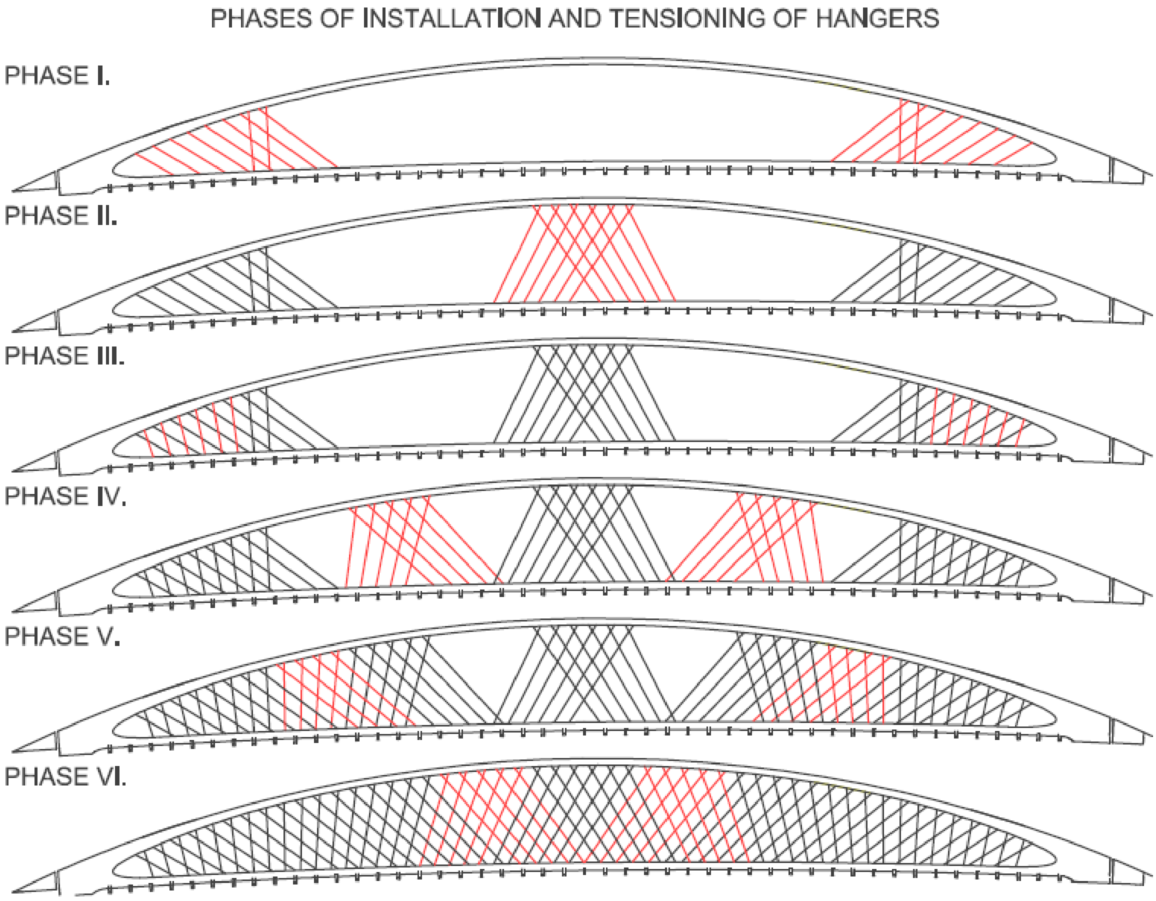

Figure 26 Troja Bridge, phases of hanger installation

The arch itself after release from the supports had extremely low bending stiffness. The installation and prestressing procedure of the hangers was carried out symmetrically across the longitudinal and transverse axes of the bridge in order to ensure the correct shape of the arch. The prestressing procedure was carried out on the basis of a matrix of mutual interaction of individual hangers calculated on partial models comprised of only the hangers present in the structure in the appropriate phase. The installation and tensioning of 200 tendons (Fig. 27, 28) was carried out during 25 working days using 92 tensioning steps. The forces in the hangers are measured by strain gauges. The measuring system makes it possible to follow on-line all forces in currently installed on the bridge. The second time the hangers were tensioned after releasing the deck from the supports in the river to optimise internal forces in the arch and to avoid theoretical compression forces in hangers in any future load combination. At the end, after the installation of all permanent loads, the eigenfrequencies measurement of all hangers will be measured. The measured frequencies will be compared with ones measured in the future in terms of the regular inspection of the bridge.


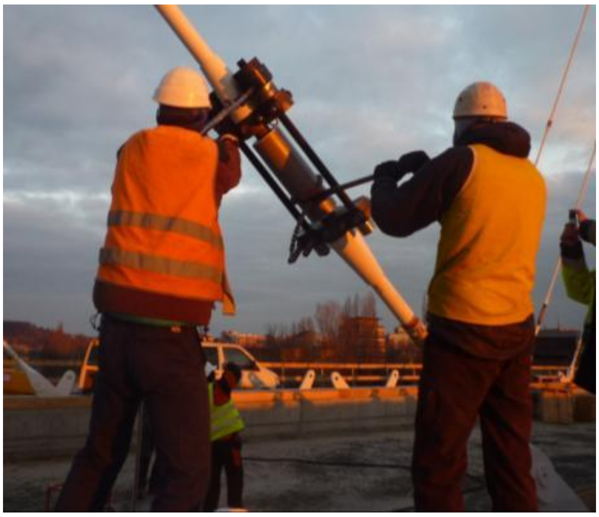

Figure 27, 28 Troja Bridge, installation and tensioning of the hangers

2.8 Brief survey of other realized or designed tensioned structures

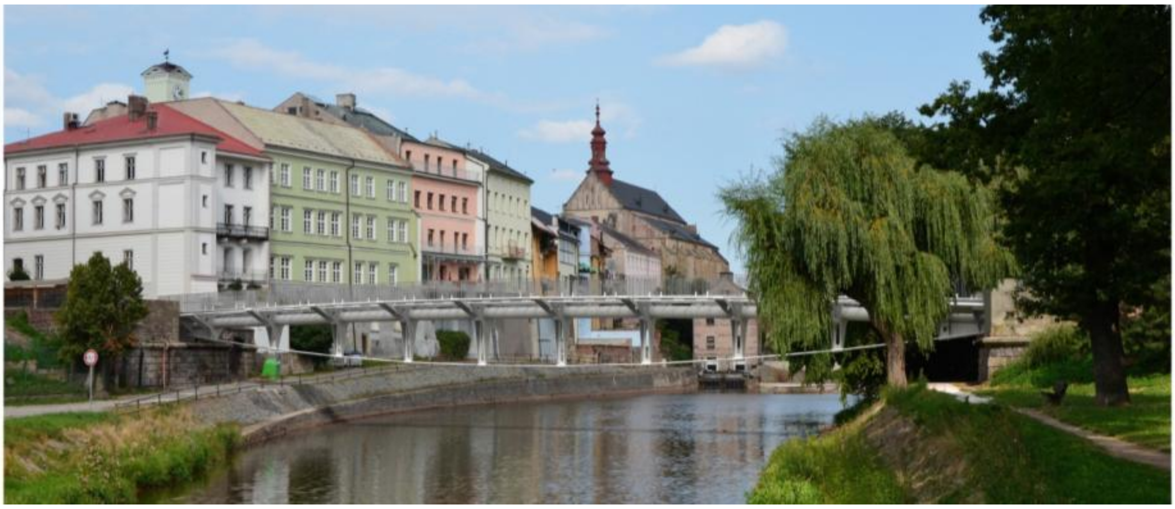

Figure 29, 30 Foot bridge in the town Jaroměř with a span of 61 m. Three prestressed tendons and central tube are the main bearing units of the structure (construction will start in July 2014).

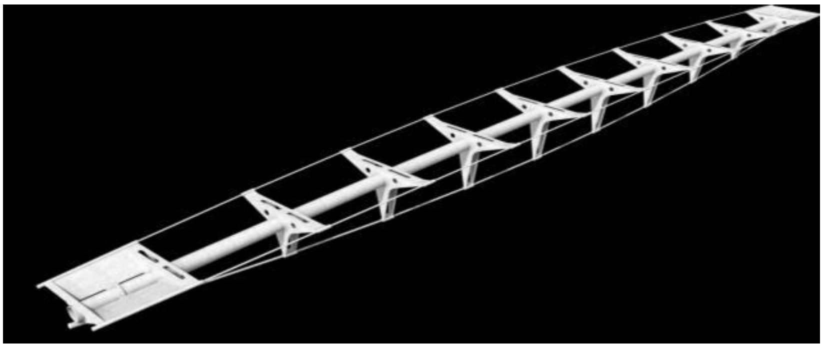

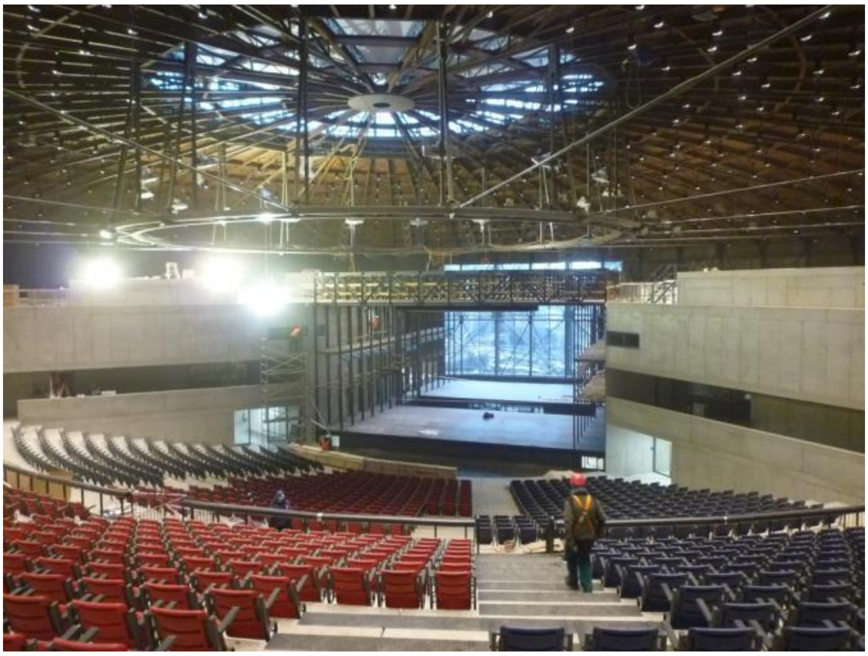

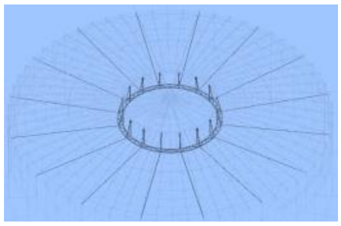

Figure 31, 32 The conversion of the gasholder into a multipurpose hall was finished in the year 2013. Redistribution of internal forces was realized by an additional prestressed beam–string structure.

Figure 33, 34 The roof of the new arena in Třinec finished in the year 2014 is supported by ten lattice prestressed beam-string girders.

3 METHODS OF TENSIONING AND MEASURING FORCES IN TIE-RODS

3.1 Tensioning methods

The tensioning of tendons is performed mostly by using turnbuckles and a hydraulic device (Fig. 28) or manually by chain wrench when forces are low. Alternative methods such as pre-deforming the structure before attaching the tendons can be applied.

3.2 Hydraulic, strain gauges and changing geometry method of measuring of forces

Tensile forces can be monitored directly on a hydraulic device and strain–gauges (Fig. 35, 36) at the same time. The level of the tensioning can be checked by monitoring of changing geometry of the structure (Fig. 16).

Strain gauges are attached to the bar in arrangement as a full bridge and the signal is transmitted to the measuring station, enabling the simultaneous processing of all tendons on site.

Forces in the bars can be monitored on-line on a computer display anywhere at the construction site or on the web.

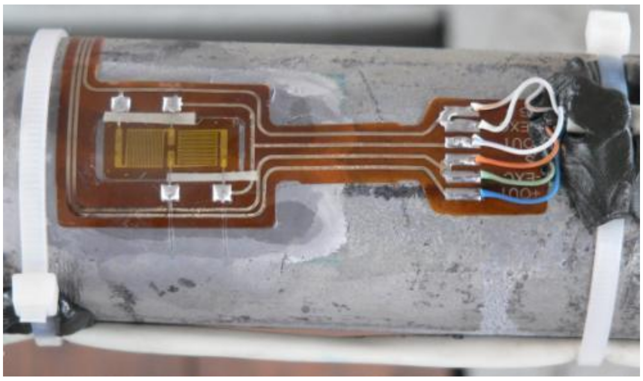

Figure 35 On-site strain gauge measurements   Figure 36 Strain gauges attached on the bar

3.3 Frequency method of measurement on tendons – solid bars

The pretension of the bars can be alternatively measured with accelerometers. The record of vibration initiated by an impact (Fig. 37) is processed into a frequency spectrum using the FFT method (Fig. 38), from which the forces in the bars can be calculated. It is used for measurement of forces on bars that are already loaded. Only one bar can be checked at one moment.

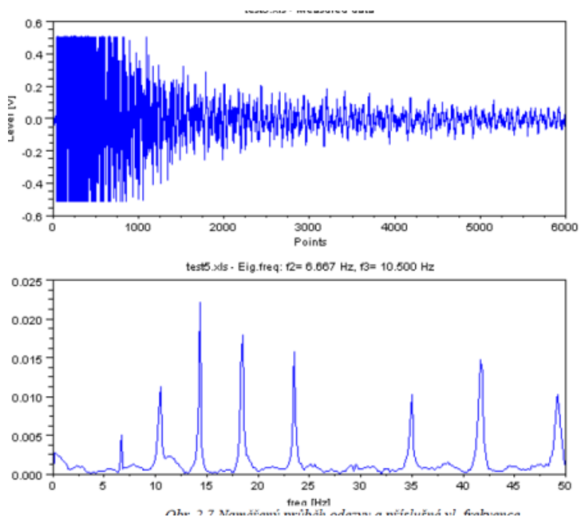

Figure 37 Accelerometer and excitation of vibration   Figure 38 Record and frequency spectrum

The frequency spectrum can be analyzed by formulas 1 or 2. The boundary conditions and the stiffness of the structure where are the bars attached, should be taken into account.

Force in the slender stiff beam pinned at the ends

$$F_n = \frac{4l^2 \rho A}{n^2}\left(f_n^2 - \frac{n^2 EI\pi^2}{4l^2 \rho A}\right) \tag{1}$$

Force for the slender stiff beam fixed at the ends

$$F = \frac{\left(\sqrt{t^2 - 4yz} \pm t\right)^2}{4y} \tag{2}$$

where

$$t = \frac{n}{l^2}\sqrt{\frac{EI\pi^2}{\rho A}}\ ,\ y = \frac{n}{2l}\frac{l}{\sqrt{\rho A}}\ \text{ and }\ z = \frac{n}{2l}\frac{l}{\sqrt{\rho A}}(4+\frac{n^2\pi^2}{2})\frac{EI}{l^2}$$

F - force in the tie-rod
l – length of the tie-rod
E – modulus of elasticity
I – moment of inertia
A – cross-sectional area
ϱ - density
f - eigenfrequency

3.4 Frequency method of measurements on ropes

The determination of the frequency spectrum from the record of vibration caused by impact to the rope is needed first (Fig. 38). The first estimation of the force can be done from the formula (3) valid for vibrating string

$$N = f_k^2 \mu L^2 \frac{4}{k^2}, k = 1,2,3,4 ... \tag{3}$$

where

F – force in the tie-rod
fk – natural frequency
µ - dead weight per unit weight
L – length of the rope
k – number of natural frequency

The forces in the ropes calculated from various frequencies are not identical. This means that the influence of the bending stiffness of the rope cannot be neglected. The bending stiffness of the rope is a non-linear function of the force N, which means that N must be determined by an indirect method. The method described in [3] can be used. This method is based on a formula for vibrating string, taking into account transversal dimensionless stiffness which can be described by the parameter:

$$\xi = L \cdot \sqrt{\frac{N}{EI}} \tag{4}$$

This stiffness determines the relationship between the real and idealized natural frequency:

$$f_k = f_{ks} \cdot \left[1 + \frac{2}{\xi} + \left(4 + \frac{k^2\pi^2}{2}\right) \cdot \frac{1}{\xi^2}\right] \tag{5}$$

If the part of equation is expressed as the parameter α_k,

$$\alpha_k = 1 + \frac{2}{\xi} + \left(4 + \frac{k^2\pi^2}{2}\right) \cdot \frac{1}{\xi^2} \tag{6}$$

The relationship for idealized first frequency f1s and measured frequency fk can be found as:

$$\frac{f_k}{f_{1s}} = k \cdot \alpha_k \tag{7}$$

Idealized first frequency f_{1s} and parameter ξ can be determined by means of the optimization function of minimum deviation of all measured natural frequencies. The Levenberg-Marquat algorithm has been chosen to minimize the deviations.

The resulting tensile force N can be calculated from the equation (3), EI from equation (4). Software for practical use has been developed in the mathematic system Scilab (www.scilab.org), which provide results from [4] according to Fig. 39 and Fig. 40. The good coincidence of measured and calculated natural frequencies determined by the optimization function is evident.

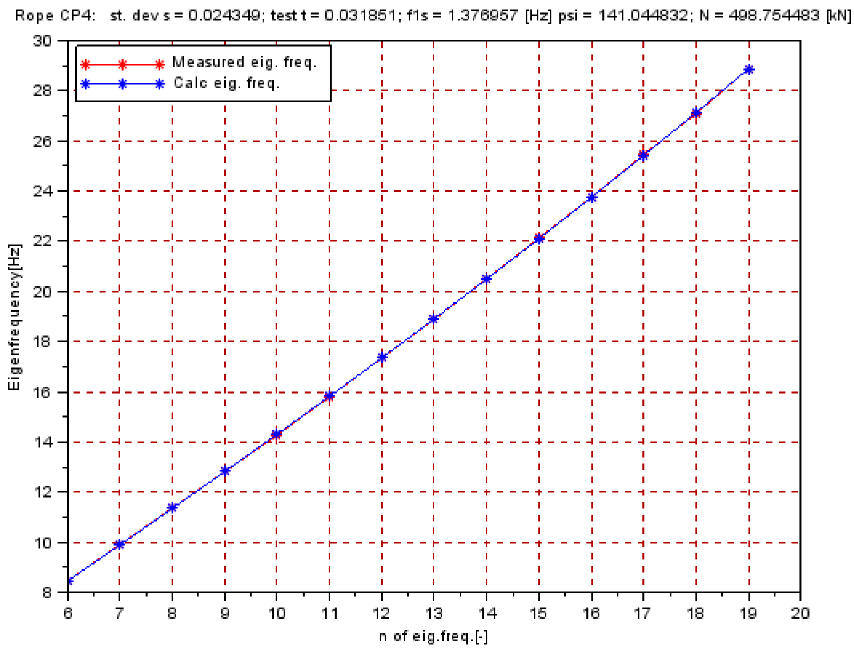

Figure 39 Calculation of natural frequency and normal force

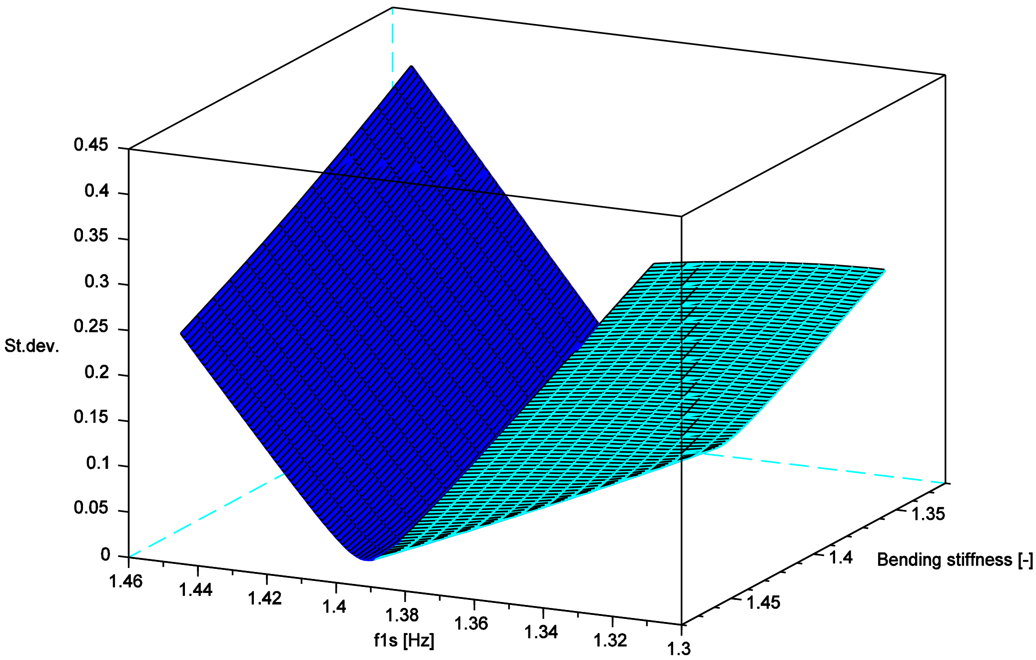

Figure 40 Output from optimization function

3.4 Tensioning procedure and tuning of the forces in tendons already installed

Tensioning procedure should be prepared properly to achieve the designed values of the forces in tendons with the required accuracy and to minimize on-site erection time. The matrix of mutual interaction of tendons must first be calculated. This matrix describes the change of the forces in all tendons installed in the structure when one tendon is tensioned. The matrix (9) presents an example of the matrix of mutual interaction of the hangers from the 2nd phase of the installation of hangers 23-28 on Troja Bridge [5].

	Normalized matrix					
	ZaP23	ZaP24	ZaP25	ZaP26	ZaP27	ZaP28
23	1	-0,1928	-0,1375	-0,1169	-0,125	-0,1795
24	-0,2025	1	-0,2	-0,1818	-0,175	-0,1795
25	-0,1392	-0,1928	1	-0,2597	-0,2125	-0,1667
26	-0,1266	-0,1807	-0,25	1	-0,2375	-0,1795
27	-0,1392	-0,1687	-0,225	-0,2597	1	-0,2308
28	-0,1899	-0,1807	-0,175	-0,1948	-0,225	1

(9)

The tuning of forces in hangers to projected values is a problem similar to the tuning of a guitar. The forces in the individual hangers are in the mutual interaction described by the matrix (9). The problem of finding the optimum process for tie-rod tensioning and accessible accuracy from actually measured forces to designed ones can be solved by the method of linear programming. The computer program (Fig. 41) works with basic formula 10:

$$Fp + A * x = Fk \tag{10}$$

Where

n – number of tie rods
Fp – measured forces (n-vector)
Fk – required (designed) forces (n-vector)
A – n x n matrix of the mutual interferences of the tie-rods
x – increments of the tie-rod forces (n-vector)

Boundary conditions should be taken into account:

- minimum force in tie rods within tensioning
- maximum force in tie rods within tensioning
- maximum force for tightening the individual bar
- maximum deviation in % from designed value

Troja Phase2-3

Hanger NO:	Final force [kN]	Diferece from ideal [%]	Diference from ideal [kN]	Forces [kN]	Aded forces [kN]	Forces to be aded [kN]	Max can be aded [kN]	1	2	3	4	5
25	247	0%	-0,1	247,1	61	0,1	0,1			61		
26	226	0%	0,5	225,5	115	0,5	0,5		115			
27	230	0%	-0,3	230,3	175	0,0	0,0	167				8
	Min	0%	-0,3	225,5	61,0	0,0	0,0	167	115	61	0	8
	Max	0%	0,5	247,1	175,0	0,5	0,5	167	115	61	0	8

Down limit of the force [kN]	20,0
Upper limit of the foce [kN]	500,0
Max. force in hydraulics [kN	300,0

Figure 41 Example of tuning the forces of three hangers of Troja Bridge

3.4 Tensioning procedure and tuning of the forces in tendons during installation

The tensioning procedure can also be determined during the installation of the tendons. The matrix of mutual interaction must be calculated for each partial model structure (model with tendons which have been in actual phase already installed). This procedure makes it possible to predict all changes of already installed tendons during the installation and tensioning of the next tendons. Although time consuming, this in advance prepared theoretical procedure significantly reduces the time of on-site erection needed for tuning the tendons. The example of a calculated tensioning procedure for six tendons (phase II of Troja Bridge) is presented in Fig. 42. The forces on diagonal are applied during installation. Hanger no. 26 is installed first. The numbers under diagonal present the decrease of the forces due to the installation of the following hangers. The final forces after installation of all hangers are in the right column. The detailed design of the installation and tensioning procedure make it possible to achieve the resulting forces corresponding to the designed forces (Fig. 43).

	Initial forces are on diagonal						**Final forces**
	ZaP23	ZaP28	ZaP24	ZaP27	ZaP25	ZaP26	
23	**287**	0	0	0	0	0	**287**
28	-54,494	**262,494**	0	0	0	0	**208**
24	-58,127	-55,262	**257,388**	0	0	0	**144**
27	-39,962	-69,077	-71,12	**271,16**	0	0	**91**
25	-39,962	-51,808	-74,507	-113,32	**342,598**	0	**63**
26	-36,329	-55,262	-67,734	-121,41	-258,45	**587,19**	**48**

Figure 42 Tensioning procedure of hangers 26-23 of Troja Bridge

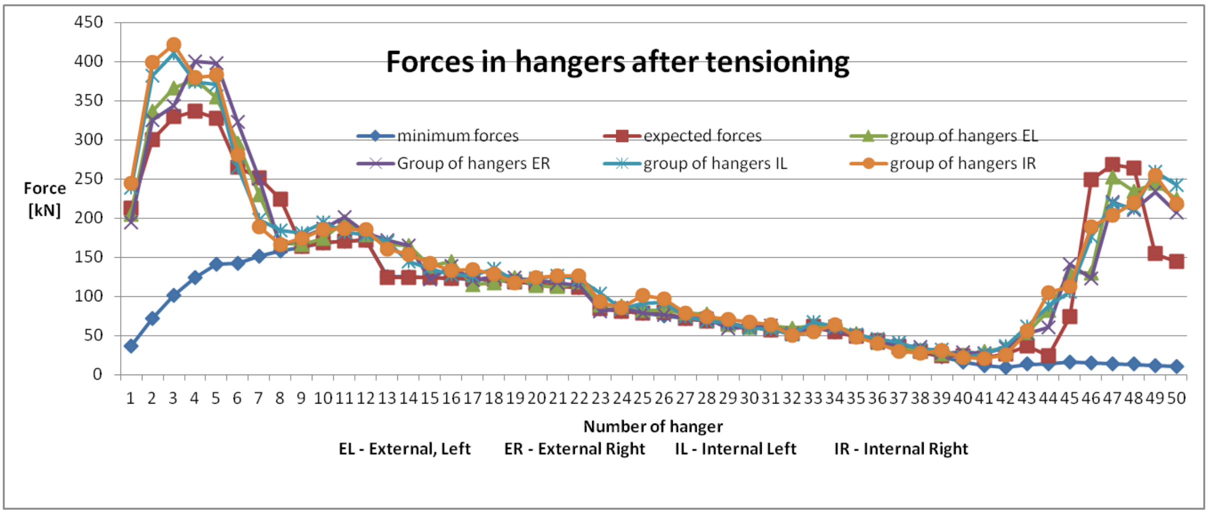

Figure 43 Expected - designed (red) and achieved forces in the hangers of Troja Bridge after installation and tensioning the forces

4 CONCLUSIONS

A considerable number of tensioned structures were built in Czech Republic over the last ten years. The application of prestressed tendons in the global static schema of steel structures has an essential influence on their architectural expression. Slender tensioned steel structures are mostly cost effective (considering the ratio of weight and cost to load bearing capacity). Advanced methods of tensioning, measuring the forces and the design of tensioning procedures have been developed.

REFERENCES

[1] V. Janata, *Sazka Arena, Prague, Czech Republic*, Structural Engineering International Vol 15, Number 1, 40-43.

[2] V. Janata, M. Lukeš, D. Gregor., D. Jermoljev, *Application of tendons in the structure of large span hangar in Mošnov, Czech Republic*, IASS Venetia, 2007.

[3] R.Geier, G.DeRoeck, R.Flesch, *Accurate cable force determination using ambient vibration measurements,* Structure and Infrastructure Engineering, Vol.2, No.1 March 2006, 43-52

[4] M. Necas, *Report of measuring of forces in guy ropes in pipe-line bridge in Kralupy nad Vltavou*, Excon, a.s. Praha, Czech (2013).

[5] V. Janata, *Report of installation and tensioning of the hangers of Troja bridge*, Excon, a.s. Praha, Czech (2013).

KEYNOTE PAPERS

12th International Conference on
Steel, Space and Composite Structures
28-30 May 2014, Prague, Czech Republic

COMPOSITE BEAMS WITH FRICTION-GRIP BOLTED SHEAR CONNECTION

M.A. Bradford

The University of New South Wales, Australia
UNSW Sydney, NSW 2052, Australia
e-mail: m.bradford@unsw.edu.au, webpage: http://www.cies.unsw.edu.au

Keywords: Deconstructability, composite beams, friction-grip bolting, partial interaction.

Abstract. *Many new medium-sized office building structures are temporary, insofar as they are demolished within ten years or even less of their construction. Composite steel-concrete structural systems are very popular for medium-sized office buildings, but deconstruction and re-use in deference to demolition is difficult because the headed stud shear connectors in the composite slab and steel beam flooring system cannot be detached easily, and reuse is virtually impossible. As an alternative, it is proposed that precast geopolymer concrete panels can be attached to steel beams using pre-tensioned high-strength bolts, instead of cast in-situ floors with pre-welded headed stud connectors. The proposed floor system can be deconstructed by unbolting the precast panels, enabling recyclability of the system and providing significant advantages in a paradigm within the construction industry focussed on low emissions. A computational modelling of this structural system using ABAQUS software is presented in the paper, so that the influence of the various parameters can be undertaken without the need for expensive full-scale testing. Following calibration with push-out tests, some parametric studies are presented and an empirical equation for the strength of the shear connection is proposed.*

1. INTRODUCTION

Many new medium-sized office building structures in urban environments will have a somewhat short lifespan, because of changes of land use and increases in land value. With composite steel-concrete structural systems being very popular in constructing medium-sized office buildings, deconstruction and re-use in deference to demolition is very difficult because headed stud shear connectors in the composite slab and steel beam flooring system cannot be detached easily, and reuse is virtually impossible (Fig. 1). As an alternative, it is proposed that (1) precast concrete panels can be attached to steel beams using (2) friction-grip or pre-tensioned bolts, instead of cast-*in-situ* floors with pre-welded headed stud connectors. The proposed demountable floor system, with high-strength friction-grip bolt (HSFGB) shear connectors, can be deconstructed by unbolting the precast panels, enabling recyclability of the system and providing significant advantages in a paradigm in the construction industry focused on low emissions [1-4].

Additional advantages in low-emissions (or low-carbon) design can be achieved if the slab is precast from geopolymer concrete [5]. These concretes utilise industrial aluminosilicate waste materials such as fly ash and blast furnace slag as the binder, and they are a viable replacement for traditional concretes, whose manufacture is known to be a significant contributor to greenhouse gas emissions [6,7]. Apart from their low-emission attributes, these concretes also possess excellent compressive strength and durability, with reduced shrinkage deformations compared with traditional concretes [5], but because they are not batched as readily on-site, their use as a precast slab element is also ideal.

The behaviour of HSFGB shear connectors in composite beams with precast geopolymer concrete slabs has been investigated experimentally from push-out tests [8,9]. Although the push-out tests provided a clear insight to the behaviour of these connectors, the tests are costly and time consuming. Therefore, the main objective of this paper is to develop an accurate and efficient three-dimensional finite element (FE) model to investigate the behaviour of HSFGB shear connectors in composite beams with precast geopolymer slabs, by modelling push-out tests initially. Because ABAQUS software is deployed [10], geometric and material non-linearity are taken into account by default in the model. The results obtained from the FE analysis are verified against the experimental results from the push-out tests conducted as part of the research programm3. Extensive parametric studies are then performed to investigate the effects of the variations in the bolt pretension, the clearance between the hole and the bolt, the diameter and tensile strength of the bolt connector and compressive strength of the geopolymer concrete. A practical design recommendation for the shear connection capacites and an algebraic load-slip curve for HSFGB shear connectors are also proposed in the paper.

Figure 1*:* Demolition of framed structure in Epping, NSW, Australia.

(a) preparation (b) experimental set-up

Figure 2*:* Arrangement of push-out tests.

2. DESCRIPTION OF PUSH-OUT TEST SPECIMENS

Fig. 2 shows the arrangement of the push tests used to determine the shear resistances and the load-slip behaviour of HSFGB shear connectors in composite beams with precast geopolymer concrete slabs. The push test specimens consist of an Australian 360 UB 56·7 steel beam and two concrete slabs that are 450 mm long, 500 mm wide and 100 mm thick attached to the flanges of the steel beam. At the bottom of the specimen, the concrete slabs recess 50 mm into to the steel beam to accommodate for the interface slip during testing. Square SL102 reinforcement mesh (having 9·5 mm diameter wire and 200 mm pitch) were cast in the concrete slabs in two layers to limit the splitting of the slabs. Two types of high strength structural bolts, *viz.* M20 8·8 bolts and M16 8·8 bolts, were installed through prefabricated holes in the concrete slabs and the steel beam flanges to assemble the specimen by applying bolt pretension. The bolt pretension was applied by using an electric torque-control wrench and direct tension indicating washers were used to confirm the applied pretension. To eliminate any horizontal resistance being imposed by the slabs, a roller support was inserted at one end of the specimen. The test load was applied vertically on the upper part of the steel beam by a hydraulic jack. The slip between the steel beam and the concrete slabs was measured using Linear Variable Displacement Transducers (LVDTs). Details of the geometry of the push test specimens are shown in Fig. 3.

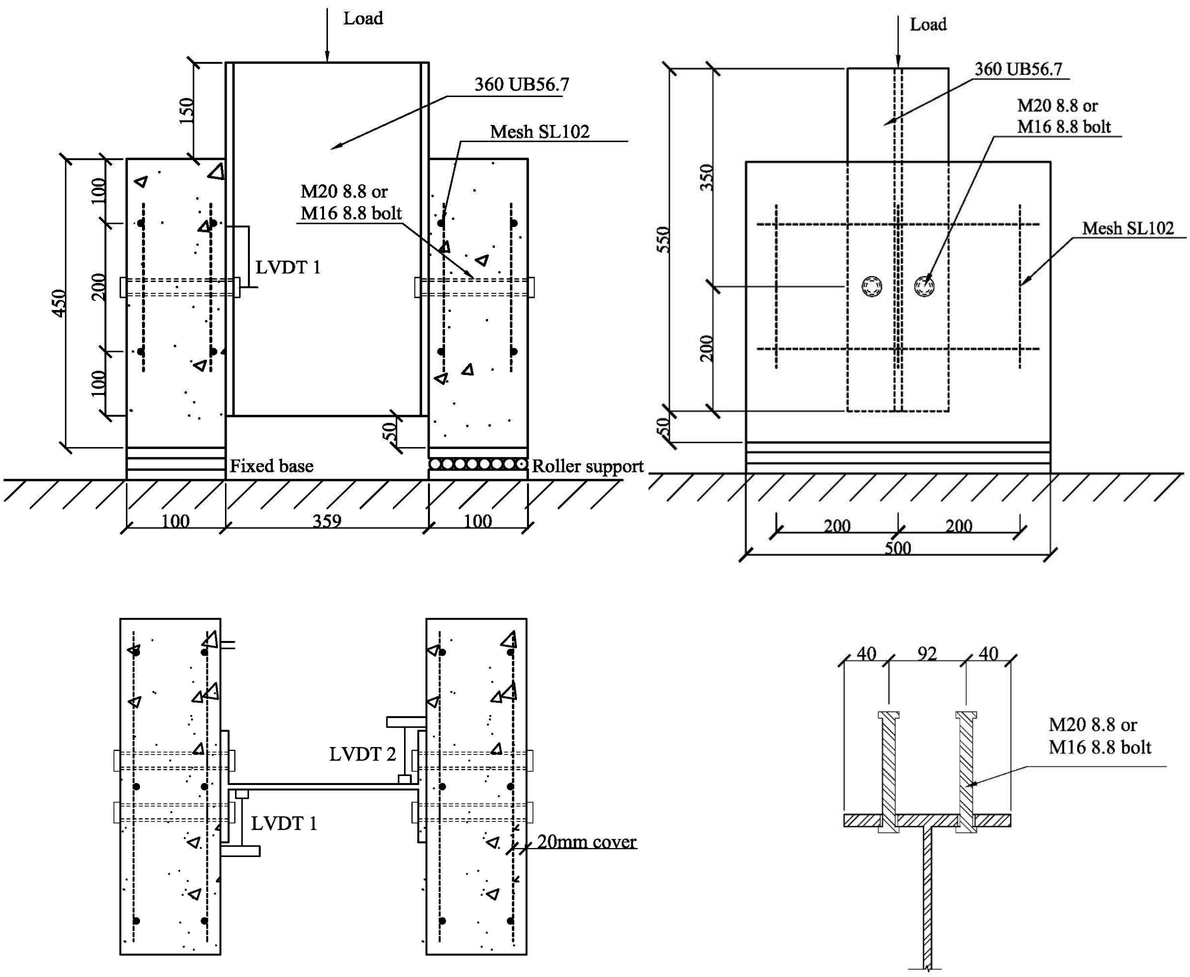

Figure 3*:* Details of push-out tests.

3. FINITE ELEMENT MODEL

ABAQUS software was used in the current study [10]. In order to obtain accurate results from the FE analysis, all components influencing the behaviour of the shear connection were properly modelled. The pertinent components are the concrete slabs, steel beams, HSFGB shear connectors with washers and the steel reinforcement. Both geometric and material non-linearities were taken into consideration in the FE analysis.

Because of the symmetry of the specimens, only one quarter of the push test arrangement was modelled, with combinations of three dimensional solid elements being used for these specimens. For both the concrete slabs and the structural steel beams, a three dimensional eight node element (C3D8R) was used, which also improves the rate of convergence. A three-dimensional twenty node quadratic brick element (C3D20R) was chosen for the bolt shear connectors because of its ability to capture stress concentrations more efficiently as well as for its favourable geometric modelling features. A two node linear three dimensional truss element (T3D2) was adopted for the steel reinforcement. In order to reduce the computation time, a coarse mesh was used for the overall member, with a fine mesh being adopted for the bolt shear connectors and for the region around the shear connectors in order to achieve accurate results. The approximate overall mesh scale was 20 mm, with the smallest mesh scale being about 3 mm. The FE mesh of the push test model is depicted in Fig. 4.

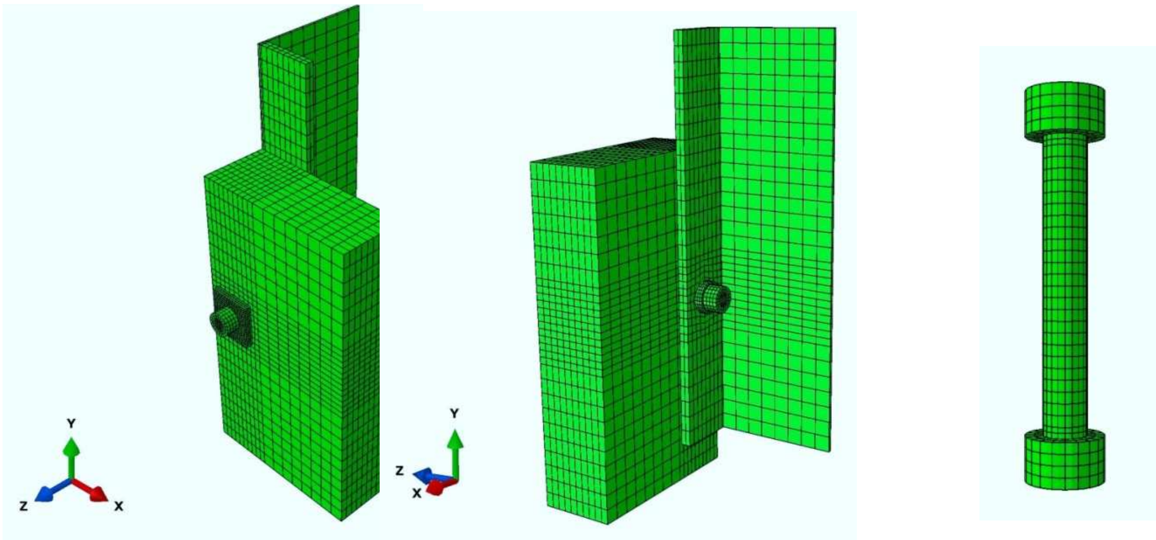

Figure 4: Finite element meshing in ABAQUS.

Once all components of the FE model were properly positioned and configured into the assembly, appropriate interaction and constraint conditions were defined among the various components. The surface-to-surface contact interaction available in ABAQUS was applied at all of the interfaces in the model, by specifying a hard contact property in the direction normal to the interface plane and the PENALTY option being used for the tangential behaviour. The penalty frictional formulation with a friction coefficient equal to 0·45 [8,9] was used for the contact interaction between the steel and concrete components, while the friction coefficient was taken as 0·25 for all of the other interactions. The embedded constraint was applied between the reinforcement and the concrete slab, so that the bars were embedded inside the slab by constraining the translational degrees of freedom of the nodes on the bar elements to the interpolated values of the corresponding degrees of the freedom of the concrete elements. The effects of the relative slip and debonding of the reinforcement with respect to the concrete slabs were ignored.

For the application of the boundary conditions shown in Fig. 5, all nodes of the concrete slab in the opposite direction of loading (surface 1) were restricted from moving in the *Y* direction to resist the compression load. All nodes along the middle of the steel beam web (surface 2) were restrained from translating in the *Z* direction and rotating in the *X* and *Y* directions due to symmetry. All nodes of the steel beam flange and concrete slab that lie on the other symmetry surface (surface 3) were prevented from translating in the *X* direction and rotating in the *Y* and *Z* directions.

The uniformly distributed test load was applied as an imposed downward displacement of the top (cross-sectional) surface of steel beam as shown in Fig. 5. The analysis consisted of several steps. In the first step, the contact interactions were established to ensure that numerical problems due to the contact formulation will not be encountered during the following steps. The pre-tensioning forces were applied during the second step of the analysis by using the BOLT LOAD function available in ABAQUS. It should be noted that in usual practice the diameter of a pre-drilled hole is between 2 mm and 3 mm larger than the diameter d_b of a bolt. In this case, the magnitude of the bolt load should be same as that of the applied bolt pretension. However, for an oversize hole that is 3 mm larger than but not exceeding $1{\cdot}25d_b$ or $(d_b + 8)$ mm in diameter (whichever is the greater), the magnitude of the bolt load should be reduced by a factor that allows for the shape and size of the hole in relation to the bolt [11] which was taken as 0·5 herein. In the subsequent step, the initial adjustment of the pre-tension section was maintained by using the FIX AT CURRENT LENGTH method in ABAQUS. This technique enables the load across the pretension section to change according to the externally applied loads to maintain equilibrium. If the initial adjustment of a section is not maintained, the force in the bolt will remain constant. Lastly, displacement-controlled non-linear analysis was performed by using the RIKS method, which is generally used to predict the unstable and non-linear collapse of a structure. It is based on the arc-length control procedure that is invoked to trace the non-linear load-deformation path. The initial increment can be adjusted if the FE model fails to converge. Subsequently, the value of load after each increment was computed automatically. The final result was either the maximum value of the load or the maximum value of the displacement. To identify the bolt fracture failure in the push-out test, the strains in the bolts were monitored during the analysis. Most of the strains in the weakest cross-section of the shank approached the expected fracture limit value, indicating bolt shear connector fracture.

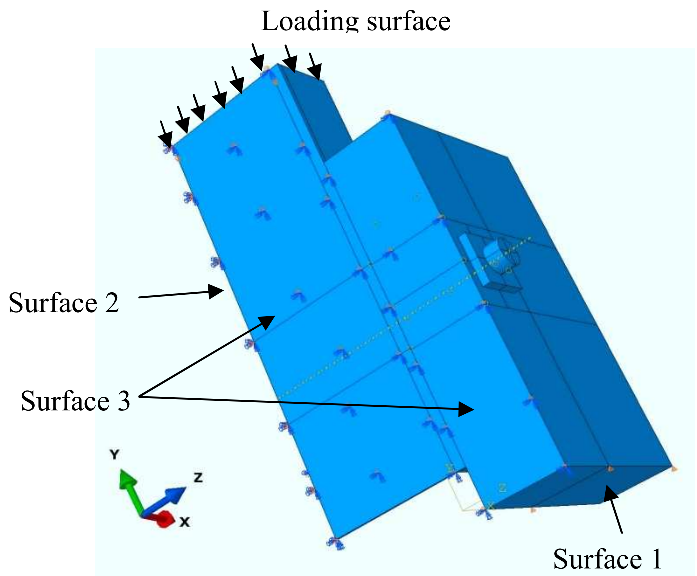

Figure 5: Boundary conditions and loading surfaces.

For structural computations with geopolymer concrete, little research is available in the open literature and so some assumptions are needed [2,3], these being essentially derived from the computational modelling of normal concretes. The non-linear behaviour of the geopolymer concrete material in the push-out tests was represented by an equivalent uniaxial stress-strain curve as shown in Fig. 6(a). Three parts of the idealised curve can be identified. The first part is assumed to be in the elastic range initially, up to the limit of proportionality stress. As has been suggested [12], the value of this stress is taken as $0{\cdot}4f_{ck}$, where f_{ck} is the compressive cylinder strength of the concrete, which is equal to $0{\cdot}8f_{cu}$, where f_{cu} is the compressive cube strength of the concrete. The Australian Standard AS3600 [13] recommends that the elastic modulus of concrete with ordinary Portland cement be taken as

$$E_c = \rho^{1{\cdot}5}\left(0{\cdot}024\sqrt{f_{cm}} + 0{\cdot}12\right) \text{ (MPa)}, \quad (1)$$

where ρ is the density of the concrete in kg/m^3 and f_{cm} the mean compressive cylinder strength in MPa. For geopolymer concrete, Rangan [5] found that the elastic modulus is approximately 25% lower than that of ordinary Portland cement, so a value of $0{\cdot}75E_c$ was used here. Poisson's ratio was taken as 0·2. The second part of the curve is the non-linear parabolic portion starting from the proportional limit stress $0{\cdot}4f_{ck}$ to the peak stress f_{ck}. This part of the curve can be determined from the empirical equation

$$\sigma_c = f_{ck}\left(\frac{\varepsilon_c}{\varepsilon_{ck}}\right)\left[\frac{n}{n-1+\left(\varepsilon_c/\varepsilon_{ck}\right)^{nk}}\right], \tag{2}$$

where ε_{ck} is the strain at the peak stress, $n = 0{\cdot}8 + f_{ck}/17$, and $k = 0{\cdot}67 + f_{ck}/62$ when $\varepsilon/\varepsilon_{ck} > 1$ or $k = 1$ when $\varepsilon/\varepsilon_{ck} \leq 1$. This equation was first proposed [14] to predict the stress-strain relationship for ordinary Portland cement-concrete in compression, and its use was recommended by Hardjito and Rangan [15] for geopolymer concrete as well. The strain at the peak stress is assumed to be 0·002 for ordinary Portland cement based concrete and 0·0033 for geopolymer concrete based on empirical data. The third part of the curve is the constant without a decrease of stress after the peak compressive strength is reached. This perfect plastic behavior is assumed for the modelling, since the benign behaviour of the concrete in compression has been observed in composite beam tests [12]. This behaviour is probably because the concrete is confined in a triaxial stress state in the regions around the shear connectors, which would be expected to be more profound with HSFGB shear connectors because of the tension in the bolts. The PLASTIC model available in ABAQUS was used to specify the plastic part of the concrete material model that uses a von Mises yield surface. It was assumed that the tensile splitting of the concrete slab was prevented. Of course, this simplifying assumption precludes the consideration of tensile stresses in the concrete greater than its tensile strength around $0{\cdot}4\sqrt{f_{ck}}$.

The effect of the steel beam is insignificant on the overall performance of a push-out test, whose main function is to allow for the transmission of the applied loads to the connectors. The stress-strain response of the steel beam was represented by the bi-linear relationship shown in Fig. 6(b). The stress-strain curves for the reinforcement and HSFGB shear connectors, as measured by Loh *et al.* [16] were also simulated as having a bi-linear stress-strain model. They behave as linear elastic materials with a modulus of elasticity E_s up to the yield stress f_{ys}, followed by fully plastic behaviour, but with the HSFGB response being limited by a fracture strain of 0·15 [17]. The modulus of elasticity for the steel beam, reinforcement and HSGFB shear connectors was taken as 200 GPa, with respective yield stresses of 390 MPa, 500 MPa, and 1020 MPa.

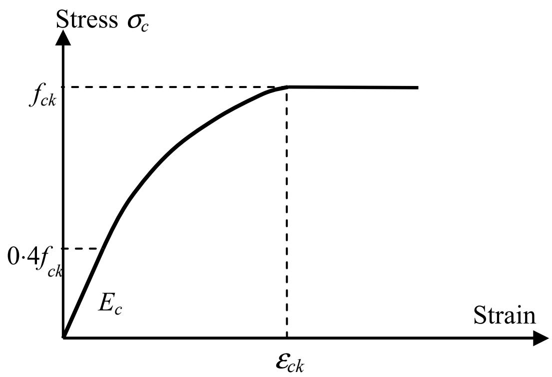

(a) geopolymer concrete

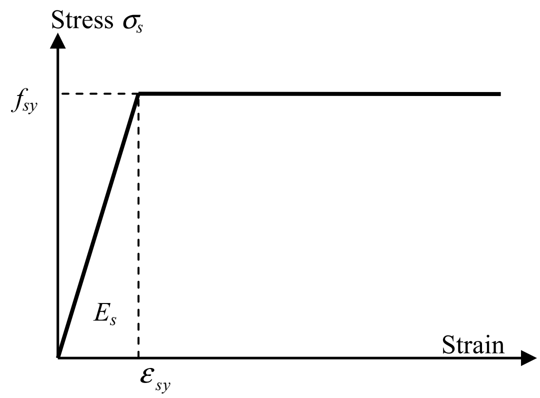

(b) bolt, reinforcement and steel beam

Figure 6*:* Material stress-strain relationships.

4. RESULTS AND DISCUSSION

As part of the present study, experimental push-out tests were undertaken to evaluate the accuracy of the FE modelling. Five specimens with different pretension forces, diameters of the holes in the slabs and diameters of the bolts were tested; the diameter of the hole in the steel flange was 24 mm for each. The testing procedure was carried out according to Eurocode 4, with each specimen being loaded initially to 40% of the expected failure load, and then cycled 25 times between 5% and 40% of the expected failure load. Following this, each specimen was loaded monotonically under displacement control until failure. The average compressive cylinder strength of the geopolymer concrete on the day of testing was measured as 47 MPa and its modulus of elasticity was measured as 23 GPa. (The density ρ was not measured, but by comparison Eq. (1) with ρ = 2400 kg/m^3

produces $0{\cdot}75E_c$ = 26 GPa). Table 1 gives detailed information for the five push-out test specimens, and a comparison of the ultimate shear connection resistance per bolt obtained from the tests Q_{Test} and from the FE analysis Q_{FE}. The ultimate resistance of the shear connector was determined based on the obtained maximum load from the push-out test. It can be seen that there is good agreement between the experimental and numerical results for all of the push-out tests, with a maximum difference of 7% was observed between both of the results for specimen SP3. The mean value of Q_{Test}/Q_{FE} is 1·02 with the coefficient of variation (COV) being 4·7%. The experimental load-slip curves measured for the specimens are compared with the numerical curves obtained from the FE element analysis in Figs. 7(a) to 7(d). It can be seen that the load–slip response obtained from the FE analysis has close agreement with the experimental response for each.

Table 1: Comparison of shear connection strengths.

Specimen	Pretension force (kN)	Slab hole diameter (mm)	Bolt diameter (mm)	No. of bolts	No. of slabs	Q_{Test} per bolt (kN)	Q_{FE} per bolt (kN)	Q_{Test}/Q_{FE}
SP1	145	24	20	4	2	216	214	1·01
SP2	145	24	20	4	2	223	214	1·04
SP3	95	24	16	4	2	153	143	1·07
SP4	70	28	20	4	2	202	214	0·94
SP5	145	28	20	8	4	216	214	1·01
Mean								1·02
COV								0·047

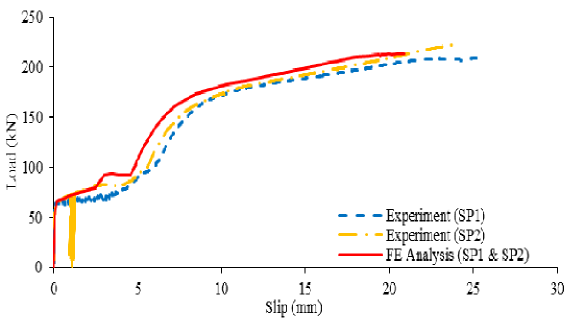

(a) SP1 and SP2

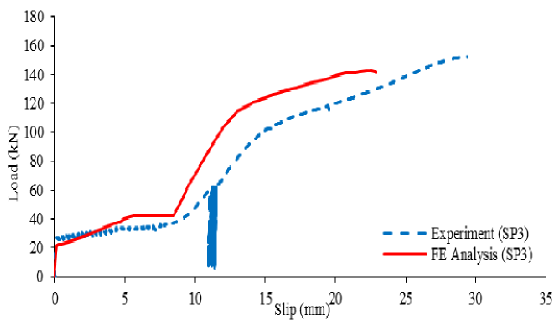

(b) SP3

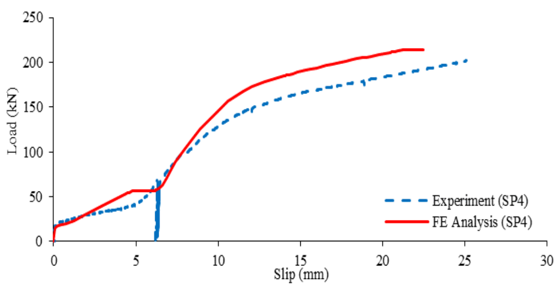

(c) SP4

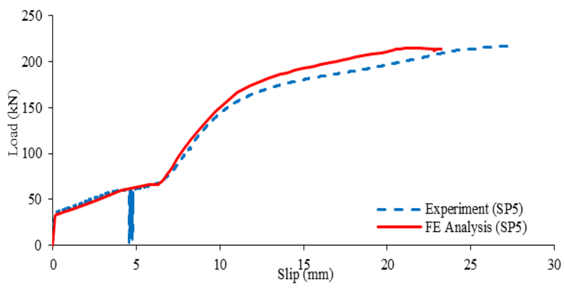

(d) SP5

Figure 7*:* Comparison of FE results and tests.

For specimen SP1, 20 mm diameter bolts pretensioned with a 145 kN standard bolt load were used. The diameter of the hole in the slab is 24 mm for each. The load-slip response exhibited three distinct regimes [18]. At the early stage of loading, the shear connection had a very high stiffness because the pretensioning of the HSFGB shear connectors induces mechanical friction between the slab and steel flange as being the mechanism of shear transfer. As can be seen, the slip at 50 kN of load is less than 0·1 mm. After the friction at the steel-concrete interface induced by the pretension in the shear connectors was overcome, significant slip occurred at the steel-concrete interface because effective installation of the shear connectors always requires significant clearance between the prefabricated holes and the bolts. The critical slip in test SP1 was approximately 4 mm, being close to the sum of the clearance between the hole in the steel beam flange and the bolt and the clearance between the hole in the concrete slab and the bolt. After the bolt commenced to bear against the surface of the hole in the slab, the HSFGB shear connectors showed similar load-slip characteristics to traditional headed stud shear connectors, except for a slightly lower initial stiffness. Specimen SP1 was not loaded to connector failure due to the significant cracking in both concrete slabs. Fig. 8 shows the stress contours and the deformed shape obtained from the FE model close to failure, from which it can be observed that the maximum stresses in the concrete are in the regions around the shear connectors in the form of a cone. However, unlike push-out tests with large headed stud shear connectors which have conical concrete failure modes [19] the concrete in the regions of the shear connectors with pretensioned bolts has an additional confinement and no conical concrete failures were observed in any of the push-out tests.

Specimen SP2 had the same dimensions and material properties as SP1. Firstly, it was loaded to 50 kN per bolt, which is in the expected range of serviceability loads at which slip is to be prevented to achieve close to full shear interaction. The specimen was then unloaded and the HSFGB shear connectors were unbolted as shown in Fig. 9, to illustrate the feasibility of the procedure for the deconstruction of the shear connection. The specimen was then reassembled and loaded until failure occurred, with the load-slip response being similar to that of SP1.

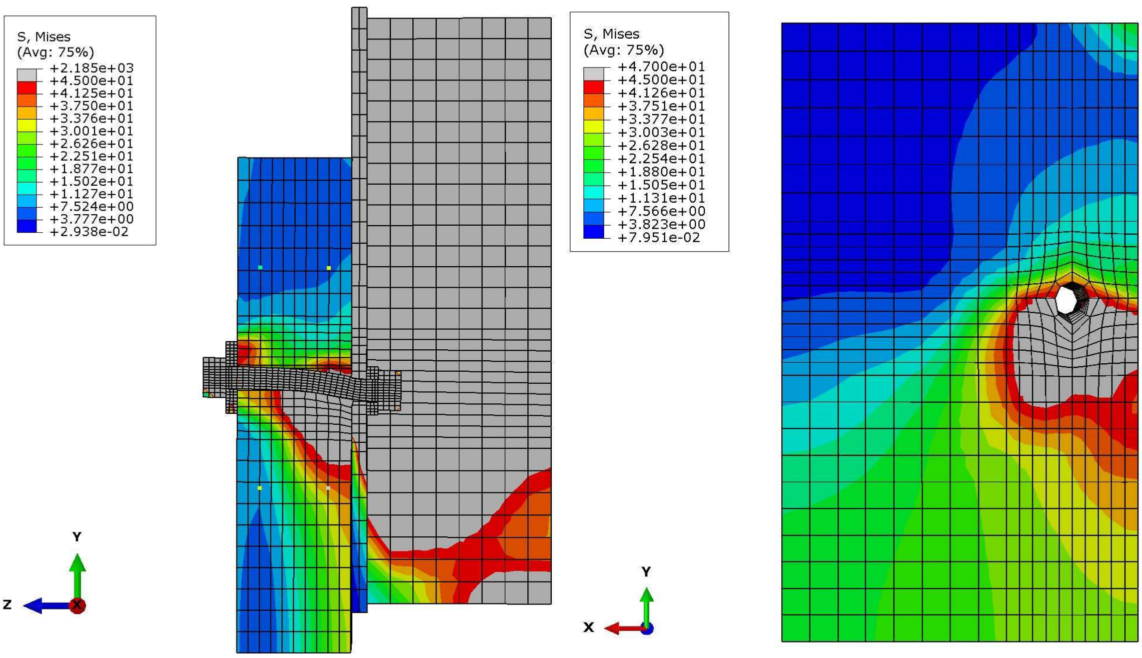

(a) section view (b) slab view

Figure 8: Stress contours and deformed shape for specimen SP1.

Figure 9: Deconstructability of HSFGB shear connection.

Specimen SP3 had smaller sized bolts (16 mm) pretensioned with a 95 kN standard bolt load, as well as oversized holes in the slabs. The first significant slip occurred at a load of 22·8 kN, compared with at 21·8 kN from the numerical analysis. The critical slip was about 6 mm. The specimen then failed by shear fracture of the bolt connector as shown in Fig. 10, with only a few small cracks being observed on the concrete surface after the test. On the other hand, 20 mm diameter bolts tightened with a smaller pretension of about 70 kN in oversized holes were used in specimen SP4. The first significant slip occurred at a load of 17·8 kN, compared with 16·7 kN from the numerical analysis, and the critical slip was also about 6 mm.

Figure 10: Shear fracture of bolt in specimen SP3.

Test specimen SP5 as shown in Fig 2(b) was specially designed with the number of bolts and concrete slabs being increased twofold, by stacking up two single slabs on each side of the push test specimen as would occur with the juxtaposition of precast geopolymer concrete slabs in a real beam. It can be seen from Fig. 7(d) that the load-slip curves obtained experimentally and numerically agree very well, the maximum experimental load being 216 kN per bolt at a slip of 26·8 mm compared with 214 kN at a slip of 23·6 mm obtained from the FE analysis. Based on its modelling of the push-out tests, the FE model developed in this study can successfully predict the ultimate shear resistances and load-slip response of shear connection that uses precast geopolymer concrete slabs and HSFGB shear connectors, and because of this it is able to provide a numerical modelling of the behaviour of push-out tests and real composite beams.

5. PARAMETRIC STUDIES

Parametric studies were carried out using the FE modeling of the push-out tests developed in this paper. The effects of variations in the bolt pretension, its clearance between the hole in the slab, its diameter and tensile strength and the compressive strength of the precast geopolymer slab on the shear connection resistances and load-slip behaviour were investigated. The dimensions and material properties of the push-out specimens for the parametric studies are given in Table 2 and the corresponding ultimate shear connection resistances obtained from the FE analysis are summarised in Table 3.

Fig. 11 shows the load-slip relationships for the push-out test specimens in group G1. *Different bolt pretensions*, *viz.* 75 kN, 100 kN, 120 kN and 145 kN, were considered in this group. It is shown in Fig. 11 that by increasing the bolt pretension, the force needed to overcome the friction at the interface between the steel and the concrete leading to the first significant slip is increased. However, the change in the bolt pretension has no significant effect on the ultimate shear connection resistance. Fig. 12 shows the load-slip relationships for the push-out test specimens with different diameters of the prefabricated holes in group G2. The same 20 mm diameter bolts were installed in all of the three specimens but different diameters for the holes, viz. 22 mm, 24 mm and 28 mm, were chosen. It can be seen that, and as expected, the clearance between the prefabricated hole and the bolt directly affects the value of the first critical slip. In addition, specimen G2-3 with a significantly larger clearance hole had not only a larger first critical slip, but it also required a smaller force to cause first slip, compared with specimens with the normal sized holes such as G2-1 and G2-2.

The effects of the *diameter and tensile strength of the bolt connectors* on the load-slip response are illustrated in Figs. 13 and 14 respectively. The group of push-out specimens with bolt diameters of 16 mm, 20 mm, 22 mm and 24 mm is denoted as group G3 in Table 2, while the group of push-out specimens with tensile strengths of 830 MPa, 900 MPa, 1020 MPa and 1100 MPa is denoted as group G4 in Table 2. The figures show that both the load-slip relationship and the ultimate shear connection resistance are affected signficantly by changing either the diameter or the tensile strength of the bolt connectors. The shear connection stiffness, strength and ductility increase with an increase of either the diameter or the tensile strengths of the bolt shear connectors. For example and as shown in Fig. 13, when the diameter of the bolt connectors is increased from 16 mm to 24 mm, the ultimate shear connection resistance increases by 113%, given that the tensile strengths of both bolts are 1020 MPa. In addition, and as shown in Fig. 14, when the tensile strength of the 20 mm diameter bolt connectors increases from 830 MPa to 1100 MPa, the ultimate shear connection resistance increases by 34%.

Table 2: Dimensions and material properties for parametric studies.

Group	Specimen	Pretension (kN)	Hole diameter (mm)	Bolt diameter (mm)	Tensile strength of bolt (MPa)	Compressive strength of concrete (MPa)
G1	G1-1	75	24	20	1020	47
	G1-2	100	24	20	1020	47
	G1-3	120	24	20	1020	47
	G1-4	145	24	20	1020	47
G2	G2-1	145	22	20	1020	47
	G2-2	145	24	20	1020	47
	G2-3	145	28	20	1020	47
G3	G3-1	95	20	16	1020	47
	G3-2	95	24	20	1020	47
	G3-3	95	26	22	1020	47
	G3-4	95	28	24	1020	47
G4	G4-1	145	24	20	830	47
	G4-2	145	24	20	900	47
	G4-3	145	24	20	1020	47
	G4-4	145	24	20	1100	47
G5	G5-1	145	24	20	1020	45
	G5-2	145	24	20	1020	50
	G5-3	145	24	20	1020	60
	G5-4	145	24	20	1020	80

Fig. 15 shows the load-slip curves for the push-out specimens in group G5, having *different compressive strengths of the geopolymer concrete*. It can be seen that the effect of the concrete compressive strength on the ultimate strength of the shear connection is negligible. This observation assumes that there is sufficient transverse reinforcement to ensure the tensile splitting of the concrete slab is prevented, because the tensile behaviour of the slab is not modelled in the FE analysis. However, the change in concrete strength produces distinct influences on the load-slip behaviour, because this is influenced by the elastic modulus of the concrete and so is influenced by the concrete compressive strength by virtue of Eq. (1).

6. DESIGN RECOMMENDATION

Kwon *et al.* [20] proposed that the ultimate strength of post-installed shear connectors Q_u under static loading is given by

$$Q_u = 0\cdot 5 A_{sc} F_u \quad \text{(N)}, \tag{3}$$

where A_{sc} is the cross-sectional area of the bolt in mm^2 and F_u the tensile strength of the high strength bolt shear connector in MPa. To more accurately predict the ultimate strength of a HSFGB shear connector, the results from the present study suggest that Eq. (3) be modified to

$$Q_u = 0\cdot 66 A_{sc} F_u \text{ (N)}. \tag{4}$$

Table 3: Comparison of shear connection strengths from FE analysis and design recommendation (DR).

Group	Specimen	Q_{FE} (kN)	Q_{Kwon} (kN)	Q_{DR} (kN)	Q_{FE}/Q_{Kwon}	Q_{FE}/Q_{DR}
G1	G1-1	212	160	211	1·32	1·00
	G1-2	212	160	211	1·33	1·00
	G1-3	211	160	211	1·32	1·00
	G1-4	214	160	211	1·33	1·01
G2	G2-1	212	160	211	1·32	1·00
	G2-2	214	160	211	1·33	1·01
	G2-3	213	160	211	1·33	1·01
G3	G3-1	141	103	135	1·38	1·04
	G3-2	212	160	211	1·33	1·00
	G3-3	255	194	256	1·31	0·99
	G3-4	301	231	305	1·31	0·99
G4	G4-1	173	130	172	1·33	1·00
	G4-2	186	141	187	1·32	1·00
	G4-3	214	160	211	1·33	1·01
	G4-4	232	173	228	1·34	1·02
G5	G5-1	214	160	211	1·34	1·01
	G5-2	212	160	211	1.32	1.00
	G5-3	212	160	211	1·32	1·00
	G5-4	211	160	211	1·32	1·00
	Mean				1·33	1·01
	COV				0·011	0·011

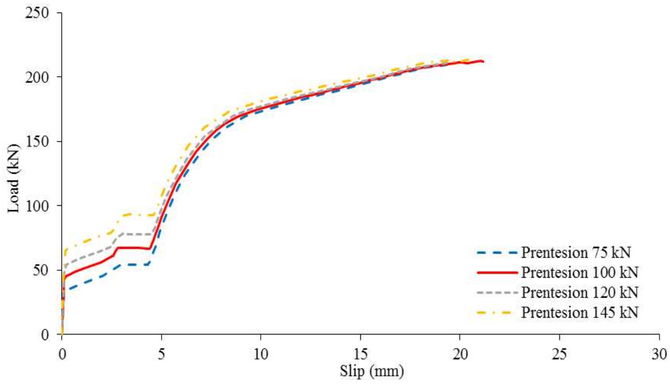

Figure 11: Effects of bolt pretension.

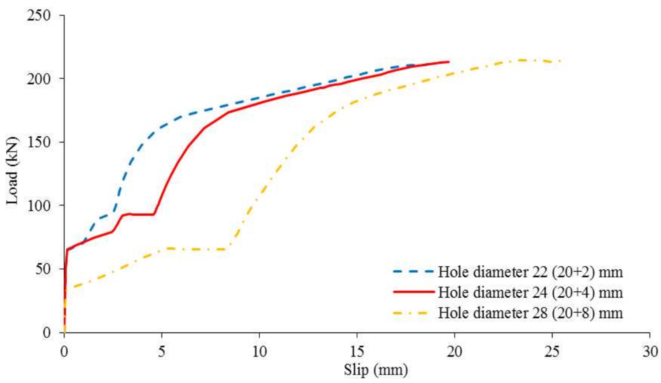

Figure 12: Effects of size of clearance holes.

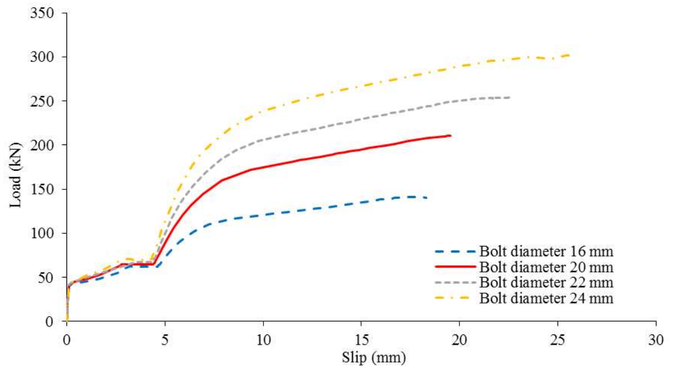

Figure 13: Effects of diameter of bolted shear connector.

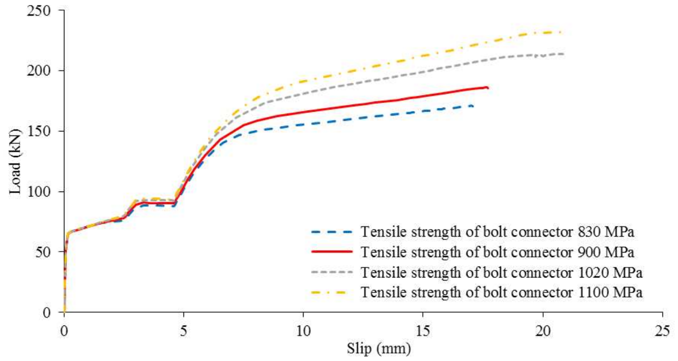

Figure 14: Effects of tensile strength of bolted shear connector.

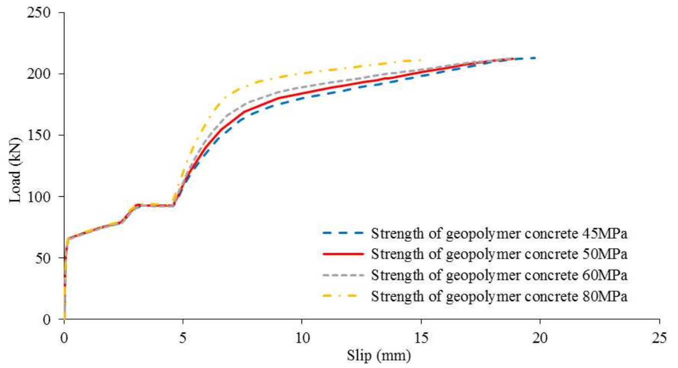

Figure 15: Effects of compressive strength of geopolymer concrete slab.

In order to propose equations to predict the load and slip displacement relationship of HSFGB shear connectors as shown in Fig. 16, the three distinct regimes of the load-slip response are taken into consideration. At the early stage of loading, the slip is almost zero because the connection uses friction as the means for shear transfer at the initial loading. Based on friction-grip bolt design methodologies [21] the first significant slip occurs after the friction at the steel-concrete interface from the pretension of the shear connectors is overcome at shear force Q_0 that is given by

$$Q_0 = \mu_f k_h N_t \, , \tag{5}$$

in which μ_f is the coefficent of friction between the slab and the steel beam and N_t the bolt tension. The factor k_h in Eq. (5) allows for the shape and size of the hole in relation to the bolt. Normally k_h is taken as 1·0. However, when either the diameter of the hole in the concrete slab d_c or in the steel beam flange d_s exceeds the diameter of the bolt d_b by more than 3 mm, k_h is taken as 0·5. The critical slip Δ_1 in Fig. 16 can be obtained from

$$\Delta_1 = \left(d_c + d_s - 2d_b\right)/2, \tag{6}$$

for which the corresponding load in Fig. 16 is given by $Q_1 = (Q_0 + 20)$ kN. After the bolt bears against the steel and concrete, the empirical formula for load-slip relationship of the shear connection is proposed as being

$$Q_{sh}(\Delta_{slip}) = Q_1 + \left(Q_u - Q_1\right)\left\{1 - \exp\left[-0\cdot 005 f_{ck}\left(\Delta_{slip} - \Delta_1\right)\right]\right\}^{0\cdot 8}, \tag{7}$$

where f_{ck} is the compressive strength of the geopolymer slab. This equation differs from that of Bradford and Pi [2] for non-pretensioned bolted shear connectors, and is a refinement of the algebraic formulations which are usually adopted for the load-slip response of conventional headed stud shear connectors reported in the literature. A slip capacity Δ_u of at least 6 mm is considered to be sufficient to ensure ductile behavior of composite beams as suggested in Eurocode 4. The ultimate shear connection resistances obtained from the parametric studies have been compared with the ultimate strength of the shear connection using the proposed design recommendation. Table 3 lists comparisons of the ultimate shear connection resistances obtained from the FE analysis and the design rules proposed by Kwon *et al.* [20] as well as the design rules suggested in the present study. It can be seen that the mean values of the ratios Q_{FE}/Q_{Kwon} and Q_{FE}/Q_{DR} are 1·33 and 1·01 respectively, and both with a COV of 0·011. The design rules proposed in this study are therefore able to predict the the ultimate shear resistances of HSFGB shear connectors more accurately than the proposals of Kwon *et al.* [20]. Fig. 17(a) shows comparisons of the load-slip curves for the specimens SP1 and SP2 obtained from the experiments and the design recommendations; Fig. 17(b) shows comparisons of the results from the FE analysis and the proposed design recommendations for specimens with different bolt diameters; and Fig. 17(c) shows comparisons of the results from the FE analysis and the proposed design recommendation for specimens with different geopolymer compressive strengths. Good agreement can be observed between the curves obtained from the proposed design recommendations and the results from the experiments or the FE analysis.

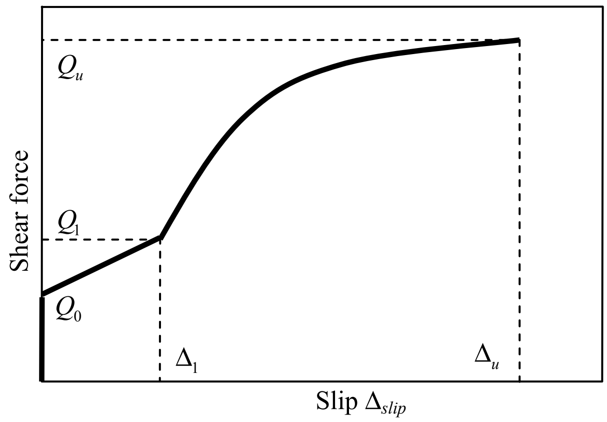

Figure 16*:* Design recommendation for HSFGB shear connection in composite beams.

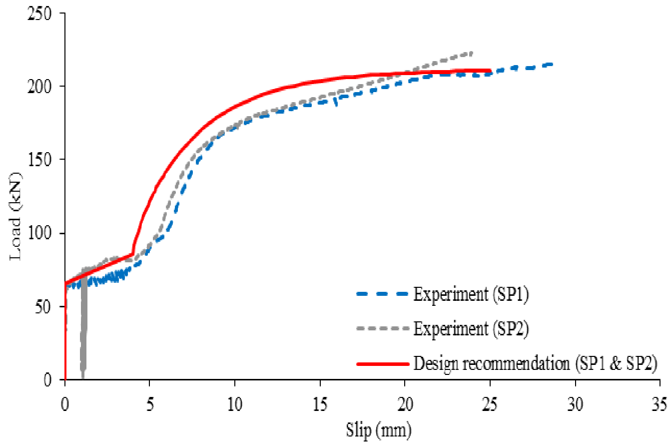

(a) SP1 and SP2

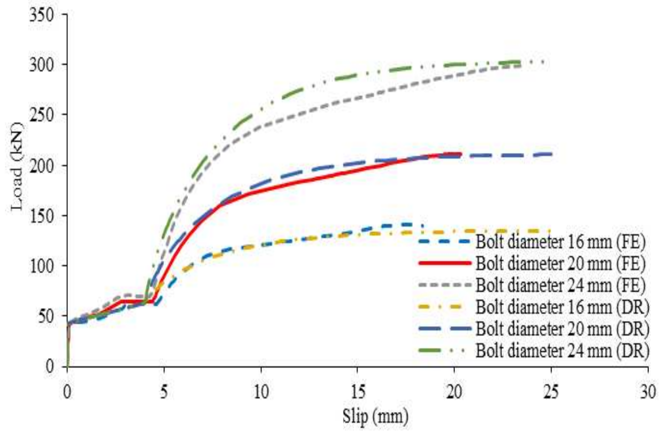

(b) FE and DR for different bolt diameters

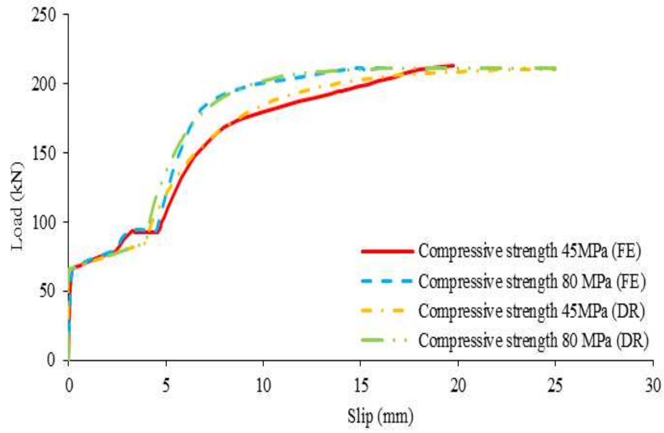

(c) FE and DR for different compressive strengths

Figure 17: Load-slip curves.

7. CONCLUSIONS

A finite element model of push-out tests has been developed to investigate the behavior of HSFGB shear connectors in composite beams with precast geopolymer slabs using ABAQUS software. This type of shear connection is proposed to expedite deconstructability within a paradigm of infrastructure sustainability. The model took into account the non-linear material properties of the concrete, the steel beam and bolt shear connectors. Comparisons of the numerical solution with experimental results showed that the numerical model developed was capable of accurately and efficiently predicting both the ultimate strength and the load-slip curves for the shear connection. Compared with conventional headed stud shear connectors, the load-slip response of the HSFGB shear connectors exhibited three distinct regimes. At the early stage of loading, the slip almost vanished because of the pre-tensioned connection. After the friction at the steel-concrete interface induced by the pretension of the shear connection was overcome, significant slip took place due to the clearance between the prefabricated holes and the bolts. After the bolt commenced to bear against the surface of the hole in the slab, a third regime for the behaviour developed.

Extensive parametric studies of push-out specimens with different bolt pretensions, clearances between the holes and the bolts, diameters and tensile strengths of the bolt connectors and compressive strengths of the geopolymer concrete were performed by using the numerical model. The results showed that the diameter and tensile strength of the bolt connectors had very significant effects on the ultimate shear resistances of the HSFGB shear connectors.

Practical design formulae for estimating the ultimate strengths and the load-slip relationships of shear connection achieved using HSFGB shear connectors in composite beams were also proposed, and the results were compared well with the experimental and numerical results. Because these formulae are in algebraic form, they form a useful design aid for determining deflections and strengths.

ACKNOWLEDGEMENTS

The work in this paper was supported by an Australian Laureate Fellowship ((FL100100063) awarded to the author by the Australian Research Council. Dr Xinpei Liu is acknowledged with thanks for preparing the computational model, as are the technical staff at the UNSW Randwick Heavy Structures Research Laboratory for their assistance in the testing programme.

REFERENCES

[1] Bradford MA. Designing structures for end-of-life deconstructability. *Engineers Australia Eminent Speaker Series,* https://www. engineersaustralia.org.au/eminent-speaker-series/professor-mark-bradford 2013.

[2] Bradford MA, Pi Y-L. Numerical modelling of deconstructable composite beams with bolted shear connectors. Numerical Modeling Strategies for Sustainable Concrete Structures, Aix-en-Provence, France, May 2012, II-2, 1-8.

[3] Bradford MA, Pi Y-L. Numerical modelling of composite steel-concrete beams for life-cycle deconstructability. 1st International Conference on Performance-Based and Life-Cycle Structural Engineering, Hong Kong, December 2012, 102-109.

[4] Bradford MA. Structural modelling of deconstructable beams fabricated using friction-grip shear connection. 4th International Conference on Mobile, Adaptable and Rapidly Assembled Structures, Ostend, Belgium, June 2014.

[5] Rangan BV. Engineering Properties of Geopolymer Concrete. Chapter 13 of Geopolymers: Structures, Processing, Properties and Applications (JL Provis, JSV van Deventer eds.), Woodhead Publishing, London, 2009.

[6] McCaffery R. Climate change and the cement industry. Global Cement and Lime Magazine (Environmental Special Issue), 15-19, 2002.

[7] National Sustainability Council. http://www.environment.gov.au/sustainability/measuring/council.html. Australian Government, Canberra, Australia, 2013.

[8] Lee SSM, Bradford MA. Sustainable composite beam behaviour with deconstructable bolted shear connectors. Composite Construction VII, Palm Cove, Queensland, Australia, July 2013.

[9] Lee SSM, Bradford MA. Sustainable composite beams with deconstructable bolted shear connectors. 5th International Conference on Structural Engineering, Mechanics and Computation, Cape Town, South Africa, September 2013.

[10] Dessault Systemès. ABAQUS 6.10.1. Vèlizy Villacoublay, France.

[11] AS4100. Steel Structures. Standards Australia, Sydney, 1998.

[12] Nguyen HT, Kim SE. Finite element modeling of push-out tests for large stud shear connectors. *Journal of Constructional Steel Research* 65 (2009): 1909-1920.

[13] AS3600. Concrete Structures. Standards Australia, Sydney, 2009.

[14] Collins MP, Mitchell D, MacGregor JG. Structural design considerations for high strength concrete. *ACI Concrete International* 15(1993): 27-34.

[15] Hardjito D, Rangan BV. Development and properties of low calcium fly ash based geopolymer concrete. Research Report CG1, Curtin University of Technology, Perth, Australia, 2005.

[16] Loh HY, Uy B, Bradford MA. The effects of partial shear connection in composite flush end plate joints. Part I – experimental study. *Journal of Constructional Steel Research* 62 (2006): 378-390.

[17] Shi G, Shi Y, Wang Y, Bradford MA. Numerical simulation of steel pretensioned bolted end-plate connections of different types and details. *Engineering Structures* 30 (2008): 2677-2686.

[18] Rowe M, Bradford MA. Partial shear interaction in deconstructable composite steel-concrete beams with bolted shear connectors. International Conference on Design, Fabrication and Economy of Welded Structures, Miskolc, Hungary, 585-590, 2013.

[19] Lam D, Ellobody E. Behavior of headed stud shear connectors in composite beams. Journal of Structural Engineering ASCE 131 (2005): 96-107.

[20] Kwon G, Engelhardt MD, Klinger RE. Behavior of post-installed shear connectors under static and fatigue loading. Journal of Constructional Steel Research 66 (2010): 532-541.

[21] Trahair NS, Bradford MA, Nethercot DA, Gardner L. The Behaviour and Design of Steel Structures to EC3. Taylor and Francis, London, 2008.

PERFORMANCE EVALUATION OF 2-D MOMENT FRAMES WITH HIGH STRENGTH STEEL END-PLATE CONNECTIONS

Murude Celikag*, Hashem Alhendi* and Onur Ejder*

*Department of Civil Engineering, Eastern Mediterranean University
Gazimagusa, North Cyprus
e-mail: murude.celikag@emu.edu.tr, webpage:http://civil.emu.edu.tr

Keywords: High strength steel (HSS), end-plate connection, non-linear dynamic

Abstract. *The structural use of high strength steel (HSS) provides numerous advantages. Hence HSS became more widely used in recent years. However, so far, there has been limited research on the behaviour of HSS beam to column connections and their effect on the performance of structures. This study aims at investigating the performance of 2-D moment frames using HSS end-plate beam to column connections in terms of strength, stiffness and ductility. The results of this study were compared with those of similar frames using mild steel end-plate connections. For this purpose, FEM was used to validate the experimental results available from past research on HSS end-plate connections. Through this approach the moment curvature relationships were captured for the purpose of finding hinge properties. Time-history (non-linear dynamic) analysis was carried out according to FEMA 356 to determine the global inelastic response of 2-D moment frames. It is found that the usage of HSS would allow the use of a thinner end-plate without compromising the frame seismic behaviour. However, the minimum thickness for the HSS end-plate may need to be determined to avoid buckling instability of the frame.*

1. INTRODUCTION

During the last two decades there has been increase in the usage of High Strength Steels (HSS). This was partly due to the increase in the demand for constructing tall structures and also the problems encountered with the steel beam-to-column connections during Northridge and Kobe earthquakes [1,2]. This increased demand for HSS encouraged researchers to embark on research into moment connections employing HSS columns [3-8] beams [9], end plates [10-13] and bolts [13]. This popularity of HSS originates from the numerous advantages it provides when compared to mild steel grades, for example; reduction in the steel consumption and thus overall weight of the structure, which results in savings during the process of fabrication, transportation to site and erection. Construction has negative impact on the environment and the reduction of steel consumption would reduce the construction impact on environment and contribute to the sustainability of natural resources [4]. In addition, HSS sections are lighter, more slender members, which are more desirable for architecture and allow for more space and freedom within the Buildings [13]. HSS exhibit high yield ratios and limited deformation capacity when compared to mild steel grades. The increase in the popularity of HSS can also be linked to its mechanical properties. It offers higher performance in tensile stress, toughness, weldability, cold forming and corrosion resistance when compared to mild steel grades [14]. Furthermore, the usage of HSS may cause a change in the structural seismic performance [15]. Hence, the necessity for understanding HSS behaviour under different loading, in particular, seismic loading, became inevitable.

On the other hand, there are a number of adverse effects of using HSS. HSS have higher elastic strength but this does not mean higher modulus of elasticity. Therefore, in the case of design being governed by stiffness, the servicability limit state criteria may not be achieved [4,13]. Research work carried out in recent year's also revealed significant differences between HSS and mild steel in terms of stress-strain curves, residual stress distributions and different effects of initial imperfections [5,6]. These would lead to significant differences in local and overall buckling behaviour of structures which may cause frame stability problems. Therefore, there is need to do more research with the objective of understanding the behaviour of HSS frame. However, this would only be possible through the understanding of the behaviour of HSS beam to column joints. Beam to column joints must be designed for strength, stiffness, rotation capacity and ductility. The full non-linear moment-rotation responses of joints are required for the global frame analysis. So far there is limited study on HSS frame behaviour. Most of the work done is about HSS connections [10-13] and column members [3-8]. In 2004, and Coelho et al. [10] and Coelho and Bijlaard [13] carried experimental research on end plate moment connections under static loading. They found that thicker end plates dramatically increased the joint's both initial stiffness and moment resistance while reduced the rotation capacity. Similar conclusions are drawn by Qiang et al. [11,12] from the research on end plate connections under fire conditions. Shi et al [6] and Ban et al [5] investigated the buckling strength and deformation of pin ended ultra-high strength steel columns (up to S960 MPa). Similarly Ban et al [7] and Wang et al [8] tested welded box and I-section columns, fabricated from S460, for their buckling deformation and capacity. Therefore, more research is needed on HSS frame behaviour, particularly, when frames are subjected to abnormal loading, such as, earthquake, fire or blast loading.

This study aims at investigating the performance of 2-D moment frames using HSS and mild steel end-plate beam to column connections in terms of strength, stiffness and ductility. For this reason a typical 2-D moment frame from an existing steel framed residential building is used as a case study so that the behaviour of frames can be compared. First of all, FEM was used to validate the experimental results available from past research on HSS end-plate connections. Through this approach the moment curvature relationship was captured for the purpose of finding hinge properties. Then time-history analysis (dynamic analysis) was used with real earthquake data in SAP2000 v15.1 [16] software to obtain the local and global performance. This performance was then compared with the performance levels given by FEMA 356 [17].

2. CASE STUDY

2.1 Description of the existing steel framed residential building

The case study is a residential house with 550 square meter floor area located in the Famagusta Bogaz, North Cyprus. The building has grade S275 steel frame, which is moment resistant in one direction and braced in the other direction. According to Turkish Earthquake Code, the building is located in an earthquake region Zone 2. Design ground acceleration was taken as 0.3 and importance factor 1.0. The behaviour factor was taken as 5.0 for the braced direction and 8.0 for the moment frame direction. The allowable bearing capacity of soil is 18 kN/m^2.

The 2-D moment frame selected from the residential building as a case study has IPE and HEB beams and columns, respectively. It has four floors and four bays with the column elevations and beam spans as shown in Figure 1. Beams are connected to column flanges via 20mm thick grade S275 extended end-plate connections and 8M16 grade 10.9 bolts. For analysis purpose, the numbering for joints and members are also shown in Figure 1.

The definition of plastic hinges for beams is important. The selected frame has same beam sections for each floor level. Therefore, there are 5 different hinges to be formed in the frame. The hinges are labeled as H1, H1R, H2, H4, and H4L, where H is for the hinge; numbers are for the bays starting from axis E and letters L and R for the hinge being on the left or right side of the beam. The hinges for the case frame with 20 mm plate is group 1 and labeled as G1 in the Table 1. The hinges for the 8 mm plate and 8 mm HSS plate are groups 2 and 3 and labeled as G2 and G3 respectively in Table 1. Hence beam section, column section and end plate geometrical dimensions are the same for each group other than the end plate thickness and steel grade.

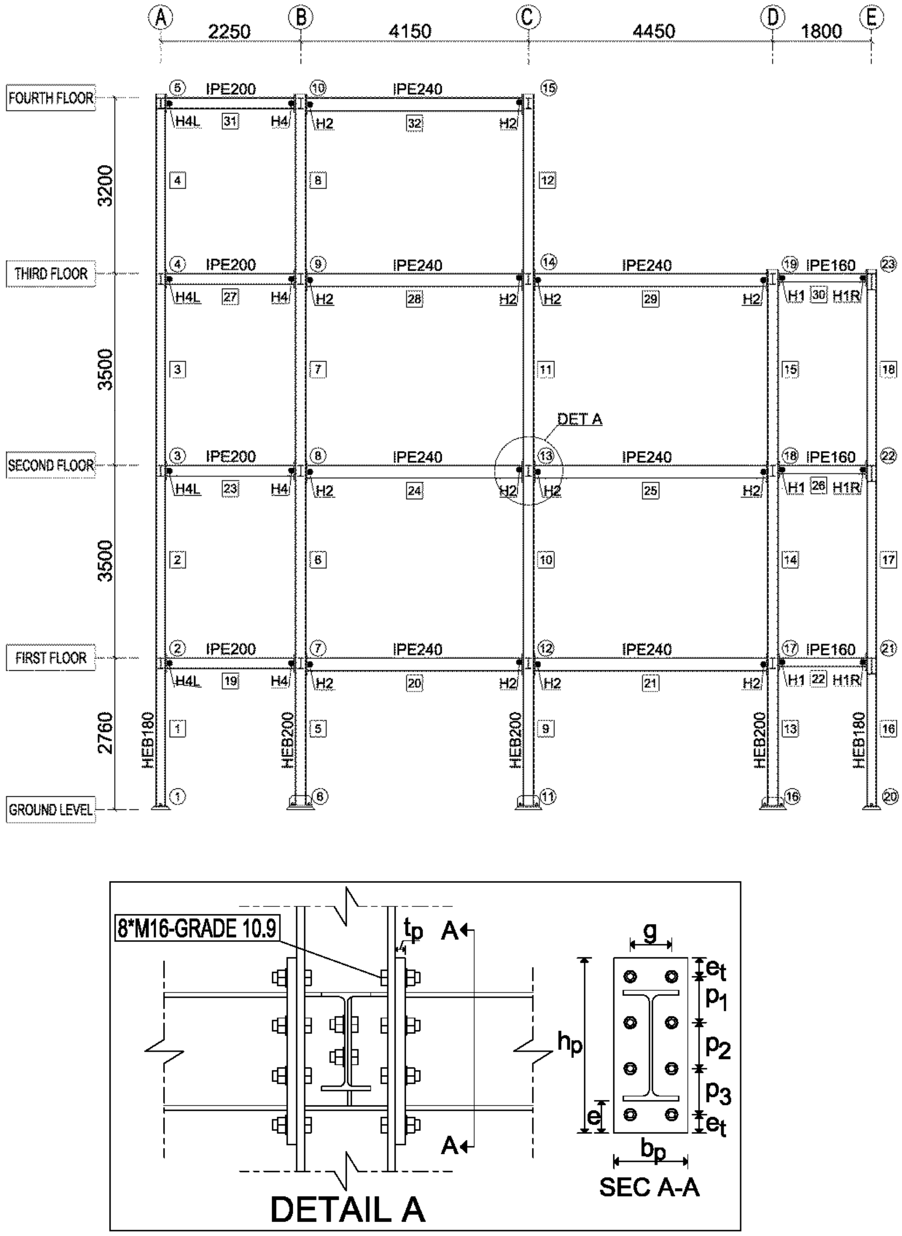

Figure 1: Analytical model for the selected case frame

Table 1: The details of rotational inelastic hinges, beam, column sections and end-plates

G1 Specimen (tp=20mm) (S275)	G2 Specimen (tp=8mm) (S275)	G3 Specimen (tp=8mm) (S690)	Column Sections (S275)	Beam Sections (S275)	End-plate							
					h_P	b_p	g	e_t	e	p_1	p_2	p_3
H1-20	H1-8	HSS-H1-8	HE200B	IPE160	295	160	90	30	67	85	65	85
HR1-20	HR1-8	HSS-HR1-8	HE180B	IPE160	295	160	90	30	67	85	65	85
H2-20	H2-8	HSS-H2-8	HE200B	IPE240	380	160	90	30	70	80	160	80
H4-20	H4-8	HSS-H4-8	HE200B	IPE200	380	160	90	30	70	80	160	80
H4L-20	H4L-8	HSS-H4L-8	HE180B	IPE200	380	160	90	30	70	80	160	80

2.2 Finit element modelling of joints

The general-purpose finite element explicit solver, ABAQUS/ Standard [18], was employed to conduct 3-D nonlinear FE simulations. A cantilever arrangement suggested by Díaz et al. [19] (Figure 2) is used for the 3-D FEM. The length of the column, Hcol, and the length of the beam were set to be equal to 3625 mm and 1550 mm, respectively. In addition, the stiffener thickness under the applied load was considered to be equal to that of the flange thickness of the beam [19]. Taken the advantage of symmetry, half of the structure was modelled. The bottom of the columns was pinned in all three directions and the top of the columns was pinned in two directions but movement along the column axis was allowed.

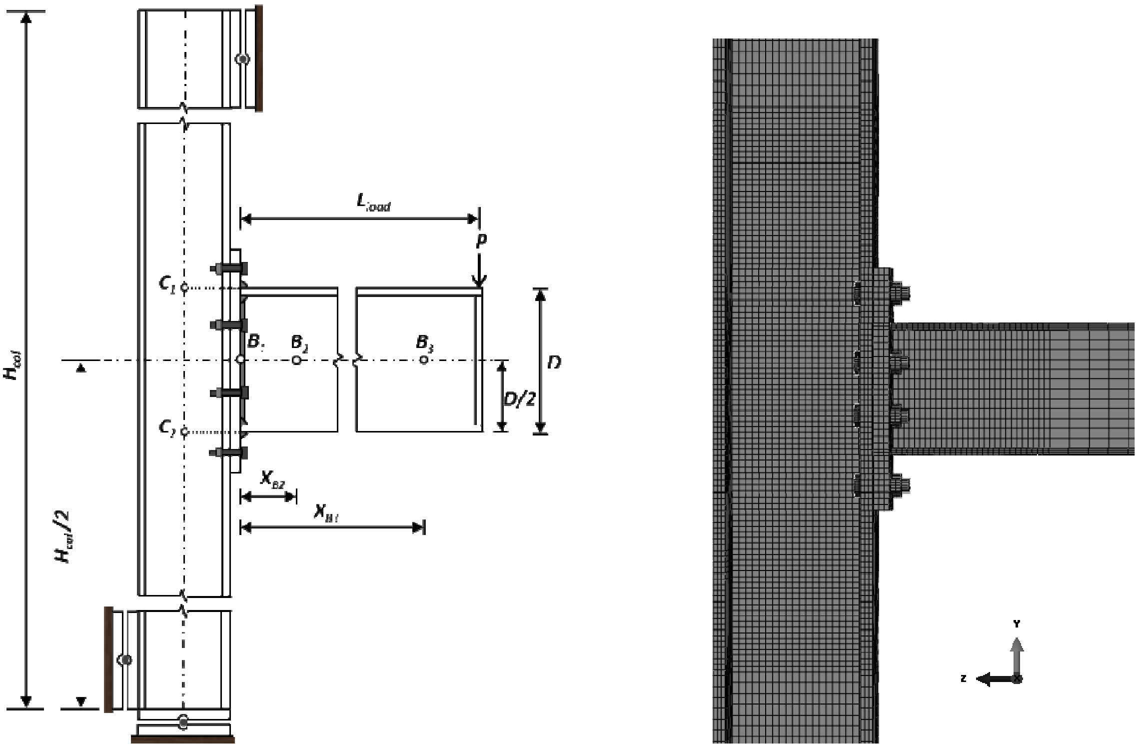

(a) (b)

Figure 2: The cantilever arrangement: (a) locations of the reference points that are used to measure the displacements (b) The typical FE mesh.

In order to define the materials properties for the joint components, the quadrilinear stress–strain curve (as given by Mohamadi-shooreh and Mofid [20]) was adopted with the values of the yield stress and ultimate stress obtained from EC3 [4]. With the purpose of capturing the large deformation and local instability effects in the 3-D FE models, both material and geometric non-linearities were considered.

The solid element C3D8R available in the ABAQUS [18] element library was used to model the HSS connection components. Figure 2(b) shows a typical finite element mesh for the cantilever arrangement. Three parameters which controls the generation of the FE mesh are noted. These are: the number of elements through the thickness, n_{et} = 3), the length of the elements in the region near the connection, l_{en} = 7 mm and the length of the elements in the region far from the connection, l_{ef} = 25 mm.

The flexural behaviour of extended end-plate connection is best described by the moment-rotation (M-ϕ) curve that describes the applied bending moment, M, as a function of the rotational deformation of this joint, ϕ. The bending moment is produced by multiplying the applied load, P, with the distance between the load application point and the face of the reverse channel, L_{load} (Figure 2(a)). On the other hand, the rotational deformation of this joint is equal to the sum of the connection rotational deformation, ϕ_c, and shear deformation of the column web panel zone, γ, [22].

The relevant equations proposed by Díaz et al. [22] and Coelho and Bijlaard [13] are used to determine the rotational deformation of the joint. It is based on the vertical displacement measurements of the reference points B_1 *to* B_3, C_1 and C_2 (Figure 2(a)).

2.2.1 Verification of finite element simulations

Three tests on HSS end-plate connections conducted by Coelho and Bijlaard [13] were used to verify the finite element model presented in this study. Table 2 summarizes the measured dimensions and grades of materials for the selected connections. The beam and column sections used were HE320A and HE300M, respectively, for all tests. Two different end-plate thicknesses; 10.1 mm and 14.62 mm, and two different bolt grades; 12.9 and 8.8, were also used, as shown in Table 2. The mechanical properties of the end-plates were obtained from tensile coupon tests. The average characteristic values are detailed in [13]. The steel grade used for beams and columns was S355J2 and for extended end-plates was S690. Six M24 (24 mm diameter) bolts were employed for each test and the details are given in Table 2. All of these bolts were hand tightened without any preloads.

Table 1: Details of test specimens [13]

Test	Column Section (S355J2)	Beam Section (S355J2)	Endplate (S690) h_P	b_p	t_p	g	e_t	e_c	e	p_1	p_2
EEP_10_2a*	HE300M	HE320A	435	300	10.10	150	40	100	25	160	135
EEP_10_2b¤	HE300M	HE320A	435	300	10.10	150	40	100	25	160	135
EEP_15_a*	HE300M	HE320A	435	300	14.62	150	40	100	25	160	135

* Grade 12.9 was used for 6 M24 standard bolts

¤ Grade 8.8 was used for 6 M24 standard bolts

Table 3 summarizes the comparison between the tests and the finite element analysis results. The results included the initial stiffness of the joint, $S_{j,in,}$ the ultimate flexural resistance of the joint, $M_{j,max}$, and the rotation corresponding to the ultimate flexural resistance, $\phi_{j,max}$. It can be seen from Table 2 that the results of tests and FE models are in very good agreement. The mean values of $S_{j,in,Exp}$ / $S_{j,in,FE}$, $M_{j,max,Exp}$ / $M_{j,max,FE}$ *and* $\phi_{j,max,Exp}$ / $\phi_{j,max,FE}$ ratios are 0.98, 1.03 and 0.93 and the coefficient of variation (COV) values are 0.11, 0.04 and 0.03, respectively.

Table 3: Comparison between test and finite element results

Test	Test [13] $S_{j,in,Exp}$ (kN.m/rad)	$M_{j,max,Exp}$ (kN.m)	$\phi_{j,max,Exp}$ (rad)	FE $S_{j,in,FE}$ (kN.m/rad)	$M_{j,max,FE}$ (kN.m)	$\phi_{j,max,FE}$ (rad)	$\frac{S_{j,in,Exp}}{S_{j,in,FE}}$	$\frac{M_{j,max,Exp}}{M_{j,max,FE}}$	$\frac{\phi_{j,max,Exp}}{\phi_{j,max,FE}}$
EEP_10_2a	17200	244.00	0.0360	17298	239.36	0.0373	0.994	1.019	0.964
EEP_10_2b	17308	252.00	0.0370	19900	233.66	0.0405	0.870	1.079	0.913
EEP_15_a	35300	366.00	0.0200	32684	367.17	0.0219	1.080	0.997	0.912
Mean	-	-	-	-	-	-	0.981	1.032	0.930
COV	-	-	-	-	-	-	0.108	0.041	0.032

2.2.2 Finite element results

Figure 3 gives the moment-rotation comparison for the same hinges from three different groups. Based on group comparison, hinges with 8mm end plate has the best rotational capacity except for the hinge 2 while hinges with 20 mm has the lowest rotational capacity. Considering the initial stiffness and the strength of the hinges, Group 1 has the highest strength and initial stiffness among the three groups. H4L-20 has 26%, 39% more strength and initial stiffness than H4L-8, respectively.

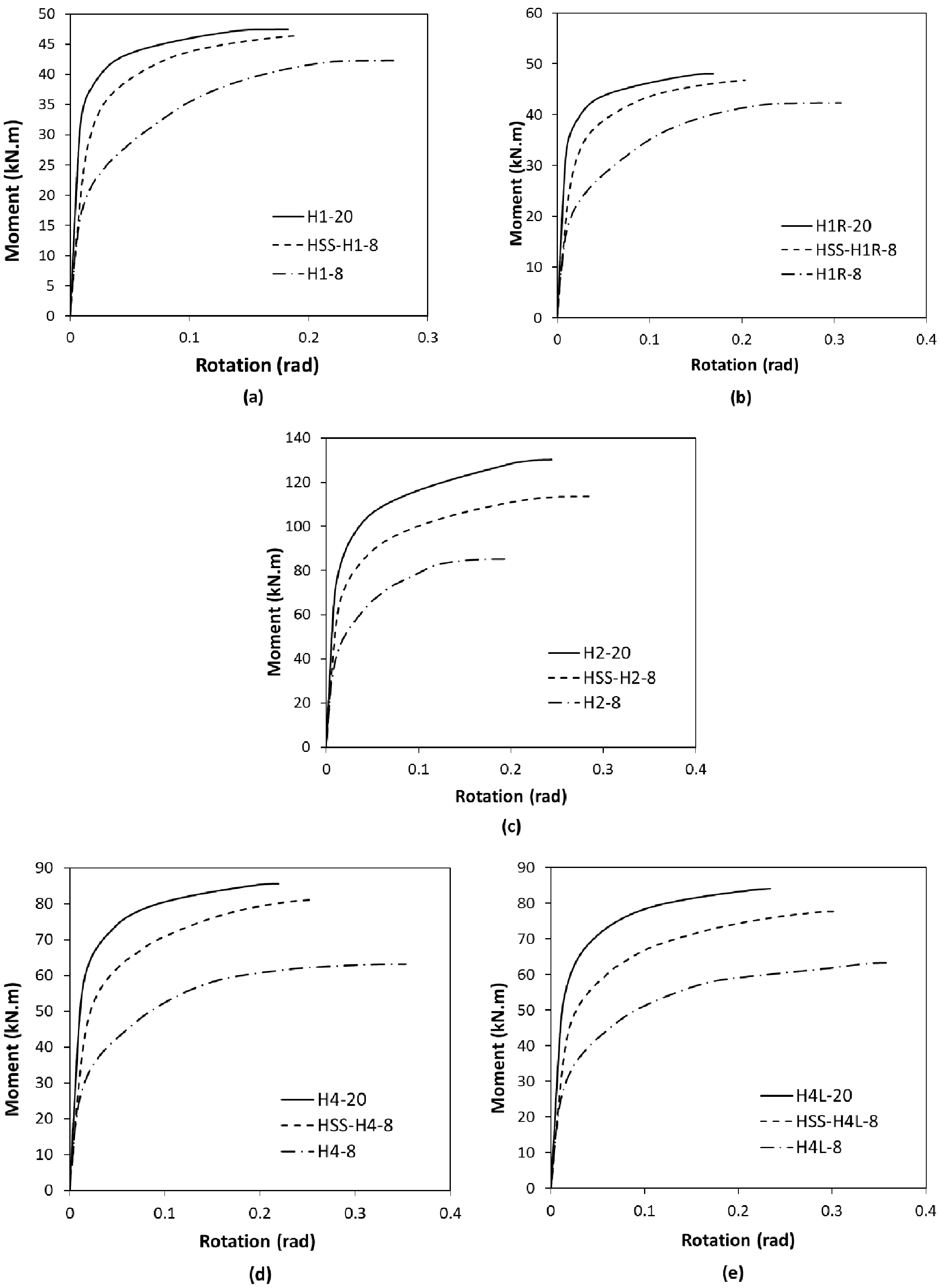

Figure 3: The moment-rotation comparison for the same hinges from three different groups.

The initial stiffness and the post yield stiffness values are computed by means of regression analysis of the elasto-plastic branches before and after the knee range. The plastic flexural resistance $M_{j,R,FE}$, and maximum bending moment $M_{j,max,FE}$, as well as the rotation values corresponding to these moments are given in Table 4. In addition the failure mode of these hinges can be found in Table 4. Through this approach the idealized (elasto-plastic) moment curvature relationships are captured for the purpose of finding hinge properties.

Table 4: The main characteristics of idealized moment-rotation curves

Group	Specimen	Resistance (kN.m)		Rotation (rad)		Failure mode
		$M_{j,R,FE}$	$M_{j,max,FE}$	ϕ_y	$\phi_{j,max,FE}$	
G1	H1-20	42.9	48.3	0.0106	0.1863	BF
	HR1-20	43.1	48.9	0.0116	0.1810	BF
	H2-20	106.7	133.2	0.0132	0.2480	BF
	H4-20	74.8	87.4	0.0155	0.2266	BF
	H4L-20	75.1	85.9	0.0165	0.2603	BF
G2	H1-8	35.1	43.1	0.0153	0.2708	EF
	HR1-8	34.5	43.1	0.0169	0.2840	EF
	H2-8	77.8	85.2	0.0143	0.1991	EF
	H4-8	57.2	63.3	0.0187	0.3302	EF
	H4L-8	51.8	63.5	0.0186	0.3419	EF
G3	HSS-H1-8	40.5	47.3	0.0177	0.2005	BF
	HSS-HR1-8	40.5	47.9	0.0194	0.2181	BF
	HSS-H2-8	97.2	113.7	0.0176	0.2646	EF/BOF
	HSS-H4-8	65.3	84.5	0.0211	0.2711	BF
	HSS-H4L-8	64.7	78.8	0.0231	0.3004	EF/BOF

Note: BF denotes Beam Faliure , EF denotes End-plate Faliure, BOF denotes Bolt Faliure.

3. TIME HISTORY ANALYSIS

3.1 Earthquake hazard levels

Four different hazard levels, 50%, 20%, 10% and 2% and three different earthquake hazard levels 50%, 10% and 2% in accordance to probability of exceedance in 50 years are presented by Federal Emergency Management Agency (FEMA 356 [17]) and Turkish Earthquake Code (TEC [23]), respectively. The case study under consideration was designed according to TEC and therefore 2% probability of exceedance in 50 years was used in the analysis to push the structure loading to upper limits to cause failure.

3.2 Performance level definitions and evaluation

According to FEMA 356 [17], there are four main structural performance levels; Operational Level (OP) Immediate Occupancy (IO), Life Safety (LS), and Collapse Prevention (CP). Structural performance will be assessed both at global and member level by considering the drift and plastic rotation, respectively [24]. Permanent and transient drift limit values suggested by FEMA 356 [17] for steel frames are used for this study. Columns and beam ends are the places that take most stresses during the earthquake excitation [25].

3.3 Target building performance levels

TEC [23] specifies minimum performance levels for buildings according to their usage purposes. However, it should be taken into account that the usage can change within time. The case study building is designed for residential purposes and therefore its performance level is expected to be a minimum of Life safety in case of design earthquake. The probability of earthquake to be exceeded is 10% in 50 years for the design earthquake. Design earthquake is used for the structural analysis of the selected building.

3.4 Nonlinear dynamic analysis

Nonlinear dynamic analysis, also known as time history analysis, was developed to investigate the response of the structures within the real ground motions [26]. It requires a step by step process to have dynamic response of a structure to specified acceleration algorithm. The step sizes are important parameter to have more accurate results.

In this study real ground motions accelerations are applied to the structure in terms of time. According to TEC [23], the selected ground motions shall be scaled according to desired earthquake level spectrum. If there are three data sets, the maximum of the results can be used to determine design acceptability. The case study building is located in Cyprus. Turkey is the closest country with reasonable seismic activity. However, there are only few earthquake data sets available for this country. Duzce earthquake is one of the most recent ones in 1999, with a magnitude of 7.14. From previous research carried out by Ejder [27] it was found that the highest damage occurred on analytical models were due to Duzce earthquake when compared with the worldwide known earthquake data, such as Northridge and El Centro. In order to achieve the objectives of this study, SAP2000 v15.1 software [16] was used with real data from Duzce earthquake for analysis of the 2-D moment frames.

4. RESULTS AND DISCUSSIONS

4.1 Member level evaluation

In order to evaluate the seismic performance of the analytical models, structural members of the frame are monitored on the basis of resulting rotation at the member ends. Thus, the maximum plastic rotations collected from dynamic analysis for beams and columns are summarized in Tables 5 and 6, respectively, depending on the formation sequence of the plastic hinges. In addition, the maximum plastic rotations are compared with the limitations given in FEMA 356 [17] in terms of performance level.

According to the results in Table 5, the beam evaluations of three group models show that the most severe damage is with G1 model. The members of G1 model are within the following limits; 21 members-IO level, 4 members-LS level and 1 member-CP level. It can also be observed that G3 (8 mm HSS end-plate) has the best performance and no member reached LS level. On the other hand, the evaluation of column members (Table 6) shows that the performance of G2 can be considered as the best among all groups; 3 members-IO level and 3 members-LS level. As for G1 and G3, they had similar performance with 3 members being at CP level.

4.2 Global level evaluation

The transient and permanent interstory drift ratios are investigated according to the given limitations in FEMA 356 [17]. Peak values are illustrated for all groups in Figure 4. Figure 4 (a) shows that all groups are in LS level. In addition, the maximum transient interstory drift ratios for G1 and G3 occurred at first story level while for G2, it is occurred at second story level. The ratio for G1, G2 and G3 are 4.4%, 4.13% and 4.20%, respectively. In Figure 4 (b), the structure in analytical models reached the plastic limits and permanent drifts were occurred. Permanent drift ratios did not exceed the LS limit for G1 and G3 while G2 is in the LS limit.

5. CONCLUSION

The primary aim of this research was to investigate the performance of 2-D moment frames using HSS and mild steel end-plate beam to column connections in terms of strength, stiffness and ductility. A typical 2-D steel moment frame from an existing residential building was taken as a case study. FEM was used to capture the moment curvature relationship for the purpose of finding hinge properties in SAP2000 v15.1 [16]. The time-history analysis (dynamic analysis) was carried out according to FEMA 356 [17] to determine the global inelastic response of 2-D moment frames. It is clear from the findings of this study that more research is needed on HSS to help in the development of a guideline to be added in the existing design codes. The following are the main conclusions of this study.

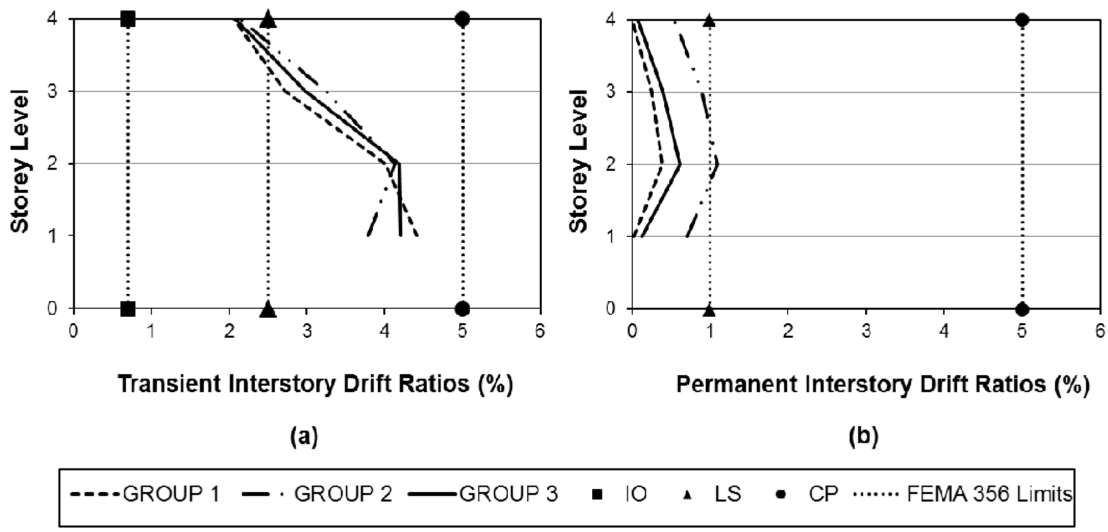

Figure 4: The maximum transient and permanent interstory drift ratios of three groups

1. Comparison of hinging patterns indicates that model with HSS end-plate beam to column connections (G3) had 14 hinges yielded as oppose to 11 and 12 hinges being yielded for group numbers 1 and 2 (G1 and G2).

2. Reducing the mild steel end-plate thickness marginally improved the ductility of the joints and hence it enhanced the behaviour of the structural members. However, it may cause increase in lateral drift of the joints which lead to instability of the frame. On the other hand, reducing the end-plate thickness together with increasing the yield strength to HSS may provide a better control of the stability of the frame.

3. From the moment-rotation behaviour achieved for the three groups it is clear that the plastic hinges locations of the models for group 1 (G1) behaved as designed and the strong column and weak beam variation was achieved. On the other hand, HSS end-plate beam to column connections (G3) did not achieve this in some cases where the damage or failure occurs at the end-plate and bolts. Therefore, the thickness of the HSS end-plate can be the key factor in determining the failure mode.

4. The usage of HSS would allow the use of a thinner end-plate without compromising the frame seismic behaviour. However, the minimum thickness for the HSS end-plate may need to be determined to avoid buckling instability of the frame.

Table 5: Plastic formations and performance levels for beams of three groups

		GROUP 1 (G1)					GROUP 2 (G2)					GROUP 3 (G3)				
		Moments	Rotation	FEMA 356 limits (rad)			Moments	Rotation	FEMA 356 limits (rad)			Moments	Rotation	FEMA 356 limits (rad)		
Mem.	Joint	(kNm)	(rad)	IO	LS	CP	(kNm)	(rad)	IO	LS	CP	(kNm)	(rad)	IO	LS	CP
19	2	76.22	*0.0279*	**0.0041**	0.0329	0.0494	52.88	*0.0326*	**0.0046**	0.0371	0.0557	65.99	*0.0287*	**0.0058**	0.0461	0.0692
19	7	76.49	*0.0318*	0.0039	**0.0310**	0.0466	57.82	*0.0326*	**0.0047**	0.0373	0.0560	67.57	*0.0328*	**0.0053**	0.0422	0.0633
20	7	110.01	*0.0307*	0.0033	**0.0264**	0.0396	78.94	*0.0327*	0.0036	**0.0286**	0.0428	99.19	*0.0319*	**0.0044**	0.0352	0.0528
20	12	109.39	*0.0250*	**0.0033**	0.0264	0.0396	78.96	*0.0330*	0.0036	**0.0286**	0.0428	99.05	*0.0297*	**0.0044**	0.0352	0.0528
21	12	109.32	*0.0244*	**0.0033**	0.0264	0.0396	78.94	*0.0326*	0.0036	**0.0286**	0.0428	99.02	*0.0291*	**0.0044**	0.0352	0.0528
21	17	110.02	*0.0309*	0.0033	**0.0264**	0.0396	78.95	*0.0327*	0.0036	**0.0286**	0.0428	99.17	*0.0316*	**0.0044**	0.0352	0.0528
22	17	43.86	*0.0333*	0.0027	0.0212	**0.0319**	36.05	*0.0334*	0.0038	**0.0306**	0.0460	41.57	*0.0333*	**0.0044**	0.0353	0.0530
22	21	44.05	*0.0297*	0.0029	**0.0231**	0.0347	35.46	*0.0330*	**0.0042**	0.0338	0.0507	41.53	*0.0307*	**0.0049**	0.0389	0.0583
23	3	75.95	*0.0212*	**0.0041**	0.0329	0.0494	52.79	*0.0299*	**0.0046**	0.0371	0.0557	65.84	*0.0253*	**0.0058**	0.0461	0.0692
23	8	75.72	*0.0174*	**0.0039**	0.0310	0.0466	57.67	*0.0251*	**0.0047**	0.0373	0.0560	66.76	*0.0209*	**0.0053**	0.0422	0.0633
24	8	108.48	*0.0165*	**0.0033**	0.0264	0.0396	78.68	*0.0252*	**0.0036**	0.0286	0.0428	98.45	*0.0201*	**0.0044**	0.0352	0.0528
24	13	108.43	*0.0161*	**0.0033**	0.0264	0.0396	78.66	*0.0245*	**0.0036**	0.0286	0.0428	98.43	*0.0198*	**0.0044**	0.0352	0.0528
25	13	108.37	*0.0155*	**0.0033**	0.0264	0.0396	78.64	*0.0241*	**0.0036**	0.0286	0.0428	98.40	*0.0193*	**0.0044**	0.0352	0.0528
25	18	108.37	*0.0173*	**0.0033**	0.0264	0.0396	78.70	*0.0256*	**0.0036**	0.0286	0.0428	98.49	*0.0206*	**0.0044**	0.0352	0.0528
26	18	43.46	*0.0198*	**0.0027**	0.0212	0.0319	35.84	*0.0262*	**0.0038**	0.0306	0.0460	41.21	*0.0223*	**0.0044**	0.0353	0.0530
26	22	43.84	*0.0230*	**0.0029**	0.0231	0.0347	35.35	*0.0292*	**0.0042**	0.0338	0.0507	41.36	*0.0258*	**0.0049**	0.0389	0.0583
27	4	75.61	*0.0127*	**0.0041**	0.0329	0.0494	52.38	*0.0175*	**0.0046**	0.0371	0.0557	65.33	*0.0139*	**0.0058**	0.0461	0.0692
27	9	75.38	*0.0109*	**0.0039**	0.0310	0.0466	57.49	*0.0154*	**0.0047**	0.0373	0.0560	66.16	*0.0123*	**0.0053**	0.0422	0.0633
28	9	107.80	*0.0102*	**0.0033**	0.0264	0.0396	78.35	*0.0158*	**0.0036**	0.0286	0.0428	97.91	*0.0114*	**0.0044**	0.0352	0.0528
28	14	107.51	*0.0076*	**0.0033**	0.0264	0.0396	78.35	*0.0140*	**0.0036**	0.0286	0.0428	97.76	*0.0090*	**0.0044**	0.0352	0.0528
29	14	107.45	*0.0070*	**0.0033**	0.0264	0.0396	78.28	*0.0137*	**0.0036**	0.0286	0.0428	97.73	*0.0085*	**0.0044**	0.0352	0.0528
29	19	107.32	*0.0058*	**0.0033**	0.0264	0.0396	78.35	*0.0157*	**0.0036**	0.0286	0.0428	97.82	*0.0100*	**0.0044**	0.0352	0.0528
30	19	43.12	*0.0078*	**0.0027**	0.0212	0.0319	35.57	*0.0165*	**0.0038**	0.0306	0.0460	40.87	*0.0116*	**0.0044**	0.0353	0.0530
30	23	43.55	*0.0143*	**0.0029**	0.0231	0.0347	35.09	*0.0200*	**0.0042**	0.0338	0.0507	41.03	*0.0016*	**0.0049**	0.0389	0.0583
31	5	75.31	*0.0052*	**0.0041**	0.0329	0.0494	51.19	*0.0119*	**0.0046**	0.0371	0.0557	65.07	*0.0082*	**0.0058**	0.0461	0.0692
31	10	74.85	*0.0009*	0.0039	0.0310	0.0466	57.32	*0.0066*	**0.0047**	0.0373	0.0560	65.56	*0.0038*	0.0053	0.0422	0.0633
32	10	106.73	*0.0002*	0.0033	0.0264	0.0396	78.03	*0.0067*	**0.0036**	0.0286	0.0428	97.37	*0.0028*	0.0044	0.0352	0.0528
32	15	107.43	*0.0068*	**0.0033**	0.0264	0.0396	78.21	*0.0117*	**0.0036**	0.0286	0.0428	97.74	*0.0087*	**0.0044**	0.0352	0.0528

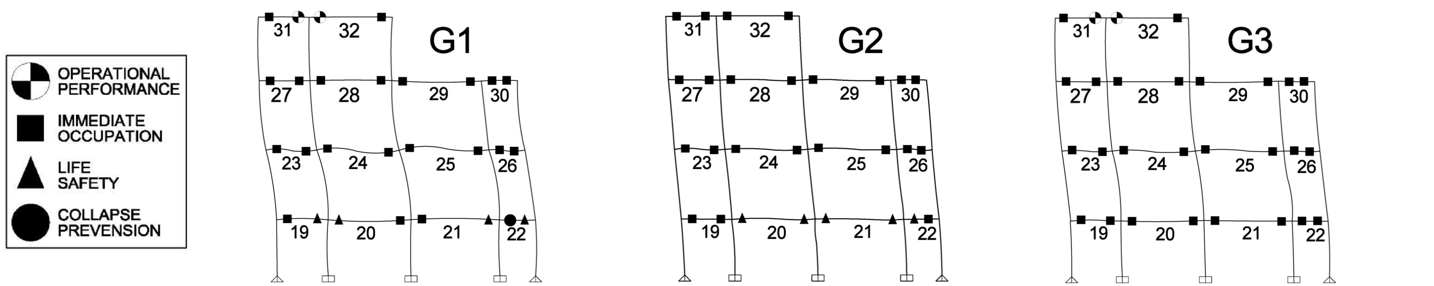

Table 6: Plastic formations and performance levels for columns of three groups

		GROUP 1 (G1)					GROUP 2 (G2)					GROUP 3 (G3)				
		Moments	Rotation	FEMA 356 limits (rad)			Moments	Rotation	FEMA 356 limits (rad)			Moments	Rotation	FEMA 356 limits (rad)		
Mem.	Joint	(kNm)	(rad)	IO	LS	CP	(kNm)	(rad)	IO	LS	CP	(kNm)	(rad)	IO	LS	CP
2	2	147.25	*0.0033*	**0.0021**	0.0166	0.0250	145.51	*0.0002*	0.0021	0.0166	0.0250	146.95	*0.0028*	**0.0021**	0.0166	0.0250
5	6	215.03	*0.0333*	0.0024	0.0188	**0.0282**	209.91	*0.0251*	0.0024	**0.0188**	0.0282	213.35	*0.0306*	0.0024	0.0188	**0.0282**
5	7	195.86	*0.0022*	0.0024	0.0188	0.0282	194.82	*0.0005*	0.0024	0.0188	0.0282	195.00	*0.0008*	0.0024	0.0188	0.0282
6	7	201.10	*0.0107*	**0.0024**	0.0188	0.0282	199.66	*0.0084*	**0.0024**	0.0188	0.0282	201.35	*0.0111*	**0.0024**	0.0188	0.0282
6	8	195.94	*0.0023*	0.0024	0.0188	0.0282	194.71	*0.0004*	0.0024	0.0188	0.0282	195.83	*0.0021*	0.0024	0.0188	0.0282
7	8	194.85	*0.0005*	0.0024	0.0188	0.0282	-	-	-	-	-	-	-	-	-	-
9	11	215.13	*0.0335*	0.0024	0.0188	**0.0282**	210.23	*0.0255*	0.0024	**0.0188**	0.0282	213.79	*0.0313*	0.0024	0.0188	**0.0282**
9	12	197.30	*0.0045*	**0.0024**	0.0188	0.0282	195.64	*0.0018*	0.0024	0.0188	0.0282	195.35	*0.0015*	0.0024	0.0188	0.0282
10	12	200.50	*0.0097*	**0.0024**	0.0188	0.0282	200.36	*0.0095*	**0.0024**	0.0188	0.0282	201.25	*0.0109*	**0.0024**	0.0188	0.0282
10	13	198.23	*0.0061*	**0.0024**	0.0188	0.0282	195.88	*0.0023*	0.0024	0.0188	0.0282	197.08	*0.0042*	**0.0024**	0.0188	0.0282
11	13	195.68	*0.0019*	0.0024	0.0188	0.0282	-	-	-	-	-	195.07	*0.0009*	0.0024	0.0188	0.0282
11	14	195.10	*0.0009*	0.0024	0.0188	0.0282	-	-	-	-	-	194.69	*0.0003*	0.0024	0.0188	0.0282
13	16	214.80	*0.0329*	0.0024	0.0188	**0.0282**	209.77	*0.0248*	0.0024	**0.0188**	0.0282	213.18	*0.0303*	0.0024	0.0188	**0.0282**
13	17	194.69	*0.0004*	0.0024	0.0188	0.0282	194.82	*0.0005*	0.0024	0.0188	0.0282	194.71	*0.0003*	0.0024	0.0188	0.0282
14	17	200.50	*0.0097*	**0.0024**	0.0188	0.0282	199.43	*0.0080*	**0.0024**	0.0188	0.0282	200.97	*0.0105*	**0.0024**	0.0188	0.0282
14	18	195.49	*0.0016*	0.0024	0.0188	0.0282	194.88	*0.0007*	0.0024	0.0188	0.0282	195.38	*0.0014*	0.0024	0.0188	0.0282
15	18	194.85	*0.0005*	0.0024	0.0188	0.0282	-	-	-	-	-	194.71	*0.0004*	0.0024	0.0188	0.0282
17	21	145.74	*0.0005*	0.0021	0.0166	0.0250	-	-	-	-	-	146.06	*0.0011*	0.0021	0.0166	0.0250

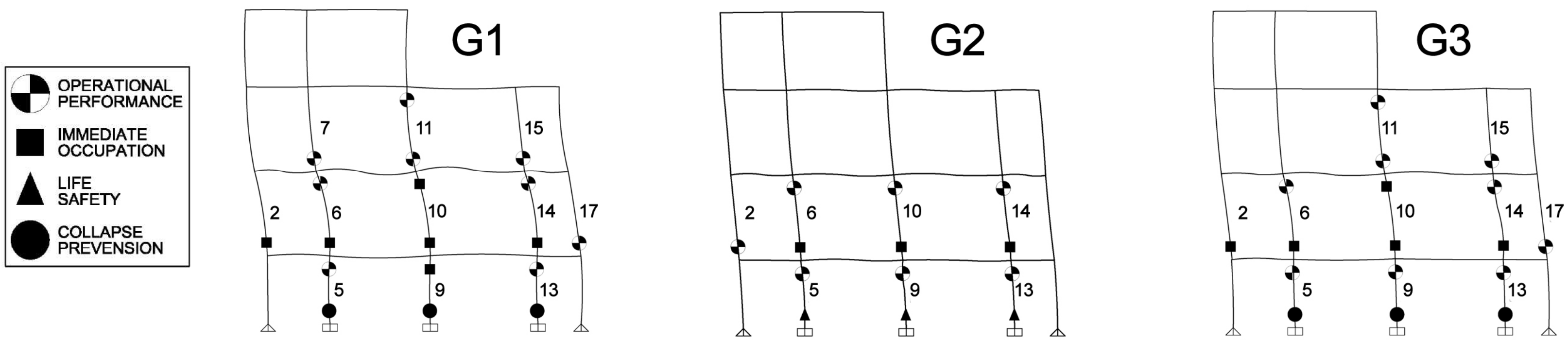

REFERENCES

[1] S. Wilkinson, G. Hurdman and A. Crowther, "A moment resisting connection for earthquake resistant structures," *Journal of Constructional Steel Research,* vol. 62, p. 295–302, 2006.

[2] C. Scawthorn and P. I. Yanev, "Preliminary report 17 January 1995, Hyogo-ken Nambu, Japanese earthquake," *Engineering Structures,* vol. 17, no. 3, pp. 146-157, 1995.

[3] L. Gao, H. Sun, F. Jin and H. Fan, "Load-carrying capacity of high-strength steel box-sections I: Stub columns," *Journal of Constructional Steel Research,* vol. 65, pp. 918-924, 2009.

[4] A. M. G. Coelho, F. S. Bijlaard and H. Kolstein, "Experimental behaviour of high-strength steel web shear panels," *Engineering Structures,* vol. 31, pp. 1543-1555, 2009.

[5] H. Ban, G. Shi, Y. Shi and M. A. Bradford, "Experimental investigation of the overall buckling behaviour of 960 MPa high strength steel columns," *Journal of Constructional Steel Research,* vol. 88, p. 256–266, 2013.

[6] G. Shi, H. Ban and F. S. Bijlaard, "Tests and numerical study of ultra-high strength steel columns with end restraints," *Journal of Constructional Steel Research,* vol. 70, p. 236–247, 2012.

[7] H. Ban, G. Shi, Y. Shi and Y. Wang, "Overall buckling behavior of 460 MPa high strength steel columns: Experimental investigation and design method," *Journal of Constructional Steel Research,* vol. 74, p. 140–150, 2012.

[8] Y.-B. Wang, G.-Q. Li, C. Su-Wen and S. Fei-Fei, "Experimental and numerical study on the behavior of axially compressed high strength steel box-columns," *Engineering Structures,* vol. 58, p. 79–91, 2014.

[9] H. Ban and M. A. Bradford, "Flexural behaviour of composite beams with high strength steel," *Engineering Structures,* vol. 56, p. 1130–1141, 2013.

[10] A. M. G. Coelho, F. S. K. Bijlaard and L. S. d. Silva, "Experimental assessment of the ductility of extended end plate connections," *Engineering Structures,* vol. 26, p. 1185–1206, 2004.

[11] X. Qiang, F. S. Bijlaard, H. Kolstein and X. Jiang, "Behaviour of beam-to-column high strength steel endplate connections under fire conditions – Part 1: Experimental study," *Engineering Structures,* vol. 64, p. 23–38, 2014.

[12] X. Qiang, F. S. Bijlaard, H. Kolstein and X. Jiang, "Behaviour of beam-to-column high strength steel endplate connections under fire conditions – Part 2: Numerical study," *Engineering Structures,* vol. 64, p. 39–51, 2014.

[13] A. M. G. Coelho and F. S. Bijlaard, "Experimental behaviour of high strength steel end-plate connections," *Journal of Constructional Steel Research,* vol. 63, p. 1228–1240, 2007.

[14] R. Bjorhovde, "Development and use of high performance steel," *Journal of Constructional Steel Research,* vol. 60, p. 393–400, 2004.

[15] G. Shi, M. Wang, Y. Bai, F. Wang, Y. Shi and Y. Wang, "Experimental and modeling study of high-strength structural steel under cyclic loading," *Engineering Structures,* vol. 37, p. 1–13, 2012.

[16] C. Inc. Berkeley, "SAP2000 Version 14, Non-Linea," Computers and Structures. [Online].

[17] Federal Emergency Management Agency, FEMA-356, "Prestandard and commentary for seismic rehabilitation of buildings," Washington (DC), 2000.

[18] "ABAQUS standard user's manual: Vol. 1, 2 and 3; version 6.12," Hibbitt, Karlsson and Sorensen, Inc., USA, 2012.

[19] C. Díaz, M. Victoria, P. Martí and O. M. Querin, "FE model of beam-to-column extended end-plate joints," *Journal of Constructional Steel Research,* vol. 67, p. 1578–1590, 2011.

[20] M. R. Mohamadi-shooreh and M. Mofid, "Parametric analyses on the initial stiffness of flush end-plate splice connections using FEM," *Journal of Constructional Steel Research ,* vol. 64, p. 1129–1141, 2008.

[21] EC3, "Eurocode 3: Design of steel structures - Part 1-1: General rules and rules for buldings," UK: British Standered Institution, Londen, BS EN 1993-1-1;2005.

[22] C. Díaz, M. Victoria, P. Martí and O. M. Querin, "FE model of beam-to-column extended end-plate joints," *Journal of Constructional Steel Research,* vol. 67, p. 1578–1590, 2011.

[23] TEC, "Specifications for structures to be built in disaster areas," Ministry of public works and settlement government of republic of Turkey, İstanbul, 2007.

[24] . M. B. D. Hueste and J. W. Bai, "Seismic retrofit of a reinforced concrete flat-slab structure: Part I-seismic performance evaluation," *Engineering Structures,* vol. 29, pp. 1165-1177, 2007.

[25] Z. Celeb, Betonarme taşıyıcı sistemlerde doğrusal olmayan davranış ve cözümleme, İstanbul, 2008.

[26] A. &. S. Pecker and International Centre for Mechanical, Advanced earthquake engineering analysis, Wien; New York: Springer, 2007.

[27] O. Ejder, Seismic performance evaluation of 2-dimensional reinforced concrete, steel and mixed frames, Gazimagusa, North Cyprus: MS. thesis, Department of Civil Engineering, Eastern Mediterranean University, 2012.

[28] Y. C. Wang and L. Xue, "Experimental study of moment–rotation characteristics of reverse channel connections to tubular columns," *Journal of Constructional Steel Research* , vol. 85, pp. 92-104, 2013.

[29] M. Wang, Y. Shi, Y. Wang and G. Shi, "Numerical study on seismic behaviors of steel frame end-plate connections," *Journal of Constructional Steel Research,* vol. 90, p. 140–152, 2013.

12th International Conference on
Steel, Space and Composite Structures
28-30 May 2014, Prague, Czech Republic

INTENSIFICATION OF LOW DENSITY DEVELOPMENT – FUNCTIONAL BRIDGING BUILDINGS

S.P. Chiew*, C.K. Lee, M.S. Zhao, Y.F. Jin, Y.Q. Cai and C. Chen

School of Civil and Environmental Engineering
Nanyang Technological University, Singapore
e-mail: *cspchiew@ntu.edu.sg

Keywords: intensification, functional bridging building, high strength steel, stack-up building, mega-truss, pre-stressed tendon

Abstract: *In highly urbanized Singapore, the needs to provide more usable space and horizontal connectivity between high-rise buildings are increasing. Unfortunately, it is getting harder for the common and traditional 1-D pencil-like vertical and serial intensification to meet these requirements. Under this background, the new functional bridging buildings based on the concept of utilizing mega-trusses with stack-up structures sitting on top appear to be a feasible and viable alternative. The novelty of this new structural form lies in its ability to intensify and optimize land use among existing buildings and across existing infrastructures by creating space for functioning buildings to sit over the bridging structures. However, it is foreseeable that such structural form is going to face many challenges in material, design and construction due to its long span. In this paper, the buildability of such functional bridging buildings (FBB) is discussed and a prototype FBB system is proposed. Some preliminary studies regarding the use of high strength S690 steel for the bridging mega-truss and volumetric modular construction for the stack-up buildings in the proposed FBB system are carried out. The use of quenched and tempered high strength S690 steel has proven its merits over conventional steel whereas the light-weight volumetric modular construction for the stack-over buildings can be very effective in reducing construction time and improving construction productivity.*

1. INTRODUCTION

Since the independence of the island state, Singapore underwent rapid development and urbanization in the last few decades. Both the population and population density have been increased for many times. It is of little doubt that land optimization and urban development – space demand for sustainable urban living will increase exponentially with time in Singapore. In general similar to many other major cities in the world, Singapore followed a very similar course of urbanization: formation of skyline mainly consist of many “pen-shape” skyscrapers: gradual extension of CBD areas with the demolishment of old and historical buildings; development of new “satellite” towns with rapid increase in residual building height and population per unit land area. However, due to the very limited size of the country, such traditional development phase, especially paradigm of “intensification by height” which tends to generate more and more crowed living conditions and overloading the energy and transportation infrastructures of the city, is unlikely to meet the expectations of most residents in terms of living standard and to deliver a long term sustainable urban living solution. Unfortunately, such problems will be further intensified with the increasing average heights of the skyline of the city.

To address the above challengers and to meet the objectives of sustaining Singapore’s long-term growth through crating new space cost-effectively and developing a livable, sustainable and resilient city, the critical turning point is to give up the traditional paradigm of 1D (vertical) intensification approach and moves towards the more effective and sustainable 2D (both vertical and horizontal) intensification approach. While intensification in the vertical direction is familiarly linked to those ubiquitous pen-shaped skyscrapers, extension into the second dimension (horizontal) requires the relative less appreciated and new concept of bridging building, whose merit and potential has only been partially explored to a very limited extent so far.

While bridges have been built for many millennia to span geographical obstacles such as rivers, there are only a few historical examples that a bridge bares other functions such as to provide residential or commercial spaces (Figure 1). The main reason for the absence of functional bridge building in the past was largely due to shortcoming of contemporary construction materials, structural engineering knowledge (both analysis and design) and building technology limitations as well as safety concerns. As a result, the main function of most bridges with buildings is still largely remained as a bridge, i.e. to provide linage across physical obstacles. However, with the advancements of bridge engineering, structural engineering knowledge and the use of modern building construction technology as well as advanced building materials, it is now possible to build functional bridging structures by combing vertical and horizontal developments, and that both the problems of space creation and improving the livable in compact precincts could be solved simultaneously. One good example of bridging structures connecting residential buildings is shown in Figure 2. Since the design load and span of such structures are not very big, normal strength structural steels are good enough for this type of structure.

Figure 1: The Ponte Vecchio, Florence, Italy

Figure 2: Pinnacle @ Duxton – Skybridges, Singapore

Next step is to really take this technology further. It should be stressed that the main novelty of the current proposal is to fully extend those “other functions” of bridges to such an extent that they will be at least as important of the function of providing linkage. As a more sustainability friendly approach for the intensification of low-density developments, this proposal is to ‘marry’ existing practices of bridge engineering and structural engineering, and develop new and safe technologies for design and construction for innovative buildings called “Functional Bridging Buildings” (FBB). This paper addresses some challenges the FBB are going to face, and proposed a prototype system comprising bridging mega-truss and stack-up structures incorporating the use of some innovative technologies regarding high strength steel material, external pre-stressing and volumetric construction approach.

2. CHALLENGES

2.1 Building high and wide

While structural engineering are experts in building heavy and tall buildings over a short span, bridge engineers are very skillful to launch long but relatively light weight bridges over a long span. None of them frequently works on building or launching a heavy structure over a long span at very high elevation. To overcome such technical difficulties, it is necessary to develop new and safe technologies for bridging structural engineering, as well as design and construction for the next generation of buildings. Towards this end, one critical factor is the use of high strength-to-weight steel and composite materials to reduce the weight of the structures so that it is both physically possible and economically cost effective to construct the functional bridge building over a large span at elevated height.

Currently, the focus of the material side is on the application of the reheated, quenched and tempered structural steel plate, RQT-S690, which comply with the EN 10025-6 grade S690 specification[1]. It has nominal yield strength of 690 N/mm2, and tensile strength between 790 N/mm^2 and 930 N/mm^2. However, the ductility of this material about 15% might be a bit short since it is only half of the values of normal carbon and alloyed structural steel.

2.2 Adopting modular design approach

While the use of high strength to weight materials would be able to reduce the weight of the FBB, it is expected that the buildability of the whole structure could still be an important issue for the final structures due to its large span. To overcome this issue, one possible way is to adopt a new structural form in a modular design approach which is commonly employed in the design of complex systems. The whole FBB which may need to span for a long distance or level up to a large height could be designed as an assembly of some discrete, repeating and scalable sub-modules or sub-structures which could be easily built and assembled. Furthermore, adopting such modular design shall be able to lower the design and fabrication costs as well as proving a partial solution to the buildability problems. However, it also implies that much research efforts will be needed on the development and testing of new connections design among different modules.

2.3 Vibration control

While in principle the long span FBB could provide very attractive solution to the space creation and sustainability problems, much research efforts would be needed on improving the vibration control, especially when modular design is adopted and many structural connections are present in the final structure. Bridge engineers have long studied and understood that long span bridge is vulnerable to all sort of vibrations. While most of the time they could reduce and control the vibration level down to a level that is acceptable by their users, i.e. car drivers or train passengers, who pass through the bridge in a short time, there exists a technology capability gap in vibration control to address and reduce the vibration level for such long span structure down to an comfort level that would be acceptable to all the occupants, who obviously have to spend much more time to stay and work inside the buildings.

2.4 Buildability and safety

Since the proposed FBB are supposed to be deployed in both new developments as well as span over existing low density development or a built above major highways and rivers, buildability and safety are definitely two crucial concerns when constructing any FBB. While to use of high strength to weight materials and modular design could be able to provide a feasible solution in terms of scalability and very long span construction, much more research works are still needed to be tackle and solve problems on how to lift and assemble the FBB modules safely over existing buildings, highways and rivers without any major interruption of the normal activities of all the buildings / utilities underneath.

3. PROPOSED PROTOTYPE SYSTEM OF FBB

3.1 Current research focus

The FBB is just a general name for structures that are able to perform functions of both bridges and buildings at the same time, while its form can vary according to the requirements. The aim of the current study is to propose a viable and cost-effective FBB over one of the important expressways in Singapore. Besides the required connection for both sides of the expressway, functional buildings are to be built on top of the structure as part of land intensification and creation as shown in Figure 3.

Figure 3: Prototype for Current Study (Source: NST 2 April 2014)

3.2 Design Actions on FBB

The system can be viewed as a long-span girder supporting a few buildings sitting on top. A mega-truss built with high strength steel is a good option for the girder while the volumetric modular design could be viable for the upper stack-up building as shown in Figure 4.

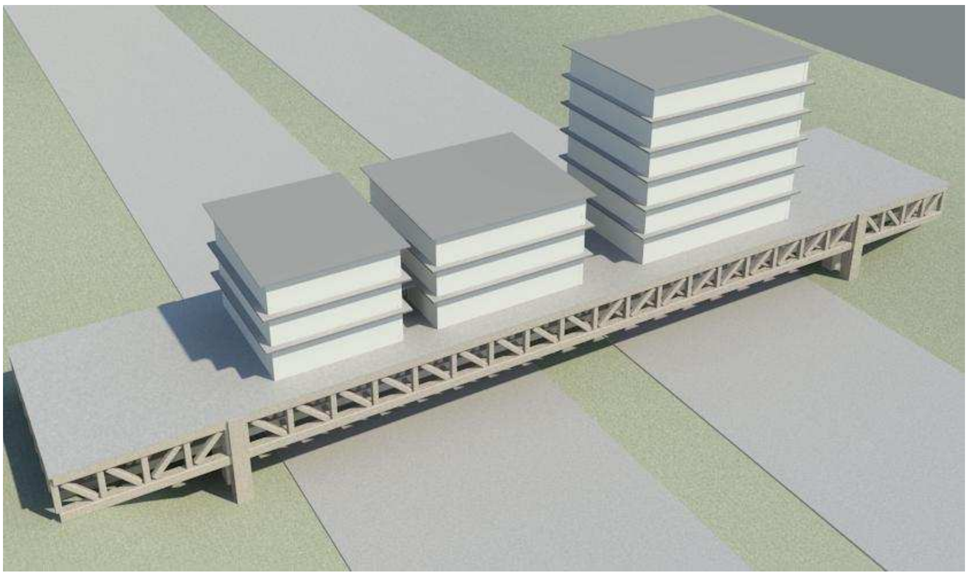

Figure 4: Simplified Structural Model

Now that the basic structural form has been confirmed, one basic question remained to be answered: is the FBB to be designed as a bridge or a building system? From action to resistance calculations point of view, bridges and buildings in fact share little in common.

Since it is built over a major road, the structure would normally be regarded as some kind of a bridge. However, the upper loads like the stack-up building are obviously very different from the normal actions applied to bridge structure such as Tandem System (TS) and Uniformly Distributed Load (UDL) specified in Eurocodes, and there is little traffic loads above the structure. The stack-up building would be used as office building or commercial hub after their construction; and a walkway would also be provided to link the two communities on both sides. Both future functions of FBB show that the mega-truss mainly bearing static action. Therefore, the rules which applicable to design steel bridge may not be suitable to this project.

The steel truss structure normally used as roof in civilian and industry buildings, which usually bear and transfer no loads but their self-weight. That's different from the mega-truss in this project which would be subjected to total permanent and imposed loads transferred from the stack-up building, the pedestrian loads transferred from the walkways, and the accidental load like fire engines. Therefore, to design the FBB as a footbridge system seems to be more appropriate.

The whole structure can be divided as three substructures: the stack-up building, the ground and its appendant, and the steel mega-truss. For the stack-up building, the permanent actions included self-weight of main structure and decoration would be calculated according to the design plan; and the value is taken as 5.4kN/m^2. The value of imposed load which refers to part 1 of EC1 is taken as 3.0kN/m^2 for the most unfavourable condition. For the ground, which would be served as walkway, small garden, or landscape pond, the most unfavourable loads combination would be adopted. If treating the ground as a walkway, the thickness of the concrete floor is assumed as 400mm; and the characteristic imposed loads, inferred to long span footbridge, can be taken as:

$$q_{fk} = 2.0 + \frac{120}{L+30} = 2.0 + \frac{120}{80+30} = 3.1kN/m^2 \tag{1}$$

If the space served as garden, the thickness of the clay layer is given as 1.5 meter according to the design plan. The self-weight of the clay layer combined with the concrete floor is taken as 24.5kN/m^2. So, the latter condition is taken into account to determine the final loads combination, as shown in Figure 5. For the mega-truss, the self-weight is calculated by the software. To get a more safe and conservable design, all upper uniform distributed loads are applied to the most unfavorable zone of the influence line of single truss. The space between two trusses is taken as 5.0m.

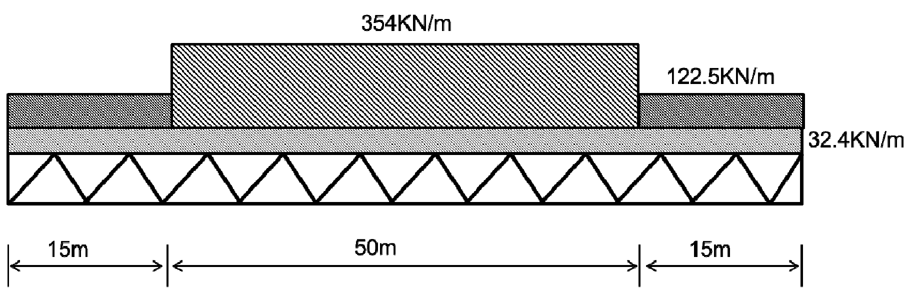

Figure 5 Loadings on the Mega-truss

3.3 Preliminary analysis

In the preliminary analysis stage, three problems are to be addressed: stress, weight and deflection. The commercial design software, MIDAS/Civil (Trial version) was used to analyze theses issues. The first model focused on the stress and weight. The stress states of all the members in a 2D elevation view are shown in Figure 6. It was quite clear that the high strength steel is quite necessary for this project. Even for S690, the stresses of many members have exceeded 70% of the nominal yield strength. At this moment, the weight could be controlled to be within 800 Kg/m^2. However, the deflection turned out to be a huge challenge. The maximum deflection reached about 400mm, which was almost twice the limit stated in chapter 3.2. Despite that improvement could be achieved by changing the structural form or detail optimizations, it was hardly possible to solve the deflection problem without adding a huge amount of additional material. This was when the idea of pre-stressing system coming into the FBB.

A simple pre-stressed tendon was added into the Mega-truss, while other structural components including the truss remain unchanged, as shown in Figure 7. As a result, the pre-stressed tendon successfully changed the stress distribution in the members and the structural deformation shape. The stress level remained almost the same, while the deflection was lowered down to a favorable level in the way shown in Figure 8, i.e. the maximum deflection was decreased to about 30mm. Accordingly, the mega-truss seemed to feasible to bear the load of the whole FBB system.

Figure 6: The Stress Distribution under Designed Load for a Warren Truss

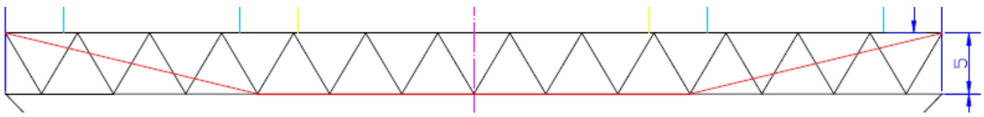

Figure 7: Elevation View of the Mega-truss with Pre-stressed Tendon

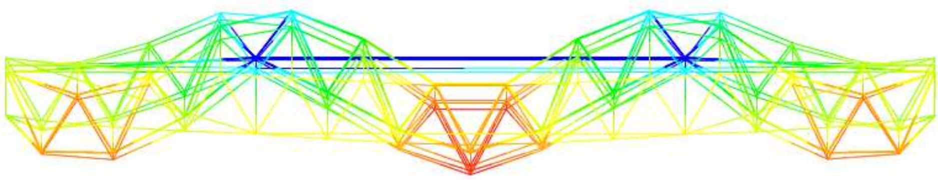

Figure 8: Deflection of the Mega-truss

4. PRELIMINARY STUDIES ON BUILDABILITY

4.1 Use of high strength S690 steel

Responding to the market demand for high strength materials, quenched and tempered steel plates with yield strength more than 690MPa for structural usage was developed in the 1960s[2]. Due to the huge raise in load carrying capacities of common structural forms and improved economies of construction, such steels are supposed to be the mainstream of the future[3-8]. As for the drawbacks, research demonstrated that it was not possible to achieve sufficient deformation capacity[9-12], and was susceptible to heat as inherited from the heat-treatment hardened microstructures[13]. Although welding for heat treated high strength steels may cause a lot of troubles for the global behavior of joints, researchers showed great interests in their welding properties. Reports have shown that the amount of residual stress in welded quenched and tempered steel structures are high[14,15] and the deterioration of mechanical properties in the heat affected zone including strength, hardness and toughness is inevitable[16]. However, few reports regarding the effects of those drawbacks to the global behavior of virtual structures could be found.

This study investigated the tensile behavior of reheat, quenched and tempered steel plate to plate joints fabricated by manual shield metal arc welding method. Joints in angles 45° and 90° with different thicknesses are tested. Further, the effects of post weld heat treatment are studied for those joints, including the influences to residual stress distribution and the tensile behavior of the joints.

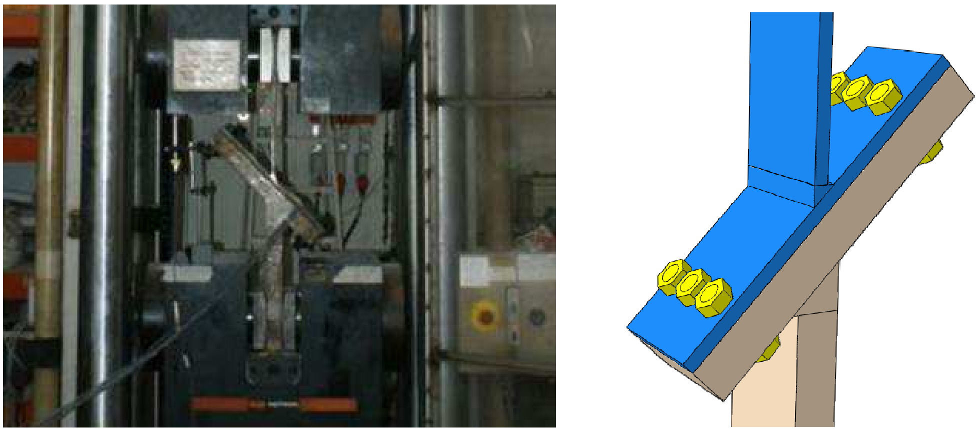

Figure 9: The Tensile Test for the High Strength Steel S690 Plate-to-Plate Joints

As the tensile loads at the brace end increased, the chord deformed into triangular shape correspondingly. Obvious plastic hinges could be found at the bolted area and near weld toes. Two types of failure are observed, i.e. fracture at the weld toe and the bolt area. Unfortunately, most of the specimens showed the fracture failure at the weld toe, which is more brittle and unfavorable in this case.

Since two major problem with welding including high residual stress level[14] and the mechanical property deterioration in the heat affected zone[17] have been confirmed, the second step of this study looked into the potential effects of post weld heat treat (PWHT) in improving the behavior of high strength steel plate-to-plate joints. It took one hour to heat the specimens from 25°C to 600°C and 15 min for the temperature inside the specimens to stabilize, as designed according to minimum requirements of the AWS structural steel welding code[18]. It turned out that PWHT still had potential to lower down the residual stress level as well as improve the load carrying capacity and global deformation ability if the specimens are properly heat treated. An example of the 45 degree joints made of the 16 mm thick plate is shown in Figure 10. As expected, PWHT-800°C heat treated overly the joints and harms the strength too much, although it is still below the eutectoid temperature of steel. Meanwhile, PWHT-600°C is proven to be effective in improving the total load carrying capacity of the investigated joints. Both the final strength and ductility of all the joints are improved after heat treated to 600°C. The most important thing is, the dangerous sudden through thickness fracture is avoided after post weld heat treatment.

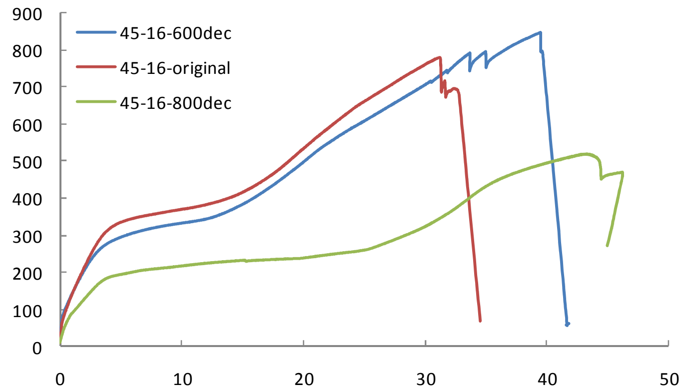

Figure 10: The Load-Displacement Curves of the 45 Degree Joints under Different Conditions

4.2 Fatigue resistance of S690 steel built up rectangular hollow section T-joints

High strength steels have been proven their merits in statically loaded structures. However, the use of high strength steel is still questionable in non-strength dominant occasions including fatigue. Unfortunately, fatigue is one of the crucial problems that all the bridge-related structures have to face. Although the extraordinarily long elastic stage and lower stress ratio are favorable in fatigue resistance[19], it is easy to find a lot of potential unfavorable facts against the fatigue life of high strength steel structures. Welding alone brings a lot of troubles such as high residual stress[14,15], the homogeneity loss in hardness[20, 21] and drop of fracture toughness in the heat affected zone (HAZ)[21, 22], yet it is necessary during the fabrication of QT steel structures since this material is only available in plate form as a structural steel. Besides, reducing the self weight on the other hand may lead to member stiffness lose and increase of stress fluctuations due to live load. From material property to load conditions, the accumulated favorable and unfavorable facts make the fatigue life of high strength steel extremely complex and difficult to be predicted. It is possible that high strength steel may behave differently from normal strength steel when subjected to fatigue loadings.

Literature shows that opinions about the fatigue strength of welded high strength steel structures fall into two groups, none of which stands against the high strength steel. Some reports claim that high and ultra-high strength steels manufactured by newly developed manufacturing techniques acquired better fatigue resistance than traditional steels with much lower yield strength[23, 24], while the others think that welded high strength steels have a fatigue life not much different to conventional steels and they still heavily rely on the post-welding techniques to improve the fatigue resistance[25-27].

Therefore, an experimental study was carried out to investigate the potential fatigue issues of built-up rectangular hollow section joints made of reheated, quenched and tempered high strength steel RQT-S690 as shown in Figure 11. Experiments are carried out to study two identical joints' fatigue behaviors: Specimen I was subjected to a high stress range while Specimen II at a relatively lower stress range. Firstly, static loads in three directions (axial force, in-plane bending and out-of-plane bending) are applied on the brace end to measure the SCFs and the hot spot stresses (HSS) under designed fatigue load cases. Subsequently, the fatigue tests are launched under the continuous monitoring of the ACPD crack monitoring system, as shown in . Three-direction-combined cyclic loadings are applied at the brace end to generate the fatigue loadings. Finally, the test results are verified against S-N curves for rectangular hollow section joints with the same geometrical parameters[28].

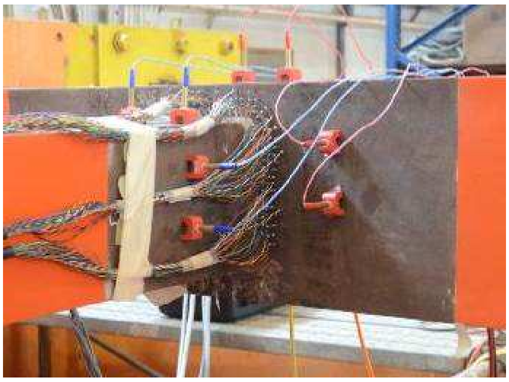

Figure 11: Fatigue Test for the S690 RHS T-Joint (right) with ACPD Installed (left)

Test results indicated that the hot spot stress methods are still applicable for the built-up section joints. The fatigue behavior of high strength steel rectangular hollow section T-joints quite similar to those made of normal strength steel as shown in Figure 12, while the effects of residual stress are of no importance. These findings are in accord with researches done to high strength bridge steels SBHS-500 and SBHS-700[25], whose yield strengths are between S355 and S690.

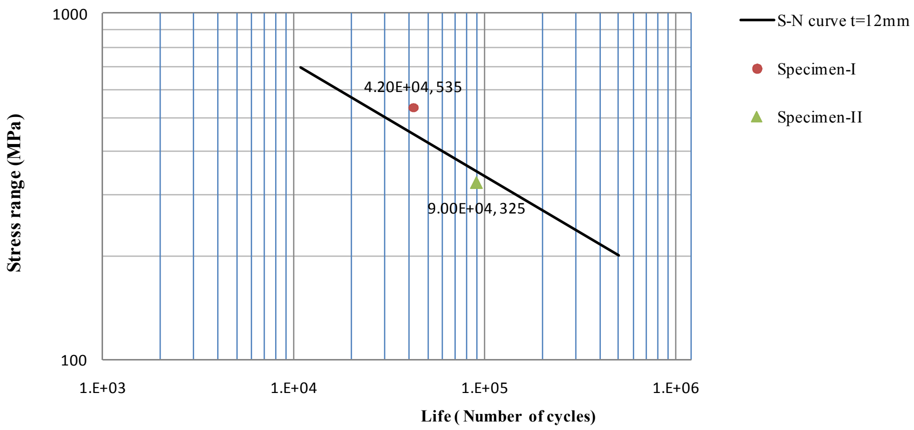

Figure 12: Fatigue Test Results in the S-N Diagram

4.3 Up-down steel connectors for volumetric construction of stack-up buildings

Volumetric modular construction for buildings is gaining popularity in Singapore due to its inherent advantages over conventional construction such as flexible design, low construction time and cost, as well as reduction of dust pollution and labor on site. The pre-fabrication of the modules can vary widely and it is possible to have the entire module fitted up in the factory before moving to the site for assembly. In most cases, this is preferred to reduce construction time and with better quality control as the internal fittings are carried out under controlled indoor factory environments and then delivered to site in complete modules. Figure 13 illustrates several modular buildings typically used as temporary site and holding offices in Singapore.

Figure 13 Typical Modular Buildings

In this type of building construction, the connection plays a crucial key role in transferring load and in maintaining structural integrity. The connections for steel structures are divided into bolted connections and welded connections. From these two basic components, numerous joint profiles are developed[29]. To enable inexpensive and fast construction of buildings, there are many proposals to utilize prefabricated building methodologies, including the steps of connecting adjacent units to one another in each level and connecting units in one level to corresponding units in at least one adjacent level that is vertically above or below the one level[30-32]. Based on the study of existing patents of interconnections of vertically and horizontally adjacent building assembly modules, a new type of up-down steel connector comprising I-beam, rectangular hollow section column and cruciform base is proposed as shown in Figure 14. The rectangular hollow section column and I-beams are welded to the cruciform base, and the bolts are used to connect the up and down beam-column connections.

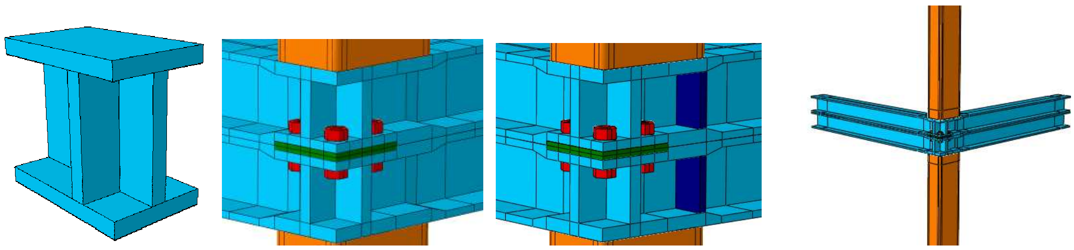

(a) cruciform base (b) connectior (c) strengthened connector (c) overview

Figure 14 Up-down Steel Connectors

Numerical analysis on several models are carried out using software ABAQUS to evaluate the compression and bending behavior of up-down steel connections. The numerical analysis includes four types of connections: L-Connection (LC), Strengthen L-Connection (SLC), T-Connection (TC) and Strengthen T-Connection (STC). Compared to connections LC and TC, two plates are added in SLC and STC to reinforce the up-down connection. The results indicated that for compression load the failure of up-down connector occurs at the up column and the endplate of cruciform base and for bending moment the failure occurs at the interconnection of the beam and cruciform base. For compression load, the ultimate strength of unstrengthen connector and strengthen connector is almost equal. Similarly, for bending moment, reinforced plate in strengthening connections SLC and STC has a little effect on the ultimate capacity of the up-down connector.

5. CONCLUSIONS

As an alternative to the 2D intensification requirements for future urbanization in Singapore, the concept of functional bridging buildings is put forward. This paper discusses the many challenges the FBB is going to face in terms of design and construction of its proposed structural form. Some preliminary studies regarding the choice of material and construction methods have confirmed that the proposed prototype for the FBB is feasible and workable.

REFERENCES

[1] BSI, hot rolled products of structural steels: part 6 technical delivery conditions for flat products of high yield strength structural steels in the quenched and tempered condition, BS EN 10025-6, in, British Standards Institution, London, 2004.

[2] R. Bjorhovde, Development and use of high performance steel, Journal of Constructional Steel Research, 60 (2004) 393-400.

[3] L. Gao, H. Sun, F. Jin, H. Fan, Load-carrying capacity of high-strength steel box-sections I: Stub columns, Journal of Constructional Steel Research, 65 (2009) 918-924.

[4] G. Shi, H. Ban, F.S.K. Bijlaard, Tests and numerical study of ultra-high strength steel columns with end restraints, Journal of Constructional Steel Research, 70 (2012) 236-247.

[5] X.-L. Zhao, D. Van Binh, R. Al-Mahaidi, Z. Tao, Stub column tests of fabricated square and triangular sections utilizing very high strength steel tubes, Journal of Constructional Steel Research, 60 (2004) 1637-1661.

[6] C. Miki, K. Homma, T. Tominaga, High strength and high performance steels and their use in bridge structures, Journal of Constructional Steel Research, 58 (2002) 3-20.

[7] H.V. Long, D. Jean-François, L.D.P. Lam, R. Barbara, Field of application of high strength steel circular tubes for steel and composite columns from an economic point of view, Journal of Constructional Steel Research, 67 (2011) 1001-1021.

[8] G. Pocock, High strength steel use in Australia, Japan and the US, Structural Engineer, 84 (2006) 27-30.

[9] R. Bjorhovde, M. Engestrom, L. Griffis, L. Kloiber, J. Malley, Structural steel selection considerations, Reston (VA) and Chicago (IL): American Society of Civil Engineers (ASCE) and American Institute of Steel Construction (AISC), 2001.

[10] P. Može, D. Beg, Investigation of high strength steel connections with several bolts in double shear, Journal of Constructional Steel Research, 67 (2011) 333-347.

[11] J.M. Ricles, R. Sause, P.S. Green, High-strength steel: implications of material and geometric characteristics on inelastic flexural behavior, Engineering Structures, 20 (1998) 323-335.

[12] A.M. Girão Coelho, F.S.K. Bijlaard, Experimental behaviour of high strength steel end-plate connections, Journal of Constructional Steel Research, 63 (2007) 1228-1240.

[13] H.K.D.H. Bhadeshia, R.W.K. Honeycombe, Steels: microstructure and properties, 3th ed., Elsevier Science & Technology, Oxford, United Kingdom, 2006.

[14] C.K. Lee, S.P. Chiew, J. Jiang, Residual stress study of welded high strength steel thin-walled plate-to-plate joints, Part 1: Experimental study, Thin-Walled Structures, 56 (2012) 103-112.

[15] Y.-B. Wang, G.-Q. Li, S.-W. Chen, The assessment of residual stresses in welded high strength steel box sections, Journal of Constructional Steel Research, 76 (2012) 93-99.

[16] T. Mohandas, G. Madhusudan Reddy, B. Satish Kumar, Heat-affected zone softening in

high-strength low-alloy steels, Journal of Materials Processing Technology, 88 (1999) 284-294.

[17] M.S. Zhao, Y.F. Jin, C.K. Lee, S.P. Chiew, Influence of welding to high strength steel plate-to-plate Y joints, part II: the heat affected zone, 11th Internation Conference on Steel Space and Composite Structures, Qingdao, China, 2012, pp. 311-315.

[18] AWS, Structural Welding Code, American National Standards Institute, Miami, 2008.

[19] T. Sakai, Y. Sato, Y. Nagano, M. Takeda, N. Oguma, Effect of stress ratio on long life fatigue behavior of high carbon chromium bearing steel under axial loading, International Journal of Fatigue, 28 (2006) 1547-1554.

[20] G.M. Castelluccio, J.E. Perez Ipiña, A.A. Yawny, H.A. Ernst, Fracture testing of the heat affected zone from welded steel pipes using an in situ stage, Engineering Fracture Mechanics, 98 (2013) 52-63.

[21] P. Yayla, E. Kaluc, K. Ural, Effects of welding processes on the mechanical properties of HY 80 steel weldments, Materials & Design, 28 (2007) 1898-1906.

[22] C.-H. Lee, H.-S. Shin, K.-T. Park, Evaluation of high strength TMCP steel weld for use in cold regions, Journal of Constructional Steel Research, 74 (2012) 134-139.

[23] J.D.M. Costa, J.A.M. Ferreira, L.P.M. Abreu, Fatigue behaviour of butt welded joints in a high strength steel, Procedia Engineering, 2 (2010) 697-705.

[24] H. Jiao, F. Mashiri, X.-L. Zhao, Fatigue behavior of very high strength (VHS) circular steel tube to plate T-joints under in-plane bending, Thin-Walled Structures, 68 (2013) 106-112.

[25] T. Hanji, K. Tateishi, S. Ono, Y. Danshita, S.M. Choi, Fatigue strength of welded joints using steels for bridge high performannce structures, in: 13th East Asia-Pacific conference on structure engineering and construction, Sapporo, Japan, 2013.

[26] The application of high strength steels for fatigue loaded structures: Sperle, J. O. and Nilsson, T. Proc. Conf. HSLA Steels: Processing, Properties and Applications, Beijing, China, 28 Oct.–2 Nov. 1990, pp 353–364, International Journal of Fatigue, 15 (1993) 536.

[27] X. Long, S.K. Khanna, Fatigue properties and failure characterization of spot welded high strength steel sheet, International Journal of Fatigue, 29 (2007) 879-886.

[28] X. Zhao, S. Herion, J. Packer, R. Puthli, G. Sedlacek, J. Wardenier, Design guide for circular and rectangular hollow section joints under fatigue loading, CIDECT, TUV Germany, (2000).

[29] Y.H. Lee, C.S. Tan and S. Mohammad. Review on cold-formed steel connections, The Scientific World Journal, Vol 2014.

[30] L. Don, V. Lissiak. Construction system for manufactured housing units. US 20020170243 A1 [P]. 2002.

[31] E. Katsalidis. Unitised building system. WO 2010031129 A1 [P]. 2010.

[32] R. P. Beattie. A multi- storey apartment building and method of constructing such building. WO 2012072971 A1 [P]. 2012.

12th International Conference on
Steel, Space and Composite Structures
28-30 May 2014, Prague, Czech Republic

RETROFITTING SOLUTION OF STEEL-CONCRETE SHEAR WALLS WITH STEEL ENCASED PROFILES USING CFRP

Daniel Dan[1], Alexandru Fabian[2], Valeriu Stoian[1] and Nagy Gyorgy Tamas[3]

*Politehnica University of Timisoara
Timisoara, 2 T. Lalescu, 300223, Romania
e-mail: daniel.dan@upt.ro

Keywords: Composite steel-concrete shear walls, seismic behavior, static cyclic tests, flexural stiffness, deformation capacity, CFRP

Abstract. *This paper presents the results of an experimental program, conceived in order to study the retrofitting of the reinforced concrete shear walls built up with steel encased profiles (CSRCW), using CFRP. The reinforced concrete (RC) elements were tested initially cyclic under lateral loads. The experimental program was performed on two shear walls with steel encased profiles tested prior to failure, thereafter retrofitted and retested. The retrofitting solution consists in rehabilitation of tested elements using Carbon Fiber Reinforced Polymer (CFRP) composites. Before retrofitting, the damaged specimens were repaired by replacing the crushed concrete with high-strength repair mortar. The experimental specimens were provided with CFRP strips and plates, to restore the bending resistance of the walls and to provide confinement effect at the ends. The aim of this study is to analyze the possibilities of using CFRP materials for strengthening the shear walls affected by seismic action. The retrofitting solution used and the failure mode is presented for each tested element. The behavior and envelope curves, ductility and energy dissipation and the stiffness degradation are presented comparatively for the strengthened and for the reference elements.*

1 INTRODUCTION

Composite steel-concrete walls (CSRCW) are developed from reinforced concrete walls by encasing additional structural steel members, usually at the extremities of the wall. As reinforced concrete walls, CSRCW elements are able to withstand high in-plane forces making them particularly suitable for earthquake resisting purposes. The research and specifications for composite steel-concrete walls show a limited level of knowledge related to the seismic behavior, energy dissipation capacity, stiffness degradation, failure modes and retrofitting solutions for damaged elements.

According to a literature survey the number of experimental campaigns on RC walls retrofitted by FRP composites is much less in comparison to the large number of programs involving other FRP-strengthened RC members on one hand and bare RC walls or wall-systems on the other. Of

---

[1] Professor, PhD, Civ. Eng., Politehnica University of Timisoara, Romania
[2] PhD, Civ. Eng., Politehnica University of Timisoara, Romania
[3] Lecturer, PhD, Civ. Eng., Politehnica University of Timisoara, Romania

particular interest for the present research are the programs with slender cantilever walls. In the framework of the CAMUS dynamic shaking table test series one of the wall system mockups was retrofitted by vertical CF sheets subsequently that it was damaged in a previous test (Sollogoub et al., 2000 [1]; Bisch and Coin, 2007[2], [3]). Also post-damage retrofitting was carried out on medium slenderness walls with aspect ratio of 1.5 (Antoniades et al., 2005 [4]) using carbon or glass FRP strips for flexural and GFRP wrapping for shear strengthening. Real scale slender walls were strengthened by horizontal CFRP strips and wrapping in the as-built condition (Paterson and Mitchell, 2003 [5]). Nagy-György et al. [6] (2005) investigated slender wall-systems retrofitted by CFRP strips

2 EXPERIMENTAL PROGRAME DESCRIPTION

An experimental program was conducted in the Civil Engineering Department at the Politehnica University of Timisoara, Romania. Five composite walls called (CSRCW1 to 5) and one reinforced concrete typical shear wall (CSRW6), were designed and tested in laboratory. From these five composite specimens, two were tested prior to failure, then were retrofitted using CFRP composites and retested.

The experimental program consists of six 1:3 scale elements (CSRCW1 to 6), designed using the principles from the existing European codes applied to composite steel-concrete elements. Specimens CSRCW2 and CSRCW4 were selected for retrofitting using CFRP composites. These elements were tested prior to failure and after retrofitting were tested again in order to investigate the strengthening effect and efficiency related to the seismic behavior. The retrofitted elements were renamed CSRCW2_R and CSRCW4_R. The experimental specimens had 3000 mm height, 1000 mm width and 100 mm in thickness. The design details of the two selected specimens for strengthening are presented in Figure 1.

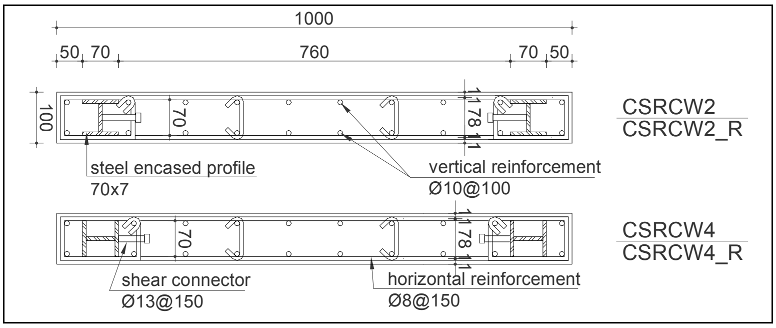

Figure 1: Experimental elements details

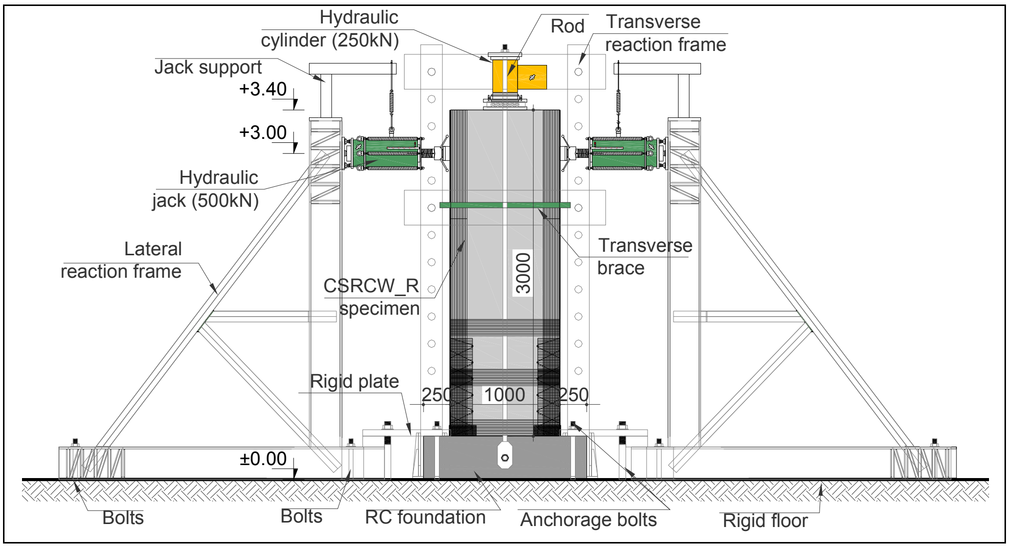

Figure 2: Test set-up and testing equipment

The specimens were tested under quasi-static reversed cyclic horizontal loads and constant vertical load. A general view of the testing equipment is presented in Figure 2.

The recommended ECCS short testing procedure was used, as it defines the loading levels as submultiples and multiples of the elastic displacement. The horizontal forces were applied under controlled cyclic displacements until the strength of the specimens decreased to 85 % of the peak horizontal load.

3 BEHAVIOR OF REFERENCE ELEMENTS

The tested composite shear walls showed a bending behavior. In the initial loading stages, horizontal cracks appeared in the tensioned zone due to the transfer of the stresses between steel and concrete. Diagonal cracks appear in the cycle when the elastic limit of the element was attained and developed in the specimens until a series of rhombic concrete blocks separated by these inclined cracks resulted. The measured strains indicated yielding of the vertical reinforcing bars located at the extremities and yielding of the steel encased profiles. In the case of the two selected elements for retrofitting (CSRCW2 and CSRCW4), the test was stopped at a displacement level of approximate 85 mm (3% drift). At that moment, the compressed concrete crushed and the strains in the vertical reinforcements and in the encased steel profile of 1.98% respectively 1.62%. A complete description related to the behavior of the reference elements is presented in (Dan et al. [7], 2011).

4 RETROFITTING SOLUTIONS

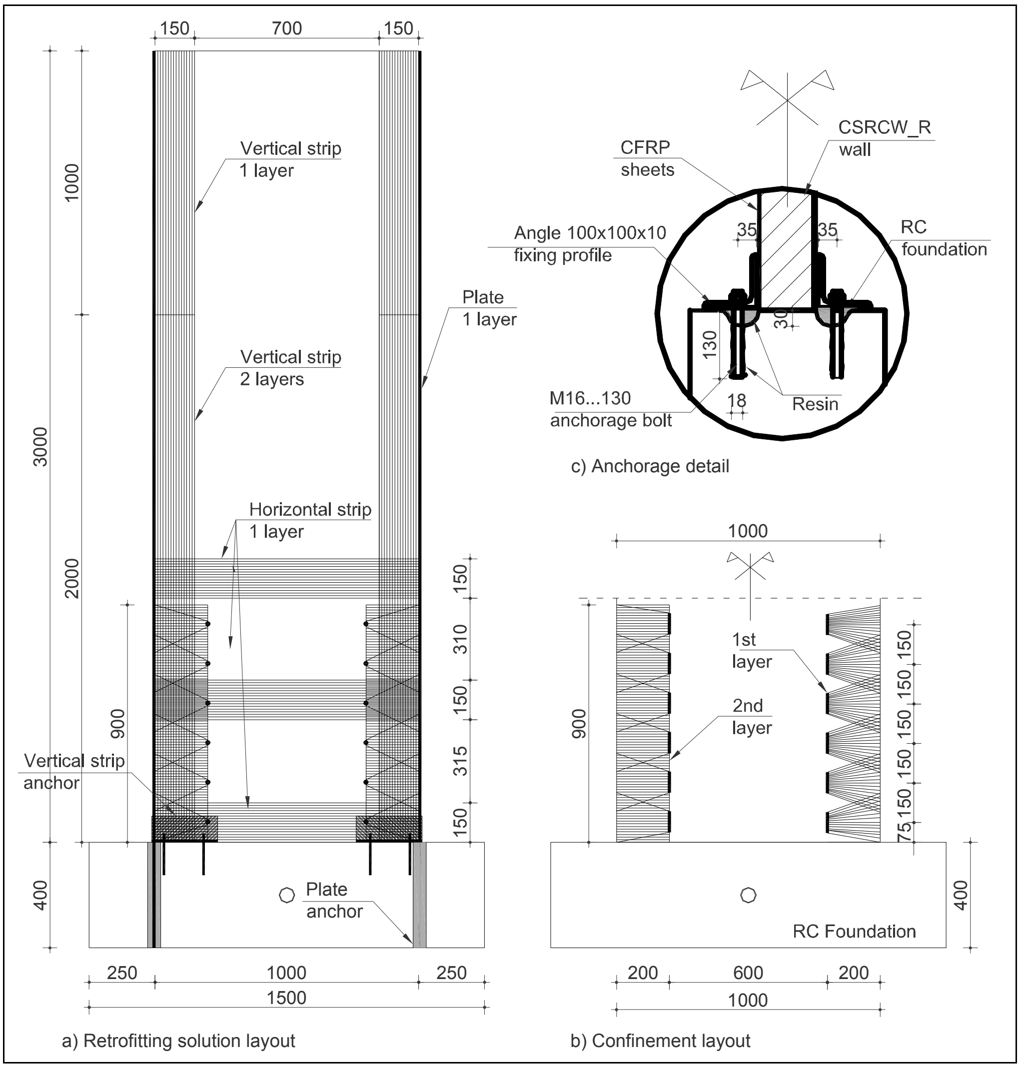

Figure 3: Retrofitting solution layout and details

Based on the behavior and failure mode observed during the test performed on the reference elements, the strengthening strategy was divided in three directions: (1) to offer flexural capacity along the edges, (2) to provide confinement effect and (3) to increase the shear capacity of the wall, especially at the wall base, (Demeter et al.[8], 2010).

The retrofitting of the specimens was performed by Externally Bonded Carbon Fiber Reinforced Polymer Reinforcement (CFRP EBR), symmetrically on both faces of the wall, in order to restore the initial load bearing capacity of the reference elements. The used composites were two types, utilizing unidirectional carbon fiber sheets in form of strips with 150 mm and 200 mm width, as well as plates of 50 mm width. The mechanical characteristics of these materials were in conformity of the producer’s datasheets given as mean values.

Before retrofitting, the damaged specimens were repaired by replacing the crushed concrete with high-strength mortar. The substrate preparation consisted in grinding the concrete surface, rounding the edges for confinement, drilling holes and creating the anchorage zone and vacuum-cleaning.

A description of the order, form and position and the application procedures for the walls are presented below. As shown in Figure 3, the retrofitting for flexure was placed vertically along the edges, and consisted in strips and plates. The 150 mm width strips were placed on the front and rear faces of the wall margins. The first layer was applied on the entire height of the specimen, while the second layer was disposed up to 2000 mm. The plates were placed on the sides of the wall in one layer on the whole height of this. The strips were anchored with a special device, as is depicted in Figure 3c, the plates being anchored in a hole created through the foundation, filled with epoxy resin. In the second step the stirrup-like confinement was realized, using 200 mm width strips. The 150 mm width shear strips were placed horizontally in one layer, anchored through superposing with 150 mm at the ends.

4 EXPERIMENTAL TEST RESULTS

The behavior of the two retrofitted and retested specimens under reversed cyclic lateral loads was similar with the behavior of the reference elements under similar load conditions. The behavior of the two retrofitted and retested specimens CSRCW_R, under reversed cyclic lateral loads, showed an expected behavior, in accordance with the design process. The anchorage provided for CFRP strips and plates were efficient, and no weakening of anchorage was observed during the tests.

For the two retrofitted elements, the obtained load displacement hysteretic responses are presented in Figure 4. The hysteretic response shows a ductile behavior. If the hysteretic curves are compared for the reference element with those obtained for the retrofitted elements it can be observed that the area bounded by the hysteretic loop of each performed cycle is smaller for the retrofitted elements than for the reference elements. The dissipated energy obtained for the retrofitted elements is smaller than for the reference elements. The hysteretic curves show that the retrofitted elements recovered the initial strength, in the positive loading cycle direction, and were stronger than the reference elements in the negative loading cycle direction.

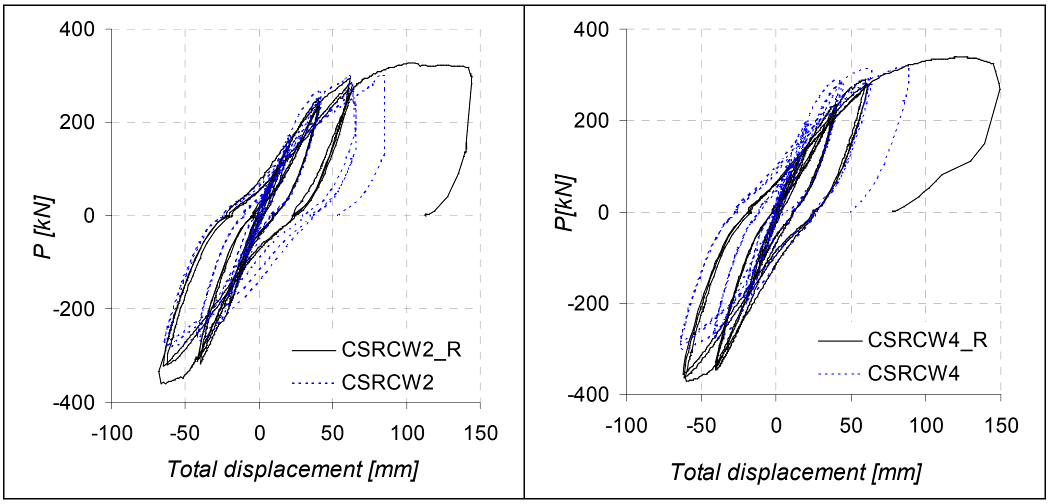

Figure 4: Load – displacement response for retrofitted elements

In terms of stiffness was observed that the initial stiffness of the retrofitted elements relatively to the initial stiffness of the reference elements is approximately 80%.

The strain measurements are fundamental in analyzing the response of an experimental element as it reveals precisely the local behavior. In the case of this experimental research, it was considered important to monitor the strains in the vertical and horizontal reinforcements, vertical steel profiles, vertical and horizontal CFRP strips and vertical CFRP plates applied at the edges. Related to the steel encased profiles and vertical reinforcements, the measured strains exceeded the yielding strains, these components of the composite wall contributing to dissipating the energy. Related to the strains measured on the vertical CFRP plates, placed on the side edges of the specimens, it was observed that, in both cases the CFRP plates were activated from the beginning of the test and worked very well during testing. Also the CFRP vertical and horizontal strips were activated from the beginning of the test and worked very well until the failure of the specimens occurred. Although the measurements did not indicate high strain values, the confinement effectiveness was evident.

5 FAILURE CONDITIONS

The failure of the retrofitted specimens is characterized by the fracture of the vertical strips and vertical plates at the base of the element, simultaneously with the tearing of the vertical reinforcements. In element CSRCW4_R also the steel encased profile fractured in tension. The confinement from the base of the element made by CFRP failed due to cyclic loading before the fracture of the vertical CFRP composites. Locally the horizontal strips debonded in their middle part (Fig. 5c) before the failure of the element. The strains measured before debonding on these composites reached only 0.35%. Simultaneously the vertical strip debonded above the level of the last horizontal strip (Fig. 5d) which practically provided its confinement. Also local debondings due to the substrate preparation technology were observed for the horizontal strips. All the anchorage systems provided for the vertical plates and for the strips behaved excellent, no slip between the composite material and the support was observed in the anchorage zone. The crack pattern and the hysteretic response diagrams show a flexural-shear behavior during the applied cyclic load. In Figure 5 are presented some aspects with the failure conditions of the tested specimens.

a) Confinement fracture

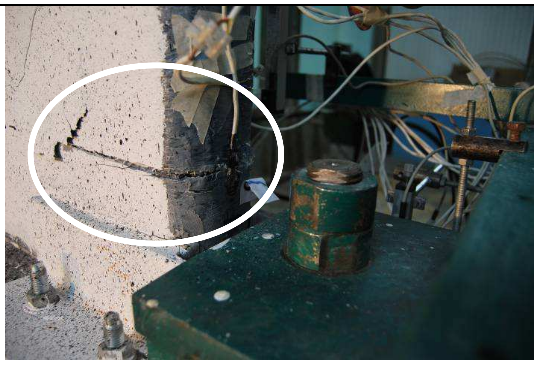

b) Fractured strip and plate

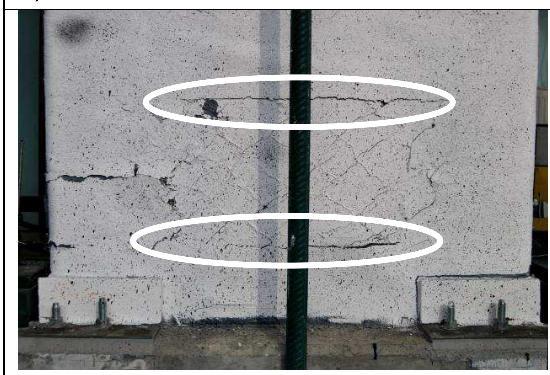

c) Debonding of the horizontal CFRP strips

d) Debonding of the vertical CFRP strips

Figure 5: Failure details of retrofitted specimens

6 CONCLUSIONS

The tested CSRCW and CSRCW_R behavior was in bending up to failure, with no major influence of the shear effects.

The strengthening solutions for composite steel concrete walls using CFRP composites are efficient in terms of load bearing capacity, the ultimate load of the reference element being restored.

The use of the horizontal FRP strips, to confine the ends of shear walls flexural strengthened with vertical strips and plates, assisted in preventing buckling and debonding.

The confinement of the compressed concrete zones from the edges was efficient.

The initial stiffness of the retrofitted elements was about 80% of the initial stiffness of the reference element and decreased more rapidly than for the reference elements during the performed cyclic tests.

The energy dissipation capacity until the fracture stage is smaller for the strengthened elements than for the reference elements.

The failure mode of the retrofitted elements was similar with the failure mode of the other three composite elements which were tested up to failure. The failure mechanism consists in the compressed concrete crushing while the tensioned steel and CFRP strips and plates fractured.

The anchorage provided for CFRP strips and plates were efficient, no weakening of anchorage has been observed during the tests.

The presented work was supported by CNCSIS – UEFISCSU project number PNII - IDEI ID_1004, Contract 621/2009, entitled „Innovative Structural Systems Using Steel-Concrete Composite Materials and Fiber Reinforced Polymer Composites”.

REFERENCES

[1] Sollogoub, P., and Queval J-C, *“Essais (CEA),” Projet CAMUS 2000 Rapport final, Vol. 6, Section 4,* Paris, (in French), (2002).

[2] Bisch, P. and Coin, A., “*The CAMUS research,”Proc. of the Eleventh European Conference on Earthquake Engineering*, Paris, CD-ROM, Vol. 2, (1998).

[3] Bisch, P. and Coin, A, *“The CAMUS 2000 research,” Proc. of the Twelfth European Conference on Earthquake Engineering*,London, CD-ROM, (2002).

[4] Antoniades, K.K., Salonikios, T. N. & Kappos, A.J, *Evaluation of hysteretic response and strength of repaired R/C walls strengthened with FRPs*. Engineering structures, 29, pp. 2158 – 2171.(2007).

[5] Paterson, J. and Mitchell, D, *Seismic Retrofit of Shear Walls with Headed Bars and Carbon Fiber Wrap*. ASCE Journal of Structural Engineering. 129:5, 606-614. (2003).

[6] Nagy-György, T., Moşoarcă, M., Stoian, V., Gergely, J. & Dan, D, *Retrofit of reinforced concrete shear walls with CFRP composites. Proceedings Keep Concrete Attractive*, 2, pp. 897-902. (2005).

[7] Dan, D., Fabian, A. & Stoian, V, *Theoretical and experimental study on composite steel–concrete shear walls with vertical steel encased profiles*, Journal of Constructional Steel Research, 67, pp. 800 – 813. (2011).

[8] Demeter, I., Nagy-György, T., Stoian, V., Dăescu, C. & Dan, D, *Seismic performance of precast RC wall panels with cut-out openings retrofitted by externally bonded CFRP composites*. Proceedings of 3rd fib International Congress (fib 2010), PCI, Paper No. 593 (2010).

12th International Conference on
Steel, Space and Composite Structures
28-30 May 2014, Prague, Czech Republic

STRAIN GAUGE MEASUREMENTS TO SUPPORT RESEARCH OF STEEL STRUCTURES

Hans De Backer*, Amelie Outtier*, Ken Schotte*, Dries Stael*, Wim Nagy* and Philippe Van Bogaert*

*Department of Civil Engineering, Ghent University,
Technologiepark Zwijnaarde 904, 9052 Zwijnaarde, Belgium
e-mail: Hans.DeBacker@UGent.be

Keywords: Strain gauges, tubular arch bridges, fatigue, viaducts, movable bridge, monitoring, temperature loads

Abstract. *This keynote paper discusses a number of research cases where strain gauge measurement, on site and in laboratory, where used to support ongoing research projects. A first project deals with the fatigue behavior of tubular arch bridges. As a second example, the expansion of a large concrete viaduct with a steel box girder section is discussed. A third project which is discussed in detail deals with the refurbishment of some steel port infrastructure in Belgium. This article gives an overview of these experiences and on the lessons learned concerning optimal placement of strain gauges, how to design optimal laboratory tests, possible noise sources and how to deal with them and the influence of unexpected force behavior. Furthermore, the most important results of all test cases are discussed in short.*

1 INTRODUCTION

When studying the behavior of steel and composite structures, it often becomes necessary to resort to testing and monitoring of certain structural parameters. This keynote paper discusses a number of research cases where strain gauge measurement, on site and in laboratory, where used to support ongoing research projects. The area of application is extremely wide.

A first project deals with the fatigue behavior of tubular arch bridges. Tubular arch bridges comprise many welded tubular nodes, which are the most critical parts, since they reduce the fatigue strength of the bridge. Due to geometric discontinuity and the welding process, various stress concentrations are introduced at the nodes, making this type of bridge prone to fatigue damage caused by the varying traffic loads. High peak values of stresses, so-called hot spot stresses, are reached near the weld toe of the nodes. The objective of the present research is to increase the fatigue strength of these nodes or to reduce the hot spot stresses. The study is supported by a series of strain gauge tests during load tests on a recently build tubular arch bridge and by laboratory fatigue testing of six tubular nodes.

As a second example, the expansion of a large concrete viaduct with a steel box girder section is discussed. The 523 m long historic viaduct crossing the Pede valley in Belgium consists of 16 three-hinged reinforced concrete arches with a span of 32 m and a maximum height of 20 m. With respect to the protected work of art, two additional lateral fly-overs consisting of steel box girders with variable hollow section are integrated in the existing viaduct. This paper shows the results of the detailed monitoring program verifying the design and behavior of the newly built superstructure. Extensive strain measurements were performed during a two-day load test, together with acceleration measurements in order to evaluate the dynamic response of the structure. In addition long term strain monitoring is carried out in order to study the effect of temperature gradients on the closed steel box girders of the fly-overs.

A third project which is discussed in detail deals with the refurbishment of some steel port infrastructure in Belgium. Apart from the measurements on a set of lock doors, this is mainly concerned with the refurbishment of part of the counterweight structure of one of the bascule bridges crossing one of the most important locks allowing entrance to the Port of Antwerp, Belgium. Because of uncertainty about the size of the stress cycles in the movable part during bridge operation, a number of strain gauges are installed during renovation. Afterwards, stress build up will be monitored during the remaining construction phases, as well as during test operation of the bridge to verify design assumptions. Monitoring will continue afterwards during the first few months of operation.

2 FATIGUE OF TUBULAR ARCH BRIDGES

2.1 Introduction

Circular hollow sections are used in various types of modern bridges. The use of tubes offers structural advantages since the bending stiffness, strength and buckling resistance is equal in all directions. High torsion stiffness and a high strength-to-weight ratio are additional advantages of circular hollow sections. Although tubular arch bridges are highly appreciated because of their aesthetic value, they are considered to be costly, mainly due to the use of welded nodes. Welded nodes can be assembled thanks to modern cutting, preparation and fabrication processes making these bridges more feasible and competitive. The fatigue strength of these structures is important because high stress concentrations are reached near the weld toes of the nodes. These are due to geometric discontinuities and to the welding process, thus making this type of bridge prone to fatigue damage caused by the varying traffic loads. In tubular bridges, the struts, connected to the main tube also introduce local bending of the arch tube, according to the ratio of the tube diameters. Consequently these welded nodes are the weakest parts and determine the global strength of the structure. The hot spot stresses must be kept sufficiently low to increase the fatigue resistance of the welded nodes. The thickness of the tubes must often be increased to decrease the in-plane deformation of the main tube, reducing the hot spot stresses in the weld. This means that the main tube is larger than strictly necessary and is not used up to its actual capacity. The larger main tube increases the weight and the cost of the bridge, making this type of bridge uninteresting. In addition, thicker tubes also show lower fatigue strength[1]. A local reinforcement of the main tube at the welded nodes without damaging the aesthetics of the structure is being used and improves the design of the tubular arch bridge.

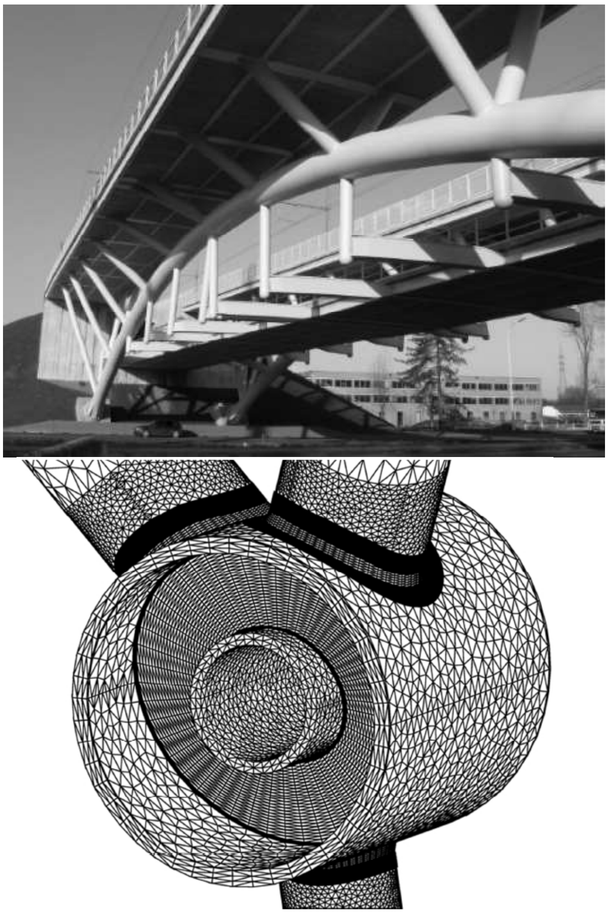

Figure 1: Woluwe Lane Bridge: overview (left) and FE model of a node (right)

The Woluwe Lane Tubular Arch Bridge[2] is a three-track elevated railway bridge, as shown in Figure 1. It consists of two tubular arches, each having a diameter of 1.2 m, supporting the two upper level railway tracks with tubular strut members. The central track is suspended in-between the arches. The arch span equals 72 m. The rise of each arch is limited to 9 m. At each node, two secondary strut tubes exist, with a diameter of 0.55 m, connected to the main arch. The bending moments in these vertical tubes are higher and no longer negligible, making this bridge an example of a framework tubular bridge. Each node contains two internal diaphragms to reinforce the main tube. The double diaphragm is able to transfer bending moments from the struts to the main arch. Due to in-plane ovalization stresses occurring in the edges of the diaphragms, additional stiffening of the diaphragms themselves has been provided, by a small tube through the diaphragms. The latter are also not perpendicular to the main tube. They continue in the direction of the strut tubes. Figure 1 shows a cross-section of an actual node as it has been constructed for the Woluwe Lane Bridge.

2.2 Strain measurements

In order to validate the numerical finite element calculations, strain gauge measurements were carried out on the Woluwe Lane Bridge in March 2011 and March 2012. The strain gauges are uniaxial, have a lead resistance of 120 ohm and a measuring grid of 1.5 mm. The strain gauges are connected with shielded and twisted cables to the measurement system. Three wires are soldered to each strain gauge, because a quarter bridge connection has been chosen for the Wheatstone bridge. The influence of the cable length on the measured resistance is filtered by using these three wires. The temperature influence is not filtered out, because the measurement time is very short. In this case the influence of the temperature on the measured resistance is negligible. The strain gauges are connected to a system 6000 of Vishay. It is a complete system that consists of a scanner, measuring cards and software.

A total of 454 strain gauges were installed on the arch and on the vertical struts. The majority of the strain gauges were placed in the vicinity of three welded in order to measure the hot spot stresses. Close to the intersection of a strut with the main arch, 48 gauges are installed, 24 on the arch and 24 on the strut. They are located in eight groups of three gauges, spread out equally around the perimeter of the weld between strut and arch as shown in Figure 2 (left). This is repeated for six strut-arch intersections (two intersections per node) in total. The three uniaxial gauges on the arch are each positioned in a direction perpendicular to the weld and between the borders of the extrapolation area. They are placed in a row at a distance of exactly 10 mm (Figure 2 (middle)). The strain gauges on the strut are positioned in a direction parallel to the strut axis. Three gauges are needed because a second order polynomial needs to be fitted through the measuring points in order to extrapolate to the hot spot strain value. The remaining strain gauges will be placed on the arch and struts at larger distance from the nodes. These gauges will measure the nominal strains. 22 sections are equipped with four gauges equally spread across the circumference of the tube. Two cross-sections between each welded node are needed allowing linear extrapolation of the nominal strain to the welded nodes (Figure 2 (right)).

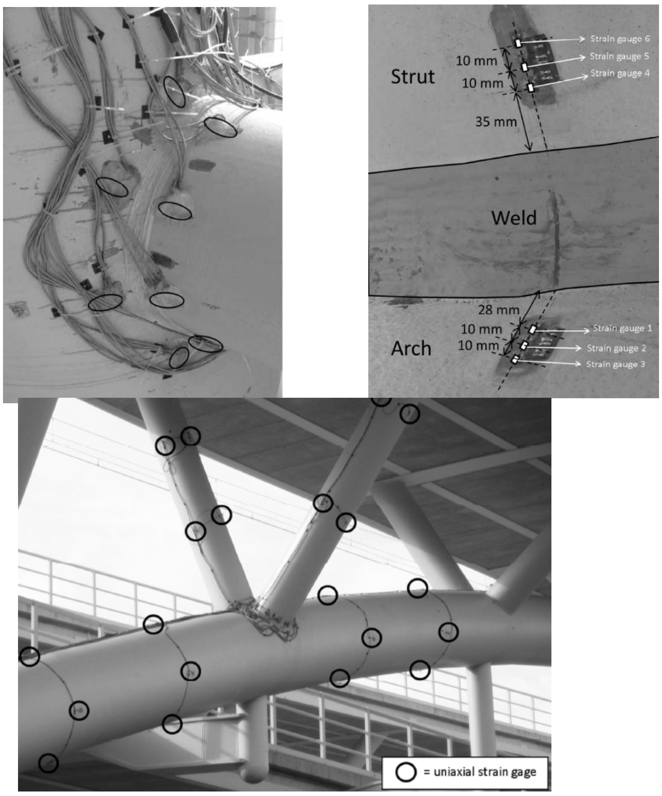

Figure 2: Location of the uniaxial strain gauges around the weld between strut and arch (left), location of the uniaxial strain gauges close to the weld (middle) and locations of the uniaxial strain gauges for measuring nominal strains (right)

After concreting of the bridge decks, static load tests with lorries have been carried out. The advantage of lorries is that they can be placed in various positions on the decks. Exactly 30 lorries have been placed in 5 different positions in order to measure the strains. All lorries were weighed before the load test, hence the total weight of each lorry is exactly known. Before the lorries drive onto the decks, the strain gauges have been calibrated and zeroed. Then the strains are measured continuously during the positioning of the lorries. All lorries are correctly positioned, this load position is held for a short period, so that a constant strain is measured for that position. During one measurement multiple positions have been measured in sequence. The strain difference between the zeroing and a static position is retained. Hence, for each position one strain value has been determined for each strain gauge. The results of three uniaxial strain gauges, installed on arch AL close to the weld of node ALK09, are shown in Figure 3. These three gauges are numbered as shown in Figure 2 (middle). One can see clearly that the strain increases rapidly when one comes closer to the weld toe. The hot spot stress method is then applied to the three constant strain values measured during position 3. The measurements also show that both arches work independently. The strains on one arch are negligible when the other arch is loaded (position 5 on Figure 3).

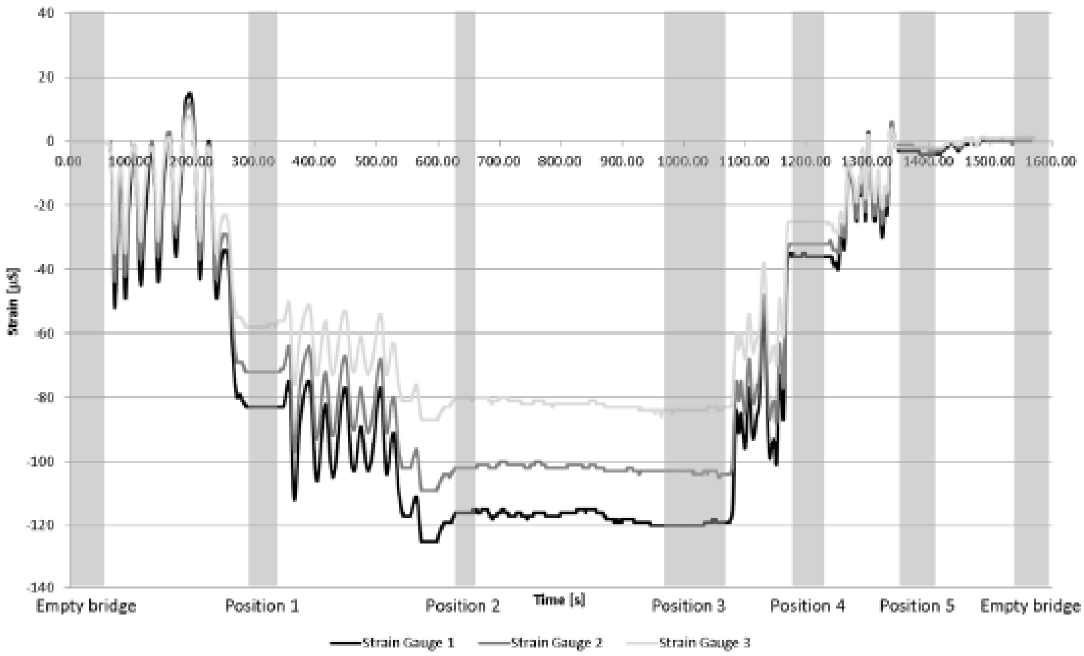

Figure 3: Measured strains in three gauges caused by various positions of the lorries

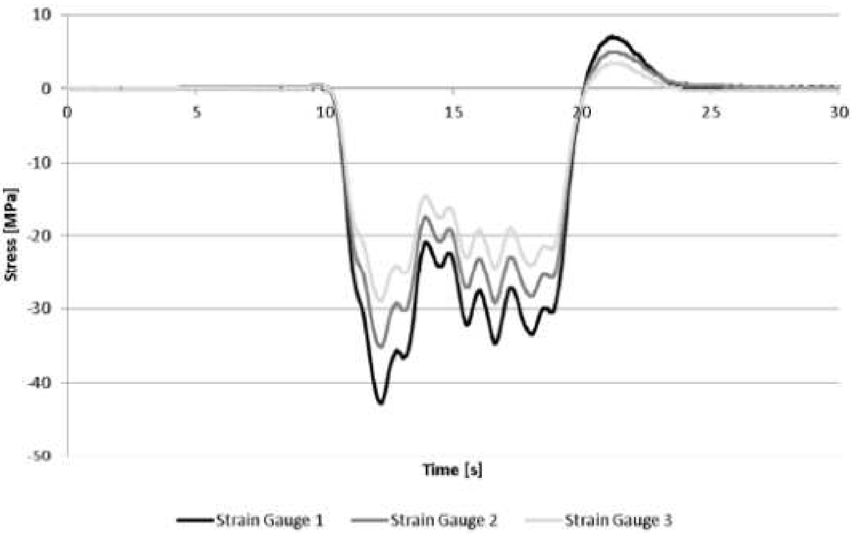

Figure 4: Measured strains in three gauges due to one train passage

After installation of railway tracks on the upper bridge decks a second load test was carried out with a small freight train. The advantage of using a loaded train is that the loads are higher and the measured strains are representative for the strain that will occur in the structure during its lifetime. The freight train consists of 2 locomotives and 5 fully loaded ballast wagons in between. The axle load of each wagon is known, because these were weighed before the load test. The strain gauges are also calibrated and zeroed before the train drove with a small and constant speed across the bridge deck. The measurement was stopped after the train had completely left the bridge. Only bridge deck AL has been loaded, because only one track was available for this test. Hence, strain gauges on arch AL have been measured only. The strain gauges on the other arch were already removed. For each strain gauge continuous strain values have been registered and can be used to execute a rainflow count, in order to determine the fatigue damage due to one load train passage. The results of the same three strain gauges as in Figure 3 are shown in Figure 4.

2.3 Validation of FEM

In order to validate the finite element model, the strain measurements of the Woluwe Lane Bridge are compared to the FE calculations. The measured strains are converted to stresses using the 2D Hooke's law. It is assumed that the strain in the direction perpendicular to the weld is significantly larger than the strains in the other direction. Since the Poisson's ratio equals 0.3 for steel, the equation is reduced to $\sigma x = 1.1 \cdot E \cdot \varepsilon x$. Investigations on a large database[4] have shown that a ratio of 1.17 is more appropriate, this value being used to convert the strains into stresses. The converted stresses are compared to the stresses determined with the FE models. First all SCFs of a node of the Woluwe Lane Bridge are determined with the alternative method[3]. Then a wireframe model of the whole bridge is used to calculate the forces in the node. Only the steel tubes and the concrete decks of the bridge are modelled. The tubes are modelled with linear elements and the bridge decks with 2D triangular elements, on which the lorry loads or train loads are placed. The forces determined with this wireframe model are then transformed to nominal stresses. These nominal stresses multiplied with the corresponding SCFs render the hot spot stresses of the node. This method also allows calculating the stresses on the measured locations close to the weld instead of the hot spot stresses located on the weld toe. This is done by replacing the hot spot stresses with stress values at a certain distance from the weld toe when determining the SCFs. The 3D FE model is not directly placed inside the loaded wireframe model because this gives wrong stress values. The nodal forces in a wireframe model are different from the forces in the same wireframe model in which a 1D node is replaced by a 3D FE model. A simple wireframe node has not the same stiffness as a 3D FE node. Hence it is more accurate to derive the forces from a complete wireframe model, converting them to nominal stresses and multiplying them with the corresponding SCF. This method also allows to calculate fast the stress ranges caused by a moving train load, because a complete wireframe model with a large number of load cases requires much less computation time than a wireframe model with the same load cases with a 3D FE model inside.

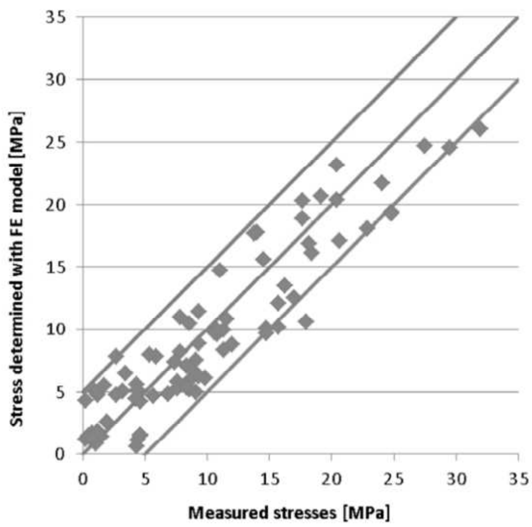

Figure 5: Comparing measured and computed stresses of node ALK09

The strains of node ALK09 that are measured when the bridge deck above the node is loaded with 10 lorries are compared to the computed stresses. To determine these stresses, the point loads of the 10 lorries are placed on bridge deck AL of the wireframe model. All measured and determined stress values of node ALK09 are plotted in Figure 5, which clearly shows a good agreement between the calculated and measured values. The scatter of some values is due to the difficult circumstances encountered during installation of the gauges. The upper and lower bound lines show the difference between calculated and measured values to be mostly smaller than 5 MPa. This deviation is because the real location and orientation of the strain gauges does not always correspond to the intended location and orientation. Shifting a gauge closer or further to the weld causes a large difference in stress because of the steep stress gradient close to the weld. Also, shifting the gauge in circumferential direction causes a stress difference. Because three individual strain gauges were used, it is also not certain that the gauges are perfectly aligned in a direction perpendicular to the weld or parallel to the strut axis. Finally, the positions of the axle loads of the lorries on the bridge deck are approximated. Due to all of this, it can be concluded that the model is validated and can be used to calculate the hot spot stresses of this node for various loading conditions.

In order to determine the stresses with the FE model, the moving freight train load is placed on the bridge deck of the wireframe model. The axle loads of the lorries could be placed directly on the concrete deck. The train loads are being spread across the concrete deck due to the ballast layer, the sleepers and the rails. This distribution is taken into account by making use of Eurocode 1[5]. The axle loads of the train are divided in multiple point loads across the bridge deck of the wireframe model. The comparison in Figure 6 (left) also shows that there is a good agreement between the calculated and measured stresses of strain gauge 1 located on arch AL close to node ALK09. The ballast wagons coincide almost perfectly with the computed values. The loads of the locomotives seem to be overestimated by the FE calculations. The computed stresses are higher than the measured stresses. The locomotives were weighed before departure from the depot, but because they run on fuel, the load was probably decreased when the strains were measured. The train has already travelled a significant distance. The difference between computed and measured stresses due to the train loads is smaller than the difference due to the lorry loads. The train load test has fewer uncertainties because the position of the train loads is well known: the tracks have a fixed position on the bridge deck and the distance between the axle loads is registered. Furthermore the loads are more spread out thanks to the rails, sleepers and ballast.

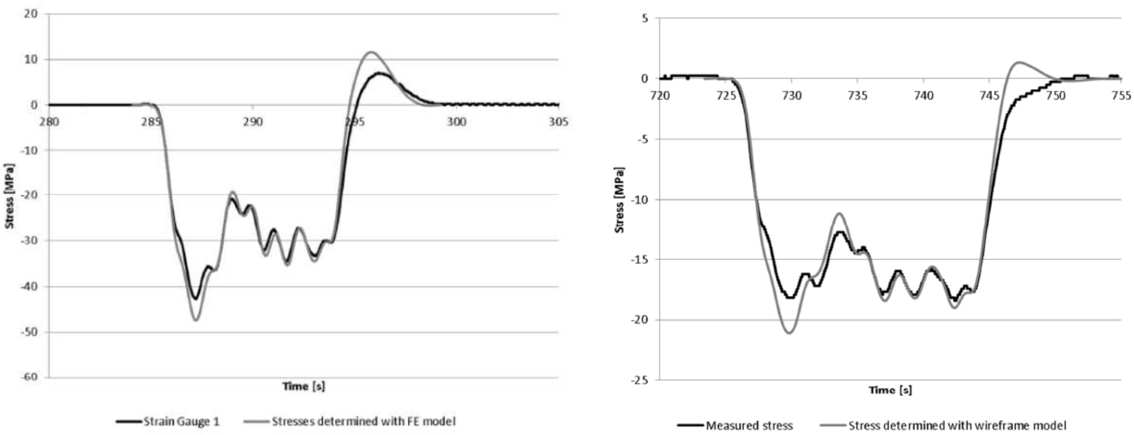

Figure 6: Comparing measured and computed stresses close to weld toe during the train load (left) and comparing measured and computed nominal stresses caused by the train load (right)

The computed nominal stresses are also compared to the measured nominal stresses in the arch at a distance from the nodes. The calculated normal forces and bending moments of the wireframe model have been converted to stresses and are compared with the measured strains on the arch during the train load. This comparison shows that the forces in the wireframe model are sufficiently accurate and the wireframe model can be used to calculate the forces in the bridge (Figure 6 (right)).

2.4 Conclusions

The strain measurements show that the stress increases rapidly when coming closer to the weld toe. However these stresses remain small enough thanks to the internal diaphragm stiffening. It has also been verified that the two arches work independently as was assumed during design. If the measured strains are compared to the finite element calculations, then a good agreement between the measured and determined stress values is demonstrated. The small difference is caused by the difficult circumstances during installation of the strain gauges and because the loads are approximated, especially when using different lorries. Also converting accurately the strains into stresses requires rosette gauges. Uniaxial gauges measure only the strain in one direction. To know the entire stress state of one location, the strains in three directions must be measured. However replacing all uniaxial strain gauges by rosettes requires much more time to install and increases the number of measured values by three. Furthermore, because the stresses grow rapidly close to the weld, very compact rosette gauges should be needed.

3 REFURBISHMENT OF HISTORIC VIADUCT

3.1 Introduction

As part of a large-scale project in order to improve the accessibility of the Belgian capital by train, the existing railway line between Brussels and Ghent is expanded from 2 to 4 tracks over a length of 25 km. This line crosses the valley of the river Pede by a 523 m long historic viaduct, built in the 1930's[6]. In those days the viaduct was chosen over large backfills in the valley due to poor soil conditions. The structure consists of 16 three-hinged reinforced concrete arches with a span of 32 m and a maximum height of 20 m. Four arches form an independent group, as they are separated from the rest of the viaduct by double pier structures, allowing for compensation of the thrust force of each group. Figure 7 gives a front view of the concrete structure.

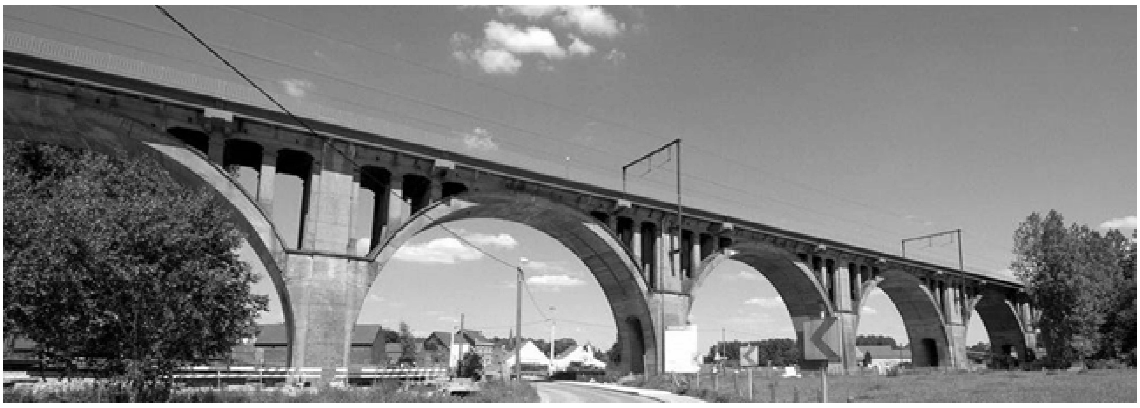

Figure 7: Front view of the historic Pede viaduct

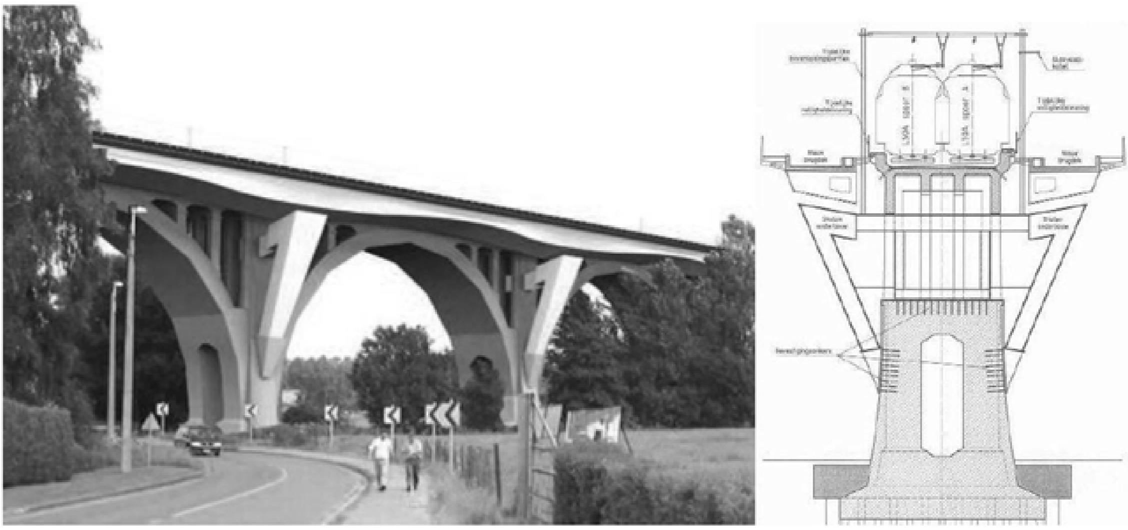

Figure 8: Final design of the integrated steel fly-overs

The viaduct is a benchmark in the rural environment through its dominance midst the gentle slopes of the Pede valley. Extension of the railway facilities to 4 tracks needs to widen the existing structure by two additional lateral viaducts, with respect to the protected work of art. Therefore the arch structure and the existing piers should be left apparent as much as possible. The arches should keep their function and continue to behave as a four-span group. Important guidelines in making the new design were the contrast of old and new technology, keeping the four-span static behavior with the repetition of 32 m spans and leaving the characteristic view of the hollow piers. In order to comply with these conditions, the new structure must not be of imposing character.

After consideration of various alternatives during the pre-design stage, the final design consists of a steel superstructure with variable hollow sections supported by integrated cantilever pier structures, as shown in Figure 8.

The steel box girders of the superstructure are continuous over 4 spans, in accordance with the existing arches. The box section is characterized by waving patterns, both in the plan view as in the cross-sections. The upper flange of the box section is constant and stays horizontal along the structure's length. The lower flange however has a variable width of minimum 3,65 m at the piers and maximum 5,15 m at the span center. The lower flange rises according to a sine wave from the supports towards the span center obtaining less height and is twisted about a horizontal axis as it becomes wider. As a result, the vertical box web near the existing concrete arches has variable height, whereas the outer web plate shows torsion along the bridge axis. This creates a waving pattern of the steel structure complying with the existing arches, both in horizontal plane as in the front view, as illustrated in Figure 9. To raise the torsion stiffness, internal diaphragms of 20 mm thickness on a distance of approximately each 2 m were installed. An additional stiffness is realized by providing a concrete deck plate of 0,25 m thickness, which allows for spreading the traffic loads and limiting local fatigue problems of the steel structure. The total construction height remains limited in order to guaranty a full front view on the existing viaduct.

The new superstructure is supported by steel cantilever structures, fixed to the existing piers. Each vertical pier has a rectangular box section in a conical shape and fades into the lower part of the concrete pier. Two cantilever piers are joined by a transverse internal steel framework located in the hollow parts of the existing piers to ensure horizontal stability in transverse direction. As for the horizontal stability in longitudinal direction, the new superstructure is made continuous over 4 spans as mentioned earlier, in order to lead the horizontal traction and braking forces to the double pier structures.

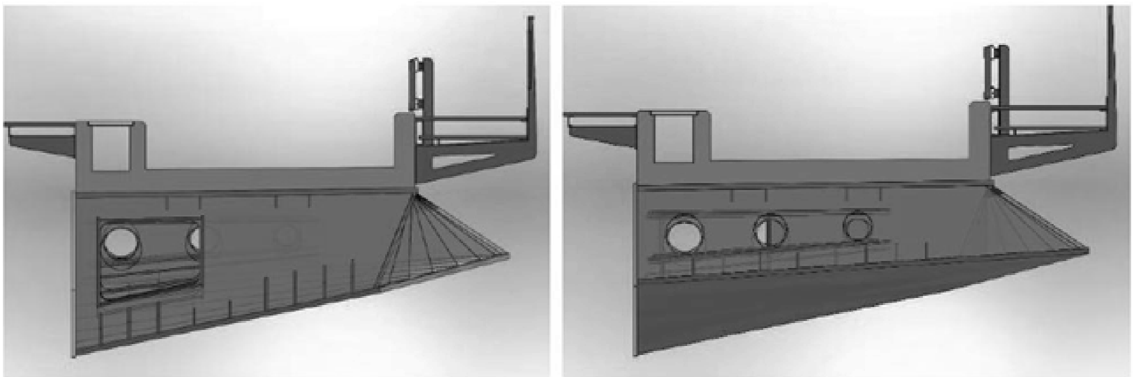

Figure 9: Cross-sections of the steel box at the supports (left) and at mid span (right)

Since the new superstructure is supported by a construction which is fixed to the existing piers, strengthening of the existing foundation was needed due to the additional load. This was realized by grouted piles drilled around the existing footings. The grouting piles are designed to replace the existing concrete piles and are founded on a deeper level to carry the additional load. After drilling of the grouting piles, the existing foundation slab was extended by a new concrete slab and post-tensioning cables were used to put together both the new and existing slab.

3.2 Measurements

In order to verify the design and behavior of the newly built superstructure, a monitoring program was set up comprising several components. Extensive strain measurements were performed during a two-day load test on the steel fly-overs as well as their supports. At the same time the dynamic response of the structure was evaluated by acceleration measurements. Furthermore long term strain monitoring is carried out in order to study the effect of temperature gradients on the closed steel box girders of the fly-overs.

The structure was equipped with a total of 326 strain gauges, of which 216 were attached to the steel superstructure and 110 were installed on the newly built piers and their transverse steel framework. Measurement points were concentrated in several cross-sections of the fly-overs on both flanks of the historic bridge, mostly monitoring strains of the lower flange and vertical web plates in longitudinal direction of the viaduct. However, some strain gauges were used to monitor the diaphragms above the supports or the longitudinal stiffeners of the lower flange. Because of the danger and inconveniences of working on greater heights, all strain gauges of the superstructure were glued inside the steel box, which allowed rather easy access and moving from one compartment to the next through the holes in the diaphragm stiffeners. The strain gauges installed on the pier structures are located on the outside of the conical box sections or on the transverse framework located in the hollow parts of the existing piers. Shielded cables were used for data transfer to the measurement unit in order to protect the strain results from undesirable effects due to adjacent rail traffic.

A total of 12 heavy lorries were applied as loads during the load test, each lorry having a mass of approximately 44 tons. Over the course of two days, the lorries were placed in various positions along the longitudinal bridge axis, in order to investigate the effect on different structural members. As an example, the full loading condition of a 4-span deck is shown in Figure 9. Lorries could be placed on both sides of the bridge, for example to obtain maximum loading of the local pier structure, or only on one side, for instance to investigate the asymmetric loading of the internal pier framework. During the test, strains were recorded with an accuracy of 1 microstrain (µS) as has been proven on many other cases. Prior to every monitored sequence of consecutive lorry configurations, a zero measurement of the unloaded viaduct was registered in order to discard the measurement results from daily thermal effects.

In addition to the static load cases, dynamic strain measurements were carried out during the two-day testing program. These included brake tests of five lorries stopping at the same time as well as continuous monitoring of the longitudinal stiffeners on the lower flange during passage of a 10-lorry convoy at low speed.

In the period after the load test, long term monitoring of a selected number of strain gauges was initialized. Therefore a fully autonomous measurement system was installed, consisting of a data logging set-up powered by 4 lithium-ion D-cell batteries to assure the independency of the system and the continuation of the monitoring process in case of power failure on the construction site. Strains are monitored continuously in 15 well-chosen points of the superstructure, mainly to study the effect of temperature gradients on the closed steel box girders of the fly-overs. For this reason, temperatures are being measured on 8 locations of the steel structure. As the superstructure is made continuous over 4 spans, temperature effects are also monitored on 14 points of the steel supports integrated in the hollow concrete piers. A Wheatstone half-bridge configuration was applied for every measurement point thanks to the use of two orthogonal measuring grids on each strain gauge. This should result in more stable long-term measurements due to a nearly complete elimination of unwanted temperature effects and influences of the leadwires on the resistance.

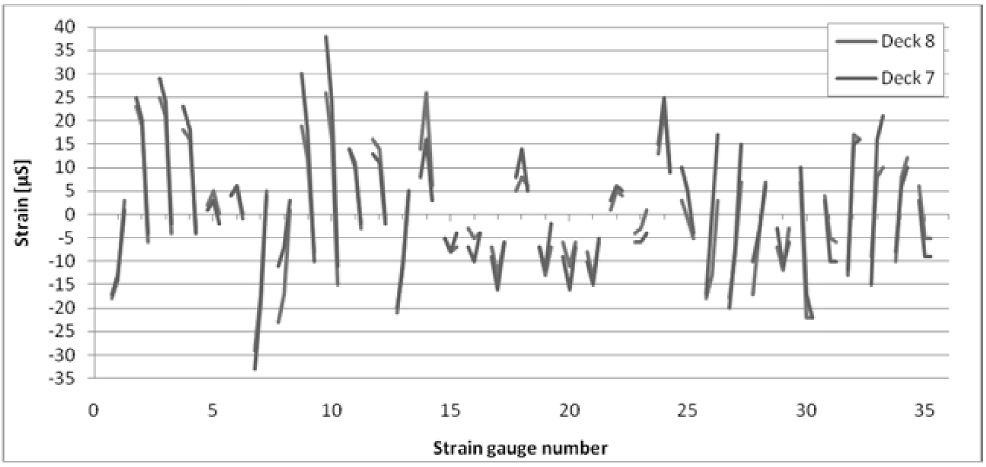

Figure 10: Comparison of strain variations of deck 7 and 8 over three lorry configurations

3.3 Results

In the following paragraphs, a selection of the large amount of measurement results is presented to demonstrate the accuracy and reliability of the measurement set-up and operating procedures. By convention, tensile stresses correspond to positive strains, compressive stresses to negative values.

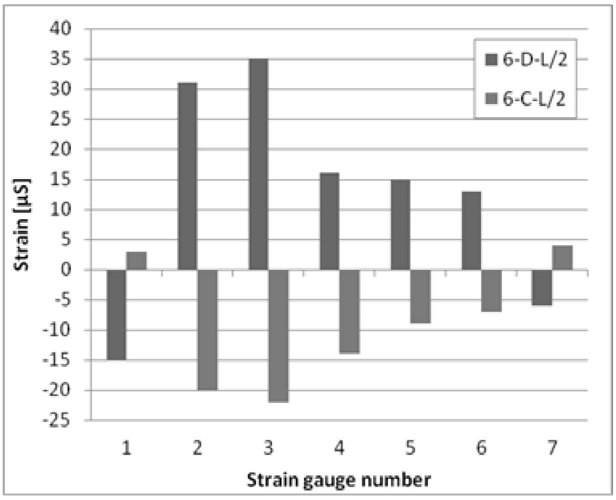

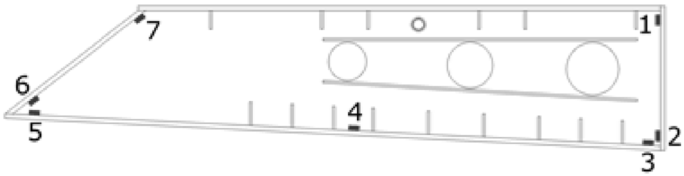

Figure 11: Strain results of deck 6 (only span D loaded) (above)
and location of strain gauges in deck 6 (below)

As part of the two-day load test, strains were measured in corresponding sections of deck 7 and 8. Both are continuous 4-span decks, but located on opposite sides of the historic arch bridge at the same position along the longitudinal axis. Figure 10 shows the comparison of strain results from deck 7 and 8 in 35 measurement points for three consecutive lorry configurations. In each of these configurations, the positioning of the lorries was identical for deck 7 and deck 8. Each line in Figure 10 corresponds with the strain variation of a single measurement point over the three load states. As the graph shows, strain results from deck 7 correspond well to strains measured in deck 8 and their variation over the sequence of lorry configurations shows the same tendency for every measurement location. As the absolute values of the measured strains are quite small, some caution is advised in performing extensive statistical analysis on the monitored data. Nonetheless, an average difference of 3 µS between results of deck 7 and 8 can be noted, with a standard deviation of 3 µS, which demonstrates the good agreement between the corresponding measurement sections.

Figure 11 shows strain results of deck 6, where only the first span (D) was loaded and no lorries were positioned on the other spans (A,B,C). Strain gauges 1 and 7 are located at the top of the box section, while the other gauges are located at the bottom. Loading of span D results in compressive stresses at the top of the cross-section at mid span and tensile stresses at the bottom. Simultaneously, the upward response of the adjacent and unloaded span C (due to the deck being continuous over four spans) results in tensile stresses at the top and compressive stresses at the bottom of the cross-section at mid span.

Figure 12 shows strain results of the same cross-sections in span C and D of deck 6, this time under simultaneous loading of both spans. This condition was found in two different lorry configurations, being positions 3 and 13, which allows for a comparison of monitored strains in both positions. The results depicted in Figure 12 show a good resemblance between positions 3 and 13 in both cross-sections of deck 6. In general, the strains in span C remain smaller as in span D, which corresponds to the smaller bending moment in span C under the applied loading condition.

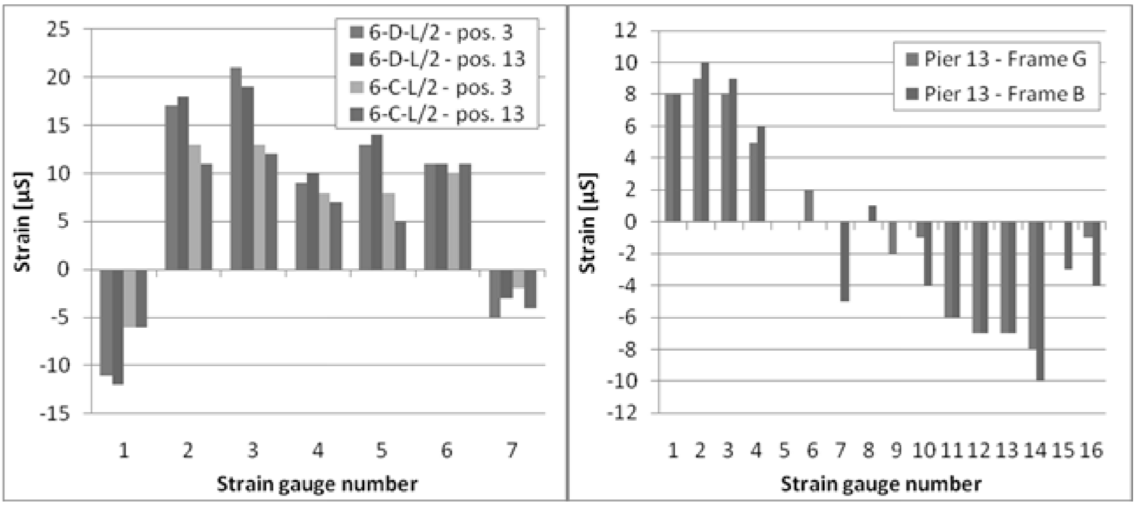

Figure 12: Strain results of deck 6 (spans C and D loaded) (left) and strain results of both frames of pier 13 (maximum loading condition) (right)

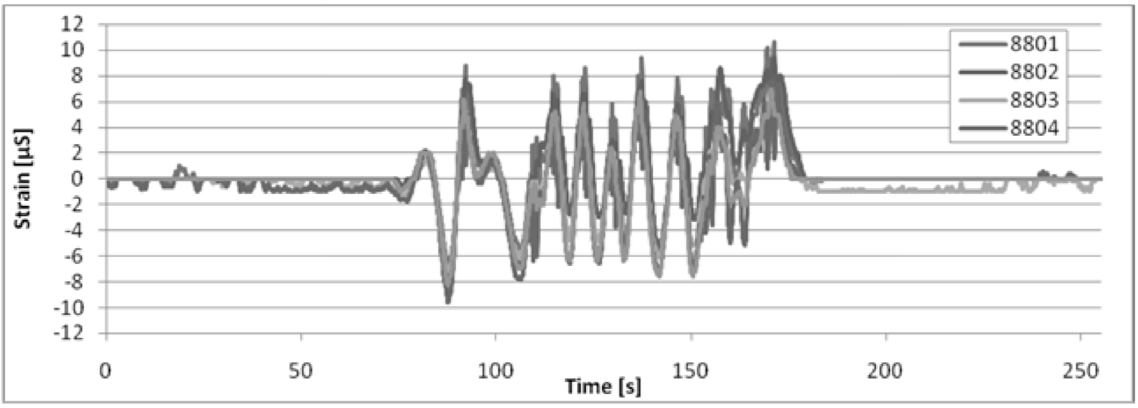

Figure 13: Strain variations of longitudinal stiffeners of deck 8 during passage of 10-lorry convoy

During the load test, the maximum loading condition of the piers was simulated by positioning lorries on both sides of the pier in longitudinal direction and at the same time on both decks of the fly-over in transverse direction. As the cantilever piers of a double pier structure are joined by two separate transverse internal frameworks, strain data from corresponding locations on both frameworks can be compared.

Therefore, results of this loading case for the double pier structure of pier 13 are shown in Figure 12 (right). Despite of the small absolute values of the measured strains, a good resemblance of the results for both frames can be observed.

All these examples give an illustration of the acquired accuracy and reliability of the measurements for the static load cases. In addition, dynamic strain measurements were performed during the load test. Figure 13 shows an example of the strains monitored in the longitudinal stiffeners on the lower flange of deck 8 during passage of 10 lorries, crossing the viaduct as a low-speed convoy. The results allow following the strain response of the structure to the passage of the trucks continuously. However, the values of the strain data prove a rather small impact of the convoy on the stiffeners.

Long term monitoring of the steel box section of the fly-overs allows for evaluating the effect of temperature gradients on the superstructure. Figure 14 gives an illustration of the daily temperature variations during the summer in several cross-sections of deck 8, which is oriented to the southwest. The graph shows that the temperature of the inner web plate near the existing concrete arches ('in') is almost identical along the entire length of span D of deck 8, and shows rather small variations between day and night temperatures. On the other hand, temperatures on the outer web plate ('out') become much higher during daytime and cause a temperature gradient in the steel box section. In addition, the outer web plate at mid span shows significant higher temperatures than the cross-sections at L/4 and the supports, due to a larger exposure to solar radiation on the inclined steel surface (see Figure 9). As a result, the largest temperature gradient between inner and outer web plate occurs at mid span and reaches almost 15°C, while this difference is only 6°C at the supports.

As an example, Figure 14 also shows the impact of the temperature variations on monitored transverse strains in the cross-section at L/4. The numbering of the strain gauges is similar to Figure 11. When temperatures rise during daytime, an increase of tensile stresses can be observed due to the thermal expansion of the steel superstructure. The largest strain variations occur in gauge numbers 5 and 6, which are located at the lower outer corner of the steel box section. The temperature effects on the superstructure can also be observed in the monitoring results of the pier structures, as illustrated in Figure 14. Corresponding measurement locations in piers 10 and 13 give a comparable response to the thermal effects, with maximal tensile stresses generated in strain gauge number 3, located on the lower connection plate between the conical box section of the piers and the internal framework.

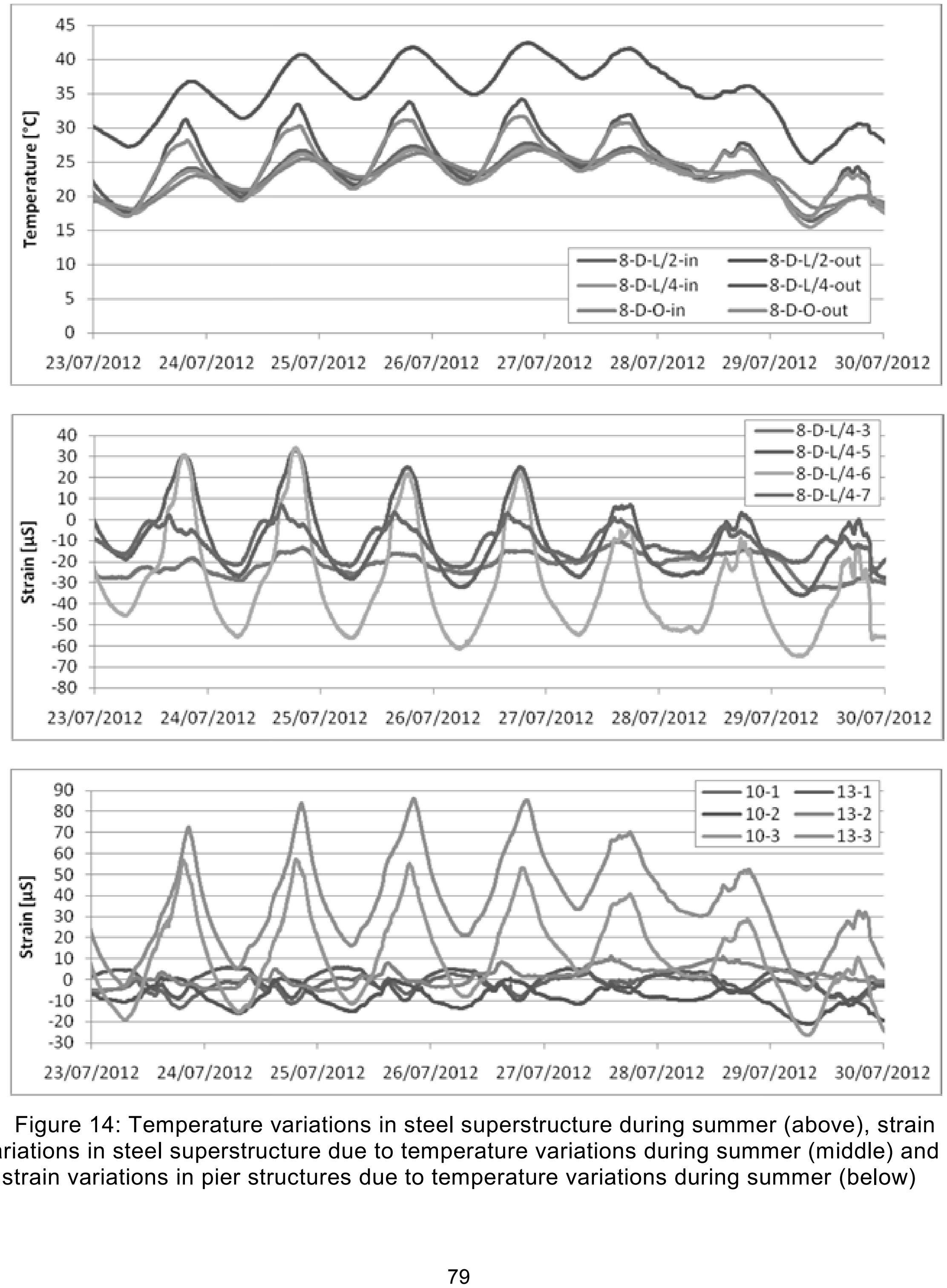

Figure 14: Temperature variations in steel superstructure during summer (above), strain variations in steel superstructure due to temperature variations during summer (middle) and strain variations in pier structures due to temperature variations during summer (below)

3.4 Conclusions

This example showed a selection of the results of the extensive monitoring program verifying the structural behavior of the newly built lateral fly-overs in extension of the historic multiple-arch viaduct crossing the Pede valley. During a two-day load test and following long term measurements, detailed strains, temperatures and frequencies were monitored which allow for evaluating the conceptual design. The accuracy and reliability of the results were illustrated in various examples of the structural response. The performed measurements provide the designers the ability to assess the behavior and stiffness of the structure under static, dynamic and thermal loading cases.

Figure 15: “Kruisschans” Bridge in the Port of Antwerp: in operation (above and left) and during renovation (right)

4 MONITORING STEEL MOVABLE BRIDGES

4.1 Introduction

The “Kruisschans” Bridge, shown in Figure 15, is one of the movable bridges bracketing the “Van Cauwelaert” lock, which is one of the main entrances to the inner harbor of the Port of Antwerp, protected from tidal effects. The renovation of the “Van Cauwelaert” lock together with the modernization of the close by “Royers” lock and the raising of the bridges over the nearby Albert canal forms part of the waterways project aimed at making the canal and river transportation an attractive alternative for road transport. Raising the bridges over the Albert Canal will enable barges to travel the inner harbor and the Albert canal, which travels to Liege and Germany, carrying containers stacked four high. This forms part of the on-going effort to achieve a modal shift away from road transportation and thus better mobility.

The modernization of the “Van Cauwelaert” lock is also significant for the Port of Antwerp, as the renovated lock doors will make it possible to handle the growing number of barges travelling on rivers and canals quickly and more efficiently. Furthermore, extreme weather conditions such as high winds and heavy rain will no longer interfere with operation of the lock, ensuring that it can remain in operation permanently.

The movable “Kruisschans” Bridge is situated at the right bank of the river Scheldt. In 1992, this bridge replaced the original movable bridge from 1928, during a previous renovation project of the locks. This bascule bridge is of the Strauss trunnion type. This type of bascule bridge is preferred over other types of movable bridges because it offers the fastest operation, and a greater level of safety. It can open a channel for large ships upon approach, without danger of collision. Bascule bridges also have the ability to allow smaller vessels to pass by opening only partially when necessary.

4.2 Experimental setup

One of the determining factors in the redesign of a trunnion type bascule bridge is the low-cycle fatigue due to the movements of the bridge. In order to verify all design assumptions, it was decided by the client to install 36 strain gauges, mainly on the balance beams, but also on the hoist beams and gear rods. In addition, it was decided to install most strain gauges at the steel construction plant where all the parts are strengthened and repainted in an unloaded condition. This allows for monitoring the stress cycles during normal bridge operation and in theory also for registering the stress build-up during assembly of the bridge. This last factor would allow for determining the absolute stress values.

Since the actual measurements would be several months after installation and zeroing of the strain gauges, a half bridge installation scheme was chosen, as shown in Figure 16 (left). However, the stress field in the balance beams is not strictly unidirectional, making it more difficult to determine the overall stresses in a certain cross-section, based on a single strain gauge. This necessitates a more complicated strain gauge application method.

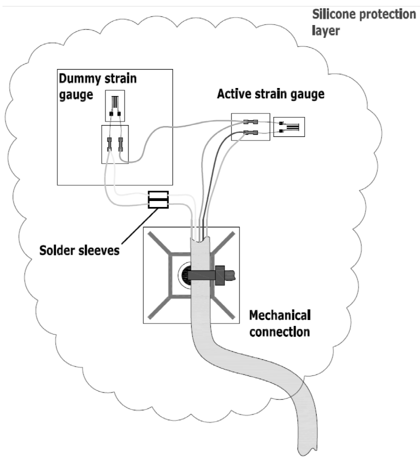

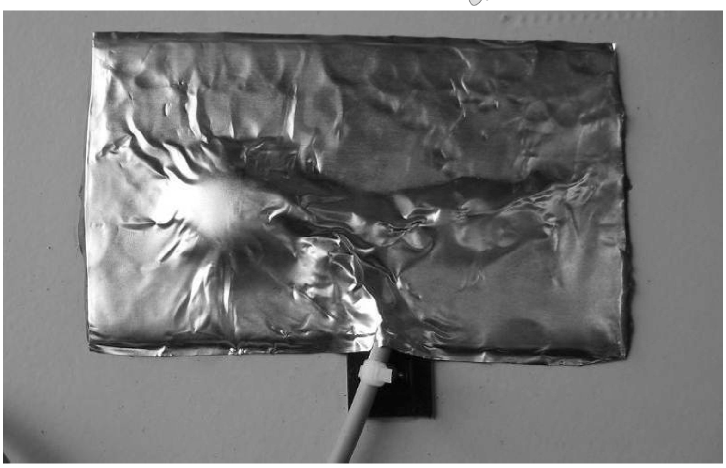

Figure 16: “Kruisschans” Bridge in the Port of Antwerp: half bridge strain gauge configuration (left) and strain gauge protection layer (right)

The dummy strain gauge, which is responsible for filtering out all of the temperature and electromagnetic noise influences on the recorded measurement signal of the active strain gauge, cannot simply be glued to the balance beam surface in a perpendicular direction to the active strain gauge, since transverse stresses would influence the measured stress values because of the Poisson-effect. The dummy strain gauges are thus installed on a separate 3 cm by 3 cm steel plate, which can entirely be prefabricated in the controlled conditions of the laboratory. Afterwards, this steel plate is attached to the steel of the balance beam using a heat transmitting tape, ensuring that a thermal connection exists between the balance beam and the dummy plate, but allowing no transfer of mechanical stresses to the steel of the dummy plate. The connection is thus only relevant for thermal and electromagnetic effects but not for the structural behavior of the structure.

Since the strain gauges will not be removed after the end of the measurement period, the entire setup has to be permanently protected against weather conditions. The protection has to ensure that the untreated steel upon which the strain gauges have to be glued, in order to end up with relevant results, cannot lead to corrosion problems. Because of this, the entire strain gauge setup is protected using a synthetic viscous knead able putty, creating a sealed-off environment around the strain gauge setup, but inducing no mechanical resistance in the strain gauge. The surface of this putty is finished with a thin aluminum layer, as can be seen in Figure 16 (right), which allows for repainting of the entire area using the same paint procedure as used for the entire “Kruisschans” Bridge. This results in the monitoring system being quite invisible, the measurement cables notwithstanding, although they will be guided to the corners and behind the stiffeners of the balance beam where possible. The location of most of the strain gauges is shown in Figure 17.

To allow for easy interpretation of the stress and strain results, the angle of the movable part of the bridge will also be recorded in the machine chamber and registered using the same data-acquisition system with identical measurement frequency. This allows for interpretation of the stresses for each step in the bridge operation.

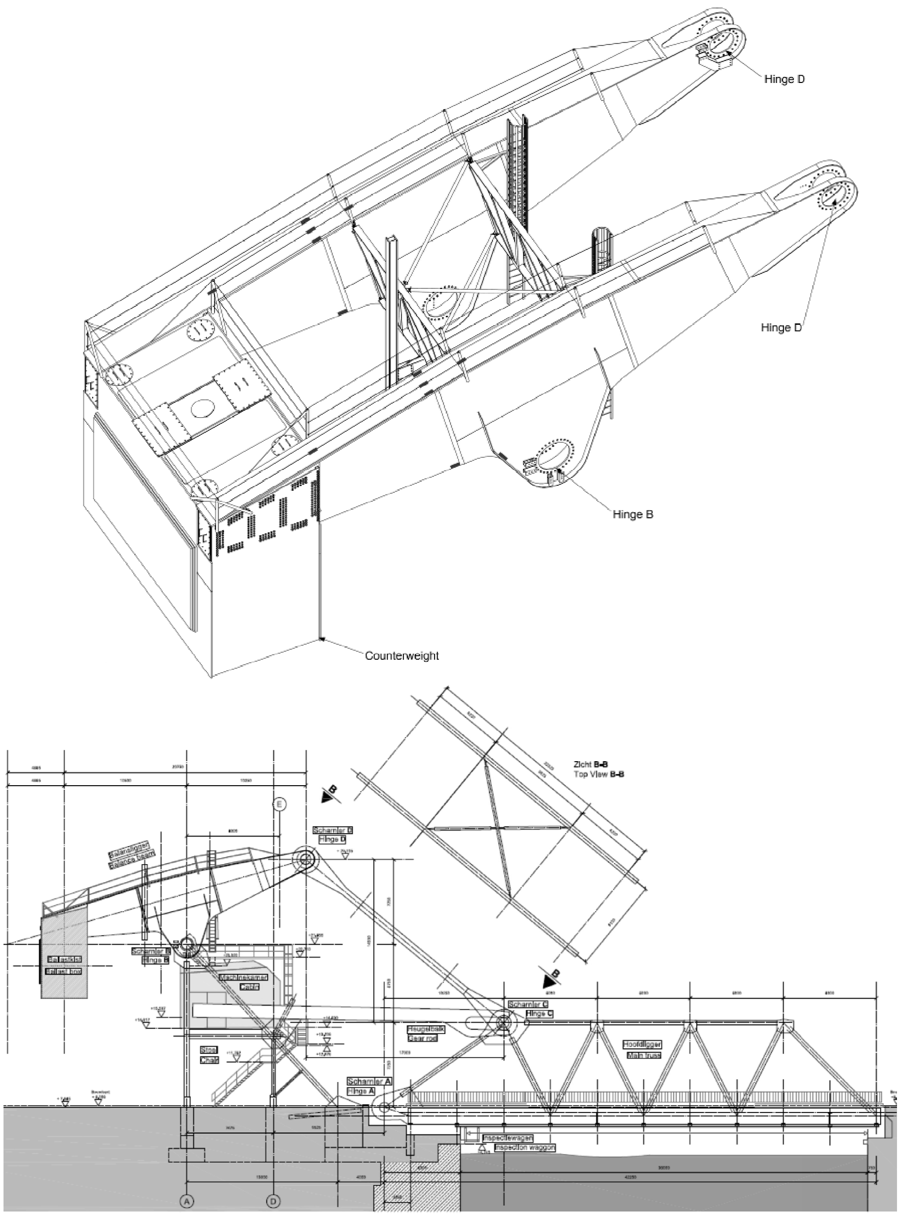

Figure 17: “Kruisschans” Bridge in the Port of Antwerp: strain gauge positions

4.3 Results

Some results concerning the movement of the bridge and the maximal strains which were measured are summarized in Figure 18. Each diagram represents the variation of a number of sensors during one operation of the entire bridge, i.e. opening and closing of the bridge. The quality and stability of the measurements is quite clear. The maximal value, being 740 μS, clearly illustrates the importance of design verifications using measurements, since it corresponds with a stress variation of 155 MPa, which is quite considerable.

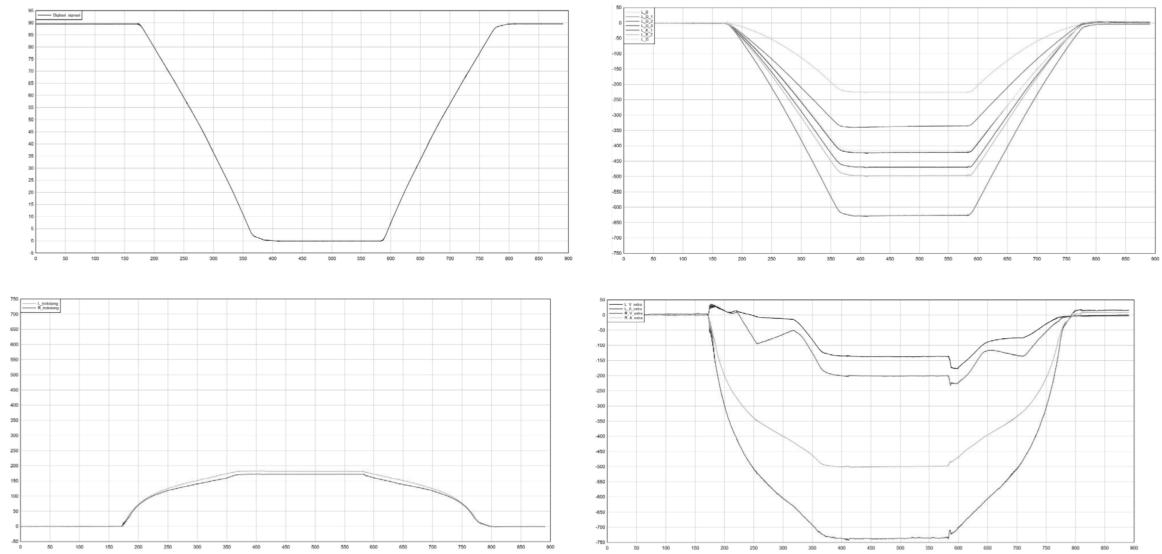

Figure 18: “Kruisschans” Bridge in the Port of Antwerp:
Registration of the position of the movable part of the bridge (between 0° and 90°, above left);
Variation of the strains in the balance beam (between 0 and -630 μS, above right);
Variation of the strains in the traction beam (between 0 and 180 μS, below left);
Variation of the strains in the support structure (between 0 and -740 μS, below right)

5 CONCLUSIONS

This article gives an overview of these measurement experiences and on the lessons learned concerning optimal placement of strain gauges, how to design optimal laboratory tests, possible noise sources and how to deal with them and the influence of unexpected force behavior. Furthermore, the most important results of all test cases are discussed in short.

REFERENCES

[1] A. Schumacher, *Fatigue Behaviour of Welded Circular Hollow Section Joints in Bridges*, EPFL Thesis 2727, (2003).

[2] P. Van Bogaert, *Stability and Node-Detailing of Tubular Steel Arch Bridges*, Proceedings ARCH’07 – 5th International Conference on Arch Bridges, pp 831-838, September (2007).

[3] D. Stael, H. De Backer and P. Van Bogaert, *Extending the Fatigue Life of Welded Tubular Bridge Joints Thanks to Internal Diaphragm Stiffening*, Report IABSE Conference Rotterdam 2013, pp 442-443, (2013).

[4] A. M. Van Wingerde, D. R. V. Van Delft, J. Wardenier and J. A. Packer, *Scale Effects on the Fatigue Behaviour of Tubular Structures*, Proceedings of the IIW International Conference on Performance of Dynamically loaded welded structures, pp 123-135, (1997).

[5] *Eurocode 1: Actions on Structures - Part 2: Traffic Loads on Bridges*, CEN, (2003).

[6] B. De Pauw, P. Van Bogaert, *Integrated Steel Viaducts for Railway in Extension of a Historic Multiple-Arch Concrete Viaduct*, Proceedings of 8th International Conference on Short and Medium Span Bridges, Niagara Falls, Canada, pp. 198.1-198.10, (2010).

EXPERIMENTAL RESEARCH ON MODULAR THIN-WALLED STEEL STRUCTURES

Markku Heinisuo, Juuso Lahdenmaa and Timo Jokinen

Tampere University of Technology
Kampusranta 9 C, 60320 Seinäjoki, Finland
e-mail: markku.heinisuo@tut.fi, webpage: http://www.metallirakentaminen.fi

Keywords: Modular structures, thin-walled steel panels, experimental research, Eurocodes

Abstract. *A new type of all-steel double skin panel has been developed, which is used to manufacture 3-dimensional modules for residential and other types of buildings. This modular system has been used in Finland for both new buildings and building extensions, such as adding new lift shafts and 1 to 2 new storeys to existing buildings. The all-metal panels are made of cold-formed members using the patented FICXEL® technology. Comprehensive experimental research has been conducted during the last 3 years on the structural resistance and stiffness of these all-metal panels. The results presented in this paper deal with the resistance of complete modules (floor + walls + ceiling) with supports only at the ends of the module, buckling and shear of panels, with and without stiffening boards (plaster, OBS) screwed to the surfaces of the panels. The tests were made to determine design values and methods for different loading cases of the panels. The test results were evaluated based on the principles of Eurocodes to provide design values for use in European markets.*

1 INTRODUCTION

A new type of all-steel double skin panel has been developed, which is used to manufacture 3-dimensional modules for residential and other types of buildings. This modular system has been used in Finland for both new buildings and building extensions, such as adding new lift shafts and 1 to 2 new storeys to existing buildings. The all-metal panels are made of cold-formed members by the patented FIXCEL® technology and they consist of two parallel thin steel faces and orthogonal steel webs located at equal intervals between the faces. The nominal steel thickness is from 0.7 to 1.25 mm and a typical steel grade is S355GD+Z. The manufacturing dimensions are: panel depth 70 to 200 mm and web spacing 100 to 200 mm. The sheet grades, thicknesses, height and width of the final panels can vary depending on the intended use of the panel. Typical panel width in floors of residential buildings is about 6 m and height in walls about 3.3 m. The cold-forming machine also punches along the joint at even intervals which can be input into the manufacturing process. Typically the punches are delivered 100 to 300 mm apart. When the sheets are joined together, the zinc surface is not damaged which ensures the corrosion resistance of the finished panel. Figure 1 shows the principle of the panel joint and a completed panel surface.

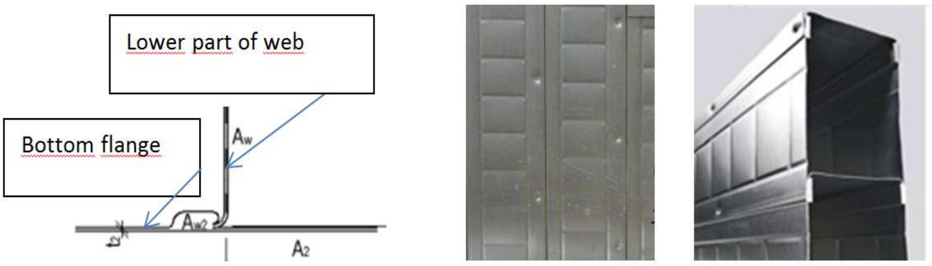

Figure 1: Panel joint principle and completed panels

Figure 2 illustrates modules for buildings made of Fixcel® panels.

Office module fabrication and transport

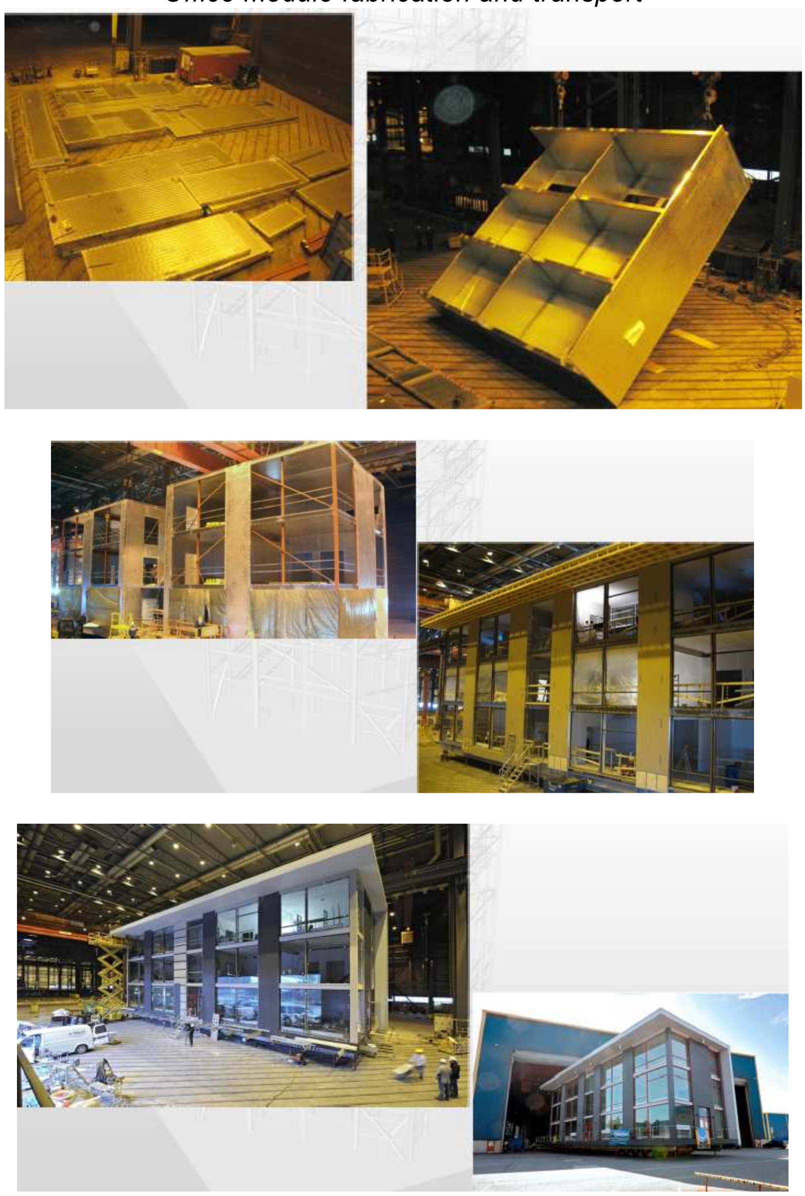

Residential building

Figure 2: FIXCEL applications

The pre-fabrication of the products can vary widely. The logistics from the factory to the site allowing, the module can be a complete house. In most cases the module is part of a house, e.g. one apartment or half of an apartment in a multi-storey residential building.

The reasons for using the panels include:

- Possibility to manufacture complete light-weight modules for buildings at the factory, avoiding manual work at the site;
- Light weight makes it easier to transport and lift the modules;
- Speeds up installation at the site (time is money at the site);
- Provides better quality (eliminates moisture problems, better tightness, tolerances) of components through controlled work indoors;
- Eliminates waste problems at the site.

Requirements for other activities at the construction site are also of importance, such as strictly following the tolerances necessary for erection of modules and logistics at the site (transport, heat, ventilation, automation and other installations).

All modules include walls, floors and ceilings. This means a double structure with an air gap between apartments which provides excellent acoustics for occupants. The thermal insulation is located outside the panels and thermal behavior of the module is good and has been tested in practice in demanding Finnish winter conditions.

One motivation for the use of these panels is that they form the load bearing structure of the building. The panels resist bending and axial loads. The floor and ceiling panels resist shear loads by diaphragm action with boards connected to the panels. The walls are not yet taken into account as stiffening elements against horizontal loads. Stiffening against horizontal loads has been complemented with steel frames embedded in the panel walls, and the structure is anchored to the foundation with vertical steel bars between the modules.

Comprehensive experimental researches have been conducted during the last 3 years both in the Finnish national Tekes project CONCELLS and the FP7-SME project MODCONS dealing with structural resistance and stiffness of these all-metal panels and modules made of them. These researches are essential because the present codes of practice do not include design rules for these kinds of structures. Architects require applications where the modules act as cantilevers and are supported only partially along their length. Moreover, specific design rules for these structures are needed to win new markets e.g. in seismic areas.

So far, 5-storey residential buildings have been constructed successfully using this technology: load bearing all-metal panels of a sheet thickness of about 1 mm. The horizontal panels can resist loads on floors and ceilings, and the vertical panels can take the loads of up to five storeys. Stiffening with different boards means more resistance both in compression and shear, which makes it possible to build higher buildings.

The results presented in this paper deal with the resistance of full modules (floor + walls + ceiling) with supports only at the ends of the module, buckling and shear of panels with and without stiffening boards (plaster, OBS) screwed to the surfaces of the panels. The tests have been done to get design values and methods for different loading and support cases of the modules. The test results have been evaluated based on the principles of Eurocodes to prove safe design values for use in the European markets.

2 AVAILABLE DESIGN RULES FOR ALL-METAL PANELS

The all-metal panel under consideration resists out of plane loads from bending and shear, and axial loads. In addition, to provide transverse stiffness to reduce vibration of the floor panels, profiled steel decking is fixed to the top of the panel perpendicular to its webs to improve bending stiffness in that direction. Figure 3 illustrates the cross-section of the part of the panel for structural analysis. External boards are also used to provide weather resistance and some additional diaphragm action.

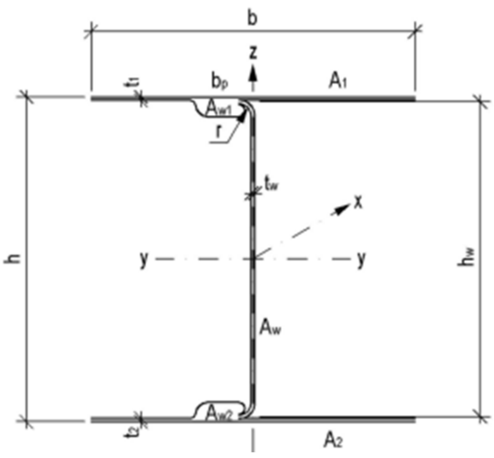

Figure 3: Cross-section of the double skin panel

The general theory of sandwich panels is well established and has been known for a long time[1, 2, 3]. Different theories have been presented for panels with thin and thick faces. Here, the faces are thin. A common feature of sandwich panels is that their faces are connected by a material which undergoes considerable shear deformation when subjected to a shear force. When the cross-section shown in Figure 3 bends, shear forces are created in the axial direction (x in Figure 3), provided that the joints between the faces and the web can withstand forces in the x direction. These joints were tested in this loading case and the corresponding stiffness and resistance of the joints were defined in [4] using the safety concepts of [5]. When these quantities are known, the general theory of sandwich panels can be used in design. In [4] the design method for floor and wall panels is presented including normal use and vibration of floor panels based on the general theory of sandwich panels and the European standard of cold-formed steel structures [5]. The design method was validated by tests.

Architects are interested in more exotic solutions. One research question was: How long openings can be located below the entire module? The normal situation is that the wall panels are supported continuously below the walls. Openings cause large shear forces at the plane of the panel above the opening. Two other research questions were: How many boards outside the panels are needed to stiffen the panels against axial and shear load. The idea was to build higher than 5-storey buildings and to use boards for stiffening the modules to avoid conspicuous stabilizing frames in the modules. No design rules are available for stiffened panels and the design of panel shear. So, these research questions were solved by the experimental researches described below. Other researches on these structures are reported in [6]. All tests were performed in the laboratory of the Department of Structural Engineering at Tampere University of Technology, Finland, during 2011–2013.

3 BRIDGE TESTS

In these tests the goal was to determine how long openings can be located below a module. Tests were made on four modules, each of which included a floor, two walls and a ceiling joined by normal methods. Normal joining of walls and floor and walls and ceiling requires special steel purlins (t =3 mm, S350GD+Z) and screws. The length of modules was 5.7 m, height 3.05 m and width 1.3 m. The modules were open at the ends. At the open ends of the module there were two tubular steel columns and one beam at the roof and floor levels, to which the panels were screwed; all were made of 100x100x5 (S355J2H) tubes. The columns extended down to the supports in the tests. Figure 4 illustrates the tested modules which were made in a module factory and transported to the laboratory.

Figure 4: Tested modules

One module (on the left in Figure 4) was a standard product while one was a similar product except for the joints which connected the faces and the web (see A_{w1} and A_{w2} in Figure 3) which had been strengthened by SFS-Intec SD14-H15-5,5x46 screws at 100 mm c/c spacing. One module (middle of Figure 4) was strengthened with diagonal steel (grade S235) plates 3x120 mm^2 and fastened with 20 screws (same screws as at the joints) at the ends to the modules. One module was strengthened using screws at panel joints and included symmetric openings (1600x1600, 1600x800) at the opposite walls, as shown in Figure 4 (on the right).

All modules were made of steel grade DX51D+Z. The thicknesses of sheets of floor and ceiling panels were 0.7 mm and those of wall panels 1.2 mm. The height of ceiling and wall panels was 100 mm and that of floor panels 200 mm. Web spacing was 150 mm in floor and ceiling panels and 100 mm in wall panels. Punch spacing of floor and ceiling panels was 230 mm and that of walls 100 mm. The modules were supported vertically at the ends of the modules, meaning a free span of 5.6 m. This support condition simulates the situation with the largest possible opening below the module, or an accidental case where the structures below the module fail.

A uniform dead load of 2 kN/m^2 (total 1200 kg) was applied over the entire floor panel. Then, a total load of 40 kN was exerted on four points in both walls, as shown in Figure 5. The load was subsequently removed and then applied to failure using four 460 kN cylinders below the strong floor.

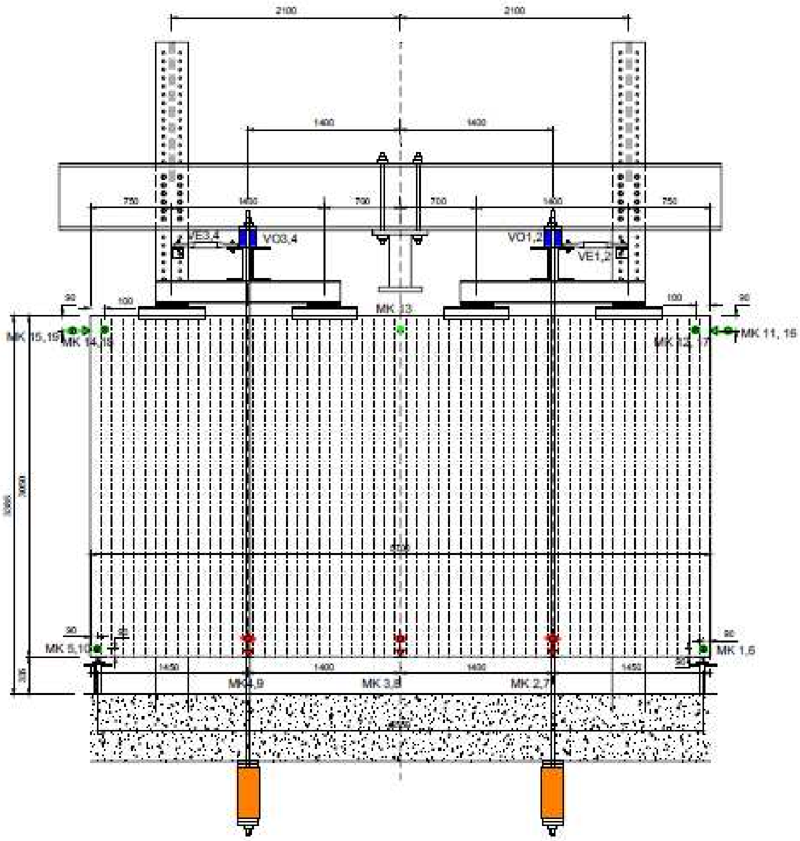

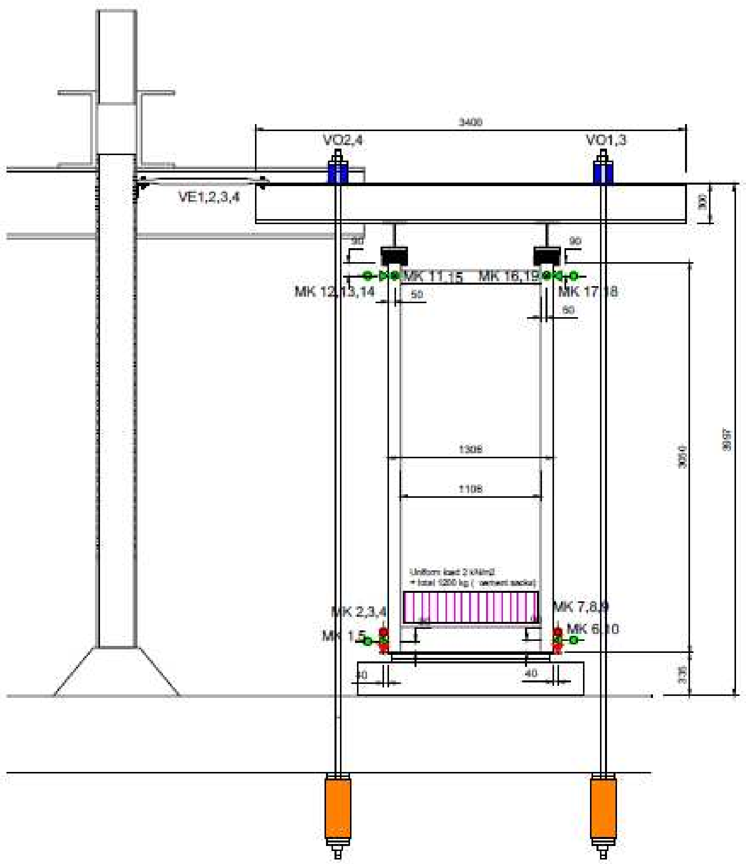

Figure 5: Bridge test arrangement

The total applied loads (sum of cylinder loads) versus mid-point deflections are shown in Figure 6 for all four tests.

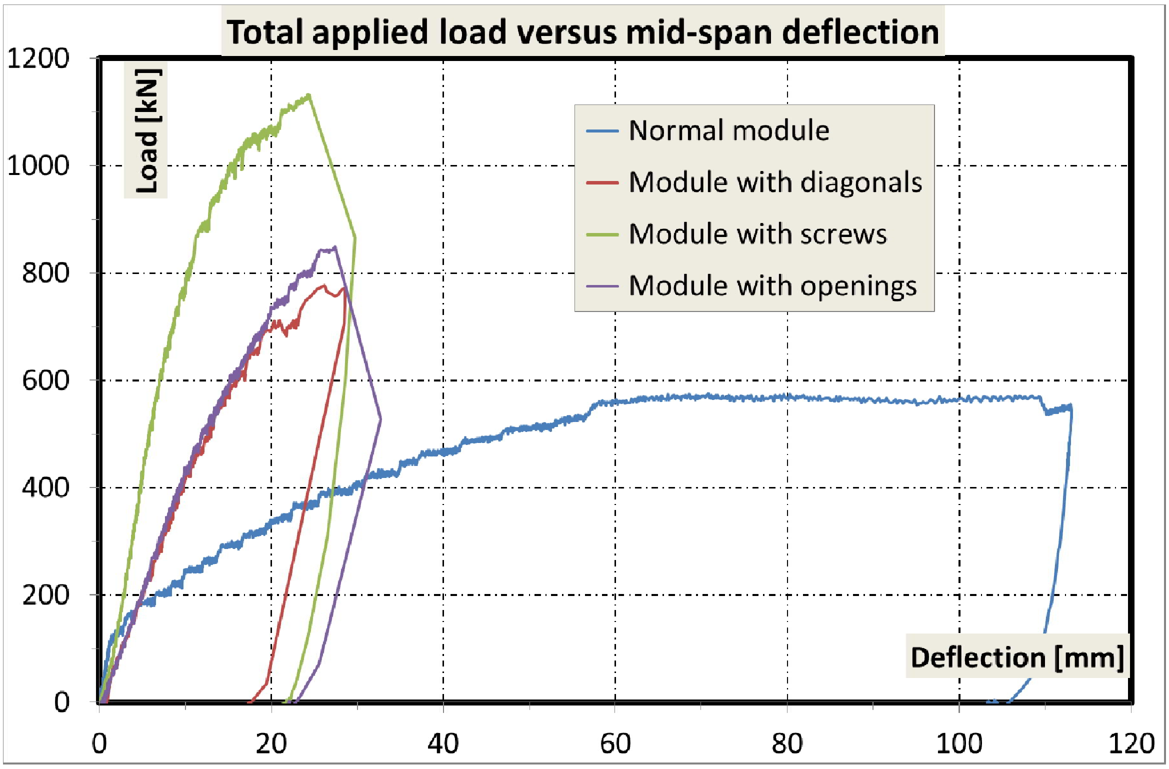

Figure 6: Applied total load versus mid-point displacement in bridge tests

It can be seen that the screwed module resisted an applied load of over 1000 kN plus the dead load of the module and the floor load. In fact, the module did not fail, but the tubular columns at the ends of the module. The standard module without screws or diagonals resisted about 550 kN but displacements started to increase after an applied load of about 100 kN. Considerable shear deformations were observed both at the panel joints between faces and webs and between purlins and modules at the joints connecting the floor and walls. The resistance of 550 kN corresponds closely to the axial resistance of the purlins at the joints between the floor and walls. The stiffness and resistance of the screwed module with openings and that without openings but with diagonals were about the same.

The resistance of the normal module in the accidental case was monitored in the tests. The test results were also used to define the design rules of the maximum opening below the module if the wall panels are stiffened by screws or with diagonal braces. Theoretical research on the shear resistance of the panels is the subject of further studies aimed at a unified theory for these kinds of panels in shear load. Stabilization of the panels against panel shear may be achieved using boards screwed outside the panels. The usability of this method was tested in the shear tests.

4 COMPRESSION TESTS AND ANALYSIS

The research question in this case was how much the compression resistance of the panel increases if some boards are fixed to the outer surfaces of the panels? Typical boards which are used in buildings available in the market were used in the tests.

The interaction of axial force and moment is given in EN 1993-1-3 as:

$$\left(\frac{N_{Ed}}{N_{b,Rd}}\right)^{0.8} + \left(\frac{M_{Ed}}{M_{c,Rd}}\right)^{0.8} = 1.0 \qquad (1)$$

where N_{Ed} and M_{ed} are the actions on the panel and $N_{b,Rd}$ and $M_{c,Rd}$ are the axial resistance and the bending resistance of the panel. When deriving the axial resistance of the panel local and global flexural buckling are taken into account, as stated in the standard. When deriving the bending resistance local buckling is taken into account in this case. Imperfection factor α in flexural buckling for these kinds of panels may be assumed to be 0.34, applying the standard. Large axial forces occur in wall panels, which is why the main interest of this study was the validity of Equation (1) in cases where the bending moment is small. When designing walls in practice, small bending moments due to load eccentricities and wind should always be considered.

A total of 20 tests were made on panels in compression. The heights of the panels were 100 mm in each case simulating a normal wall panel. The width of the panels was 1 m. Two types of steel panels were tested. One was a panel with a web spacing of 150 mm, nominal sheet thickness of 0.7 mm and steel grade S350. The other type had a web spacing of 100 mm, sheet thickness of 1.0 mm and steel grade S280. Three identical full steel panels with a span of 5 m of both panel types were tested. One test was made using a panel of S350 steel 3 m long and one test with the same panel 6 m long, their slenderness values being in the range 0.76–1.51. The panels were located horizontally in the tests. A small vertical load was due to the dead weight of the panel and, moreover, small dead loads were located at the mid-spans of the panels. A 25 mm eccentricity occurred at the loading point.

The same 5 m long steel panels were tested using three identical specimens with:

- A 15 mm thick fire protection plaster board on the upper side, screws (dia. 4.8 mm) spaced at 300 mm in both directions, (3 + 3 tests);
- Same as above but with a 15 mm thick OSB board (class OSB/3) on the other side, screws as above, (3 + 3 tests).

Figure 7 illustrates typical results of the compression tests. Figure 7 presents the results of three tests on S350 panels with boards on both sides, displacements were measured at two points at mid-span.

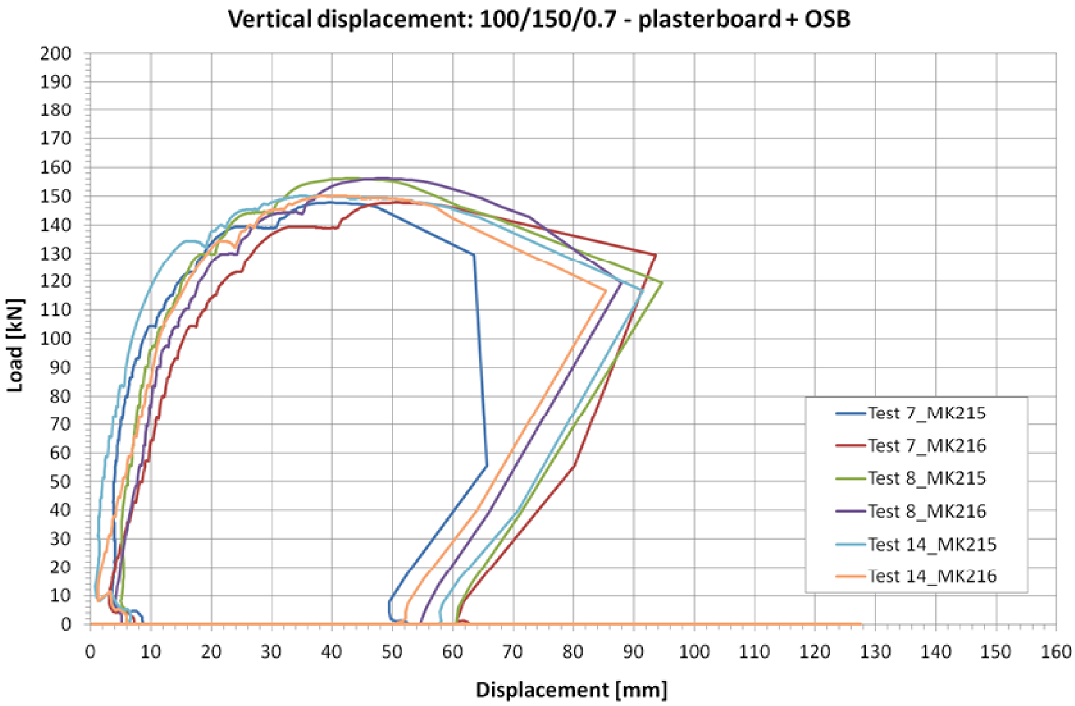

Figure 7: Axial load versus vertical displacement at mid-point of an S350 panel with boards

Generally a board on the compressed side increased the maximum axial load by 30–50 % compared to full steel panels. If there were boards on both sides, the maximum axial load did not increase much. The failure mode in each test was the same: forming of a plastic hinge at the mid-span of the panel, see Figure 8.

Figure 8: Failure modes of compression tests

Based on these tests, a design method for the compressed panels was derived from the statistical safety concept of EN 1990[7]. The target safety constant was γ^* = 1.0. The details of that analysis can be found in [8]. As a result the flexural buckling load may be calculated as:

With boards — Without boards

$$N_{cr} = \frac{\pi^2 EI_{gross}}{L_{cr}^2} \qquad N_{cr} = \frac{\pi^2 EI_{eff}}{L_{cr}^2} \tag{2}$$

and, moreover, imperfection factor α can be assumed to be 0.21 with boards on the compressed side and 0.34 without the boards. Other design rules are given in the standard[5]. The calculation of the flexural buckling load without boards differs from the recommendation of the standard. The standard does not require reduction due to local buckling. There are no rules in the standard for the design of the compressed panel with boards, but an imperfection factor of 0.21 was shown to be possible for these panels.

5 SHEAR TESTS

The research question in this case was how much does the shear resistance of the panel increase if some boards are fixed to the outer surfaces of the panels? The tests were made with the same full steel panels and panels with the same boards as in the compression tests. A total of 19 tests were made on 1 m wide and 2.35 m long panels in a special test frame. The goal of the study was not to derive an analytical method for the design of panels but to determine characteristic shear resistance based on tests and evaluation of the tests applying EN 1993-1-3, Annex A[5]. The test plan is shown in Table 1.

Table 1: Shear tests

Specimen	Client coding	Sheeting	Length [mm]
Test 1	100/ k100 1,0x1,0x1,0	No sheeting	2350
Test 2	100/ k100 1,0x1,0x1,0	Plaster board + osb	2350
Test 3	100/ k100 1,0x1,0x1,0	Plaster board + osb	2350
Test 4	100/ k100 1,0x1,0x1,0	Plaster board + osb	2350
Test 5	100/ k100 1,0x1,0x1,0	No sheeting	2350
Test 6	100/ k100 1,0x1,0x1,0	No sheeting	2350
Test 7	100/ k100 1,0x1,0x1,0	No sheeting	2350
Test 8	100/ k100 1,0x1,0x1,0	Plaster board	2350
Test 9	100/ k100 1,0x1,0x1,0	Plaster board	2350
Test 10	100/ k100 1,0x1,0x1,0	Plaster board	2350
Test 11	100/ k150 0,7x0,7x0,7	No sheeting	2350
Test 12	100/ k150 0,7x0,7x0,7	No sheeting	2350
Test 13	100/ k150 0,7x0,7x0,7	No sheeting	2350
Test 14	100/ k150 0,7x0,7x0,7	Plaster board	2350
Test 15	100/ k150 0,7x0,7x0,7	Plaster board	2350
Test 16	100/ k150 0,7x0,7x0,7	Plaster board	2350
Test 17	100/ k150 0,7x0,7x0,7	Plaster board + osb	2350
Test 18	100/ k150 0,7x0,7x0,7	Plaster board + osb	2350
Test 19	100/ k150 0,7x0,7x0,7	Plaster board + osb	2350

The test arrangement is shown in Figure 9.

Figure 9: Shear test arrangement

All specimens failed when the joints within the panels failed. The displacements at these joints were negligible when the load was small. At a certain load level the joint started to slide, but the panel could still resist high shear loads during sliding. For the design of these panels in shear, two design values based on these tests may be proposed: the load at which sliding starts (i.e serviceability limit) and ultimate failure. The serviceability condition relates to the absence of physical damage. The ultimate failure condition is used when some damage is visible in the structure, but the structure can resist the loads up to this level.

After the statistical evaluation a simplified design rule was derived[8]. A bi-linear shear forcé-displacement curve is proposed, as shown in Figure 10.

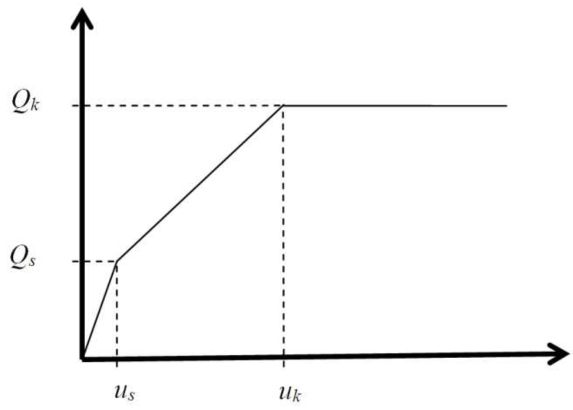

Figure 10: Idealised shear force-displacement relationship for tested panels

Characteristic values for shear are given in Table 2.

Table 10. Characteristic values for shear. Values are given for one 1.2 m x 2.8 m (width x height) panel

Panel	Boards	Q_s (kN)	u_s (mm)	Q_k (kN)	u_k (mm)
100/100/1.0 S280	No	3	0.1	16	40
	One size	8	0.1	38	40
	Both sides	11	0.1	51	40
100/150/0.7 S350	No	4	0.1	7	40
	One size	7	0.1	22	40
	Both sides	15	0.1	49	40

6 CONCLUSION

This study describes experiments completed during 2011–2013 dealing with the resistance properties of the new innovative all-metal sandwich panel. The bridge tests were made to provide design guidelines for entire modules with large openings below. The ultimate resistance of the standard module was monitored, and the results can be used to estimate the resistance of the module in the accidental case when the supporting structures below the module fail. Two kinds of stiffening systems were studied for that case: screws at the panel joints, and diagonal bracing. Both systems worked well and considerable axial force resistances were observed in the tests. Screw fastening is a more expensive than using diagonals.

The goal of the compression tests was to specify a design rule using the interaction equation in EN 1993-1-3 for cold-formed structures under axial load and bending. Statistical evaluation based on EN 1990 using the target safety constant γ^* = 1.0 showed that the equations in EN 1993-1-3 can be used if the flexural buckling load is calculated using the effective moment of inertia for the panel cross-section. If boards are screwed to the surfaces of the panel that stiffen the steel sheets, the equations of EN 1993-1-3 can be used as they are, but the imperfection factor for flexural buckling can be α = 0.21, instead of 0.34.

The goal of the shear tests was to define the characteristic values for shear design of full steel panels and panels with boards using the statistical evaluation of EN 1993-1-3, Annex A. The bi-linear shear force-displacement curve is proposed for shear analysis of panels together with numerical values for typical panels similar to the tested panels.

In future studies a theoretical model will be developed for the design of these kinds of panels in bending, axial and shear loads. Furthermore, entire modules should be analysed theoretically by numerical methods, such as FEM. The experimental results presented in this paper may be used in future researches for the validation of the developed theories.

7 ACKNOWLEDGEMENTS

The financial support of Tekes and companies of the CONCELLS project is gratefully acknowledged. The research leading to this paper was also funded by the European Commission through the project to support SME 'MODCONS' through GRANT AGREEMENT 315274.

REFERENCES

[1] H. Allen, *Analysis and Design of Structural Sandwich Panels*, Pergamon Press, London (1969).
[2] F. Plantema, *Sandwich Construction*, John Wiley & Sons, New York (1966).
[3] K. Stamm and H. Witte, *Sandwichkonstruktionen*, Springer-Verlag, Wien (1974).
[4] I. Toppila, *FIXCEL®-kennopalkin suunnittelu*, Master's thesis, Tampere University of Technology, Tampere, Finland, Draft (2012). (in Finnish)
[5] EN 1993-1-3
[6] J. Sorri (ed.). *Moduulirakentaminen: Teräskennoteknologian mahdollisuudet*. Tampere University of Technology. Department of Civil Engineering. Construction Management and Economics. Report 14, Tampere, Finland (2013). (in Finnish)
[7] EN 1990
[8] J. Lahdenmaa, M. Heinisuo, T.Jokinen and M. Lawson, *Tests on Thin Double Skin Wall Panels in Compression and Shear*, to be published.

INNOVATIVE CONNECTIONS FOR THE DEMOUNTABILITY AND REHABILITATION OF STEEL, SPACE AND COMPOSITE STRUCTURES

Brian Uy*

*Centre for Infrastructure Engineering and Safety,
The University of New South Wales, Sydney, NSW 2052, Australia
e-mail: b.uy@unsw.edu.au, webpage: http://www.cies.unsw.edu.au

Keywords: Composite structures, demountability, rehabilitation, space structures, steel structures

Abstract. *Steel, space and composite structures are the common predominant structural form for structural steel used in construction and infrastructure. With the ever increasing trend internationally to build structures and infrastructure sustainably, the use of structural steel has the ability to allow structures to be designed for both deconstructability and rehabilitation. Deconstruction techniques allow structures to be designed so that they may be conveniently dismantled in the future. This will allow potential reuse of recycling of steel for future use. Rehabilitation allows structures to have their life extended. Both deconstruction and rehabilitation techniques have the potential to significantly reduce the amount of use of structural steel in construction which has the potential to have significant benefits for sustainable construction methods. One of the key elements for developing solutions for the demountability and rehabilitation of steel and composite structures are the connections between the various structural elements. This paper will detail recent research into various aspects of shear connectors, beam-beam, beam-column and column-column connectors. Future research will also be detailed that will highlight the various loading regimes that these connections need to be designed for, in order to make them suitable for robust construction.*

1 INTRODUCTION

This paper will investigate innovative connections to enable steel and steel-concrete framed structures to be made demountable. The four broad primary aims of the paper include:

1. Promote the ***reduction*** of the use of structural steel through composite steel-concrete approaches;

2. Promote the ***reuse*** of structural steel by using innovative connections that allow demountability;

3. Promote the ***recycling*** of structural steel unable to be reused after the structure is made demountable;

4. Promote the concepts of ***safety in design*** which is a new Australian mandatory requirement for building construction, (Safework Australia[1])

The concepts of demountable buildings and prefabricated construction can be traced back two millennia to the bible, Teutsh[2]. More recently in ***Australia***, the Green Building Council of Australia has provided guidelines for best practice in the use of structural steel and concrete in construction projects, (Green Building Council of Australia[3,4,5]). Furthermore, more recent discussion has centred around construction and demolition waste where demountable buildings which allow for the reuse of materials, (Green Building Council of Australia[6]). Current estimates in Australia have determined that approximately 40% of landfill waste is directly attributed to building and construction, (Green Building Council Australia, 2009[2]). Methods for lowering this rate can be achieved through changes in construction materials, methods of construction and demolition. This project will employ the use of innovative connectors between steel and concrete elements that will allow structures to be made demountable. Current Australian practice in steel building construction encourage steps that structural designers can take to maximise the potential for re-using steel buildings including using bolted connections in preference to welded joints and ensuring easy access to connections, (Ng[7]). Recent examples of this concept include the Olympic Stadium project in Sydney completed in 2000, (Figure 1). The end stands of this stadium were made demountable using innovative blind bolts and the structural steel was reused to upgrade the Wollongong Stadium south of Sydney (Figure 2), (One Steel[8]). In addition to the economic and environmental benefits that are promoted by demountable buildings, proper design of connections that ensure buildings are able to be systematically disassembled also promotes safety in design, (Safework Australia[1]).

Figure 1: The most significant demountable steel structure in Australia, Olympic Stadium Sydney

Figure 2: The most significant reused steel structure in Australia, WIN Stadium Wollongong

Significant research in Canada into the reuse of structural steel has been ongoing since 2006. This work was funded by the Enhanced Recycling Component of the Government of Canada Action Plan 2000 and by the Canadian Institute for Steel Construction, (Gorgolewski[9]). The research looks at the specific issue of reuse and recycling for the design of steel buildings, (Gorgolewski et al.[10]). Further outcomes of this work have then looked at the design of buildings using reclaimed steel, (Gorgolweski et al.[11]). Some prominent examples of this concept include the University of Toronto Scarborough Campus Student Centre. This project completed in 2005 facilitated the reuse of structural steel components from initiation of a reuse strategy and accessing a source of salvaged steel through deconstruction, fabrication, and erection of the new building.

Recent research in Europe, has highlighted methods in Sweden, promoted by the Swedish Institute of Steel Construction[12] into the sustainability of steel framed buildings. Highlighted in this report is the issue of recycling and reuse. Whilst recycling rates are as high as 100% in some jurisdictions, actual reuse of steel is only about 10-15%. Thus there are significant opportunities to grow the reuse market of structural steel. Research in Germany has also focussed on the ability to make connections demountable in precast construction (Apol[13]). Furthermore, significant research in the Netherlands has been ongoing to develop demountable connections for steel and steel-concrete composite buildings, (Brekelmans and Bijlaard[14]).

Significant research has been ongoing in Japan into the reuse and dismantling of steel buildings. Fujita and Iwata[15] firstly identified a reuse system of building steel structures and they expanded this to look at the key aspects of dismantling and evaluation of the performance of reusable members, (Fujita and Iwata[16]). Fujita et al.[17] also presented a model to diagnose stock with reusable steel members and presented a reuse business model including integrated circuit tags on the steel members, (Fujita et al.[18,19]). More recently Fujita et al.[20] have moved toward looking at a trial construction test on reused steel members not containing fireproofing materials.

In the United Kingdom, WellMet2050 is a program investigating novel methods of meeting global carbon emission targets for steel and aluminium that go beyond improving process efficiency by reconsidering the entire product lifecycle. One of the major outcomes of this program is a major publication focussing on sustainable materials which particularly advocates for the reuse of metal components without melting them, (Allwood and Cullen[21]). The London 2012 Olympics put in practice many such practices which has also received significant backing from the steel construction industry, (Bioregional Development Group[22]),

In the United States of America, there have been significant efforts to promote the concepts of sustainable aspects of structural steel, including its ability to be made demountable, (Hewitt[23]; Pulaski et al[24] and American Institute of Steel Construction[25]). One of the most significant recent examples is the newly opened gift shop on Liberty Island, the home of the Statue of Liberty. The building had to achieve a Leadership in Energy and Environmental Design (LEED) gold certification and since the owners of the new building only had a 10-year lease, they wanted the building to be designed to be easily deconstructable in case they lost their lease and needed to relocate. The building was therefore designed entirely in steel with all connections being bolted, (Koklanos[26]). More recent efforts in the USA have also been ongoing to promote the use of reclaimed structural steel and significant structural engineering practices have developed procedures to incorporate Salvaged Structural Steel (SSS) into future projects, (Winters-Downey[27]).

One of the major practical/technical limitations of the reuse of steel is the ability to make structures demountable and thus this paper will highlight the development of innovative connectors for both beams and columns that will promote the concepts of demountability. The paper will thus develop the following range of demountable/removable connectors to promote the reuse of steel: ***Beam connectors***; Beam-beam connections **(BB)**; Beam-column connections **(BC)**; and Beam-Slab connections **(BS)**, for hollowcore **HC** and profiled steel **PS** as well as ***Column connectors***; Column-baseplate connections **(CB)**; and Column-column connections **(CC)**.

2 BEAM CONNECTORS

The three major beam connectors to promote demountability include beam-beam **(BB)**; beam-column **(BC)**; and beam-slab **(BS)** connectors. The project will consider web side plate (**WSP**) connections for beam-beam **(BB)** connections. Web-side plates are the most common method of connecting primary beams to secondary beams in Australian steel framed connections. Their use will facilitate deconstruction of steel framed buildings. Key issues that need to be considered include the stiffness, strength and ductility of these connections. Uy et al. [28] has already carried out experimental and analytical studies for these types of connections in the beam-column arrangement. Figure 2 illustrates a typical photograph of a beam-beam connection using a web-side plate. The schematic shown will be evaluated. Primarily it is not expected that any rotational stiffness will be derived from this connection and it is expected that pin jointed behaviour will ensue. The primary objective is to evaluate the shear loads that will be able to be transferred and the ability to unbolt these connections after significant service loads have been applied. Current practice uses oversized holes for tolerances of these types of connections. Oversized and slotted hole arrangements will be evaluated to determine which is more reliable in being able to achieve demountability.

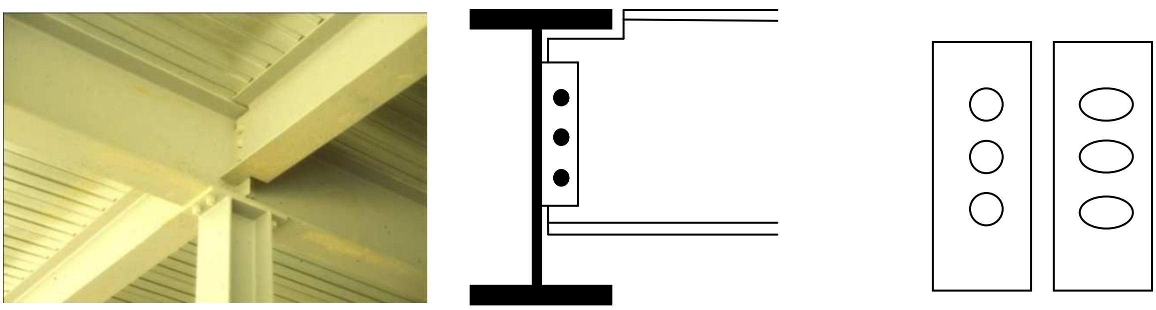

(a) Typical **BB** connection (b) **BB** connection with **WSP** (c) **WSP** options for holes

Figure 3: Beam-beam **(BB)** connections, web-side plates

Beam-column **(BC)** connections that can be used to promote demountability include the use of flush-end plate connections. Flush end plate connections possess the advantage of large initial stiffness (close to rigid) with partial strength capacity. This study will evaluate a typical connection which relies on composite capacity from the arrangement rather than continuous reinforcement. Significant research by Loh, Uy and Bradford[29,30], Wang, Han and Uy[31] and Mirza and Uy[32] illustrated the benefits of using blind bolted connections to concrete filled steel tubular columns. These types of joints are also able to be made demountable using some minor modifications as illustrated in Figure 4 (b). The main requirement would be to ensure that the slab is made discontinuous in the hogging moment region. Given that the major benefit of these joints is to provide increased stiffness in the service load range, removal of hogging moment reinforcement in these zones, should only have a minor effect on the strength and stiffness of the joints, whilst promoting demountability.

(a) Typical flush end plate (**FEP**)

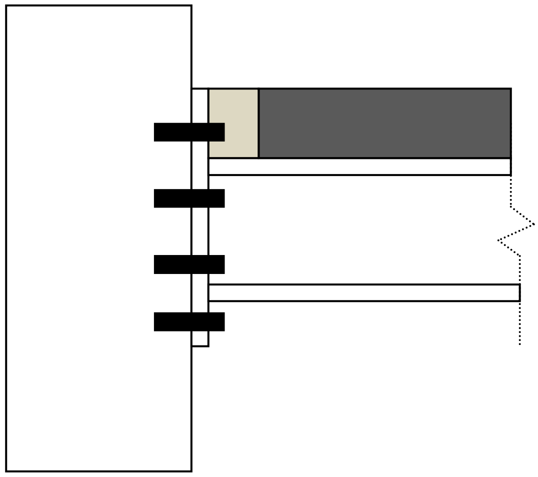

(b) **FEP** connection showing detail for demountability

Figure 4: Beam-column (**BC**) connections, flush end plates

Typical beam-slab **(BS)** connections are illustrated in Figures 5 and 6. Figure 5 illustrates typical cases of solid slabs, precast slabs and composite metal decking slabs and the shear connection between the slab and the steel beam, whilst Figure 6 highlights pretensioned hollowcore planks and their shear connection with steel beams. Recent work has been carried out to evaluate the shear connector behaviour for demountable (accessible bolted) construction by Mirza, Uy and Patel[33] and Mirza and Uy[34]. These studies showed how blind bolts could be used to make the shear connection between solid slabs demountable and the tests would apply to the cases in Figures 5 (a), (b) and (c). Further work on full scale beams by Henderson et al[35] and Pathirana et al.[36] also illustrated that beams could be loaded to very high service loads and the blind bolts could still be removed. Lam and Saveri[37] carried out further work using tapped headed shear studs into solid slabs. Since composite metal decking is by far the most commonly used method for forming slabs in composite construction, it is necessary to carry out a study to develop methods of achieving a demountable connection for these structural forms, where the metal decking and its preparation will play a critical role in the development. Furthermore, hollowcore planks on steel beams are also a very popular method of construction and demountable connection to these structural forms will also be evaluated.

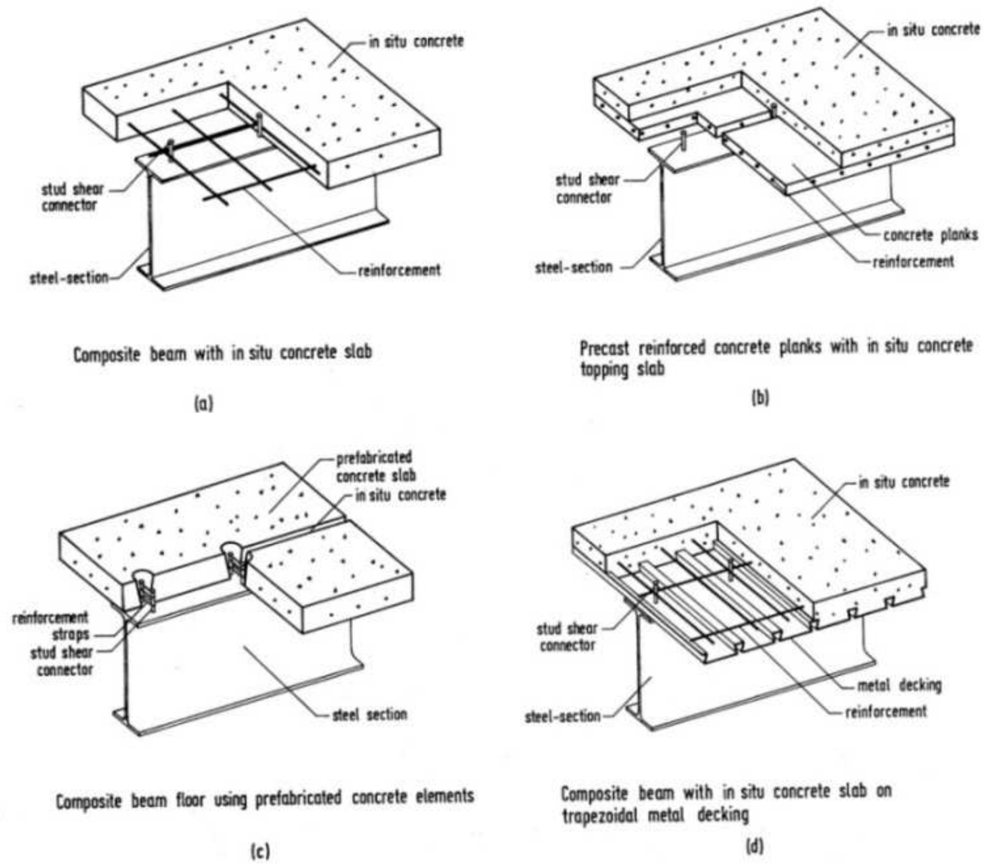

Figure 5: Typical beam-slab **(BS)** connections, (Uy and Liew[38])

Figure 6: Beam-slab hollowcore **(BS-HC)** connection, (Uy and Bradford[39])

3 COLUMN CONNECTORS

For column construction the two major forms of connectors that are necessary in erection and dismantling of steel or steel-concrete structures are column-baseplates **(CB)** and column-column **(CC)** splices. Figures 8 and 9 illustrate typical bolted configurations for steel I section columns. In Australia, steel framed multi-storey construction tends to be dominated by the use of concrete filled steel columns. Major multi-storey buildings projects such as Perth Tower (Australian Steel Institute[40]), Latitude (Chaseling[41]), Casselden Place (Webb and Peyton[42]) and Forrest Plaza (Gillet and Watson[43]) all used concrete filled steel columns because of the construction economy provided by the use of thin-walled steel tubes filled with high strength concrete. In order to provide demountable connections, for what is clearly the most dominant form of column construction in steel-framed buildings, a **CB** and **CC** connection for concrete filled steel columns will be developed herein

Figure 7: Steel column-baseplate **(CB)** connections

Figure 8: Steel column-column **(CC)** splice

Previous research into column baseplates has been carried out by Thambiratnam and Paramasivam[44], Melchers[45] and Del Savio et al. [46]. These studies dealt specifically with bare steel sections. More recent work on baseplates has been carried out by DiSarno et al. [47] and Pecce and Rossi[48] on composite encased sections. The only reported work on baseplates for concrete filled steel columns has been carried out by Park et al. [49] however this work dealt with connections where reinforcing bars are continuous through the connection, which would make the concept of demountability cumbersome to achieve. Research on column splices has primarily carried out on steel column splices. Seminal work by Lindner[50], Snijder and Hoenderkamp[51] and Girao Coelha et al.[52] has primarily focussed on stability and strength of steel column splices. The research to be carried out herein will focus on splices for concrete filled steel columns. The behaviour of concrete filled steel column splices is influenced significantly by the bond behaviour of the steel and concrete interfaces. Recent research by Tao et al[53] and Tao, Uy and Han[54] has found that the bond strength between steel tubes and concrete reduces significantly as the cross-section size increases. This project will further investigate this issue to ensure that the transfer of loads through bolts can sufficiently compensate for the reduced bond stress values which have been observed by recent research. Potential demountable connections for a concrete filled column baseplate and column splice are illustrated in Figures 9 and 10.

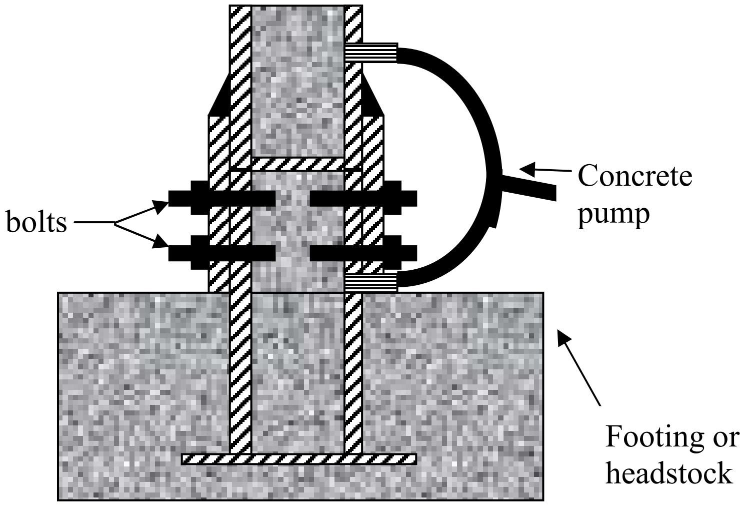

Figure 9: CFT column-baseplate **(CB)** connection

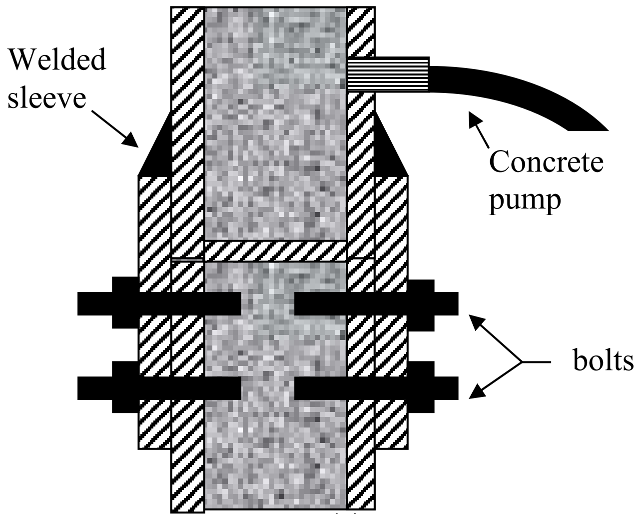

(c)

Figure 10: CFT column-column **(CC)** splice connection

4 FURTHER RESEARCH AND CONCLUSIONS

This paper has provided a background to the concepts of promoting innovative connections to enable steel, space and composite structures to be made demountable. The paper has provided an international perspective of the current regulatory frameworks that exist as well as ongoing research in this area. Typical connections for beams, slabs and columns have been postulated herein. In order to develop these types of innovative systems it will be necessary to carry out signifcant experimental testing and numerical modelling of these types of connections under typical service and ultimate load conditions. The results of these will be expected to be reported at the next SS Conference.

5 ACKNOWLEDGEMENTS

The author would like to acknowledge the support of the Australian Research Council Discovery Project Schemes which have supported this project titled “The use of innovative anchors for the achievement of composite action for rehabilitating existing and deployment in demountable steel structures” under project DP110101328 and the project “The behaviour and design of innovative connections to promote the reduction and reuse of structural steel in steel-concrete composite buildings” under project DP140102134.

REFERENCES

[1] Safework Australia. Safe design of structures, Code of Practice, July, (2012).

[2] Teutsh, M. Building in the bible - Biblical buildings, *Concrete Precasting Plant and Technology*, 67 (12), pp. 12-21, (2001).

[3] Green Building Council of Australia *Green star overview*, April, (URL:www.gbca.org.au), (2009).

[4] Green Building Council of Australia *Green star steel credit*, September, (URL:www.gbca.org.au), (2010).

[5] Green Building Council of Australia *Green star concrete credit*, November, (URL:www.gbca.org.au), (2010).

[6] Green Building Council of Australia *Construction & Demolition Waste Management in Green Star: Discussion Paper*, November, (URL:www.gbca.org.au), (2012).

[7] Ng, A. *Design for deconstruction*, Design Note No. D6, One Steel, (2009).

[8] OneSteel Why is recycling steel not the best option ?, *World Steel Dynamics*, (2004).

[9] Gorgolewski, M. The implications of reuse and recycling for the design of steel buildings, *Can. J. Civ. Eng.* 33: 489–496, (2006).

[10] Gorgolewski, M., Straka, V., Edmonds, J. and Sergi, C. Facilitating greater reuse and recycling of structural steel in the construction and demolition process, *Dept of Arch. Sc. at Ryerson Univ. with the Canadian Institute for Steel Construction*, (2006).

[11] Gorgolewski, M. , Straka, V., Edmonds, J. and Sergio-Dzoutzidis, C. Designing buildings using reclaimed steel, *Journal of Green Building*, Volume 3, Issue 3, Pages 97-107, (2008).

[12] Swedish Institute of Steel Construction Sustainability of steel framed buildings, SBI, (2005).

[13] Apol, E.J. Effects of recent trends in construction methods on connection method on connections between precast concrete elements, Part 2:How to Achieve a Demountable Connection? *Concrete Precasting Plant and Technology* 53 (11), pp. 775-777, (1987).

[14] Brekelmans, J.W.P.M. and Bijlaard, F.S.K. Design requirements for plug and play type joints in mixed and steel-concrete composite construction, *Connections in Steel Structures IV*, Roanoke, (2000).

[15] Fujita, M., and Iwata, M. Reuse system of building steel structures, *Structure and Infrast Engineering*, 4(3), pp. 207-220, (2008).

[16] Fujita, M., and Iwata, M. Reuse Dismantling and Performance Evaluation of Reusable Members, *Structural Engineering International* 3, pp. 230-237, (2008).

[17] Fujita, M., Murai, M., Fumikura, R., and Iwata, M. Reuse system of building steel structures Stock diagnosis of reusable members - Stock D, *J of Env Engg*, 73 (630) pp. 1061-1067, (2008).
[18] Fujita, M., Murai, M., and Iwata, M. Reuse system of building steel structures, *J of Env Engg*, v76 (669), pp.1025-1031, (2011).
[19] Fujita, M., Okamoto, K., Nakamura, H., Iwata, M. Reuse system of building steel structures Reuse business model using integrated circuit tag, *J of Env Engg*,, 74 (638), pp. 531-537, (2009).
[20] Fujita, M., Shibuya, A., and Iwata, M. Trial construction test on reuse of building steel structural members with fireproofing protection, *AIJ Journal of Technology and Design*, 18 (39), pp.795-799, (2012).
[21] Allwood, J.M. and Cullen, J.M. Sustainable materials with both eyes open, Chapter 15 Re-using metal components without melting them, UIT Cambridge, (2012).
[22] Bioregional Development Group Reuse and recycling on the London 2012 Olympic Park, (2011).
[23] Hewitt, C. The real deal: sustainable steel, *Modern Steel Construction,* September*, (*2003).
[24] Pulaski, M., Hewitt, C., Horman, M. and Guy, B. Design for deconstruction, *Modern Steel Construction,* June, (2004).
[25] American Institute of Steel Construction The Sustainable aspects of structural steelwork, Chicago, (2009).
[26] Koklanos, P. Built for deconstruction, *Modern Steel Construction,* January*,* (2011).
[27] Winters-Downey, E. Reclaimed structural steel and LEED Credit MR-3 – Materials Reuse, *Modern Steel Construction, May,* (2010).
[28] Uy, B., Diedricks, A.A., Bradford, M.A., and Oehlers, D.J. Behaviour of semi rigid composite connections for continuous composite beams in braced frames, *Australasian Struct. Engg Conf, Auckland, New Zealand,* pp. 221-228, (1998).
[29] Loh, H.Y., Uy, B. and Bradford, M.A. The effects of partial shear connection in composite flush end plate joints: Part I: Experimental study, *J of Constructional Steel Research,* 62 (4), pp. 378-390, (2006).
[30] Loh, H.Y., Uy, B. and Bradford, M.A. The effects of partial shear connection in composite flush end plate joints: Part II: Analytical study and design appraisal, *J of Constructional Steel Research,* 62 (4), pp. 391-412, (2006).
[31] Wang, J-F. Han, L-H. and Uy, B. Behaviour of flush end plate joints to concrete-filled steel tubular columns, *Journal of Constructional Steel Research, An International Journal*, 65 (4), pp. 925-939, (2009).
[32] Mirza, O. and Uy, B. Behaviour of composite beam-column flush end plate connections subjected to low probability, high consequence loading, *Engineering Structures, An International Journal*, 33 (2) pp. 647-662, (2011).
[33] Mirza, O., Uy, B. and Patel, N. Behaviour of shear stud connectors utilising blind bolting, *4th International Conference on Steel and Composite Structures, 21-23 July, Sydney,* pp. 429-431, (2010).
[34] Mirza, O. and Uy, B. Numerical modelling and parametric studies of shear connectors using blind bolting, *PSSC2010, Ninth Pacific Structural Steel Conference, 19-22 October, 2010, Beijing, China,* pp. 463-469, (2010).
[35] Henderson, I. Mirza, O. Zhu, X. and Uy, B. Dynamic assessment of composite structures with different shear connection systems, *ASCCS'2012 10th Int. Conf. on Steel-Concrete Composite and Hybrid Structs, Singapore,* pp. 1163-1170, (2012).
[36] Pathirana, S. Mirza, O. Zhu, X. and Uy, B. Experimental study on the behaviour of composite steel-concrete beams using innovative blind bolts, *ASCCS'2012 10th Int. Conf. on Steel-Concrete Composite and Hybrid Structs, Singapore,* pp. 1163-1170, (2012).

[37] Lam, D. and Saveri, E. Shear capacity of demountable shear connectors, *ASCCS'2012 Tenth International Conference on Steel-Concrete Composite and Hybrid Structures, 2nd-4th July, Singapore,* pp. 767-774, 2012.

[38] Uy, B. and Liew, J.Y.R. Composite steel-concrete structures, Chapter 51, *Civil Engineering Handbook*, CRC Press, (2002).

[39] Uy, B. and Bradford, M.A. Composite action of structural steel beams and precast concrete slabs for the flexural strength limit state. *Special Issue Australian Journal of Structural Engineering*, 7 (2), pp. 123-134, (2007).

[40] Australian Steel Institute. Perth tower agape to grand views, *Steel Australia*, pp. 16-17, (2009).

[41] Chaseling, C. Star attraction, *Modern Steel Construction*, 37:36-42, (2004).

[42] Webb, J. and Peyton J.J. Composite concrete filled steel tube columns. *The Institution of Engineers Australia, Structural Engineering Conf.*, pp. 181-85, (1990).

[43] Gillett, D.G. and Watson, K.B. Developments in steel high rise construction in Australia, *Steel Construction, Journal of the Australian Institute of Steel Construction*, 21 (1), pp. 2-8, (1987).

[44] Thambiratnam, David P., Paramasivam, P. Base plates under axial loads and moments, *Journal of Structural Engineering.*, 112 (5), pp. 1166-1181, (1986).

[45] Melchers, R. E. Column-base response under applied moment. *J of Constructional Steel Research*, 23(1–3), 127–143, (1992).

[46] Del Savio, A.A. , Nethercot, D.A., Vellasco, P.C.G.S., De Lima, L.R.O, Andrade, S.A.L., Martha, L.F. An assessment of beam-to-column endplate and baseplate joints including: The axial moment interaction *Advanced Steel Construction* 6 (1), pp. 548-566, (2010).

[47] Di Sarno L., Pecce, M.R and Fabbrocino, G. Inelastic response of composite steel and concrete base column connections *Journal of Constructional Steel* Research 63, pp. 819–832, (2007).

[48] Pecce, M. and Rossi, F. The non-linear model of embedded steel-concrete composite column bases, *Engineering Structures*, 46, pp. 247-263, (2013).

[49] Park, Y.-M. , Hwang, W.-S., Yoon, T.-Y., Hwang, M.-O. A new base plate system using deformed reinforcing bars for concrete filled tubular column, *Steel and Composite Structures*, 5 (5), pp. 375-394, (2005).

[50] Lindner, J. Old and new solutions for contact splices in columns*, J of Constructional Steel Research*, 64, pp. 833–844, (2008).

[51] Snijder, H.H. and Hoenderkamp, J.C.D. Influence of end plate splices on the load carrying capacity of columns, *Journal of Constructional Steel Research*, 64 (2008) 845–85, (2008).

[52] Girão Coelhoa, A.M, Simão, P.D. and Bijlaard, F.S.K. Stability design criteria for steel column splices *Journal of Constructional Steel Research* 66, pp. 1261–1277, (2010).

[53] Tao, Z., Han, L.H., Uy, B. and Chen, X. Post-fire behaviour of bond between steel tube and concrete in concrete-filled steel tubular columns, *Journal of Constructional Steel Research, An International Journal,* 67 (3), pp. 484-496, (2011).

[54] Tao, Z. Uy, B. and Han, L.H. Bond between the steel tube and concrete in concrete filled steel columns, *Abstracts of the Inaugural IIE Annual Conference, Sydney, 30 November, 2012*, Pages 22-23, (2012).

VALIDATION AND VERIFICATION PROCEDURES FOR CONNECTION DESIGN IN STEEL STRUCTURES

František Wald*, Leslaw Kwasniewski, Lukáš Gödrich* and Marta Kurejková***

*Czech Technical University in Prague
Thákurova 7, 166 29 Praha 6, Czech Republic
e-mail: wald.fsv.cvut.cz, webpage: http:/steel.fsv.cvut.cz

Keywords: Steel structures, structural connections, validation, verification, component method, research finite element model, design finite element model, component based finite element model, T stub, compresses stiffener

Abstract. *The paper refers to aspects related to benchmark studies, validation and verification (V&V) of structural connections. The considerations emphasize questions encountered in the V&V process, principles of comparison of numerical results and experimental data, the importance of sensitivity study, new ideas regarding the relationship between the research and design finite element model, differences between the Component based model and the Design finite element model. The V&V is demonstrated on modelling of the T stub and on buckling of compressed stiffener.*

1 INTRODUCTION

1.1 Validation and Verification and Connection Design

In publications dealing with computational mechanics the authors express a need for V&V studies which could be used by code users and software developers, see [1]. However, there are different opinions on how such reference material should be developed, how complex problems should be considered, theoretical or with practical meaning, and if benchmark questions should refer only to analytical and numerical solutions or should also include experimental data. These inquiries are related to the differences between validation and verification. In the formal procedure called Validation and Verification, validation compares the numerical solution with the experimental data, whereas verification uses comparison of computational solutions with highly accurate (analytical or numerical) benchmark solutions. According to [2], code verification can be conducted through tests of agreement between a computational solution and four types of benchmark solutions: analytical, highly accurate numerical solutions, and manufactured solutions [3]. In contrast to numerical solutions used in the validation stage, the numerical solutions applied for verification can represent mathematical models with little physical importance. The verification on the analyst's side is based on the test of agreement with the known correct results, if such are available. Most of commercial codes, such as ANSYS, ABAQUS. see [4], and MIDAS support lists of well-documented benchmark tests. For example, ABAQUS in three manuals provides a wide variety of benchmark tests (including 93 NAFEMS benchmarks) from simple one-element tests to complex engineering problems and experiments (validation benchmarks). These example problems, containing input files, are advantageous for a user not only as material for verification but also as a great help in individual

** Warsaw University of Technology

modelling, see [5] and [6]. Nevertheless, there is still lack of benchmark studies for some specific research areas such as, for example, connection design.

The design models of structural connections developed in last hundred year from interpolation and extrapolation of experimental results in tables and curve fitting models, see [7], to simple component based model (CBM), see [8] and advanced approaches for CBM [9] and [10]. The interpolation of experimental results is very safe procedure and was used for almost hundred years in structural steel and was replaced recently CBM. The curve fitting models has the only advantage in the simplicity of description in case of cyclic loading are still used in seismic design procedures. The major advantage of the component based models is the decomposition of the joint into components, which are well described based on engineering practice, as bolts, weld, compressed plated or by special the experiments. From this point of view is CBM taking the best historical solutions from the structural engineering in case of resistance, see [12], stiffness and deformation capacity of the structural steel connections. The simple CBM composes the final behaviour in one plane in terms of initial stiffness, ultimate resistance and deformation capacity. The extreme of such assembling is the model by one component only, see [13], which is very efficient in prediction of stiffness, where the accuracy is not necessary. It is also not surprisingly accurate for prediction of resistance in connections with one guiding component, as top angle or base plate. The advanced models are enable prediction of behaviour in 3M. The research finite elements models of structural connections were used for sensitivity studies from seventies. The question of reproduction of numerical simulation in the times of traditional calibrations procedures of major parameters were studied also at European scale, see [14]. The component the end plate in bending and the bolt in tension (or the column flange in bending and the bolt in tension) is one of the most complex part of the structural steel connections. Its component based model allow to take the prying forces into consideration. The complexity of FE modelling is deeply studied in last twenty years, see [15] and [16]. Later were commonly accepted the procedures to reach proper results in scientific oriented FE models and the strong limits for application of design FE models. Based on numerical experiments validated on experiments were developed behaviour of the well described and published components loaded by elevated temperature, as tying forces, moment normal interaction and torsion and of the new less described components, as backing channel. The fast development of the computer assisted design of steel and composite structures in field of complex structures, as plated structures in bridges, excavators and wind towers, glass structures and cold formed structures, clarified the design procedures in accuracy of models and its application in civil engineering. Today are CBM´s commonly supported by the Design finite element models (DFEM) not only to areas of design of hollow section connections. The design of this connections is still based on curve fitting models limited to only experimentally approved solutions. For connection of hollow sections of class 3 and 4 are available and used the DFEM. New generation advanced models was developed from simple tools, see [14], to Component based finite element model CBFEM, which are taken the advantages of both, finite elements assembly and plate modelling and the best engineering practice integrated into design of components, bolts, welds and compressed plates, with latest technology of design modelling and database based drawings.

The experimental data which can be used for validation should be treated separately and in a different way comparing to benchmark solutions applied for verification. The reasons for that are unavoidable errors and uncertainties associated with the result of experimental measurement. An error of a measurement (calculation) can be defined as the result of a measurement (calculation) minus the value of the measured (accurate solution), see [17]. As the accurate solution is usually unknown (eventually for simplified cases) the user can only deal with estimates of errors. Uncertainty can be thought of as a parameter associated with the result of a measurement (solution) that characterizes the dispersion of the values that could reasonably be attributed to the measured.

Experimental validation in the structural connections design through comparison between numerical results and experimental data obtained using the beam tests with for simple connections loaded in shear and cruciform tests for moment resistant connections loaded by bending moments are especially difficult and has limitations which are not economical, connection tests compare to most simple ones, but are due to inevitable uncertainties characterising the specimen behaviour. The limitations of experimental validation increase the importance of verification which is supposed to deliver evidence that mathematical models are properly implemented and that the numerical solution is correct with respect to the mathematical model.

1.2 Benchmark examples

Even though examples of experimental studies and examples of calculations following the

Structural Eurocodes procedures are also useful and can be helpful for other users, here the term benchmark studies refers to computer simulations (numerical analysis). A well-developed benchmark example should satisfy the following requirements. The problem considered should be relatively simple, easy to understand. In authors' opinion for more complex problem less reliable solution can be provided. For complex problems, for example with actual material properties of steel or concrete, only numerical solutions can be obtained. Comparison among the numerical solutions obtained with the help of different software shows quite often unexpected discrepancy among the results as well. Even if the results are similar this should not be considered as a strong evidence of the solution's reliability. Two different numerical solutions can be only compared based on a solution sensitivity analysis.

Seeking for the simplicity we should accept that a considered case can show little of practical meaning. It is supposed to be used for verification of computational models not to solve an engineering problem. Critical is the material model taken into account. If the material models developed for actual structural materials are used, for example based on EC, with all required nonlinearities, only approximate solutions are possible and can substantially vary for different software. It is difficult to find a good balance between simplicity and a practical meaning of the chosen benchmark case. To solve this difficulty it is recommended to use in benchmark studies a hierarchical approach where a set of problems is considered, starting from simple cases with analytical solutions and then more complex problems, closer to the practice are investigated numerically. Such approach gives more confidence towards obtained solutions.

As a part of benchmark study the complete input data must be provided in the way easy to follow. All assumptions such as of material properties, boundary conditions, temperature distribution, loading conditions, large/small deformations and displacements must be clearly identified. For experimental examples all measurements and detailed description of the test procedure should be provided. For numerical benchmark examples mesh density study should also be conducted. It should be shown that provided results are within the range of asymptotic convergence. If possible the recommended solution should be given as the estimate of the asymptotic solution based on solutions for at least two succeeding mesh densities. For finite element calculations the complete procedures such as Grid Convergence Index (GCI), based on Richardson extrapolation, are recommended [18]. During the development of benchmark studies it also should be considered to check alternative numerical models. e. g. using different codes or solid vs. shell finite elements (if possible). Such approach increases the validity of the solution.

1.3 Numerical experiments

Parametric study is a desired element of the experimental work and an indispensable element of the numerical analysis. The cost needed to perform multiple experiments related to structural connections is usually small but a probabilistic distribution of the system response is rarely available. However, in the case of simulated benchmark problems computational cost of running multiple instances of a simple numerical experiment with varying input parameters is competitive.

The variance of a system response depends on the variance in the input parameters but also on the range at which it is tested. Nonlinearity of the response has to be taken into account as well when designing the benchmark tests. The numerical experiments should be performed out in the range where a reasonable variation in an input parameter causes a reasonable change in the system's response. Designing a benchmark test producing either a non-sensitive or overly sensitive response is undesirable. The sensitivity study for a system with multiple variable input parameters and multiple responses should be performed by regression analysis or variance based methods.

Actually selection of the System Response Quantity (SRQ), see [19], is important for both, verification and validation. However, in both cases it is subject to different limitations. In verification, SRQ means a quantity which describes the response of the structure and is selected for comparison with the value obtained from the benchmark solution. A user is less limited here as in the case of validation where the experimental data is always limited with the number of gauges and other instrumentation. The selection of the SRQ should reflect the main objective of the analysis and for structures in fires it usually refers to quantities describing heat transfer or mechanical response. For heat transfer problems temperatures obtained at the specific time instance at selected locations seems to be an optimal choice. For mechanical structural response usually we can choose between local and global (integral) quantities. Engineers are usually interested in stresses and internal forces, which are local quantities. They are subject to larger uncertainties especially in the case of validation. More appropriate are global quantities such as deflection which reflects deformation of the whole (or a large part of) structure and its boundary conditions

1.3 Experimental validation

As the experimental data is stochastic by nature and is always subject to some variation it should be actually defined by a probability distribution such. For complete comparison the numerical results should also be presented in analogous probabilistic manner using a probability distribution, generated by repeated calculations with some selected input data varying following prescribed distributions (so called probability simulations). Such extensive calculations can be conducted automatically with the help of specialised optimization packages (e.g. LS-OPT®, HyperStudy® or ModeFrontier®) which are more often included in nowadays commercial computational systems.

For many authors working on principles of validation and verification [1] the term calibration has negative meaning and describes a practice which should be avoided in numerical modelling. Calibration means here unjustified modification of the input data applied to a numerical model in order to shift the numerical results closer to the experimental data. An example of erroneous calibration is shown in Figure 1, where at the begging it is assumed that the numerical model well reflects the experiment however, due to some uncertainties associated with the experiment the first numerical prediction, differs from the first experimental result. Frequently in such cases the discrepancy between the experiment and the numerical simulation is attributable to some unidentified by the analyst input parameter and not to a limitation of the software and then through hiding one error by introducing another, the calibration process itself is erroneous. Calibration, applied for example through variation of material input data, shifts the result closer to the experimental response but at the same time changes the whole numerical model whose probability is now moved away from the experimental one. Due to the calibration, the new numerical model may easily show poorer predictive capability. This fact is principally revealed for modified input data (e.g. loading conditions).

There is a situation when the calibration process actually makes sense. If a full stochastic description of experimental data is known and probabilistic analysis was performed for the simulation and there is a difference between means of measured and simulated responses then calibration of physics models may be needed. The adjustment of the model introduces a change in the response that brings the entire spectrum of results closer to the experimental set of data. The calibration defined that way is much more complex process than just tweaking of the models and must be confirmed on different simulated events.

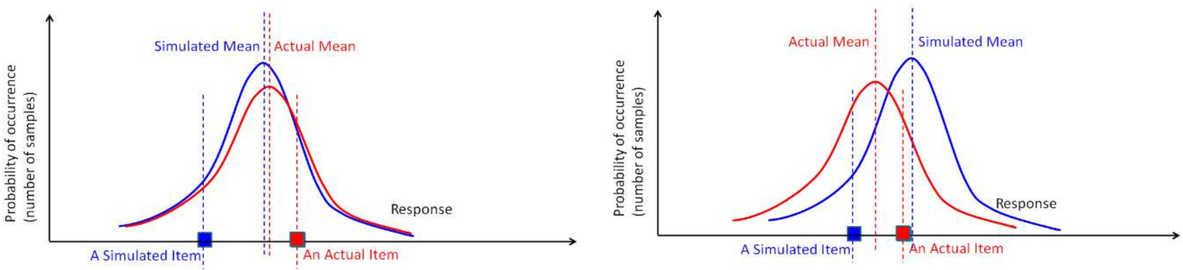

Figure 1: Example of calibration meaning unjustified shifting the numerical results closer to the experimental data, see [5]

2 VALIDATION OF REASERCH MODEL OF T STUB

2.1 Experiment

As very classical procedure is presented further a validation of T-stub with 2 bolts. Numerical model was validated according to results of two experiments performed on CTU Prague. MIDAS software was used for numerical simulation.

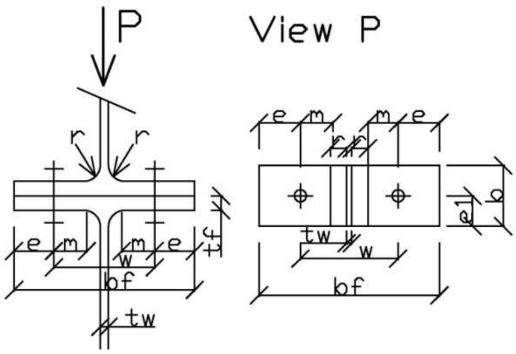

Figure 2: Geometry of T stub samples

Table 1: Measured geometry of T stubs, mm

Sample	Section	t_f	t_w	b_f	r	b	w	e_1	m	e	f_y	f_u	R
1	HEB 300	17,8	10,6	300	27,0	98,8	164	49,4	5,1	68,0	355	530	62 %
2	HEB 400	23,1	13,6	300	27,0	99,6	169	49,8	6,1	65,5	263	443	58 %

Two samples of T-stubs connected by two bolts M24 8.8 were designed and experimentally tested. T-stubs were performed by separating the upper flange of rolled HEB-sections. Dimensions of the samples are given in Figure 2 and Table 1. T-stub's webs were fixed to clamps and samples were subjected to tension force.

2.2 Material and Imperfections

Tensile tests of T-stubs material were performed, see Table 1 with yield stress f_y, ultimate stress f_u and deformation capacity R. The Multi-linear truth stress truth strain stress-strain diagram with statically determined values was used for material of T-stubs in numerical model. For the material of the bolts is considered a bilinear stress-strain diagram with strain hardening, Young´s modulus E = 210000 MPa, yield strength f_{yb} = 640 MPa and ultimate strength f_{ub} = 800 MPa. Maximal plastic strain is expected as ε_b = 5%.

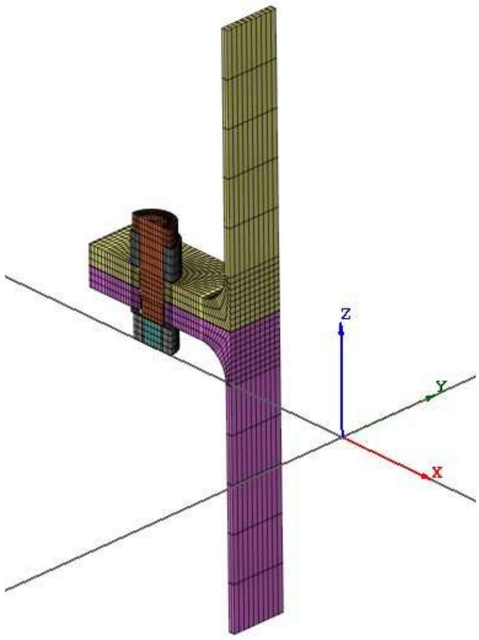

Figure 2: Numerical model of T sub

2.4 Validation procedure

Numerical model of the bolt was verified at the first step. Verification of the bolt numerical model was based on comparison with several analytical models and numerical model according to Wu et al

[20]. Influence of the element size, number of elements through thickness of the flange, geometric imperfections, the choice of stress-strain diagrams and others were investigated as part of the validation process. Minimal three elements through flange thickness provide sufficient accuracy of numerical model. Element edge size 5 mm provides sufficient accuracy of calculation. It was found that only the thickness of the flange, bolts location and radius of curvature at the connection of the web to flange significantly affect results of numerical model. It is important to consider multilinear stress-strain diagram with static values for the material of T-stub.

Results obtained from validated numerical models are compared to experimental data. Comparisons of T-stub deformations are shown in Figure 3. It can be concluded that in both cases are numerical results very similar to the experiment. Comparisons of strains on the flange in plastic lines of bolt and plastic lines by web were done and similar conclusions have been reached.

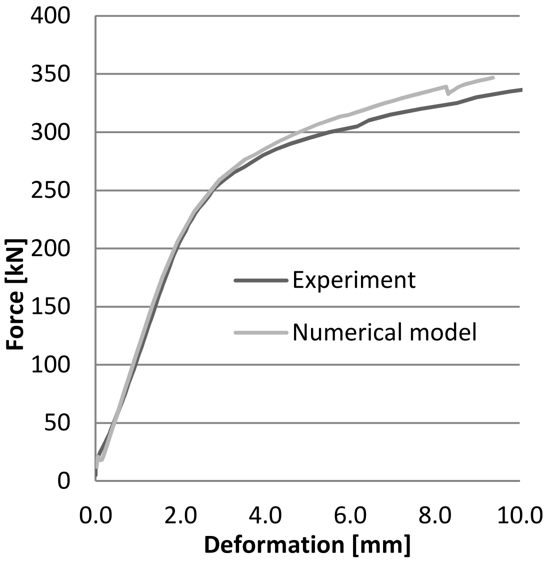

a)

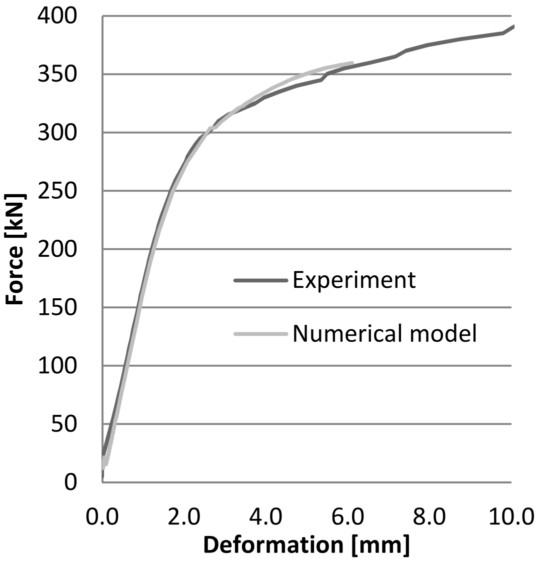

b)

Figure 3: Force-deformation diagrams for T-stubs, a) sample HEB300, b) sample HEB400

3. VERIFICATION OF DESIGN MODEL OF COMPRESSED PLATE

3.1 Focus and geometry

In this part is presented a verification example of steel plate under uniform uniaxial compression with changing slenderness. The numerical results calculated in MIDAS are compared to reduction curve in Chapter 4 and Annex B, EN1993-1-5:2007 [21]. For each case is considered the same boundary conditions, material model and imperfections. A similar analysis using code ANSYS was published by Braun [22]. In the numerical analysis is used a square steel plate with dimensions a = b = 1000 mm and thickness changing from 7 mm to 30 mm.

3.2 Load cases and boundary conditions

The investigation is concentrated on a simple load case namely uniform uniaxial compression as shown in Figure 4. Boundary conditions are used hinged at all edges, the loaded edges are constrained in the y direction and unloaded are unconstrained.

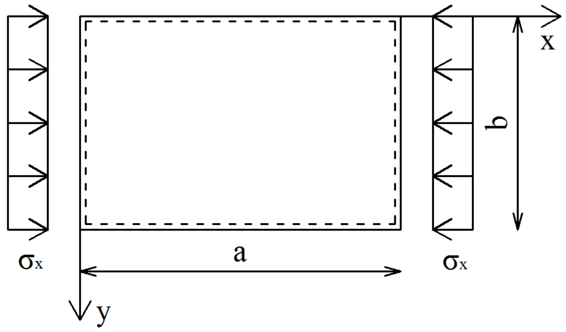

Figure 4: Load case and boundary conditions for verification example

3.3 Material model and imperfections

For the calculation is used isotropic material model to assure that mechanical behavior is same in all directions. The characteristic material properties of steel were utilized, Young´s modulus E = 210 000 MPa, Poissson´s ratio v = 0,3 and yield strength f_y = 355 MPa. The bilinear stress-strain curve with strain hardening was selected with maximal strain is ε = 5 % at ultimate strength f_u = 510 MPa as shown in Figure 5.

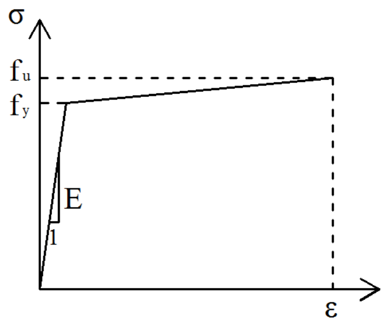

Figure 5: Material model for verification

Imperfections are modelled in the shape of first eigenmode coming from a linear bifurcation analysis (LBA) with amplitude recommended in Annex C, EN 1993-1-5 [21], i.e. a/200.

3.4 Numerical model

Plates are modelled using shell elements in MIDAS. The same material model, imperfections, loading and boundary conditions are considered as described previously. The load was applied only on one of the edges to assure symmetrical behavior. Supports were modelled in every node: constrained displacement degree of freedom in z direction at the unloaded edges, constrained displacement in y and z at the loaded edge, where is the stress load applied and constrained displacement in x,y and z at the loaded edge without the stress load. FE elements dimension is 100 x 100 mm as shown in Figure 6.

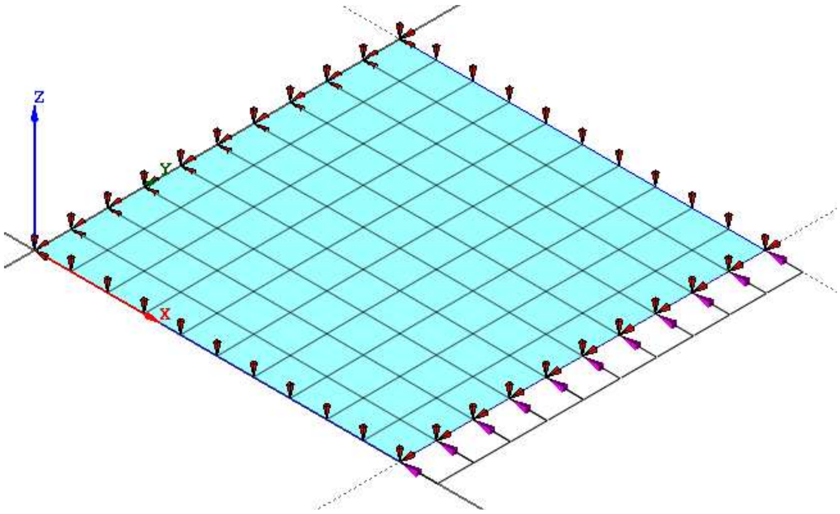

Figure 6: Numerical model

3.5 Verification on buckling curves

The reduction factor ρ depends on the boundary condition and slenderness and is chosen from EN 1993-1-5 section 4 or Annex B.

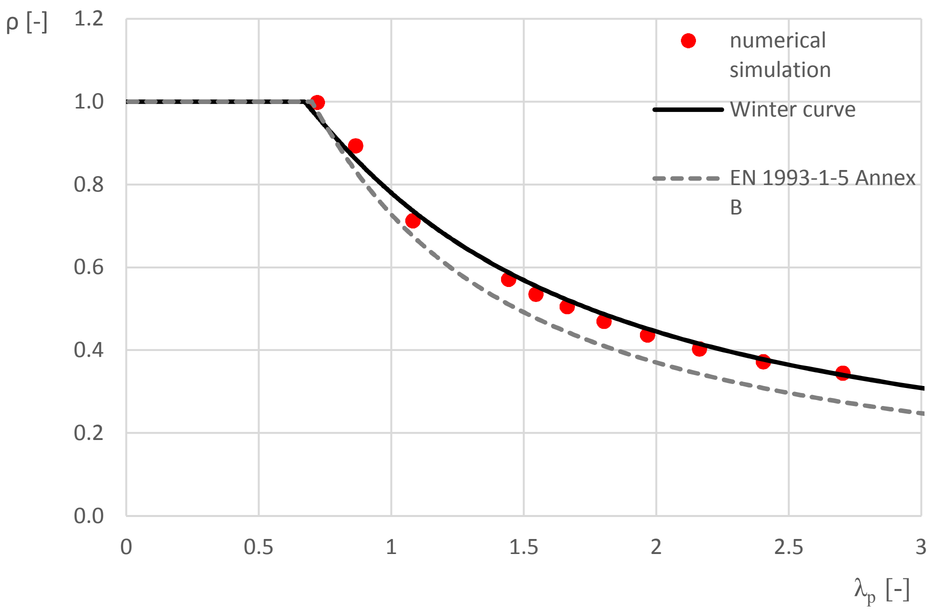

Figure 7: Buckling curves and numerical simulations

The reduction factor according to Chapter 4 for may be determined:

$$\rho = 1{,}0 \text{ for } \overline{\lambda}_p \leq 0{,}673 \tag{1}$$

$$\rho = \frac{\overline{\lambda}_p - 0{,}055(3+\psi)}{\overline{\lambda}_p^2} \text{ for } \overline{\lambda}_p > 0{,}673 \tag{2}$$

The reduction factor according to Annex B is determined:

$$\rho = \frac{1}{\phi_p + \sqrt{\phi_p^2 - \overline{\lambda}_p}} \tag{3}$$

where $\overline{\lambda}_p$ is the modified plate slenderness,

$$\phi_p = \frac{1}{2}\left(1 + \alpha_p\left(\overline{\lambda}_p - \overline{\lambda}_{p0}\right) + \overline{\lambda}_p\right) \tag{4}$$

where α_p is 0,13 for hot rolled and 0,34 for welded or cold formed sections, $\overline{\lambda}_{p0}$ is 0,7 for direct stress and 0,8 for shear and transverse stress buckling mode.

Results from numerical simulation are shown in Figure 7. It can be concluded that in all cases are numerical results very similar to the Winter curve. The numerical study could be further extended by FE mesh density investigation and influence of different boundary conditions.

4 CONCLUSIONS

Four decades ago computational analysis of structural connection was treated by some researchers as a non-scientific matter. Two decades later it was already a widely accepted addition or even extension of experimental and theoretical work, see [24]. Today computational analysis, in particular computational mechanics and fluid dynamics, is commonly used as an indispensable design tool and a catalyst of many relevant research fields. The recommendation for design by advanced modelling in structural steel is already hidden but ready to be used in Chapter 5 and Annex C of EN 1993-1-5:2005 [21]. Development of modern general-purpose software and decreasing cost of computational resources facilitate this trend. As the computational tools become more readily available and easier to use, even to relatively inexperienced engineers, more scepticism and scrutiny should to be employed when judging one's computational analysis. The only way to prove correctness of simulated results is through a methodical verification and validation process. Without it the analysis is meaningless and cannot be used for making any decisions. In the case when the analysed event is too complex or overly expensive to test experimentally, hierarchical validation is recommended, see [25].

However for structural connections with thousands experiments available the validation process may be executed. But even in such situation the verification process performed through benchmark tests gains crucial importance. Seeing the need of making the results of research more transparent to the public, the office of science and technology policy in the United States issued a memorandum stipulating increased access to the results of federally funded scientific research, see [26]. Such data can be easily verified or used for verification (or benchmarking), of some other work. The trend of making extended data available together with a report or publication persists in order to build confidence in growing number of performed numerical simulations. To achieve this goal it seems even more beneficial at this point to develop a standard set of smaller benchmark tests that can be used as a reference in the verification process of simulations, see [24]. The source and the extent of such benchmark tests for the field of structural connections is yet to be established.

ANNOUNCEMENT

The work was prepared under work the project MERLION of Czech Republic Technical No. TA02010159.

REFERENCES

[1] Kwasniewski L., Numerical verification of post-critical Beck's column behavior, *International Journal of Non-Linear Mechanics,* 45 (3), 2010, 242-255.

[2] AIAA, Guide for the Verification and Validation of Computational Fluid Dynamics Simulations, American Institute of Aeronautics and Astronautics, AIAA-G-077-1998, Reston, VA, 1998.

[3] Oberkampf W.L., Trucano T.G., Verification and validation benchmarks, Nuclear Engineering and Design 238, 2008, 716–743.

[4] SIMULIA, Abaqus 6.11 Benchmarks Manual, © Dassault Systèmes, 2011.

[5] Wald F., Burgess I., Kwasniewski L., Horová K, Caldová E., *Benchmark studies, Experimental validation of numerical models in fire engineering*, CTU Publishing House, 2014, 198 p., ISBN 9788001054437.

[6] Wald F., Burgess I., Kwasniewski L., Horová K., Caldová, E., *Benchmark studies, Verification of numerical models in fire engineering*. CTU Publishing House, 2014. 328 p., ISBN 9788001054420.

[7] Chen, W.F., Abdalla K.M., Expanded database of semi-rigid steel connections, Computers and Structures, 56, (4), 1995, 553-564.
[8] EN 1993-1-8, Eurocode 3, Design of steel structures, Part 1-8, Design of Joints, CEN, Brussels 2005.
[9] da Silva L. S, Towards a consistent design approach for steel joints under generalized loading, *Journal of Constructional Steel Research,* 64 (2008) 1059–1075.
[10] Block FM, Davison JB, Burgess IW & Plank RJ, Deformation-reversal in component-based connection elements for analysis of steel frames in fire. *Journal of Constructional Steel Research*, 86, 2013, 54-65.
[11] Zoetemeijer, P.: *Summary of the Researches on Bolted Beam-to-Column Connections*. Report 6-85-7, University of Technology, Delft 1985.
[12] Steenhuis M., Gresnigt N., Weynand K., *Pre-Design of Semi-Rigid Joints Ii Steel Frames*, Proceedings of the Second State of the Art Workshop on Semi-Rigid Behaviour of Civil Engineering Structural Connections, COST C1, Prague, 1994, 131-140.
[13] Agerskov, H.: *High-strength bolted connections subject to prying*, Journal of Structural Division, ASCE, 102 (1), 1976, 161-175.
[14] Virdi K. S. et al, *Numerical Simulation of Semi Rigid Connections by the Finite Element Method*, Report of Working Group 6 Numerical, Simulation COST C1, Brussels Luxembourg, 1999.
[15] Bursi O. S., Jaspart J. P., Benchmarks for Finite Element Modelling of Bolted Steel Connections*, Journal of Constructional Steel Research,* 43 (1-3), 1997, 17-42.
[16] Brito P. H., Rocha C.R., Filho F.C., Martins E., Rubira C.M.F., A Method for Modeling and Testing Exceptions in Component-Based Software Development, Dependable Computing, Lecture Notes in Computer Science, 3747, 2005, 61-79.
[17] ISO, Guide to the Expression of Uncertainty in Measurement, ISO Geneva, 1993.
[18] Roache P.J., Verification and Validation in Computational Science and Engineering, Computing in Science Engineering, Hermosa Publishers, 1998.
[19] Kwasniewski L., Nonlinear dynamic simulations of progressive collapse for a multistory building *Engineering Structures*, 32 (5), 2010, 1223-1235.
[20] Wu, Z., Zhang, S. and Jiang, S., *Simulation of tensile bolts in finite element modeling of semi-rigid beam-to-column connections*, International Journal of Steel Structures, Vol. 12, No. 3, pp. 339-350, 2012.
[21] EN 1993-1-5*, Eurocode 3: Design of steel structures - Part 1-5: Plated Structural Elements,* CEN, Brussels, 2007.
[22] Braun B., *Stability of steel plates under combined loading*, Institut für Konstruktion und Entwurf, Stuttgart, 2010.
[23] Jetteur P., Cescotto S. *A mixed finite element for the analysis of large inelastic strains*, International Journal for Numerical Methods in Engineering, 31, 1991, 229-239.
[24] NAFEMS, National Agency for Finite Element Methods, http://www.nafems.org/, 2013.
[25] ASME Guide for Verification and Validation in Computational Solid Mechanics, The American Society of Mechanical Engineers, ISBN 079183042X, 2006.
[26] Holdren J. P., Increasing Access to the Results of Federally Funded Scientific Research, Memorandum for the Heads of Executive Departments and Agencies, Office of Science and Technology Policy, Washington, D.C, 2013.

12th International Conference on
Steel, Space and Composite Structures
28-30 May 2014, Prague, Czech Republic

PREVENTING FIRE-INDUCED PROGRESSIVE COLLAPSE OF STEEL FRAMED STRUCTURES – A SCENARIO ANALYSIS

Y.C. Wang

School of Mechanical, Aerospace and Civil Engineering,
University of Manchester, United Kingdom
e-mail: yong.wang@manchester.ac.uk
website: http://www.mace.manchester.ac.uk/our-research/research-themes/structural-fire/

Keywords: progressive collapse, fire, scenarios, steel structures, Class 3 building, multi-hazard

Abstract. *This paper presents some suggestions on credible scenarios that may be considered when assessing the risk of fire-induced progressive collapse of steel framed structures. Fire-induced progressive collapse of building structures has been brought into prominence after collapse of the World Trade Center buildings on September 11, 2001. Although there have been many research studies to understand the mechanisms of, and possible methods for reducing, progressive collapse of steel framed structures in fire, there is a lack of debate on what constitutes as credible scenarios from which to start the structural robustness assessment.*

At ambient temperature, member removal, in particular column removal, is considered an acceptable scenario for assessment of robustness of a structure. However, this is not a suitable scenario for assessing robustness of the structure in fire. This is because member removal is already the consequence of an extreme loading condition and its addition to another one, fire, would be too severe and should only be considered under the rarest conditions. For most structures, it would not be possible for them to withstand simultaneous member removal and high temperatures from fire exposure.

The scenario analysis in this paper is based on the following definition of structural robustness: the ability of a structure to accept a certain amount of local damage without failing to any great extent. It proposes a "20%" rule: there should be no additional structural failure when performance of any member of the structure suffers a reduction by 20%. Thus, for example, if the load-carrying capacity of the supporting column to the supported beams is reduced by 20% against its expected performance in fire, it should not lead to the supported beams to collapse. Or if the design limiting temperature is exceeded by 20%, the structure can find an alternative load carrying mechanism to resist this increased temperature.

Based on the above definition, this paper will present some detailed results to assess the criticality of different scenarios, based on testing the sensitivity of various generic structural arrangements to 20% reduction in performance in a number of design parameters.

The results of this analysis suggest that a 20% degradation in thermal performance (e.g. due to increase in fire severity, or degradation of fire protection material performance) results in temperature increase in the structure of about 20% above the limiting temperature. This temperature increase can lead to over 50% reduction in the member's load carrying capacity. With this level of reduction in column load carrying capacity, increasing the column fire protection by 20% is the most effective way of minimising the risk of fire-induced progressive collapse. Even with a loss of 50% in load carrying capacity, the lateral stability (e.g. bracing) system can still resist the lateral loads because at fire limit state, the dominant lateral load, wind, is only a very small fraction of that at ambient temperature. If steel beam temperature is increased by 20% over the limiting temperature calculated based on bending resistance, it is possible for the beam to survive without progressive collapse, by developing catenary action. However, the connections should be able to resist the catenary action force and have very high rotation capacity. The possible method of achieving these requirements is by using Fire Resistant steel for the critical connection components (bolts).

1. INTRODUCTION

Design for structural fire safety has traditionally been relegated to activities by non-engineering professions. Since about 20 years ago, structural fire engineering has been identified as an effective tool, practised by specialist fire engineers with structural engineering background, to help reduce the cost of construction, improve design and construction flexibility [1]. Structural fire engineering can also lead to improved structural safety because the structural fire engineering approach forces the engineer to understand how the structure behaves under the design fire scenario and to focus on the critical aspects of the structure to ensure their safety [2], whilst the blanket deemed-to-satisfy approach is tick box and may overlook some of the critical aspects of structural safety in fire.

However, publicity since the World Trade Center collapse on 11th September 2001 seems to have over swung the pendulum so much so that there is now a tendency to overestimate the risk of fire. Many researchers are now investigating how to design and construct structures to survive extremely severe fire attacks without suffering progressive collapse. However, in these research studies, the question is seldom asked about the credible scenarios which may trigger progressive collapse in fire.

If the assumed design scenario is too severe (such as multi-hazard) and the structure is as currently designed and constructed, it is often not possible to prevent fire-induced progressive collapse [3]. However, it would not be realistic to change the existing construction and it would be prohibitively expensive to design the structure to survive the extremely severe fire attack. A rational assessment of scenarios that may cause progressive collapse in fire is necessary so that structural fire design can achieve the desired balance of safety and economy.

This paper presents some thoughts on possible scenarios that may lead to fire-induced progressive collapse and then assesses whether they should be considered in structural fire safety design. This paper does not include structures which have their specialist requirements on safety. For example, the consequence of nuclear structural failure is such that they have to be designed for very severe scenarios often involving multi-hazards. Other specialist structures include petrochemical plants and offshore oil platforms. This paper is for buildings that are covered in Eurocode 1 Part 1.7[4] and the Building regulations of England and Wales [5] but without hazardous materials and processes. Such building structures are divided into 3 classes which are broad indications of the risk of failure. For Class 3 buildings (e.g. residential/office/education/retail buildings over 15 storeys, hospitals more than 3 storeys high, grandstands accommodating more than 5000 spectators), the risk of failure is deemed to be sufficiently high that a systematic risk assessment for disproportionate collapse (progressive collapse) should be carried out. The discussions of this paper are within the context of such Class 3 buildings and are intended to provide suggestions for determining possible scenarios for the required systematic risk assessment.

In the latest publication by the Institution of Structural Engineers [6] providing guidance on systematic risk assessment of high-risk structures against disproportionate collapse, it states that "a number of adverse events have a high likelihood of causing a secondary event that is not statistically independent, and should therefore be considered in combination (consequential hazards). Many of these consequential hazards involve fire". However, the example given for this statement, World Trade Center, 11 September 2011, is far from being typical. In fact, it may be argued that collapse of the World Trade Center buildings was mainly a result of deficiencies in fire resistance, rather than the combined hazard of impact and fire. Had the fire protection spraying material on the floor trusses of the buildings not been defect, the floor trusses would not have experienced high temperatures and would not have gone into catenary action which pulled down the supporting columns.

Within this building class, this paper argues that multi-hazards involving fire, such as fire and earthquake, fire and explosion, fire and impact, should only be considered if the client of the project considers the likelihood is credible (e.g. chemical plants, offshore oil platform) and the consequence of structural failure under such multi-hazards cannot be tolerated (e.g. iconic super tall structures). Otherwise, the cost of construction can become prohibitively high.

For the majority of structures, this paper argues that consideration of fire-induced progressive collapse should only have to address issues related to possible inadequacy of fire resistance. Because there are uncertainties on many aspects of structural fire safety design (specification of fire behaviour, thermal properties/application/durability/maintenance of fire protection materials, understanding of structural material and structural behaviour at high temperatures) such inadequacies have a reasonably high probability of occurring. This paper poses the following question: if the performance on any of these uncertainties leads to degradation of expected performance, say by 20%, would progressive collapse occur? If the answer is no or if alternative load carrying mechanisms can be identified to compensate for the lost performance, then the structure may be considered to have sufficient robustness and that the risk of fire-induced progressive is sufficiently low to be acceptable. If the answer is yes, additional strengthening of the structure is necessary.

For the above scenario, this paper will outline some methods of assessing residual structural resistance for degradation of 20% performance on a number of design parameters, and identify some alternative load carrying mechanisms and evaluate their feasibility to compensate for the loss of performance.

2. SCENARIO ASSESSMENT

Fire is already an accidental loading condition that has to be included in structural design for buildings. Therefore, it can be argued that the building structure should not fail in fire and consequently there would be no fire-induced progressive collapse. The fact that fire-induced progressive collapse has occurred means that the design fire scenario cannot cover all eventualities. What is important is to identify credible scenarios that may happen but that have not been considered during the design stage. These scenarios may be considered under two generic headings: (1) multi-hazard and (2) inadequate fire resistance. Often multi-hazard scenarios are not explicitly considered; instead, a default notional damage, such as removal of a structural member, is assumed. In the case of inadequate fire design assumptions, it may be argued that there must be a limit in how far the real condition departs from the design assumption. Without any scientific basis to quantifying such departure, it is difficult to present a definitive value. This paper suggests a nominal value of 20%, based on the belief that if the real condition departs from the design condition by 20%, then this represents a relatively high level of inaccuracy. Given that existing fire resistant design has a credible level of accuracy, assuming 20% inaccuracy is considered acceptable for testing structural robustness under fire exposure. Thus, there are three possible specific scenarios:

- Multi-hazards involving fire;
- Member removal in fire;
- 20% degradation in performance of fire precaution measures.

The latter two represent two levels of damage that may be assumed as the initial condition for assessing risk of fire-induced progressive collapse of building structures: 100% damage (member removal) or a notional 20% damage. Member removal is linked to the first scenario of multi-hazard when it is not possible to specify the exact magnitude of the other hazards, while the 20% damage is relevant to inherent uncertainties in fire resistance. Currently, member removal is often used as the starting point of assessing progressive collapse of structures under normal loading without fire exposure. Since it is already quite difficult for a structure to survive progressive collapse after member removal at ambient temperature, it is expected that the structure with member removal would be almost impossible to resist progressive collapse at elevated temperatures. The following section argues that unless sources exist and there are special considerations, it is not appropriate to assume multi-hazard as a design scenario for assessment of fire-induced progressive collapse, and consequently it is not reasonable to assume member removal as the initial damage.

3. MULTI HAZARD SCENARIO ASSESSMENT

Under the multi-hazard scenario, fire acts in conjunction with other accidents, which may be the cause or result of fire attack.

Following on from collapse of the Twin Towers, which happened after the Twin Towers were impact by an aeroplane followed by fire, there has been wide interest in research studies on building structural performance under multi-hazards. These include earthquake and fire, explosion and fire, and impact and fire.

3.1 Earthquake followed by fire

The co-existence of fire and earthquake has long been noticed, however, their effects have been separately considered [7] and it appears that it is only recently this is being considered in structural design. When discussing post-earthquake fire resistance, one should separate strengthened and un-strengthened buildings. If post-earthquake, the building is repaired and strengthened so that the strengthened building achieves the original fire resistance performance requirements, the building may be considered to be “as new” so far as fire resistance is considered and earthquake should be ignored in assessing further fire-induced progressive collapse. It is expected that post-earthquake, repairable buildings would be repaired and strengthened to meet the requirements of new buildings.

Combined earthquake and fire refer to the case when fire attacks the building immediately after the earthquake. In this case, it may be argued that fire after earthquake does not pose more risk than from earthquake alone. This is because when an earthquake strikes, it can be assumed that building occupants have either evacuated or perished before the fire attack. In addition, fire occurs after an earthquake due to fracture of gas pipes. If the building structure has survived the earthquake remaining intact, it is reasonable to assume that the gas pipes inside the building would remain intact and would not cause a fire. If coincidence of fire and earthquake has to be considered in building design, it would be more effective to ensure that fire does not occur if the building structure does not collapse. This may be possible if the gas pipes can survive the building deformations expected during earthquake.

If the building collapses and causes the gas pipes to fracture and hence leading to fire, it is inconsequential as far as the building structure is concerned because the structure has already collapsed.

The risk of fire following earthquake therefore would come from external, not internal, fire exposure.

In summary, the additional risk due to fire following earthquake, over that already caused by the earthquake, is likely to be very small. Designing the building structure for combined earthquake and fire appears an ineffective strategy for reduction of risk.

3.2 Fire and Explosion

In order for explosion to occur, there must be sources of explosion. Consider accidental gas explosion first. Domestic gas explosion is a possible source, but its occurrence has been very rare with ever improving gas safety systems. Gas explosion in petrochemical plants, including offshore oil platforms, is a credible scenario. In such facilities, existing practices for safeguarding, particularly in prevention of fire and explosion, are strenuous and the control of risk is acceptable. Existing safety control methods include explicit consideration of both fire and explosion and the structure is designed to survive the design fire and explosion. Therefore, when explosion is combined with fire, the probability of member removal due to explosion followed by a severe fire attack can be considered to be very low.

Impact followed by fire may happen, as illustrated by the World Trade Center buildings [8]. However, such an incident should not become the norm of structural fire design. Impacts to buildings happen frequently, but they rarely cause a fire to break out. When fire follows impact, it is usually because the building is iconic and the accident is malicious with impact being used as incendiary to start the fire. For such buildings, the design team should consider the multi-hazards.

In summary, multi-hazard should only be considered in the following situations:

- Specialist structures whose consequence of failure is unimaginable. The example is nuclear structures.

- Specialist structures with explosion sources. Examples include petrochemical plants and offshore oil platforms.
- Iconic tall structures: structures that may become targets for malicious attack (impact) which may lead to consequential fire attack.

For other types of Class 3 structures, fire should be considered independently. In fact, the worked example in the recent Institution of Structural Engineers' design manual for systematic risk assessment of fire-risk structures against disproportionate collapse identifies impact, explosion and fire as possible hazards, but does not consider their combination.

3.3 Quality of information for fire safety design of structures

Whilst the above two sections focus on initiating events that are not fire related, progressive collapse may still occur due to inadequacy of design input data. Such possibilities include:

Inadequate specification of fire loading: prediction of fire behaviour is a young science and there are still many uncertainties. Furthermore, the specification of fire load for the quantification of fire behaviour is based on data that dates back many years ago.

Damage to fire protection materials due to wear and tear: when fire protection material is applied on steel structures, the assumption is that they would remain unchanged during the life of the structure. However, some fire protection materials may easily suffer wear and tear, especially if the fire protection materials are subject to everyday activities.

Degradation of fire protection materials due to aging: some fire protection materials may degrade in their performance due to aging. Collapse of the World Trade Center buildings is largely attributed to the loss of fire protection function of the fire protection spray materials [8] (Figure 1). Intumescent coating fire protection materials are chemically reactive and weathering can cause their fire protection performance to suffer [9].

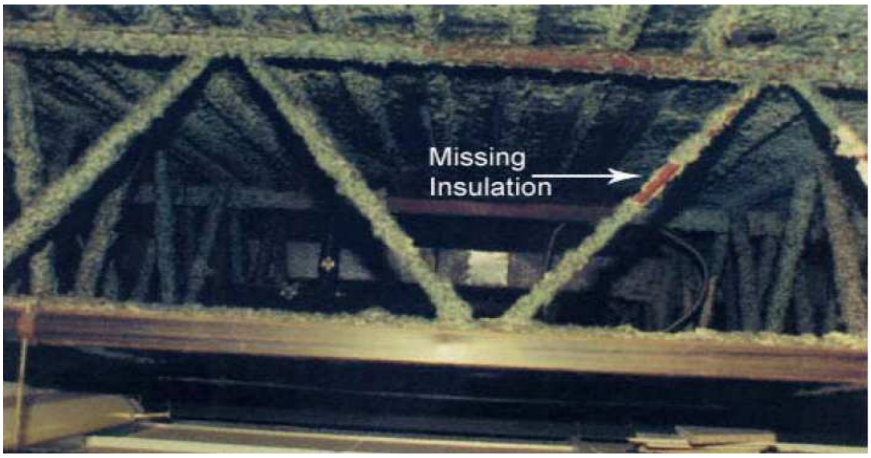

Figure 1: Floor truss with damaged spray fire protection, from [8]

Thermal properties of fire protection materials: reliable data for elevated-temperature applications are virtually non-existent. Manufacturers of fire protection materials provide ambient temperature properties at best. However, the elevated temperature thermal properties of some fire protection materials can be considerably different from those at ambient temperature. In particular, the thermal conductivity of some fire protection materials may be much higher than those at ambient temperature, thus causing the protected structural temperature to be much higher than calculated in design [2].

Mechanical properties at elevated temperatures: whilst data at ambient temperature for different structural loadbearing materials are abundant and extensively researched, quality of the corresponding data at elevated temperatures is much poorer. This comes about because (1) the probability of structural collapse under fire attack is considerably lower than under normal loading conditions: (2) obtaining high-quality data for resistant design in inherently much more time consuming. Consider the stress-strain curve of steel as a simple example. It is a routine task to carry out tensile coupon testing at ambient temperature. However, at elevated temperatures, not only is obtaining tensile stress-strain relationships much more complicated, but also it is difficult to establish the exact condition under which the steel acts when it is affected in fire.

Accuracy of structural fire calculation models: structural behaviour in fire is inherently much more complicated than at ambient temperature.

It is difficult to be precise about the how the values in real use may be different from those assumed in design. However, since robustness is defined as insensitivity to a small amount of initial damage, it is sufficient to choose a nominal value above which it is considered that the design parameter contains gross inaccuracy. A value of 20% is considered. The reminder of this paper will demonstrate how sensitivity of structural performance to 20% degradation in performance of some design parameters may be tested and whether some of the 20% degradation may be tolerated by the structure under fire condition.

4. IMPLICATIONS OF “20%” RULE

According to Eurocode 3 Part 1.2 [10], the temperatures of unprotected and protected steel sections can be calculated using the following equations:

For unprotected steel section:

$$\Delta T_s = \frac{h}{\rho C_s}\frac{A_s}{V}\left(T_{fi} - T_s\right)\Delta t \tag{1}$$

For protected steel section:

$$\Delta T_s = \frac{\left(T_{fi} - T_s\right)A_p / V}{\left(t_p / k_p\right)C_s\rho_s\left(1+\frac{1}{3}\phi\right)}\Delta t - \left(e^{\phi/10} - 1\right)\Delta T_{fi}\text{, with } \phi = \frac{C_p\rho_p}{C_s\rho_s}t_p\frac{A_p}{V} \tag{2}$$

Increasing the fire temperature (T_{fi}) in the above equations by 20% will increase the steel temperature (T_s) by a similar amount. Also, if any of the fire protection properties (thickness t_p, thermal conductivity k_p) is degraded by 20%, the increase in the steel temperature is also about 20%. Changing the specific heat of the fire protection material (C_p) has much less effect.

Therefore, adversely changing the fire behaviour or fire protection material performance individually is likely to result in an increase in the steel temperature by about 20%.

As an approximate guidance, the reduction in strength of steel/composite beams and steel/composite columns can be calculated based on the limiting temperature-load ratio relationships of BS 5950 Part 8 [1]. Table 1 and Table 2 present the results.

Steel limiting temperature (^oC)	510	540	580	615	635	710
Load ratio at above limiting temperature	0.7	0.6	0.5	0.4	0.3	0.2
Steel temperature after 20% increase (^oC) ($\lambda \le 70$)	612	648	696	738	763	852
Load ratio at increased steel temperature	0.41	0.28	0.22	<0.2	<0.2	<0.2
Reduction in column strength	41%	53%	56%	>50%	-	-

Table 1: Reduction in steel/composite column strength due to 20% increase in steel temperature

Steel limiting temperature (^oC)	590	620	650	680	725	780
Load ratio at above limiting temperature	0.7	0.6	0.5	0.4	0.3	0.2
Steel temperature after 20% increase (^oC)	708	744	780	816	870	936
Load ratio at increased steel temperature	0.34	0.27	0.2	<0.2	<0.2	<0.2
Reduction in column strength	51%	55%	60%	-	-	-

Table 2: Reduction in steel/composite beam strength due to 20% increase in steel temperature

The results in tables 1 and 2 reveal some interesting, yet important trends. Firstly, an increase in steel temperature of 20% can result in a reduction of more than 50% in strength of the steel structure. A clear message is that when striving to improve accuracy of prediction of structural fire resistance, it is more effective in achieving the relatively easy gain of improving understanding on thermal properties of fire protection materials, instead of the more difficult endeavour of achieving ever more demanding accuracy in structural analysis. Secondly, in order to avoid the severe reduction in structural strength (more than 50%), it is much more cost effective to achieve this by increasing the fire protection thickness by 20%. Thirdly, on the assumption that the values for the various design parameters necessary for calculating steel temperatures (e.g. fire temperature, fire protection thickness, fire protection material properties) are their characteristic values so that an increase in steel temperature by 20% is a credible scenario, then when assessing the risk of fire-induced progressive collapse, it would be necessary to assume that the strength of the structural member is reduced by 50%.

The following section will investigate whether and how a structure may avoid progressive collapse after suffering a reduction in strength by 50% of any of its structural members.

5. SOME POSSIBLE MECHANISMS OF RESISTING PROGRESSIVE COLLAPSE

Consider the steel frame illustrated in Figure 2. The frame is in simple construction with nominally simple beam-column connections and bracing for lateral stability. The discussions will consider the effects of a 50% reduction in strength of the bracing members, the edge columns, the internal columns and the beams in turn.

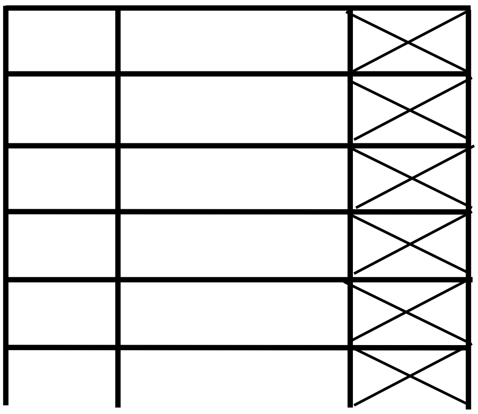

Figure 2: A steel frame in simple construction

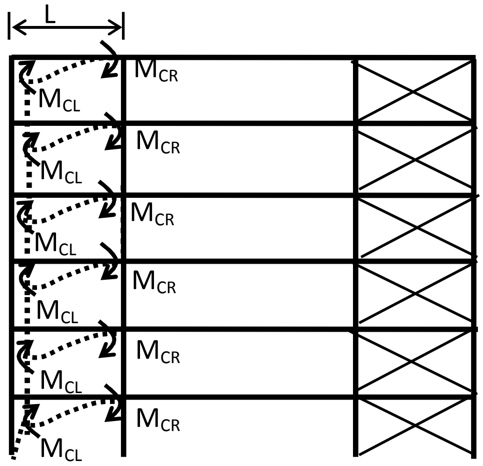

Figure 3: Frame with damaged edge column

5.1 Bracing members

The bracing members resist the lateral loads, mainly from wind. Therefore, the safety factors for wind can be used to give a measure of the required strength for the bracing members in fire. According to EN 1990, the partial safety factor for wind load at ambient temperature is 1.5. Under fire condition, the safety factor for wind load is 0.2. Thus, the required strength for bracing members (lateral stability system in general) in the fire situation is very low, about 13% (0.2/1.5) of the ambient temperature strength. This is significantly lower than the available strength of the bracing members after a reduction of about 50%. Therefore, bracing member failure is unlikely to be a problem for progressive collapse in fire.

5.2 Edge columns

Refer to Figure 3. Assume the distributed load on each floor is w. If the beam-column connections are pinned, the structure is determinate and the total axial force in the edge column is N.wL/2 where N is the number of storeys supported by the column. If the edge column resistance suffers 50% reduction, as assumed above, then the structure would experience progressive collapse. Without restoring the column resistance to N.wL/2, the only way to prevent progressive collapse is by using moment-resisting connections.

Consider steel construction only without composite action in the beams and in the connections. The structure with reduced axial resistance in the edge column would behave in a combination of cantilever action and propping with deformed shape as illustrated by the dotted lines in Figure 3. This deformation mode induces clockwise bending moment in all the connections. Assume all the beams have the same connection bending moments. The equilibrium equation for the free-body diagram consisting of all the beams supported by the fire damaged column is:

$$N\left(M_{CL}+M_{CR}\right)+\frac{N.wL}{4}L-N\frac{wL^2}{2}=0 \tag{3}$$

where M_{CL} and M_{CR} are bending moment resistances of the left and right connections respectively. The second term in the above equation is the bending moment from the total shear force on the left hand side of all the beams, which is equal to the resistance of the fire damaged column (N.wL/4).

This gives:

$$\left(M_{CL}+M_{CR}\right)=\frac{wL^2}{4} \tag{4}$$

With pin connections, the beam would be designed such that:

$$M_s=\frac{wL^2}{8} \tag{5}$$

where M_s is the beam bending moment resistance.

Combining the above two equations gives:

$$\left(M_{CL}+M_{CR}\right)=2M_s \tag{6}$$

This means that each connection must be full strength being able to reach the bending moment resistance of the beam.

This is unlikely to be achievable unless very expensive fully welded or haunched connections are used. If composite beams are used, which is almost always the case, then it would be impossible to satisfy the above equilibrium equation because it would be impossible for a composite connection to achieve the bending moment resistance of the composite beam. It may be argued that if fire attack is a few floors below the top, then cold connections above the fire attacked floor may be able to offer the required resistance. However, such an argument pre-determines where the fire damage should be limited, which is unlikely to be acceptable given the random nature of accidental damage in robustness design. Furthermore, the fire damaged column must be able to resist the total bending moments in all the connections on the left side of all the beams.

The only strategy for reducing the risk of fire-induced progressive collapse, as a result of a possible 20% increase in the edge column temperature, is to make sure that after such a 20% increase in temperature, the edge column temperature does not exceed the original limiting temperature of the column. This means that in design of Class 3 building structures to prevent fire-induced progressive collapse, the edge columns should be designed to limiting temperatures that are 20% lower than those without considering progressive collapse. Effectively, this means increasing the fire protection thickness of the columns by 20%.

5.3 Internal columns

When the strength of an internal column is decreased by 50%, it is possible for the connected beams to remain stable under a combination of bending resistance by the connections and catenary action in the beams. Refer to figure 4 which shows the deformed shape of the structure and force diagram of the left side beam connected to the damaged column.

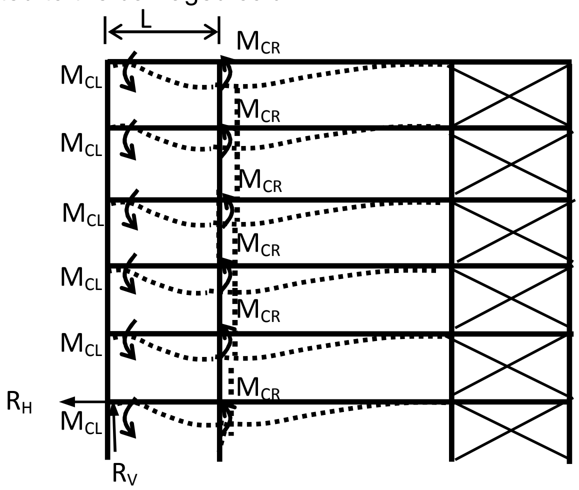

Figure 4: Frame with damaged internal column

The equilibrium equation is:

$$\left(M_{CL}+M_{CR}\right)+R_H\delta+V_H L-\frac{wL^2}{2}=0 \tag{7}$$

where R_H and V_H are the catenary force in the beam and vertical reaction force in the column from the connected beam. Assuming that the vertical resistance of the column is only 50% of its required resistance, then V_H=WL/4. The above equation becomes:

$$(M_{CL} + M_{CR}) + R_H \delta = \frac{wL^2}{4} \tag{8}$$

Without catenary action ($R_H \delta = 0$), the above equation becomes the same as equation 6. This means that completely full capacity connections are necessary. This is unlikely to be achievable.

Using typical flush endplate connections, the connection bending moment resistance can reach about 50% of the beam bending moment resistance. If this is the case, then:

$$(M_{CL} + M_{CR}) \cong M_s = \frac{wL^2}{8} \tag{9}$$

Equation (8) becomes:

$$R_H \delta \cong \frac{wL^2}{8} \tag{10}$$

The right hand side of the equation is the required bending moment resistance of the beam if assuming simple connection. The above equation means that catenary action would need to be sufficient to resist the applied load for one span of the beam. Again, this is a very challenging requirement and will be very difficult to achieve.

As with the edge column situation, the most reliable way would be to increase the fire protection thickness on the internal column by 20%.

In summary, to reduce the risk of fire-induced progressive collapse for the situation that the column temperatures may be 20% higher than expected, the reliable method is to increase the column fire protection thickness by 20% than required for normal fire limit state design. Since fire protection on columns is a relatively small part of the total fire protection to steel structures, the additional cost will be low. However, this would give considerable enhancement to resistance of the structure to fire-induced progressive collapse.

5.4 Beams

The majority of fire protection in a steel structure is on beams. Therefore, increasing the fire protection thickness on all beams by 20% would represent a significant increase in fire protection cost. For beams, if the bending moment resistance is not sufficient to resist the applied loads, it is possible to make use of catenary action.

The topic of catenary action in steel beams has been researched quite extensively by the author's research group [11-16] and has been demonstrated to be a reliable load carrying mechanism for steel beams in fire. The key is to ensure that the connections do not fracture. If using normal carbon bolts, development of catenary action is very limited. However, if Fire Resistant (FR) bolts [17] could be used, the beam failure temperature (defined as when fracture occurs) can reach about 150^{o}C higher than the beam's limiting temperature (defined as reaching its bending moment resistance). For example, figure 5 (taken from [11]) compares the effects of using different sizes and grades of bolts on the development of catenary action in a beam. Using FR bolts is the most effective. FR bolts have higher strength retention factors than normal bolts. More importantly, FR bolts have much superior elongation ability than normal bolts.

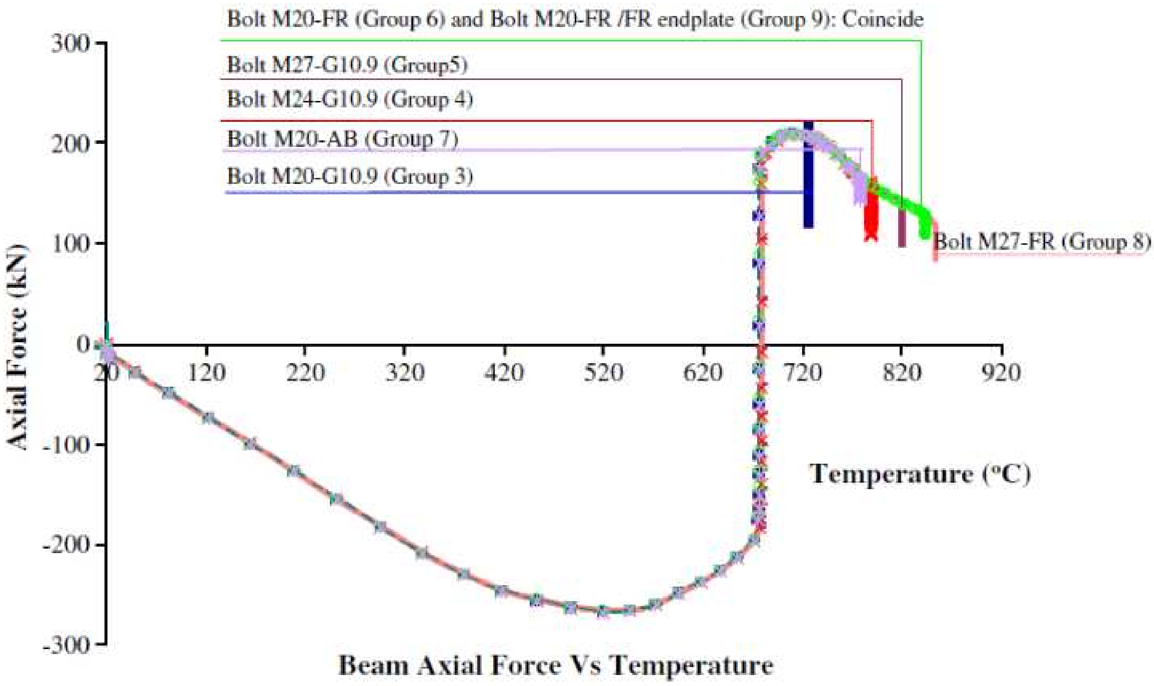

Figure 5: Effects of using different bolts on behaviour of axially restrained beam, from [11]

6. CONCLUSIONS

This paper has presented a scenario analysis for assessment of fire-induced progressive collapse of steel framed structures. This paper argues that consideration of fire-induced progressive collapse is only necessary for Class 3 buildings of EN 1991-1-7 [4] or Approved Document A of England and Wales [5] as part of systematic risk assessment. For such buildings, unless specialist high risks of combined hazards exist, such as nuclear structures and petrochemical plants, or the building clients demand design for combined hazards due to iconic and high risk nature of the building that may attract combined hazards, systematic risk assessment of fire-induced progressive collapse should only consider fire exposure.

Under fire exposure only, it is necessary to consider the potential risk due to any aspect of the fire resistance system not being able to meet the expected performance, due to uncertainties in quantification or degradation in performance. A value of 20% degradation in performance has been suggested. The most severe implication of 20% degradation in performance may lead a structural member to suffer 50% reduction in load carrying capacity.

If any column load carrying capacity decreases by 50%, it is unlikely for the structure to retain its structural integrity. Therefore, to minimise the risk of fire-induced progressive collapse, the fire protection thickness to columns should be increased by 20% compared to the fire protection thickness specified for normal fire limit state design without explicit consideration of fire-induced progressive collapse. Such an increase in fire protection cost is likely to be very small because fire protection to columns is a small part of the total fire protection cost.

If beam load carrying capacity decreases by 50%, it is possible to make use of catenary action. However, in order for the increased beam failure temperature to be sufficiently high to compensate for a possible 20% increase in the steel temperature, Fire Resistant (FR) bolts would be necessary. FR bolts have better retention of strength and much superior elongation ability than normal bolts at high temperatures.

REFERENCES

[1] British Standards Institution, *BS 5950: Structural Use of Steelwork in Buildings. Part 8: Code of Practice for Fire Resistant Design*, British Standards Institution, London, UK, 1990

[2] Y.C. Wang, I.W. Burgess, F. Wald and M. Gillie, *Performance-based fire engineering of structures*, Spon Press, ISBN 978-0-415-55733-7, 2013

[3] A.S. Usmani, Y.C. Chung and J.L. Torero, How did the WTC Towers Collapse: A New Theory, *Fire Safe Journal*, Vol. 38, pp. 501-533, 2003

[4] Committee of European Standardisation, *EN 1991-1-7: 2006, Actions on Structures Part 1–7: General Actions – Accidental Actions*, CEN, Brussels, 2006
[5] Office of the Deputy Prime Minister. *The Building Regulations 2000 — Approved Document A: Structure. A3 — Disproportionate Collapse*, 2004 edition with 2004 amendments. NBS, 2004
[6] The Institution of Structural Engineers, *Manual for the systematic risk assessment of high-risk structures against disproportionate collapse*, The Institution of Structural Engineers, London, 2013
[7] T. Tanaka, Characteristics and problems of fires following the Great East Japan earthquake in March 2011, *Fire Safety Journal*, Vol. 54, pp. 197-202, 2012
[8] National Institute of Standards and Technology, *Federal Building and Fire Safety Investigation of the World Trade Center Disaster: Final Report of the National Construction Safety Team on the Collapses of the World Trade Center Towers (Draft)*, NIST NCSTAR 1 (Draft), National Institute of Standards and Technology , 2005
[9] L.L. Wang, Y.C. Wang, and G.Q. Li, Experimental study of hydrothermal aging effects on insulative properties of intumescent coating for steel elements, *Fire Safety Journal*, Vol. 55, pp. 168-181, 2013
[10] Committee of European Normalization, *EN 1993-1-2-2005, Eurocode 3: Design of Steel Structures, Part 1-2: Structural Fire Design*, Brussels, 2005
[11] L. Chen and Y.C. Wang, Methods of improving survivability of steel beam/column connections in fire, *Journal of Constructional Steel Research*, Vol. 79, pp. 127–139, 2012
[12] X.H. Dai, Y.C. Wang and C.G. Bailey, Numerical Modelling of Structural Fire Behaviour of Restrained Steel Beam-Column Assemblies using Typical Joint Types, *Engineering Structures*, Vol. 32, pp. 2337-2351, 2010
[13] J. Ding and Y.C. Wang, “Experimental Study of Structural Fire Behaviour of Steel Beams to Concrete Filled Tubular Column Assemblies with Different types of Joints, *Engineering Structures*, Vol. 29, pp. 3485-3502, 2007
[14] S. Elsawaf and Y.C. Wang, Methods of improving the survival temperature in fire of steel beam connected to CFT column using reverse channel connection, *Engineering Structures*, Vol. 32, pp. 132-146, 2012
[15] Y.C. Wang, X.H. Dai and C.G. Bailey, An Experimental Study of Relative Structural Fire Behaviour and Robustness of Different Types of Steel Joint in Restrained Steel Frames, *Journal of Constructional Steel Research*, Vol. 67, pp. 1149-1163, 2011
[16] Y.Z. Yin and Y.C. Wang, “A Numerical Study of Large Deflection Behaviour of Restrained Steel Beams at Elevated Temperatures”, *Journal of Constructional Steel Research*, Vol. 60, pp. 1029-1047, 2004
[17] Y. Sakumoto, K. Keira, F. Furumura, F. and Ave, T., Tests of fire-resistant bolts and joints, *ASCE Journal of Structural Engineering*, 119(11), 3131-3150, 1994

12th International Conference on
Steel, Space and Composite Structures
28-30 May 2014, Prague, Czech Republic

APPLICATION OF HIGH-PERFORMANCE STEEL TO GIRDER OF COMPACT I-SHAPED SECTION

Eiki Yamaguchi, Yuji Sugimura and Kenjiro Ohmichi

Department of Civil Engineering, Kyushu Institute of Technology
Tobata, Kitakyushu 804-8550, Japan
e-mail: yamaguch@civil.kyutech.ac.jp

Keywords: High-Performance Steel, Steel Girder, Compact I-Section

Abstract. *The maximum width-to-thickness ratios for compact I-shaped sections are first studied for three girders: the SM490Y girder, the SBHS500 girder and the hybrid girder. SM490Y is a conventional steel and SBHS500 is a high-performance steel specifically for bridge construction. Both steel grades are registered in Japanese Industrial Standards. The hybrid girder consists of a SM490Y web and SBHS500 flanges. The maximum width-to-thickness ratio thus obtained is quite different from that of AASHTO. A cause is investigated, and the difference is found attributable to analysis conditions. The three girders with compact sections are then designed for a given plastic moment. The result shows that the SBHS500 girder is the lightest: 19％ lighter than the heaviest girder, the SM490Y girder. The price varies from steel to steel. From the viewpoint of cost, the optimum girder is looked for as well. The result shows that the hybrid girder is the most competitive at the current steel price.*

1 INTRODUCTION

Conventional steel girder bridges are rather complicated steel structures, having quite a few secondary members such as cross girders, cross frames, lateral bracings and stiffeners in addition to main girders (Figure 1). In recent years, an effort has been made to reduce the number of secondary members for saving construction cost. Figure 2 shows an example of such a bridge, which has no cross girders, no cross frames, no lateral bracings, and no stiffeners in the main box girders except on bridge piers. The bridge is so simple that portions susceptible to fatigue cracks and corrosion are very few: the inspection of the bridge is much easier. Therefore, durability is considered high and maintenance cost is expected low. In fact, the owner has a much simpler inspection scheme for this bridge than usual. Since the expectation of a bridge service life is very long, in a range of 100 years or so, such a simple structure is much favored.

In 2008, high performance steels were registered in Japanese Industrial Standards (JIS): SBHS500 and SBHS700. They are high strength steels developed specifically for bridge construction. In addition to high yield strength, they have various advantages such as good weldability over conventional steels. That is why they are called high-performance steels.

Focusing on the high yield strength, the present study explores a possibility of its effective use. To this end, the maximum width-to-thickness ratios for compact I-shaped sections are first obtained by nonlinear analysis. Based on those maximum width-to-thickness ratios, three I-section girders are studied, two of which have homogeneous sections and one of which has a hybrid section. The homogeneous sections are made of SM490Y and SBHS500, respectively, and the hybrid section is of SM490Y for a web and SBHS500 for flanges, where SM490Y is a conventional steel given in JIS. The three girders are called the SM490Y girder, the SBHS500

Figure 1: Conventional Steel Bridge

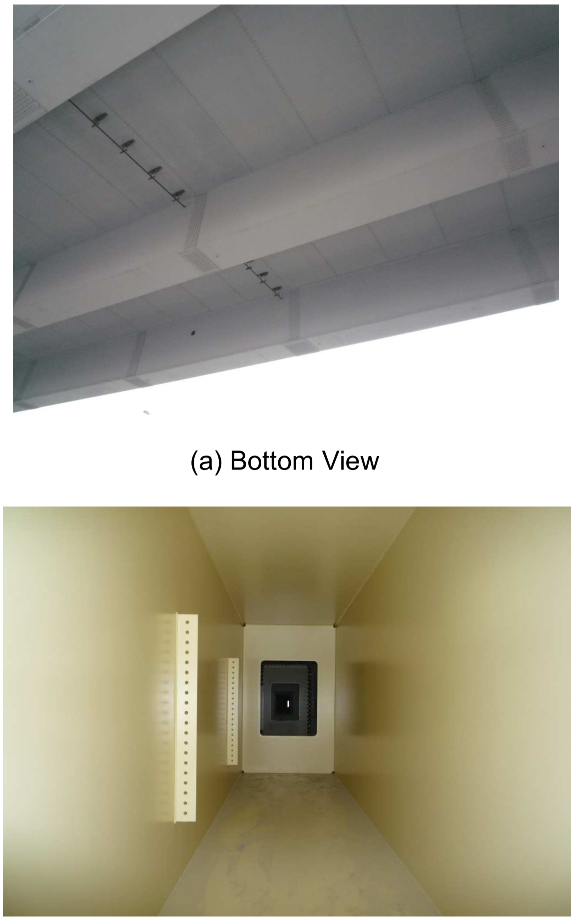

(a) Bottom View

(b) Inside Main Girder

Figure 2: Steel Bridge of New Type

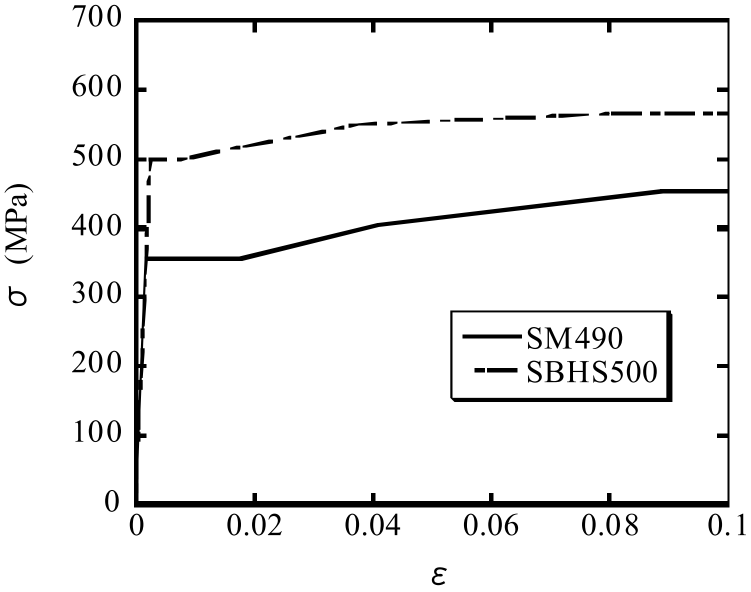

Figure 3: Stress-Strain Relationship

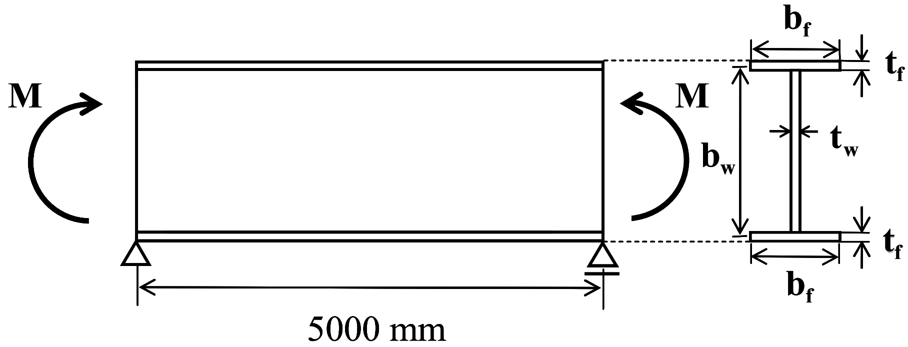

Figure 4: Steel Girder Model

girder and the hybrid girder, respectively. The optimum compact sections are then designed for the three girders under a given plastic moment. The results are compared and discussed.

All the analyses in the present study are conducted by ABAQUS[1] with shell elements

2 ANALYSIS MODELS

2.1 Material Properties

JIS specifies the yield stress, the tensile strength and the elongation of the structural steel, but it does not give the stress-strain relationship beyond the yield point. The present study follows the stress-strain relationships proposed by the JSSC committee[2]. Young's modulus E and Poisson's ration ν are 2.0×10^5 N/mm^2 and 0.3, respectively, for both steels of SM490Y and SBHS500. The yield stresses σ_y are assumed to be the minimum values that JIS requires. Figure 3 shows the stress-strain relationships used in this study.

2.2 Material Properties

Figure 4 presents the girder model to be analyzed. It is a simple girder subjected to equal bending moments at the ends. The girder length is 5 m. The cross section is I-shaped and doubly symmetric. As is mentioned earlier, two homogeneous girders and one hybrid girder are

3 COMPACT SECTIONS (MAXIMUM WIDTH-TO-THICKNESS RATIO)

Not all the cross sections can reach the plastic moments M_p due to the occurrence of buckling. The maximum width-to-thickness ratio that ensures the attainment of M_p is specified, for example, in AASHTO[3] while it is not available in Japanese Specifications for Highway Bridges[4]. In the first phase of the present study, therefore, the maximum width-to-thickness ratio is to be obtained in conjunction with Japanese Specifications for Highway Bridges[4].

Both material and geometrical nonlinearities must be considered for evaluating the maximum width-to-thickness ratio for the compact section. The initial imperfection of the girder needs be taken into consideration as well. In general, the initial imperfection consists of residual stress and displacement, but the residual stress has been found barely influential on the maximum width-to-thickness ratio in the preliminary analysis, so that only the initial displacement is taken account of. Following the fabrication tolerance specified in Japanese Specifications for Highway Bridges[4], the maximum initial deflection of the flange is assumed 1/100 of the distance between the web and the free edge of the flange; the maximum initial deflection of the web is 1/250 of the web height. For the initial-deflection mode, the buckling mode for the lowest elastic buckling load is employed.

Unless the constituent material is perfectly plastic, the compact section cannot be defined well. Herein by neglecting the strain hardening portion and thus treating as if the material is perfectly plastic, M_p is computed, and the cross section is considered compact if the maximum moment M_u exceeds M_p.

The girder height b_w and the flange width b_f are fixed at 2500 mm and 600 mm, respectively. For various combinations of the flange thickness t_f and the web thickness t_w, then M_u is evaluated numerically. The combination of the width-to-thickness parameter of the flange R_f and the width-to-thickness parameter of the web R_w that gives $0.99 < M_u / M_p < 1.01$ is the maximum width-to-thickness ratio for the compact section in the present study. Herein the width-to-thickness parameters are defined as follows:

$$R_f = \frac{b_f}{t_f}\sqrt{\frac{\sigma_y}{E}\cdot\frac{12(1-\nu^2)}{0.426\pi^2}} \tag{1}$$

$$R_w = \frac{b_w}{t_w}\sqrt{\frac{\sigma_y}{E}\cdot\frac{12(1-\nu^2)}{23.9\pi^2}} \tag{2}$$

The maximum width-to-thickness ratio thus obtained is shown in Figure 5. The figure has three curves, which are the results of the three girders analyzed. Large difference between the girders is observed. The usage of SBHS500 tends to increase the maximum width-to-thickness ratio for the compact section. The cross sections whose width-to-thickness parameters lie below the corresponding maximum width-to-thickness ratio curve are compact.

The present result is plotted together with the design maximum width-to-thickness ratio of AASHTO[3] in Figure 6. The difference is quite large. A cause for it is possibly the difference in the analysis conditions such as the initial displacement: as for the initial deflection of the web, AASHTO[3] allows up to 1/250 of the web height while the fabrication tolerance in Specifications for Highway Bridges is only 1/100, for instance.

To verify the deduction above, further analysis is conducted using the same conditions as those of AASHTO[3]. The maximum moments Mu of the five girders corresponding to five points a-e in Figure 6 are evaluated. The results are summarized in Table 1. The present numerical procedure has yielded M_u close enough to M_p, the largest discrepancy between M_u and M_p being less than about 2.7%. The result thus confirms that the difference in the maximum width-to-thickness ratio between AASHTO[3] and the present study is attributable to the analysis conditions: the present numerical procedure itself can be considered valid.

4 COMPARISON OF THREE GIRDERS

Under the condition of $M_p = 5.0 \times 10^{10}$ mm, the compact cross section having the smallest area is obtained for each of the three girders. Table 2 gives the dimensions of the cross sections thus designed. The smallest area of the three is attained by the SBHS500 girder, the second smallest by

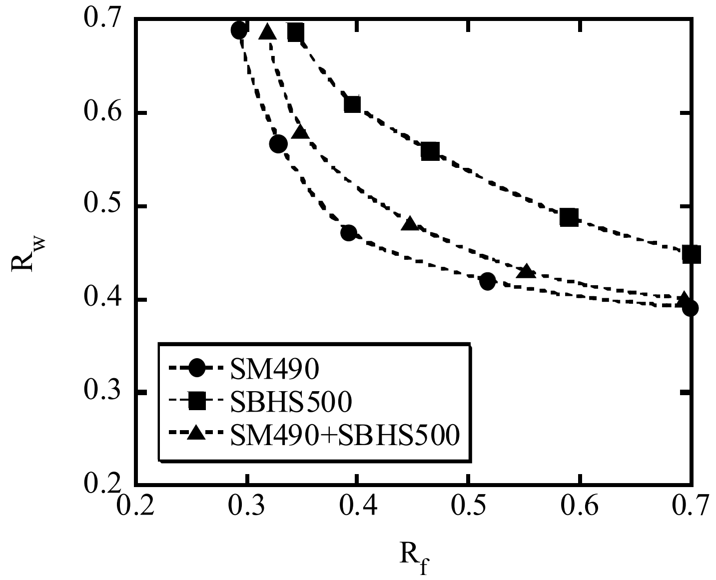

Figure 5: Maximum Width-to-Thickness Ratio for Compact Section

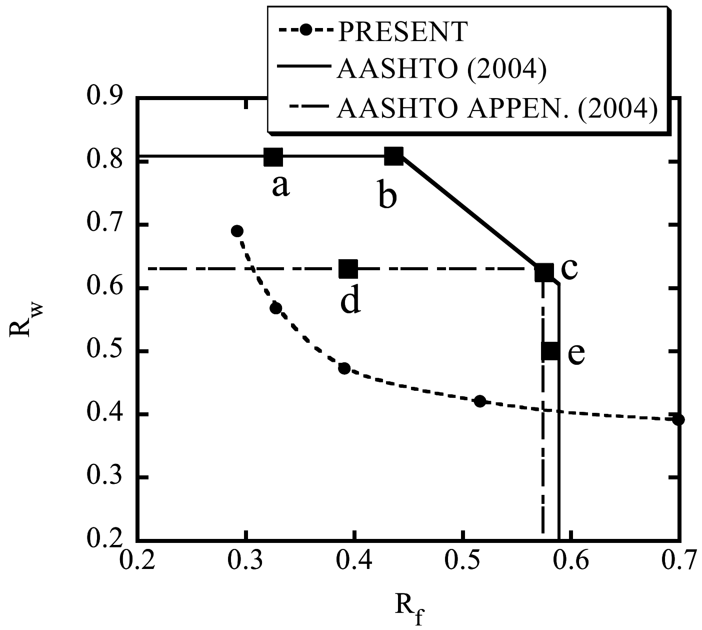

Figure 6: Comparison of Maximum Width-to-Thickness Ratios (SM490Y)

Table 1: Numerical Results with AASHTO Conditions

Girders	M_u/M_p
A	0.979
B	0.973
C	0.988
D	1.012

Table 2: Cross Section of Minimum Area (Unit: mm)

Girder	Flange	Web
SM490Y	540 x 52	2566 x 39
SBHS500	461 x 50	2237 x 36
Hybrid	450 x 52	2527 x 34

Table 3: Comparison of Costs of Three Girders

		Price Ratio (SBHS500/SM490Y)						
cost		<	1.08	<	1.23	<	1.50	<
	Low	SBHS500	SBHS500	Hybrid	Hybrid	Hybrid	Hybrid	SM490Y
	Middle	Hybrid	Hybrid	SBHS500	SBHS500	SM490Y	SM490Y	Hybrid
	High	SM490Y	SM490Y	SM490Y	SM490Y	SBHS500	SBHS500	SBHS500

constructed for the study. The difference between the three girders lies in the constituent steel grades the hybrid girder and the largest by the SM490Y girder. The weight of the SBHS500 girder can be 19% less than that of the SM490Y girder.

For the selection of the optimum girder, the cost is also an important factor. The price varies from steel to steel. To be specific, SBHS500 is more expensive than SM490Y. Table 3 presents the comparison of the three girders in terms of the cost. Depending on the price ratio of SBHS500/SM490Y, the optimum girder varies. When the price ratio is less than 1.08, the SBHS500 girder is the best. When the price ratio exceeds 1.08, the hybrid girder becomes better until the ratio reaches 1.50, beyond which the SM490Y girder is the most superior. Since the current price of SBHS500 is about 33% higher than that of SM490Y, the hybrid girder is considered the most competitive at present.

Taking the current steel prices into account, the adjustment of the cross section of the hybrid girder is made so as to further reduce the cost. The area of the flange then becomes smaller while the area of the web becomes larger slightly than those of the cross section having the minimum area. The total area increases by 0.7%, but the girder cost reduces by 0.6%. The cost of the adjusted hybrid girder is 14% and 7% lower than those of the SBH500 and SM490Y girders, respectively.

5 CONCLUDING REMARKS

The maximum width-to-thickness ratios for the compact section are obtained for three girders: the SM490Y girder, the SBHS500 girder and the hybrid girder consisting of the two steel grades. With the usage of SBHS500, the maximum width-to-thickness ratio for the compact section tends to be larger. The present maximum width-to-thickness ratio is different from that of AASHTO[3], which is found attributable to the difference in the conditions for the analysis.

Using the maximum width-to-thickness ratios obtained in the present study, the optimum compact sections that attain the same M_p are designed for the three girders. Depending on the price ratio of SBHS500 to SM490Y, the best girder from the viewpoint of the girder cost varies. At the current steel price, the hybrid girder is found the most competitive: its cost is 14% and 7% lower than those of the SBH500 and SM490Y girders, respectively.

ACKNOWLEDGEMENTS

Financial support from the Japan Iron and Steel Federation for the present research is gratefully acknowledged.

REFERENCES

[1] ABAQUS, *User's Manual, ABAQUS*, Ver. 6.6., Dassault Systemes Simulia Corp. (2006).
[2] Japanese Society of Steel Construction, *Reference Document for 1st Meeting*, Committee for Rationalized Bridge Design (2010).
[3] AASHTO, *LRFD Bridge Design Specifications*, 3rd ed. (2004).
[4] Japan Road Association, *Specifications for Highway Bridges Part 2 Steel Bridges*, Maruzen, Japan (2012).

TECHNICAL PAPERS

12th International Conference on
Steel, Space and Composite Structures
28-30 May 2014, Prague, Czech Republic

LOAD DISTRIBUTION ON MULTI COMPOSITE STEEL GIRDER BRIDGES UNDER AASHTO LRFD LIVE LOADS

Essam Ayoub*, Charles Malek† and Gamal Helmy‡

*Cairo University and Dar Al-Handasah
e-mail: Essam.Ayoub@dargroup.com

Keywords: Bridges, steel girders, AASHTO LRFD, live loads, load distribution

Abstract: *The present paper studies the transverse loads acting on each steel composite girder of single span multi-composite steel girder bridges when subjected to AASHTO LRFD live loads. The AASHTO LRFD live loads considered are the 325 KN truck load, the 220 KN tandem load and the 9.3 KN/m lane load. 3-D finite element models are developed to predict the percentage of the live loads carried by each composite steel girder for maximum moment effect. In the 3-D finite element models the steel bottom flange, the steel web, the steel upper flange and the reinforced concrete slab are modeled as 3-D shell elements; while, the steel girder-concrete slab connection is realized by using rigid body constraints to ensure full steel-concrete composite action. Several bridges with different transverse cross sections and different spans are considered to come up with reasonable load distribution factors which can be used for the longitudinal analysis of the bridge composite steel girders. Comparisons with the load distribution factors as presented by AASHTO LRFD are investigated and discussed.*

1 INTRODUCTION

Many papers dealing with the transverse load distribution on bridges appear in the literature; however, more comprehensive study is needed to come up with reasonable approach suitable for accurate bridge analysis. In 2001, Eom and Nowak[1] in their analytical study concluded that AASHTO LRFD[2] girder distribution factors for live loads are not accurate and lead to conservative values for long spans and large girder spacing; however, these factors are liberal for short bridge spans and small girder spacing. They conducted field testing program on steel girder bridges up to 45 m and they concluded that the field measurements are lower than AASHTO LRFD code specified values for all tested steel girder bridges. In 2011, Li and Chen[3] introduced a method to compute live load distribution for bridge girders. They used elastic springs to simulate the bridge main girders in the transverse direction. They concluded that the results obtained from the proposed model are comparable with current design standards. In 2012, Razaqpur et al.[4] developed a non-linear finite element program for the analysis of composite steel bridges and compared the outcome results of simply supported and continuous bridges with the 1/3 scale composite bridge tested by the authors. Good agreement was found between both results concerning load deflection responses and strains. In 2012, Razaqpur et al.[5] investigated the effects of concrete nonlinearity and steel yielding on the

† Dar Al-Handasah
‡ Dar Al-Handasah

truck load distribution in simply supported composite bridges. They concluded that the load carrying capacity of existing bridges will be higher compared to elastic limit state. In the present paper, the load distribution factors of multi girder steel composite bridges are calculated based on AASHTO LRFD live loads. The live loads consist of 9.3 KN/m lane load in addition to 325 KN truck or 220 KN tandem (figure 1). An impact factor of 1.33 is applied for truck and tandem loads only.

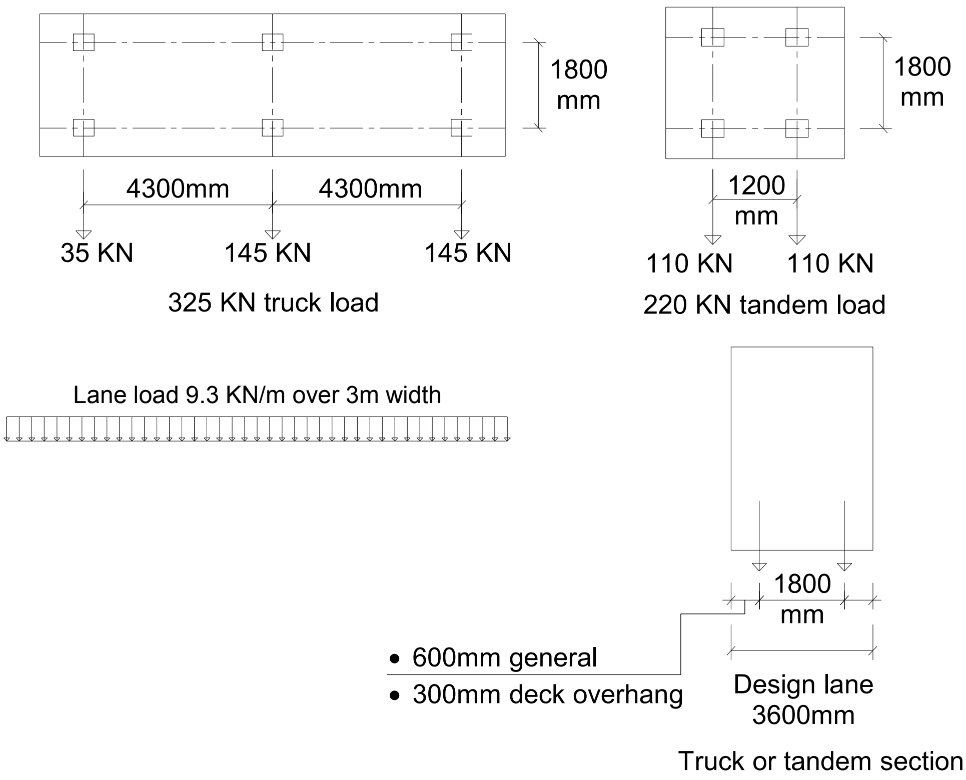

Figure 1: AASHTO LRFD live load description

Figure 2 shows a general arrangement of the simply supported composite steel bridges used in the current work. The bridge deck consists of 4 steel girders with spacing S varying from 2 to 4m and topped with R.C. slab (20 to 25 cm thickness). The bridge span (L) ranges from 20 to 40 m. Cross bracings are provided in the longitudinal direction at distances less or equal to 7.5m. 3-D finite element models are developed to compute the load distribution factor (D.F.) applied to exterior and interior composite steel girders for maximum moment effect. In these 3-D finite element models, the steel bottom flange, the steel top flange, the steel web and the R.C. slab are modeled as 3-D shell elements. The shear connectors assuring the steel-concrete composite action is achieved by imposing rigid body constraints between the top steel beam flange and the R.C. slab. The distribution factor (D.F.) for moment is determined using the above models and compared with the corresponding AASHTO LRFD values for exterior and interior beams.

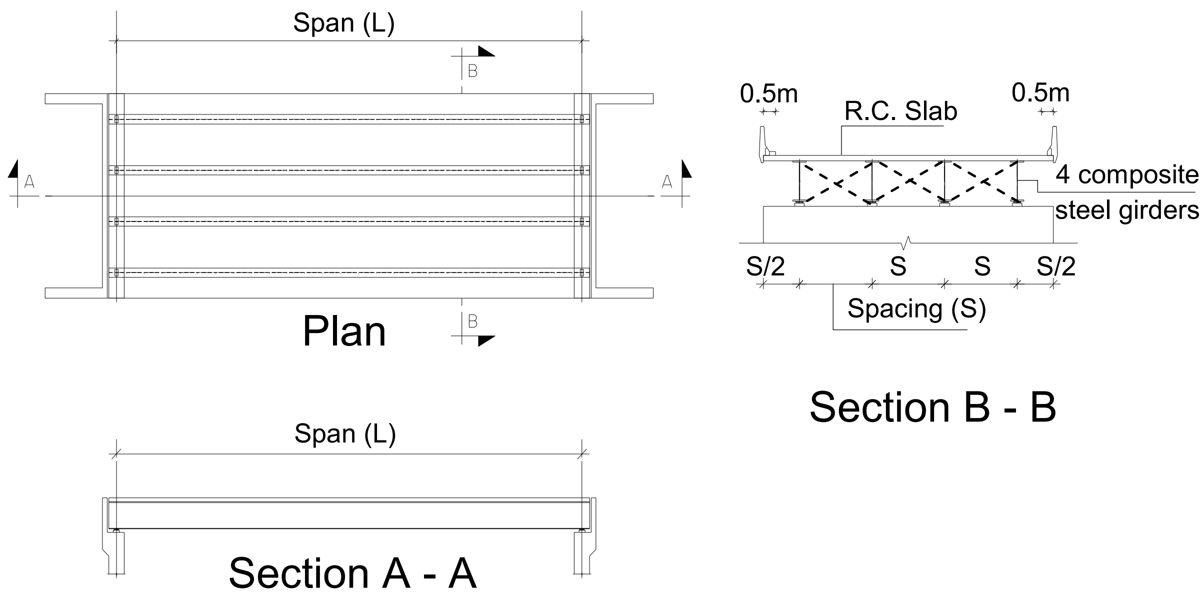

Figure 2: Plan, elevation and cross section of composite steel girder bridge used in the current study

2 FINITE ELEMENT MODELS DESCRIPTION

Figure 3 shows the 3-D finite element model used for the composite steel girder bridge analysis. Shell elements are chosen to introduce all structural bridge deck elements including R.C. deck slab, steel girder upper flanges, steel girder bottom flanges and steel girder webs. Cross bracing diaphragms (2 angles 100x100x10 mm) represented by frame elements are introduced all over the bridge span at distances not exceeding 7.5 m as per AASHTO LRFD requirements. The dimensioning of the steel girder elements is determined based on preliminary analysis and design of the steel girder bridges under AASHTO LRFD loads and strength requirements. The top steel flange-R.C. slab connection is realized using rigid body constraints. The composite steel bridge analysis is achieved using SAP2000 program[6]. Three simple span bridges with 20, 30 and 40 m are considered in the current paper. For each bridge span, five different girder spacing (2.0, 2.5, 3.0, 3.5 and 4.0m) are examined.

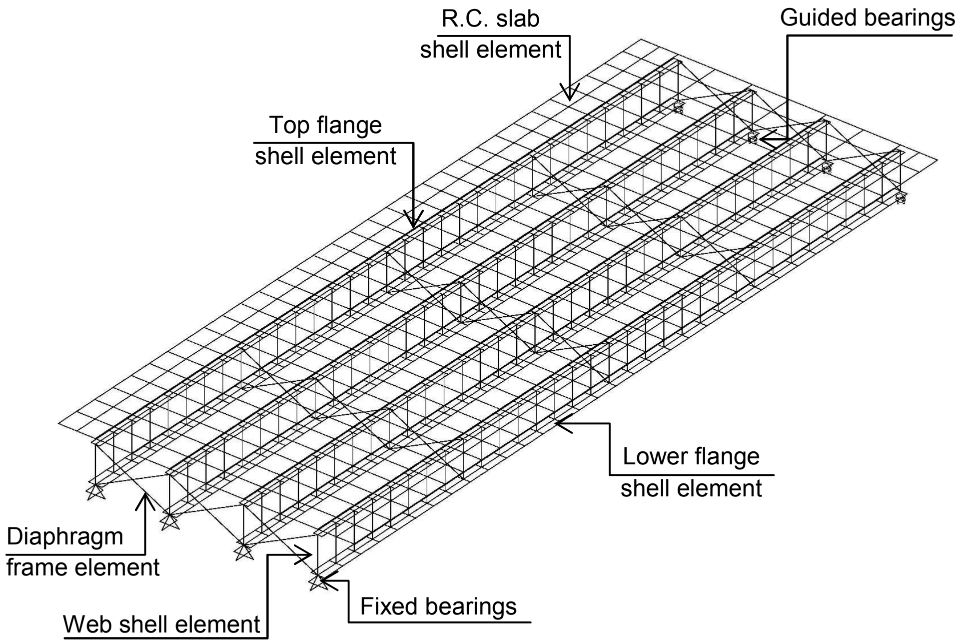

Figure 3: 3-D finite element model for the composite girder bridge used in the present study

Table 1 displays the superstructure bridge data including the R.C. slab thickness (t_{slab}), the steel upper flange dimensions (A_u), the steel lower flange dimensions (A_l) and the steel web dimensions (A_w) considered in the present work.

Bridge span (m)	Girder spacing (m)	t_{slab} (mm)	A_u (mm2)	A_l (mm2)	A_w (mm2)
	2.00	200	300x20	400x26	1000x12
	2.50	200	300x22	400x32	1000x12
20.00	3.00	220	320x24	450x36	1000x12
	3.50	220	320x30	450x42	1000x12
	4.00	250	350x32	500x44	1000x12
	2.00	200	300x30	500x34	1500x16
	2.50	200	320x32	500x42	1500x16
30.00	3.00	220	350x36	550x50	1500x16
	3.50	220	400x40	550x58	1500x16
	4.00	250	450x42	600x60	1500x16
	2.00	200	320x30	500x38	2000x20
	2.50	200	320x36	500x46	2000x20
40.00	3.00	220	350x40	550x52	2000x20
	3.50	220	400x42	550x60	2000x20
	4.00	250	450x44	600x66	2000x20

Table 1: Steel sections and slab thickness used for the current bridge study

To obtain the maximum straining actions effect on exterior and interior composite steel beams the live loads are positioned in the bridge transverse direction as shown in figures 4a and 4b. Two cases of loading are considered in the present analysis; these include one lane and two lanes loaded. In the longitudinal direction the AASHTO LRFD live loads are moving on the composite girder bridges to acquire the maximum straining actions acting on the composite steel girders. The concrete grade used in the current analysis is fc' 28 Mpa with Young's modulus equals to 28500 Mpa; while the steel sections are of grade 420 Mpa yield stress and 200000 Mpa Young's modulus. .

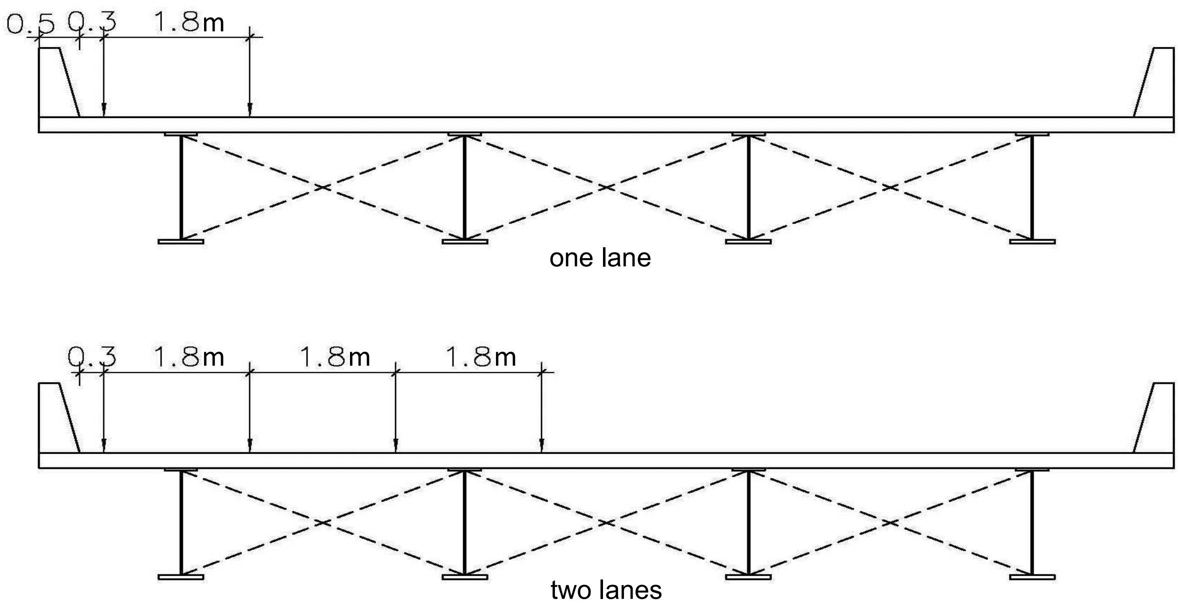

Figure 4a: Transverse position of live loads for exterior girder

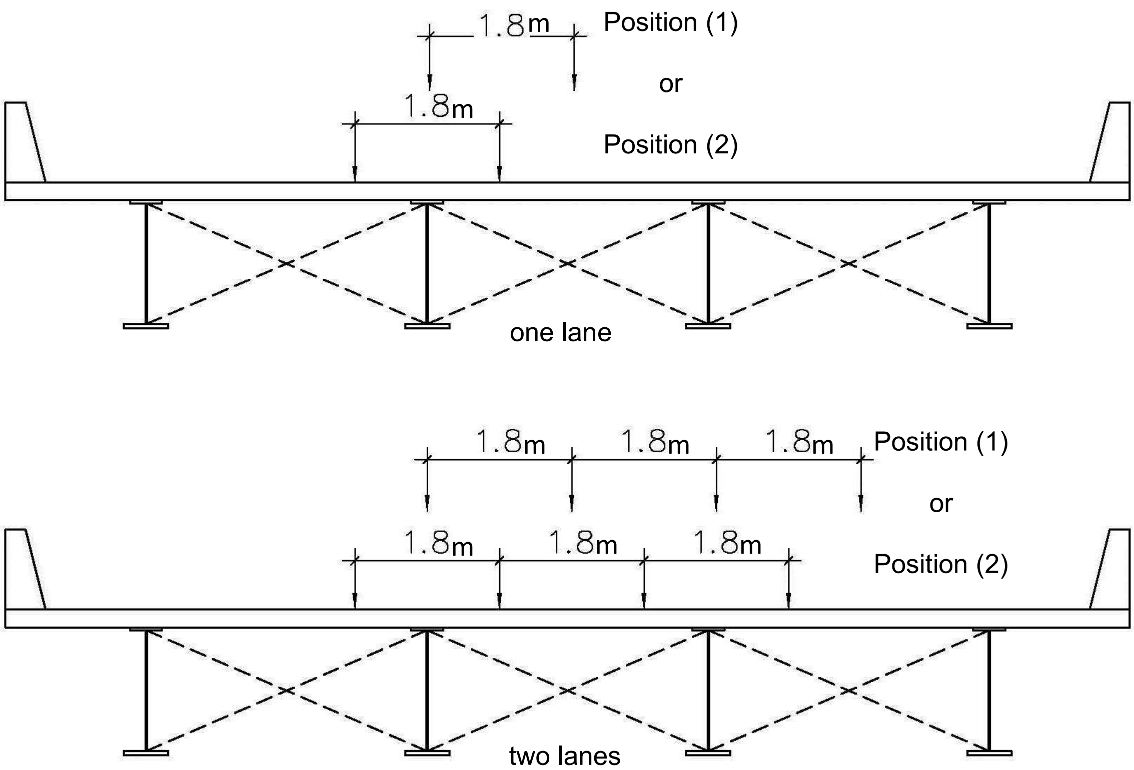

Figure 4b: Transverse position of live loads for interior girder

3 LOAD DISTRIBUTION RESULTS AND COMPARISON WITH AASHTO LRFD FACTORS

3.1 Load distribution factors as per AASHTO LRFD

According to AASHTO LRFD the live load moments on interior and exterior composite steel beams can be calculated in a simplified way for one and two or more loaded design lanes as follows:

$M_{interior}$ = f1 x M_{total} on bridge due to one loaded lane

$M_{exterior}$ = f2 x M_{total} on bridge due to one loaded lane

Where f1 = load distribution factor for interior beam moment

$$f1 = 0.06 + (S/4300)^{0.4} (S/L)^{0.3} (Kg/L\ ts^3)^{0.1} \text{ for one design lane loaded} \quad (1)$$

$$f1 = 0.075 + (S/2900)^{0.6} (S/L)^{0.2} (Kg/L\ ts^3)^{0.1} \text{ for two design lane loaded} \quad (2)$$

and f2 = load distribution factor for exterior beam moment

For one lane loaded f2 is calculated based on the lever rule method

$$\text{For two lanes loaded, } f2 = e \times f1 \text{ where } e = 0.77 + (de/2800) \quad (3)$$

In the above equations

S = beam spacing in mm

L = bridge span in mm

ts = R.C. slab thickness in mm

Kg = n (I + A e_g^2) where n = modular ratio = $E_{steel}/E_{concrete}$

I = moment of inertia of the steel beam about horizontal axis passing through center of gravity

A = area of steel beam

e_g = distance from c.g. of steel beam to c.g. of deck slab

de = distance from exterior beam to the interior edge of curb in mm

Table 2 displays the load distribution factors (D.F.) for exterior and interior beam moments based on the above AAHTO LRFD equations for the various bridges given in table 1.

Bridge span (m)	Girder spacing (m)	D.F. - one lane loaded		D.F. - two lanes loaded	
		exterior beam	interior beam	exterior beam	interior beam
20.00	2.00	0.65	0.42	0.54	0.57
	2.50	0.82	0.49	0.70	0.68
	3.00	0.93	0.55	0.86	0.77
	3.50	1.01	0.61	1.06	0.87
	4.00	1.08	0.65	1.22	0.94
30.00	2.00	0.65	0.41	0.54	0.57
	2.50	0.82	0.48	0.71	0.69
	3.00	0.93	0.53	0.87	0.77
	3.50	1.01	0.59	1.06	0.87
	4.00	1.08	0.63	1.23	0.94
40.00	2.00	0.65	0.40	0.54	0.57
	2.50	0.82	0.46	0.70	0.67
	3.00	0.93	0.51	0.86	0.76
	3.50	1.01	0.57	1.04	0.86
	4.00	1.08	0.60	1.21	0.93

Table 2: Distribution factors (D.F.) for exterior and interior composite beams as per AASHTO LRFD

3.2 Load distribution factors based on 3-D finite element analysis

Tables 3 and 4 display the total live loads bridge moment due to one lane loaded in addition to the maximum live load moment values due to one and two lanes loaded for exterior and interior beams; respectively. These results are based on the 3-D finite element models created in the present work. The distribution factors (D.F) which represent the fraction of one lane load carried by the exterior and the interior beams are then calculated and presented in tables 3 and 4; respectively.

Bridge span (m)	Girder spacing (m)	M bridge (one lane loaded) (KN.m)	M external (KN.m)		D.F.	
			one lane	two lanes	one lane	two lanes
20.00	2.00	2096.23	1130.80	1268.84	0.54	0.61
	2.50	2096.23	1294.63	1559.07	0.62	0.74
	3.00	2096.23	1417.66	1879.80	0.68	0.90
	3.50	2096.23	1541.46	2126.38	0.74	1.01
	4.00	2096.23	1625.05	2324.93	0.78	1.11
30.00	2.00	3742.92	2027.23	2289.10	0.54	0.61
	2.50	3742.92	2286.20	2894.44	0.61	0.77
	3.00	3742.92	2480.64	3410.51	0.66	0.91
	3.50	3742.92	2665.47	3832.17	0.71	1.02
	4.00	3742.92	2797.90	4157.77	0.75	1.11
40.00	2.00	5622.73	3046.56	3441.51	0.54	0.61
	2.50	5622.73	3417.59	4360.63	0.61	0.78
	3.00	5622.73	3673.29	5139.36	0.65	0.91
	3.50	5622.73	3908.73	5759.21	0.70	1.02
	4.00	5622.73	4082.58	6227.31	0.73	1.11

Table 3: Distribution factors (D.F.) for exterior composite beams based on 3-D finite element analysis

Bridge span (m)	Girder spacing (m)	M bridge (one lane loaded) (KN.m)	M internal (KN.m)		D.F.	
			one lane	two lanes	one lane	two lanes
20.00	2.00	2096.2332	691.0245	—	0.33	—
	2.50	2096.2332	736.9004	1262.6536	0.35	0.60
	3.00	2096.2332	785.2044	1405.9519	0.37	0.67
	3.50	2096.2332	848.7788	1480.2248	0.40	0.71
	4.00	2096.2332	898.1217	1529.9862	0.43	0.73
30.00	2.00	3742.9176	1191.1023	—	0.32	—
	2.50	3742.9176	1240.3322	2118.5668	0.33	0.57
	3.00	3742.9176	1302.2745	2384.8428	0.35	0.64
	3.50	3742.9176	1382.7235	2449.9416	0.37	0.65
	4.00	3742.9176	1450.6511	2509.4107	0.39	0.67
40.00	2.00	5622.7305	1776.7401	—	0.32	—
	2.50	5622.7305	1823.8192	3135.2555	0.32	0.56
	3.00	5622.7305	1875.4356	3485.5904	0.33	0.62
	3.50	5622.7305	1942.7357	3489.6965	0.35	0.62
	4.00	5622.7305	2015.3908	3522.5745	0.36	0.63

Table 4: Distribution factors (D.F.) for interior composite beams based on 3-D finite element analysis

Figures 5a and 5b outline a comparison between the D.F. obtained from both AASHTO LRFD equations and 3-D finite element analysis. It is observed from figure 5a that D.F. resulting from AASHTO LRFD are upper bound for exterior beam under one lane loaded; while, they are not conservative for exterior beam under two lanes loaded with small girder spacing. Regarding interior beam, ASHTO LRFD distribution factor (D.F.) results shown in figure 5b are always upper bound compared to 3-D finite element results for both one and two lanes loaded.

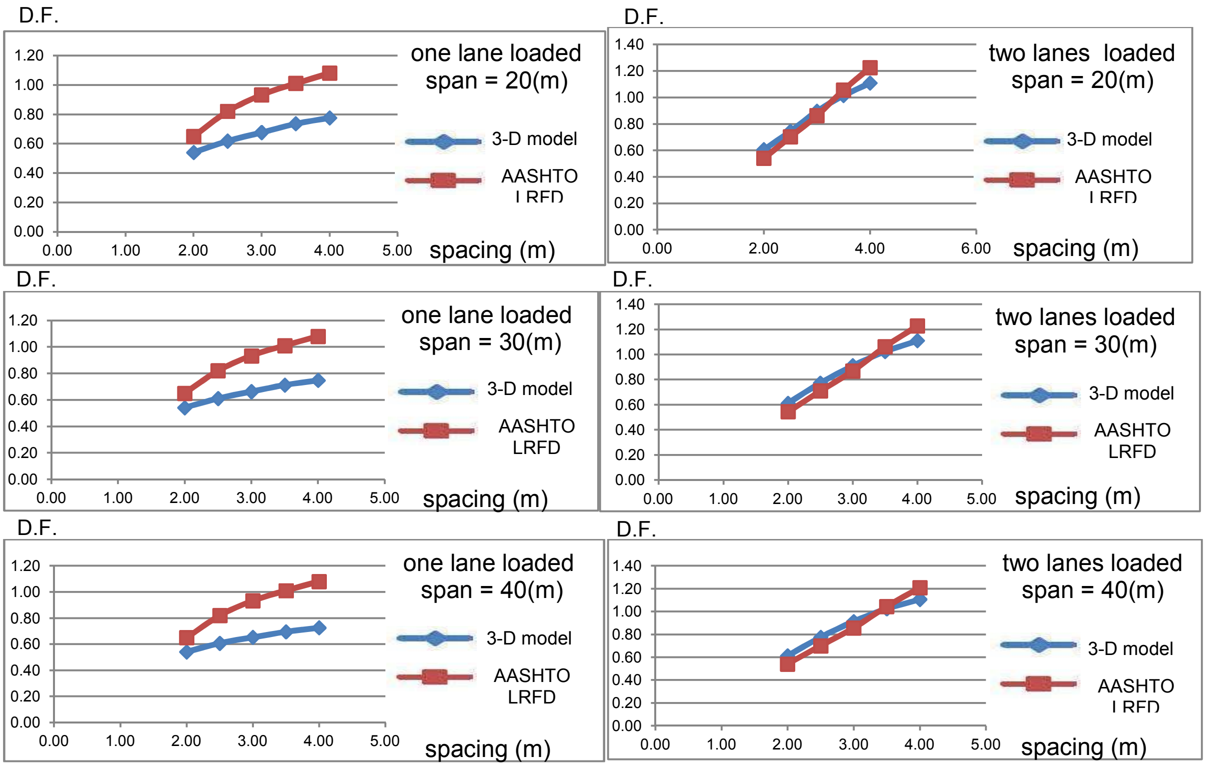

Figure 5a: Comparison between distribution factors (D.F.) obtained from AASHTO LRFD and 3-D finite element analysis for exterior beam

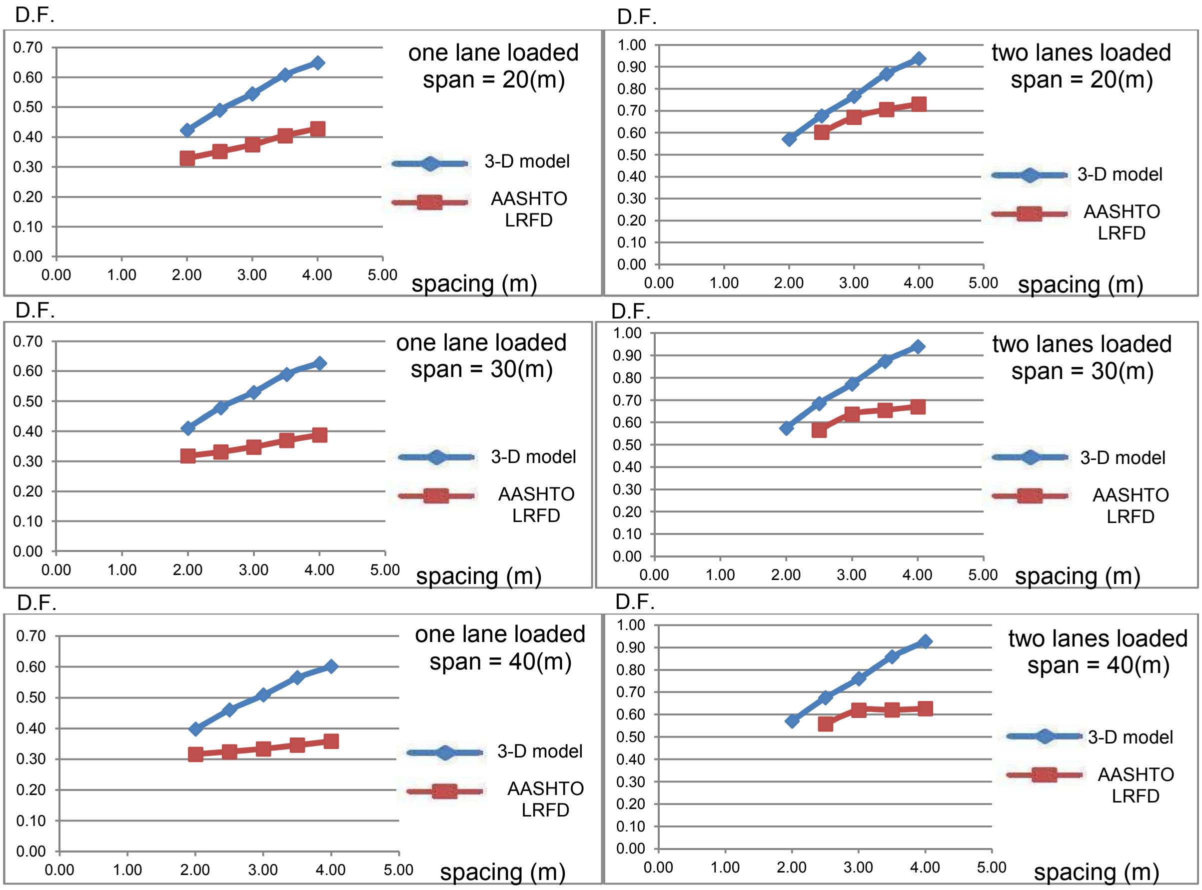

Figure 5b: Comparison between distribution factors (D.F.) obtained from AASHTO LRFD and 3-D finite element analysis for interior beam

Also it is noticed from tables 2 to 4 and figures 5a and 5b that the bridge span has no significant effect on the D.F. values from both AASHTO LRFD and 3-D finite element model results.

4 CONCLUSIONS

Based on the above study the following main remarks can be concluded:

1. The distribution factors (D.F.) obtained from AASHTO LRFD for live load analysis of exterior beams are conservative compared to 3-D finite element results for one lane loaded especially for bigger beam spacing.
2. For case of two lanes loaded, the D.F. of exterior beam resulting from 3-D analysis give higher values for small girder spacing and lower values for big girder spacing compared to AASHTO LRFD values.
3. For interior beam, AASHTO LRFD distribution factors are conservative compared to the 3-D finite element analysis factors notably for higher composite beam spacing.
4. Bridge span is not considerably significant for the D.F. calculations for both AASHTO LRFD method and the current 3-D finite element analysis.

REFERENCES

[1] J. Eom and A. Nowak , *Live Load Distribution for Steel Girder Bridges,* Journal of bridge engineering, volume 6, 489-497 (2001)

[2] AASHTO LRFD Bridge design specifications, 2007.

[3] J. Li and G. Chen, *Method to Compute Live Loads Distribution in Bridge Girders,* Practice Periodical on Structural Design and Construction, volume 16, 191-198 (2011)

[4] A, Razaqpur et al., *Nonlinear Behaviour of Steel-Concrete Composite bridges: Finite Element Modeling and Experimental Verification,* Canadian journal of civil engineering, 39 (2), 191-202 (2012)

[5] A, Razaqpur et al., *Inelastic Load Distribution in Multi-Girder Composite Bridges,* Journal of engineering structures, volume 44, 234-247 (2012)

[6] Computers and Structures, Inc. Berkely, SAP2000 Program 2011, California, USA. .

12th International Conference on
Steel, Space and Composite Structures
28-30 May 2014, Prague, Czech Republic

INFLUENCE OF SELECTED PARAMETERS ON DESIGN OPTIMISATION OF ANCHOR JOINT

Miroslav Bajer*, Martin Vild*, Jan Barnat* and Josef Holomek*

*Brno University of Technology, Faculty of Civil Engineering, Institute of Metal and Timber Structures
Veveří 95, 602 00 Brno
e-mail: vild.m@fce.vutbr.cz, webpage: http://www.fce.vutbr.cz

Keywords: Cast-in anchors, concrete pad, rigid joint, experiment

Abstract. *Main topic of this article is description of real behaviour of selected statically loaded anchor joints — design of individual anchor joint components in context of determination of selected parameters used during the anchor joint optimisation process.*

The standard design approach is Component method used in codes which is not able to solve more complex and atypical anchoring joints especially when the character of load is complicated. First the parameters which should be used in design process are determined and described. Then the parameters are surveyed in detail. These parameters should be used not only in further development of component method but also as inputs for other methods such as Finite Element Method (FEM). Models of the anchor joint based on FEM usually demand solid modelling approach, which is very complicated, time consuming and very difficultly applied in practice. Thus the aim is to simplify the model as much as possible with similar accuracy.

This paper is mainly focused on description of experiments which were prepared and realised in laboratories of Brno University of Technology. Joints of columns and concrete using base plate were realized to monitor the real behaviour of individual parts of anchor joint (concrete, anchor bolts, base plate, welds etc.) Results are presented and compared to models. Data obtained from these tests could be further used in design of anchor joints.

1 INTRODUCTION

The article presents a research which is focused on developing a simplified engineering model of a steel or steel-concrete joint of a structure. Both creation and solution of this simplified model should require only the most necessary material parameters, geometry and short duration of solution. Therefore, the aim is to use simple beam or shell elements instead of solid elements, complex contact parameters and areas with detail modelling with keeping the same quality and accuracy of results.

For example, to model an anchor bolt it is possible to use a beam element and to replace a complex behaviour of a mechanical (e.g. expansion anchor) or glued (bonded anchor) contact between the bolt and concrete by an appropriate setting of the beam element, e.g. see [1]. In addition, the whole concrete pad including a grout can be simplified to Winkler foundation model. Then, with the correct setting of stiffness, the model will provide forces and stresses, which can be evaluated according to analytical solutions. Steel structures mostly comprise of plates which can also be modelled using shell elements.

In current praxis it is very difficult or impossible and always expensive to determine all necessary parameters which are required in complex nonlinear material models and contact settings. General effort is to find the parameters that mostly influence the accuracy of results and the ones that can be neglected. In the design phase an engineer does not know some values of the most important parameters and thus a default values should be recommended at least for common types of joints. Ideally, the sensitivity analysis is performed, e.g. see [2].

The values of these parameters have to be based on experimental research. The execution of experiments can lead to another problems concerning methods of measuring of forces or deformations. For example, there are two most widespread methods to measure the tensile force in an anchor bolt: strain gauges glued to bolt surface and force washers.

At Brno University of Technology a basic type of steel-concrete joint was selected for an experiment. The joint is simple enough so its resistance can be calculated by Component Method used in Eurocode and to be modelled by FEM. The experiments described below were performed to acquire data used in software for creation of simple engineering models, for example IdeaCON. Another useful result was verification of measuring methods.

2 METHODS

The intention was to subject a steel-concrete joint to a constant compressive force and an increasing bending moment. Hence, four specimens consisting of reinforced concrete pad, cast-in anchors and steel column were prepared. The cast-in anchors were made of threaded rods M20, steel grade 8.8, corresponding nuts and a steel plates with dimensions 60 x 60 x 20 mm and a hole in the middle, which served as a head of the bolt and big washers to cover the holes in base plate. The head of the bolt, which resisted the pull-out failure mode, was created by pulling the threaded rod through the small hole in the steel plate, which was fixed in place with a nut from each side. A small part of a thread adjacent to the upper concrete surface was milled off and a strain gauge was applied on each anchor which was to be subjected to tension.

First the formwork of OSB was prepared, then reinforcement cage and anchors were fixed in place using wooden frame. The reinforcement was standard for concrete pad: rods of steel grade B 490 with 12 mm diameter with spacing 150 mm at the bottom and 300 mm at the top. The cover to reinforcement was 40 mm. Four reinforcing bars for crane hooks were added for manipulation. Polystyrene was attached to the wooden frame to keep the place for shear lug. Three strain gauges were fixed to the wooden frame in a position where an area of concrete in compression was expected. Hereby the pad was ready for pouring of concrete. The formwork with all the above described elements can be seen in Fig. 1.

Figure 1: On the left: formwork, reinforcement, anchors and strain gauges ready for casting; on the right: column, base plate and shear lug

The grade of concrete was C16/20 and 4 concrete pads (1500 mm length, 1000 mm width and 400 mm height) and 9 testing specimens (5 cubes and 4 prisms) were cast from one batch. The concrete was sufficiently vibrated and cured for 2 days against shrinkage.

A base plate with holes for anchors and a spreading plate, both with 20 mm thickness, were welded to bottom and top of column HEB 240, respectively. A shear lug was welded to the bottom of the base plate. The shear lug was IPE 100 with length 100 mm. All these components were from steel grade S 235. The base plate with the shear lug and the bottom part of the column is shown in Fig. 1.

One month after the casting of the concrete the columns welded with plates and shear lugs were attached to the concrete pads using grout Groutex 603 and cast-in anchors.

Strain gauge was applied in the height of 150 mm to each side of a column flange which was in tension when the sufficient bending moment was applied. Another gauges were glued to the base plate: one near the flange where maximum deformation of the base plate was expected and a rosette between two anchors in tension. Additionally the lifting of a base plate above the concrete pad and the horizontal and vertical displacement on loading cylinders was measured.

Two independent forces were applied by the loading cylinders on the top of the column: the axial force, which was applied first and then held constant at 400 kN, and the horizontal force, which varied and caused a bending moment in the joint. The axial force was applied using a special set-up of rigid steel beams not to interfere greatly with the horizontal force and not to cause any unwanted stresses in the concrete pad. The loading cylinder was held by two rods attached by pins to a short beam which was bolted to two larger beams fastened to the ground in the laboratory, which is specially designed to withstand great loads. The beams also stabilized the specimen in place. Ideally the pins should be in the point around which the column would turn. In our case the pins were 485 mm above this point and therefore the axial force slightly stabilized the column when horizontal deflection raised. The horizontal force was applied by loading cylinder pinned in the height of 1.83 m above the base plate, thus causing bending moment and shear force in the joint. Specimens 1 and 2 were subjected to in-plane axial force along the stronger axis of the column. Specimens 3 and 4 were rotated by 26.56˚ along the vertical axis, thus bended in out-of-plane direction. The scheme and the photograph of the set-up with in-plane bending is shown in Fig. 2 and Fig. 3, respectively.

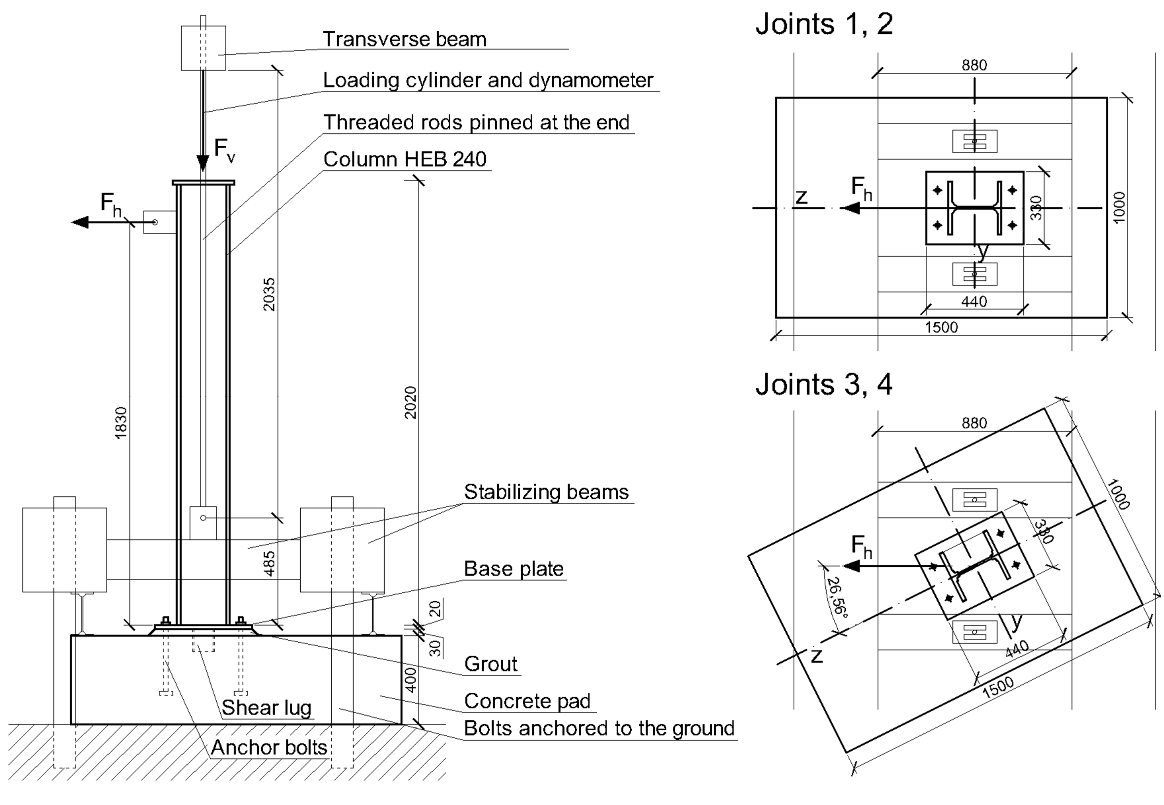

Figure 2: The test set-up scheme

Figure 3: The test set-up of joint 2 — axial force and in-plane bending

3 RESULTS AND DISCUSSION

Tests to determine the compressive cube strength and modulus of elasticity of the concrete were performed 136 days after the casting of both the concrete pads and the test specimens. The average compressive cube strength and modulus of elasticity were 22.6 MPa and 20.9 GPa, respectively. These values were used for calculation purposed in Eurocodes and in FEM models.

The resistances N_{Rk} and M_{Rk} and stiffness S_j of the above described joint were calculated according to the Component Method in ČSN EN 1993-1-8 [3], the concrete resistance according to ČSN EN 1992-1-1 [4] and the interaction curve was determined using the guideline in [5]. The axial resistance N_{Rk} was 1760 kN. The joint resistance in in-plane bending moment perpendicular to the stronger axis is dependent on the axial force. With the chosen compressive axial force, F_v = 400 kN, the resistance was M_y = 128 kNm. The stiffness is also dependent on the direction and magnitude of forces. For the above described case the initial stiffness $S_{j,ini}$ was 22.168 MNm/rad. According to the Component Method in Eurocode the stiffness starts to decrease at 2/3 of maximal resistance in bending moment. The bending moment resistance and stiffness can be calculated only for simple joint set-ups, in-plane case and for specific points in the joint interaction diagram.

The anchor bolts can fail in 3 modes — steel rupture, pull-out failure and concrete cone breakout. Calculation according to ETAG [6] was performed and although the concrete cone breakout mode had the lowest characteristic resistance (230 kN for both bolts in tension). However, it did not occur during any of the experiments. In all cases the steel failure was governing the ultimate resistance of the joint. Nevertheless the concrete cone breakout is known to have great variation of results and the concrete pad exhibited many cracks and in case of cyclic loading the concrete cone breakout could be decisive.

The evaluation of the tests involved reducing horizontal force F_h with stabilizing effect of vertical force F_v caused by the difference of heights of the point around which the column turned and the pins connecting the threaded rods holding the cylinder inducting vertical force F_v. Also the elastic deformation of the column was subtracted to determine the value of rotation φ of the joint. Initial stiffness $S_{j,ini}$ was calculated from the difference between M_y = 100 kNm and 20 kNm and corresponding values of rotation φ. In both experiments the initial stiffness was more than twice lower than according to the Component Method in Eurocode: $S_{j,ini}$ = 9,32 MNm/rad for joint 1 and 10,77 MNm/rad for joint 2.

The bending moment - rotation diagram of calculation and results of two experiments of joints with in-plane bending can be seen in Fig. 4.

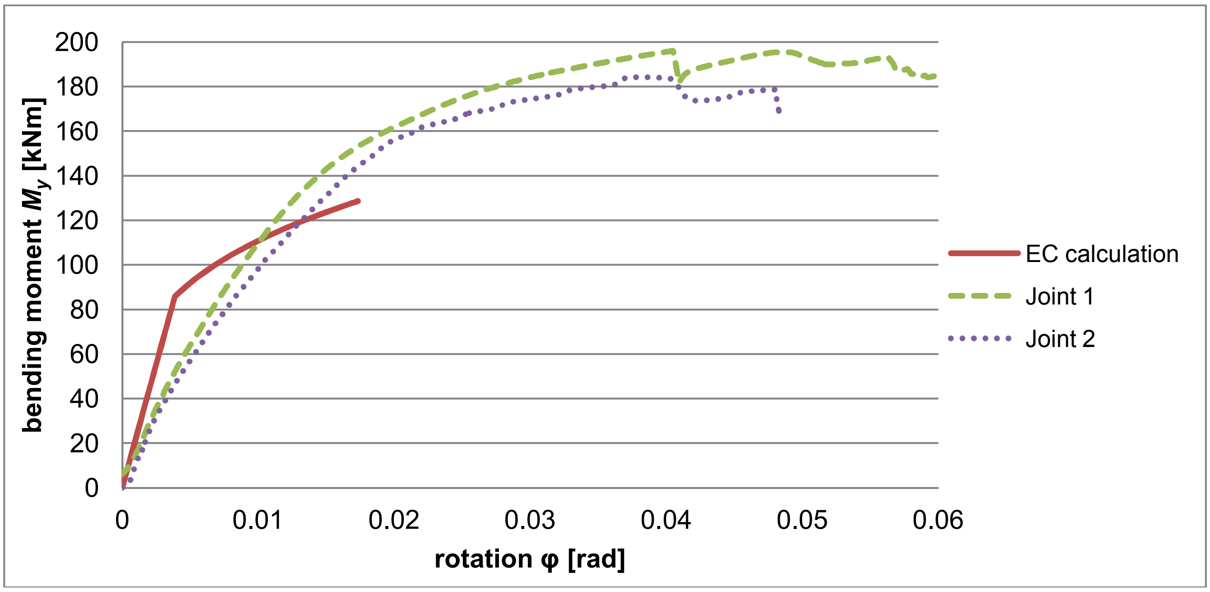

Figure 4: Bending moment - rotation diagram of specimens 1 and 2 subjected to axial force and in-plane bending moment and calculation according to EC

The M-φ diagram plotting the results of 2 experiments of joints with out-of-plane bending can be seen in Fig. 5. Curves φ, φy and φz show the dependence of bending moment M on rotation φ in the direction of the horizontal force, perpendicular to the stronger axis y and perpendicular to the weaker axis z, respectively. The instant when the anchor bolts in tension were torn are clearly seen in the graph where bending moment plummets. This occurred at the horizontal displacement of 270 mm in case of joint 3, where only one anchor was cut, and 185 mm and 268 mm in case of joint 4, where both anchors were torn. The maximal horizontal displacement allowed by the cylinder was about 300 mm.

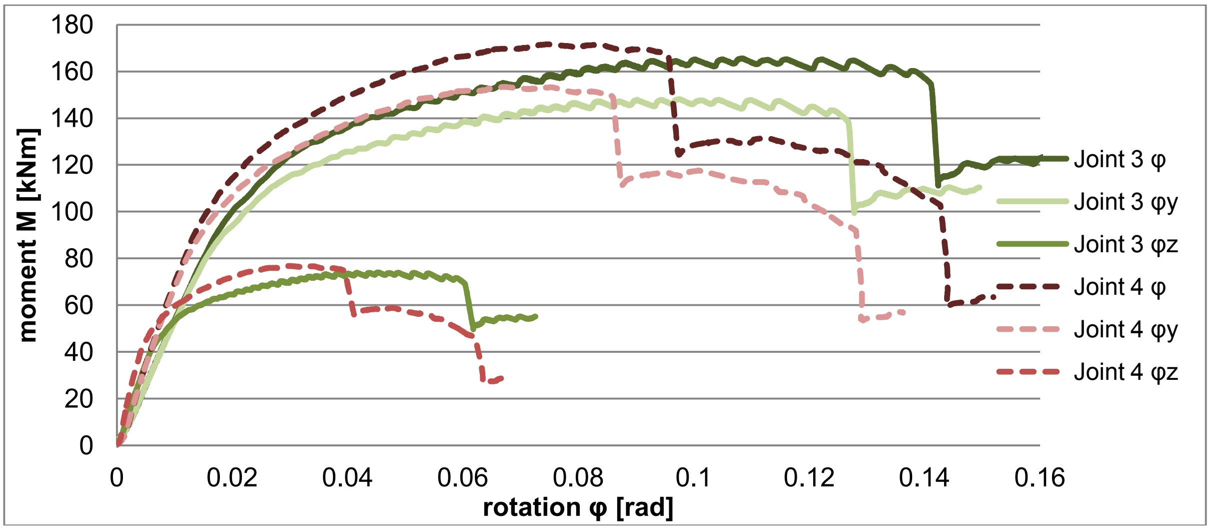

Figure 5: Bending moment - rotation diagram of specimens 3 and 4 subjected to axial force and out-of-plane bending moment

The forces on anchors in tension were measured by strain gauges and force washers. Force washers measure directly the force but the strain obtained from strain gauges had to be multiplied by modulus of elasticity (E = 210 GPa) and reduced cross sectional area of an anchor bolt (A = 220 mm^2) in the place where parts of the thread on the anchor bolts in tension were milled off so the strain gauge could be glued to the bolts' surface. The results are plotted in Fig. 6.

The manufacturer guarantees the error of measurement only 2 % for strain gauges and 12 % for force washers. On the other hand, if a bolt is subjected also to bending moment, it is paramount to place a strain gauge to a neutral axis or to use more strain gauges. In case of in-plane bending (joints 1 and 2) the results of forces obtained from force washers show good agreement with results calculated from strain acquired from strain gauges. In the experiments with out-of-plane bending moment (joints 3 and 4) the strain gauges were glued to the sides parallel to the flange of the column and showed results completely corrupted by significant strain caused by bending. With only one strain gauge on each bolt, it is impossible to differentiate the parts of the strain caused by tension and bending. Another disadvantage of strain gauges is the fact that after the yield strength is reached, the real stress-strain diagram has to be used to calculate stress and force. The moment when results from strain gauges starts to differ from results from force washers and rise sharply is the moment of yielding.

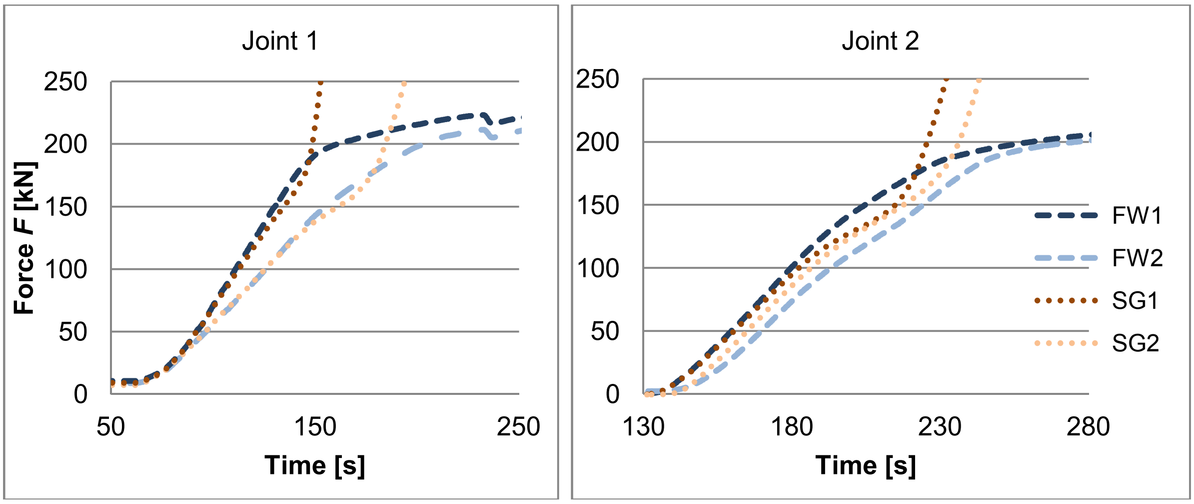

Figure 6: Forces on anchors measured with force washers (FW) and strain gauges (SG)

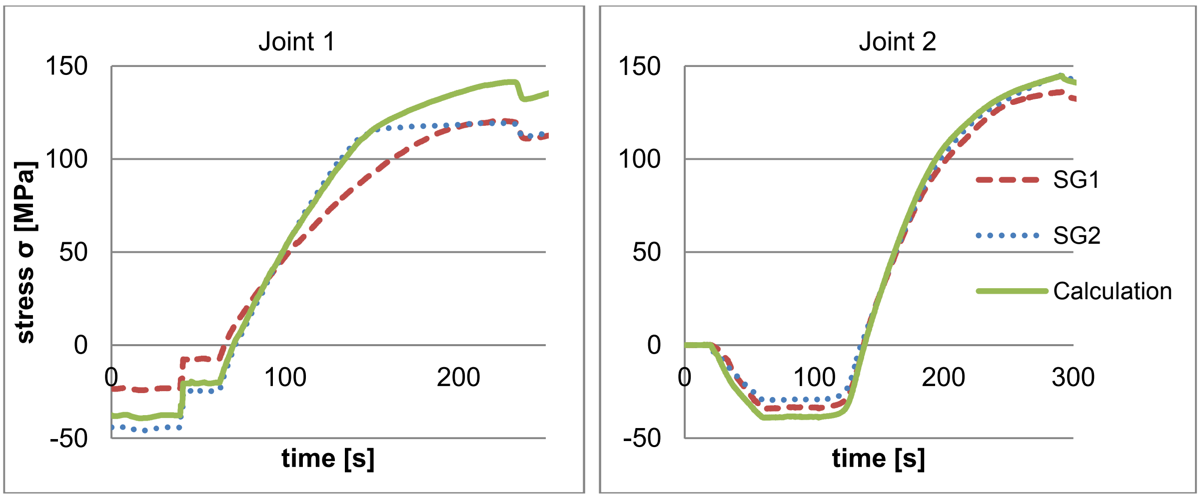

Figure 7: Stress obtained from strain gauges on the edges of the flange and by calculation

Stress on the edges of a flange in tension is plotted in Fig. 7. The stress was rising very differently on two edges of the flange of the column in joint 1. The same behaviour can be seen in

Fig. 6. At the time around 140 s the bolt reached its yield stress and also the stress on this edge of the flange near yielding bolt flattened out. Later the stress on both flanges remained very similar on both edges and slightly lower than the calculation which was caused by yielding of bolts. The initial differences could be ascribed to joint imperfections, e.g. not completely straight column, non-uniform grout or slightly eccentric application of forces. In case of joint 2 all three curves fit each other very well.

The case of out-of-plane bending is plotted in Fig. 8. The increment of stress from bending was higher in direction perpendicular to the weaker axis even though the angle between force and direction perpendicular to the stronger axis was 26.65˚. This means that the flanges of a column started to yield much sooner than in in-plane bending case. The yielding caused the stress on the most tensioned edge of a flange to decrease and the stress on the other side of this flange to get from compression into tension.

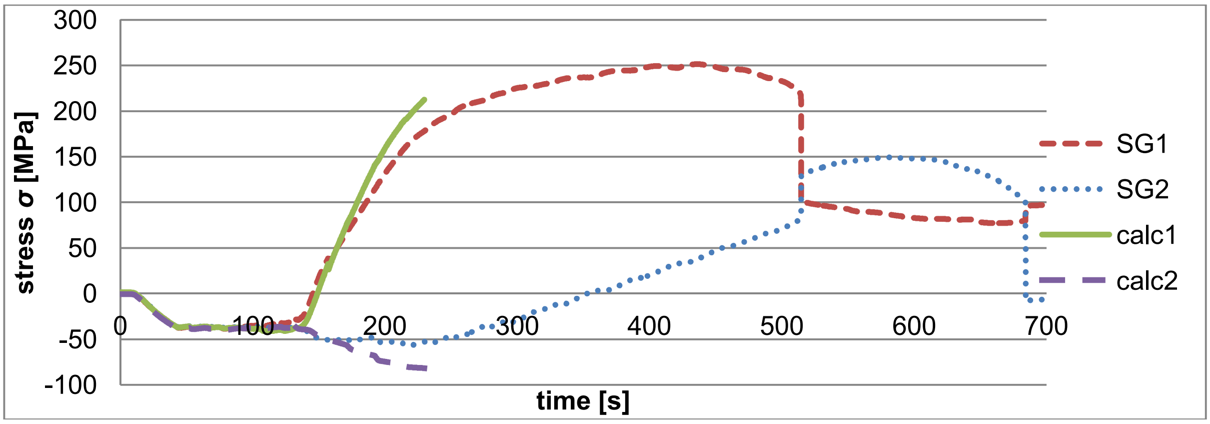

Figure 8: Joint 4 — Stress on the edges of flanges — out-of-plane bending

The typical sequence of resistance failing is described on the case of joint 2. First the cracks in concrete could be heard around M_y = 100 kNm and soon they started to be visible on the surface. At t = 175 s and M_y = 110 kNm the base plate started to yield according to the strain gauge near the flange in tension. Then at t = 215 s and M_y = 163 kNm the first anchor bolt started to yield and soon after, at t = 222 s the second anchor bolt as well. The elastic resistance of a column was reached at t = 255 s and M_y = 185 kNm according to the calculation. Then the bending moment stayed nearly constant around 195 kNm until the maximum horizontal displacement allowed by the loading cylinder was reached. At that moment the joint was practically destroyed, many cracks with about 1 mm thickness could be seen in the concrete pad and steel components were extensively yielded, which can be seen in Fig. 9.

Figure 9: Joint 2 — deformed base plate and bolts after the experiment

Results from engineering model from software IdeaCON with axial force F_v = 400 kN and bending moment M_y = 128 kNm are shown in Fig. 10. The anchor bolts were modelled only as truss element and the concrete pad was only a Winkler foundation model. Von Mises stress on steel shell elements corresponds well with calculation and experiment. Future work is to set the correct stiffness parameters to anchor bolts and Winkler foundation model for various types of anchorage, concrete and shapes of foundation pad.

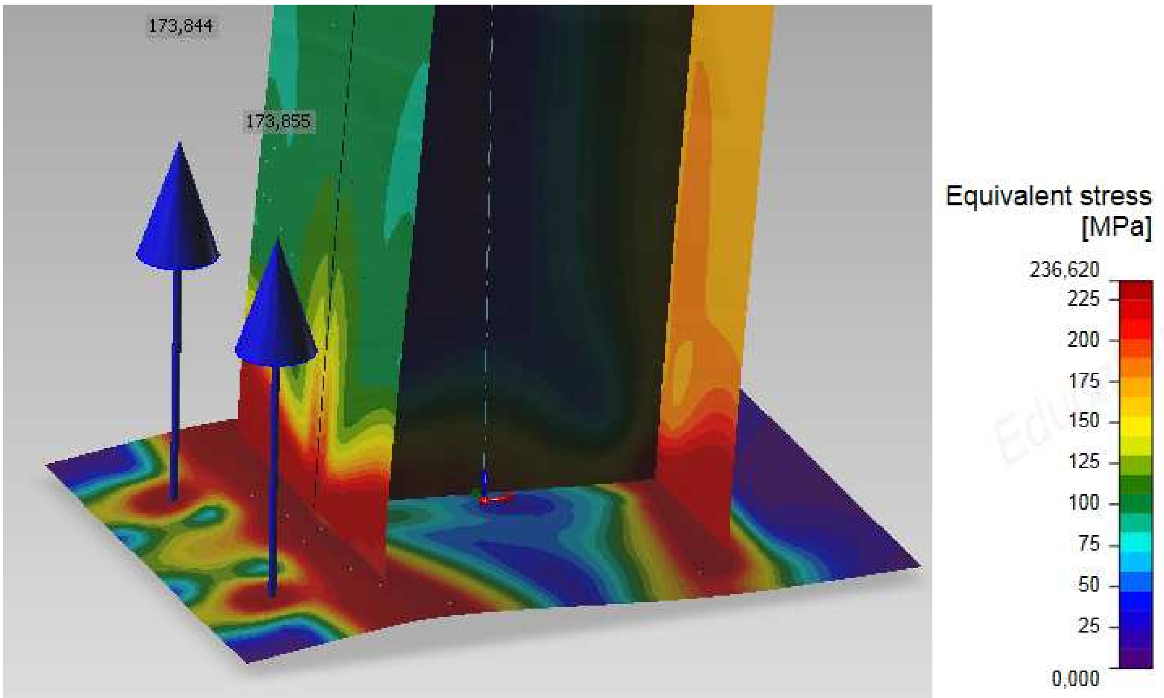

Figure 10: Von Mises stress on deformed shape and forces on anchor bolts from IdeaCON

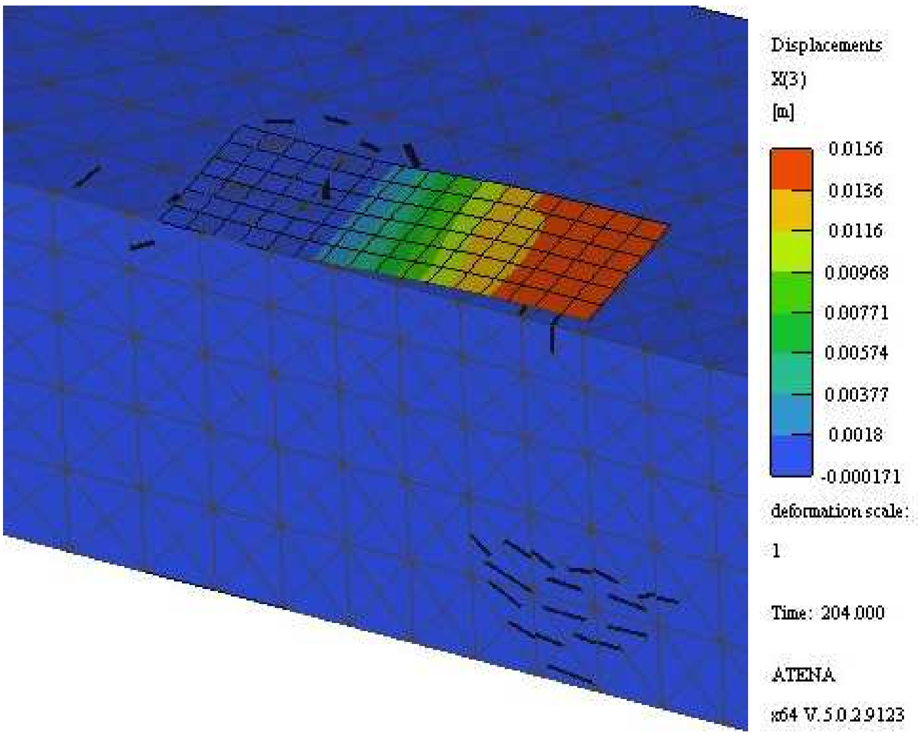

Figure 11: Vertical displacement and cracks in concrete from ATENA

Detailed FEM model was created in ATENA [7], which is a software especially dedicated to nonlinear analysis of concrete material. The detailed FEM model is used for comparison with the experiment, to determine magnitude and direction of main stresses in concrete, the contact area between steel base plate and concrete pad and to create parametrical studies, for example with various external forces, properties of concrete, interface bond between anchor bolt and concrete or various dimensions and shapes of steel column and concrete pad. The results of vertical displacement of base plane and cracks in concrete of this detailed FEM model is shown in Fig. 11. The comparison of forces acting on anchor bolts between FEM model and force washer readings from experiments can be seen in Fig. 12.

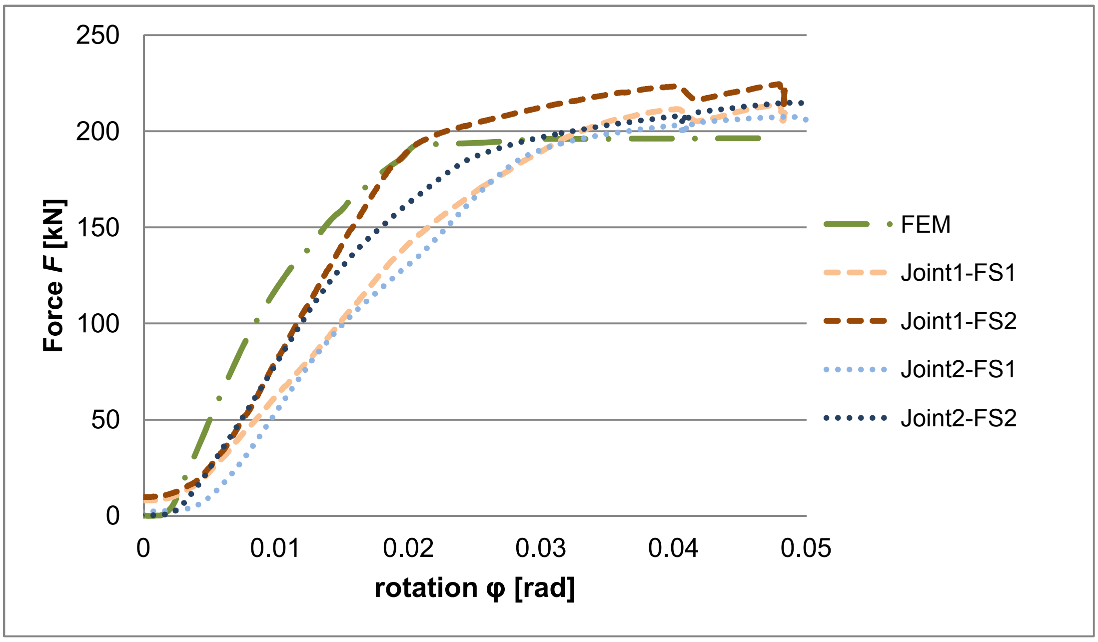

Figure 12: Comparison of forces on anchors

4 CONCLUSION

Even a very simple joint of steel into concrete is a very complex problem with many various modes of failure. Different failure modes, e.g. concrete cone failure or steel yielding, can occur at different load and rotational displacement and some are allowable under certain conditions, for example anchor bolts yielding under the condition of sufficient rotational capacity of the joint and calculation of ultimate strength. There are many types of anchors to concrete, which are dependent on many factors. While steel is more ductile and engineers often allow yielding, concrete is quasi-brittle material with very low strength in tension. Thus, both materials exhibit different behaviour in monotonic and cyclic loading.

Analytical solution for such problems is possible only for certain shapes of column, position of bolts and in-plane bending. Even simplified and not accurate, it is very time consuming. Detailed FEM modelling requires vast knowledge about material and contact parameters, elaborate software and good hardware equipment. Still, to achieve accurate results, it is often necessary to validate the detailed model with an experiment. Therefore simplified engineering model, allowing to create and solve a joint in minutes is very welcome. In this simplified model, it is clear that certain problems have to be solved analytically rather than using detailed FEM elements, for example the resistance of anchor bolts.

Regarding the experiment, it is very convenient to apply redundant measuring devices; for example force washers and strain gauges can be used together and in case of malfunction of one device, there are still results from the other one available. Also, even though strain gauges should be more accurate, force washers can be used to measure force even without the precise knowledge of stress-strain diagram.

The experiments provided necessary inputs into both engineering model and detailed FEM model. Both of them are going to be updated and the simplified engineering model is to be provided to engineering society.

5 ACKNOWLEDGEMENT

The article was elaborated with the financial support of TA03010680, FAST-S-13-2077 and GAČR P104/11/0703.

REFERENCES

[1] M. Bajer, J. Barnat, *The Glue-Concrete Interface of Bonded Anchors,* In Construction and building materials, (2012), 34(9). p. 267 - 274. ISSN 0950-0618.

[2] Z. Kala, J. KALA, *Sensitivity Analysis of Stability Problems of Steel Columns using Shell Finite Elements and Nonlinear Computation Methods*, In Proc. of the 17th Int. Conf. Engineering mechanics 2011, Svratka, Czech Republic (2011), pp.271-274, ISBN 978-80-87012-33-8.

[3] *ČSN EN 1993-1-8 Eurokód 3: Navrhování ocelových konstrukcí - Část 1-8: Navrhování styčníků*, Český normalizační institut, Prague, Czech Republic (2006).

[4] ČSN *EN 1992-1-1 Eurokód 2: Navrhování betonových konstrukcí - Část 1-1: Obecná pravidla a pravidla pro pozemní stavby*, Český normalizační institut, Prague, Czech Republic (2006).

[5] F. Wald, *Column Bases*, Ediční středisko ČVUT, Prague, Czech Republic (1995).

[6] Europian Organization for Technical Approvals, *ETAG 001 Guideline for European Technical Approval of Metal Anchors for Use in Concrete*, EOTA, Brussels, Belgium (2001).

[7] V. Červenka, L. Jendele, *ATENA program documentation - Part 1 - Theory,* Červenka Consulting, s.r.o., Prague, Czech Republic (2013).

ON PROBLEM OF STABILIZATION OF STEEL THIN-WALLED BEAMS IN BENDING BY SANDWICH PANELS

Ivan Balázs* and Jindřich Melcher*

*Institute of Metal and Timber Structures
Faculty of Civil Engineering, Brno University of Technology
Veveří 331/95, 602 00 Brno, Czech republic
e-mail: balazs.i@fce.vutbr.cz, webpage: http://www.fce.vutbr.cz

Keywords: Beam, sandwich panel, stability, steel

Abstract. *Planar members such as sandwich panels have been widely used in building industry as roof or wall cladding. Besides covering of large spaces there is another significant feature of such members. When fastened to a supporting beam in bending or compression these members contribute to stabilization of such beam against buckling. It is particularly appreciable when a beam of a thin-walled cross-section is utilized. It involves purlins, wall substructure beams and others. The presence of planar members considerably increases buckling resistance of beams of slender thin-walled sections that are prone to buckling. There is number of factors influencing performance of these structural systems and stabilizing effect of planar members. Since these factors are mostly independent on each other and have a large dispersion, a pure mathematical solution of this problem is not practicable or even feasible. Influence of some factors on overall behavior may be efficiently assessed by experiments or numerical simulations.*

This paper focuses on investigation of behavior of steel beams of cold-formed thin-walled sections stabilized by sandwich panels fastened at the top flange of beams. Sandwich panels are specific structural members that consist of several layers of different material characteristics. They can work as simple or continuous members. This study particularly deals with influence of sandwich panel thickness and its effect on stabilization of steel beams. Geometrically nonlinear numerical analysis is conducted and substantial results are summarized and presented.

1 INTRODUCTION

Sandwich panels consist of insulation core (rigid polymer foam or mineral wool) and of thin metal facings. Their good heat insulation and fire safety characteristics predetermine their application to roof or wall cladding. These members also considerably contribute to buckling resistance of supporting beam in bending or compression. The buckling resistance is increased due to certain shear and rotational stiffness of planar members[1]. There is number of factors having influence on overall behavior of these constructional systems such as mechanical properties of fasteners used, way of load transfer from the planar member to the beam[2] and others. It is a problem of bound deformation of the beam along the span[3]. Lateral displacement of fastened part of the beam is prevented. This prevention can be either full or partial[4]. Due to complexity of the problem a pure analytical solution is practically not feasible or even possible. It is efficient to use numerical or experimental analysis to investigate the effect of selected factors on overall stabilizing performance of sandwich panels. This paper presents results of numerical analysis performed using ANSYS 14.0 code based on finite element method. Influence of the sandwich panel thickness on behavior of steel supporting beam of cold-formed thin-walled section in the point of view of global stability is investigated.

2 SUBJECT OF THE STUDY

Steel beams of cold-formed thin-walled Z-sections are considered. The steel grade is S355. The beam span is 3 m, depth 150 mm and thickness 3 m. Sandwich panels are considered to be fastened at the top flange of the beam using self-drilling screws. Each panel is supported by three beams i.e. the panels work as continuous beams with two equal spans. The beam constituting the intermediate support of the panels is investigated in detail. The system can be seen in Figure 1. The points of jointing of panels to beams are visible there.

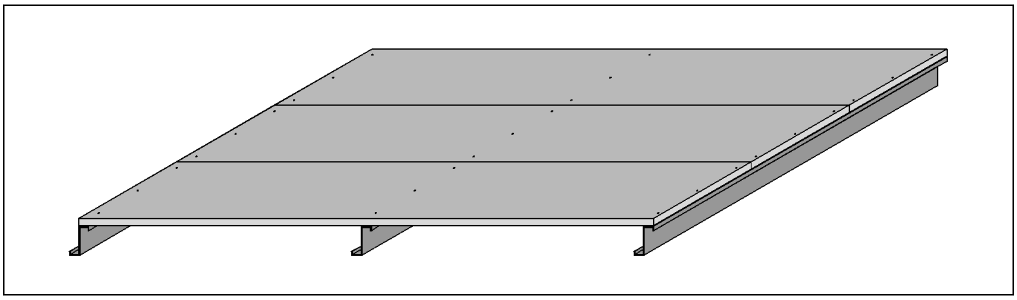

Figure 1: Constructional system

Isolation panels with rigid polyurethane foam core from the S. C. Plastsistem S. A. company series production are considered[5]. Length of each panel is 3 m and width 1 m. Three values of panel thickness H are considered: 40 mm, 80 mm and 120 mm. Thin steel facings of thickness of 0,5 mm (steel grade S280) are utilized. Their profilation is very shallow and is neglected in the numerical analysis. In Figure 2 there are schematic cross-sections of the steel beam and sandwich panel utilized. In case of beam, there is also orientation of coordinate system. The x-axis is longitudinal axis of the beam.

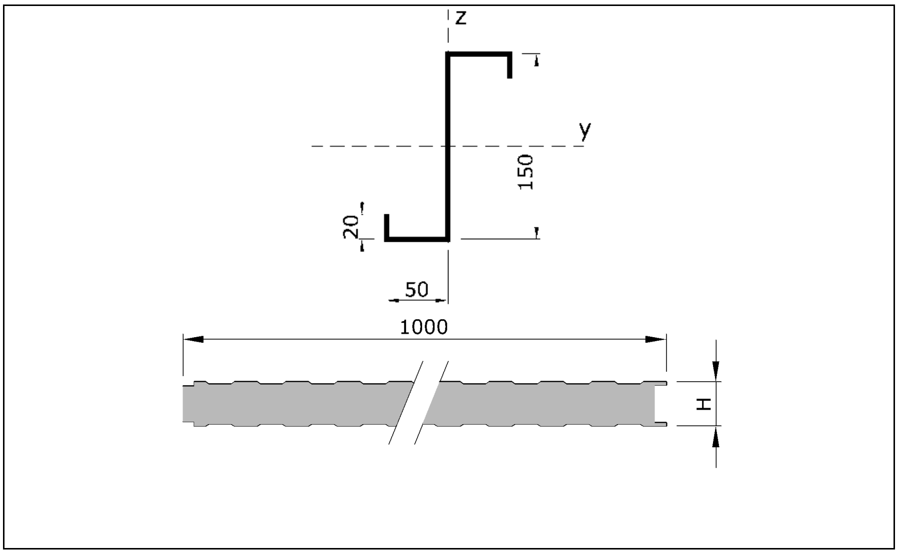

Figure 2: Beam and panel Sections

Longitudinal jointing of the panels is assumed. In practice longitudinal edges of the panels might not be connected by fasteners but by feather and groove system only[4]. In that case, shear forces transfer is ensured by friction only[6].

Polyurethane (PUR) constituting the core of the panel is polymer with some convenient characteristics. Its mechanical properties differ significantly from the properties of thin steel facings. In literature some approximate values can be found. Since these values were determined mostly by experiments, they can differ slightly from each other depending on sample utilized for experiments and on specific composition of polyurethane foam. The density of PUR can be taken as $\rho = 38 \div 43\ kg \cdot m^{-3}$ and Young's modulus of PUR $E_{PUR} = 3{,}4 \div 4{,}6$ MPa[7] or $\rho \approx 40\ kg \cdot m^{-3}$ and $E_{PUR} \approx 3{,}4$ MPa[8], respectively. There are also empirically established formulae for approximate Young's modulus value determination[8]. The Poisson's ratio of polyurethane can be taken as $\nu = 1/3$[8].

The bending moment is assumed to be transferred by steel facings, the core transfers shear forces[9].

The steel beams are considered to be supported at the lower flange i.e. simple beams in bending are dealt with. Areal uniformly distributed uplift load applied at the external surface of the panels is considered. This load causes lower (free) flange to be in compression and thereby prone to buckling.

3 NUMERICAL ANALYSIS

Numerical analysis was performed using the ANSYS 14.0 code based on finite element method. For the sandwich panel the layered SHELL181 element suitable for sandwich constructions is utilized. It consists of three layers of different materials and thickness according to sandwich panel composition. Steel beams were also modeled using SHELL181 elements with appropriate thickness (3 mm) assigned. The element size is 25 mm (beam and sandwich panel areas adjacent to steel beam) and 50 mm (sandwich panel). The bilinear material model without hardening was utilized for sandwich panel facings as well as for steel thin-walled beams. Regarding polyurethane, there are several material models in literature based on results of experiments (isotropic, elastic[7]; isotropic, bilinear[9]). For the purposes of this numerical study an elastic isotropic material model was utilized with Poisson's ratio equal to 1/3 and elasticity modulus 4,6 MPa. After some experiments data will be obtained the finite element model might be improved. The finite element mesh is generated by the code with respect to specified finite element sizes. Detail of finite element network can be seen in Figure 3.

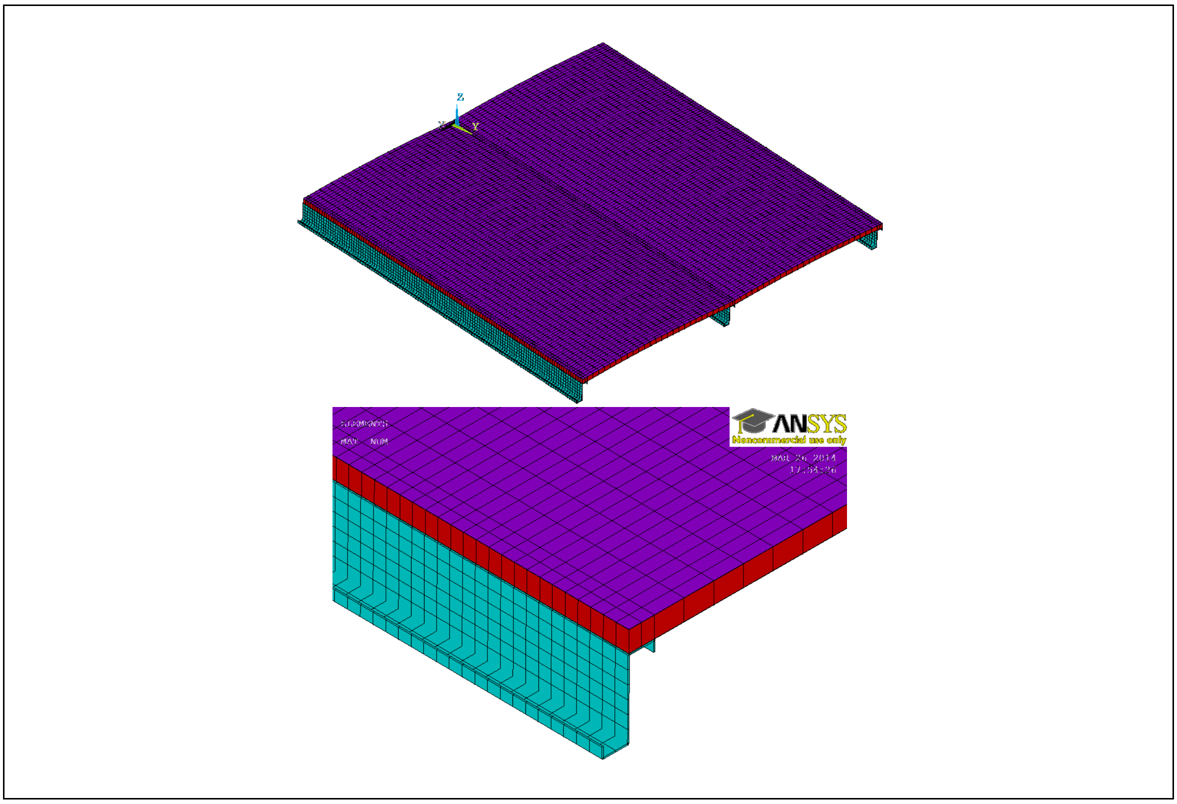

Figure 3: Finite element model and detail

The panels are placed at the top flanges of the steel beams. In numerical model it is taken into account by contacts between beam and panel elements with specified friction coefficient equal to 0,1 (steel – steel). Contact elements CONTA174 and TARGE170 were utilized. For the purposes of numerical model the fastenings are simplified using elements passing through the panel and connected to the top flange of the beam in given points of jointing. Appropriate material (high-strength steel) is assigned.

The geometry of the constructional system was updated according to deformation caused by unit uplift load with respect to imperfections specified in European standard for design of steel structures.[10]

The imperfection of steel beam is taken into account by initial curvature of the beam with given amplitude of $k \cdot e_{0,d}$ where $e_{0,d}$ is the initial equivalent bow imperfection of the weak axis of the section considered.[10] The value of k is taken equal to 0,5.[10] Initial bow imperfection e_0 / L for the lateral torsional buckling curve b (recommended for cold-formed sections[11]) should be taken as 1 / 250.

After the model had been completed the geometrically nonlinear analysis of imperfect system was performed.[12]

4 RESULTS OF NUMERICAL ANALYSIS

Selected results of numerical analysis focusing on influence of sandwich panel thickness on behavior of steel beams are presented. The chart in Figure 4 shows the load – deformation relationship for all the investigated values of sandwich panel thickness. It is possible to compare the influence of each value of thickness.

For the purpose of comparison with beam with no stabilization, numerical analysis of an isolated beam of identical Z-section in bending was performed. All the assumptions of the analysis remained unaltered including element type (SHELL181) and material model.

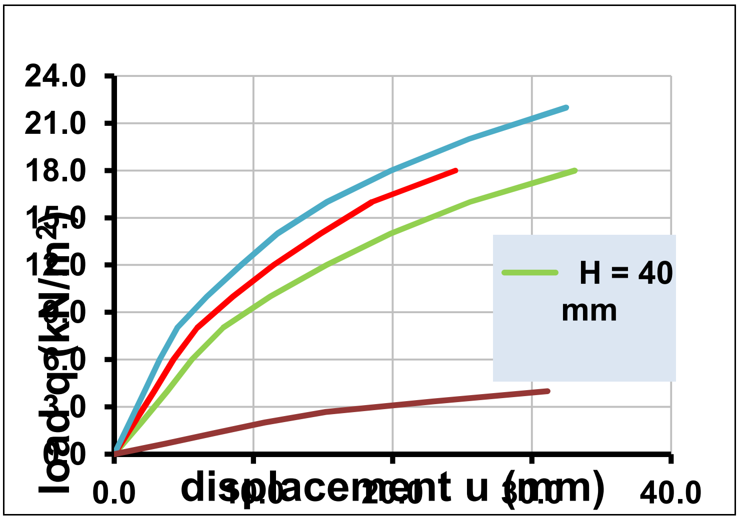

Figure 4: Load – deformation relationship

In Figure 5 there is Mises stress (intermediate beam, sandwich panel thickness 40 mm).

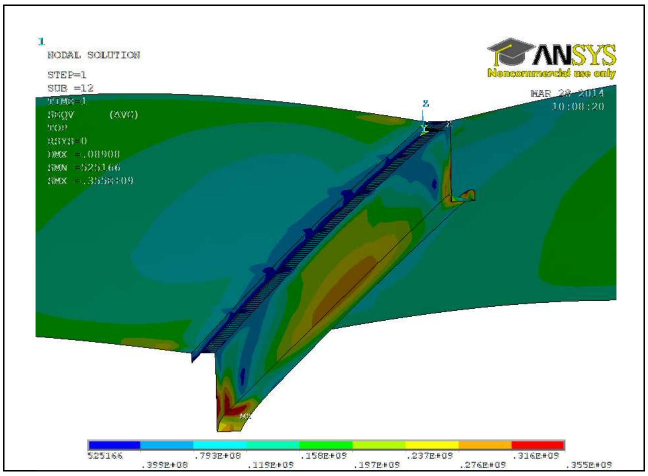

Figure 5: Mises stress

5 CONCLUSION

This paper summarizes selected results of geometrically nonlinear numerical analysis of steel beams of thin-walled Z-sections stabilized by sandwich panels of various values of thickness. The values of displacements at midspan of the beam in case of the sandwich panel thickness 80 mm are about 25 % lower than in case of the thickness of 40 mm. For the thickness of 120 mm this difference is about 41 %.

From the chart in Figure 4 it is visible that the beam behavior is significantly influenced by linkage to sandwich panel. An isolated beam with no stabilization under the same appropriate load as stabilized member exhibits larger magnitudes of displacement in comparison with stabilized beams.

This paper focuses particularly on problem of the global stability of steel beam in bending only. In the general point of view the problem is very complex. Particularly in case of thin-walled cold-formed sections problem of local or distortional buckling might occur. These local stability problems might be combined with each other or with the problem of lateral torsional buckling (coupled instabilities). Investigation of these demanding issues can be efficiently assisted by testing or by more extensive numerical models. Experiments might be used also for verification of numerical models. More accurate results of numerical models can be achieved by the finite element mesh refinement or by volume elements instead of the shell elements.

The load bearing capacity of these systems can be limited by sandwich panel limit states. Better inclusion of material model of polyurethane foam might lead to more accurate results. It is conditioned by exact knowledge of its material properties which can be most conveniently gained by experiments. Another substantial question is influence of fasteners on overall behavior and stabilization of thin-walled beams. Some of these issues might be an aim of forthcoming research.

6 ACKNOWLEDGEMENT

This paper has been elaborated within the frame of the projects of the Czech Science Foundation No. P105/12/0314 and of the Specific Research Program of the Brno University of Technology No. FAST-J-14-2345.

REFERENCES

[1] S. Käpplein, K. Berner and T. Ummenhofer, Stabilisierung von Bauteilen durch Sandwichelemente (Stabilization of substructure by sandwich panels), *Stahlbau*, Ernst & Sohn, Berlin, Germany (2012).
[2] J. Melcher, *Ohyb, kroucení a stabilita ocelových nosníků (Bending, torsion and stability of steel beams)*, Brno University of Technology, Brno, Czech Republic (1975).

[3] V. Březina, *Vzpěrná únosnost kovových prutů a nosníků (Buckling resistance of metal bars and beams)*, Czechoslovak Science Academy Publishing, Prague, Czech Republic (1962).
[4] S. Käpplein, T. Misiek and T. Ummenhofer, Aussteifung und Stabilisierung von Bauteilen und Tragwerken durch Sandwichelemente (Bracing and stabilization by sandwich panels), *Stahlbau*, Ernst & Sohn, Berlin, Germany (2010).
[5] *Wall panels – visible fastenings*, http://www.plastsistem.ro/p.aspx?t=Panou-termoizolant-de-perete-cu-imbinare-vizibila.
[6] M. Georgescu, V. Ungureanu and D. Dubina, Diaphragm effect in sandwich panel roofing: Experimental approach, *EUROSTEEL 2011: 6th European Conference on Steel and Composite Structures*, European Convention on Steel and Composite Steelwork, Budapest, Hungary (2011).
[7] M. Dürr, R. Podleschny and H. Saal, Untersuchungen zur Drehbettung von biegedrillknickgefährdeten Trägern durch Sandwichelemente (Investigation of the torsional restraint of sandwich panels against lateral torsional buckling of beams), *Stahlbau*, Ernst & Sohn, Berlin, Germany (2007).
[8] P. Hassinen and T. Misiek, Einfluss von Inhomogenitäten im Kernwerkstoff von Sandwichelementen auf die Tragfähigkeit (Influence of structural imperfections and inhomogeneities of the core material of sandwich panels on load-bearing capacity), *Stahlbau*, Ernst & Sohn, Berlin, Germany (2012).
[9] F. Rädel and J. Lange, Tragfähigkeit von Sandwichelementen mit profilierten Deckkschichten und Öffnungen (Load bearing capacity of sandwich panels with profiled faces and openings), *Stahlbau*, Ernst & Sohn, Berlin, Germany (2011).
[10] EN 1993-1-1, *Eurocode 3: Design of steel structures – Part 1-1: General rules and rules for buildings*, Czech Standard Institute, Prague, Czech Republic (2006).
[11] EN 1993-1-3, *Eurocode 3: Design of steel structures – Part 1-3: General rules – Supplementary rules for cold-formed members and sheeting*, Czech Standard Institute, Prague, Czech Republic (2008).
[12] R. Kindmann and C. Wolf, Geometrische Ersatzimperfektionen für Tragfähigkeitsnachweise zum Biegeknicken von Druckstäben (Member imperfections for verifications against lateral buckling of compression members), *Stahlbau*, Ernst & Sohn, Berlin, Germany (2009).

12th International Conference on
Steel, Space and Composite Structures
28-30 May 2014, Prague, Czech Republic

COMBINED MOMENT AND WEB CRIPPLING BEHAVIOR OF RE-ENTRANT PROFILED STEEL SHEETING

Y.Q. Cai*, C. Chen and S.P. Chiew

School of Civil and Environmental Engineering
Nanyang Technological University, Singapore
e-mail: *yqcai@ntu.edu.sg

Keywords: Re-entrant, Profiled steel sheeting, Section failure, Web crippling, Hogging moment, Numerical analysis.

Abstract: *Continuous profiled steel sheeting is often subjected to large hogging moment over internal support. Section failure of profiled steel sheeting over internal support under combined hogging moment and support reaction is often critical. Therefore, accurate prediction to the combined bending and web crippling behavior of profiled steel sheeting in an internal support is important. This paper presents an experimental study of the behavior of high strength re-entrant profiled steel sheeting under combined bending moment and web crippling. Test results are compared with design resistance obtained from design codes EN1993-1-3. It is found that Eurocode 3 gives conservative values for re-entrant profiled steel sheeting with high strength steel. Based on experimental study, finite element analysis is also carried out to predict the combined bending and web crippling behavior of profiled steel sheeting. Parameters investigated involve the thickness of profiled steel sheeting, the load bearing width and effective span. The comparison of numerical results and design values indicates that the design equations are over-conservative by 35%. It is demonstrated that a set of new design rules specifically for re-entrant profiled steel sheeting is needed for both improved efficiency and reliability.*

1 INTRODUCTION

Cold-formed profiled steel sheeting is widely used in composite slabs due to various advantages. They act as formwork during construction to support construction loads and self-weight of concrete. Profiled steel sheeting is able to develop reliable composite action with concrete and act as tensile reinforcement against sagging moment. Moreover, they also stabilize the supporting beams against lateral-torsional buckling. In the practical application, section failure under a combination of web crippling force and hogging moment at the internal support is often found to be critical during the construction stage which limits the capacities of the profiled steel sheeting.

Empirical interaction formula for the design of combined bending and web crippling is adopted in many design codes. Such an empirical formula was originated from a series of one-point load tests with specimens at various span lengths. For one-point load tests with short span lengths, failure is primarily caused by web crippling while the effect of bending moment is considered to be small. The effect of bending moment to web crippling resistance becomes more noticeable with increasing span length. A graphic representation of the empirical interaction formula is proposed by bakker[1]. It is shown that in the absence of a concentrated force, the moment capacity of a member can be fully achieved. Moreover, in the absence of bending moment, the web crippling resistance can also be fully achieved. If both bending moment and concentrated force are present at the same location, then interaction effect occurs, leading to significant reduction in both resistances.

Current provisions of design codes EN1993-1-3, BS5950-6 and other advanced specifications and codes such as NAS and AS4600 for estimating the web crippling resistance and moment resistance over internal support are known to be overly conservative [2-5]. Specially, the accuracy of the design rules is often in doubt for modern profiled steel sheeting with different geometry and high yield strength. In general, web crippling behavior and combined bending and web crippling behavior of profiled steel sheeting is an important research topic in recent years. Many researchers have carried out a lot of experimental investigation and numerical analysis to predict the behavior of profiled steel sheeting.

Combined web crippling and bending moment failure of trapezoidal sheeting profiles is studied based on yield line method by Hofmeyer et al [6]. A design rule with improved accuracy is proposed to predict the resistance of profiled steel sheeting. However, this rule is considered to be rather complicated for practical design and it is not applicable to re-entrant profiled steel sheeting. Combined flexure and web crippling strength of a low-ductility high strength steel sheeting is studied by Akhand[7] based on both experimental investigation and finite element analysis. A finite element model has been presented to predict the combined flexure and web crippling strength and moment-rotation capacity with sufficient accuracy. A comprehensive study of web crippling behavior and section failure under combined moment, shear and web crippling is reported by Chung and Tse[8-11] who carried out systematic tests on the web crippling failure of laterally restrained cold-formed profiled steel sheeting R50 and section failure under combined action over internal support. Comparison between tests results and design codes reveals that design rules are overly conservative to predict profiled steel sheeting R50 especially with high steel grades.

Although many research studies have been carried out during recent years, it is still important to have reliable and rational prediction methods in assessing the section failure of typical profiled steel sheeting. It will facilitated data interpretation against variations in both cross-sectional geometry and yield strength of profiled steel sheeting. In a word, it is highly desirable to develop a rational prediction capability to quantify the section failure of high strength re-entrant profiled steel sheeting under combined hogging moment and web crippling.

This paper presents an experimental study of section failure of high strength re-entrant profiled steel sheeting under combined action over internal support. Test results are compared with design code EN1993-1-3 to examine the applicability of current design rules in predicting combined bending and web crippling behavior of high strength profiled steel sheeting. Finite element analysis is also conducted to predict the behavior of profiled steel sheeting with various parameters.

2 EXPERIMENTAL INVESTIGATION

2.1 Profiled steel sheeting

The profiled steel sheeting used in this experimental investigation is re-entrant steel sheeting RF 55, which is formed from high strength sheet steel of Grade G550 of Australian standard AS1397. Figure 1 shows cross-sectional dimensions of the profiled steel sheeting. For present study, thicknesses 0.75 mm and 1.0 mm were used. In order to obtain the mechanical properties of the profiled steel sheeting, a total of 6 coupon tests are carried out, three for each profiled steel sheeting of different thicknesses. The yield strength f_{yb} for 0.75mm thickness and 1.0mm thickness are 592 N/mm^2 and 637 N/mm^2 respectively. And the Young's modulus E is 206 kN/mm^2 and 212 kN/mm^2 respectively.

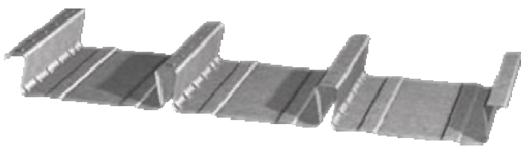

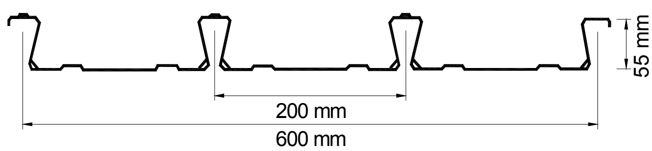

Figure 1 cross-section of profiled steel sheeting

2.2 Test setup

The experimental test is carried out according to EN 1993-1-3 to investigate the section failure behavior of continuous sheeting under combined bending and crippling force at internal support. All the test specimens are loaded in reverse position on a simple span of equivalent length using a central beam in order to simulate the actual loading condition of profiled steel sheeting over internal support. Figure 2 shows the general setup of the one point load test of the profiled steel sheeting. The span length tested is 1.6 m which corresponds to actual continuous sheeting span of 4 m, under uniformly distributed loading condition. The width b_B of the beam used to apply the test load is 100 mm, which represents closely to the actual support width to be used in practice. Three LVDT are used to measure deflections at mid-span of the specimens, as shown in Figure 2. A total of 6 tests are carried out where each thickness was tested on 3 specimens to determine the average value of the failure load.

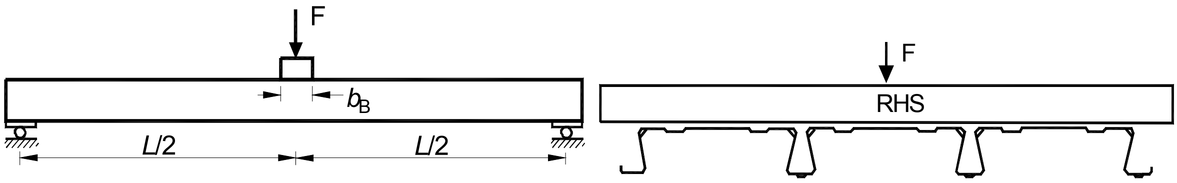

(a) Elevation view (b) Side view

(c) General view of test setup

Figure 2 Typical setup of one point loading test

2.3 Test results

Typical load-displacement curves of the profiled steel sheeting are presented in Figure 3. The graphs are plotted with the same scales in both axes for easy comparison. For each group tests, the failure loads of the three specimens are relatively consistent with a maximum difference of 9% between the highest and lowest values recorded. Similarly, the deflections of three nominally identical tests at the failure load are consistent. The average failure load of 0.75 mm and 1 mm thicknesses profiled steel sheeting under combined actions of hogging moment and web crippling force at internal support are 8.3 kN and 16.9 kN respectively. Obviously, profiled steel sheeting with 1 mm thickness could withstand twice the loading applied to 0.75 mm thickness steel sheeting.

Typical failure mode of profiled steel sheeting of one point loading test is shown in Figure 4. The failure modes for both 0.75 mm and 1 mm thick specimens are relatively similar. It can be seen that local buckling is observed at the compression trough in load bearing width in all test specimens, as shown in Figure 4(a). Section failure against web crippling is also observed at mid-span, as shown in Figure 4 (b). In general, the failure of all the specimens is through simultaneous buckling of trough flanges and crippling of webs under the loading bearing width.

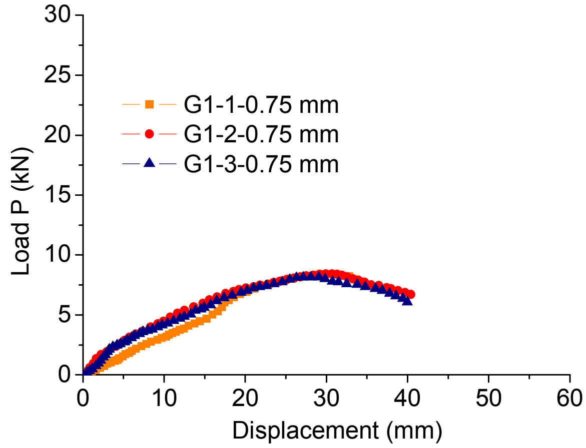

(a) Thickness 0.75 mm

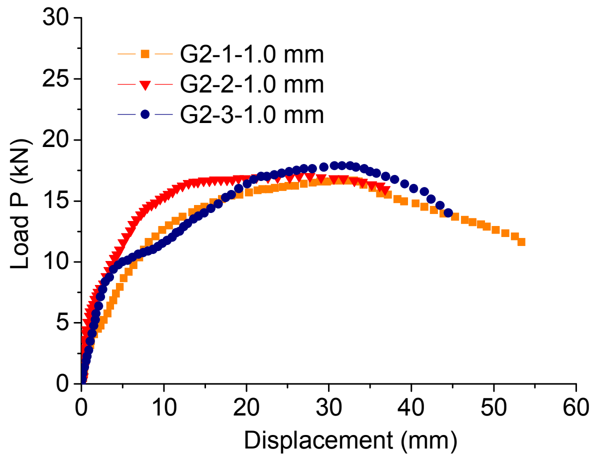

(b) Thickness 1.0 mm

Figure 3 Load-displacement curves of tests

(a) Significant local buckling in trough

(b) Section failure over load bearing area

(c) Local failure in web-trough corner

Figure 4 Typical failure mode of profiled steel sheeting

2.4 Comparison with design codes

In general, continuous profiled steel sheeting is subjected to large hogging moment over internal support. Section failure of profiled steel sheeting over internal support under combined hogging moment and concentrated load is often critical. Both British code BS 5950-6 and Eurocode EN 1993-1-3 recommend that such failure is assessed with a simple interaction rule as follows.

$$\frac{F}{R_{\mathrm{w,Rd}}}+\frac{M}{M_{\mathrm{c,Rd}}}\leq 1.25 \tag{1}$$

Where F and $R_{\mathrm{w,Rd}}$ are support reaction or concentrated load and web crippling resistance respectively; M and $M_{\mathrm{c,Rd}}$ are the bending moment at internal support and moment resistance under hogging moment respectively.

According to EN1993-1-3 (2006), in cross-sections with two or more webs, including sheeting, the local transverse resistance of an unstiffened web should be determined as specified, provided that both of the following conditions are satisfied: (1) The clear distance c from the actual bearing length for the support reaction or local load to a free end is at least 40mm;(2) The cross-section satisfies the following criteria: $r/t\leq 10;\quad h_{\mathrm{w}}/t\leq 200\sin\theta;\quad 45^{\circ}\leq\theta\leq 90^{\circ}$ where h_{w} is the web height; r is the internal radius of the corners; θ is the angle of the web relative to the flanges. Web crippling resistance per web of the cross-section should be determined from:

$$R_{\mathrm{w,Rd}}=\alpha t^{2}\sqrt{f_{\mathrm{yb}}E}\left(1-0.1\sqrt{\frac{r}{t}}\right)\left(0.5+\sqrt{\frac{0.02l_{\mathrm{a}}}{t}}\right)\left(2.4+\left(\frac{\theta}{90}\right)^{2}\right) \tag{2}$$

According to EN 1993-1-3 and EN 1993-1-5, moment resistance of profiled steel sheeting is determined from:

$$M_{\mathrm{c,Rd}}=W_{\mathrm{eff}}f_{\mathrm{yb}} \tag{3}$$

The web crippling resistance and moment resistance obtained from Equation (2) and (3) are presented in Table 1 for easy comparison with the test data. To evaluate the efficiency of the design codes, factor c is established to denote the ratio of test data to design data, as shown in Table 1. All the factors are larger than 1.0 indicating that the current design codes are generally conservative for re-entrant profiled steel sheeting.

t (mm)	F_{test} (kN)	M_{test} (kNm)	$R_{\mathrm{w,Rd}}$ (kN)	$M_{\mathrm{c,Rd}}$ (kNm)	$a=\frac{F_{\mathrm{test}}}{R_{\mathrm{w,Rd}}}$	$b=\frac{M_{\mathrm{test}}}{M_{\mathrm{c,Rd}}}$	$c=\frac{a+b}{1.25}$
	8.16	3.26	29.7	2.74	0.27	1.19	1.17
0.75	8.42	3.37	29.7	2.74	0.28	1.23	1.21
	8.38	3.35	29.7	2.74	0.28	1.22	1.20
	16.04	6.42	51.9	4.65	0.31	1.38	1.35
1.0	17.08	6.83	51.9	4.65	0.33	1.47	1.44
	17.60	7.04	51.9	4.65	0.34	1.51	1.48

Table 1: Comparison between test data and design code

3 FINITE ELEMENT ANALYSIS

Finite element analysis is carried out using software ABAQUS 6.10. Shell element S4R with six degrees of freedom at each node is adopted in the present study to model the profiled steel sheeting. The load bearing beam utilized in the test is modeled using 3-D solid element with 10 mm thickness. The measured material property from tensile coupon tests is used in the numerical analysis. Only a portion of the profiled steel sheeting corresponding to the half width of an interior repeating section was modelled due to symmetry in geometry and loading configurations. The boundary conditions are generally modelled in accordance with the tests conducted in the laboratory. As observed in the experimental test, major part of the flanges of the profiled steel sheeting lose contact with the loading beam because of local buckling of the trough, and the load is transferred through a narrow strip of the flange adjacent to the line of web-trough junctions. The interfaces between the loading beam and the profiled steel sheeting are modelled using surface-to-surface contact. The loading control used in numerical analysis is similar to that used in experimental test, where the load is applied by imposing vertical displacement to the loading beam.

The FE models are validated by the comparison against test results. Figure 5 illustrates the experimental and numerical load-displacement curves for test specimens. The ultimate strength of 0.75mm and 1.0 mm thick profiled steel sheeting obtained from FE analysis are 9.0 kN and 16.8 kN respectively. There is a 8% difference between FE and test results. In general, good agreement between the experimental and numerical results is observed, though for 1mm test specimens, the stiffness of numerical load-displacement curves deviated to some extent from the test results.

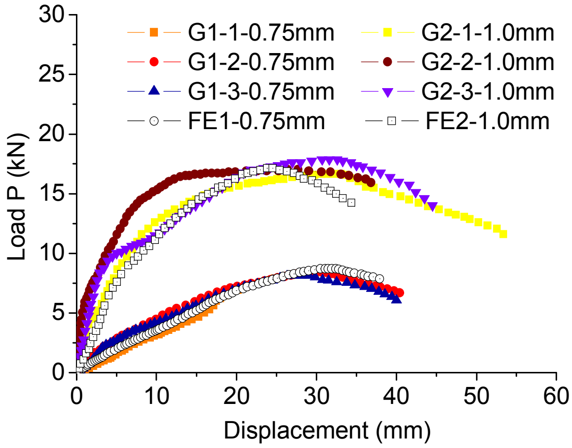

Figure 5 Experimental and numerical load-displacement curves

A parametric study aims to obtain behavior of profiled steel sheeting with different thickness t, load bearing length b_B and span L is conducted using the validated FE model. In the parametric study, the values of parameters are summarized as follows: thickness of profiled steel sheeting t = 0.75 mm or 1.0 mm; load bearing length b_B = 50mm, 100 mm, 150 mm or 200 mm; span L = 800 mm, 1200 mm, 1600 mm and 2000 mm. A total of 32 models are performed to build up a large database of indeterminate profiled steel sheeting and therefore to assess the design approaches. The material property obtained from tensile coupon tests as mentioned above is used to define the material property of profiled steel sheeting in this parametric study.

Based on the parametric study, the numerical results are shown in Table 2. In the numerical analysis, the failure load of all models is taken as the peak load of load-displacement curves. The results are also compared with the values determined from equation (1)-(3) in accordance with EN 1993-1-3. The results are illustrated in Figure 6 by several moment web crippling curves. It can be found that the numerical results are larger than the values determined form design codes, as the numerical values are higher than the interaction curve determined from the equation (1). Therefore, Eurocode 3 part 1-3 gives conservative values of high strength re-entrant profiled steel sheeting. The ratio of numerical results to design values c defined in Table 1 is used to calculate the accurate ratio values. The mean value of the 32 models is 1.35 indicating that the design equations are over-conservative by 35%.

t (mm)	L (mm)	b_B (mm)	F_{FE} (kN)	t (mm)	L (mm)	b_B (mm)	F_{FE} (kN)
0.75	800	50	13.7	1.0	800	50	26.0
		100	17.2			100	32.7
		150	20.1			150	36.1
		200	22.5			200	38.3
	1200	50	10.8		1200	50	20.2
		100	12.8			100	23.0
		150	13.6			150	23.5
		200	14.2			200	24.0
	1600	50	8.4		1600	50	16.3
		100	9.1			100	16.8
		150	9.7			150	17.3
		200	10.1			200	17.4
	2000	50	6.9		2000	50	13.2
		100	7.4			100	13.6
		150	7.7			150	13.9
		200	7.8			200	14.0

Table 2: Comparison between numerical analysis and design codes

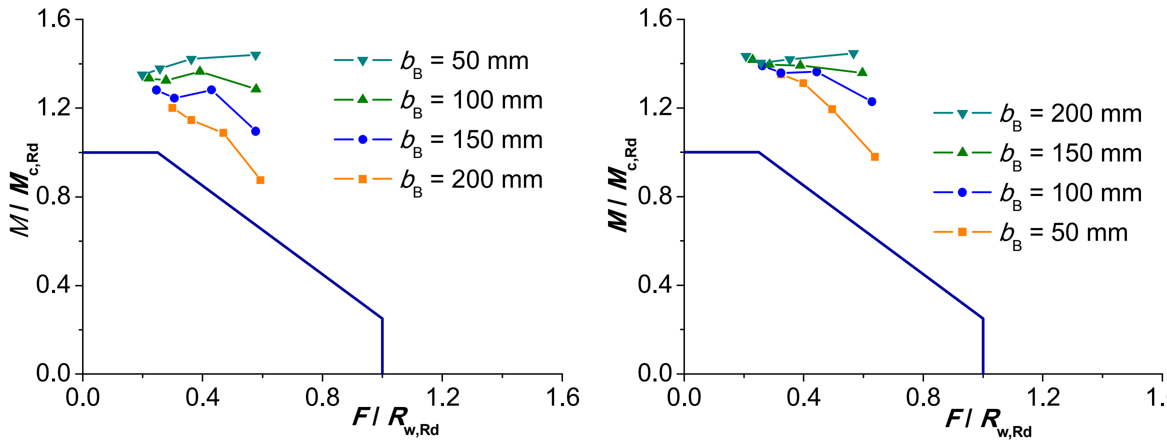

(a) 0.75 mm (b) 1.0 mm

Figure 6 Section failure resistances

4 CONCLUSIONS

This paper presents an experimental study of the behaviour of a low ductility high strength re-entrant profiled steel sheeting under combined bending moment and web crippling. Comparison between the Tested resistance and the design resistance obtained from Eurocode 3: Part 1.3 is also carried out. Based on the experimental study, finite element analysis is also carried out to predict the behaviour of profiled steel sheeting. Parameters investigated involve the thickness of profiled steel sheeting, the load bearing width and effective span. It is found that the failure of all the specimens is through simultaneous buckling of trough flanges and crippling of webs under the loading bearing width. The comparison of numerical results and design values indicates that the design equations are over-conservative by 35%. It is demonstrated that a set of new design rules specifically for re-entrant profiled steel sheeting is needed for both improved efficiency and reliability.

REFERENCES

[1] M.C.M. Bakker. *Theoretical and experimental research on web crippling of cold formed flexural steel members*. Thin-Walled Structures. 18 (1994) 261-290.

[2] British Standards Institution. *Eurocode 3: Design of steel structures. Part 1.3: General rules and supplementary rules for cold-formed steel structures*. BSI, London, 2006.

[3] Britishe Standards Institution. *BS 5950: Structural use of steelwork in building. Part 6: Codes of practice for design of light gauge profiled steel sheeting*. BSI, London,1995.

[4] American Iron and Steel Institute. *North American Specification for design of cold-formed steel structural members*. AISI, Washington, DC,2002.

[5] Australian Standard, AS/NZS 4600 Cold-formed steel structures, 2005

[6] H. Hofmeyer, J.G.M. Kerstens, H.H. Snijder and M.C.M. Bakker. *Combined web crippling and bending moment failure of first-generation trapezoidal steel sheeting*. Journal of Constructional Steel Research, 58 (2002) 1509-1529.

[7] A.M. Akhand, W.H. Wan Badaruzzaman and H.D. Wright. *Combined flexure and web crippling strength of a low-ductility high strength steel decking: expetiment and a finite element model*. Thin-Walled Structures, 42 (2004) 1067-1082.

[8] W.T. Tse, K.F. Chung. *Web crippling failure of cold-formed steel deckings*. Proceedings of international colloquium on stability and ductility of steel structures. 2006, pp721-728.

[9] W.T. Tse, K.F. Chung. *Section failure due to combined moment, shear and web crippling forces in cold-formed steel deckings*. Proceedings of international colloquium on stability and ductility of steel structures. 2006, pp729-734.

[10] W.T. Tse, K.F. Chung. *Web crippling behaviour of laterally restrained cold-formed steel re-entrant profiled deckings*. Journal of Constructional Steel Research, 64 (2008) 785-801.

[11] W.T. Tse. *Web crippling behaviour in cold-formed steel profiled deckings under lateral concentrated loads*. Master thesis, The Hong Kong Polytechnic University, 2007.

[12] British Standards Institution. *Eurocode 3: Design of steel structures. Part 1.5: Plated structural elements*. BSI, London, 2006.

12th International Conference on
Steel, Space and Composite Structures
28-30 May 2014, Prague, Czech Republic

FINITE ELEMENT ANALYSIS OF UP-DOWN STEEL CONNECTORS FOR VOLUMETRIC MODULAR CONSTRUCTION

C. Chen*, Y.Q. Cai and S.P. Chiew

School of Civil and Environmental Engineering
Nanyang Technological University, Singapore
e-mail: *cchen013@e.ntu.edu.sg

Keywords: Modular construction, Finite element method, Up-down steel connector, Bending strength, cruciform base, Failure mode.

Abstract: *Volumetric modular construction for buildings is gaining popularity in Singapore due to its inherent advantages over conventional construction such as flexible design, low construction time and cost, as well as reduction of dust pollution and labour on site. In the design for modular construction, the connector plays a crucial key role of transferring load and maintaining structural integrity. In this paper, a new type of up-down steel connector comprising I-beam, rectangular hollow section column and cruciform base is proposed. A series of finite element models with different types of connectors are established to study the compressive and bending behaviour of the new up-down connector. It was found that the connector transfers bending load efficiently and that the stiffness of cruciform base has considerable impact on bending strength of the connectors. The results also revealed that the failure of the up-down connector occurs at up column and end plate of cruciform base under compression load and failure takes place at interconnection of beam and cruciform base under bending moment. For LC and SLC, failure is more likely to occur under bending in weak axis, while in major axis for TC and STC. It should be noted that the use of reinforced plate in SLC and STC has a little effect on ultimate strength of the up-down connector.*

1 INTRODUCTION

Volumetric modular construction has been developed in Singapore, which is used to manufacture 3-dimensional modules for residential and other types of building. This modular system has been used for both new buildings and building extensions, such as adding new storeys to existing building. The pre-fabrication of the modules can vary widely. The logistics from the factory to the site allowing the modules can be a complete house. In most cases, the module is part of a house, such as one room of a hotel/ motel, one office room, one classroom for a school, one apartment room and one patient room for a hospital, which is manufactured in factory and then delivered to site to erect with minimal site work.

There are many advantages of using the volumetric modular construction: (1) all modules are constructed and integrated into the system in a factory, avoiding manual work at the site; (2) it can speed up installation at the site and cut down the construction time; (3) better quality of components can be provided through controlled work indoors; (4) reduces noise, dust pollution and labor intensive wet trades on site. Due to these advantages, volumetric modular construction has been used widely in recent years. Figure 1 illustrates several modular buildings such as site offices, Singapore cancer center and Singapore children cancer centre.

Figure 1 Application of modular construction

Connections play a crucial key role in the design of construction. In general, connection is defined as the physical component which mechanically fastens the structural elements. Structural joints can be classified into several categories by referring to its strength and stiffness according to EN 1993-1-8[1]. The connections for steel structures are divided into bolted connections and welded connections. From these two basic components, numerous joint profiles are developed. A review of commonly used steel connections is reported by Lee et al[2] who described the performance and application of these connections in cold-formed steel structures. In general, behavior of connection in steel structure is an important research topic over the past few decades and many researchers had performed a large number of experimental studies and numerical analysis to predict the behavior of connection in practical conditions. There is a wide range of research findings reported in the literature including the static behavior, seismic behavior, dynamic behavior of numerous connections[3-6]. However, the connections studied by researchers are often used in traditional building.

Nowadays, to enable inexpensive and fast construction of buildings, several types of connection which are facilitated to install prefabricated modules have been invented recent years[7-14]. In these international patents applications the inventors describe the steps of connecting adjacent units to one another in each level and connecting units in one level to corresponding units in at least one adjacent level that is vertically above or below the one level. For example, WO2010/031129 Unitized building system (UBS) provides a method of building a building having a plurality of levels using. In this method, top and down columns are welded to the top and down beams respectively. Top and down beams in a vertically adjacent level as well as beams in laterally adjacent building units are bolted together. This easy connection between one unit and adjacent unit speeds up the modular construction, which takes 50% less time than a conventionally constructed on site building. Although numerous modern connections have been proposed, behavior of modern connections used in modular construction is rarely studied[15-17]. Therefore, accurate prediction to the behavior of connections in modular construction is highly desirable.

In this paper, a new type of up-down steel connector comprising I-beam, rectangular hollow section column and cruciform base is proposed. A series of finite element models with different types of up-down connectors are established to study the compressive and bending behavior of the new up-down connector.

2 UP-DOWN STEEL CONNECTIONS

A new type of up-down steel connector comprising I-beam, rectangular hollow section column and cruciform base is proposed, as shown in Figure 2. The rectangular hollow section column and I-beams are welded to the cruciform base, and the bolts are used to connect the up and down beam-column connections. The reason for using this type connection includes: speeds up installation at the site and saves space (up and down I-beams can work together to resist loading, which could reduce the section size of I-beam).

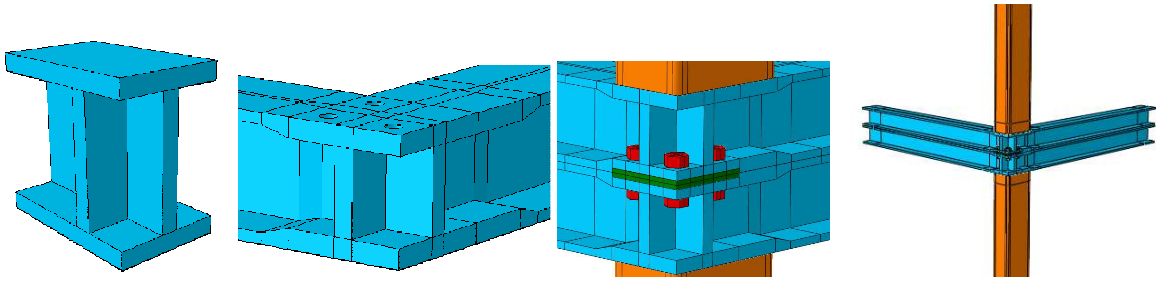

(a) cruciform base (b) down joint (b) up-down steel connection (c) overview of the connection

Figure 2 Up-down steel connection

3 FINITE ELEMENT ANALYSIS

To evaluate the compression and bending behavior of up-down steel connections, finite element analyses on 12 models are carried out using software ABAQUS. In the numerical analysis, there are total four types of connections: L-Connection (LC), Strengthen L-Connection (SLC), T-Connection (TC) and Strengthen T-Connection (STC), as shown in Figure 3. Connections LC and TC are simulated the external column and internal column respectively. Compared to connections LC and TC, two plates with thickness 10mm are added in SLC and STC to reinforce the up-down connection. For all the eight models, the rectangular hollow section column RHS 160x100x8mm and the I-beam 100x100x9x6 mm are adopted to comprise the connection. The thickness of all plates of cruciform base is equal to 16 mm. It should be noted that four models are established to simulate the compressive strength of the up-down connector, one model for each type of connection. While eight models are established to simulate the uniaxial bending behavior of up-down connector, two models for each type of connection in which one model is subjected to bending moment in major axis (strong axis) of the connector, namely LC-S, SLC-S, TC-S and STC-S respectively, and the other one for bending moment in minor axis (weak axis), namely LC-W, SLC-W, TC-W and STC-W.

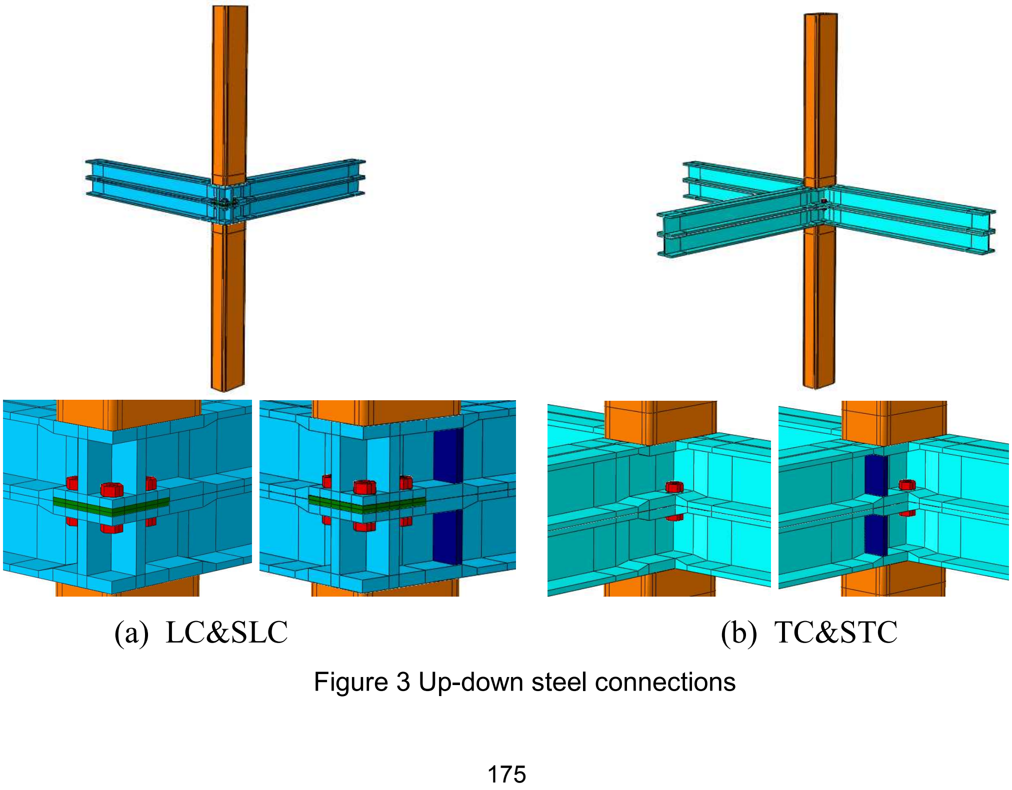

(a) LC&SLC (b) TC&STC

Figure 3 Up-down steel connections

In the finite element analysis, 3-D solid elements are used to model the entire up-down steel connector. The element type named C3D8I is chosen to generate the mesh. C3D8I is a linear brick element with 8 nodes in each element. This element type is used to define contact. In the definition of the contact, the bottom surface of the up joint and the up surface of the down joint are two contact surfaces. The bolts surface and the inner hole of the end plate in cruciform base are also contact surface. The column is connected to the endplate of cruciform by using “tie” command. For steel material, isotropic hardening property is used to define the nonlinear character of the material after yielding. The yield strength of beam, column, cruciform base and reinforced plate is 355 N/mm^2. The yield strength of bolts is 640 N/mm^2. The Young’s modulus and the Poisson’s ratio are 206x10^3 N/mm^2 and 0.3 respectively. The weld is not simulated in the finite element model because the weld has little effect on the static strength of the up-down steel connection although it has much influence on the fatigue life. In the numerical analysis, the column of up-down steel connector is first subjected to axial compression to obtain the ultimate compressive strength. And then half of the ultimate load is applied to the end of top column as a constant value and the vertical displacement is applied to the end of beam step by step to simulate the actual bending on connector.

4 RESULTS OF NUMERICAL ANALYSIS

4.1 Failure modes

Failure mode of up-down steel connector under compression is shown in Figure 4-5. It can be seen that the failure of connector under compression occurs at the up column and the endplate of cruciform base in all models. Both unstrengthen and strengthen connection have similar failure modes, which can also be proved by the load-displacement curves. Based on the analysis results, using thicker plates in cruciform base would be possible to improve the connector.

Typical failure mode of up-down connector under bending moment is illustrated in Figure 6-7. In all models, failure occurs at the interconnection of beam and cruciform base. For both LC and SLC connections, failure is more likely to occur under bending moment in weak axis. However, for TC and STC connections, failure is more likely to occur under bending moment in strong axis. This rule can also be found in moment-rotation curves illustrated in the following section.

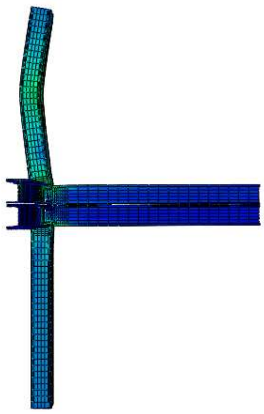

(a)

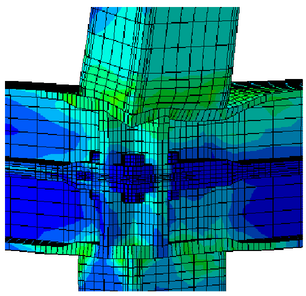

(b)

Figure 4 Failure mode of column for LC

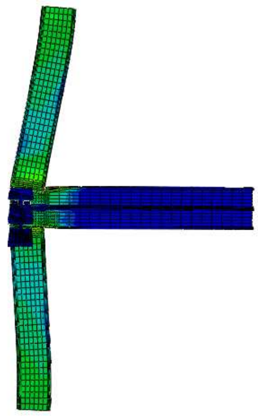

(a)

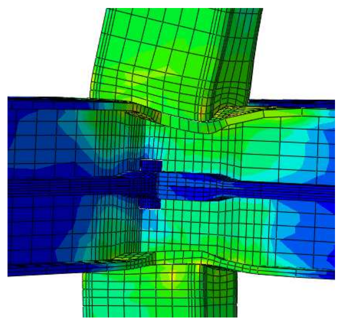

(b)

Figure 5 Failure mode of column for TC

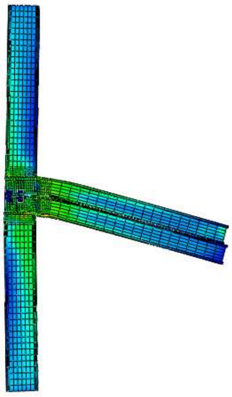

(a)

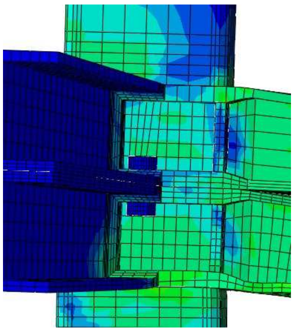

(b)

Figure 6 Failure mode of beam for LC

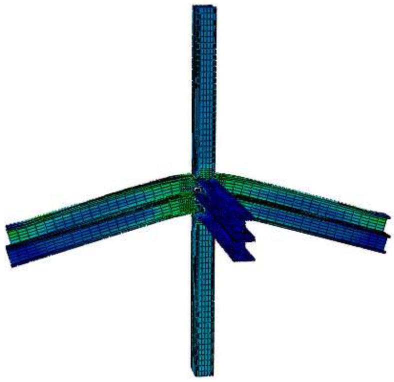

(a)

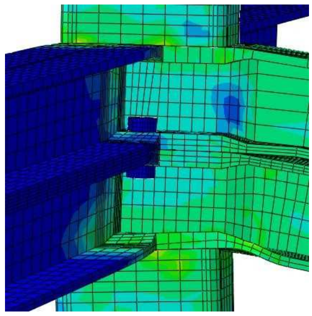

(b)

Figure 7 Failure mode of beam for TC

4.2 Ultimate strength

The load-displacement curves of up-down steel connection under compression load are shown in Figure 8(a)-(b). It can be seen from the Figure 8(a) that the ultimate capacity of LC connection and TC connection are 1200 kN and 1350 kN respectively. Compared to LC connection, the ultimate strength of TC connection increased 12.5%. Similarly, the ultimate capacity of strengthen connection SLC and STC are 1270 kN and 1350 kN respectively, as shown in Figure 8(b). The ultimate capacity of STC connection has a 6% increase compared with SLC connection. In general, the ultimate compressive strength of TC connection with or without reinforced steel plates are all larger than the values of corresponding LC connections. However, the ultimate capacity of strengthen connection SLC and STC is approximately equal to the ultimate strength of corresponding unstrengthen connection LC and TC. Therefore, the reinforced plate has little effect on the improvement of compressive strength of the up-down connections.

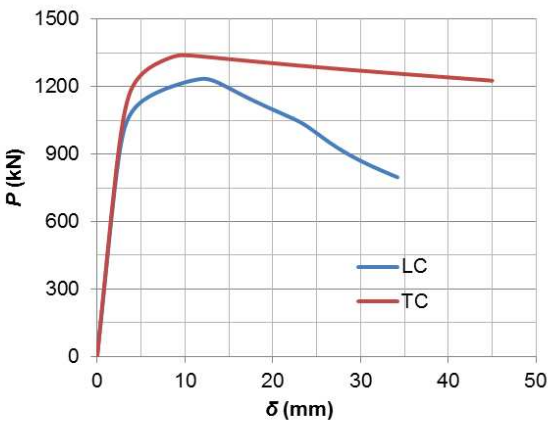

(a) Connection LC&TC

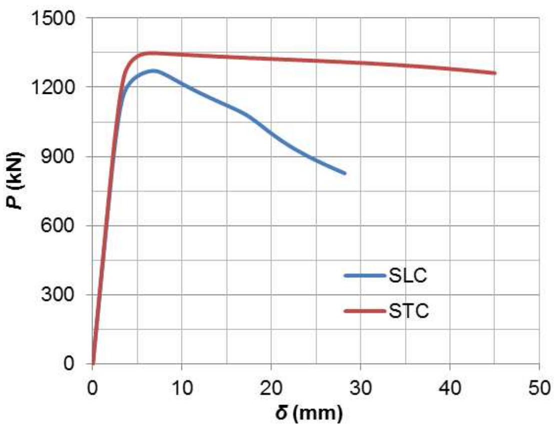

(b) Strengthen Connection SLC&STC

Figure 8 Load-displacement of up-down connctors

The Rotation-moment curves of up-down steel connection are shown in Figure 9-12. It can be seen from Figure 9 that the ultimate moment capacity of LC connection under bending moment in major axis (strong axis) and minor axis (weak axis) are 84 kNm and 50 kNm respectively. The ultimate strength under bending moment in major axis increased 68% compared to the value in minor axis. Similarly, the ultimate capacity of strengthen connection SLC under bending moment in major and minor axis are 84 kN and 65 kN respectively, as shown in Figure 10. The ultimate capacity of SLC-S has a 30% increase compared with SLC-W. For both connector TC and STC, the bending strength in minor axis is 95 kNm, which has a 12% increase compared to the bending strength in major axis 85 kNm. In general, for both strengthen and unstrengthen LC connections, the ultimate capacity under bending moment in major axis is larger than that in minor axis, while for TC and STC, the ultimate capacity in weak axis has a larger value compared to strong axis.

It should be noted that the ultimate capacity of strengthen connections SLC-S, STC-S and STC-W is approximately equal to the ultimate strength of unstrengthen connection LC-S, TC-S and TC-W correspondingly. The reinforced plate has little effect on the bending strength of the up-down connections in most case. Only for bending strength of SLC-W, the use of reinforced plate could increase the bending strength by 30% compared to LC-W.

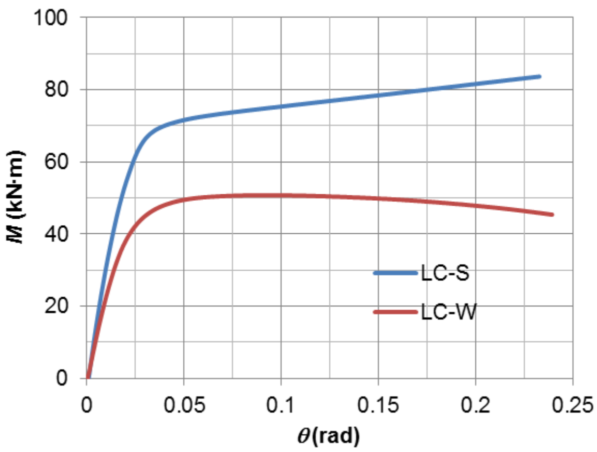

Figure 9 Rotation-moment curves of LC

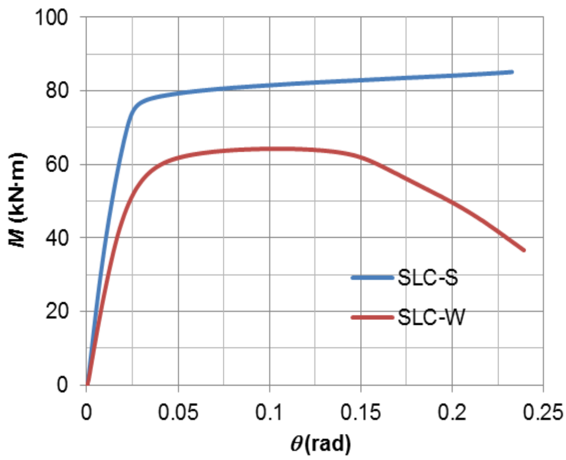

Figure 10 Rotation-moment curves of SLC

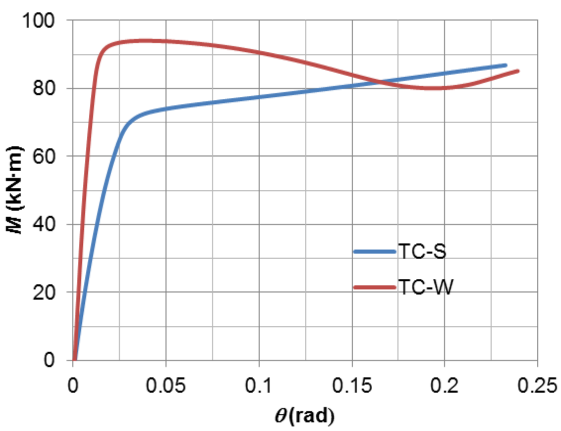

Figure 11 Rotation-moment curves of TC

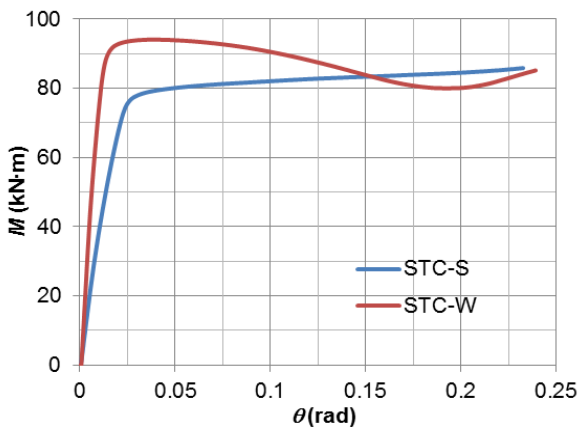

Figure12 Rotation-moment curves of STC

5 CONCLUSIONS

A new type of up-down steel connector comprising of rectangular hollow section column, I-beam and cruciform base is proposed. The ultimate strength of the up-down connector under compression and bending is studied by numerical analysis using software ABAQUS 6.10. Total 12 finite element models include four types of connectors, namely, L-Connector, T-Connector, Strengthen L-Connector and Strengthen T-Connector. Based on the numerical study, the following conclusions can be obtained.

(1) Typical failure of the up-down connector under compression takes place at up column and end plate of cruciform base for all the four type connections.
(2) The failure of the up-down connector under bending occurs at the interconnection of the I-beam and the cruciform base. For LC and SLC connectors, failure is more likely to occur under bending moment in minor axis, while, failure is easily to occur under bending moment major axis for TC and STC connectors.
(3) The ultimate capacity of T-Connector under compression is 1350 kN, which has a 12.5% increase compared to the ultimate strength of L-Connector 1200 kN. However, the reinforced plate used in SLC and STC has little effect on improving the compression strength of up-down connector.
(4) For both LC and SLC connectors, moment capacity in strong axis is larger than the value in weak axis, whereas moment capacity of TC and STC has a larger value in weak axis. Similar to compression, the use of reinforced plate increases the moment strength slightly.

REFERENCES

[1] British Standards Institution, Design of steel structures. Part 1-8: Design of Joints. BSI, London,2005.
[2] Y.H. Lee, C.S. Tan and S. Mohammad. Review on cold-formed steel connections, The Scientific World Journal, Vol 2014.
[3] F.R. Mashiri, X.L. Zhao and P. Grundy. Fatigue tests and design of welded T connections in thin cold-formed square hollow sections under in-plane bending. Journal of Structional Engineering. 128(11): 14133-1422, 2002.
[4] M.F. Wong, K.F. Chung. Structual behavior of bolted moment connections in cold-formed steel beam-column subframes. Journal of Constructional Steel Research, 58(2): 254-274,2002.
[5] R. Zaharia, D. Dubina. Stiffness of joints in bolts connected cold-formed steel trusses. Journal of constructional Steel Research. 62(3): 240-249, 2006.
[6] C. Bernuzzi, C.A. Castiglioni. Experimental analysis on the cyclic behavior of beam-to-column joints in steel storage pallet racks. Thin-Walled Structures, 39(10): 841-859, 2001.
[7] L. Don, V. Lissiak. Construction system for manufactured housing units. US 20020170243 A1. 2002.
[8] J. Quesada. Pre-fabricated building modules and method of installation. US 20050108957 A1. 2005.
[9] J. Ruano. Modular building systerm and method for level assembling of prefabricated building modules. US 2006019132 A1. 2006.
[10] A.C. Gines. Perfabricated reinforced-concrete single-family dwelling and method for erecting said dwelling. US 20090165399 A1. 2009.
[11] E. Katsalidis. Unitised building system. WO 2010031129 A1. 2010.
[12] A.E. Collins, M.L. Woerman. Premanufactured structures for constructing building. US 20110296769. 2011.
[13] B.L. Liberman. Modular building systerm for constructing multi-story buildings. US 20120110928 A1. 2012.
[14] R. P. Beattie. A multi- storey apartment building and method of constructing such building. WO 2012072971 A1. 2012.
[15] C.D. Annan, M.A. Youssef, M.H. El Naggar. Experimental evaluation of the seismic performance of mudular steel-braced frames. Engineering Structures. 31 (2009) 1435-1446.
[16] C.D. Annan, M.A. Youssef. M.H. El Naggar. Seismic overstrength in braced frames of modular steel buildings. Jounral of Earthquake Engineering. 13 (2009) 1-21.
[17] C.D. Annan, M.A. Youssef, M.H.El Naggar. Seismic vulnerability assessment of modular steel buildings. Journal of Earthquake Engineering. 13 (2009) 1065-1088.

EFFECT OF HUMAN-INDUCED VIBRATION ON THE DESIGN OF STEEL PEDESTRIAN BRIDGES

Ahmed S. El-Robaa*, Sherif M. Ibrahim†, Sameh M. Gaawan‡ and Charles I. Malek††

Dar Al-Handasah Consultants
14 Gezieret El-Arab – Mohandessin, Giza 12411
webpage: http://www.dargroup.com

Keywords: Vibration, pedestrian bridges, footfall analysis, Robot structural analysis.

Abstract. *The importance of vibration becomes a dominate criterion for design of footbridges. Modern design and construction techniques produce structures which are competitive in terms of overall cost. To achieve this goal, longer spans and lightweight bridges have been comprised in most of design trends. This leads to lower the natural frequencies of the system which have a great effect on the dynamic performance of bridges subjected to human activities. Although the design of steel footbridges could reach the optimum level of design in terms of strength criterion, it might not reach the acceptance level for vibration condition. This will enforce the designer to choose section profiles with higher inertia to enhance stiffness of the whole system. For such cases, it is required to examine the factors affecting the design of steel structures due to vibration concern. The main goal of this research study is to investigate the range of spans and deck's finish loads of footbridges which are governed by human comfort requirements due to vertical forces induced by pedestrians. The footfall method presented by concrete center "CCIP-016" is adopted in this study to evaluate the response factor and acceleration of pedestrian bridges using a FEA software package "Robot Structural Analysis".*

1 INTRODUCTION

The goal of the current design trends is to reach the most efficient and low cost structural design. This is achieved by utilizing high strength materials which lead to long spans - lightweight structures. By this approach, the vibration problem due to human walking forces is raised and human comfort needs to be considered as serviceability limit. For many decades, the design approach for serviceability was limited to checking deflection values due to live load against specified code value or limiting the span-to-depth ratio. However, current design practice reveals that such approach could not ensure acceptable levels for human comfort for all cases. The design guidelines for vibration serviceability of footbridges in the vertical direction depend on estimation of vibration response to single person walking at a pacing frequency that matches the

* Senior Structural Steel Engineer, Dar Al-Handasah Consultants, Cairo- Egypt
† Associate Professor of structural Engineering, Ain Shams University, Cairo-Egypt / Associate, Structures Department, Dar Al-Handasah Consultants, Cairo –Egypt
‡ Associate Professor of structural Engineering, Helwan University, Cairo-Egypt / Principal, Structures Department, Dar Al-Handasah Consultants, Cairo –Egypt
†† Director, Structures and Bridges Departments, Dar Al-Handasah Consultants, Cairo – Egypt

natural frequency of the relevant vibration mode. Footbridges which exhibit vibration serviceability problems are mostly low-frequency flexible structures. Many measurements were conducted to quantify vertical loads executed by walkers on structures. The continuous vertical force produced by a walking person is indicated in Figure 1 based on measured time history.

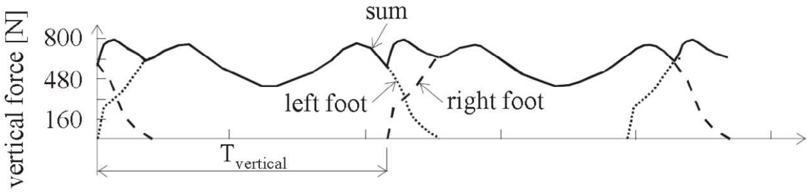

Figure 1 : Time history for vertical human induced force due to walking[1]

As one foot is always in contact with the bridge deck, the loading does not disappear completely at any time. During the transition period of the motion sequence, the body weight is shifted from one foot to the other and the two load curves for each foot overlap. According to [2], the human perception of vibrations is subjective and depends on individual characteristics and psychological influences. The perception is influenced by the physical factors, vibration frequency, acceleration and the time period of exposure. The discomfort depends much on the environmental conditions and the attitude towards the vibration cause. One of the powerful design guides to assess vibration problem due to human induced forces is the one published by “The Concrete Center” - CCIP-016[3].This design guide illustrates a rigorous analysis method for calculating structural response due to single walking person which is called footfall analysis method. In this analysis two different responses are calculated due to vertical human force; the resonant and the impulsive vibration responses. These types of response are associated with low or high frequency floors. Structures with fundamental vertical natural frequencies less than 4.2 times the fastest walking frequency will be designed for resonant response.

In this analysis a response factor (R) is calculated. This factor is a multiplier of the base line curve for RMS acceleration (vertical direction) as per BS 6472-1992[4]. This curve corresponds to the level of the average threshold of human perception in continuous vibration. A response factor of 1 represents the magnitude of vibration that is just perceptible by a typical human. The performance criteria given in [3] are applicable for bridges of all spans and natural frequencies. These criteria are given for indoor and outdoor bridges as follows[3]:

a) For external bridges: R < 64.
b) For indoor bridges: R < 32.
c) For indoor bridges that are exposed, high in an atrium or heavily trafficked R ~< 24.

This method is used in this study which emphasizes on the effect of floor vibration on optimized steel bridges.

2 ANALYSIS AND PARAMETERS:

This paper focuses on the study of the vertical vibration due to human induced forces on footbridges whose sections are optimized for both strength and deflection limit states.

The study is investigating the behavior of a footbridge composed of two simply supported composite steel beams. A reinforced concrete (R.C.) composite slab cast on metal decking is forming the bridge deck and supported on the two main beams. The total depth of the R.C. slab with the corrugation of the metal decking is 160 mm as shown in Figure 2. The bridge width is selected as 3.0 m which is common value for typical footbridges. This footbridge is analyzed for spans ranging from 10 m to 50 m.

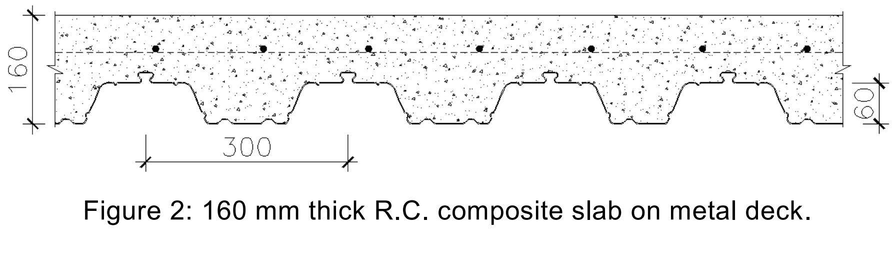

Figure 2: 160 mm thick R.C. composite slab on metal deck.

The analysis models are chosen with different finish and installtion loadings. The total finshes and installtions loads are considerd as 100 Kg/m^2 for low-finished brdiges, 300 Kg/m^2 for average-finish types and 800 Kg/m^2 for heavy-finish which is suited for footbridges in special locations such the Holy Haram at Makkah. The live load is considered as 90 psf as per AASHTO LRFD guide specifications for the design of pedestrian bridges[5]. High strength steel with yield strength of 345 MPa is assumed in the design of the composite main girder. The concrete strength is considered as 30 MPa. These values of steel and concrete strength represent the common values in the construction industry. The span-to-steel beam depth ratio is selected to be about 30.

Thus a total of fifteen footbridges were designed based on strength and deflection limit states. The optimized cross sections are obtained based design requirements of AISC 360-10[6] for design of composite beams. The level of steel main beam strength optimization can be expressed in terms of the ratio applied external bending moment to the cross section bending strength. This ratio is referred hereafter as strength unity check. The Deflection due to live load is compared to a value of (span/360) ratios. Deflection unity check is expressed as the ratio between the live load deflection to the value of (span/360). The required steel cross section for most of the studied cases was controlled by the strength limit state. For the few cases which controlled by deflection limit state, the strength optimized steel cross section was increased.

These strength or deflection optimized steel cross sections were checked for human comfort by footfall analysis afterwards. To compute the overall response factor of a structure, the following points illustrate the required steps in accordance with CCIP-016[3]:

a) First, a range of walking frequencies is chosen (typically 1 to 2.8 Hz) to generate various number of step frequencies. Then, the forcing function is calculated for a selected step frequency in that chosen range.
b) Secondly, this forcing function is applied at chosen nodes in the structure, and the response at these nodes and at all the other nodes is then calculated. This is carried out for each of the four harmonic components of the forcing function with their corresponding harmonic frequencies.
c) Thirdly, based on the obtained accelerations, a total response factor is calculated from combination of each of the four harmonic responses for the selected step frequency.
d) Finally, these steps are repeated until the whole range of frequencies is covered, and the maximum response factor R is the value that sets the acceptance of a structure.

Robot Structural Analysis software[7] is used for footfall analysis. The concrete slab is simulated with 100 mm shell element, which is the solid part above the steel profile deck, and with an offset to account for the composite action as shown in Figure 3. The dynamic modulus of elasticity for concrete is chosen as 38 KN/mm^2. The R.C. slab is simulated as 4-noded quadrilateral finite element with mesh size of 0.5 m by 0.5 m.

The walker weight is assumed as 76 kg and the damping ratio considered in the analysis is 1% for composite footbridges.

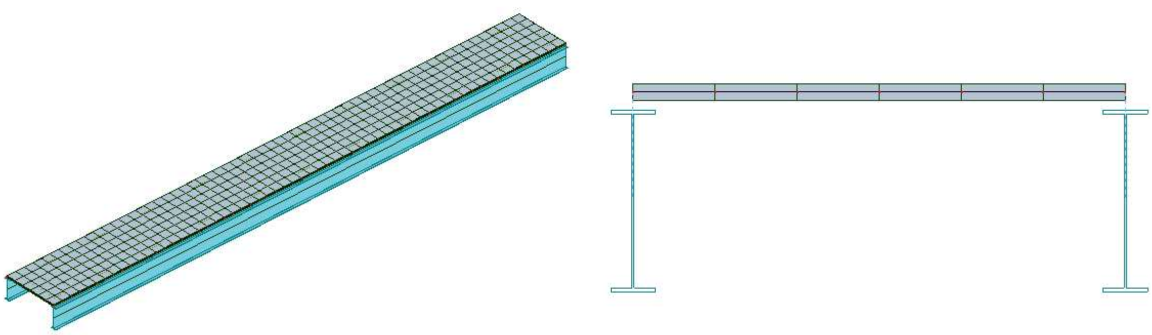

(a) (b)

Figure 3 : (a) 3D FE analysis model. (b) Cross section of the bridge with offset in slab.

3 RESULTS DISCUSSION:

The optimized steel cross sections of the fifteen footbridges along with the strength and deflection unity checks and the overall response factors are shown in Table 1. For heavy-finish bridges the optimized steel cross sections were controlled by the strength limit state as the strength unity check is always greater than the deflection unity check. Only for the 50 m span with light and average finish, the optimized steel cross sections were controlled by deflection limit state. The overall response factor (R) for all the optimized fifteen bridges resulted from all types of finishes are higher than human comfort level for heavily trafficked indoor bridges (R<24). If the studied footbridges are considered as external bridges (R<64), only the case of heavy-finish can be considered satisfying or close to satisfy (for R slightly higher than 64) the human comfort level as shown in Table 1. The overall response factor (R) for the other two finishes (low and average) is not satisfying the human comfort level for external bridges except two cases. A sample for the contour distribution of the response as obtained from FE model is shown in Figure 4 for finish weight of 100 kg/m^2 and 30 m span. It is evident from that figure that the maximum vibration response will be noticed at the mid-span of the footbridge. The fundamental vertical natural frequency for all footbridges is also listed on Table 1. Some international standards such as AASHTO[5] recommend that the fundamental frequency shall not be less than 3 Hz to achieve human comfort. One of the obvious remarks from the natural frequency results that although the frequency is larger than 3Hz for some cases (the 10 m spans), the human comfort is still not achieved. The reason of this is that the method of footfall analysis method used in CCIP-016[3] takes into account the first four harmonics of the human forcing function. As for the case of higher harmonics, the frequency of the walker is coincident with the natural frequency of the footbridge, which could lead to higher response factor.

As discussed above, most of the optimized steel main beams have not satisfied the human comfort acceptance level either for internal or external footbridges. Accordingly, the cross section sizes were increased in order to satisfy the human comfort level for indoor/external bridges. Such increase in cross section size has an impact on the total self-weight of the bridge. Another round of analysis for footfall analysis has been performed to achieve two target levels, one to satisfy response factor less than 24 and another one for response factor of 64. The target of this is achieved by increasing the cross section properties more than the optimized ones. The ratio of new cross section weight to the optimized cross section weight is used to quantify the required increase in the cross section to satisfy the human comfort level and is referenced hereunder as “weight increase ratio”.

Figure 5 illustrates the weight increase ratio for different type of finishes in order to achieve a comfort level of R<24. It is observed from this figure that footbridges with heavy finishes (800 kg/m^2) shall requires lesser increase in beam weight to achieve the comfort level compared to light and average finishes. The maximum required increase is observed in light weight finish (100 kg/m^2) and shorter spans. Since the comfort criteria of R<24 is very stringent one, the weight increase ration reach 8 to 10 times the original weight. On the other hand, it reaches 2 times the original weight for large spans up to 50 m.

Figure 6 illustrates the weight increase ratio for different type of finishes in order to achieve a comfort level of R<64. For this case, the required weight increase ratio is much smaller than those required for indoor bridges. It is also observed that for footbridges with heavy finish (800 kg/m^2) the weight increase ratio is minimal for all spans ranging from 10m to 50m. The maximum weight increase ration is observed for short span with light or average finish and it reaches a value of 1.75 to 1.8 ratios for 10 m span. However, for longer spans (20 to 50 m), such increase is very minimal and its value is lesser than 1.17.

The fundamental natural frequency is recalculated for the increased steel main beam for the case of R<24 and R<64 as shown in Table 2. It worth noting that although the natural frequency of some footbridges shown on Table 2 is lesser than 3 Hz, the human comfort is satisfied. Thus, it can also be concluded that it is not practical to impose certain single value limit on fundamental natural frequency to achieve human comfort. Generally, if a limit on the natural frequency is to be thought, such limit must be related mainly to the span of the footbridge. The limit on natural frequency shall be set higher for shorter spans and decrease with the increase of the footbridge span. A wider range of spans, loading, widths of footbridge need to be further investigated to reach a generalized limit of the fundamental natural frequency of footbridges.

Finish weight = 100 Kg/m^2							
Span (m)	Optimized section	Frequency of first mode (Hz)	Strength unity check	Live load deflection unity check	Overall response factor (R)	External bridge R<64	Heavily trafficked indoor bridge R<24
10	330x75x 8x5	4.43	0.97	0.84	132.91	No comfort	No comfort
20	670x120x 12x8	2.95	0.91	0.99	92.12	No comfort	No comfort
30	980x100x 20x15	2.45	0.99	0.79	102.32	No comfort	No comfort
40	1300x280x 15x15	2.11	0.99	0.81	55.24	Comfort	No comfort
50	1650x210x 25x18	1.87	0.84	1	92.36	No comfort	No comfort
Finish weight = 300 Kg/m^2							
Span (m)	Optimized section	Frequency of first mode (Hz)	Strength unity check	Live load deflection unity check	Overall response factor (R)	External bridge R<64	Heavily trafficked indoor bridge R<24
10	330x100x 8x5	3.91	0.99	0.74	122.17	No comfort	No comfort
20	650x155x 15x8	2.65	0.99	0.91	123.27	No comfort	No comfort
30	1000x160x 15x12	2.08	0.99	0.98	56.74	Comfort	No comfort
40	1330x240x 15x15	1.82	0.98	0.99	118.18	No comfort	No comfort
50	1650x260x 20x18	1.63	0.99	1	73.84	No comfort	No comfort
Finish weight = 800 Kg/m^2							
Span (m)	Optimized section	Frequency of first mode (Hz)	Strength unity check	Live load deflection unity check	Overall response factor (R)	External bridge R<64	Heavily trafficked indoor bridge R<24
10	330x110x 15x5	3.51	0.99	0.51	63.1	Comfort	No comfort
20	620x260x 25x8	2.57	1	0.54	69.93	No comfort	No comfort
30	1000x320x 22x12	1.99	0.99	0.63	29.87	Comfort	No comfort
40	1300x335x 32x15	1.7	0.99	0.68	68.38	No comfort	No comfort
50	1650x340x 40x18	1.53	1	0.68	42.19	Comfort	No comfort

Table 1: Data results obtained for optimized cross-sections with different finish weights.

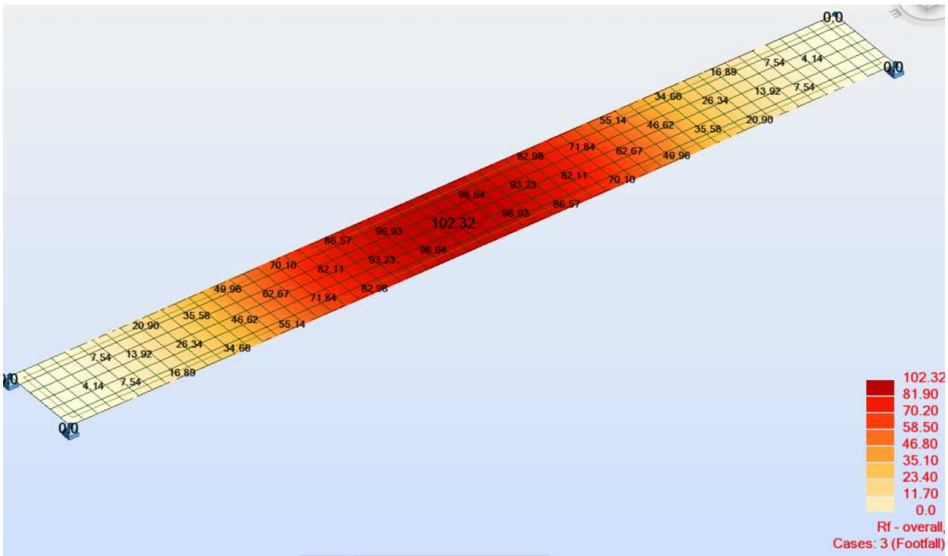

Figure 4 : Overall response factor resulted for 30 m span footbridge with finish weight of 100 kg/m^2.

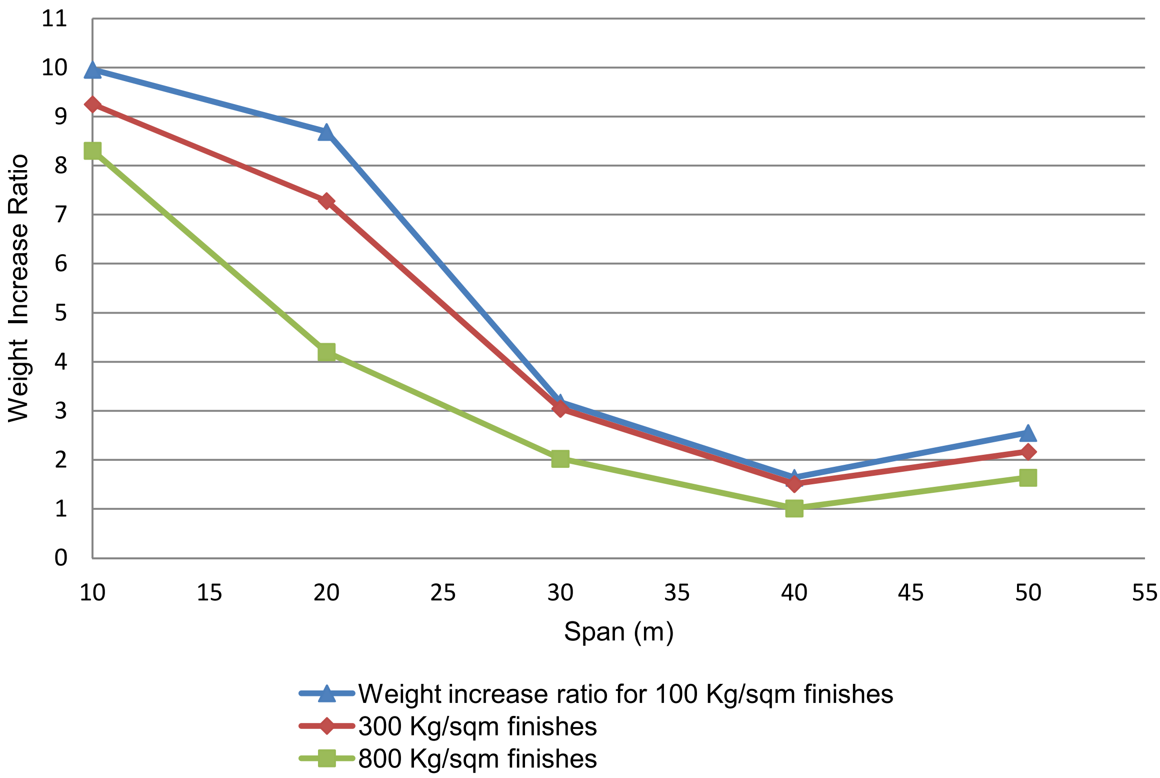

Figure 5 : The weight increase ratio to satisfy an overall response factor of R<24 for heavily trafficked indoor bridges.

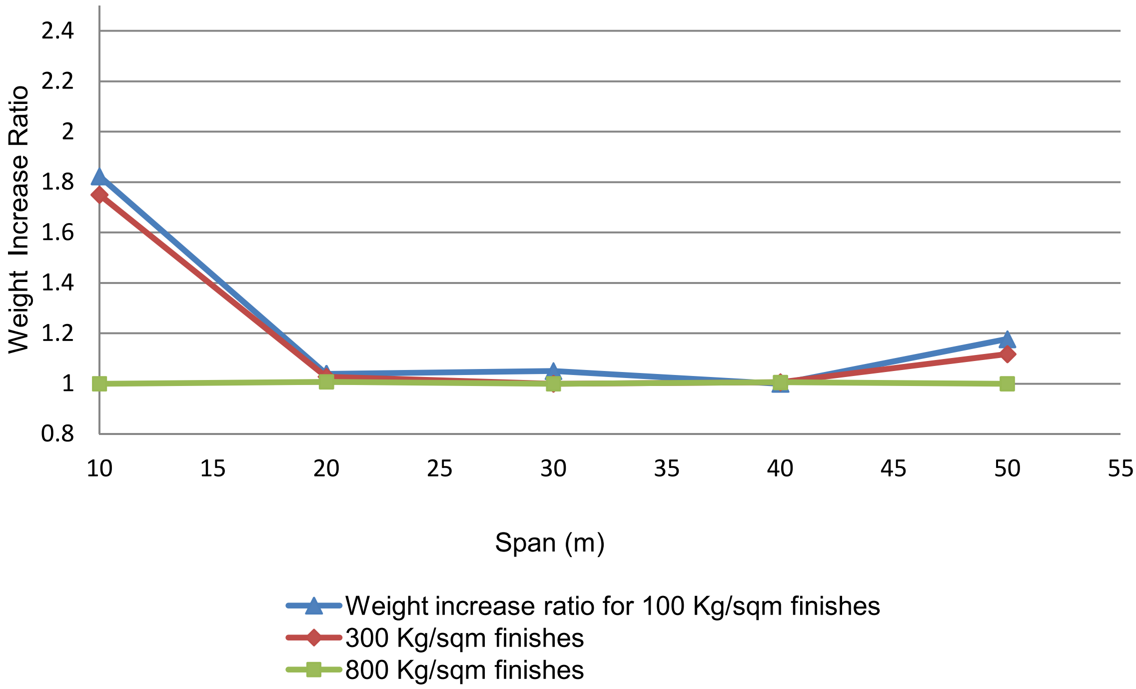

Figure 6: The weight increase ratio to satisfy an overall response factor of R<24 for external bridges.

Frequency (Hz) if R<24 is reached					
Finish weight (Kg/m^2)	Span (m)				
	10	20	30	40	50
100	11.44	6.85	4.3	2.87	2.83
300	11.35	6.02	3.62	2.86	2.84
800	8.82	4.93	2.93	1.9	2.05
Frequency (Hz) if R<64 is reached					
Finish weight (Kg/m^2)	Span (m)				
	10	20	30	40	50
100	6.06	3.23	2.84	2.11	2.14
300	6.1	2.95	2.08	1.88	2.05
800	3.51	2.83	1.99	1.85	1.53

Table 2: Frequency results to reach the required limits for indoor and external bridge.

4 CONCLUSION:

The present study presented the effect of satisfying human comfort level on the optimized composite steel footbridges. The following can be concluded from the current research:

1- The effect of applied finish weights on human comfort has a big influence on the design of footbridges. If the weight of finish is relatively heavy (800 Kg/m^2), the required design alterations to satisfy vibration limit is smaller than those required for lighter weight (100 Kg/m^2). In addition to that, heavily trafficked indoor bridges need more design refinements than those required for external bridges to overcome vibration problem.
2- The human comfort level of R< 24 is very stringent and substantial increase in the cross section dimensions shall be required. It is easier and much less costly to achieve human comfort level of R<64.

3- It is concluded that despite of remarkable decrease in natural frequency in some longer spans (mainly 40 to 50 m) of the footbridge than 3Hz; the human comfort is achieved according to recommended limits of CCIP-016[3] for both indoor and outdoor footbridges. On the other hand for some footbridges for which fundamental natural frequency is higher than 3 Hz, human comfort is not achieved.
4- Any limit on fundamental natural frequency must be inversely proportional with the bridge span. The longer the span the lower required limit on natural frequency.
5- It is important to emphasize that the vibration problem should not be controlled by 3 Hz criterion as recommended by AISC design guide no. 11[8] or AASHTO LRFD guide for pedestrian bridge[5]. Instead, dynamic footfall analysis shall be performed to take into account the full range of walking frequencies and the first four harmonics of the walker's forcing function. The latter will lead to more accurate assessment of vibration problem due to human induced forces.

REFERENCES

[1] S. Živanović, A. Pavić and P. Reynolds, *Vibration serviceability of footbridges under human-induced excitation: a literature review*, Journal of Sound and Vibration, Vol. 279, No. 1-2, pp. 1-74, Elsevier, Maryland Heights (2005) .
[2] M. Schlaich and J. Francois, *Guidelines for the design of footbridges* , Féderation Internationale du Béton (International Federation for Structural Concrete), FIB Bulletin 32 ,Switzerland (2005).
[3] M. Willford and P.Young, *A design guide for footfall induced vibration of structures (CCIP-016)*, The Concrete Centre, Blackwater, Camberley (2006).
[4] British Standard Insitutiton, *Guide to evaluation of human exposure to vibration in buildings (1 Hz to 80 Hz)*, BS 6472, London (1992).
[5] AASHTO, *LRFD guide specifications for design of pedestrian bridges, American Association of State* Highway and Transportation Officials,Washington DC (2009).
[6] AISC, *Specification for structural steel* buildings, AISC 360-10, American Institute of Steel Construction, Chicago, (2010).
[7] Autodesk, *Autodesk Robot Structural Analysis Proffesional*, San Rafael, USA, Version (2012).
[8] T.Murray, D. Allen and E. Ungar, *Floor vibration due to human activity*, Steel design guide series no. 11, American Institute of Steel Construction, Chicago, (2003).

12th International Conference on
Steel, Space and Composite Structures
28-30 May 2014, Prague, CzechRepublic

HUMAN COMFORT ACCEPTANCE CRITERIA OF PEDESTRIAN BRIDGES

Ahmed S. El-Robaa*, Sherif M. Ibrahim†, Sameh M. Gaawan‡ and Charles I. Malek††

Dar Al-Handasah Consultants
14 Gezieret El-Arab – Mohandessin, Giza 12411
webpage: http://www.dargroup.com

Keywords: Vibration, pedestrian bridges, human comfort.

Abstract. *The assessment of vertical vibrations due to human induced force becomes an inevitable procedure in the design process of footbridges. In past decades the deflection due to live load is limited by span to length ratio and the depth to span length ratio, however such approach had not lead to bridges with acceptable level of vibrations. Nowadays many codes of practices describe the human discomfort in terms of the perceived acceleration of the footbridge or by avoiding specific limit of natural frequency. Many standards apply the concept of baseline curves and its multipliers for specifying floor vibration criteria. The human perception of vibrations is subjective and depends on individual characteristics, psychological influences, and the attitude of people towards the vibration cause. Several standards require a calculation of the dynamic response of a footbridge due to a footfall force; others provide simplified procedures to predict accelerations. The purpose of this study is to investigate the variety of vibration limits and acceptance criteria as stated in international standards and design guides. A comparison study between different methods prescribed in international codes is presented for different pedestrian bridges configurations.*

1 INTRODUCTION

As a result of utilizing high strength materials and attaining lightweight structures to save project's overall cost, structures become more susceptible to vibration due to human activity. Currently, the most significant serviceability limit that should be considered in the design stage is the vibration due to human induced forces. If the pace frequency of a walking pedestrian is the same as the natural frequency of the structure, resonance problem is occurs. This will not only happen with the fundamental frequency of the structure but also for higher natural frequencies. This is attributed to the fact that higher harmonics of walker's footstep frequency might coincide with the natural frequency of the system. For such case, the vibration becomes perceptible and it will reduce the comfort level of the walkers. This discomfort depends on many factors that are related to the receiver of such vibrations or the location of the structure. From these factors, the walking speed of the pedestrian, type of pedestrian traffic, the environmental conditions around

* Senior Structural Steel Engineer, Dar Al-Handasah Consultants, Cairo- Egypt
† Associate Professor of structural Engineering, Ain Shams University, Cairo-Egypt / Associate, Structures Department, Dar Al-Handasah Consultants, Cairo –Egypt
‡ Associate Professor of structural Engineering, Helwan University, Cairo-Egypt / Principal, Structures Department, Dar Al-Handasah Consultants, Cairo –Egypt
†† Director, Structures and Bridges Departments, Dar Al-Handasah Consultants, Cairo – Egypt

the structure (whether it is located in rural or urban areas), some physical aspects (like age, health, mood, etc…), the prediction of the walker to the vibration, duration of vibration and the frequency of the vibration. Moreover, the reaction of different people to the same vibration conditions might also be different.

At design stage, the human comfort level should be considered and preliminary dynamic model should be established to assess the vibration issue. However, the damping ratio for footbridges at design stage is one of the uncertainties in the vibration problem as the damping ratio will only be identified when they are built[1].

Earlier, the only serviceability limit stated in international standards was the one related to limit the live load deflection against a ratio of the span. At present, international codes and design guides provide some regulations for vibration assessment due to human induced forces. There are two approaches which are provided in those codes & design guides[2]. The first approach is based on avoiding natural frequencies of footbridges to match the walking frequencies for the pedestrians[2]. The second approach depends on calculating the dynamic response in terms of acceleration of footbridge and to check if they are within acceptable limits or not[2]. Illustration of various international standards and design guides are given in the following section to show how these concepts are implemented.

2 INTERNATIONAL STANDARDS AND GUIDELINES

There are many different methods and comfort limits which are provided in international codes or design guidelines, the following represents a literature review study to reveal such approaches.

2.1 BS 5400-2:2006[3]

The vibration serviceability requirements for footbridges are stated in annex B of that standard. In order to satisfy it, the fundamental natural frequency f_o of a pedestrian bridge should exceeds 5 Hz for the unloaded bridge in the vertical direction. However, if the fundamental frequency of the footbridge f_o is equal to, or less than 5 Hz, the maximum vertical acceleration is limited to 0.5 $\sqrt{f_o}$ m/s^2. A simplified method to calculate the maximum acceleration given in this standards but it is limited to bridges with up to three continuous spans.

Calculations for maximum vertical acceleration are based on simplified method presented in Annex B of that standard.

$$a = 4\pi^2 f_0^2\, y_s\, k\, \psi \tag{1}$$

Where: f_0 is the fundamental natural frequency (Hz). y_s is the static deflection taken due to vertical concentrated load of 0.7 KN applied at mid-point of the span (m). k is the configuration factor, taken as 1.0 for simple span. ψ : is the dynamic response factor depends on span length and damping ratio.

2.2 BS EN 1990:2002+A1:2005[4]

The comfort criterion is defined in terms of maximum acceptable acceleration of any part of the deck as specified in Annex A of that standard. The recommended maximum value is considered as 0,7 m/s^2 for vertical vibrations. It is not confirmed in this standard, if this value is related to any type of pedestrian traffic or it is related only to single person walking on the bridge. It is recommended also that a verification of the comfort criteria should be performed if the fundamental frequency of the deck is less than 5 Hz for vertical vibrations. However, no guidelines are included for such methodology of verifications. However, the comfort criteria are suggested to be satisfied with a significant margin, otherwise it may be necessary to make provision in the design for the possible installation of dampers in the structure after its completion. In such cases the designer should consider and identify any requirements for contracting tests.

2.3 UK national annex for BS EN 1991-2:2003[5]

In this national annex, the maximum vertical acceleration is essentially required to be not less than the design acceleration limit given by:

$$a_{limit} = 1.0\, k_1\, k_2\, k_3\, k_4 \text{ m/s}^2 \text{ and } 0.5 \text{ m/s}^2 \le a_{limit} \le 2{,}0 \text{ m/s}^2 \tag{2}$$

Where: k_1 *is* site usage factor which is ranged from 1.6 to 0.6 depends on the location of the bridge if it is in rural areas or in primary route for hospitals or high sensitivity routes. k_2 is route redundancy factor, this factor is ranged from 1.3 to 0.7, it depends on if there any possibility of other routes that pedestrians could use it for crossing the same location (k_2 = 1.3) or if it is the only way for crossing (k_2 = 0.7). k_3 is height of structure factor which is ranged from 1.1 to 0.7. If the structure height is less than 4m, it reaches 1.1. If the height is greater than 8 m , its value is 0.7. k_4 is an exposure factor which is to be taken as 1.0 unless otherwise determined specifically to the project. It may be assigned as a value between 0.8 and 1.2 to reflect other conditions that may affect the users' perception towards vibration. These may include consideration of parapet design, quality of the walking surface (such as solidity or opacity) and provision of other comfort-enhancing features. These values of k_1, k_2, k_3 and k_4 are considered as response modifiers. The graph shown in Figure 1 explains some of these modifiers.

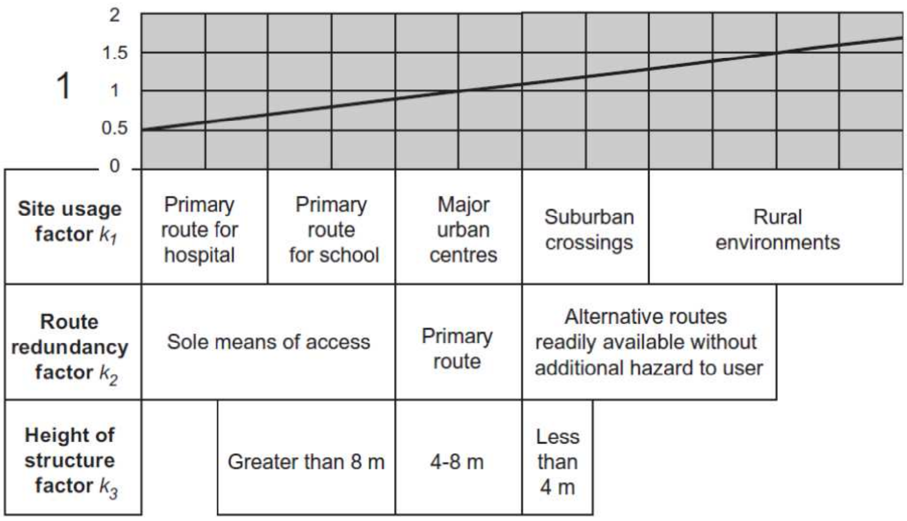

Figure 1: Response modifier factors as given in UK national annex for BS EN 1991-2:2003, where "1" denotes to response modifiers k_i.

2.4 ISO 10137:2007[6]

This standard gives some guidelines for the level of vibrations in the vertical direction (z-axis) for walkways over roads or waterways, it is recommended to not exceed a multiplying factor of 60 to the R.M.S. base curve as shown in Figure 2. However, for the case where one or more persons standing still on the walkway, such as one person walking across the walkway and another-the receiver- standing at mid-span, a multiplying factor of 30 is suggested to be accounted for.

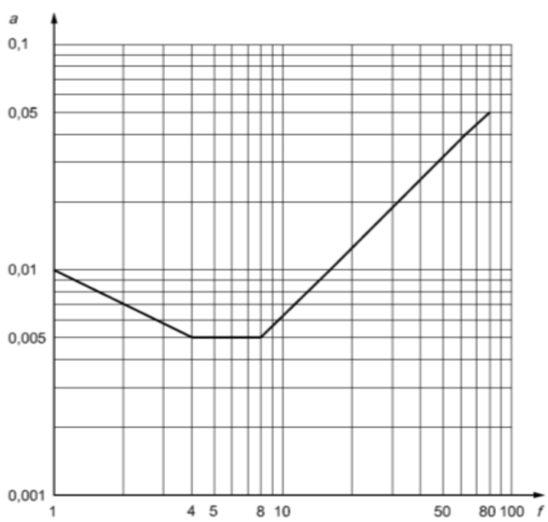

Figure 2: Z-axis's vibration base curve (vertical direction) for r.m.s. acceleration.

2.5 AASHTO LRFD guide specifications for the design of pedestrian bridges (Dec. 2009)[7]

The fundamental frequency in a vertical mode of pedestrian bridge without live load is considered to be greater than 3 Hz to avoid resonance due to first harmonic. However, it was mentioned in this guide that if the fundamental frequency cannot satisfy this limitation or if the second harmonic is of a concern, an evaluation of the dynamic performance shall be made. Nevertheless, such dynamic analysis or calculations is not clarified in that guide. In lieu of that evaluation in the vertical direction, the bridge is recommended to be proportioned so that either of the following criteria is satisfied:

$$f \geq 2.86 \ln(180/W) \text{ or } W \geq 180\, e^{(-0.35 f)} \tag{3}$$

Where: W is the weight of the supported structure, including only dead load (kips). f is the fundamental frequency in the vertical direction (Hz).

2.6 AISC steel design guide no. 11 "Floor vibration due to human activity" (Oct. 2003)[8]

In this design guide, recommended value for acceleration limit of indoor footbridges is equal to "1.5 % g" or 0.15 m/sec^2. However, for outdoor footbridges, the recommended value for acceleration limit is equal to "5 % g" or 0.5 m/sec^2. These criteria should be compared with the peak acceleration "a_p" which is calculated as follows:

$$(a_P/g) = P_o\, e^{(-0.35 f_n)}/\beta W \tag{4}$$

"P_o" is a constant force representing the excitation (taken as 0.41 KN for indoor/outdoor footbridges). "f_n" is the fundamental natural frequency of a joist panel, girder panel or combined panel modes whichever is applicable. "β" is modal damping ratio taken as 0.01 for indoor/outdoor footbridges. "W" is the effective weight supported by the joist panel, girder panel or combined panel modes, as applicable. It was mentioned in that guide, that floor systems with fundamental frequencies less than 3 Hz should generally be avoided.

2.7 Design guide for footfall induced vibration of structures "CCIP-016" (December 2006)[9]

This design guide illustrates a rigorous analysis method for calculating structural response due to single walking person which is called footfall analysis method. In this analysis two different responses are calculated due to vertical human force; the resonant and the impulsive vibration responses. These types of response are associated with low or high frequency floors. The resonant response is calculated for structures with fundamental vertical natural frequencies less than 4.2 times the fastest walking frequency. The impulsive response is calculated for structures with fundamental vertical natural frequencies higher than 4.2 times the fastest walking frequency. In this analysis the overall response factor "R" is calculated, which is a multiplier of the Z-axis base line curve for RMS acceleration (vertical direction) according to BS 6472 1992[10]. A response factor of 1 represents the value of vibration that is just noticeable by a typical human. The performance criteria given in this guide are applicable for bridges of all spans and natural frequencies. For external bridges "R" should be less than 64. For typical indoor bridges "R" should not exceed a value of 32. For heavily trafficked indoor bridge the value of "R" should be less than 24. Most of the structures that include the vibration problem are the ones which suffer from resonant response. In this analysis, this type of structures is susceptible to the first four harmonics of footfall forces.

These harmonics are sinusoidal forces applied to the structure at frequencies of 1, 2, 3 and 4 times the walking frequency (1 Hz to 2.8 Hz). All modal frequencies of up to 15 Hz contribute in the response calculations. The total response factor, R, is calculated by considering the 'square root sum of the squares' combination of the response factor for each of the four harmonics.

2.8 JRC report - Design of lightweight footbridges for human induced vibrations "EUR 23984 EN"[11]

This technical guide provides some procedures which link the dynamic response with the natural frequency and pedestrian traffic density to check the comfort level. The comfort criteria are classified into 4 levels with degree of comfort varies from maximum comfort level to discomfort level. To compute the dynamic response the following steps shall be followed:

a) Estimation of natural frequencies and their critical range: If the modal mass of the pedestrians is more than 5 % of the modal deck mass, it is recommended to account for the mass of pedestrians when calculating the natural frequencies. The next step is to check whether these frequencies are placed at critical range or not. The critical range is specified as 1.25 Hz to 2.3 Hz for first harmonic and 2.5 Hz to 4.6 Hz for the second harmonic. Dynamic calculations to pedestrian excitation should be performed if the natural frequencies are located within these ranges.

b) Specify design situation and pedestrian density: Determination of design situations is based on the events or real conditions that might occur during certain time intervals, like the inauguration of bridge and commuter traffic. Based on these events the traffic situation can be specified. Five categories are presented for pedestrian traffic; their ranges vary from 0.2 pedestrian/m^2, for weak traffic up to 1.5 pedestrian/m^2 for exceptionally dense traffic.

c) Then the comfort class is specified according to the expected occurrence for the design situation, if it is occurred once in the life time then lower level of comfort can be chosen, if it is occurred daily then higher comfort class shall be selected. The comfort classes are specified in terms of vertical accelerations. Maximum level of comfort is 0.5 m/sec^2, medium level is from 0.5 -1.0 m/sec^2, minimum level of comfort is in range 1.0 to 2.5 m/sec^2 and the unacceptable discomfort is for accelerations more than 2.5 m/sec^2.

d) The maximum accelerations can be determined by application of load models based on pedestrian traffic, or by using response spectra method for pedestrian streams. The latter is a straight forward method , where the maximum characteristic acceleration is defined by the product of peak factor $k_{a,d}$ and a standard deviation of acceleration σ_a:

$$a_{max,d} = k_{a,d}\, \sigma_a \tag{5}$$

Where "σ_a", is the standard deviation of the response. Its value depends on the modal mass, the damping ratio and other constants which are specified in terms of natural frequency. "$k_{a,d}$", is the peak factor that transform the standard deviation of response to the characteristic value $a_{max,d}$. In serviceability states, the characteristic value is the 95th percentile, $k_{a,95\%}$. Both factors are resulting from Mont Carlo simulations based on numerical time step analysis of several pedestrian streams on various bridges geometries. The following equation represents the empirical equation for the determination of the variance of the acceleration response:

$$\sigma_a{}^2 = k_1\, \xi^{k_2}\, \frac{C \times \sigma_F^2}{m_i^{*2}} \tag{6}$$

Where:

$\sigma_F{}^2 = k_F\, n,$ is the variance of the pedestrian induced forces.

k_F is a constant shown in Table 1.

n = is number of pedestrians on the bridge based on pedestrian traffic density "d".

$k_1 = a_1 f_i^2 + a_2 f_i + a_3$

$k_2 = b_1 f_i^2 + b_2 f_i + b_3$

$a_1, a_2, a_3, b_1, b_2, b_3$ are constants shown in Table 1.

ξ is the structural damping ratio.

C is the constant describing the maximum of the load spectrum.

f_i is the natural frequency that coincides with the step frequency of the pedestrian stream.

m_i^* is the modal mass of mode i.

d Ped./m^2	k_F	C	a_1	a_2	a_3	b_1	b_2	b_3	$k_{a,95\%}$
≤ 0,5	1,20×10^{-2}	2,95	-0,07	0,60	0,075	0,003	-0,040	-1,000	3,92
1,0	7,00×10^{-3}	3,70	-0,07	0,56	0,084	0,004	-0,045	-1,000	3,80
1,5	3,34×10^{-3}	5,10	-0,08	0,50	0,085	0,005	-0,060	-1,005	3,74

Table 1: Constants used for evaluating vertical acceleration as specified in "JRC - EUR 23984 EN"[11].

3 COMPARATIVE STUDY

Fifteen pedestrian bridges that were optimized for strength, deflection and response factor shown on previous paper[12] will be used in a comparative study between the several methods listed in the literature. The chosen results, from that paper[12], are those satisfying comfort levels suitable for external bridges which mean that the overall response factor (R) is less than 64. Cross sectional profiles of main beams that achieve such limit will be used in the current study using different finish weights (100 kg/m^2, 300 kg/m^2 and 800 kg/m^2). Design checks by AISC design guide[8] is selected to satisfy the acceleration limit of outdoor footbridges.

Comparison between vertical accelerations calculated from AISC[8], CCIP-016[9] and BS 5400-2:2006[3] are shown in Table 2. It is worth mentioning that the natural frequency exceeds 5 Hz for 10 m span with 100, 300 kg/m^2 of finish weight, therefore acceleration values for BS 5400-23 are not computed for these situations and those cases consider satisfying human comfort without calculations of acceleration. All foot bridges in Table 2 which have already satisfied response factor R<64 in previous paper[12] according to CCIP-016[9] are also fulfilling the acceleration limits specified in AISC[8], and BS5400-2[3]; therefore the human comfort for all cases is satisfied. It is also evident that the acceleration computed by AISC is always the least compared to both CCIP-0169 and BS 5400-2:2006[3]. Acceleration values from BS 5400-2:2006[3] are generally consistent with CCIP-016[9]. Since the acceleration calculated by CCIP-016[9] is based rigorous footfall analysis, it is concluded that the simplified equation in BS 5400-2:2006[3] better calculate the vertical acceleration than the AISC[8]. The computed accelerations in Table 2 are proportioned to the their limits as stated in each standard and guideline to obtain vibration unity check as shown in Figure 3 (a), (b) and (c). The unity check by CCIP-016[9] represents the upper limits between the three methods.

Finish Weight	Span (m)	Freq. (Hz)	AISC Steel Design Guide[8] no. 11		Footfall Analysis CCIP-016[9]		BS 5400-2[3]	
			Acc. (m/sec^2)	Comfort Level	Acc. (m/sec^2)	Comfort Level	Acc. (m/sec^2)	Comfort Level
100 kg/m^2	10	6.06	0.344	Satisfied	0.63	Satisfied	N/A	Satisfied
	20	3.23	0.49	Satisfied	0.448	Satisfied	0.613	Satisfied
	30	2.84	0.352	Satisfied	0.523	Satisfied	0.535	Satisfied
	40	2.11	0.315	Satisfied	0.536	Satisfied	0.477	Satisfied
	50	2.14	0.22	Satisfied	0.548	Satisfied	0.398	Satisfied
300 kg/m^2	10	6.1	0.22	Satisfied	0.41	Satisfied	N/A	Satisfied
	20	2.95	0.376	Satisfied	0.458	Satisfied	0.45	Satisfied
	30	2.08	0.216	Satisfied	0.555	Satisfied	0.39	Satisfied
	40	1.88	0.159	Satisfied	0.556	Satisfied	0.35	Satisfied
	50	2.05	0.177	Satisfied	0.516	Satisfied	0.316	Satisfied
800 kg/m^2	10	3.51	0.341	Satisfied	0.448	Satisfied	0.278	Satisfied
	20	2.83	0.23	Satisfied	0.436	Satisfied	0.245	Satisfied
	30	1.99	0.195	Satisfied	0.298	Satisfied	0.23	Satisfied
	40	1.85	0.148	Satisfied	0.547	Satisfied	0.21	Satisfied
	50	1.53	0.125	Satisfied	0.398	Satisfied	0.19	Satisfied

Table 2: Comparison between vertical accelerations computed using different methods.

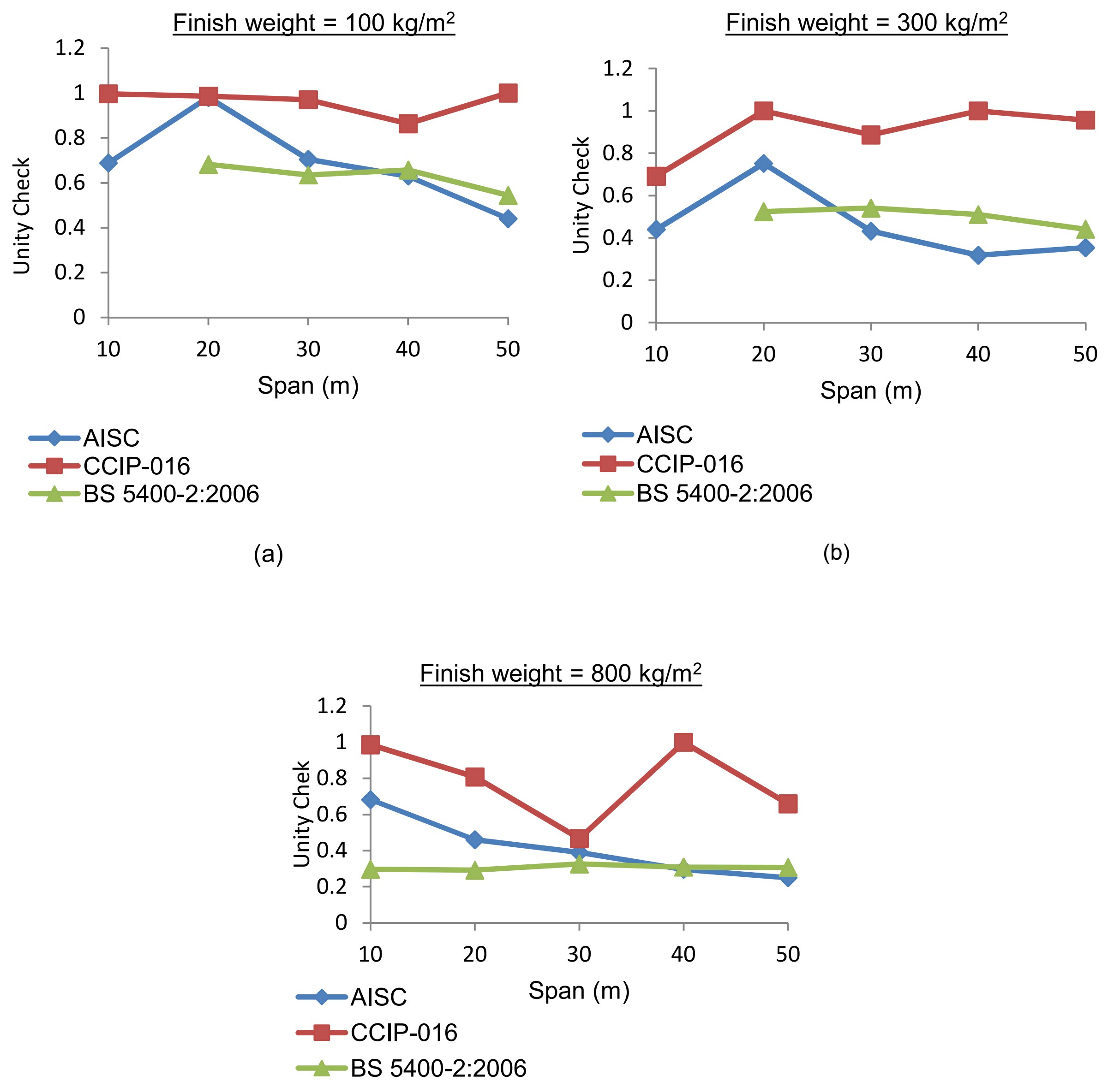

(c)

Figure 3 : (a), (b) and (c): Unity check for acceleration limits specified in AISC[8], CCIP-016[9] and BS 5400-2[3] for finish weights 100, 300 and 800 Kg/m^2 respectively.

The vertical acceleration results based on response spectra method specified in JRC - EUR 23984 EN[11] are shown in Figure 4 (a), (b) and (c) for different pedestrian traffic classes. The chosen classes are 0.5 pedestrian/m^2 representing dense traffic,1 pedestrian/m^2 representing very dense traffic and 1.5 pedestrian/m^2 representing the exceptionally dense traffic. The comfort levels obtained from these results are shown in Table 3. For 10 m span and finish weight of 100 and 300 kg/m^2, the fundamental frequency exceeds 4.6 Hz which are located outside the critical range of natural frequency. Consequently, the assessment of comfort is not required and vertical accelerations are not calculated for that case. It is evident from Figure 4 that the resulting acceleration is inversely proportion to the foot bridge span. This is mainly attributed to the increase in bridge mass. The same observation is noticed for the effect of floor finish weight as the resulting acceleration decreases with the increase of the finishes weight. The method specified in JRC-EUR 23984 EN[11] provides detailed assessment of the resulting acceleration. Although all the studied cases have fulfilled the requirements of AISC[8], CCIP-016[9] and BS 5400-2:2006[3], some cases just achieved minimum comfort level by JRC - EUR 23984 EN[11] specially for the case of light finish weight. It is worth noting that the resulting accelerations in

Table 3 are generally of higher order of magnitude when compared to the resulting acceleration in Table 2. This is attributed to the different approach used in each table. AISC[8], CCIP-016[9] and BS 5400-2:2006[3] are based on single walker response while JRC - EUR 23984 EN[11] is based on flow of pedestrian traffic. The resulting acceleration of each method must be compared to its specified limit only.

The acceleration limit of 0.7 m/sec^2 set by Eurocode 1990[4] is satisfied for all cases as computed using AISC[8] design guide, CCIP-016[9] and BS 5400-2[3]. On the other hand, when comparing this limit to acceleration obtained from JRC - EUR 23984 EN[11], it is found that most of vertical accelerations are not conforming to recommended value from Eurocode 1990[4] especially for finish weights of 100 and 300 kg/m^2. This means that the limit set by Eurocode 1990[4] is consistent with methods depending on single walker models rather than methods depending on load models following the flow of pedestrian traffics.

The design acceleration limit stated in UK NA for BS EN 1991-2[5] can be estimated as 1 m/sec^2, when the bridge is assumed to be at major urban centers (k_1=1), located at primary route (k_2=1) and its height is about 6 m (k_3=1). The load models illustrated in that standard are adequate for single pedestrian, group of pedestrians and crowded pedestrian traffics. If this limit is compared to resulting acceleration shown in Table 3 which is suited for pedestrian traffic, it can be concluded that this limit is satisfied for foot bridges having medium or maximum comfort level only. Footbridges with minimum comfort level in JRC - EUR 23984 EN[11] shall not fulfill the limits set by UK NA for BS EN 1991-2[5].

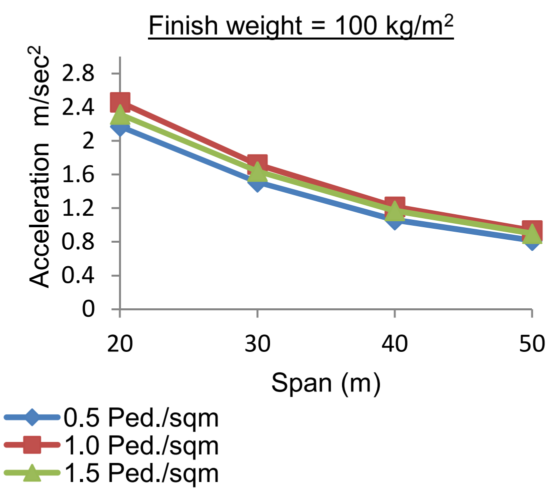

(a)

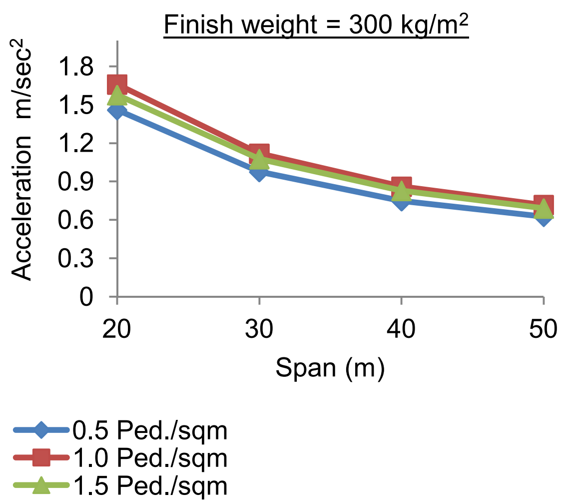

(b)

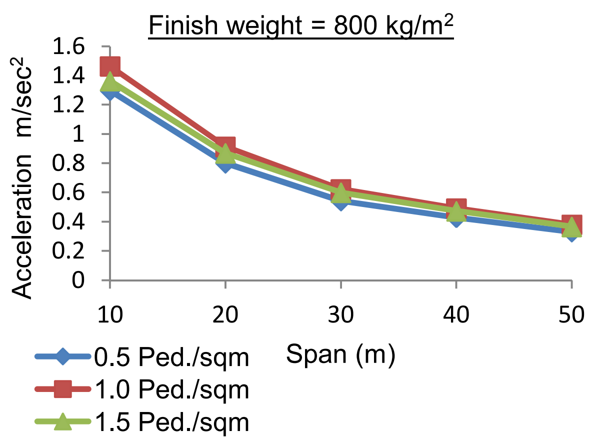

(c)

Figure 4 (a), (b) and (c) acceleration results from JRC-EUR 23984 EN[11] for different pedestrian densities and finish weights 100, 300, 800 Kg/m^2 respectively.

Finish Weight	Span (m)	JRC-EUR 23984 EN[11] (0.5 Ped./m²)		JRC-EUR 23984 EN[11] (1.0 Ped./m²)		JRC-EUR 23984 EN[11] (1.5 Ped./m²)	
		Acc. (m/sec²)	Comfort Level	Acc. (m/sec²)	Comfort Level	Acc. (m/sec²)	Comfort Level
100 Kg/m²	10	N/A	Satisfied	N/A	Satisfied	N/A	Satisfied
	20	2.171	Min. Comfort	2.459	Min. Comfort	2.315	Min. Comfort
	30	1.51	Min. Comfort	1.72	Min. Comfort	1.637	Min. Comfort
	40	1.061	Min. Comfort	1.216	Min. Comfort	1.17	Min. Comfort
	50	0.815	Medium Comfort	0.935	Medium Comfort	0.899	Medium Comfort
300 Kg/m²	10	N/A	Satisfied	N/A	Satisfied	N/A	Satisfied
	20	1.459	Min. Comfort	1.659	Min. Comfort	1.576	Min. Comfort
	30	0.975	Medium Comfort	1.118	Min. Comfort	1.076	Min. Comfort
	40	0.749	Medium Comfort	0.86	Medium Comfort	0.828	Medium Comfort
	50	0.625	Medium Comfort	0.717	Medium Comfort	0.69	Medium Comfort
800 Kg/m²	10	1.297	Min. Comfort	1.463	Min. Comfort	1.362	Min. Comfort
	20	0.801	Medium Comfort	0.913	Medium Comfort	0.869	Medium Comfort
	30	0.542	Medium Comfort	0.622	Medium Comfort	0.599	Medium Comfort
	40	0.428	Max. Comfort	0.491	Max. Comfort	0.473	Max. Comfort
	50	0.33	Max. Comfort	0.38	Max. Comfort	0.366	Max. Comfort

Table 3: Comparison between vertical accelerations computed for different pedstrian traffics using JRC - EUR 23984 EN[11].

4 CONCLUSION

Different vibration assessment methods have been compared to each other. Group of them are related to evaluating the vibration problem due to vertical forces induced by single pedestrian such as AISC[8] design guide no. 11 and CCIP-016[9]. Other group of standards and guidelines covered more cases where pedestrian traffic of different density can be used for evaluation of human comfort such as UK national annex for BS EN 1991-2[5] and JRC - EUR 23984 EN[11]. It was found that there is conformity between AISC[8], CCIP-016[9] and BS5400-2[3] for evaluating the vibration problem due to walking single pedestrian as all of them attain the same result that confirm the adequacy of footbridges to human comfort.

However, for the second group, it is found that their limits contradict with each other to obtain acceptable level of comfort. Nevertheless, they matched each other, in terms of comfort criterion, if the total self-weight is increased up to 800 kg/m² especially for long spans.

The vertical acceleration limit stated in Eurocode 1990[4] is not accompanied with clarification statement that confirm if it might be applied to crowded pedestrians case, or it is valid only to single walking pedestrian case. Form this study, the limit stated in that code fits properly with single pedestrian case as used in AISC[8], CCIP-016[9] and BS5400-2[3]. Moreover, this limit cannot be compared to crowded pedestrians traffic as obtained by JRC - EUR 23984 EN[11], where comfort level is achieved.

5 REFERENCES

[1] M. Schlaich and J. Francois, *Guidelines for the design of footbridges* , Féderation Internationale du Béton (International Federation for Structural Concrete), FIB Bulletin 32 ,Switzerland (2005).

[2] S. Živanović, A. Pavić and P. Reynolds, *Vibration serviceability of footbridges under human-induced excitation: a literature review*, Journal of Sound and Vibration, Vol. 279, No. 1-2, pp. 1-74, Elsevier, Maryland Heights (2005).
[3] British Standard Insitutiton, *Steel, concrete and composite bridges Part 2: Specification for loads*, BS 5400-2, London (2006).
[4] British Standard Insitutiton, *Eurocode - Basis of structural design*, BS EN 1990:2002 + A1:2005, London (2010).
[5] British Standard Insitutiton, *UK national annex to Eurocode 1: actions on structures - part 2: Traffic loads on bridges*, NA to BS EN 1991-2:2003, London (2008).
[6] International Organization for Standardization , *Bases for design of structures - Serviceability of buildings and walkways against vibrations*, ISO 10137,second edition, (2007).
[7] AASHTO, *LRFD guide specifications for design of pedestrian bridges, American Association of State* Highway and Transportation Officials,Washington DC (2009).
[8] T.Murray, D. Allen and E. Ungar, *Floor vibration due to human activity*, Steel design guide series no. 11, American Institute of Steel Construction, Chicago, (2003).
[9] M. Willford and P.Young, *A design guide for footfall induced vibration of structures (CCIP-016)*, The Concrete Centre, Blackwater, Camberley (2006).
[10] British Standard Insitutiton, *Guide to evaluation of human exposure to vibration in buildings (1 Hz to 80 Hz)*, BS 6472, London (1992).
[11] H. Cristoph, B. Christiane, K. Andreas, et. al, *Design of Lightweight Footbridges for Human Induced Vibrations*, JRC - EUR 23984 EN , Jonint and Research Center (JRC) Scientific and Technical Report, European Commission,(2009).
[12] A. El-Robaa, S. Ibrahim,S. Gaawan,C. Malek, *Effect of human-induced vibration on the design of steel pedestrian bridges*, 12th International Conference on Steel, Space and Composite Structures, Praque, Czech Republic (2014).

ON THE ISSUE OF RC SLABS WITH CUT-OUT OPENINGS RETROFITTED BY MEANS OF CFRP SYSTEMS

Sorin-Codruț Florut, Tamás Nagy-György, Valeriu Stoian and Daniel Dan

Politehnica Univeristy of Timisoara
2nd P-ta Victoriei, Timisoara 300006
e-mail: <codrut.florut@upt.ro> webpage: http://www.upt.ro

Keywords: reinforced concrete, two-way slabs, FRP, NSM, cut-out openings, retrofitting

Abstract. *The paper discusses the issue of Reinforced Concrete (RC) slabs retrofitted with Carbon Fibre Reinforced Polymer (CFRP) composite materials, through the perspective of experimentally obtained results within a research program that was conducted at the Politehnica University Timisoara, Romania. The program consisted in tests on two-way RC slabs with and without cut-out openings. The results presented in this paper were obtained by performing twelve tests on six full scale RC elements. Two full slabs served as control specimens, while at a corner or an edge of the other four slabs, various configurations of cut-outs were sawn in. Initially, each element was tested in as-built condition up to a certain stage. Afterwards, a mixed retrofitting solution that involves the use of both Near Surface Mounted FRP (NSM-FRP) and Externally Bonded FRP (EB-FRP) was applied. Finally, the elements were retested up to full failure. An important aspect of the research program (compared with most of those previously conducted) resides in the fact that it deals with relatively large cut-out openings. At the same time, the circular shape of the cut-out created inside one of the slabs generates attractive situations that were not completely studied up to this point. By performing the twelve experimental tests, the effectiveness of the proposed technique was assessed. The results are encouraging as they prove that the specimens' capacity can be very easily regained or increased by applying the strengthening/retrofitting system.*

1 INTRODUCTION

It is almost impossible to imagine important renovation of existing buildings without interventions on their floors and slabs. Whether the need of structural interventions is caused by increased load demands, degradations or changes in functionality, the requirements and the outcome are the same. The research program that is discussed within this paper was conducted at the Politehnica University Timisoara laboratories and covers experimental investigations on two-way RC slabs with and without cut-out openings strengthened/retrofitted using CFRP. The study was concentrated on establishing the effectiveness of the proposed solutions for the particular case of cut-outs that are inserted at the corners and along the edges of such slabs.

Two-way RC slabs supported on their entire contour are mostly subjected to flexure, with insignificant shear stresses. Thus, they are clearly susceptible to flexural failure rather than shear one, strengthening them by means of FRP materials being able to provide an efficient solution. The strengthening method for all RC elements presumes applying lamellas or fabrics (in the required amount and direction) by bonding them using resins (mostly epoxy) on the tensioned side of the member. Even though researches were carried out previously in order to find viable solutions for structural renovation of RC slabs, similar studies to those proposed within the above mentioned research program were quite scarce in literature. Using of FRP strengthening/retrofitting methods for this kind of applications is justified by its un-laborious execution. A drawback of these materials/techniques in structural strengthening of RC members is their brittle behaviour that can cause a decrease in their stiffness and could lead to brittle and sudden failure mechanisms.

For two-way slabs with cut-out openings strengthened using FRP, the available research is scarce, only several research programs being reported in literature, as work conducted by Tan & Zhao in 2004 [1], Vasquez & Karbhari in 2003 [2], Enochsson in 2005 [3] or Smith in 2009 [4] being of high importance. The solution applied by all of these researches consisted in laying up CFRP or Glass Fibre Reinforced Polymer (GFRP) strips or sheets of fabrics along the edges of the cut-out and bonding them to the concrete surface, on the tensioned side, using epoxy based resins. Different configurations for the lay-out of the strengthening materials were used, the most common being the one in which the material is placed parallel to the edges of the cut-out.

2 EXPERIMENTAL PROGRAM

The program consisted in twelve tests performed on six RC two-way slab panels, two tests on each specimen. Even though all six experimental specimens were identical in terms of geometry and material specifications (full scale 3950 x 2650 x 120 mm prismatic elements) they were split into 2 groups. The first 4 elements were included in the 1st group while the 2nd group consisted of the last 2 specimens. The 1st group of experimental elements consisted in a homogeneous slab (full slab, without any opening) and three slabs with rectangular cut-out openings. The full slab served as control element and was referred to as FS-01 (standing for Full Slab). The second slab, denoted RSC-01 (Rectangular Small Cut-out), had a small rectangular cut-out inserted into one of its corners. Into the third and fourth slabs, denoted RLC-01 and RLC-02 (standing for Rectangular Large Cut-out) a large rectangular cut-out was positioned along their entire width. The 2nd group of experimental elements consisted in a homogeneous slab referred to as FS-02 and one with a circular cut-out opening placed at one of its corners denoted CC-01 (standing for Circular Cut-out).

The specimens were placed horizontally, resting on a series of supports, 1.00 meter above the laboratory floor, in order to allow inspection during tests. The slab-support interface was provided by a layer of fresh mortar, the elements settling in horizontal position under their own weight. This type of simple support blocked gravitational displacements still allowing uplift of corners and edges of the slabs. The load was applied gravitationally, at the centre of the slabs, being distributed through a steel member over a surface of 1200 x 600 mm. The position of the load patch (i.e. centre of the full slab) was maintained throughout all 12 tests, regardless of the geometry of slabs with cu-outs; even if asymmetrical, it provided an un-favourable type of loading for all specimens. More detailed data on the experimental program are provided in reference work [5]. A view of the entire test set-up is presented in Figure 1.

Figure 1: Test setup for RSC-01 and CC-01 slabs

All elements in the 1st group were cast using concrete with cubic compressive strength of 65N/mm^2. The slabs were reinforced with steel welded wire meshes at the inferior side (4 mm in diameter with spacing of 100 mm) and with steel rebar at the superior one (6 mm and 10 mm bars). The bars in the steel welded wire meshes had average yield strength between 537 MPa and 597 MPa. The specifications for the elements in the 2nd group were identical to those in the 1st group; however, since they were constructed in two different units of pre-cast elements, some differences have occurred. Thus, elements in the 2nd group were cast using concrete with cubic compressive strength of 38N/mm^2. The lay-out of reinforcement was identical for all slabs, both in 1st and 2nd groups. The compressive strength of concrete was determined experimentally, on cubes tested at the time of the test on each slab panel. Three cubes were tested for each slab. For further details regarding materials and reinforcement configuration, please refer to [5].

The testing protocol was to test all elements in their as-built state up to a stage that would assume the need of applying strengthening/retrofitting interventions. For all of the slabs, this stage was considered as the maximum allowable deflection (L/250=2400mm/250=9.60mm) according to EN 1992-1-1 [6]. As this limitation was reached, the test was stopped and a mixed (hybrid) retrofitting solution that involved the use of both Near Surface Mounted (NSM-FRP) and Externally Bonded (EB-FRP) techniques was applied. Finally, after allowing CFRP system to cure for at least 7 days, the retrofitted elements were tested up to their complete failure.

3 RESULTS OF TESTS ON ELEMENTS IN AS-BUILT CONDITION

All tests on bare elements were denoted starting with the reference of the experimental specimens and updated with the mark “UU” standing for Undamaged Unstrengthened (e.g. FS-01 represents the specimen and FS-UU-01 represents the test on the bare specimen).

3.1 1st group of elements

One of the most important features of the specimens’ behaviour is the small number of cracks that have opened, in conjunction with crack patterns that indicate larger stresses in the area around the cut-outs. Actually, initiation points of all cracks are located in areas around the cut-outs. In the case of the FS-UU-01 test, a very predictable behaviour was identified, as four cracks opened on the direction of the yield lines, at inclinations close to 45° (36°, 44°, 52° and 56°). For all of the other tests, the first crack to appear was a longitudinal one, parallel to long edges of the slabs, located quasi-centrally. In all these tests on slabs with cut-outs, the first crack was always followed by inclined cracks, at various inclinations (ranging from 30° to 73°).

The maximum load level reached during the FS-UU-01 test was 118kN. Past this value, the strain in numerous steel reinforcement has reached yielding point and the vertical mid-span displacement has reached maximum allowable deflection as provided by EN 1992-1-1. Moreover, deflection increased without a substantial increase of load. During the test, the maximum vertical mid-span displacement had a value of 10.28 mm. The maximum load level reached during the RSC-UU-01 test was 87kN while the maximum vertical displacement had a value of 11.36mm. During RLC-UU-01 test the maximum recorded load level was 75kN while the maximum vertical displacement had a value of 9.59mm. For the RLC-UU-02 test the maximum recorded load level was 67kN while the maximum vertical displacement had a value of 8.88mm. All of the load-displacement diagrams recorded for the elements within the 1st group, in as-built condition, are presented in Figure 2. Even though it was not necessarily intended for the steel reinforcement to yield during tests on bare elements, conclusions of these test is that the steel reinforcement reaches yield strength prior to reaching the maximum Service Limit State (SLS) in terms of maximum allowable deflection (L/250=2400mm/250=9.60mm) as imposed by EN 1992-1-1.

3.2 2nd group of elements

An important characteristic of slabs in 2nd group that differentiate these specimens from those in 1st group is related to the crack patterns. Even though identical materials specifications were provided and required to the manufacturer of the slabs, the results were somehow different. The crack patterns of 2nd group slabs show a large number of cracks, opening quite early in the loading stage, in contradiction to the elements in the 1st group for which the tests on bare elements disclosed a very small number of cracks. The maximum load level reached during the FS-UU-02 test was 101kN and during test CC-UU-01 was 76kN. All of the load-displacement diagrams recorded for elements in as-built condition within the 2nd group are presented in Figure 2. The load-displacement diagrams recorded for all elements in as-built state (Figure 2) are represented at a different scale in terms of displacement from the diagrams on the strengthened elements, due to clarity and readability reasons.

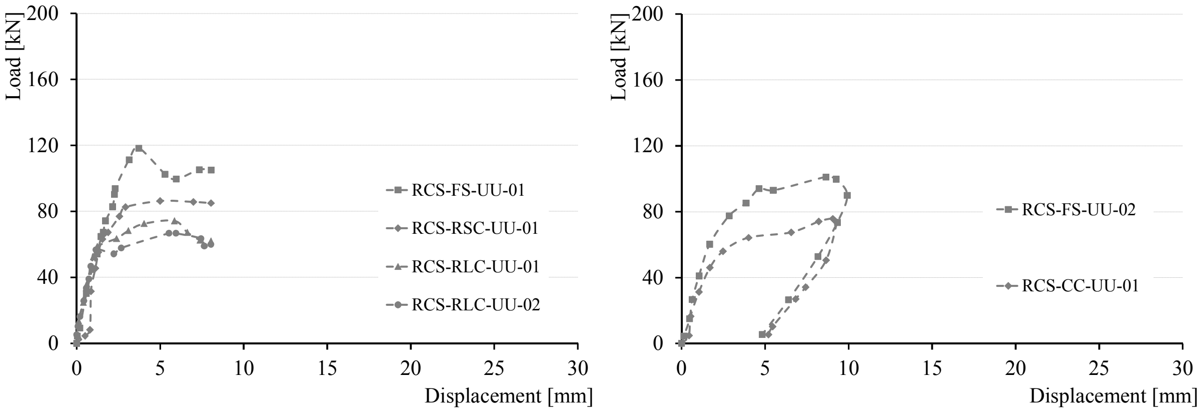

Figure 2: Load-displacement diagrams recorded for all the elements in as-built condition (left - 1st group, right - 2nd group)

4 STRENGTHENING/RETROFITTING SOLUTIONS

As mentioned previously, for all RC elements for which the enhancement of performance in flexure is intended by strengthening, the procedure consists in applying of the CFRP components on the tensioned side (i.e. the bottom side of the slab in the present cases), in the required direction and quantity. In the case of the present research program, the CFRP elements will be placed on two directions, parallel with the edges of the slab, for all specimens, with or without cut-out openings, regardless of the geometry of the cut-outs.

The required amount of CFRP is determined analytically considering the following simplified assumptions. For the full slabs, the tensile force that would have been undertaken by the steel reinforcement (which is yielded at the end of the tests on bare elements) is equalized with the tensile force that will be undertaken by the CFRP system. For the elements with cut-outs, the CFRP strengthening material will be placed around the cut-out, along its edges, parallel to the edges of the slabs. The amount of CFRP is established by equalizing the tensile force that would have been undertaken by the steel reinforcement eliminated by inserting the cut-out with the tensile force that will be undertaken by the CFRP, as provided in Equation 1.

$$F_s = F_f \quad \Rightarrow \quad A_f = \frac{f_{yd}}{E_f \cdot \varepsilon_f} A_s \tag{1}$$

where: F_s - tension force in steel reinforcement; F_f - tension force in FRP fibers; A_f - area of fibers in CFRP composite; f_{yd} - design yield strength of steel reinforcement; E_f - modulus of elasticity of fibers of CFRP composite; ε_f - strain in fibers of CFRP composite; A_s- steel reinforcement area

In the above formula, the strain in CFRP composite is limited to 0.008, this value being an accepted limit for elements subjected to flexure, according to the strain limitation approach as presented in *fib* bulletin 14 [7]. This value is much lower than the ultimate strain provided by the producers, being considered the value at which composite action is lost due to premature failure. CFRP lamellas and NSM strips with a modulus of elasticity of 165000MPa and a thickness of 1.2mm and CFRP sheets with a modulus of elasticity of 230000MPa and a thickness of 0.12mm were used for all strengthening systems. On the direction parallel to the short edges of the slabs, FRP reinforcement was applied by NSM-FRP technique while on the direction parallel to the long edges the EB-FRP technique was used. Inside Figure 3 and Figure 4 the lay-up of CFRP components for all of the tested slabs is depicted. For further details regarding materials and FRP configuration, please refer to [5].

As it can be observed in Figure 4, for slabs RLC-01 and RLC-02 the applied CFRP solution is different even though the specimens have identical geometry. The RLC-01 slab was only retrofitted, as the purpose was only to restore the initial capacity of the slab, so the CFRP components were installed only around the long edge of the cut-out. For the RLC-02 slab the objective was to enhance the behaviour and increase of the load bearing capacity, this desiderate being obtained by applying CFRP strengthening components on its entire soffit.

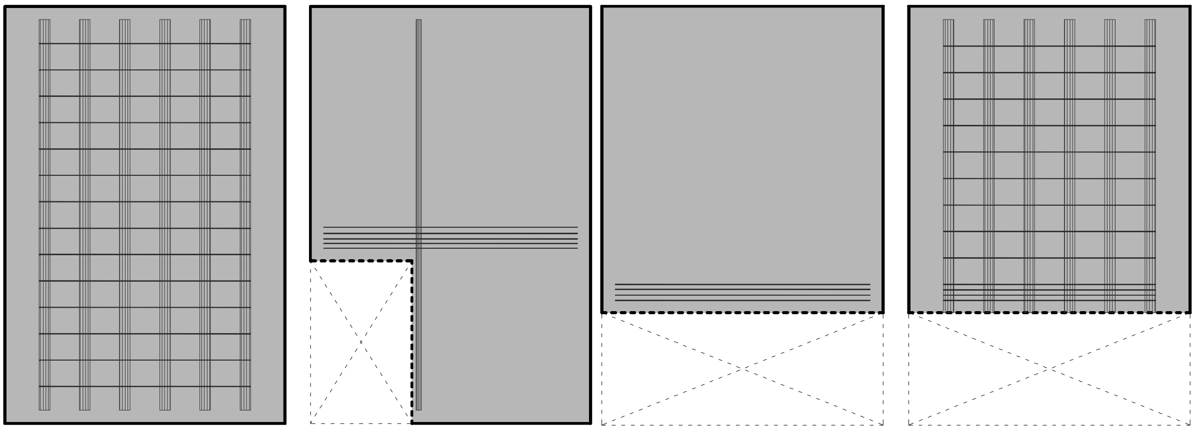

Figure 3: Lay-up of CFRP components for specimens in the 1st group
(from left to right: FS-01, RSC-01, RLC-01 and RLC-02).

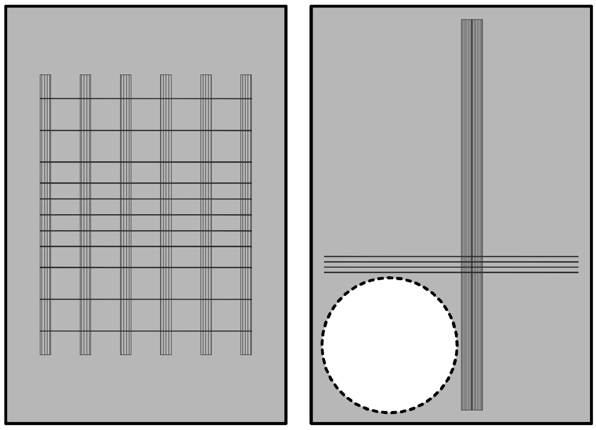

Figure 4: Lay-up of CFRP components for specimens in the 2nd group
(from left to right: FS-02 and CC-01).

5 RESULTS OF TESTS ON STRENGTHENED/RETROFITTED ELEMENTS

All tests on strengthened elements were denoted starting with the reference of the experimental specimens and updated with the mark "DS" standing for Damaged Strengthened (e.g. FS-01 represents the full specimen and FS-DS-01 represents the test on the strengthened element).

5.1 1st group of elements

The FS-DS-01 slab was tested up to failure, reaching a maximum load of 186 kN that corresponds to a vertical mid-span deflection of 50 mm. After this level, the deflection increased while the load diminished. The slab was able to deflect almost 110 mm before full failure. During the RSC-DS-01 test a maximum load of 86 kN was recorder at a central deflection of 27 mm. Maximum recorded deflection was 33 mm. The RLC-DS-01 test reached a maximum load of 75 kN at a central deflection of 8 mm. Maximum deflection was of 87 mm. The RLC-DS-02 test reached a maximum load of 147 kN at a central deflection of 63 mm. Maximum deflection was of 84 mm [5]. The load-displacement diagrams of 1st group slabs are presented in Figure 5.

5.2 2nd group of elements

The FS-DS-02 slab reached a maximum load of 199 kN with a corresponding mid-span vertical displacement of 70 mm. The CC-DS-01 test reached a maximum load of 109 kN at a central deflection of 27 mm, being however able to deflect up to 85 mm showing a relative uniform plateau in the load-displacement curve after a small drop recorded after reaching the maximum load level. The load-displacement diagrams of 2nd group of slabs are presented in Figure 5.

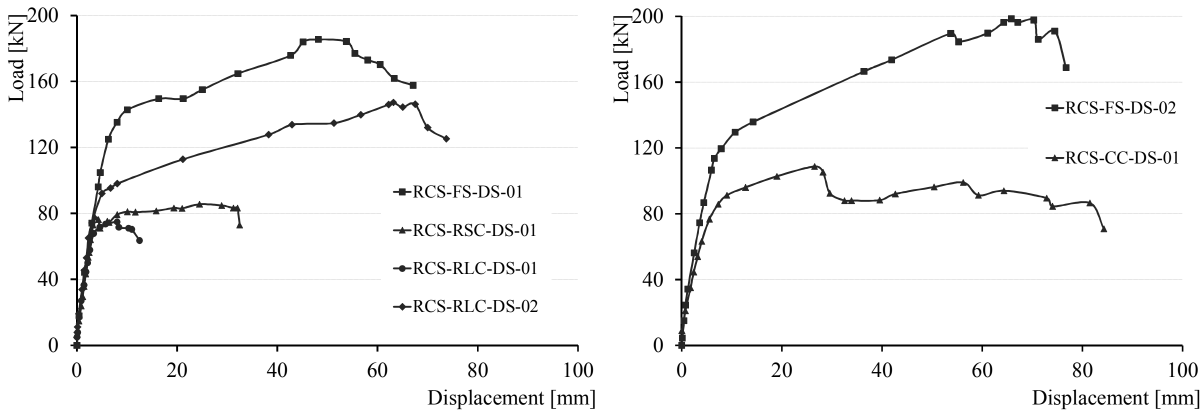

Figure 5. Load-displacement diagrams for strengthened elements (left - 1st group, right - 2nd group)

CONCLUSIONS

The goal of strengthening/retrofitting interventions is achieved as slabs prove a regain or an increase in the capacity after applying the strengthening/retrofitting solutions. The increase of capacity by 58% for slab FS-01 is an extremely important prove of the effectiveness of the applied solutions. An even larger increase is obtained in the case of slab RLC-02 (by 119%) and in the case of the full element in 2nd group (by 96%).

By applying only a retrofitting system, the capacity of the RSC-01 and RLC-01 slabs was restored. The amount of CFRP laid-up around the cut-outs was however insufficient for increasing the bearing capacity of the slabs. It is however interesting that by applying only the retrofitting system for CC-01 slab, the capacity increased by 43%, suggesting the fact that the circular configuration of the cut-out is a much more favorable one.

An important characteristic of the behavior of strengthened slabs consists in the fact that all of the CFRP components have failed due to fiber rupture; the only situation in which premature debonding had occurred was related to the failure of the laminate mounted by EB-FRP on the RSC-01 slab.

REFERENCES

[1] Tan K. H., Zhao H., *Strengthening of openings in one-way reinforced-concrete slabs using carbon fiber-reinforced polymer systems*, J. Compos. for Constr., Volume 8, Issue 5, pp. 393-402 (September/October 2004).

[2] Vasquez A., Karbhari V. M., *Fiber-reinforced polymer composite strengthening of concrete slabs with cutouts*, ACI Structural Journal, V. 100,No. 5, pp. 665-67 (2003).

[3] Enochsson O., *CFRP strengthening of concrete slabs, with and without openings. Experiment, analysis, design and field application*. Licentiate thesis, Luleå University of Technology (2005).

[4] Smith S.T., Kim S.J., *Strengthening of one-way spanning RC slabs with cutouts using FRP composites*, Construction and Building Materials, Volume 23, Issue 4, 2009, pp 1578-1590.

[5] Florut, S. C., Reinforced concrete slabs strengthened using FRP composites, Ed. Politehnica, Timisoara, 2014.

[6] EN 1992-1-1; Eurocode 2: Design of concrete structures - Part 1-1: General rules and rules for buildings (2004).

[7] Technical Report on the Design and Use of Externally Bonded FRP Reinforcement for Reinforced Concrete Structures, fib Bulletin 14, TG.

[8] Florut Sorin Codrut, Performance study of elements strengthened with FRP composite materials subjected to flexure, PhD Thesis, Ed. Politehnica, Timisoara 2011.

[9] Floruţ S. C., Stoian V., Nagy-György T., Dan D. and Diaconu D., *Experimental results of research program on RC slabs retrofitted by mixed CFRP system*, Proceedings of 14th International Conference Structural Faults and Repair, 2012, pp. 70/7e.

12th International Conference on
Steel, Space and Composite Structures
28-30 May 2014, Prague, Czech Republic

LARGE DISPLACEMENT ANALYSIS BASED ON THE CO-ROTATIONAL APPROACH FOR FUNCTIONALLY GRADED PLANAR BEAM STRUCTURES

Buntara S. Gan* and Dinh-Kien Nguyen†

*Department of Architecture, College of Engineering, Nihon University
1-Nakagawara, Tokusada, Koriyama City, Fukushima 963-8642, Japan
e-mail: buntara@arch.ce.nihon-u.ac.jp, webpage: http://www.ce.nihon-u.ac.jp

Keywords: Functionally graded material, plane beam structures, finite element method.

Abstract. *A large displacement analysis based on the co-rotational approach for functionally graded (FG) planar beam structures is presented. The material properties are assumed to be graded in the thickness direction by a defined power law distribution. A simple beam element based on the first-order shear deformation beam theory, taking the material in-homogeneity and the shift in the neutral axis position into account, is formulated and employed in the analysis. An incremental/iterative procedure in combination with the arc-length control method is employed in computing the equilibrium paths of the structures. Numerical examples are given to show the accuracy and efficiency of the formulated element. The influence of the material non-homogeneity and the shear deformation on the large displacement behavior of the structures is examined in detail and highlighted.*

1 INTRODUCTION

In recent years, many investigations have been carried out on mechanics of structures made of functionally graded materials (FGMs). These materials are formed by varying the percentage of constituents in one or more spatial directions. As a result, the effective properties of FGMs exhibit continuous change, thus eliminating interface problems and mitigating thermal stress concentrations. FGMs have great potential in applications where the operating conditions are severe, including spacecraft heat shields, heat exchanger tubes, biomedical implants, flywheels, and plasma facings for fusion reactors, etc [1].

Large displacement analysis of structures and components is often of great concerns in civil engineering, mechanical and aerospace industries. The finite element method with its versatility in spatial discretization is an effective tool for large displacement analysis. A number of finite element methods have been proposed for the FGM structures with geometrical nonlinearity in the last two decades. Praveen and Reddy[2] adopted the von Kármán plate theory in the derivation of a plate element for studying the static and dynamic response of FGM plates. Using the exact solution of the governing differential equations as interpolation functions, Chakraborty et al.[3] formulated a first-order shear deformation beam element for analyzing the thermo-elastic behavior of FGM beams. Lee et al.[4] presented a finite element procedure for computing the post-buckling response of FGM plates under compressive and thermal loads. Nguyen[5], Nguyen and Gan[6] studied the large displacement behavior of tapered cantilever beams composed of axially and transversely FGM by using the co-rotational finite element formulations. Nguyen et al.[7] derived a co-rotational Euler-Bernoulli beam element for geometrically nonlinear analysis of plane beam and frame of FGM structures.

† Department of Solid Mechanics, Institute of Mechanics, Vietnam Academy of Science and Technology, 18 Hoang Quoc Viet, Hanoi, Vietnam

This paper presents a finite element procedure for large displacement analysis of FGM structures which material properties are vertically gradually change in section. To this end, a nonlinear beam element based on the first-order shear deformation beam theory is formulated in the context of the co-rotational formulation. The shift in the neutral axis position is taken into account in the derivation of the element, and as a result there is no axial-bending coupling terms in the element formulation. Numerical examples are given to illustrate the accuracy and efficiency of the proposed beam element and to highlight the large displacement behavior of the FGM beam structures.

2 FINITE ELEMENT FORMULATION

2.1 Co-rotational formulation

Co-rotational formulation is an efficient tool in dealing with geometrically nonlinear problems in which the structures often undergo large displacements. The central idea of the formulation is to introduce a local co-ordinate system that continuously moves and rotates with the element during its deformation process. By using such a local system, the geometrical nonlinearity induced by the large body motion is separated from the total deformation and incorporated in the transformation matrices. The element formulation is firstly derived in the local co-ordinate system and then transferred into the global system with the aid of the transformation matrices. Depending upon definition of the local co-ordinate system, different types of co-rotational beam elements can be obtained. The co-rotational formulation adopted in the present work is closely related to that described by Crisfield[8], and further developed by Pacoste and Eriksson[9], and Nguyen[10].

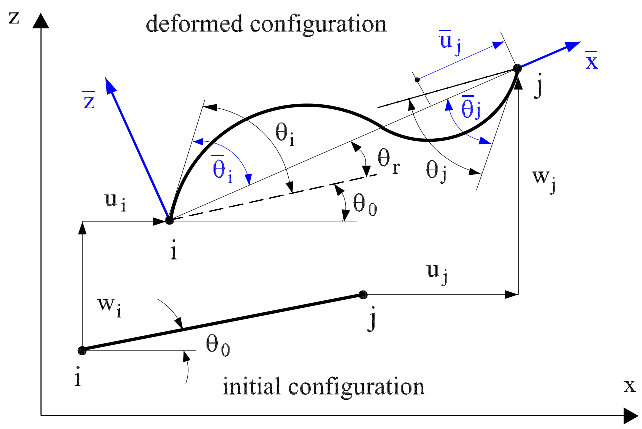

Figure 1: A co-rotational planar beam element

Figure 1 shows a co-rotational planar beam element and its kinematics in two co-ordinate systems, the local $(\bar{x},\bar{z})$, and the global (x,z). The element is initially inclined to the x-axis with an angle θ_0. The global system is fixed, while the local system continuously moves and rotates with the element during its deformation. The local system is chosen with its origin at node *i* and with the $\bar{x}$-axis directs towards node *j*. With the chosen local system, the axial displacement at node *i* and the transverse displacements at the two nodes are always zero, $\bar{u}_i = \bar{w}_i = \bar{w}_j = 0$. Thus, the element vector of local nodal displacements, $\bar{\boldsymbol{d}}$, contains only three components as

$$\bar{\boldsymbol{d}} = \{\bar{u}_j \ \bar{\theta}_i \ \bar{\theta}_j\}^T . \tag{1}$$

In Equation 1 and hereafter, a bar suffix is used to indicate a quantity defined in the local co-ordinate system. The global nodal displacements in general are nonzero, and the element vector of global nodal displacements in the global system, ***d***, contains six components as

$$\boldsymbol{d} = \{u_i \ w_i \ \theta_i \ u_j \ w_j \ \theta_j\}^T . \tag{2}$$

The local nodal displacements in Equation 1 can be computed as

$$\bar{u}_j = l_n - l_0, \ \bar{\theta}_i = \theta_i - \theta_r, \ \bar{\theta}_j = \theta_j - \theta_r \tag{3}$$

Where l_n and l_0 are respectively current and initial lengths of the element, and θ_r is the rigid rotation of the element. These quantities can be computed from the element co-ordinates and the current nodal displacements[8]. By equating the virtual work of the element written in both the local and global systems we can obtain the relation between the local and the global vectors of nodal forces as[8]

$$\boldsymbol{f}_{in} = \boldsymbol{T}^T \bar{\boldsymbol{f}}_{in} \tag{4}$$

Where $\boldsymbol{f}_{in}$ and $\bar{\boldsymbol{f}}_{in}$ are respectively the global and local vectors of nodal forces, and $\boldsymbol{T}$ is a transformation matrix which can be defined from the local and global displacements, Equation 1. By partial differentiation of the global vector with respect to nodal forces given by Equation 4 one can obtained the element tangent stiffness matrix in the global system, $\boldsymbol{k}_t$, in the form

$$\boldsymbol{k}_t = \boldsymbol{T}^T \bar{\boldsymbol{k}}_t \boldsymbol{T} + \frac{\bar{f}_u}{l_n} \boldsymbol{z}\boldsymbol{z}^T + \frac{\bar{f}_{\theta i} + \bar{f}_{\theta j}}{l_n^2} (\boldsymbol{r}\boldsymbol{z}^T + \boldsymbol{z}\boldsymbol{r}^T) \tag{5}$$

In the above equation, $\bar{\boldsymbol{k}}_t$ is the element local tangent stiffness matrix; $\bar{f}_u, \bar{f}_{\theta i}, \bar{f}_{\theta j}$ the local nodal forces; $\boldsymbol{r}$ and $\boldsymbol{z}$ are the vectors relating the local virtual displacements to the global ones. The detail expressions for the matrix $\boldsymbol{T}$ and vectors $\boldsymbol{r}$, $\boldsymbol{z}$ are given in the texbook by Crisfield[8].

As seen from Equations 4 and 5, the element formulation is completely defined provided the local nodal force vector and tangent stiffness matrix are known.

2.2 Local formulation

This subsection derives the local nodal force vector and tangent stiffness matrix for an FGM beam element. Figure 2 shows a beam element in two Cartesian co-ordinate systems (x_1, z_1), $(\bar{x}, \bar{z})$. The x_1 −axis is chosen on the bottom surface, and $\bar{x}$ − axis is on the neutral plane with its distance to the bottom surface, h_0, will be determined later. The beam is assumed to be composed of two constituents, ceramic and metal, with the effective elastic moduli follow a simple power law as

$$\begin{aligned} E(z_1) &= (E_c - E_m)\left(\frac{z_1}{h}\right)^n + E_m \\ G(z_1) &= (G_c - G_m)\left(\frac{z_1}{h}\right)^n + G_m \end{aligned} \tag{6}$$

Where n is a non-negative index defining the material variation profile; subscripts '*c*' and '*m*' stand for ceramic and metal, respectively. As seen from Equation 6, the bottom surface contains only metal, and the top surface is pure ceramic.

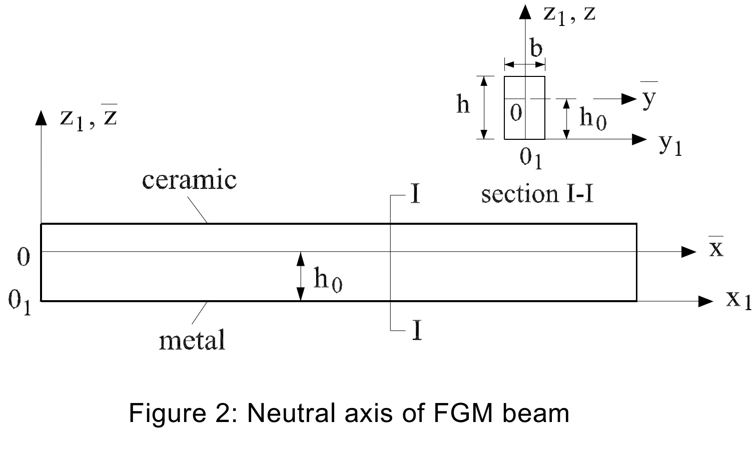

Figure 2: Neutral axis of FGM beam

Clearly, due to the asymmetric variation of the effective Young's modulus according to Equation 6, the beam neutral axis is no longer at the mid-plane. The position of the neutral axis can be determined by requiring the axial force of a beam segment in pure bending to be vanished

$$\int_A \sigma_x dA = \frac{b}{\rho} \int_{-h_0}^{h-h_0} E(\bar{z}) d\bar{z} = 0 \tag{7}$$

Where σ_x is the axial stress, and ρ is the beam curvature. By replacing $\bar{z} = z_1 - h_0$ in Equation 7, one can obtain the expression for h_0 in the form

$$h_0 = \int_0^{h_0} E(z_1) z_1 dz_1 \Big/ \int_0^{h_0} E(z_1) dz_1 = \frac{h(n+1)(2E_c + nE_m)}{2(n+2)(E_c + nE_m)} \tag{8}$$

Based on the first-order shear deformation beam theory, the strains of the beam can be written in the forms

$$\varepsilon_x = \bar{u}_{,x} + \frac{1}{2} w_{,x}^2 + z\chi \,,\ \gamma_{xz} = \bar{w}_{,x} - \bar{\theta} \tag{9}$$

In Equation 9, $\bar{u}, \bar{w}$ are the axial and transverse displacements with respect to the local system; $\chi = -\bar{\theta}_{,\bar{x}}$ is the beam curvature. Assuming linear elastic behaviour, the corresponding streesses are given by

$$\sigma_x = E(z)\varepsilon_x \,,\ \tau_{xz} = \psi G(x) \gamma_{xz} \tag{10}$$

With ψ denotes the shear correction factor.

Interpolations are introduced to the kinematics variables as

$$\bar{u} = N_u \bar{u}_j \ ,\ \bar{w} = \mathbf{N}_w^T \bar{\boldsymbol{\theta}} \,,\ \bar{\theta} = \mathbf{N}_\theta^T \bar{\boldsymbol{\theta}} \tag{11}$$

Where N_u , $\mathbf{N}_w^T$, $\mathbf{N}_\theta^T$ are respectively the matrices of shape functions for $\bar{u}$, $\bar{w}$, $\bar{\theta}$, and $\bar{\boldsymbol{\theta}} = \{\bar{\theta}_i \ \ \bar{\theta}_j\}^T$. The linear, quadratic and cubic polynomials function previously used by the authors[6] are again employed in the present work.

The membrane strain in Equation 9, however needs to be averaged for avoiding the membrane locking[8,9]

$$\varepsilon_{\text{av.}} = \frac{1}{l} \int_0^l \left(\bar{u}_{,x} + \frac{1}{2} \bar{w}_{,x}^2 \right) d\bar{x} = b_u \bar{u}_j + \frac{1}{2l} \boldsymbol{\theta}^T \int_0^l b_w b_w^T \, d\bar{x} \, \boldsymbol{\theta} \tag{12}$$

with l denotes the element length, and $b_u = N_{u,\bar{x}}$, $\mathbf{b}_w = \mathbf{N}_{w,\bar{x}}$.

From Equations 9 and 10, the virtual work can be written for the element in the form

$$\delta U = \int_V (\sigma_x \delta\varepsilon_x + \tau_{xz} \delta\gamma_{xz}) dV = \int_0^l \left(N\delta\varepsilon_{\text{av.}} + M\delta\chi + Q\delta\gamma_{xz} \right) dx \tag{13}$$

In Equation 13, N, M and Q are the stress resultants

$$N = \int_A \sigma_x dA = A_{11}\varepsilon_{\text{av.}} + A_{12}\chi,\ M = \int_A \sigma_x \bar{z} dA = A_{12}\varepsilon_{\text{av.}} + A_{22}\chi,\ Q = \int_A \tau_{xz} dA = \psi A_{33}\gamma_{xz} \tag{14}$$

with

$$(A_{11}, A_{12}, A_{22}) = \int_A E(\bar{z})(1, \bar{z}, \bar{z}^2) dA \ ,\ A_{33} = \int_A G(\bar{z}) dA \tag{15}$$

Substituting $\bar{z} = z_1 - h_0$, we can rewrite Equation 15 in the forms

$$(A_{11}, A_{12}, A_{22}) = b\int_0^h E(\bar{z}_1)(1, (z_1 - h_0), (z_1 - h_0)^2) dz_1,\ A_{33} = b\int_0^h G(\bar{z}_1) dz_1 \tag{16}$$

It is worthy to note that due to Equation 8 the axial-bending coupling term A_{12} defined by Equation 16 vanishes. From Equations 9, 10 and 12, one can compute the virtual strains and curvature in the forms

$$\delta\varepsilon_{\text{av.}} = b_u \delta u_j + \boldsymbol{c}_w^T \delta\bar{\boldsymbol{\theta}} \ , \ \delta\gamma_{xz} = \left(\boldsymbol{b}_w^T - \boldsymbol{N}_\theta^T\right)\delta\bar{\boldsymbol{\theta}} , \ \delta\chi = \boldsymbol{b}_\theta^T \delta\bar{\boldsymbol{\theta}} \tag{17}$$

With $\boldsymbol{b}_\theta = \boldsymbol{N}_{\theta,\bar{x}}$ and $\boldsymbol{c}_w = \varepsilon_{\text{av.},\bar{\boldsymbol{\theta}}}$. Substituting Equations 17 into Equation 13, one gets

$$\delta U = \int_0^l \left\{ N b_u \delta\bar{u}_j + \left[N\boldsymbol{c}_w^T + M\boldsymbol{b}_\theta^T + Q(\boldsymbol{b}_w^T - \boldsymbol{N}_\theta^T) \right] \delta\bar{\boldsymbol{\theta}} \right\} d\bar{x} \tag{18}$$

Equation 18 gives the local nodal forces in the forms

$$\bar{f}_u = \int_0^l N b_u \, d\bar{x} \ , \ \bar{\boldsymbol{f}}_\theta = \{\bar{f}_{\theta i} \ \ \bar{f}_{\theta j}\}^T = \int_0^l \left[N\boldsymbol{c}_w + M\boldsymbol{b}_\theta + Q(\boldsymbol{b}_w - \boldsymbol{N}_\theta) \right] d\bar{x} \tag{19}$$

The local tangent stiffness matrix for the element can be written in sub-matrices as

$$\bar{\boldsymbol{k}}_t = \begin{bmatrix} \bar{\boldsymbol{k}}_{uu} & \bar{\boldsymbol{k}}_{u\theta} \\ \bar{\boldsymbol{k}}_{u\theta}^T & \bar{\boldsymbol{k}}_{\theta\theta} \end{bmatrix} \tag{20}$$

The sub-matrices in (20) are computed as

$$\begin{aligned} &\bar{\boldsymbol{k}}_{uu} = \bar{f}_{u,\bar{u}_j} = \int_0^l b_u^2 A_{11} \, d\bar{x} \ , \ \bar{\boldsymbol{k}}_{u\theta} = \bar{f}_{u,\bar{\boldsymbol{\theta}}} = \int_0^l b_u \boldsymbol{c}_w^T A_{11} \, d\bar{x} , \\ &\bar{\boldsymbol{k}}_{\theta\theta} = \bar{f}_{\theta,\bar{\boldsymbol{\theta}}} = \int_0^l \left[\boldsymbol{c}_w A_{11} \boldsymbol{c}_w^T + N\boldsymbol{B} + \boldsymbol{b}_\theta A_{22} \boldsymbol{b}_\theta^T + \psi(\boldsymbol{b}_w - \boldsymbol{N}_\theta) A_{33} (\boldsymbol{b}_w^T - \boldsymbol{N}_\theta^T) \right] d\bar{x} \end{aligned} \tag{21}$$

In the above equation, $\boldsymbol{B} = \boldsymbol{c}_{w,\bar{\boldsymbol{\theta}}}^T$ is a symmetric matrix. Equations 19 and 21 together with Equation 4 and 5 completely define the element formulation.

3 NUMERICAL PROCEDURE

The nonlinear equilibrium equations for the structure can be written in the form[8]

$$\boldsymbol{g}(\boldsymbol{p}, \lambda) = \boldsymbol{q}_{in}(\boldsymbol{p}) - \lambda \boldsymbol{f}_{\text{ex.}} \tag{22}$$

where $\boldsymbol{p}$, $\boldsymbol{q}_{in}$ denote the structural nodal displacements and nodal force vectors, respectively; $\boldsymbol{f}_{\text{ex.}}$ is the fixed external loading vector and scalar λ is a load parameter. Equation 22 can be solved by an incremental-iterative procedure in which the norm of vector $\boldsymbol{g}$ is guided to zero[8]. In order to deal with the limit point, snap-through and snap-back situations, in which the structure tangent stiffness matrix ceases to be positive definite, the spherical arc-length constraint method is adopted herewith. The detail of the arc-length method and its implementation is described in detail by Crisfield[8].

4 NUMERICAL EXAMPLES

A number of numerical examples are presented in this section to illustrate the accuracy and efficiency of the formulated element and the described numerical procedure. The Poisson's ratio is assumed to be constant and a shear correction factor ψ=5/6 is chosen in all examples reported below.

4.1 Example 1: Cantilever beam under a tip moment

A cantilever beam formed from Silicon Nitride (Si_4Ni_4) and Aluminum (Al) with data: L=5 m, b=0.15 m, h=0.1 m, subjected to a moment M at its free end is considered. The Young's modulus and Poisson's ratio of Si_4Ni_4 are respectively 322.3 GPa and 0.24, and that of Al are 70 GPa and 0.3. The tip axial and transverse displacements, u and w, obtained by using an analytical method based on Bernoulli beam theory are as follows[11]

$$u = \frac{A_{22}}{M} \sin\left(L\frac{M}{A_{22}} \right) - L \ , \ w = \frac{A_{22}}{M}\left[1 - \cos\left(L\frac{M}{A_{22}} \right) \right] \tag{23}$$

Where A_{22} is the bending rigidity defined by Equation 16.

In Table 1, the normalized tip axial and transverse displacements of the Si_4Ni_4/Al beam obtained by different number of elements are given for a tip moment $M=5E_{Al}I/L$. The corresponding tip displacements computed by Equation 23 are also given in the table. As seen from the table, the results using element of the present work converge very fast, and both the axial and transverse tip displacements converge to the analytical solutions by using just six elements, regardless of the index n. Noting that the effect of the shift in the neutral axis position has been taken into account in both the present work and in reference[11], and the beam under consideration having a high aspect ratio, L/h=50.

		Number of elements				Equation 23
Response	n	1	2	4	6	
u/L	0.3	0.3063	0.3048	0.3048	0.3047	0.3047
	1	0.5805	0.5760	0.5758	0.5757	0.5757
	10	1.0310	1.0339	1.0339	1.0340	1.0340
w/L	0.3	0.5978	0.5990	0.5990	0.5991	0.5991
	1	0.7063	0.7139	0.7141	0.7143	0.7143
	10	0.5583	0.6106	0.6129	0.6130	0.6130

Table 1: Convergence of the element in computing tip response of cantilever beam

4.2 Example 2: Cantilever beam under a transverse tip load

The beam in sub-section 4.1 subjected to a transverse tip load P is analyzed. Due to the convergence stated in the previous sub-section, only six elements are employed to discrete the beam. The load-displacement curves of the beam are depicted in Figure 3 for various values of the index n. The figure clearly shows the effect of the material inhomogeneity on the response of the beam. Similar in case of the beam subjected to a tip moment, the displacements are larger for a beam associated with a higher index n, regardless of the applied load.

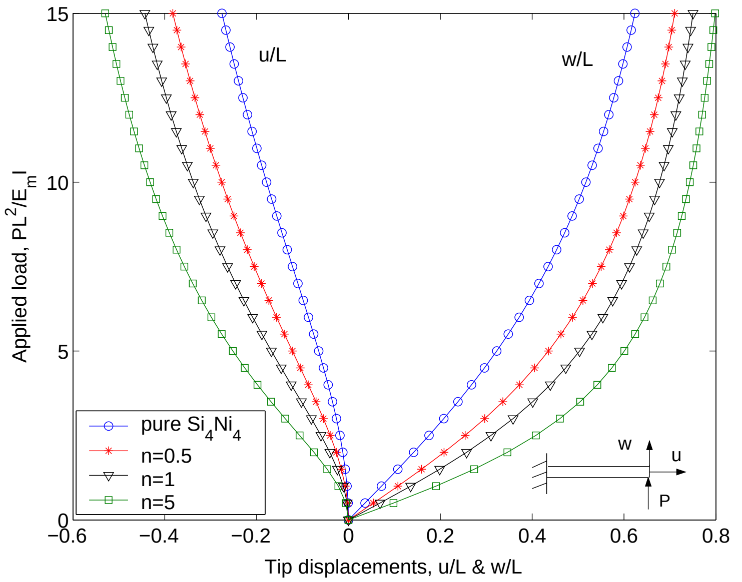

Figure 3: Load-displacement curves for Si_4Ni_4/Al cantilever beam under a tip load

		L/h				
Response	n	5	10	15	20	50
u/L	0.3	0.2455	0.2423	0.2416	0.2414	0.2412
	0.5	0.2806	0.2772	0.2765	0.2763	0.2761
	1	0.3428	0.3392	0.3385	0.3383	0.3380
	5	0.4388	0.4336	0.4326	0.4323	0.4319
w/L	0.3	0.6061	0.5939	0.5916	0.5908	0.5899
	0.5	0.6414	0.6284	0.6260	0.6252	0.6243
	1	0.6968	0.6821	0.6793	0.6784	0.6773
	5	0.7747	0.7509	0.7464	0.7449	0.7432

Table 2: Tip displacements of cantilever Si_4Ni_4/Al beam with different aspect ratios

In order to study the capability of the formulated element in modelling the shear deformation effect, the beam with different values of aspect ratio, L/h, subjected to the transverse load P at its free end is considered. Keeping the height and width of the beam as above, for L/h=5, 10, 15, 20 and 50, the computation is performed with the beam length L=0.5, 1, 1.5, 2 and 5 m, respectively.

In Table 2, the axial and transverse tip displacements of the beam with different aspect ratios at an applied load $P=10E_{Al}I/L^2$ are given for various values of the index n. As seen from the table, both the axial and transverse displacements steadily reduce when raising the aspect ratio, regardless of the index n. By examining the table in more detail one can see that the influence of the aspect ratio on the response of the beam depends upon the percentage of the constituent material which is defined through the index n. For example, when increasing the aspect ratio L/h from 5 to 50, the transverse displacement reduces 2.67% for a beam with n=0.3, but these values are 2.68%, 2.80% and 4.07% for the beam associated with n=0.5, 1 and 5, respectively. The numerical results obtained in this sub-section show the good capability of the proposed element in modeling the shear deformation of the FGM beam structures.

Constituents	$h_0 \neq h/2$	$h_0 = h/2$	Difference (%)
Al and $Zr0_2$	0.7767	0.7753	0.18
Al and Si_4Ni_4	0.7307	0.7293	0.19
Al and Al_2O_3	0.7192	0.7159	0.46

Table 3: Tip deflection of cantilever beam made of diffrenet constituent materials

To study the effect of the neutral axis position on the large displacement response of FGM beam structure, the tip deflection of the cantilever beam composed of different constituents is computed, and the numerical results are listed in Table 3. In the table, the modulus of Zirconia ($Zr0_2$) is 152.2 GPa and that of Alumina (Al_2O_3) is 390 GPa. The Poisson's ratio of both materials is 0.3. The element ignored the effect of the shift in the neutral axis position is denoted by $h_0=h/2$, and in this case the A_{ij} in Equation 16 are computed by setting $h_0=h/2$. As seen from the table, the deflection computed by the element ignoring the shift in the neutral axis position is slightly smaller than that obtained by the element taking the effect into consideration. The difference in the computed deflection increases for the beam with sharper gradient in the thickness direction.

4.3 Example 3: Lee's frame

An asymmetric frame subjected to a downward load P as shown in lower part of Figure 4 is investigated. The isotropic frame exhibits snap-through and snap-back behaviour[9], and thus this example can be used as a good example to further test the formulated beam element and computer code. The geometric data for the frame are: L=120 cm, b=3 cm and h=2 cm.

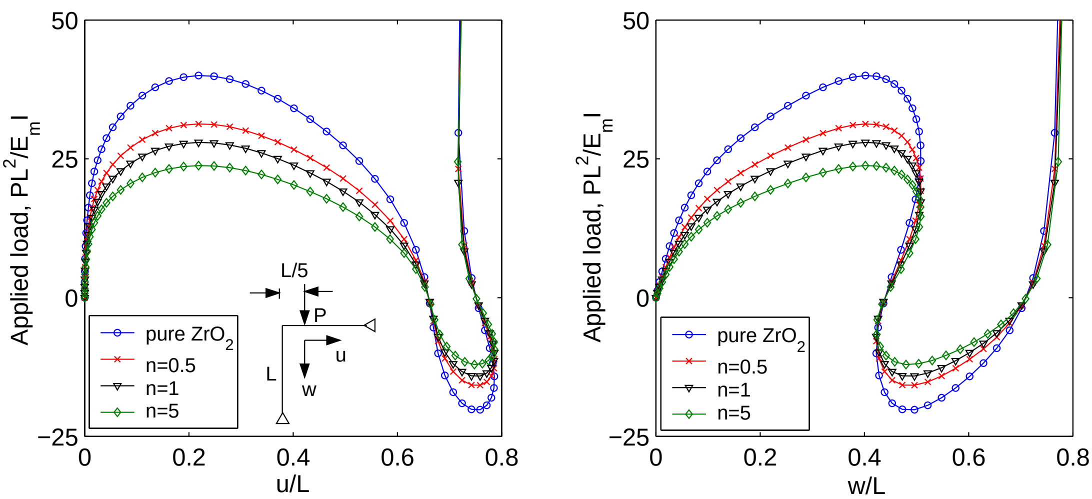

Figure 4: Load-displacement curves for Si_4Ni_4/Al Lee's frame

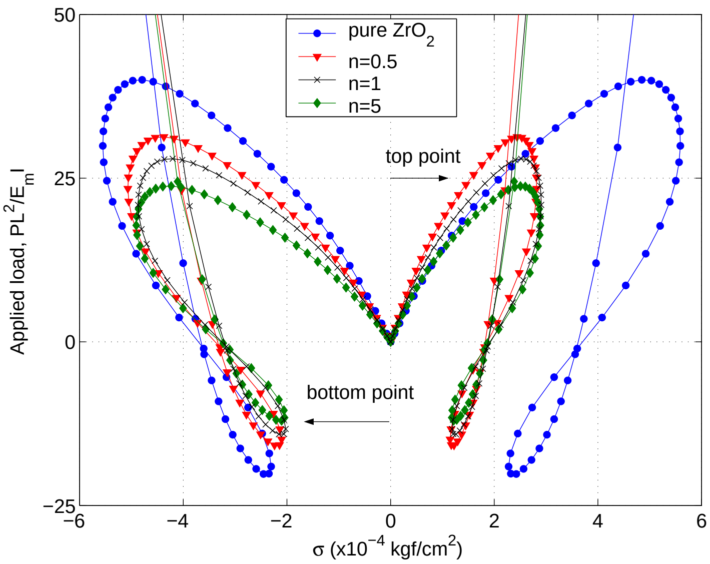

Figure 5: Axial stress versus load for ZrO_2/Al Lee's frame

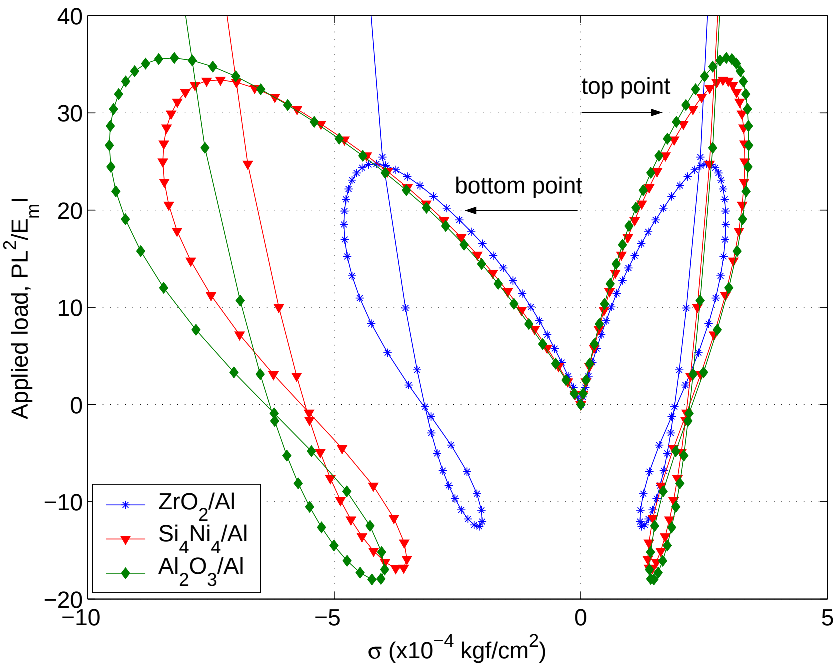

Figure 6: Axial stress versus applied load for Lee's frame composed of different materials

The load-displacement curves of the frame composed of Zirconia and Aluminum are shown in Figure 4 for various values of the index *n*. In the figure, the axial and vertical displacements were computed at the loaded point by using ten elements, five for each beam. The influence of the material distribution on the behavior of the frame is clearly seen from the figure, where the limit load of the frame steadily reduces when increasing the index *n*. In Figure 5 the axial stresses at the top and bottom points of the loaded section versus the applied load is shown for the ZrO_2/Al Lee's frame with various values of the index *n*. As seen from the figure, while the axial stress at the points of an isotropic beam is symmetric with respect to the mid-plane, the amplitude of the compressive stress is considerably higher than that of the tensile stress. In Figure 6, the axial stresses at the top and bottom points of the loaded section versus the applied load is shown for the Lee's frame composed of different constituent materials. The figure clearly shows the influence of the constituents on the stress at the points of the beam, and both the maximum compressive and tensile stresses increase for the beam composed of ceramic with higher Young's modulus.

4.4 Example 4: Williams' toggle frame

Finally, the Williams' toggle frame under a downward load P as shown in lower right part of Figure 7 is analyzed. The load-displacement curves of the homogeneous frame show snap-through behaviour[9], and thus the displacement control technique or the arc-length control method (employed herewith) is necessary to use in tracing equilibrium paths of the frame. The frame is assumed composed of Zirconia and Aluminum as above. The data for computation are as follows: L=12.934 in. (0.3285 m), H=0.386 in. (0.0098m), b=0.753 in. (0.0191 m), h=0.243 in. (0.0062 m). The frame is discretized by using eight elements, four for each beam. The vertical displacements at the loaded point versus the applied load are shown in Figure 7 for various values of the index n. The influence of material inhomogeneity defined through the index n on the limit load of the FGM frame is clearly seen from the figure, where a lower index n results in a higher limit load.

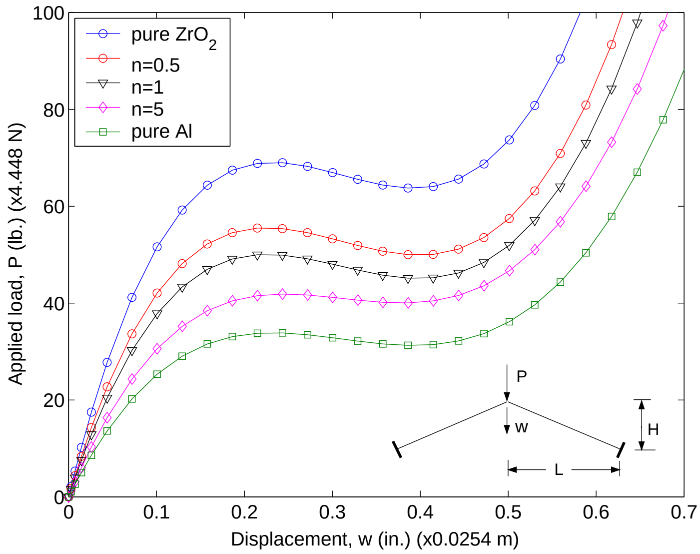

Figure 7: Load-displacement curves for Williams' toggle frame.

5 CONCLUSIONS

A finite element procedure based on the co-rotational approach for large displacement analysis of planar FGM beam structures has been presented. The material properties of the structures are assumed to be graded in the thickness direction by a power-law distribution. The finite element formulation based on the first-order shear deformation beam theory was formulated by taking the shift in the neutral axis position into account. An incremental-iterative procedure in combination with the arc-length control method was employed in solving the nonlinear equilibrium equations. Numerical examples were presented to demonstrate the accuracy and efficiency of the formulated element and illustrate its versatility. Results show that convergence of the proposed element is fast and that the large displacement response of structures can be accurately assessed using a few of the formulated elements. The numerical results have also demonstrated the capability of the formulated element in modeling the effects of shear deformation and material inhomogeneity. Results from the present set of examples have revealed that the FGM beam and frame structures associated with a larger value of the power-law index endure larger displacements than those with a smaller power-law index. It is necessary to note that the material is assumed to be linearly elastic in the present work. As demonstrated in the numerical examples, the stress increases when the structure undergoes large displacements, and it might exceed the yield stress at some points. More work is necessary to deal with the large displacement analysis of elastic-plastic FGM beam and frame structures.

ACKNOWLEDGEMENT

The support from VAST-RFBR Program (Project No.VAST.HTQT.NGA.07/14-15) to the second author is gratefully acknowledged.

REFERENCES

[1] D.K. Jha, T. Kant and R.K. Singh, A critical review of recent research on functionally graded plates, *Compos. Struct.*, 96 (2013) 833-849.

[2] G.N. Praveen, J.N. Reddy, Nonlinear transient thermoelastic analysis of functionally graded ceramic-metal plates, *Int. J. Solids Struct.*, 35 (1998) 4457-4476.

[3] A. Chakraborty, S. Gopalakrishnan, J.N. Reddy, A new beam finite element for the analysis of functionally graded materials, *Int. J. Mech. Sci.*, 45 (2003) 519-539.

[4] Y.Y. Lee, X. Zhao, J.N. Reddy, Postbuckling analysis of functionally graded plates subjected to compressive and thermal loads, *Comput. Methods Appl. Mech. Eng.*, 199 (2010) 1645-1653.

[5] D.K. Nguyen, Large displacement response of tapered cantilever beams made of axially functionally graded material, *Compos. Pt B Eng.*, 55 (2013), 298-305.

[6] D.K. Nguyen, B.S. Gan, Large deflections of tapered functionally graded beams subjected to end forces, *Appl. Math. Model.*, (2014), http://dx.doi.org/10.1016/j.apm.2013.11.032.

[7] D.K. Nguyen, B.S. Gan, T.H. Trinh, Geometrically nonlinear analysis of planar beam and frame structures made of functionally graded material, *Struct. Eng. Mech.*, 49 (2014), 727-743.

[8] M.A. Crisfield, *Non-linear finite element analysis of solids and structures*. Volume 1: Essentials, John Wiley & Sons, Chichester (1991).

[9] C. Pacoste, A. Eriksson, Beam elements in instability problem, *Comput. Methods Appl. Mech. Eng.*, 144 (1997) 163-197.

[10] D.K. Nguyen, A Timoshenko beam element for large displacement analysis of planar beams and frames, *Int. J. Struct. Stab. Dynam.*, 12 (2012) DOI: 10.1142/S0219455412500484.

[11] Y.A. Kang, X.F. Li, Bending of functionally graded cantilever beam with power-law nonlinearity subjected to an end force, *Int. J. Non-linear Mech.*, 44 (2009) 696-703.

THE BOLTS AND COMPRESSED PLATES MODELLING

L. Gödrich, M. Kurejková, F. Wald and Z. Sokol

Czech Technical University in Prague, Faculty of Civil Engineering,
Department of Steel and Timber Structures, Thákurova 7, Praha 6, Czech Republic
e-mail: lukas.godrich@fsv.cvut.cz, webpage: http://www.ocel-drevo.fsv.cvut.cz

Keywords: Steel structures, bolted connection, bolts in tension and shear, triangular stiffener, finite element method, reduced stress method.

Abstract. *The paper is focused on modelling of the bolts in tension and plate in bending and of compressed plate in structural steel connection by analytical and finite element models. The procedure for creating a Design finite element model (DFEM) with shell elements and a Component based finite element model (CBFEM) with shell elements and component elements for bolts, weld, and compressed plate, is discussed. The proposed procedure is evaluated on published and performed experiments.*

1 INTRODUCTION

End-plate joints are due to their simplicity and cost one of the most common connection type in steel structures. End-plate joints are usually designed using analytical component based method (CBM). This method allows relatively precise design of joints with usual geometry. Designed joint must contain only known components which are described in the design codes or literature. Another limitation of the CBM can be faced when the joint is loaded by combinations of internal forces, as some combinations (for example combination of strong and weak axis bending moments or combination with the axial force) are not supported. Silva (2008) [1] creates a matrix that takes into account the influence of a combination of internal forces. However, this issue of interaction is inaccurate and complex form its principle and its approval is just at the beginning.

Design finite element model (DFEM) and Component based finite element model (CBFEM) are getting common for design of joints as an alternative solution. Application of Research finite element model (RFEM) is time-consuming. Introduction of non-linearity of the bolts, welds or compressed plates exhibiting stability problems bring difficulties. Prediction of failure of individual parts of the joint is unclear because of stress peaks. Despite these problems, many numerical models have already been created in the past [2]. These models were usually used for parametric studies and were based on the results of experiments. Results of these studies are useful, however these studies did not consider the possibility of using finite element method for everyday design of joints to make it available as an alternative approach to the design of joints using component method. This paper examines numerical models of bolts and compressed plates as first step to create the Component based model (CBM) and the Design finite element model (DFEM) or Component based finite element model (CBFEM) of end plate joint.

2 BOLT IN TENSION AND PLATE IN BENDING

2.1 Bolts in tension

Several analytical models of bolts in tension have been developed. These analytical models consider linear behaviour with initial stiffness up to bearing capacity of the bolt. The most commonly used procedure is the T stub model published in chapter 6 of EN1993-1-8:2008. For bolt elongation developed Agerskov (1976) [3] an analytical model that considers the deformation of the shank and thread, nut and washers according to equations (1), (2), and (3), respectively. Initial stiffness is determined from the sum of deformations of these parts.

$$\Delta \mathrm{l_{shank}} = \Delta l_s + \Delta l_t = \frac{N_t}{EA_s} l_s + \frac{N_t}{EA_t}\left(l_t + \frac{l_n}{2}\right) \tag{1}$$

$$\Delta \mathrm{l_n} = \frac{N_t}{2EA_n} l_n \tag{2}$$

$$\Delta \mathrm{l_w} = \frac{N_t}{EA_w} l_w \tag{3}$$

where subscripts n, s, t, w refer to nut shaft, thread and washer, respectively.

Similar approach is used in the analytical model according to the German guideline VDI2230 [4] equations (4), (5), and (6) and according to Barron and Bickford (1998) [5] equation (7). These two models consider deformation caused by stripping of the threads in thread-nut contact area in addition.

$$\Delta \mathrm{l_b} = \Delta l_{b1} + \Delta l_{b2} = \frac{N_t}{EA_s}(l_s + 0{,}4 d_b) + \frac{N_t}{EA_t}(l_t + 0{,}85 d_b) \tag{4}$$

$$\Delta \mathrm{l_w} = \frac{N_t}{EA_p} l_w \tag{5}$$

where $$\mathrm{A_p} = \frac{\pi}{4}(d_h^2 - d_{w1}^2) + \frac{1}{2}(d_{w2}^2 - d_h^2) tan^{-1}\left[\frac{0{,}75 d_h (l_w - d_h)}{(d_{w2}^2 - d_{w1}^2)}\right] \tag{6}$$

in which d_b, d_h, d_{w1} and d_{w2} denotes bolt shank diameter, head diameter, washers inner and outer diameters, respectively. Stiffness is determined from the sum of deformations Δl_b and Δl_w.

$$\frac{1}{\mathrm{K_b}} = \frac{f d_b}{EA_s} + \frac{l_s}{EA_s} + \frac{l_t}{EA_t} + \frac{f d_b}{EA_t} \tag{7}$$

where f is a correlation factor determined by Swanson [6] as the average value 0,73.

Simplified procedure is used in Eurocode 3 when constant cross-section corresponding to the core is used along entire length of the bolt which is taken as the clamping length. The stiffness calculated from these data is then reduced to 80%, see equation (8).

$$K = \frac{0{,}8 EA_t}{l_b} \tag{8}$$

where $$l_b = l_s + l_t + \frac{l_h + l_n}{2} \tag{9}$$

and l_h denotes length of the bolt head.

In addition to these analytical models many numerical models of the bolts have been created. Many approaches that use different element types were applied to numerical models of the bolts in the past. Tarpy and Cardinal (1981) [7] created 2-D models and used shell elements for bolts. 3-D models started to be used when powerful computers were available. In these models, spring elements were used by Bahaari and Sherbourne (1996) [8] and beam elements by Bursi and Jaspart (1998).

Later, solid elements were applied to model of bolts. However, some simplifications were necessary in numerical models because of the time and computational limits. Kukretti and Zhou (2006) [9] created a numerical model of the bolts, which neglected the washers and considered a constant nominal diameter of the bolt shank along the entire length. Chen and Du (2007) [10] neglected washers in its model too and considered a constant effective diameter of the shanks along the entire length. Wheeler et al. (2000) [11] developed a model that considers the nominal diameter in the shank and effective diameter in the threaded part. Washers are usually introduced as increase of the height of the bolt head and nut. The length of the shank or the thread corresponds to total thickness of steel plates in all three above mentioned models. Gantes et al. (2003) [12] considered effective length of the shaft according to Agerskov's model (1976). This model takes into account the deformation of the nut and thread. Washers in this model are considered by increasing the height of the bolt head and nut.

Wu et al. (2012) [13] tried to create the accurate model of the bolt, in which the separate washers and the thread are modelled. This model cannot be used in the T-stub or the joint model due to its complexity. The results were compared to the results of the four above-mentioned simplified models. Based on this comparison, new simplified model based on the model by Wheeler et al. (2000) was created. The washers were introduced as increased height of the bolt head and nut but were separated from the bolt shank in this model. This modification takes into account the correct length of the bolt shank and the model exhibits more accurate behaviour.

2.2 Finite element model of initial stiffness

Numerical model is created in Midas FEA software. A solid numerical model of the bolt was created first and spring model was created based on the results of solid model. Spring model is much easier to create and less time consuming. Both bolts models were integrated into the T-stub model and the results of both models were compared.

Solid numerical model is based on the model by Wu et al. (2012). Nominal diameter is considered in the shank and effective core diameter is considered in the threaded part. Washers are coupled with bolts head and nut. Deformation caused by stripping of the threads in thread-nut contact area is simply modelled using interface elements. These interface elements are unable to transfer tensile stresses. Constant shear modulus was determinate to 7000N/mm^3 and normal stiffness modulus in compression is determinate as 10E/a where E is Young's modulus and is the element size. Numerical model was calibrated according to results of Wu et al. (2012) model and several analytical models.

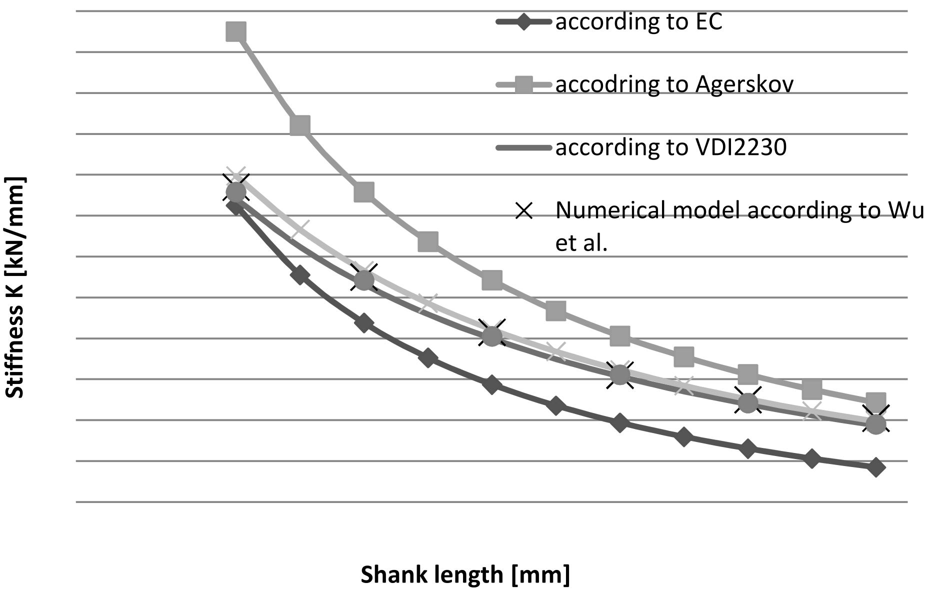

Figure 1: Parametric study of bolts initial stiffness, parameter shank length

Calibration of numerical model was done on bolt M20 with thread length of 10 mm and shank length as variable parameter. Comparison of the results is shown in Figure 1. Developed numerical model shows good agreement with model by Wu et al. Analytical model according to the VDI2230 fits good to results of numerical models and it is used for the other parametric studies of developed model. Parametric study for bolt M20 with shank length 20 mm was done. Thread length was a parameter in this case. Initial stiffness of developed numerical model was compared to analytical models because there were no data of numerical model by Wu et al. for this case of study. Results of parametric study of thread length are shown in Figure 2.

The same parametric studies were done for bolts M16, M24, M27 and M30. Initial stiffness calculated by the developed numerical model fits to results of analytical model according to the German VDI2230 very good in all cases.

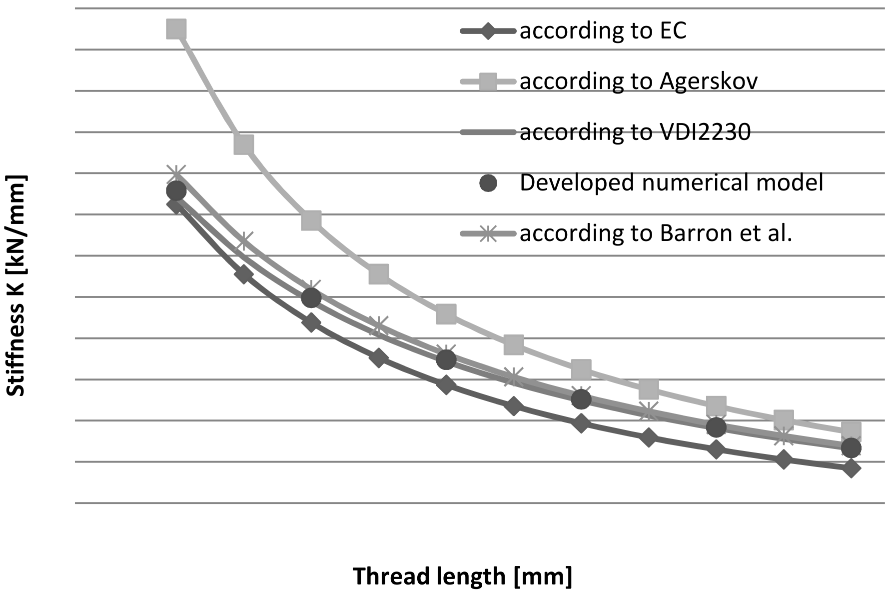

Figure 2: Parametric study of bolts initial stiffness, parameter thread length

2.3 Force-deformation diagram

Bilinear stress-strain diagrams were used in the second step. Bolt grades 4.6, 5.6, 8.8 and 10.9 were investigated. Characteristic values for yield stress f_y and ultimate strength f_u were considered. Maximal plastic strain is considered 5%. Some bolts shows bilinear or in some cases trilinear behaviour up to design tensile resistance according to EC. Such behaviour shows bolts of material with ratio f_u/f_y higher than γ_{M2}/k_2=1,25/0,9=1,39. Above mentioned analytical models consider only linear behaviour of bolt. Therefore, analytical model according to the VDI2230 was extended. Force-displacement diagram of bolt according to extended analytical model is shown on Figure 3. Initial stiffness E_{ini} is considered according to the VDI2230. Forces $F_{y,t}$, $F_{y,s}$, and $F_{u,t}$, correspond to initialization of thread yielding, shank yielding and threat rupture, respectively. Plastic deformations of the thread $\delta_{pl,t}$ and shank $\delta_{pl,s}$ are given by Eq. (10), (11). Shank yielding occurs only in some cases.

$$\delta_{\mathrm{pl,t}} = \frac{F-F_{y,t}}{E_{pl}A_t}(l_t - cd_t) \tag{10}$$

$$\delta_{\mathrm{pl,s}} = \frac{F-F_{y,s}}{E_{pl}A_s} l_s \tag{11}$$

In the above formulas, A_t, A_s, l_t, l_s, and d_t denotes thread cross section area, shank cross section area, length of thread, length of shank and threaded part diameter, respectively. Correlation factor c considers unequal stresses distribution in the threaded part shown in Figure 4. Its value depends on bolt grade, l_s/l_t ratio and is in range from 0,3 to 0,6. Plastic modulus E_{pl} is given by equation (12).

$$\mathrm{E_{pl}} = \frac{f_u - f_y}{\varepsilon_{pl}} \tag{11}$$

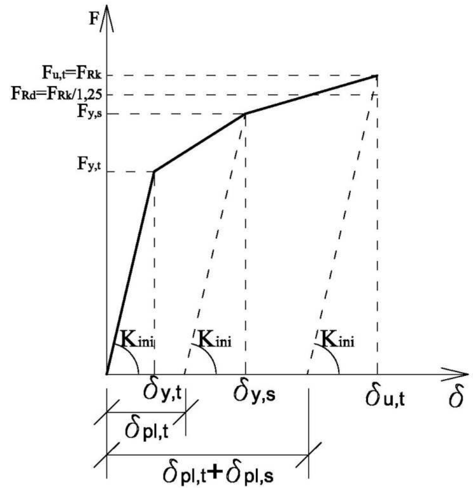

Figure 3: Force-displacement diagram according to developed analytical model

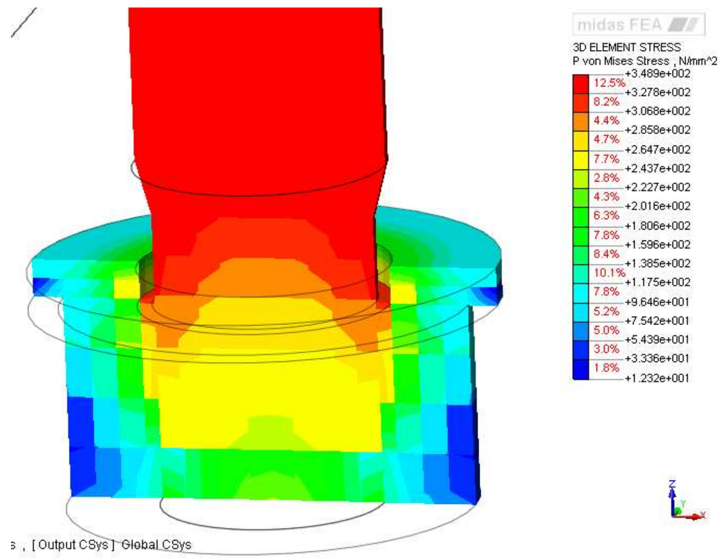

Figure 4: Unequal stresses distribution in the threaded part of the bolt

Comparison of force-displacement diagrams is shown in Figure 5. This comparison is made for two bolts M24 grade 8.8 with length of the shank 50 mm. The graph on the left shows the force-displacement diagram for bolt with thread length of 17,6 mm and the graph on the right shows force-displacement diagram for bolt with thread length of 28,2 mm.

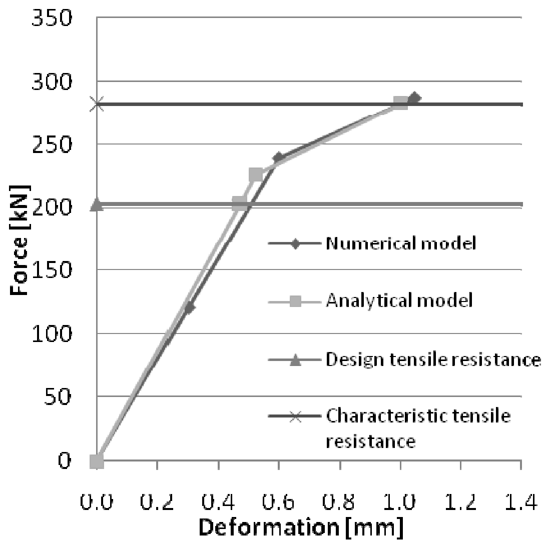

a)

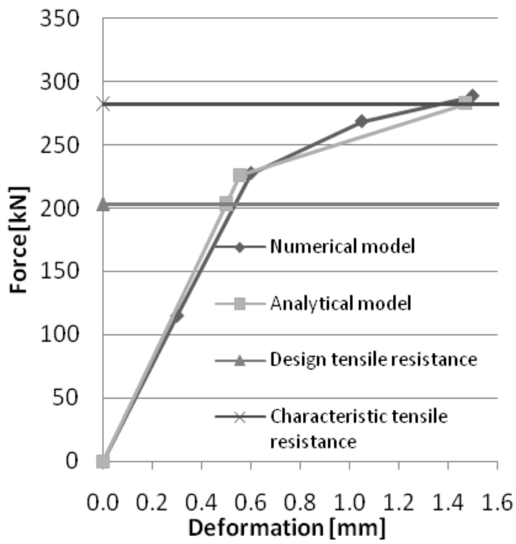

b)

Figure 5: Force-displacement diagrams for bolts M24 grade 8.8. Thread length 17,6 mm a), thread length 28,2 mm b).

2.4 T-stub

The accuracy of the bolts behaviour was subsequently validated on experiments of two T-stubs performed at the CTU Prague. T-stubs were made from hot-rolled sections HEB300 and HEB400 and were connected by two bolts M24 8.8. Two different numerical models have been created. The first numerical model considers a detailed solid model of the bolt, shown in Figure 6a. One quarter of the sample was modelled for the reason of symmetry. Comparison of results of the numerical models to experimental results for both experiments are shown on graphs in Figure 7.

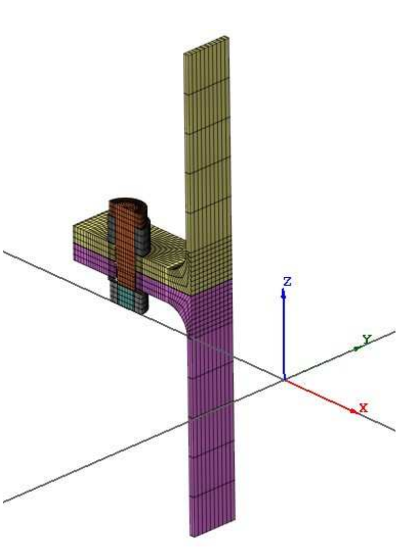

a)

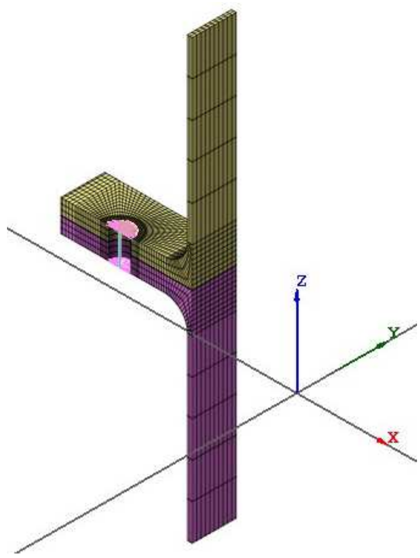

b)

Figure 6: T-stub model a) with solid element bolts, b) with spring element bolts

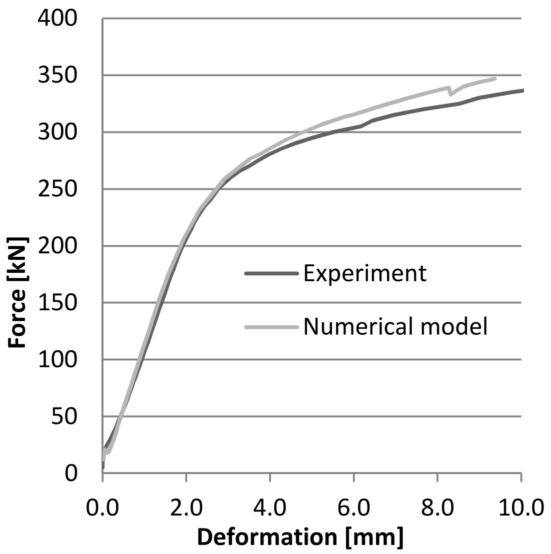

a)

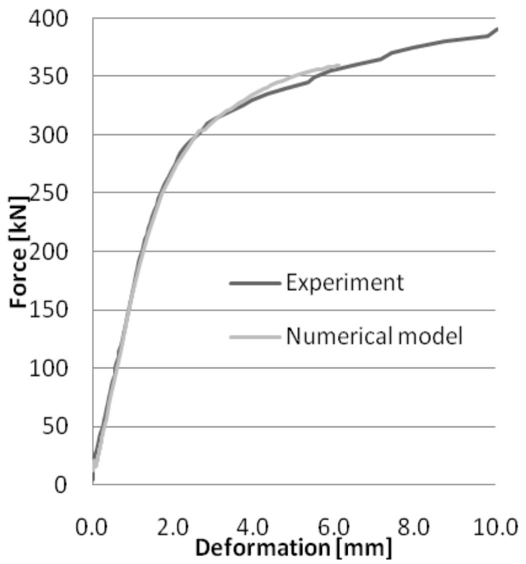

b)

Figure 7: Force-deformation diagrams for T-stubs, HEB300 sample a), HEB400 sample b).

The spring elements are used for the bolts in second model, see Figure 6b. Rigid elements are used on the ends of spring to transmit forces into the flange of the T-stub. Bilinear stress-strain diagram according to the proposed analytical model has been set for spring elements. Connection point of rigid elements to the flange significantly affects the behaviour of T-stub. The graphs in Figure 8 show influence of the radius of the rigid elements. Three different radii of rigid elements were chosen. The first corresponds to bolt-hole radius, the second corresponds to outer radius of the bolt head and the third corresponds to middle radius of the bolt head. It is clear that the radius of the rigid elements corresponds to middle radius of the bolt head shows the best agreement with experiment. Model with spring element bolts shows a slightly smaller stiffness compared to model with solid element bolts, see Figure 9. This is due to omitted bending stiffness of the spring elements.

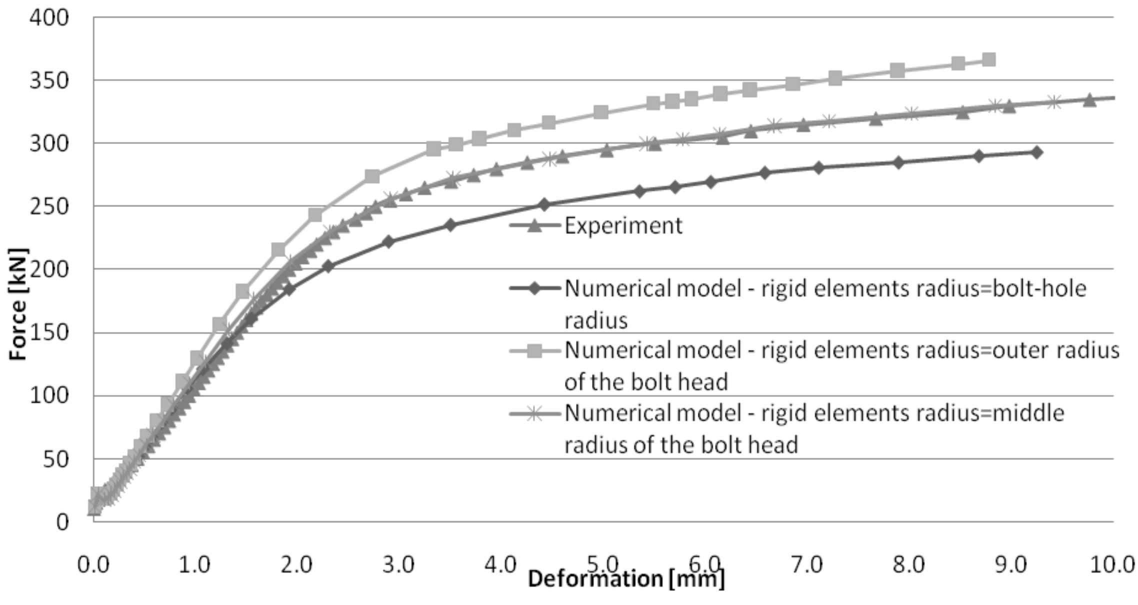

Figure 8: Influence of the radius of the rigid elements to T-stub deformation

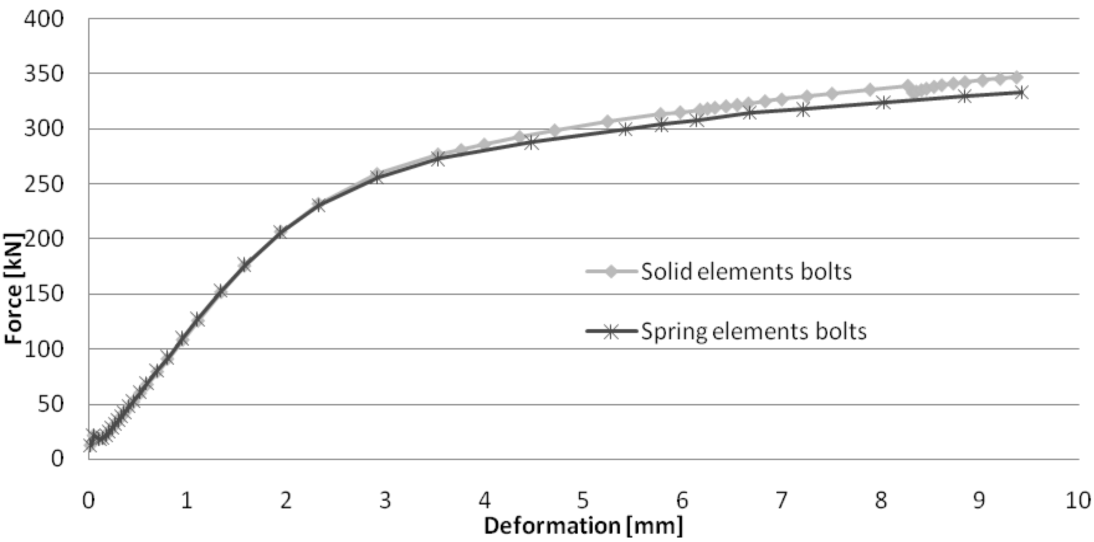

Figure 9: Comparison of solid elements bolt model and spring elements bolt model

4 COMPRESSED PLATES

4.1 Models

Generally the design of compressed plates could be solved by two approaches. The first one is based on geometric and material nonlinear analysis with imperfections. Modelling of imperfections in complex connections may be complicated task and the analysis is time-consuming. The second approach is based on material nonlinear and geometric linear analysis without imperfections and manual verification of compressed slender plates. For the verification is proposed to use reduced stress method provided in EN 1993-1-5 [14]. The verification is based on the von-Mises yield criterion and sums up the load effects of normal and shear stresses

$$\left(\frac{\sigma_{x,Ed}}{\rho_x f_y/\gamma_{M1}}\right)^2 + \left(\frac{\sigma_{z,Ed}}{\rho_z f_y/\gamma_{M1}}\right)^2 - \left(\frac{\sigma_{x,Ed}}{\rho_x f_y/\gamma_{M1}}\right)\left(\frac{\sigma_{z,Ed}}{\rho_z f_y/\gamma_{M1}}\right) + 3\left(\frac{\tau_{Ed}}{\chi_w f_y/\gamma_{M1}}\right)^2 \leq 1 \tag{13}$$

4.2 Verification

The verification procedure is divided in four steps. In first step is performed the material nonlinear analysis without imperfections of the connection model. In second step is a compressed plate separated from the connection and the boundary condition and stress distribution are determined. In the next step is carried out linear buckling analysis to obtain the first eigenmode and critical buckling factor of the separated plate. In the last step are determined reduction factors ρ_x, ρ_z and χ_w for longitudinal, transverse and shear stress and the plate is verified using reduced stress method.

An example of numerical model with triangular stiffener in beam-column connection is shown in Figure 10. The numerical model is created in Dlubal RFEM software, using shell elements and bilinear material model with strain hardening. The plasticization in stiffener is significant, although it is not clear, if the ultimate resistance is reached.

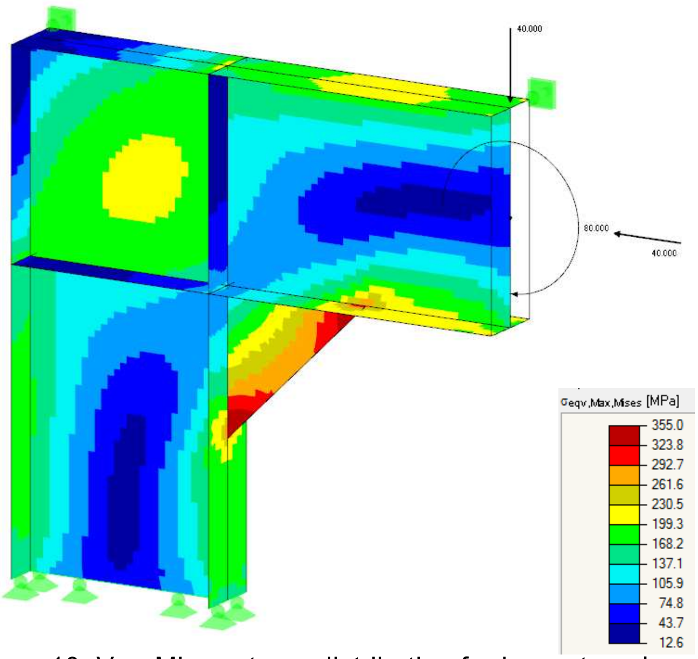

Figure 10: Von-Mises stress distribution for beam-to-column joint

The triangular stiffener is taken out of the model, boundary conditions are chosen CCF (clamped, clamped, free edge) and the stress distribution is applied, as shown in Figure 11a).In Midas FEA software are for the given boundary conditions and stress distribution calculated first eigenmode and critical buckling factor as shown in Figure 11b).

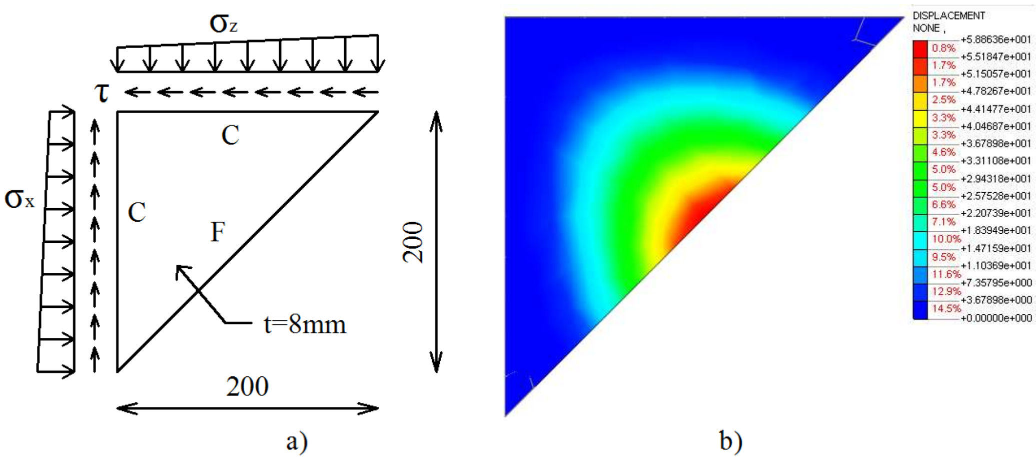

Figure 11: Triangular stiffener
a) boundary conditions and stress distribution b) first eigenmode

Reduction factors for longitudinal, transverse and shear stress may be determined from buckling curves according to EN 1993-1-5 or using geometric and material nonlinear analysis. Buckling curves are verified for square or rectangular plates but not for non-regular shapes as triangular. For this example are reduction factors determined in Midas FEA. Finally the sum of the load effects shows that the verification is not satisfied and ultimate strength is overstepped.

5 CONCLUSIONS

The current analytical models consider only linear behaviour of the bolts. This simplification may be inaccurate, especially for bolts of materials with the f_u/f_y ratio higher than γ_{M2}/k_2 = 1,25/0,9 = 1,39 for the Design finite element model (DFEM) or Component based finite element model (CBFEM). Analytical model according to the VDI2230 was extended to plastic deformations. Detailed numerical model can be used for an accurate description of the behaviour of the bolts. Numerical model, based on the model by Wu et al. (2012) was created. Developed numerical model differs by using interface elements to consider deformation caused by stripping of the thread in the thread-nut contact area. The proposed numerical model is much less time consuming. Despite the simplification, a detailed numerical model is still very time consuming and cannot be used for everyday design, therefore spring model of the bolt was created. Rigid elements are used at the ends of the spring elements to transmit forces into the flange. The spring model was validated by the results of T-stub experiments. The Research finite element model (RFEM)of T-stub with spring element bolts shows slightly lower stiffness because of neglected bending stiffness. Differences in stiffness are negligible and can be ignored. The spring element bolt is time-saving and can be advantageously used for the design by CBM, DFEM, and CBFEM of end-plate joints.

It is proposed to use the reduced stress method for the Design finite element model (DFEM) or Component based finite element model (CBFEM) of compressed plates in connections. The verification example shows that compressed plates could be in finite element models designed without applying imperfections. Essential part of the following research is verification of buckling curve for non-regular plate shapes such as triangular. Using the buckling curve instead of nonlinear analysis will reduce the calculation time. The procedure will be validated on the published and newly prepared experiments of stiffeners with different types of support, free edge, partially stiffened and clamped.

ANNOUNCEMENT

The work was prepared under work the project MERLION of Czech Republic Technical No. TA02010159.

REFERENCES

[1] Simoes da Silva, L.:*Towards a consistent design approach for steel joints under generalized loading*, Journal of Construction Steel Research, Vol. 64, pp. 1059-1075, (2008).

[2] Bursi, O. S. and Jaspart, J. P.:*Basic issues in the finite element simulation of extended end plate connections*, Computer & Structures, Vol. 69, No. 3, pp. 361-382, (1998).

[3] Agerskov, H.:*High-strength bolted connections subject to prying*, Journal of Structural Division, ASCE, Vol. 102, No. 1, pp. 161-175, (1976).

[4] VDI2230 *Systematic Calculation of high Duty Bolted Joints – Joints with One Cylindrical Bolt*, Association of German Engineers, Berlin, Germany, (2003).

[5] Barron, J. and Bickford, J. H.: *Handbook of Bolts and Bolted Joints: Computing the Strength of a Fasteners*. Marcel Dekker, Inc. (1998).

[6] Swanson J.A.:*Characterization of the strength, stiffness and duktility behavior of T-stub connections*. Ph.D. dissertation. Atlanta (USA): Georgia Institute of Technology; (1999).

[7] Tarpy, T. S. and Cardinal J. W.:*Behavior of semi-rigid beam-to-column endplate connectins*. Joints in Structural Steelwork, Pentech Press, London,(1981).

[8] Bahaari, M. R. and Sherbourne, A. N.:*Structural behavior of end-plate bolted connections to stiffened columns*, Journal of Structural Engineering, Vol. 122, No. 8, pp. 926-935, (1996).

[9] Kukreti, R. and Zhou F. F.:*Eight-bolt endplate connection and its influence on frame behavior*, Engineering Structures, Vol. 28, No. 11, pp. 1483-1493, (2006).

[10] Chen, S. M. and Du, G.:*Influence of initial imperfection on the behavior of extended bolted end-plate connections for portal frames*, Journal of Construction Steel Research, Vol. 63, No. 2, pp. 211-220, (2007).

[11] Wheeler A. T., Clarke M. J., and Hancock, G. J.:*FE Modeling of Four-bolt Tubular Moment End-plate Connections*, Journal of Structural Engineering, Vol. 126, No. 7, pp. 816-822, (2000).

[12] Gantes, C. J. and Lemonis, M. E.:*Influence of equivalent bolt length in finite element modeling of T-stub steel connections*, Computer & Structures, Vol. 81, No. 8-11, pp. 595-604, (2003).

[13] Wu, Z., Zhang, S. and Jiang, S.: *Simulation of tensile bolts in finite element modeling of semi-rigid beam-to-column connections*, International Journal of Steel Structures, Vol. 12, No. 3, pp. 339-350, (2012).

[14] EN 1993-1-5*, Eurocode 3: Design of steel structures - Part 1-5: Plated Structural Elements,* (2007).

12th International Conference on
Steel, Space and Composite Structures
28-30 May 2014, Prague, Czech Republic

NEW EUROPEAN SEISMIC REGULATIONS FOR THE QUALIFICATION AND DESIGN OF POST-INSTALLED ANCHORING

Jorge Gramaxo

Hilti Corporation
100 Feldkircherstrasse, Liechtenstein 9494
e-mail: jorge.gramaxo@hilti.com, webpage: http://www.hilti.com/seismic

Keywords: Anchors, Qualification, Design, Seismic

Abstract. *Under seismic loading, the performance of a connection in a structure is crucial either to its stability or in order to avoid casualties and major economic impacts, due to the collapse of non-structural elements. In the United States the anchor seismic resistance shall be evaluated in accordance with ACI 318 Appendix D. Created in accordance with the ACI 355.2 regulated testing procedures and acceptance criteria ICC-ES AC193 and AC308, pre-qualification reports provide sound data in a proper design format. With the release of the ETAG 001 Annex E in the first half of 2013, the seismic pre-qualification of anchors became regulated in Europe. Anchors submitted to these new test procedures will now also incorporate in the ETA (European Technical Approval) all the required technical data for seismic design. Until the release of the EN 1992-4, planned for 2015, EOTA TR045 (Technical Report) will set the standard for the seismic design of steel to concrete connections. Therefore, the design framework for the seismic design of anchors is already available through both the U.S. and European regulations.*

1 BACKGROUND AND RECOMENDATIONS

In all parts of the world, seismic design methodologies not only for primary structures, but also including equipment, installation and other non-structural element supports have significantly gained in importance over the past years. This does not apply solely to "classical" earthquake regions, but also to Central Europe where, for example, the threat from earthquakes has been underestimated in the past. As the tragic 1755 Lisbon earthquake and the seismicity distribution shown in Figure 1, large earthquakes in Europe are not just historical references.

In fact the economic and social costs associated with the failure or interruption of certain services and equipments such as water, energy or telecommunication supply systems and traffic lines are of comparable magnitude to the costs associated with structural failures, if not greater.

As post-installed anchors are often used to fix structural members and non-structural components, their adequate design and selection is of crucial importance to guarantee safety and minimize costs associated with seismic events. The connections should then be clearly detailed during design phase in order to allow a common understanding of the project specifications by contractors and building inspectors. Ultimately, this practice avoids the high risk of leaving the responsibility to subcontractors.

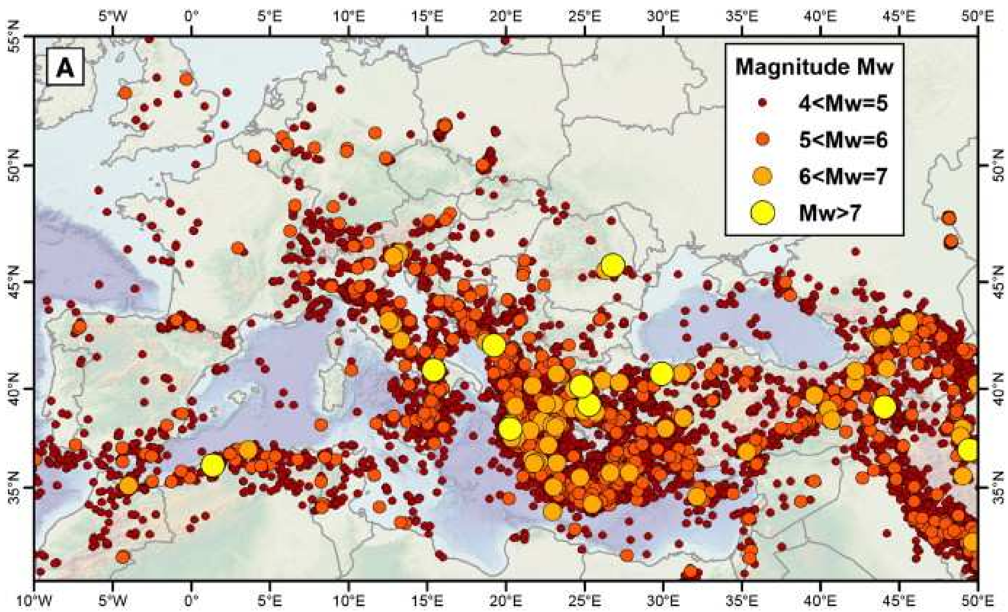

Figure 1: European Seismicity Distribution for the 1976–2009 Period (NEIC Catalog)

1.1 Influence of earthquake resulting cracks in concrete base material

As a structure responds to earthquake ground motion it experiences displacement and consequently deformation of its individual members. This deformation leads to the formation and opening of cracks in the concrete members. Consequently all anchorages intended to transfer earthquake loads should be suitable for use in cracked concrete and their design should be predicted on the assumption that cracks in the concrete will cycle open and closed for the duration of the ground motion.

Parts of the structures may however be subjected to extreme inelastic deformation as exposed in Figure 2. In the reinforced areas yielding of the reinforcement and cycling of cracks may result in cracks width of several millimetres, particularly in regions of plastic hinges. Qualification procedures for anchors do not currently anticipate such large crack widths. For this reason, anchorages in these regions where plastic hinging is expected to occur should be avoided unless apposite design measures are taken.

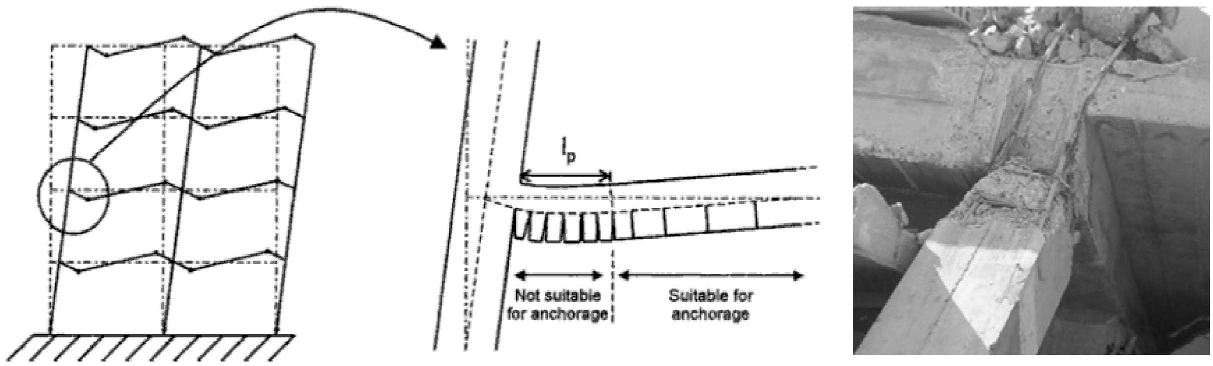

Figure 2: Member Cracking Assuming a Strong-Column, Weak Girder Design

1.2 Suitability of anchors under seismic loading

An anchor suitable (approved) to perform in a commonly defined cracked concrete, about 0.3 mm, is not consequently suitable to resist seismic actions, it's just a starting point.

During an earthquake, cyclic loading of the structure and fastenings is induced simultaneously. Due to this the width of the cracks will vary between a minimum and a maximum value and the fastenings will be loaded cyclically. Specific testing programs and evaluation requirements are then necessary in order to evaluate the performance of an anchor subjected to seismic actions. Only the anchors approved after the mentioned procedure shall be specified for any safety relevant connection.

Anchors generally suitable for taking up seismic actions are those which can be given a controlled and sustained pre-tensioning force and are capable of re-expanding when cracking occurs. Also favorable are anchors which have an anchoring mechanism based on a keying (mechanical interlock) as it is the case for undercut anchors. Furthermore, some specific chemical anchors have also been recognized good performance to resist seismic actions. Displacement controlled expansion anchors should be avoided considering that their performance under seismic is proven unsuitable.

The following Table 1 provides a rough overview of the suitability of various types of anchors to resist seismic actions. This suitability depends to a great extent on how badly the concrete has cracked and how large the cracks are in the event of an earthquake. The classifications presented are based on a generic assessment of the anchor types not reflecting a particular evaluation of any product or anchor manufacture.

Type of anchor		Displacement controlled expansion anchors	Adhesives anchors	Concrete screws	Torque-controlled expansion anchors	Adhesive-expansion anchors	Sleeved torque-controlled expansion anchors	Undercut anchors
Cracked concrete with crack width, w	small (w < 0.5mm)	-	++	++	++	++	++	++
	medium (0.5 ≤ w ≤ 1.0mm)	-	+	+	+	+	++	++
	large (w > 1.0mm)	-	-	-	-	+	+	++

Table 1: Suitability of Anchors Under Seismic Loading (- unsuitable, + suitable, ++ very suitable)

Note that the precise understanding of an anchor ability to tackle seismic loading should always be checked by consulting the anchor approvals being Table 1 guidance for a general understanding of the different anchor type capacities and limitations.

1.3 Influence of annular gaps in the anchorage resistance under shear loading

Under shear loading, if the force exceeds the friction between the concrete and the anchoring plate, the consequence will be slip of the fixture by an amount equal to the annular gap. The forces on the anchors are amplified due to a hammer effect on the anchor resulting from the sudden stop against the side of the hole (Figure 3). This justifies the new European seismic design guideline recommendation for annular gaps between the anchors and the fixture to be avoided in seismic design situations.

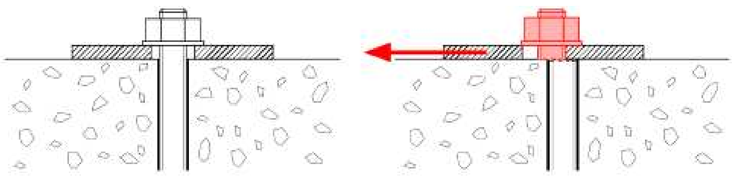

Figure 3: Unanticipated Steel Failure Possibility Resulting from Annular Gaps

Moreover, where multiple-anchor fastenings are concerned, it must be assumed that due to play of the hole on the steel plate a shear load may not be distributed equally among all anchors. In an unfavourable situation, when anchor fastenings are positioned near to the edge of a building member, only the anchors closest to the edge should be assumed loaded and this could result in failure of the concrete edge before the anchors furthest from the edge can also participate in the load transfer (Figure 4).

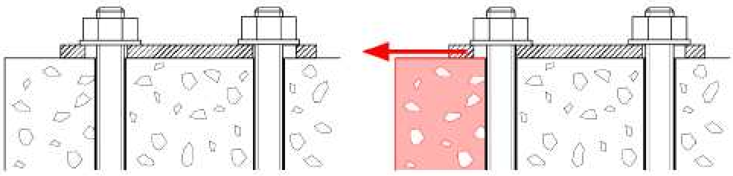

Figure 4: Unanticipated Concrete Failure Possibility Resulting from Annular Gaps

By eliminating the hole play, filling the clearance hole with an adhesive mortar e.g., the effects mentioned above are controlled with great benefit to the anchorage performance. The use of Hilti Dynamic Set (Figure 5) will ensure a professional approach for a controlled filling of the annular gaps as well as it will prevent the loosening of the nut since it also comprehends a lock nut, effect that also complies with a European seismic design guideline clear recommendation. Also according to the same guideline, in case it can be ensured that there is no hole clearance between the anchor and the fixture, the anchor seismic resistance for shear loading is doubled compared to connections with hole clearances.

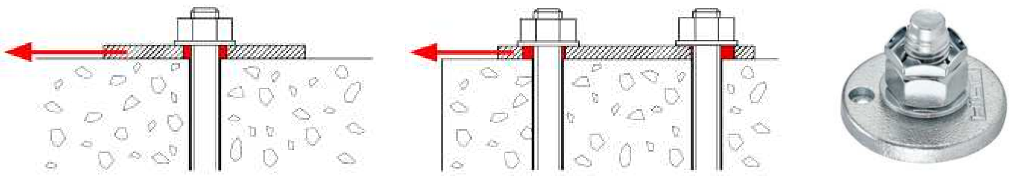

Figure 5: Predictable Steel and Concrete Behavior with Filled Annular Gaps (Hilti Dynamic Set)

2 UNITED STATES AND EUROPEAN SEISMIC REGULATIONS

For a sound seismic design of a post-installed anchorage the first step begins with the correct definition of the acting loads. In the United States ASCE 7 establishes the provisions for the definition of the seismic action and the anchor performance shall be evaluated in accordance with ACI 318 Appendix D and AC308 in case of chemical anchors. Pre-qualification reports, created in accordance with published testing procedures and acceptance criteria, (ACI 355 with ICC-ES AC193 and AC308) provide sound data in a proper format for design.

Following the same design flow, in Europe the action definition is available through the EN 1998:2004 (Eurocode 8). Until the release of the EN 1992-4, planned for 2015, EOTA TR045 (Technical Report) sets the standard for the seismic design of steel to concrete connections. This regulation is in full alignment with ETAG 001 Annex E, the new European guideline for the anchor's seismic pre-qualification testing. As such, the European framework is also already harmonized in order to allow the design of a post-installed anchorage under seismic conditions.

As an overview, Table 2 display the application ranges of the different guidelines or codes mentioned above. The presented design codes represent the state of the art for the testing of fasteners and the design of fastenings in concrete worldwide. Note that even if not all, most of the countries in the world refer to one of these frameworks for the design of anchors.

	United States	Europe
Load definition	ASCE 7	EN 1998-1:2004
Design resistance	ACI 318 Appendix D, AC308	EOTA TR045
Technical data	ICC-ES report (ESR)	ETA
Qualification criteria	ACI 355 with ICC-ES AC193/AC308	ETAG 001, Annex E

Table 2: Seismic Design Framework for Fastenings in Concrete

2.1 Seismic load definition

The starting point for the definition of the seismic actions is the seismic design spectrum. In the case of the US a seismic design category (SDC) is endorsed and the seismic design spectrum is obtained by the mapped maximum (short period, 0.2s) and 1.0s period acceleration whereas in Europe the seismic hazard is defined by the peak ground acceleration (PGA) and no SDC is established. There is however a clear definition for low and very low seismicity, based on the design ground acceleration, and in case of very low seismicity no specific seismic provisions need to be observed.

The influence of the soil type is considered in both codes by a site coefficient which is based on matching ground classifications, considering the shear wave velocity limits and soil descriptions. Based on the risk of an eventual improper seismic performance, the categorization of buildings is placed in the same way by both codes and the correspondent importance factor is assigned with similar values (even if at different phase in the design flow).

Considering the above mentioned, the equations to derive the seismic design spectrum are expected to be different between the codes but, considering equivalent importance class and ground type, the resulting shape and spectral acceleration are very much similar. In simple terms, it can be said that mathematically the two codes are just pointing different coordinates of the design spectrum (Figure 6). Note that the design response spectrum according to ASCE7 does not contemplate the influence of the building importance (being considered later in the design) and as such the comparison was made considering the resulting spectrum accordantly scaled by this factor.

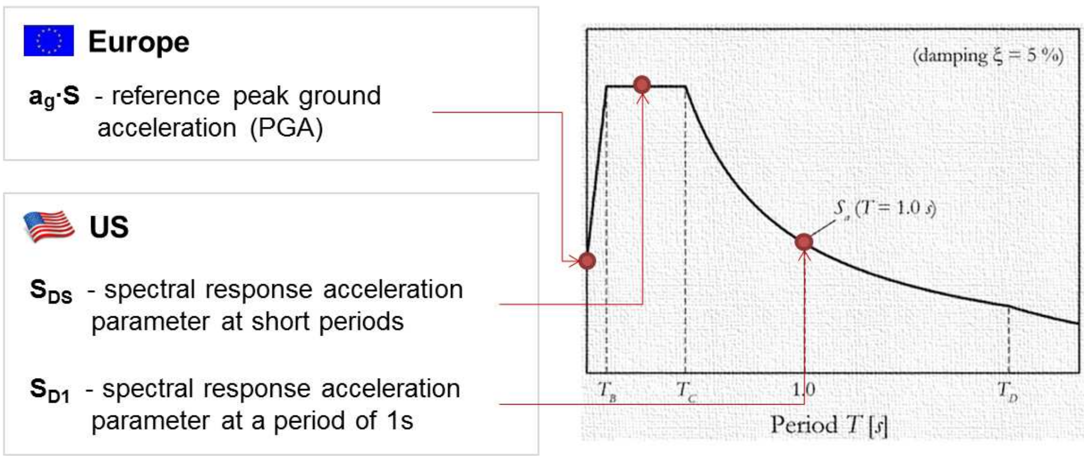

Figure 6: Design Response Spectrum According to Eurocode 8 and ASCE 7

A comparison was also established between the seismic base shear force using the EN1998-1:2004 and the ASCE7. Evaluating the different expressions as well as some practical applications of the codes we can conclude that the values are decidedly coincident. From the seismic base shear force different well-known methods can be used to determine the load acting at each level of the structure.

As such, comparing the resulting seismic design spectrums with equivalent importance classes and ground types (S being the soil factor), it's possible to correlate the European seismicity rating with the United States seismic design category, as expressed in Table 3. In summary, there is a clear relationship between the two lowest seismic classifications between the European and U.S. regulations.

As the only yet important exception to the Table 3, in case of a building with an importance class IV and a seismicity rating of low or above the corresponding seismic design category is C or above. This means that in the case of buildings that in the event of a failure could pose a substantial hazard to the environment or community (e.g. hospitals, fire stations, power plants) the design should consider all the seismic specific provisions.

EN 1998-1:2004 (Eurocode 8)		ASCE7	
Seismicity rating	Design repercussion	SDC	Design repercussion
Very low $ag \cdot S \leq 0.05 \cdot g$	No seismic specific provisions need to be observed	A	No seismic specific provisions need to be observed
Low $ag \cdot S \leq 0.1 \cdot g$	Reduced or simplified design procedures may be used	B	
$ag \cdot S > 0.1 \cdot g$	Seismic design must be attend to all the elements	C to F	Seismic design must be attend to all the elements

Table 3: European Seismicity Rating Relation to Seismic Design Category (SDC) aplicable for buildings importance class I, II, III

2.2 Anchors seismic design resistance

Design provisions for the anchor seismic design are provided by the ACI 318 Appendix D or the recent EOTA TR045. Both design regulations work with the CC-method (concrete capacity method) to calculate the characteristic resistances of fastenings. Differences between the codes occur in the basic assumptions for the design equations which partially result in different factors. According to the CC-method the design resistances are calculated for tension loading and shear loading considering all possible failure modes.

All discussed safety concepts calculate resistance and actions based on partial safety factors. The main requirement for design of the discussed codes is that the factored action E shall be smaller or equal to the factored resistance R. All codes factor the characteristic action E_k with partial safety factors γ (equations 1).

$$E_d \leq R_d \tag{1}$$

$$E_d = E_k \cdot \gamma$$

For the characteristic resistance there is a conceptual difference since the European codes divide the characteristic resistance R_k by a partial safety factor γ whereas the United States codes factor the characteristic resistance R_k with a strength reduction factor ϕ. The effect of these factors is however the same reducing the characteristic value to design level. The design resistance R_d is generally very similar for all the evaluated failure modes independently on the adopted code (equations 2).

$$R_d = R_k / \gamma \tag{2}$$

$$R_d = \phi \cdot R_k$$

As per the new European design guideline, EOTA TR045, the design incorporates three design approaches which aim to avoid any non-ductile failure of the anchorage point under seismic loading. An overview of these different design options is given in Table 4. All three approaches are acceptable within their application conditions where options a1) and a2) don’t require any requirement on the ductility of the anchors while b) envisions the ductility resulting from the anchor capacity to accommodate sufficient elongation. Even in the case option b) is considered in the design, the fastening shall not be accounted for energy dissipation in the global structural analysis or in the analysis of a non-structural element.

Note that the ACI 318 also considers thee design approaches that are conceptually the same as the ones presented by the EOTA TR045. The main difference, that nevertheless has the same background intention, comes from the fact that the “Elastic design” defined as per European guideline has a different approach in the U.S. regulations. In the ACI 318 this design option consider the loads resulting from a regular seismic design (not elastic) and introduces a reduction factor (recommended as 0.4) directly applied to all concrete failure modes. It is the authors’ opinion that the new European regulations have made the different design approaches more clear compared to the ACI 318 interpretation.

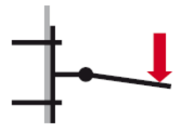	**a1) Capacity design** The anchorage is designed for the force corresponding to the yield of a ductile component or, if lower, the maximum force that can be transferred by the fixture or the attached element.
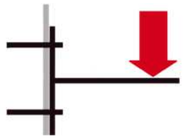	**a2) Elastic design** The fastening is designed for the maximum load assuming an elastic behaviour of the fastening and of the structure.
	**b) Design with requirements on the ductility of the anchors** Requires the use of an anchor classified as ductile and is applicable only for the tension component. Additional provisions are required to be observed in order to ensure the anchor steel resistance is governing the resistance.

Table 4: Seismic Design Options per European Seismic Guideline

2.3 Evaluation of the anchor seismic performance

For testing of fastenings in concrete three different basic guidelines must be considered. In the United States ACI 355 covers testing of post-installed mechanical anchors under static and seismic loading and prescribes testing programs and evaluation requirements for post-installed mechanical anchors intended for use in concrete under the design provisions of ACI 318. This guideline is the basis for the acceptance criteria AC193 and AC308 by the International Code Council (ICC). While AC193 covers testing of mechanical anchors, AC308 covers testing and design of adhesive anchors.

Referring the main testing procedures, the anchors are installed in a closed crack that then is open to 0.5mm. The anchors under testing are afterwards subject to the sinusoid varying loads specified, using a loading frequency between 0.1 and 2Hz as exposed in Figure 7. The maximum seismic tension and shear test load is equal to 50% of the mean capacity in cracked concrete from reference tests.

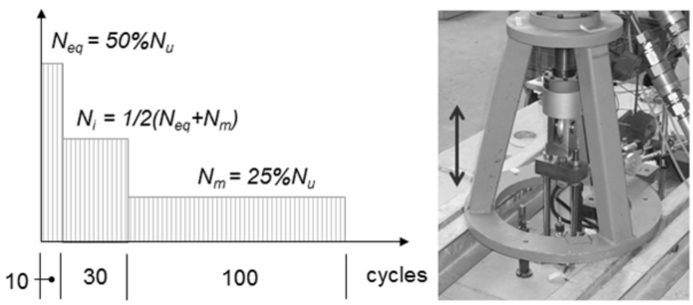

Figure 7: Loading Pattern for Simulated Seismic Tension Tests According to ACI355

After the simulated seismic-tension and seismic-shear cycles have been run, the anchors are tested to failure in static-tension and static-shear. The mean residual tension and shear capacities shall be assessed according the guideline defined limits.

In Europe the ETAG 001 is valid for testing of post- installed mechanical (Part 1 to Part 4) and bonded anchors (Part 5). With the release of the ETAG 001 Annex E in the first half of 2013, the seismic pre-qualification of anchors became regulated in Europe. Two different testing programs are presented to assess the anchor's suitability to seismic loading resulting in two seismic performance categories classified as follows:

- Seismic category C1 - similar to the US seismic pre-qualification procedure and only recommended for non-structural applications.
- Seismic category C2 - very demanding seismic crack movement tests classify an anchor as suitable for structural and non-structural applications.

While seismic category C1 is identical to the U.S. seismic pre-qualification procedure, seismic category C2 involves a set of quite more demanding seismic load and/or crack cycle tests especially considering that for assessing the tension seismic performance one of the tests involves the cycling of the cracks until a width of 0.8mm.

In practical terms, according to the EOTA TR045 and for $a_g \cdot S$ above 0.05g, anchors intended for connections between structural elements of primary or secondary seismic members should always have a seismic category C2. For anchors used in the attachment of non-structural elements, if the acceleration $a_g \cdot S$ is between 0.05g and 0.10g then a seismic category C1 can be used. Please note that these are the generic recommendations that member states can locally adjust. The map represented in Figure 8 is based on national earthquake data (for ordinary buildings and ground type A) and provides perspective on the relevance of the new ETA guidelines in various countries. For more precise information see national regulations.

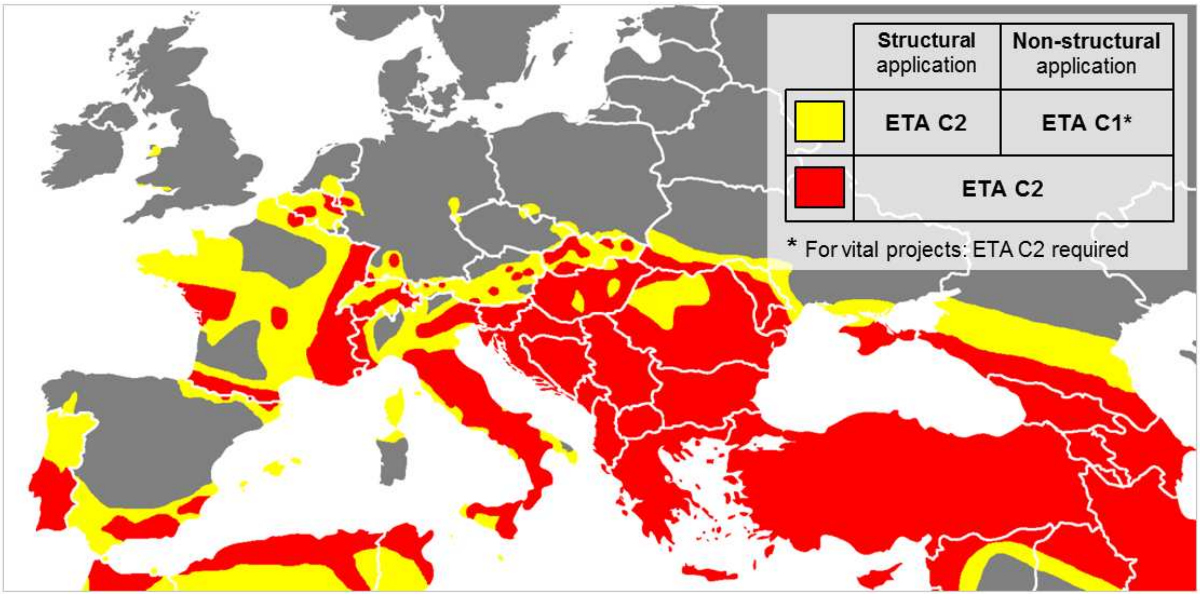

Figure 8: Representation of Required Seismic Performance Category in Europe (EOTA TR045)

12 CONCLUSIONS

Considering all the exposed above, the design framework for the seismic design of anchors is already available through both the U.S. and European regulations. This means that there it is no longer a need for an engineering judgment on the use of U.S. anchor performance provisions along with the European seismic action definition, solution suggested by the author during the last years in the absence of European seismic regulations to assess and design anchors.

It's now the responsibility of the anchoring manufactures to provide designers and the building industry with seismic design data according to the new European testing procedures. Hilti has been at the forefront of anchoring related seismic projects and investigations, Hilti has already approved for seismic performance category C2 both the chemical anchor HIT-HY 200 + HIT Z and mechanical anchor HST.

REFERENCES

[1] European Organization for Technical Approvals. EOTA TR045, *Design of Metal Anchors Under Seismic Actions*, Brussels, Belgium (2013).
[2] European Organization for Technical Approvals, ETAG 001 Annex E, *Assessment of metal anchors under seismic actions*, Brussels, Belgium (2013).
[3] Hilti Corporation, *Build a future safer from earthquakes: New EU guidelines*, Schaan, Liechtenstein (2013).
[4] Jorge Gramaxo, *Engineering judgement on the use of American's anchor performance provisions along with the European seismic action definition*, 15^{th} World Conference on Earthquake Engineering, Portugal (2012).
[5] ICC Evaluation Service, Inc., AC 193, *Acceptance Criteria for Mechanical Anchors in Concrete Elements*, United States of America (2011).
[6] ICC Evaluation Service, Inc., AC 308, *Acceptance Criteria for Post-Installed Adhesive Anchors in Concrete Elements*, United States of America (2011).
[7] Hilti Corporation, Build a future safer from earthquakes, Schaan, Liechtenstein (2011).
[8] K. Tonning, *Design of High-rise Onshore Steel and Reinforced Concrete Structures for Earthquake Resistance*, University of Stavanger, Norway (2009).
[9] Applied Technology Council, ATC-69, *Reducing the risks of nonstructural earthquake damage*, California, United States of America (2008).
[10] American Concrete Institute, ACI 318-08 Appendix D, *Building Code Requirements for Structural Concrete - Anchoring to Concrete*, United States of America (2008).
[11] American Concrete Institute, ACI 355.2, *Qualification of Post-Installed Mechanical Anchors in Concrete*, United States of America (2007).
[12] R. Eligehausen, R. Mallee and J.F. Silva, *Anchorage in Concrete Construction*, Ernst & Sohn, Berlin (2006).
[13] M. Höhler, *Behavior and testing of fastenings to concrete for use in seismic applications*, Doctor Thesis. University of Stuttgart (2006).
[14] American Society of Civil Engineers, ASCE 7-05, *Minimum Design Loads for Buildings and Other Structures*, United States of America (2005).
[15] European Committee for Standardisation, EN 1998:2004, *Eurocode 8: Design of structures for earthquake resistance*, Brussels, Belgium (2004).
[16] Hilti Corporation, *Guideline for earthquake resistant design of installations and non-structural elements*, Schaan, Liechtenstein (2004).

12th International Conference on
Steel, Space and Composite Structures
28-30 May 2014, Prague, Czech Republic

DESIGN AND NUMERICAL ANALYSIS OF COMPOSITE SLABS USING SMALL-SCALE TESTS

Josef Holomek*, Miroslav Bajer* and Jan Barnat*

*Faculty of Civil Engineering, Brno University of Technology
Veveří 331/95, 602 00 Brno, Czech Republic
e-mail: holomek.j@fce.vutbr.cz, webpage: http://www.fce.vutbr.cz

Keywords: Composite slab, longitudinal shear, prepressed embossment, small-scale test, numerical model.

Abstract. *The longitudinal shear is a typical failure mode for composite slabs. The load-bearing capacity in longitudinal shear is determined mainly by mechanical bearing capacity of embossments and friction above the support. It is also influenced by effect of curvature, longitudinal strain in the sheeting and vertical load distribution. The mechanical bearing capacity is determined by shape and dimensions of embossments and their distance from bended edge of sheeting, thickness of the sheeting, material properties etc. Moreover when slip occurs the thin-walled sheeting starts to deform and different stress distribution can change local shear bearing capacity of the interface between steel sheeting and concrete. The complexity of problem caused that nowadays methods in standards prescribe full-scale laboratory bending tests. Small-scale shear tests present a less expensive alternative to bending tests. Several design procedures using small-scale tests results has been derived in last decades. Results of two of these procedures are being compared in this paper. Obtained data from small-scale tests as well as results from bending tests which had been previously performed in our laboratory are being used for numerical analysis and parametric study of shear bearing capacity of the slab.*

1 INTRODUCTION

There are three global failure modes of steel-concrete composite slabs using thin-walled steel sheeting with prepressed embossments: vertical shear, longitudinal shear and bending. Longitudinal shear is typical and most difficult to quantify of these three. Load bearing capacity in the longitudinal shear is mainly determined by mechanical bearing capacity of embossments and friction above the support. It is also influenced by effect of curvature, longitudinal strain in the sheeting and vertical load distribution, etc. The mechanical bearing capacity is determined by shape and dimensions of embossments and their distance from bended edge of sheeting, thickness of the sheeting, material properties etc. [1] Moreover when slip occurs the thin-walled sheeting starts to deform and different stress distribution can change local shear bearing capacity of the interface between steel sheeting and concrete. It is therefore difficult to describe the behaviour of the slab analytically. Eurocode contains two methods of design of composite slabs. Both of them are based on full-scale bending test results.

2 DESIGN METHODS USING SMALL-SCALE TESTS

Various kind of test small-scale shear test set-ups have been used in past to investigate shear properties of the slab. [2] Also several methods of design have been derived in last decades using these tests. However they are not used in practice either for lack of information, either for complexity of calculations or dependence on numerical analysis. This paper deals with Slip-Block Test and New Simplified Method which do not use numerical analysis for design. Numerical analysis presented in this paper is used for possibility of parametrical studies and better understanding of the slab behaviour.

2.1 Slip-Block Test

Slip Block Test is a testing procedure and design method using push-out test set-up. The test set-up includes two loading jacks, one to produce horizontal shear force H and second to produce vertical clamping force V. The testing procedure differs from others by changing of clamping force during the test. Corresponding values of shear resistance are obtained for each level of clamping force V during the test. Thus, a friction line is obtained when plotting V – H diagram. Slope of the line indicates friction μ and by extrapolation to intersection with axes gives value of shear resistance of mechanical interlock H_{rib}; $b_1$is length of specimen [3]:

$$H = b_1 H_{\mathrm{rib}} + \mu V \tag{1}$$

Tensile force in the sheeting T is then calculated as follows:

$$T = H_{\mathrm{rib}} / b_{\mathrm{r}} \, L_{\mathrm{s}} + \mu R_u \tag{2}$$

Where b_{r} is width of rib of specimen; R_u is support reaction and L_{s} is span length. Bending resistance of the slab is calculated using this force similarly as in partial connection theory. [4]

2.2 New Simplified Method

New Simplified Method originally uses pull out test set-up. Values of shear corresponding to initial slip and maximum shear force are used for design. The method describes slab behaviour in three phases. Behaviour in phase I is linear elastic without concrete cracking and without slip. The slab leaves Phase I when first cracks occur in bottom fibres of concrete. Behaviour of phase II is elastic or elasto-plastic with concrete cracking and without slip. The slab leaves this phase when longitudinal shear force overcomes value of shear force corresponding to first slip obtained from small-scale tests. Height of cracked concrete is found iteratively. Phase III is governed by non-linear elasto-plastic behaviour with concrete cracking and with slip. Maximum bending resistance with corresponding curvature and initial strain are found iteratively using maximum shear strength from small-scale tests. A spreadsheet model has to be created to find the solution in three iterations. [5]

3 EXPERIMENTS

3.1 Small-scale tests

Test set-up was chosen similar to that described for Slip Block Test. This set-up can be used also in New Simplified Method when considering possible differences coming up from different boundary conditions of the tests. The tests were performed in two laboratories, in Brno University of Technology (BUT) and in Addis Ababa Institute of Technology (AAiT) - Fig. 1. Testing procedure in AAiT was slightly modified. The clamping force was gradually increasing instead of decreasing, which enables to perform several series of the test per each specimen.

Trapezoidal sheeting Cofraplus 60 was used in all the tests. Geometry of the sheeting was following: 60 mm height, 1 mm thickness, height of embossments in transverse direction 31 mm, depth of embossments 3 mm. The specimens had width of two waves which enabled to apply shear force in one point. The width of concrete part was then 414 mm and length 200 mm. Overlapping part of the sheeting served to bolt the specimens to base plate. Horizontal shear force was applied by hand-operated loading jack.

The tests were performed in series with constant clamping force 1.6 kN (Fig. 2a – BUT) and in series with changing magnitude of clamping force (Fig. 2b – BUT and AAiT) as used in New Simplified Method and in Slip Block Test, respectively. Input values for New Simplifies Method are shear resistance at first slip τ_1 = 0.034 MPa and maximum shear resistance τ_2 = 0.127 MPa.

Friction line for Slip Block Test method (Fig. 2b) determines coefficient of friction to be $\mu = 0.46$ and mechanical interlock resistance $H_{rib} = 12.95 / 0.2 = 64.75$ kN/m.

Ultimate bending moment obtained by New Simplified Method is $M_u = 17.763$ kNm, resulting load on half of slab in four-point bending would be $F_u = 33.51$ kN. Ultimate bending moment obtained by Slip-Block Test is $M_u = 13.124$ kNm and resulting load $F_u = 24.23$ kN.

(a) (b)

Figure 1: (a) Small scale test set-up in BUT; (b) Small scale test set-up in AAiT.

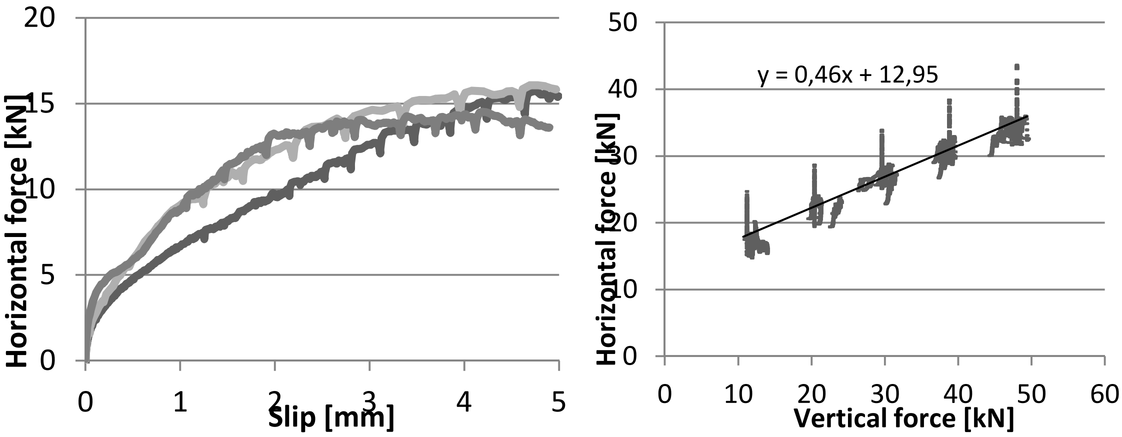

(a) (b)

Figure 2: (a) Test results of small-scale test with constant clamping force V = 1.6 kN; (b) Results of Slip Block Test procedure.

3.2 Bending tests

Four-point bending tests were previously performed in laboratory of BUT. The test set-up and procedure follows instructions in EN 1994-1-1. The slab thickness was 110 mm. At first two specimens were loaded statically up to total collapse. Then three specimens were loaded by cycling loading and subsequently statically up to total collapse. The resulting force vs. vertical deflection diagrams can be seen in Fig. 7 where a comparison with results from numerical models is presented.

4 NUMERICAL ANALYSIS

Numerical analysis shows stress distribution in structure and enable to perform parametrical studies. Modelling of composite slabs is problematic because of contact problem with large displacements in combination with bending of thin-walled steel sheeting which is bended locally around embossments and globally as a slab. Concrete cracking in tension occurs usually in bottom fibres of concrete. Small-scale tests shows that local peeling or abrasion may occur around indentations in concrete and crushing can be observed in top fibres of the slab. GiD was used for pre-processing and Atena software was used to perform the non-linear analysis.

Several failure criteria are possible to use for steel-concrete interface: linear, parabolic or hyperbolic. Mohr-Coulomb failure criterion is implemented in Atena [6] to which is the hyperbolic failure criterion asymptotically equivalent when compressive force increases [7].

4.1 2D model

Simple 2D model served to adjust contact setting. The model of sheeting had 4 layers of elements per height. Layer of interface has zero thickness and its elements have identical nodes with the elements of sheeting. Concrete mesh is coarser and is fixed with nodes of contact mesh by complex boundary condition. The bond is updated at the end of each step which enables the large displacements. [6] Load is applied in intervals. At first vertical displacement is applied on upper edge of concrete. Then horizontal displacement prescribed to its side edge. Hardening/softening functions of contact material are applied with prolonged relationship to obtain a force-slip relationship similar to real behaviour of sheeting with embossment (Fig. 4). For further possibility of comparison with results of experiments a 3D model is created since the behaviour is strongly influenced by its spatial geometry.

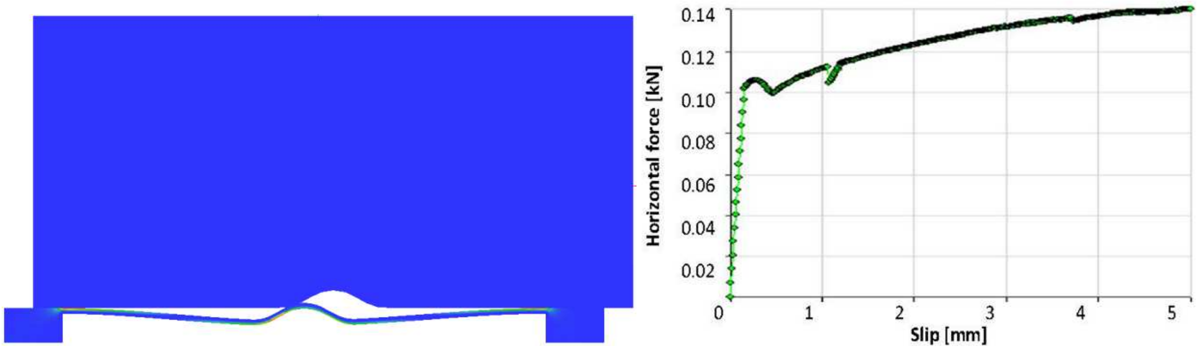

(a) (b)

Figure 3: (a) 2D model geometry; (b) Shear force vs. slip dependence.

4.2 3D shear test model

3D model of shear test is simplified to model specimen with length of one embossment and width of one side of rib. Sheeting is modelled using shell elements with implemented layers in all 3D models. [8] It enables to model bending of the sheeting out of its plane with significantly lower amount of elements. Symmetry is applied on side surfaces. The sheeting is deformed inside the rib and is sliding on the concrete surface (Fig. 4a) in the similar way as the real sheeting after the test (Fig. 5). Peak stress occurs around the edges of embossments, especially around the edge which is farther in the direction of shear force. It is in accordance with abrasion observed on the specimens after experiments (Fig. 6).

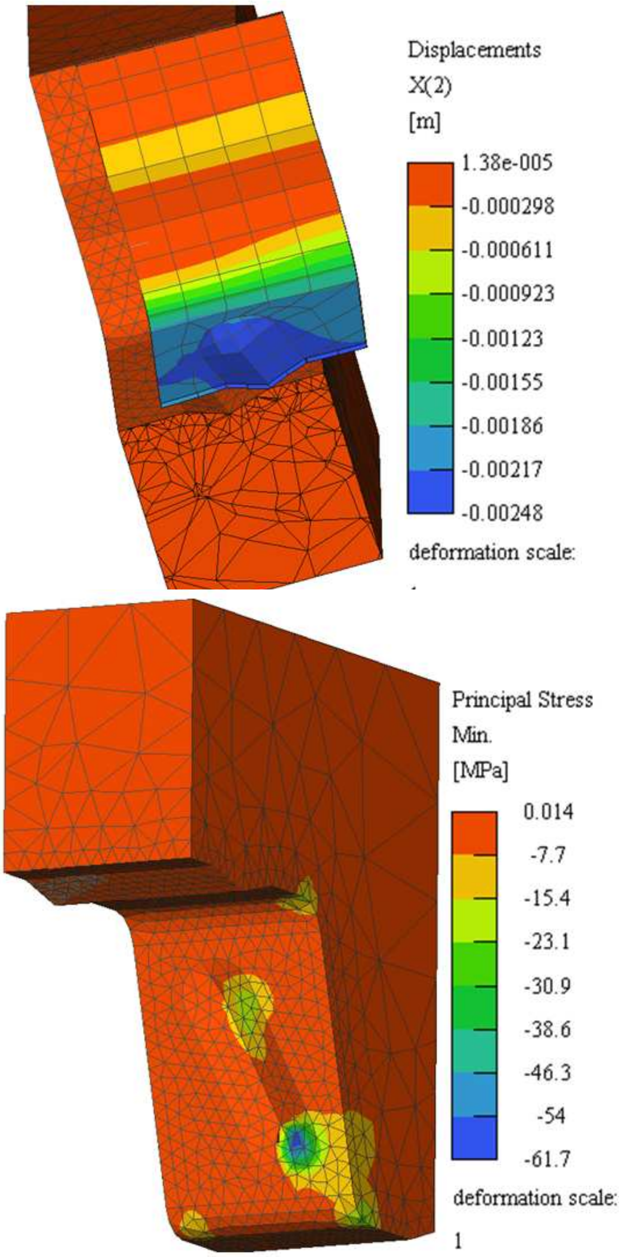

(a) (b)

Figure 4: (a) Sliding of sheeting on the concrete surface observed in clipping plane; (b) Peak stresses around the indentations in concrete.

Figure 5: Deformation of the sheeting inside rib at after the test.

Figure 6: State of indentations in concrete after experiment.

4.3 3D bending test models

3D model of bended slab is very demanding on computational time. Model simulated behaviour in four-point bending. Contact material setting is similar to that used in shear models; however number of adjusting is still needed to reach good agreement with real experiments. Symmetry enables to create model of half rib above half span. Embossments are substituted by hardening/softening function of contact material (Fig. 7). This simplification makes the analysis more feasible and enables to reach relatively agreement with bending test results (Fig. 8). Supporting plates enable rotation to avoid local peak stresses. The plates are connected with model by complex boundary conditions which makes easy to move their positions and compare results with varying magnitude of shear span L_s.

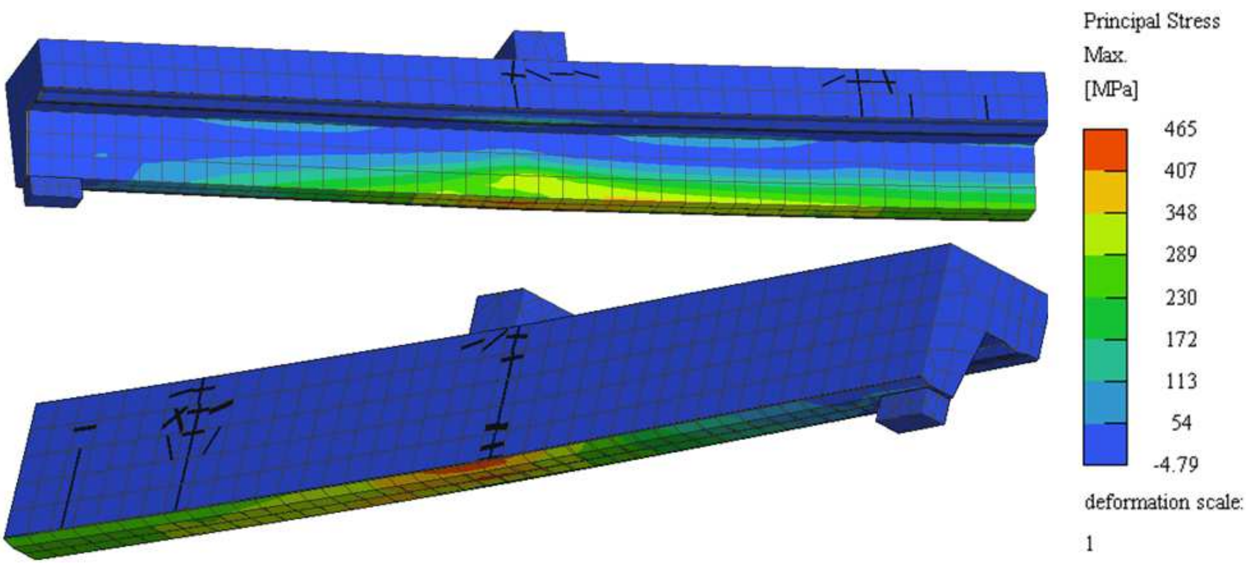

Figure 7: Model of four-point bending with shear span L_s = 500 mm
and concrete strength f_c = 33 MPa.

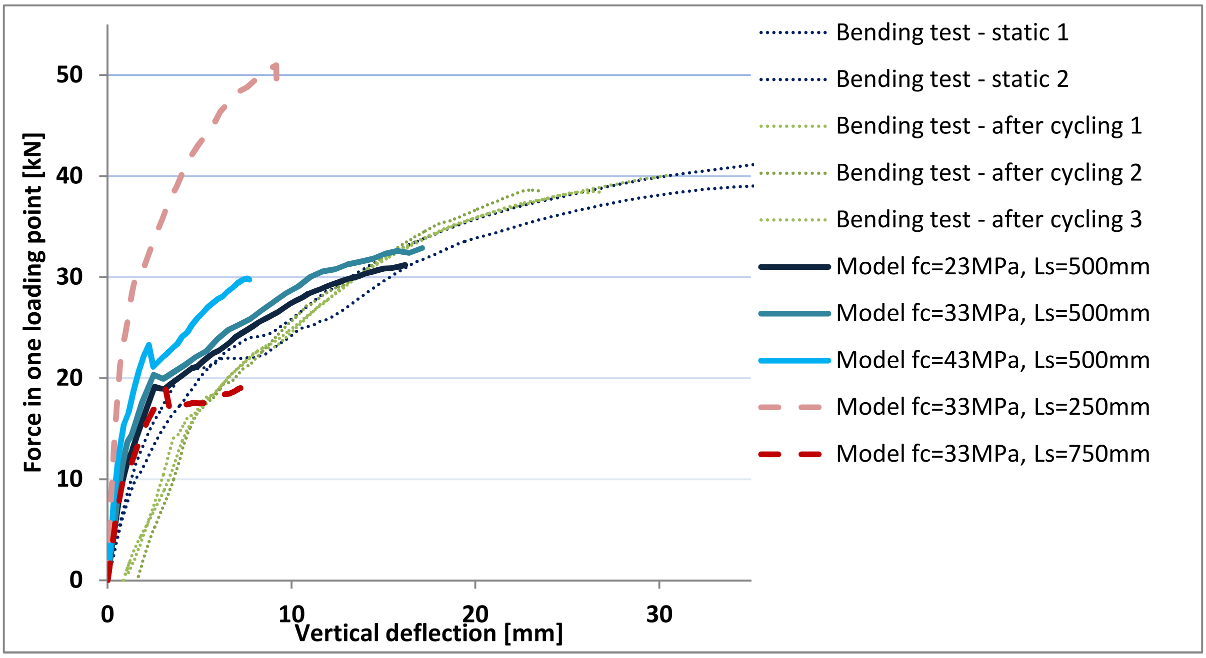

Figure 8: Comparison of four-point bending models and experiments in force vs. vertical deflection diagram.

5 CONCLUSIONS

Small-scale tests can effectively replace full-scale bending tests required for design of new types of sheeting for composite slabs. Two of the methods using small-scale tests for design are used and compared in this paper, Slip Block Test and New Simplified Method. Despite its name the New Simplified Method is significantly more arduous, but gives the designer more information about behaviour of the slab. Brief comparison was made using the same test set-up but with corresponding magnitudes of clamping forces. Under these conditions the Slip Block Test is more conservative than New Simplified Method.

Numerical simulation is very useful tool for better understanding the structure and for performing parametrical studies. Shear test model describes detailed deformation of the sheeting inside the rib and peak stresses in concrete around the edges of indentations which results in small abrasion in real experiments. Bending test model is compared with results of four-point bending test performed previously in laboratory of BUT. Variation of concrete grade does not change the results significantly. On the other hand changing of magnitude of shear span has high influence on results, which is in accordance with partial connection theory.

ACKNOWLEDGEMENT

This paper was elaborated with the financial support of the European Union's "Operational Programme Research and Development for Innovations", No. CZ.1.05/2.1.00/03.0097, as an activity of the regional Centre AdMaS "Advanced Materials, Structures and Technologies," project FAST-J-13-1918 and project FAST-S-13-2077.

REFERENCES

[1] M. Ferrer, F. Marimon, M. Crisinel, *Designing cold-formed steel sheets for composite slabs: An experimentally validated FEM approach to slip failure mechanics*, Thin-Walled Structures, Volume 44, Issue 12, Elsevier, 2001, p. 1261 – 1271.

[2] P. Guignard, A. Schumacher, M. Crisinel, *Etude des dalles mixtes et développement d'une méthode de calcul basée sur la relation moment-courbure*, ICOM REPORT, Lausanne, 2003.

[3] M. Patrick, W. Poh, *Controlled test for composite slab design parameters*, IABSE reports, Zürich, 60, 1990, p. 227-231.

[4] M. Patrick, R. Bridge, *Partial shear connection design of composite slabs*, Vol. 16, No. 5, Engineering Structures, 1994, p. 348–362.

[5] M. Crisinel, F. Marimon, *A new simplified method for the design of composite slabs*, Journal of Constructional Steel Research, 60, 2004, p. 481 – 491.

[6] V. Červenka, L. Jendele, *ATENA program documentation - Part 1 - Theory,* Červenka Consulting, s.r.o., Prague, Czech Republic, 2013.
[7] Y.-H. Lee, J. T. Job, T. Lee, D.-H. Ha, *Mechanical properties of constitutive parameters in steel–concrete interface,* Engineering Structures, Volume 33, Issue 4, April 2011, p. 1277–1290.
[8] J. Holomek, M. Bajer, *Experimental and Numerical Investigation of Composite Action of Steel Concrete Slab*, Procedia Engineering, Volume 40, 2012, p. 143–147, Elsevier

12th International Conference on
Steel, Space and Composite Structures
28-30 May 2014, Prague, Czech Republic

MATERIAL PROPERTIES OF COLD-FORMED STAINLESS STEEL

Michal Jandera and Jan Marik

Czech Technical University in Prague, Faculty of Civil Engineering
Thakurova 7, 166 29 Prague 6, Czech Republic
e-mail: michal.jandera@fsv.cvut.cz, webpage: http://www.cvut.cz

Keywords: Stainless steel, material diagram, cold forming.

Abstract. *The research is focused on material properties of cold-formed stainless steel sections made of basic grades of stainless steel, namely austenitic (1.4404), ferritic (1.4003), duplex (1.4462) and lean-duplex (1.4162). Current investigation at the Czech Technical University in Prague involves experimental research consisting of tensile tests of large number of coupons made of sheets, on which uniaxial uniform tensile plastic deformation was previously induced. The level of the induced plastic strain varies from around one to tens percent to cover the whole possible range. Subsequent tensile tests were carried both parallel and transverse to the direction of the previous loading. The influence of the sheet rolling direction was also considered.*

1 INTRODUCTION

Stainless steel is a material of many specific properties. Significant structural behaviour differences from carbon steel demand more sophisticated design. One of the main benefits that haven't been satisfactorily investigated for all stainless steel grades is the significant increase of yield and ultimate strength due to cold-working in fabrication process of structural elements. In the last decades some proposals were developed. However, the codes are usually limited on receiving the increased strength properties vie coupon tests. Based on the tests, material models for the stress-strain diagram description are given. These models use various material parameters and material strength obtained. Some of them show a good agreement in the range of strain expected in load-bearing structures, other are in good agreement at high strains. Results obtained from the recent investigations [1,2] demonstrate also different values for basic material characteristics, especially for modulus of elasticity, 0,2% proof strength, ultimate tensile strength or ductility. Particularly, material properties of steel in cold worked conditions can differ a lot.

This paper presents tensile tests results of cold rolled strip coupons made from austenitic (1.4404), ferritic (1.4003), duplex (1.4462) and lean-duplex (1.4162) grade. Apart from classic tensile test, tensile tests were carried out on cold-worked specimens respecting different behaviour parallel and transverse to the rolling directions, either parallel or transverse to the plastic strain induction directions. The results of the research will lead to more accurate material characteristics and material models of cold-formed material appropriate for FEM modelling.

2 RECENT RESEARCH AND DESIGN STANDARDS IN MATERIAL BEHAVIOUR

Mechanical properties are specified in the European standard EN 10088-1 [3]. The yield strength (0.2% proof strength) values are only given as transverse to the rolling direction property. The standard doesn´t take into account the material anisotropy. Values differ according to the product form (cold rolled strip/hot rolled strip/hot rolled plate), for example of cold rolled strip see Table 1. For the lean-duplex steel 1.4162, material characteristics similar to 1.4462 are expected. However, within the designing of structure, there is not often possible to know, what type of product form will be used. Consequently there is not applicable to employ enhanced properties of cold-worked materials.

Type of stainless steel	grade	f_y (MPa)	f_u (MPa)
ferritic	1.4003	280	450
austenitic	1.4404	240	530
duplex	1.4462	480	660

Table 1. Yield strength and ultimate tensile strength of cold rolled strip $t \leq 6$ mm [3].

The recent valid design standard EN 1993-1-4 [4] allows to use materials with the yield strength up to 480 MPa as no significant research in higher strength stainless steel members was made. This is limiting also using the material in cold-worked condition (austenitic steels only) for CP350 resp. C700 only [5]. The material characteristics are shown in Table 2.

Grade	Cold Worked Condition			
	CP350		C700	
	f_y (MPa)	f_u (MPa)	f_y (MPa)	f_u (MPa)
austenitic steel	350-500	-	-	700-850

Table 2. Nominal values of the tensile yield strength f_y and the ultimate tensile strength f_u for austenitic stainless steel according to EN 10088-2 [5] in the cold worked condition.

EN 1993-1-4 defines the Ramberg – Osgood parameter n, it is essential for the secant modulus of elasticity, appropriate for deflections estimating, and tangential modulus (essential for stability). However the current and extensive research of Afshan et. al [1] shows slightly different hardening exponent n depending on type of stainless steel, i.e. austenitic, ferritic, and duplex as opposed to recent version determining n according to steel grade and rolling direction. The same paper recommends also a lower modulus of elasticity for design purposes, which may be assumed for the global analysis and in determining the resistances of members and cross-sections.

3 EXPERIMENTS

The section describes set of experiments carried out at the Czech Technical University in Prague. The programme is focused on the establishment of stress-strain behaviour description of cold-formed stainless steel section from all types of stainless steel grades, i.e. ferritic (1.4003), austenitic (1.4404), duplex (1.4462) and relatively new grade lean-duplex (1.4162), too. The project design involves especially tensile tests. Several compression tests are also being planned in the future for the whole stress-strain behaviour description. All specimens are prepared from a cold-rolled steel sheet of 1.5 mm respectively 2.0 mm thickness.

First of all, material tensile tests of all grades were carried out, both for direction transverse and parallel to the rolling directions. Strain was measured by electrical resistance strain gauges attached to both sides of the specimens (see Figure 1) for the best accuracy of initial part of the stress-strain diagram and by an extensometer for higher strain ranges.

The next step included tensile plastic deformations induction on the coupons or special wide specimen from which the coupons were machined subsequently. A device able to induce uniform plastic deformation through the whole width of the wide specimen was used. That provides the desired stress distribution in the area from which the new coupon was created (neck of the specimen) as shown in Figure 2. The geometry of the specimen was based on a simple Abaqus 2D model presented as well.

Levels of the induced plastic strain varied significantly. Plastic strain equal to 1%, 3%, 5%, 10%, 15% and for other than ferritic grades also 20 or 50% was used. Experimental set consisted of 5 or 6 specimens depending on the rolling direction and depending on plastic strain induction direction for each grade. A total of 92 coupons were prepared and tested in accordance with EN ISO 6892-1 [6].

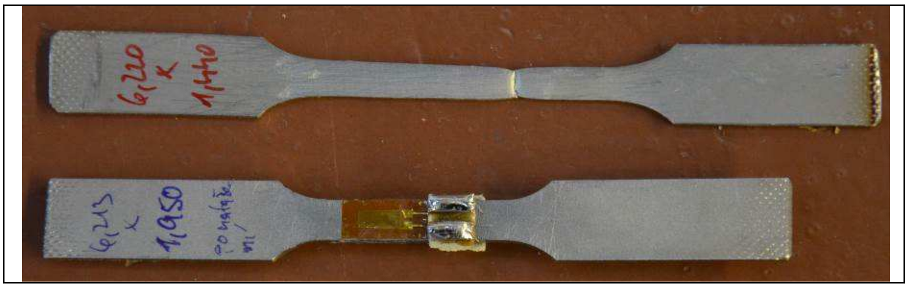

Figure 1. Coupons before and after tensile test.

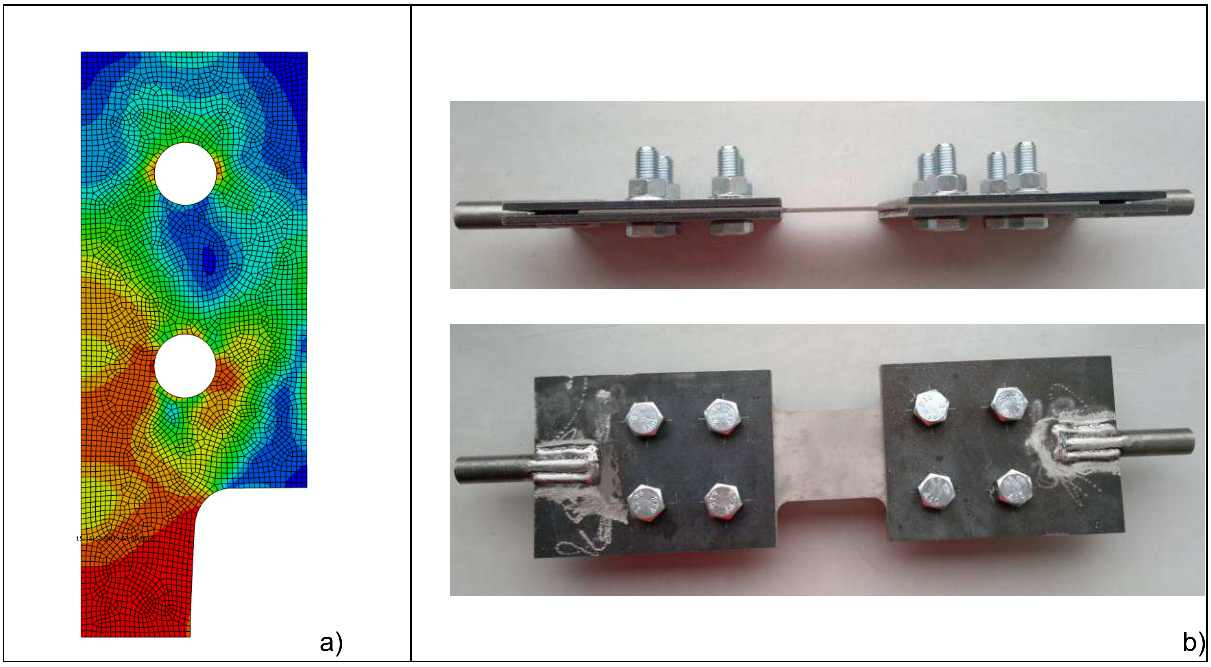

Figure 2. a) Numerical stress model (quarter of sample – symmetric); b) device with stainless steel plate.

The device consists of 2 parts, in which the sample was connected by 4 bolts M16 of 8.8 grade. There were 2 shear planes (represented by 2 plates and sample) to minimalize the eccentricity in the connection. The device was able to clamp to the testing machine by a round bar, which eliminated eventual moment influence. The middle part of specimen served for extensometer set with gage length of 50 mm or less. The device allowed load of the specimen more than 100 kN.

All tests were performed using MTS Qtest 100 kN electromechanical testing machine with all data recording at 0.2 second interval using SPIDER data acquisition system with CATMAN32 data acquisition software. Strain control was used to drive the machine – see Fig. 3. The accepted strain rate for the first period of testing was 0.007% strain per sec up to 1.5% strain and 0.2% strain per sec until fracture. The value of 1.5% strain was determined to ensure the lower stress rate was used to reach the point of 1.0% plastic deformation. The $\sigma 1.0$ value is often used for stress-strain diagram description.

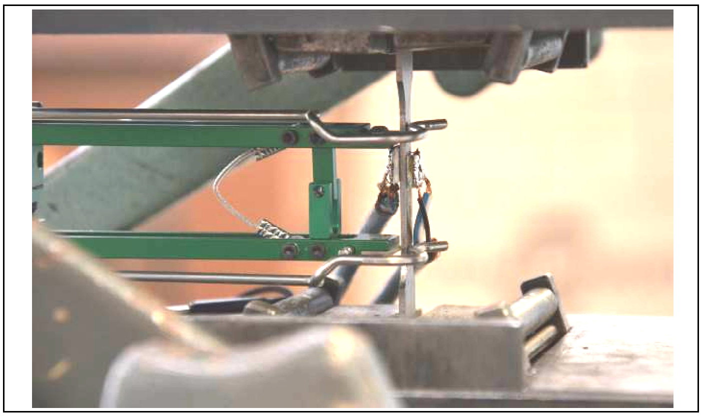

Figure 3. Detail of coupon in testing machine jaws.

4 RESULTS AND DISCUSSION

Determination of slope of linear elastic part of uniaxial stress-strain curve – Young´s modulus process was conducted in accordance with SEP 1235: Determination of the modulus of elasticity on steels by tensile testing at room temperature [7]. However difficulties with modulus of elasticity caused by short linear region of initial stress-strain curve also occurred and the initial modulus was evaluated for lower stresses than recommended. Material properties of the sheet have been assumed as average values from results of 3 samples (Table 3). For the coupons with plastic strain induced previously, only coupon was tested. Results are shown in Tables 4 to 11 and Figure 4. The evaluated characteristics are as follows:

E modulus of elasticity;
$\sigma_{0.2}$ 0.2% proof strength;
$\sigma_{1.0}$ 1% proof strength;
σ_u ultimate strength;
$\varepsilon_{pl,f}$ plastic strain at coupon fracture;
n Ramberg-Osgood hardening exponent [1];
$n'_{0.2,1.0}$ compound Ramberg-Osgood model hardening exponent [1].

The presented results show significant increase in strength by previous plastic forming. Also the influence of the forming direction in respect to the testing direction is clearly visible in comparison of yield strength and material nonlinearity.

Grade	Rolling direction	E (GPa)	$\sigma_{0.2}$ (MPa)	$\sigma_{1.0}$ (MPa)	σ_u (MPa)	$\varepsilon_{pl,f}$ (%)	n	$n'_{0.2,1.0}$
1.4003	P	198,3	326,7	357,1	492,3	18,0	8,4	1,8
1.4003	T	211,9	343,7	374,5	512,3	17,6	8,5	1,9
1.4404	P	191,0	257,2	307,7	620,6	49,5	3,9	2,2
1.4404	T	199,8	279,0	322,0	635,1	57,1	8,8	2,3
1.4162	P	193,3	551,6	623,7	785,9	24,1	7,3	3,0
1.4162	T	195,5	556,5	624,8	765,6	21,1	7,5	3,1
1.4462	P	195,8	600,1	676,6	843,0	22,6	6,9	2,9
1.4462	T	210,7	637,6	722,7	863,7	20,6	5,6	3,4

Rolling direction (tensile test direction): P – parallel to the rolling directions, T – transverse to the rolling direction

Table 3. Summary of tensile material properties for the sheet.

RD	LPSI (%)	*E* (GPa)	$\sigma_{0.2}$ (MPa)	$\sigma_{1.0}$ (MPa)	σ_u (MPa)	$\varepsilon_{pl,f}$ (%)	*n*	$n'_{0.2,1.0}$
P	1	200,6	366,6	399,9	519,6	20,2	7,3	1,7
P	3	204,8	418,5	437,0	493,4	17,8	8,2	2,0
P	5	200,8	487,0	500,6	x	x	5,3	3,0
P	10	189,8	523,7	531,5	543,2	12,6	5,9	3,1
P	15	178,5	548,8	552,1	553,0	8,2	5,2	3,1
T	1	197,3	436,4	456,3	528,1	26,1	9,6	1,7
T	3	196,5	434,7	454,6	524,0	26,0	9,6	1,9
T	5	189,0	482,5	495,3	540,4	22,0	6,2	1,8
T	10	189,8	523,7	531,5	543,2	12,6	5,9	3,1
T	15	194,6	584,0	586,1	588,0	10,4	5,3	3,0

Rolling direction (tensile test direction): P – parallel to the rolling directions, T – transverse to the rolling direction; RD = Rolling direction; PSI = Plastic strain induction in respect to the rolling direction; LPSI = Level (magnitude) of the induced plastic strain.

Table 4. 1.4003 grade tensile material properties for the coupons with plastic strain induced in the direction of the subsequent testing.

RD	LPSI (%)	*E* (GPa)	$\sigma_{0.2}$ (MPa)	$\sigma_{1.0}$ (MPa)	σ_u (MPa)	$\varepsilon_{pl,f}$ (%)	*n*	$n'_{0.2,1.0}$
P	1	192,1	354,1	407,2	455,0	x	9,2	3,1
P	3	202,6	420,2	469,1	503,2	x	4,0	4,0
P	5	194,6	453,7	517,7	526,5	x	3,9	5,0
P	10	189,2	492,0	581,4	581,4	12,0	3,3	5,0
P	15	184,9	585,7	649,6	650,6	8,0	5,3	5,0
T	1	190,7	368,0	415,7	528,0	16,0	6,3	2,5
T	3	207,3	408,2	481,7	534,1	45,2	3,4	4,9
T	5	197,6	464,7	518,2	551,0	22,0	4,7	4,5
T	10	197,2	561,1	612,3	632,4	10,0	4,2	4,0
T	15	201,8	577,1	x	643,5	6,8	4,1	4,0

Table 5. 1.4003 grade tensile material properties for the coupons with plastic strain induced transversally to the direction of the subsequent testing.

RD	LPSI (%)	*E* (GPa)	$\sigma_{0.2}$ (MPa)	$\sigma_{1.0}$ (MPa)	σ_u (MPa)	$\varepsilon_{pl,f}$ (%)	*n*	$n'_{0.2,1.0}$
P	1	195,2	336,7	369,7	655,0	56,6	8,2	2,0
P	3	184,5	356,8	398,8	656,3	56,2	3,2	2,2
P	5	170,4	416,9	440,5	643,8	51,5	5,8	1,8
P	10	198,1	513,1	539,0	695,8	45,2	2,8	1,9
P	15	199,5	564,8	589,5	700,9	40,1	2,6	2,1
T	50	193,2	927,3	954,7	960,9	7,5	2,4	2,1
T	1	201,4	336,7	369,7	655,0	56,6	8,2	2,0
T	3	210,7	356,8	398,8	656,3	56,2	3,2	2,2
T	5	202,9	416,9	440,5	643,8	51,5	5,8	1,8
T	10	188,8	506,7	525,6	653,4	49,4	3,1	2,2
T	15	197,6	548,0	571,0	748,8	56,2	2,7	1,8
T	50	197,4	925,6	960,5	981,7	17,8	3,1	15,0

Table 6. 1.4404 grade tensile material properties for the coupons with plastic strain induced in the direction of the subsequent testing.

RD	LPSI (%)	*E* (GPa)	$\sigma_{0.2}$ (MPa)	$\sigma_{1.0}$ (MPa)	σ_u (MPa)	$\varepsilon_{pl,f}$ (%)	*n*	$n'_{0.2,1.0}$
P	1	194,4	296,1	365,4	654,3	60,4	3,5	3,0
P	3	198,1	336,6	425,7	666,5	57,2	1,8	3,2
P	5	195,1	362,1	461,0	678,0	55,2	3,2	3,4
P	10	193,7	413,8	534,9	699,4	52,0	2,9	3,6
P	15	190,3	452,3	586,0	716,5	44,8	2,9	3,8
T	50	199,2	610,0	x	x	x	3,0	x
T	1	202,0	312,1	370,8	663,6	66,8	4,4	3,0
T	3	209,1	359,7	420,1	670,8	64,4	4,2	3,3
T	5	202,5	399,1	473,5	688,2	62,4	3,6	4,3
T	10	203,8	474,2	553,5	712,6	55,2	3,5	4,9
T	15	204,9	517,2	618,7	743,1	47,2	3,3	4,8
T	50	203,6	679,7	850,9	891,8	26,8	2,9	4,5

Table 7. 1.4404 grade tensile material properties for the coupons with plastic strain induced transversally to the direction of the subsequent testing.

RD	LPSI (%)	*E* (GPa)	$\sigma_{0.2}$ (MPa)	$\sigma_{1.0}$ (MPa)	σ_u (MPa)	$\varepsilon_{pl,f}$ (%)	*n*	$n'_{0.2,1.0}$
P	1	197,9	564,6	651,5	773,6	33,6	5,0	3,6
P	3	187,1	649,9	709,4	822,3	34,3	4,5	2,9
P	5	186,1	726,7	744,3	816,3	33,7	5,6	2,0
P	10	189,6	829,3	843,5	871,0	28,2	4,3	2,8
P	15	187,3	866,4	889,1	898,1	26,3	3,7	5,0
T	50	182,8	920,4	945,0	946,9	20,9	3,5	8,0
T	1	203,5	563,6	642,7	779,4	36,5	3,8	3,4
T	3	199,4	686,2	727,6	809,3	30,5	6,1	3,1
T	5	192,1	735,5	761,5	816,9	28,8	4,2	2,3
T	10	193,4	792,1	827,0	849,1	22,0	3,7	6,0
T	15	184,6	875,3	889,9	895,5	20,9	4,3	6,0
T	50	190,4	922,0	933,7	936,7	15,2	3,9	3,0

Table 8. 1.4162 grade tensile material properties for the coupons with plastic strain induced in the direction of the subsequent testing.

RD	LPSI (%)	*E* (GPa)	$\sigma_{0.2}$ (MPa)	$\sigma_{1.0}$ (MPa)	σ_u (MPa)	$\varepsilon_{pl,f}$ (%)	*n*	$n'_{0.2,1.0}$
P	1	193,6	511,8	668,2	815,5	40,4	2,6	4,5
P	3	200,3	546,4	721,6	824,6	38,0	2,9	3,3
P	5	200,2	637,6	782,3	857,9	33,2	7,2	3,1
P	10	190,3	596,0	835,0	911,4	25,2	2,7	3,1
P	15	197,1	626,9	880,1	956,1	18,4	2,5	2,7
T	50	201,8	653,6	937,0	1002,5	12,8	2,4	3,0
T	1	209,9	556,5	674,4	816,2	38,4	3,4	3,6
T	3	208,6	574,1	728,0	834,9	35,2	2,9	3,5
T	5	201,1	583,6	768,9	850,0	32,8	2,8	3,6
T	10	202,8	646,4	859,5	925,6	22,8	2,7	3,0
T	15	198,7	690,6	912,2	971,2	14,4	2,7	3,8
T	50	202,3	673,6	917,9	1006,9	12,0	1,8	3,0

Table 9. 1.4162 grade tensile material properties for the coupons with plastic strain induced transversally to the direction of the subsequent testing.

RD	LPSI (%)	*E* (GPa)	$\sigma_{0.2}$ (MPa)	$\sigma_{1.0}$ (MPa)	σ_u (MPa)	$\varepsilon_{pl,f}$ (%)	*n*	$n'_{0.2,1.0}$
P	1	193,3	665,2	713,0	834,2	39,6	6,6	2,4
P	3	195,1	741,7	763,1	843,5	28,9	5,5	1,9
P	5	195,3	745,4	790,5	867,2	29,6	3,9	3,2
P	10	188,1	876,6	888,8	913,6	24,4	4,6	2,6
P	15	192,0	931,5	959,8	961,3	19,3	3,2	8,0
T	50	192,6	981,8	997,4	1005,0	15,9	3,8	8,0
T	1	205,2	714,5	758,7	852,5	39,6	6,6	2,4
T	3	200,6	747,1	798,0	860,9	28,9	5,5	1,9
T	5	211,2	825,0	842,6	907,7	29,6	3,9	3,2
T	10	196,5	915,2	926,0	932,6	24,4	4,6	2,6
T	15	207,4	983,5	992,4	1005,3	19,3	3,2	8,0
T	50	200,2	1026,4	1036,0	1039,0	15,9	3,8	8,0

Table 10. 1.4462 grade tensile material properties for the coupons with plastic strain induced in the direction of the subsequent testing.

RD	LPSI (%)	*E* (GPa)	$\sigma_{0.2}$ (MPa)	$\sigma_{1.0}$ (MPa)	σ_u (MPa)	$\varepsilon_{pl,f}$ (%)	*n*	$n'_{0.2,1.0}$
P	1	191,1	608,2	665,8	882,4	34,0	3,2	3,0
P	3	194,5	647,5	756,6	890,3	30,8	3,8	3,4
P	5	195,0	720,2	873,6	940,4	22,8	3,2	3,8
P	10	196,2	747,7	933,9	994,1	16,8	3,0	4,2
P	15	188,2	844,5	1030,9	1072,2	10,8	2,9	4,3
T	50	188,8	897,3	1080,9	1116,0	7,6	3,0	4,2
T	1	211,0	648,4	757,2	900,9	38,8	3,7	3,6
T	3	208,9	691,6	836,8	927,6	32,4	2,7	4,0
T	5	208,4	732,3	860,3	939,3	24,8	3,3	4,0
T	10	209,2	827,2	933,9	994,1	20,4	3,5	4,3
T	15	203,1	865,9	1039,6	1117,4	16,8	3,2	4,4
T	50	213,5	887,3	1070,6	1115,4	15,6	3,1	4,8

Table 11. 1.4462 grade tensile material properties for the coupons with plastic strain induced transversally to the direction of the subsequent testing.

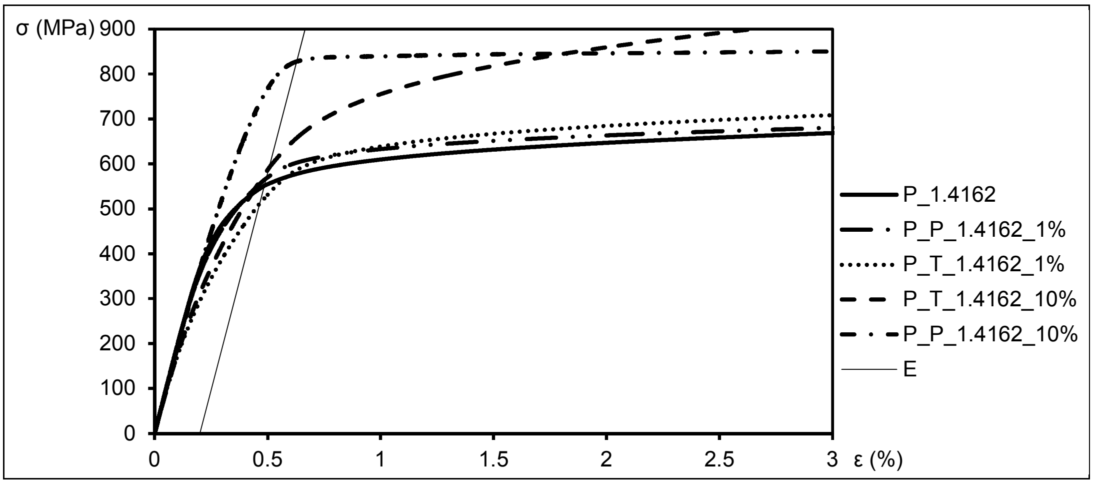

Figure 4. Stress strain diagram of selected 1.4162 samples manufactured parallel to rolling direction (P) with different direction of plastic strain induction (P – parallel, T –transverse) in respect to the direction of testing.

5 SUMMARY

A test program on 92 coupons has been carried out and its results presented. The main material characteristics and stress-strain curves have been also described. Values of non-linearity parameters n, 0.2% proof stress, ultimate tensile strength, ductility and modulus of elasticity will serve for further development of analytical model of strength increase in cold-formed stainless steel cross-sections.

The presented strength increase shows, that the influence of cold forming is important not just for the austenitic grades, but also for the other stainless steel grades. However for the ferritic grade, the ductility could be limiting. After the plastic strain induce in the specimen corresponding to strain during section cold-forming (in corners typically exceeding ten percent), the yield strength could reach about 50 % higher values.

ACKNOWLEDGEMENT

The support of the Czech Science Foundation grant P105/12/P307 “Influence of Cold-Forming on Stainless Steel Mechanical Properties” is gratefully acknowledged.

REFERENCES

[1] Afshan S., Rossi B., Gardner L., *Strength enhancements in cold-formed structural sections - Part I: Material testing*, Journal of Constructional Steel Research, Vol. 83, pp. 177-188 (2013).

[2] Afshan S., Rossi B., Gardner L., *Strength enhancements in cold-formed structural sections - Part II: Predictive models,* Journal of Constructional Steel Research, Vol. 83, pp. 189-196 (2013).

[3] EN 10088-1, *Stainless steels - Part 1: List of stainless steels*, CEN, Brussels (2005).

[4] EN 1993-1-4, *Eurocode 3: Design of steel structures - Part 1-4: General rules - Supplementary rules for stainless steels*, CEN, Brussels (2006).

[5] EN 10088-2, *Stainless steels - Part 2: Technical delivery conditions for sheet/plate and strip of corrosion resisting steels for general purpose*, CEN, Brussels (2005).

[6] EN ISO 6892-1, *Metallic materials - Tensile testing - Part 1: Method of test at room temperature*. CEN, Brussels (2009).

[7] SEP 1235, *Determination of the modulus of elasticity on steels by tensile testing at room temperature*, Verlag Stahleisen GmbH, Düsseldorf (2012).

12th International Conference on
Steel, Space and Composite Structures
28-30 May 2014, Prague, Czech Republic

POST-WELD HEAT TREATMENT OF HIGH STRENGTH S690 STEEL PLATE-TO-PLATE JOINTS - PART I: INFLUENCE OF HEAT TREATMENT

Y.F. Jin*, M.S. Zhao, C.K. Lee and S.P. Chiew

School of Civil and Environmental Engineering
Nanyang Technological University, Singapore
e-mail: *yfjin@ntu.edu.sg

Keywords: high strength steel, post-weld heat treatment, residual stress

Abstract: *Literature shows that it is a big challenge for high strength heat treated steel to achieve sufficient deformation capacity to avoid brittle fracture under as weld conditions. This study experimentally investigated the potential improvement in the ductility as well as the reduction in residual stress of welded plate to plate joints by post weld heat treatment techniques. The coupon test found out the proper temperature used to carry out the post weld heat treatment. The experimental results indicated that post weld heat treatment could significantly reduce the magnitude of the residual stress, which contributes to alleviate the risk of fatigue failure of welded structures.*

1. INTRODUCTION

Structural steel has been used in construction for more than 100 years. With the development of design ideas and fabrication abilities, the material has undergone significant changes. Responding to the market demand for high strength materials, quenched and tempered steel plates with yield strength more than 690MPa for structural usage was developed in the 1960s[1]. Due to the huge raise in load carrying capacities of common structural forms and improved economies of construction, such steels are supposed to be the mainstream of the future[2-7]. As for the drawbacks, research demonstrated that it was not possible to achieve sufficient deformation capacity[8-11], and was susceptible to heat as inherited from the heat-treatment hardened microstructures[12].

Welding is of great economic importance for steel structures, as one of most important tools available to the engineers in their efforts to reduce the production and fabrication costs. Greater freedom in design is also made possible by the use of welding. However, heat is essential to the making of most welds in the discussion on the meaning of the noun “weld”. American Welding Society defines weld as a localized coalescence of metals. This coalescence is brought about by the application of heat with or without fusion, the addition of filler metal or the application of pressure[13]. The application of heat input produces a variety of structural, thermal and mechanical effects into the heat affected zone, e.g. expansion and contraction, metallurgical changes and compositional changes. Steels are more significantly altered by the heat of welding than other metals, and heat treatment or work hardened steels are the most sensitive types[14].

Although welding for heat treated high strength steels may cause a lot of troubles for the global behavior of joints, researchers showed great interests in their welding properties. Reports have shown that the amount of residual stress in welded quenched and tempered steel structures are high[15, 16] and the deterioration of mechanical properties in the heat affected zone including strength, hardness and toughness is inevitable[17]. However, few reports regarding the effects of those drawbacks to the global behavior of virtual structures could be found.

This study investigated the tensile behavior of reheat, quenched and tempered steel plate to plate joints fabricated by manual shield metal arc welding method. Joints in angles 45° and 90° with different thicknesses were tested. Further, the effects of post weld heat treatment were studied for those joints, including the influences to residual stress distribution and the tensile behavior of the joints.

2. MATERIAL, SPECIMENS AND TEST SETUP

The research materials and specimens in this project, reheated, quenched and tempered (RQT) structural steel plate RQT-S690, have nominal yield strength of 690 N/mm^2, and tensile strength between 790 N/mm^2 and 930 N/mm^2 and elongation capacity around 15%. These RQT steel plates comply with the EN 10025-6 grade S690 specification[18], which is approximately equivalent to the ASTM A514 steel[19]. The mechanical properties of RQT-S690 acquired from standard coupon tensile test are shown in Table 1 in comparison with a randomly selected hot rolled rectangular hollow section manufactured to grade S355J2H. Although the ductility of RQT-S690 is sacrificed during the hardening processes, the extraordinarily high strength offered better serviceability under elastic stage.

	$f_{0.2,n}$ (MPa)	$f_{2.0,n}$ (MPa)	$f_{u,n}$ (MPa)	E_n (GPa)	Elongation
S355J2H	423.4	461.6	535.1	204.5	34.2%
RQT-S690	769.0	817.1	849.8	201.3	14.7%
Difference	181.6%	177.0%	158.8%	98.3%	43.0%

Table 1 Material Properties of test specimens

The specimens of coupon were cut from 8mm thick RQT-S690 HSS plates in the longitudinal direction. The configuration was designed according to EN 10025-5.

The specimens were fabricated by welding two plates in dimension of 440 mm x 150mm x 8 mm (as well as 12mm and 16mm). The joints was designed according to the AWS structural welding code[13]. The configuration of the 45° joint is shown in Figure 1. Three bolt holes were drilled at both sides of the chord to fix the specimens in the test rig. The distance between two rows of bolt holes (center to center) is 290 mm.

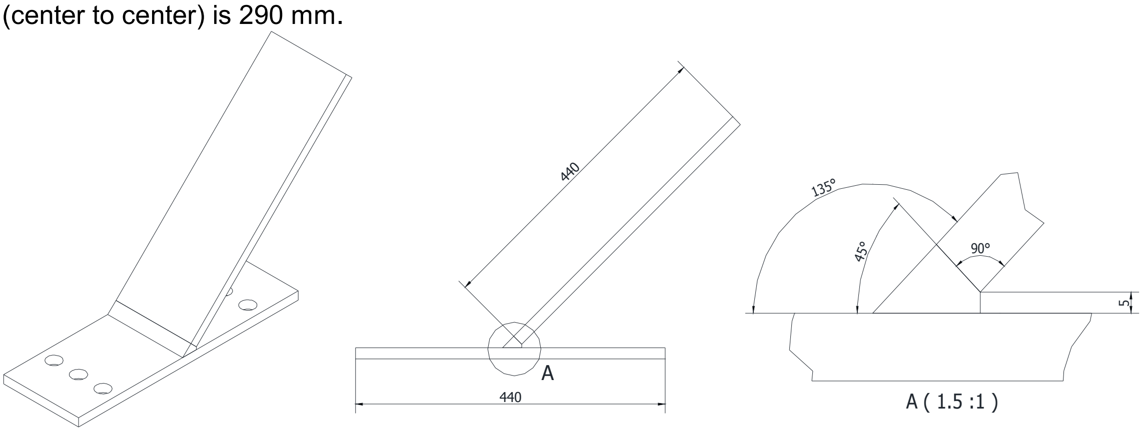

Figure 1: Configuration of Joints

The tensile tests were carried out in an INSTRON 8506 servo-hydraulic test machine with maximum loading capacity of 200 T. To fix the specimen into the uniplanner test machine, two types of support joints made of S355 with thickness of 45mm were fabricated according to the same configuration. The specimens are fixed into the support joints by 6 high strength hexagon bolts in grade 10.9HR, M24, as shown in Figure 2. As the tests go on, the load-displacement relationship is monitored in case any problem happened. The loading rate was 1 mm/min constantly until failure happened.

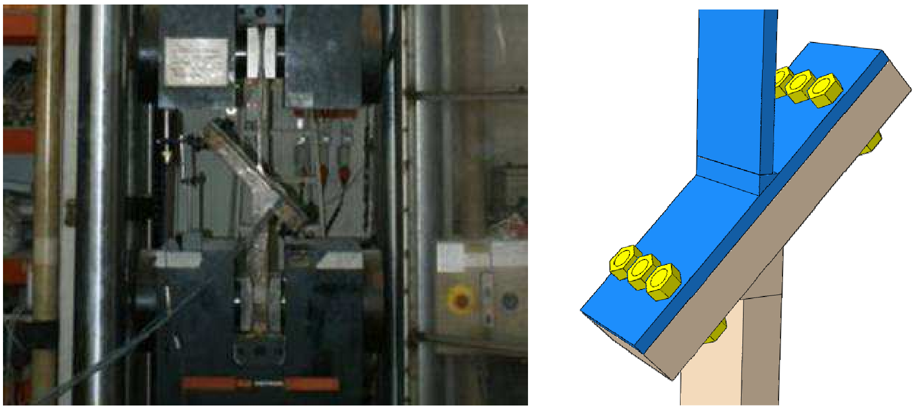

Figure 2: Test Setup

3. THE TENSILE BEHAVIOR OF AS WELD JOINTS

As the tensile loads at the brace end increased, the chord deformed into triangular shape correspondingly. Obvious plastic hinges could be found at the bolted area and near weld toes. For all specimens under as weld conditions, failures always happened as brittle fracture at the chord plate near weld toe (joints in 45°) or weld root (joints in 90°). Figure shows the test in progress for 45-16mm and its final fracture.

Figure 3: Tensile Behavior of As Weld Joints

4. POST WELD HEAT TREATMENT STUDY

4.1 The heat treatment methods

PWHT is normally applied to mild steel weldment to remove residual stress, restore deformations during welding or improve the load-carrying capability in the brittle fracture temperature range of service. In fact, the beneficial effects of PWHT are not primarily due to reduction of residual stresses, but rather to improvement of metallurgical structure by tempering and removal of aging effects. This process is widely accepted as beneficial for mild steel weldment since the microstructure, i.e. the mixture of pearlite and proeutectoid ferrite formed at temperature above normal PWHT range, would be little altered unless the time of heating is prolonged or higher than usual temperature are employed[14]. However, it may introduce unpredictable changes into the microstructure of hardened steel weldment, which is extremely complicated and normally very sensitive to heat. This is why PWHT for quenched and tempered steel as well as cold work hardened steel is forbidden by AWS (clue 3.14) [13], despite tempering is necessary in the manufacturing of quenched and tempered steel.

In order to fulfill the heat treatment task, the laboratory heating furnace Nabertherm LH216 with a maximum heating capacity of 1200°C and robust refractory bricks inside was employed. The external and internal dimensions (width × depth × height) of the oven were 900×900×1200 mm and 500×500×700 mm respectively, as shown in Figure 4. Inside the furnace, the specimens were simple supported in the oven by three ceramic bars to release the thermal expansion or contraction during the heat treatment. Besides the thermometer measuring the temperature in the furnace, a thermocouple was attached to the specimens to monitor their inner temperatures, guaranteeing the temperature to be within the range of the designed values ±3°C below 600°C and ±5°C from 600 to 1000°C.

Figure 4: The Oven Used to Fulfill Heat Treatment

4.2 The heat affected coupon

To study the residual strength of RQT high strength steel, a post heat treatment residual strength test was conducted. Standard coupon specimens were first gradually heated and cooled in a laboratory furnace and the residual strength were tested in ambient temperature condition. In this study, the targeted elevated or treatment temperatures included 400℃, 600℃, 800℃, 900℃, and 1000℃. A constant heating time rather than constant heating speed was set herein, since different parts suffers to heat in different extents yet the same period in fire conditions.

During heating, a thermocouple was used to monitor the inner temperature of the specimens, guaranteeing the temperature in the coupon to be within the range of the designed values ±3℃ below 600℃ and ±5℃ from 600℃ to 1000℃. After the preset temperature was reached, another 10 minutes were maintained for the temperature to be stabilized and uniformly distributed. Subsequently, the specimens were cooled down naturally in the furnace until 300 when they were moved out and continued to cool in air. 300℃ was chosen as the critical temperature since steel's properties would not change below it according to the elevated temperature test results.

The stress-strain curves of RQT-S690 after heated and cooled down as shown in Figure 5. The temperatures in the legend refer to the highest temperature that the specimens were once heated to in furnace. The mechanical properties were stable below 400°C or above 900°C. In between, the stress-strain curves exhibit obvious yield stage like high tensile strength. As the temperature rising, the yield and ultimate strengths of HSS kept decreasing but the ductility kept increasing. While heat treated temperature reach to 800°C, the largest elongation was obtained. 1000°C was considered to be the end of this series test, since the difference between stress-strain curve of 900°C and 1000°C almost only existed in ductility.

Through the post-weld heat treatment study of the standard coupon test, it is found out that RQT-S690 high strength steel tended to turn back to the softer but more ductile parent steel after exposure to high temperatures. 600℃ is the critical temperature above which significant loss strength will happen, with minor loss occurring between 400℃ and 600℃. Therefore, 600℃ was chosen as the heat treated temperature used in following plate-to-plate joints post weld heat treatment.

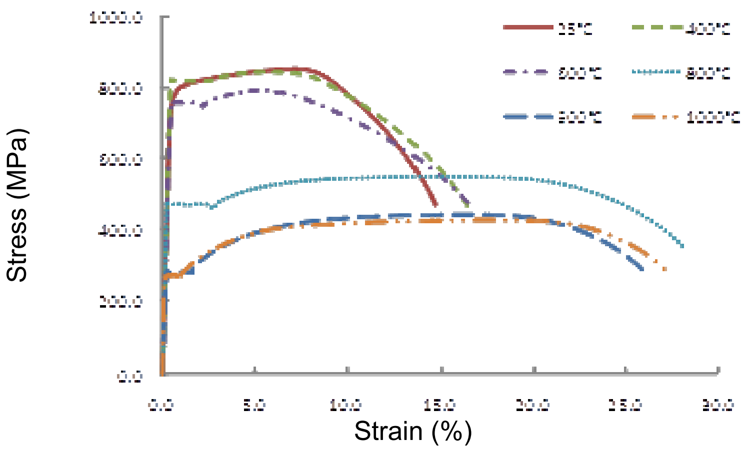

Figure 5: Stress-Strain Curves of RQT-S690 after Heated to Different Temperatures.

5. RESIDUAL STRESS STUDY FOR PWHT-600 JOINTS

5.1 PWHT-600

The post weld heat treatment was carried out for the plate-to-plate joints. It took one and half hours to heat the specimens from 25°C to 600°C and 15 min for the temperature inside the specimens to stabilize, as designed according to AWS D1.1 clue 5.7[13]. A short maintaining time is chosen due to consideration of deterioration in the mechanical properties and embrittlement of quenched and tempered steel caused by long time tempering[14]. Subsequently, the specimens were held within the furnace to be cooled slowly. To verify the effect of relieving residual stress by heat treatment, two set of specimens which included 12mm and 16mm were chosen to test and analysis the residual stress.

5.2 The residual stress measurement

The standard ASTM hole-drilling method[20] was employed to measure residual stress in this study. This method can identify in-plane residual stresses by removing localized stress and measuring strain relief in the boundaries of the drilled hole. Following ASTM, the drilling is limited to 2mm from the surface of specimen by 8 successive drilling steps. Therefore, it causes relatively little damage to the specimen and allows localized residual stress measurements. In the designed locations, a hole was drilled in the center of the special strain gauge rosette, and then the released strain was recorded for further analyzing the residual stresses.

A special type of strain rosette FRAS-2 was used to measure the released strain of specimen during drilling. As the residual stresses caused by welding are confined to areas near the weld, 9 points on the chord plate were picked out to capture the residual stress distribution near the weld toe. The strain gauge scheme in measurement is shown in Figure 6. For each point, both longitudinal (S11) and transversal (S33) residual stresses were measured. The test results of each point are shown in Figure 7-9.

5.3 The effects of PWHT to residual stress

Residual stress is induced during welding due to the highly localized heating and subsequent uneven cooling, non-linear material properties and thermal expansion / shrinkage. Although compressive residual stresses are supposed to be beneficial sometimes, e.g. surface compressive residual stresses could increase the fatigue strength of certain types of welded specimens, they are thought to be generally harmful to structures.

It could be seen from Figure 7 (a) that the gradient of residual stress changes drastically along both S11 and S33 directions. The transversal residual stresses distribution is generally symmetrical to the center plane perpendicular to the weld line. The values of residual stresses in the center plane are positive, which means the material is in tensile. When the measured points transferred to both edges, the stress state presents a downward trend and parts of the stresses shade into compressive at last. The distribution of longitudinal stress seemed to be more seriously affected by the distance to weld line. In general, the stresses far away from weld line are less than the stresses in the near points. Figure 7 (b) shows the residual stress distribution in longitudinal direction of the duplicate specimen heated to 600. It could be seen that the amount level of residual stresses after PWHT-600 was greatly decreased, while the characteristics in distribution was not fully erased. The peak value of stresses drops to 60MPa from 236MPa.

The transversal residual stresses (in S33 direction) of both as-weld and PWHT-600 specimens are shown in Figure 8. It could be found in Figure 8 (a) that the region in both starting and ending of the weld line bearing extremely compression. The stresses in the weld starting side are much bigger than that in the finish side, which seems due to the multi-pass welding as reaction stresses from extra distortion and subsequent mismatch as welding being carried out. After heat treatment, with the stress redistribution and microstructural transformation, the compressive has been a great release.

Figure 9 shows the residual stress distribution perpendicular to weld line (S11 direction) for 16mm 45° joints. Two contour diagrams were plotted to compare the PWHT effect on relieving residual stress. The residual stress distribution in Figure 9 (a) is same as that in Figure 7(a) that the center plane contains the largest and tensile stress. At point P2 (5mm from weld toe), the maximum residual stress for specimen without heat treatment reaches 285MPa. Although there is a singular point which might be caused by measuring error, it could be seen from Figure 9 (b) that the residual stresses were reduced as a low level. The heat treated effect is significant for 16mm specimens.

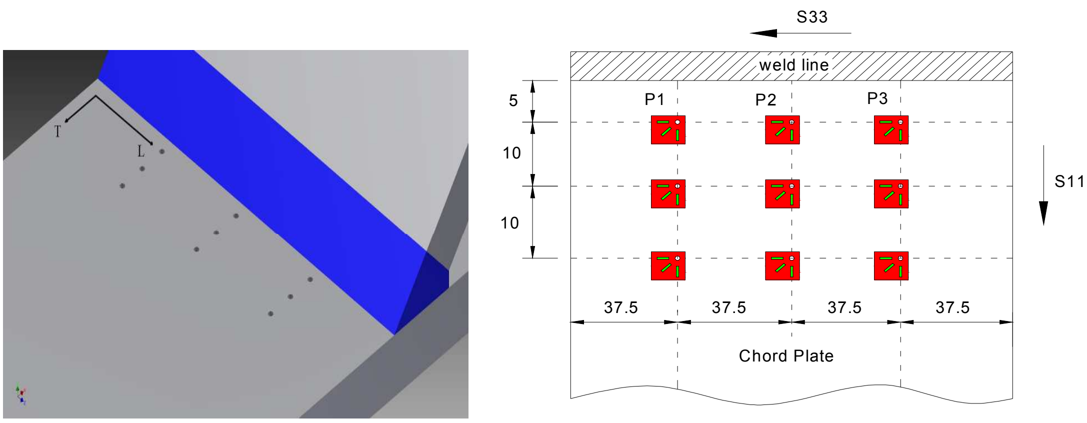

Figure 6: Strain Gauge Scheme on Chord Plate

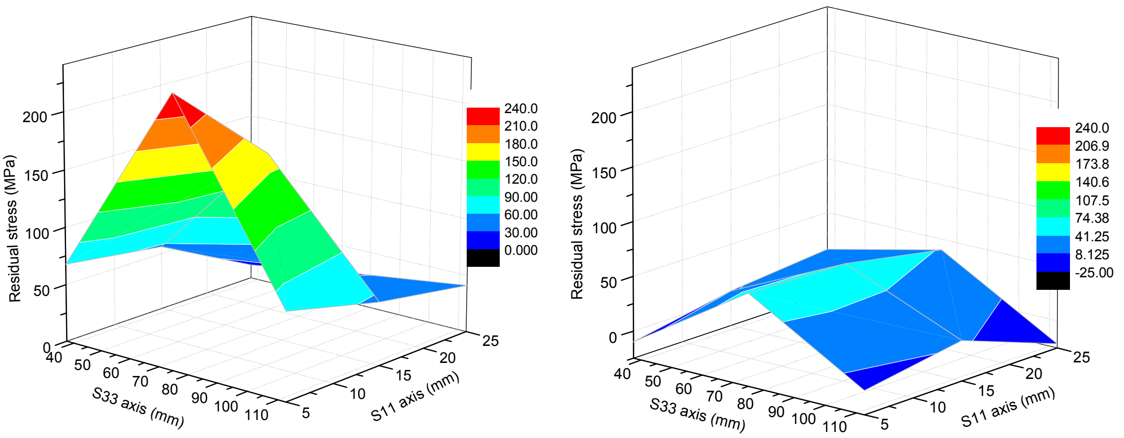

Figure 7: Residual Stress of 12mm Specimens in S11 Direction: (a) As-weld; (b) PWHT-600

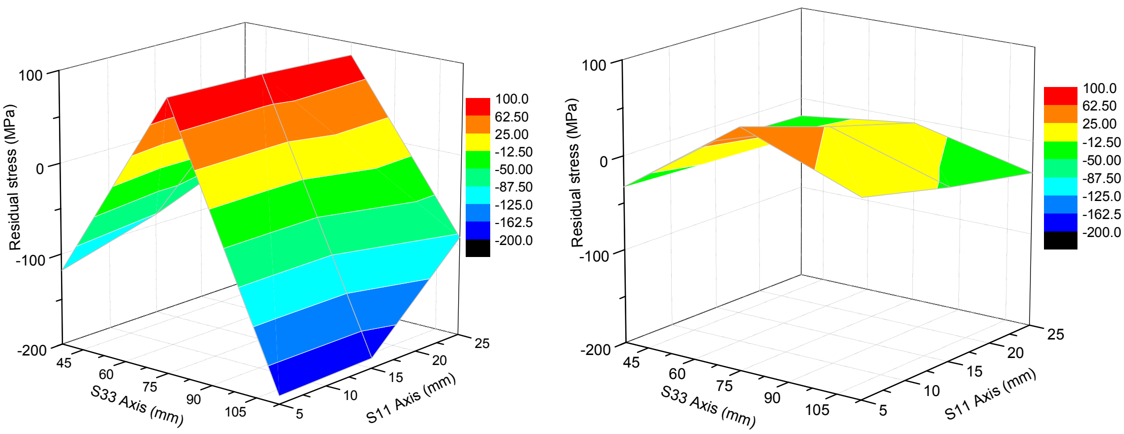

Figure 8: Residual Stress of 12mm Specimens in S33 Direction: (a) As-weld; (b) PWHT-600

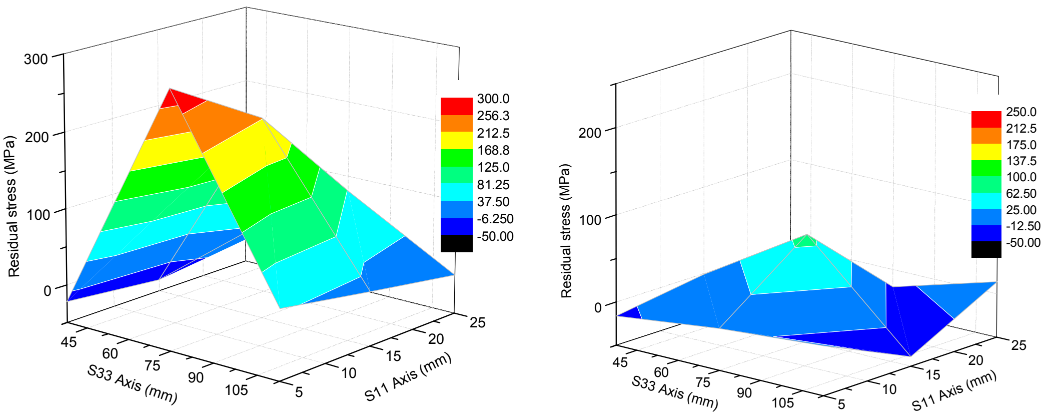

Figure 9: Residual Stress of 16mm Specimens in S11 Direction: (a) As-weld; (b) PWHT-600

6. CONCLUSIONS

this paper has presented the experimental investigations of effect of heat treatment on the material properties of reheated, quenched and tempered high strength steel RQT-S690 as well as residual stress of plate-to-plate joints. The coupons were heated to high temperatures, which range from 400°C to 1000°C, and cooled down at ambient temperature. It was found out that 600°C was the critical temperature above which serious deterioration of strength would happen, although above 85% of the nominal strength still existed at that temperature.

The standard ASTM hole-drilling method was employed to measure the value of residual stress at a critical region of the joints. The experimental results indicated that while tensile or compressive residual stresses with high magnitude could appear near the weld toe, the post weld heat treatment could significantly reduce the magnitude of the residual stress.

REFERENCES

[1] R. Bjorhovde, Development and use of high performance steel, Journal of Constructional Steel Research, 60 (2004) 393-400.
[2] L. Gao, H. Sun, F. Jin, H. Fan, Load-carrying capacity of high-strength steel box-sections I: Stub columns, Journal of Constructional Steel Research, 65 (2009) 918-924.
[3] G. Shi, H. Ban, F.S.K. Bijlaard, Tests and numerical study of ultra-high strength steel columns with end restraints, Journal of Constructional Steel Research, 70 (2012) 236-247.
[4] X.-L. Zhao, D. Van Binh, R. Al-Mahaidi, Z. Tao, Stub column tests of fabricated square and triangular sections utilizing very high strength steel tubes, Journal of Constructional Steel Research, 60 (2004) 1637-1661.
[5] C. Miki, K. Homma, T. Tominaga, High strength and high performance steels and their use in bridge structures, Journal of Constructional Steel Research, 58 (2002) 3-20.
[6] H.V. Long, D. Jean-François, L.D.P. Lam, R. Barbara, Field of application of high strength steel circular tubes for steel and composite columns from an economic point of view, Journal of Constructional Steel Research, 67 (2011) 1001-1021.
[7] G. Pocock, High strength steel use in Australia, Japan and the US, Structural Engineer, 84 (2006) 27-30.
[8] R. Bjorhovde, M. Engestrom, L. Griffis, L. Kloiber, J. Malley, Structural steel selection considerations, Reston (VA) and Chicago (IL): American Society of Civil Engineers (ASCE) and American Institute of Steel Construction (AISC), 2001.
[9] P. Može, D. Beg, Investigation of high strength steel connections with several bolts in double shear, Journal of Constructional Steel Research, 67 (2011) 333-347.
[10] J.M. Ricles, R. Sause, P.S. Green, High-strength steel: implications of material and geometric characteristics on inelastic flexural behavior, Engineering Structures, 20 (1998) 323-335.
[11] A.M. Girão Coelho, F.S.K. Bijlaard, Experimental behaviour of high strength steel end-plate connections, Journal of Constructional Steel Research, 63 (2007) 1228-1240.
[12] H.K.D.H. Bhadeshia, R.W.K. Honeycombe, Steels: microstructure and properties, 3th ed., Elsevier Science & Technology, Oxford, United Kingdom, 2006.
[13] AWS, Structural Welding Code, in: steel, American National Standards Institue, Miami, 2008.
[14] R.D. Stout, Weldability of steels, fourth ed., Welding research council, New York, 1987.

[15] C.K. Lee, S.P. Chiew, J. Jiang, Residual stress study of welded high strength steel thin-walled plate-to-plate joints, Part 1: Experimental study, Thin-Walled Structures, 56 (2012) 103-112.
[16] Y.-B. Wang, G.-Q. Li, S.-W. Chen, The assessment of residual stresses in welded high strength steel box sections, Journal of Constructional Steel Research, 76 (2012) 93-99.
[17] T. Mohandas, G. Madhusudan Reddy, B. Satish Kumar, Heat-affected zone softening in high-strength low-alloy steels, Journal of Materials Processing Technology, 88 (1999) 284-294.
[18] BSI, hot rolled products of structural steels: part 6 technical delivery conditions for flat products of high yield strength structural steels in the quenched and tempered condition, BS EN 10025-6, in, British Standards Institution, London, 2004.
[19] ASTM, Standard specification for high-yield-strength, quenched and tempered alloy steel plate, suitable for welding, in, ASTM International, West Conshohocken, United States., 2009.
[20] ASTM E837-08, Stardand test method for determining residual stresses by hole-drilling strain-gage method, ASTM international, West Conshohocken, PA 19428-2959, Unitied States, 2008.

3-D STEEL FRAME AS FLOOR DECK SLAB FOR LABORATORY

Anil Kumar

Senior Manager, Sasken Communication Technologies Limited
139/25, Ring road, Domlur, Bangalore, India
e-mail: anil.kumar@sasken.com, webpage: www.sasken.com

Keywords: 3D- Frame, Nominal bore, Tensile Bolts, Anchor fasteners, false floor tiles.

Abstract: *The main object of this paper is to highlight the methodology adopted to ensure stability of lab equipment subjected to lateral motions, if any. 3-D double layer rigid steel frame was considered as additional floor deck slab over an existing sunken concrete slab, for a laboratory in 2nd floor of 8 story RCC building, to ensure stability of series of lab equipment, each measuring 8' feet tall and 600mm X 750mm on plan, from any lateral motions caused- mainly due to Seismic forces.*

The frame was analyzed using Staad-Pro considering the equipment load & self-weight of frame and designed for maximum forces. The top and bottom frame were rectangular members and diagonal members were circular members. The existing false floor tiles were reused to form the flat surface over which the lab equipment was mounted. All lab equipment placed over false floor tiles was anchored to steel frame by high tensile bolts of 12mm dia at all four corners of each unit. The entire frame was anchored to surrounding RCC beams by anchor fasteners thereby restricting movement of entire frame. The size of steel frame grid was restricted to 600 mm X 600 mm on plan to reuse the already available false floor tiles of 600mm size. The depth of frame was restricted to 350 mm to match the available depth of sunken concrete slab.

Considering the ease of fabrication, erection & installation in terms of modules, the 3-D steel frame was adopted successfully and work was executed at a reasonable price without loss of business hours. Now, all equipment is mounted, anchored and stability is achieved. This concept of ensuring stability was conceived after Audit observation from our counterparts.

1. INTRODUCTION

Sasken Communications is a leading provider of telecommunication Software solutions and is having its Corporate Office at Ring road, Domlur, Bangalore. The office building is a eight story RCC framed structure completed during the year 2000 with all world class facilities like Auditorium, Montessori, library, cafeteria, STP plant ATM center, landscape areas etc. The office is accommodating about 1300 software professionals and lab space. The built up area of the building is 2, 98,000 sq ft with two levels of basement parking.

1.1 Current scenario of the lab areas and equipment placing.

The major portion of the lab areas in the building is by and large sunken portion and depth of sunken floor is 350mm. One of the lab areas measuring 850 Sq ft required solution for instability of lab equipment. In order to match the finished floor level of neighboring areas, the raised floor (false floor tile) system was adopted in sunken portion. All electrical and network cables in the lab area are drawn in the sunken portion of the lab area so that all cables are concealed. Dimensions of the Lab equipment, varies from 600mm X 600mm to 900 X 900mm on plan and height is 8 feet. All the lab equipment is directly mounted on the false floor system without anchoring at the base of equipment and liable for distortions due to lateral motions, if any, particularly due to Seismic forces. Thus during lab audit, this instability of the lab equipment was identified and required a solution. Ref figure 1.

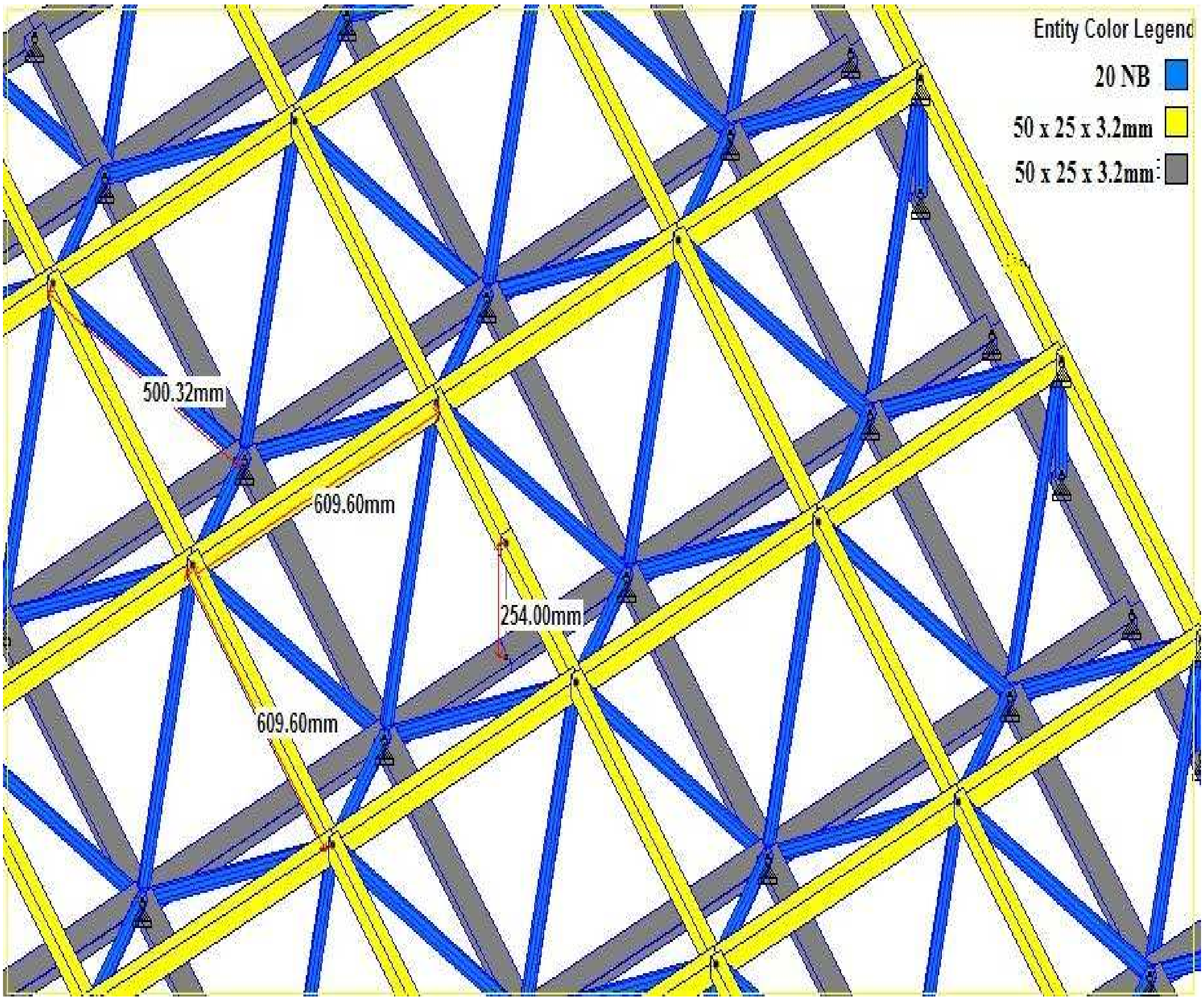

Figure 1. Details of space frame

1.2 Options explored considering site constraints.

A) Option of using I-beam sections was considered and bottom flange shall be anchored to sunken slab & the lab equipment shall be anchored to top flange and rest of the areas shall be covered with raised floor system. The site constraint was: Below the 2nd floor sunken slab, Auditorium was located and our desire was not to puncture the large span concrete slab for bottom flange anchoring. Also, considering the weight of I beams, lifting and installation at 2nd floor level it was just a difficult task

B) Welded 3-D double-layered Steel frame (space frame) in terms of modules was considered as an optimum solution with respect to the prevailing site constraints. The rigidly connected frame resists higher loads and since the entire frame is anchored to sides of existing RCC beams, the movement of the frame is restricted. The lab equipment is anchored to steel frame by high-tension bolts at base and harness belt support at top of equipment, which ensures stability of the equipment. Hence 3-D steel frame in terms of modules was preferred to I beams. (Ref fig ,2).

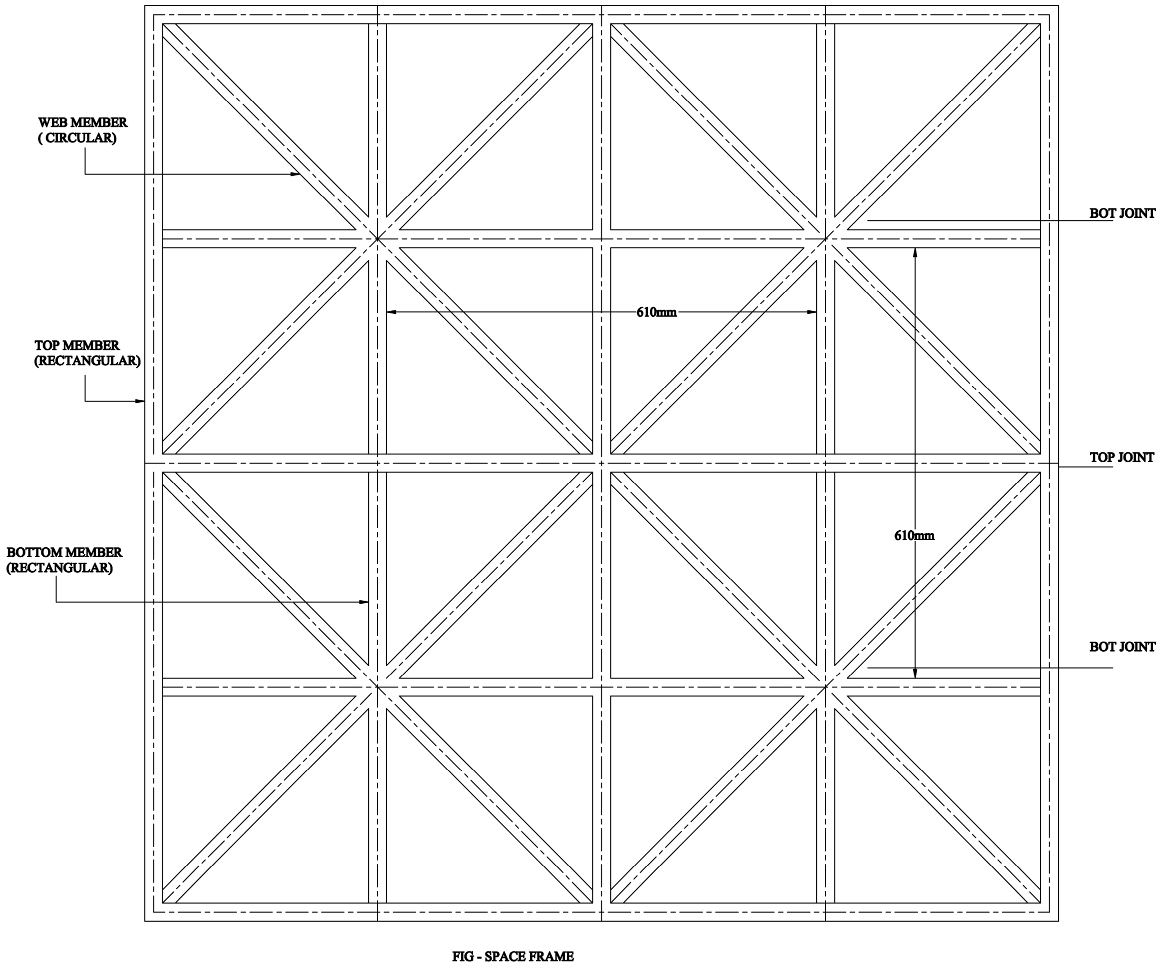

Figure 2. Space frame dimensions.

2 BEHAVIOR OF 3-D FRAME

The double layer grid also known as spatial structures are structures that resist external actions by distributing their effects in three dimensions (hence the term “Space”). Any structure that is detailed in 3D and structurally modeled and analyzed in 3D can be considered as a space structure. Welded 3D frame combines in to a lightweight structure but very rigid, highly structural efficient and ease of construction in structural applications. In fabrication of the tubular space frame, it is essential to keep the amount of fabrication and profiling of tube ends to a minimum. The critical factor in space frame is dimensional tolerance that can be achieved during the erection.

3. GRID SIZE

Generally, the space frame grid of 1.5M x 1.5M is preferred from structural point of view but here in Sasken lab area, the depth of sunken slab of 350mm restricted the grid size. Also, the existing false floor tiles of size 600mm x 600mm are to be reused to have the flat surface over which the lab equipment shall be mounted. Hence, the grid size of 600mmx 600mm is adopted with a depth of

350mm.The ends of frame were anchored to sides of existing RCC beams to restrict any movements. All top & bottom members are rectangular members of size 50mmX 25mmX 3.2 mm and diagonal members were circular pipes of 25NB,3.2 mm thickness. (Refer Fig No. 3)

Figure 3. Space Frame in position over sunken concrete slab.

4. ANALYSIS & DESIGN OF 3-D FRAME

Analysis of 3-D frame was carried out by using STAAD PRO program for different load combinations and maximum forces were tabulated. The maximum weight of individual equipment or the design Live load is considered as 750kg/m2. The boundary conditions were assumed as hinged, translations restrained.

5. MATERIAL SPECIFICATIONS

- **a.** Circular pipes (diagonal members)—NB 25 mm at 2.4 kg/m Confirming to Indian standards ----IS 1169.
- **b.** Top & bottom members 50mm x 25mm x 3.2 mm at 3.24 confirming to Indian standards IS-1239.
- **c.** Unit weight of steel – 7850kg/ Cum, Youngs modulus—2.0E+05 Mpa.
- **d.** High tensile bolts—M-12 mm dia x 1whose pull out capacity is 3300kgs.

6. GEOMETRY

- Configuration : Square on Square
- Area covered : 850 Sqft
- Grid size adopted : 600mm X 600mm
- Depth of frame : 350mm
- Joints : Welded
- Frame end : Anchored to existing RCC beams by anchor fasteners.

7. ANALYSIS OF RESULTS

Maximum Compressive force: 1.25 MT
Maximum Tensile force: 0.72 MT
Circular members of NB 25mm for all diagonal members and rectangle members of 50mmx25mmx3.2mm for top & bottom chord members with the following properties is found to be satisfactory .

Circular members: 25 NB,3.2 mm thickness with cross sectional area of 3.06sqcm, weight / m run: 2.41kg/m.
Moment of Inertia: I = 3.61 Cm4.
Modulus of section: Z = 2.14Cm3.

Rectangular sections: 50mm X 25mmX3.2 mm with C/s area of 4.13sqcm
Moment of Inertia: Ixx = 11.63 Cm4, Iyy = 3.80 Cm4
Modulus of section: Zxx = 4.65 Cm3 Zyy = 3.04 Cm3

8. CONSTRUCTIONAL METHODOLOGIES

The structure is divided into a number of modules. Individual modules of required size were assembled on ground and they are lifted and connected in the final position by welding. It is much easier to assemble the individual members on the ground to form a module compared to the same work done in the lab area. The sole intention was to reduce the welding work inside the lab area from safety point of view. The ends of the frame were anchored to existing RCC beams on all four sides by using anchor fasteners of 12 mm dia. After frame is completely installed, false floor tiles of size 600mmx600mm were laid in such a manner to have a flat surface, over which the lab equipment was mounted in a desired pattern. Four holes were drilled through false floor tiles at four corners of each equipment and 12mm bolts were used to anchor the equipment to space frame at base and harness belt support was provided at top of equipment to prevent any distortion. Thus the stability of lab equipment was ensured. The work was executed with out loss of business hours. (Ref figs 4,5,6).

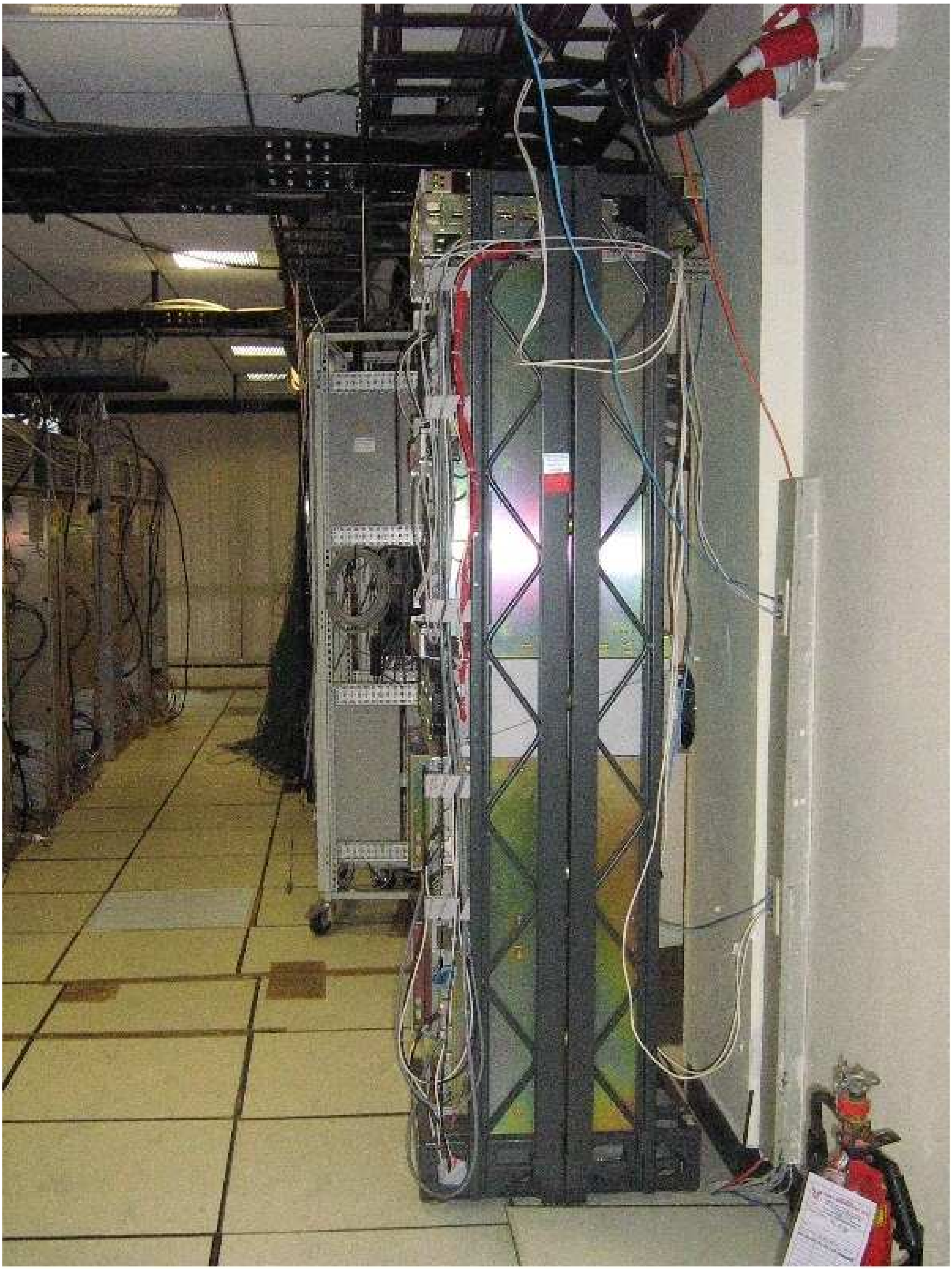

Figure 4. Lab units are in position over 3D frame.

Figure 5. Lab units in series mounted over 3 D frame.

Figure 6. Details of Anchor Fastener

9. CONCLUSION

The double-layered 3D frame with site constraints was successfully executed to cover 850 sqft of laboratory area in a limited time of 2 weeks & reduction in cost is also achieved compared to other options explored. The stability of lab equipment was achieved after anchoring the equipment to the frame & using harness belt at top. Thus the sole object of this work was completed satisfactorily. Since it is modular frame, flexibility of removal and reusable is possible depending on the need.

10. ACKNOWLEDGEMENT

The author would like to thank the Nortel lab & Facilities team members of Sasken for their support in completing the 3d Frame to achieve stability of lab equipment. Also, the author expresses thanks to Mr.S.P.Umashankar, Structural Project Management Consultants India Pvt Ltd, for technical assistance in execution of the steel frame in time.

11. REFERENCES

[1] INSDAG,'recent case studies of pre-engineered buildings and space frames in India', Institute for Steel Development & Growth Publication, Aug 2000.
[2] Hand book on Steel structures –Reynolds
[3] IS: 800 code of practice for use of structural steel in general building construction
[4] IS: 806 code of practice for use of steel tubes in general building construction
[5] IS: 961 structural steel (high tensile)
[6] IS: 1169- steel tubes for structural purposes
[7] IS: 4923 -hollow steel sections for structural use.

RETROFITTING STRATEGIES OF RC WALL PANELS WITH CUT-OUT OPENINGS USING CFRP COMPOSITES

Tamás Nagy-György*, István Demeter* and Daniel Dan*

* Politehnica University Timisoara
Department of Civil Engineering
e-mail: tamas.nagy-gyorgy@upt.ro, webpage: http://www.upt.ro

Keywords: RC wall, precast, FRP, seismic retrofit, cut-out opening

Abstract. *This paper presents the seismic behaviour of the reinforced concrete (RC) wall panels with cut-out openings retrofitted with externally bonded carbon fibre reinforced polymers (CFRP-EBR). The objectives were to investigate the seismic performance of the precast reinforced concrete walls, to assess the weakening effects caused by doorway cut-outs and to reveal the effects of the strengthening strategy. In the experimental part of the program seven quasi-static cyclic tests on near-full scale precast reinforced concrete wall specimens were conducted. The experimental variables referred to the opening and the strengthening condition. The retrofitting technique by means of CFRP-EBR yielded improved behaviour characteristics, primarily in terms of energy dissipation; however, certain limitations were identified on the use of this strengthening system in reversed cyclic applications. It was concluded that the CFRPs subjected to alternating tension-compression forces are susceptible to premature failure.*

1 INTRODUCTION

Reinforced concrete (RC) shear walls are one of the most reliable lateral load resisting systems which were proved by several earthquakes. Despite of the seismic performance the widespread use of the shear-walls is hindered by the functional rigidity of this system. However, in East- European countries, and especially in Romania, the precast large panel systems were extensively used. In the 1950-1990 period more than 40 000 five-storey large panel residential blocks of flats were constructed[1] . The architectural drawback is resolved by piercing the existing solid walls with new openings. Structural alterations by doorway cut-outs, impair the seismic performance of a RC wall member. According to the common sense of structural engineering the weakening effect should be proportional to the size of the cut-out opening, although this assumption needs further data regarding the shape and position of the opening. Moreover, the weakening should be quantified in terms of strength, stiffness, ductility and energy dissipation.

In order to enhance the seismic performance of the cut-out weakened walls retrofitting should be carried out. The strengthening technique of CFRP-EBR was introduced in the past twenty years and gained widespread application for its advantages with respect to conventional and/or traditional methods. The technique is primarily used for RC beams and column members and masonry elements.

The conceptual outline of the research is to investigate the seismic performance of the precast RC walls, assess the weakening effects caused by doorway cut-outs and reveal the effects of the seismic retrofit by CFRP-EBR. It is important that the foregoing analysis can be achieved at three structural levels of complexity, namely for a structural element, a building system or for the entire building structure.

2 EXPERIMENTAL PROGRAM

The objectives of the experimental research were to record the seismic performance of the precast large wall panels considering the outrigger effect of adjacent structural members, to assess the weakening of doorway cut-outs and to investigate the performance of the CFRP-EBR strengthening method.

An outline of the test program can be structured in three levels. The first level is represented by a bare solid wall, see Figure 1, which was the reference specimen. The second level included two bare walls with cut-out openings, which were identical in all aspects with the solid reference, except the presence of the cut-outs. The difference between the elements of this level was the width of the door opening. The third level is composed by two pairs of strengthened specimens, which corresponded in all regards to the second level walls and were additionally retrofitted. Besides the opening size, the difference between the specimens of the third level consisted in the state of the walls at the time of retrofitting: after sustaining a number of damaging load reversals, the specimens of the second level were upgraded to the third one by repair and post-damage strengthening, whereas their counterparts were prior-to-damage strengthened.

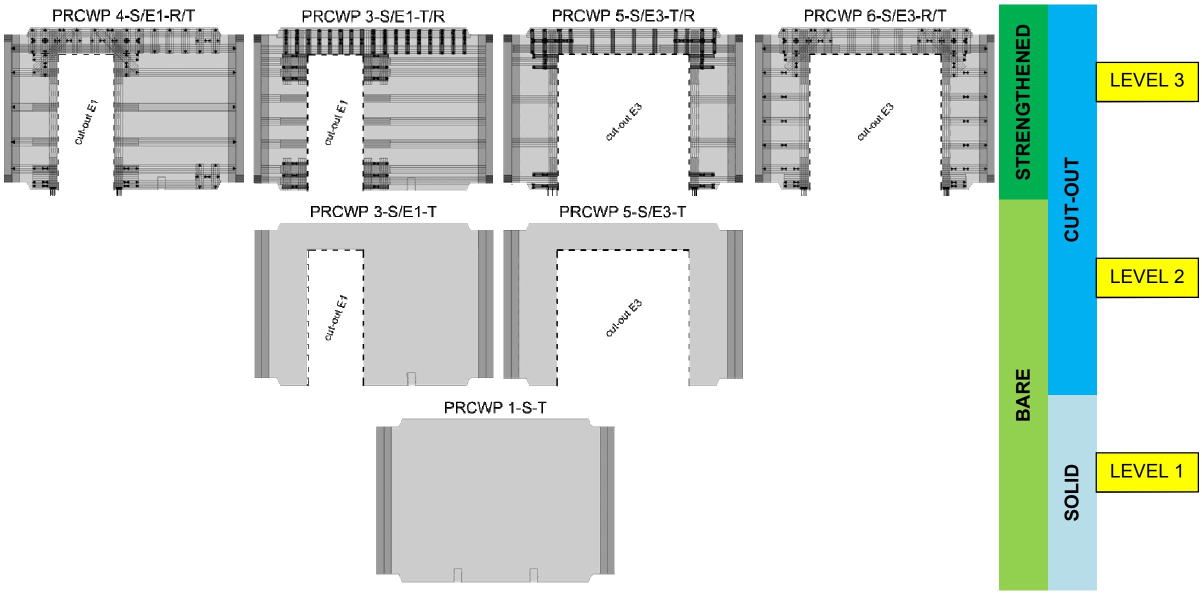

Figure 1: Variables of the experimental program

The concrete outlines and reinforcing details of the solid reference specimen are described in the following. The dimensions of the web-panel were 2750 mm length, 2150 mm height and 100 mm thickness. The cross-sectional area of the solid web-panel was 2750 cm^2 and its aspect (height-to-length) ratio was 0.8. Similarly to the original large panels, shear keys were formed along the edges of the web-panel to improve the sliding shear resistance. For the same reason larger set-backs were provided at the panel corners. The wings were composed of a short in-plane connection zone and a flange perpendicular to the wall plane. The concrete outlines and reinforcing details of the solid reference specimen are depicted in Figure 2.

A comparison line is defined as a series of at least two specimens or tests that are identical in all regards except one variable. These lines are set up in order to assess the effect of the investigated variable on the behaviour of the specimens. The present program contains three comparison lines, each of them comprising of three tests. The first comparison line was set to assess the weakening effect of doorway cut-out. The reference specimen of this line is the solid specimen while the variable is the cut-out width. The second and third comparison lines are referred to as strengthening effect of CFRP-EBR, with reference specimens being the bare walls with narrow and wide door cut-out, respectively and the variable being the strengthening condition.

The test set-up adopted in the experimental program (see Figure 3) is featuring a zero overall base moment trait by the hinged end connections, although in the case of the specimens with openings there are interior moments possible to develop through the wall to base beam interface. The development of the moments is limited in both cases by the increasing axial loads, which acts against the vertical tensile forces. Therefore it can be stated that the shear span and the shear span ratio is negligible compared with the bending moment in the case of the solid wall, while it is slightly greater for the wall piers. The exact value is quiet difficult to evaluate, due to the variable axial loads, differences in the anchored vertical reinforcement in the two loading directions and the coupling effect of the spandrel beam. Consequently, shear behaviour is extensively stimulated. The boundary conditions adopted in the experimental program were aimed to reproduce the outrigger effect, deemed to be of high importance in the behaviour of lateral load resisting structural systems.

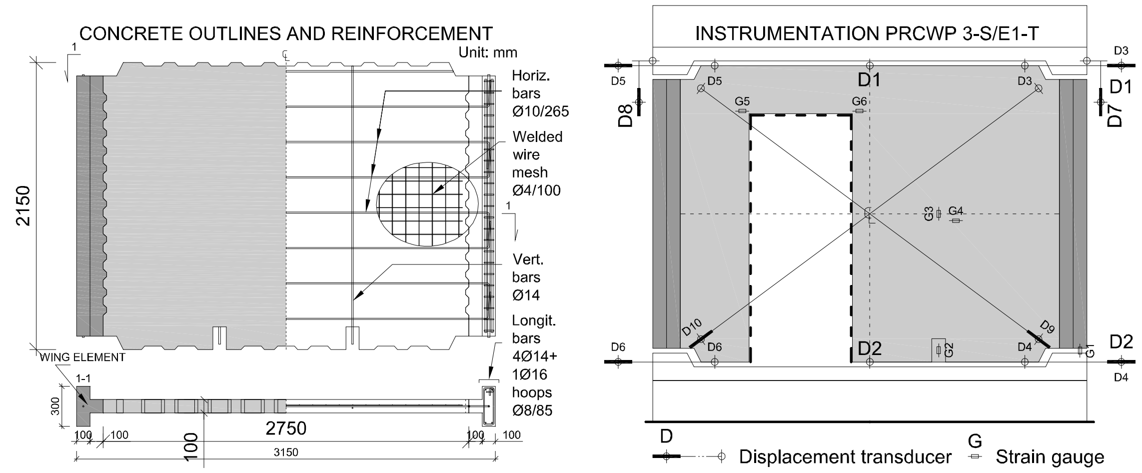

Figure 2: Concrete outlines reinforcement arrangement and instrumentation

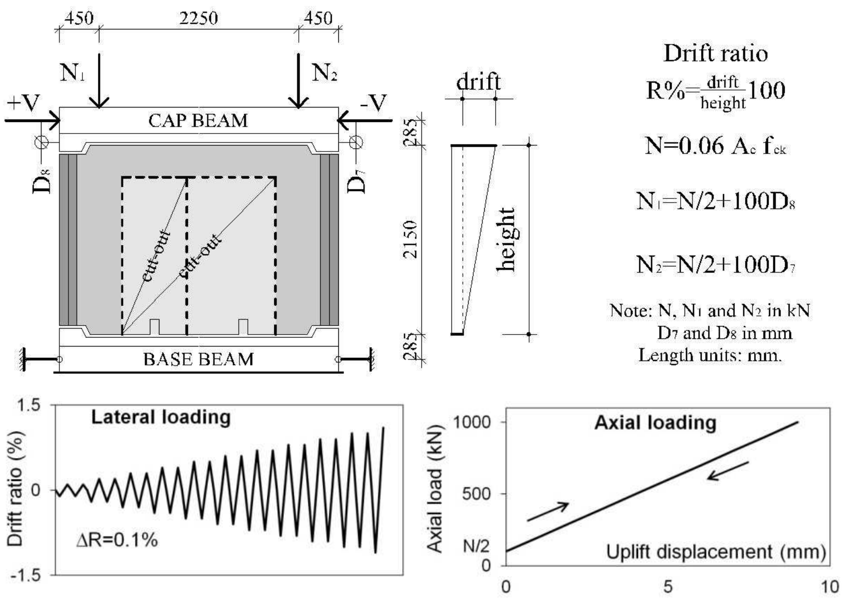

Figure 3: Test set-up used in the experimental program and the loading procedure

3 STRENGTHENING PROCEDURE

Based on the behaviour and failure mode observed during the test performed on the un-strengthened specimen, the strengthening strategy was divided in three directions: (1) to offer flexural capacity along the edges of the cut-out opening, (2) to increase the shear capacity of the wall piers, and (3) to provide confinement effect at the cut-out opening corners. Before strengthening, the damaged specimen was repaired by replacing the crushed concrete with high-strength mortar. The substrate preparation consisted in grinding the concrete surface, rounding the edges, drilling holes through the wall and vacuum-cleaning.

The strengthening was performed by the CFRP EBR technique. Two types of unidirectional Carbon Fiber (CF) sheets (S1 and S2) were applied by dry layup and wet layup process, respectively. The properties of the CF sheets and the corresponding epoxy resins are given in (Demeter, 2011). The S1 and S2 CF-sheets were utilized in form of strips with 100 mm and 50 mm width, respectively. The strengthening was carried out symmetrically on both faces of the wall.

As shown in Figure 4, the flexural strips (flx) were placed horizontally on the coupling beam and vertically on the wall piers alongside the opening. Note that for specimen #3 the flexural strips were applied in one layer and the piers were not CFRP-anchored to the foundation, while for specimen #4 the flexural strips were doubled at the opening's corners and CFRP-anchorage was provided. The shear strips (sh) were aligned parallel to the shear forces, i.e. horizontally on the piers and vertically on the coupling beam. The stirrup-like confinement (cnf) strips were closed by CFRP tows referred to as through-wall anchorages.

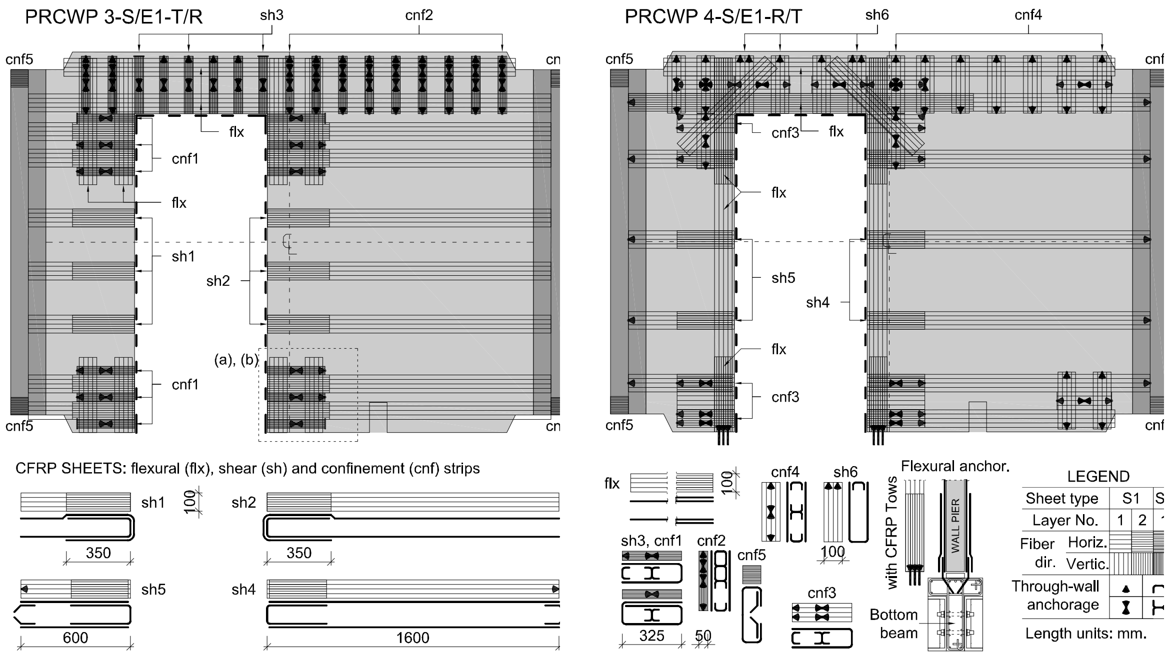

Figure 4: Example for a strengthening layout

4 EXPERIMENTAL RESULTS

In Figure 5 the lateral load vs drift ratio responses were plotted along the three comparison lines of the experimental program. As presented earlier the first comparison line was aimed to assess the weakening effect of the doorway cut-outs. It is impressive the loss of load resistance of the specimens with cut-out door with respect to the solid reference. Comparison lines 2 and 3 were meant to assess the performance improvement achieved by CFRP-EBR strengthening for the narrow and wide door cut-out conditions, respectively. Both lines comprised a bare, a post-damage strengthened and a prior-to-damage strengthened wall test of the same opening condition. One can remark the increased load and displacement capacity and the enlarged hysteresis loops of the strengthened specimens with respect to the bare references.

The experimental results regarding the weakening effect of the door cut-outs on the seismic response of the solid reference wall are presented in Figure 6. The cut-out ratio is a measure of the opening size relative to the solid reference wall calculated either as the horizontal cross section ratio or as the square root of the in-plane area ratio (peripheral ratio). The performance ratio indicates the response characteristic of the weakened specimen normalised to the corresponding characteristic of the sound (solid) reference. The proportionality between the performance ratio and the cut-out ratio is represented by the dashed line joining the unities of the two axes. One can observe that there is experimental evidence on the proportionality between specific performance and opening ratios: the strength and stiffness performance ratios are the complement of the peripheral ratio, whereas the energy dissipation rate [2] in performance ratio is proportional of the cross sectional ratio[3].

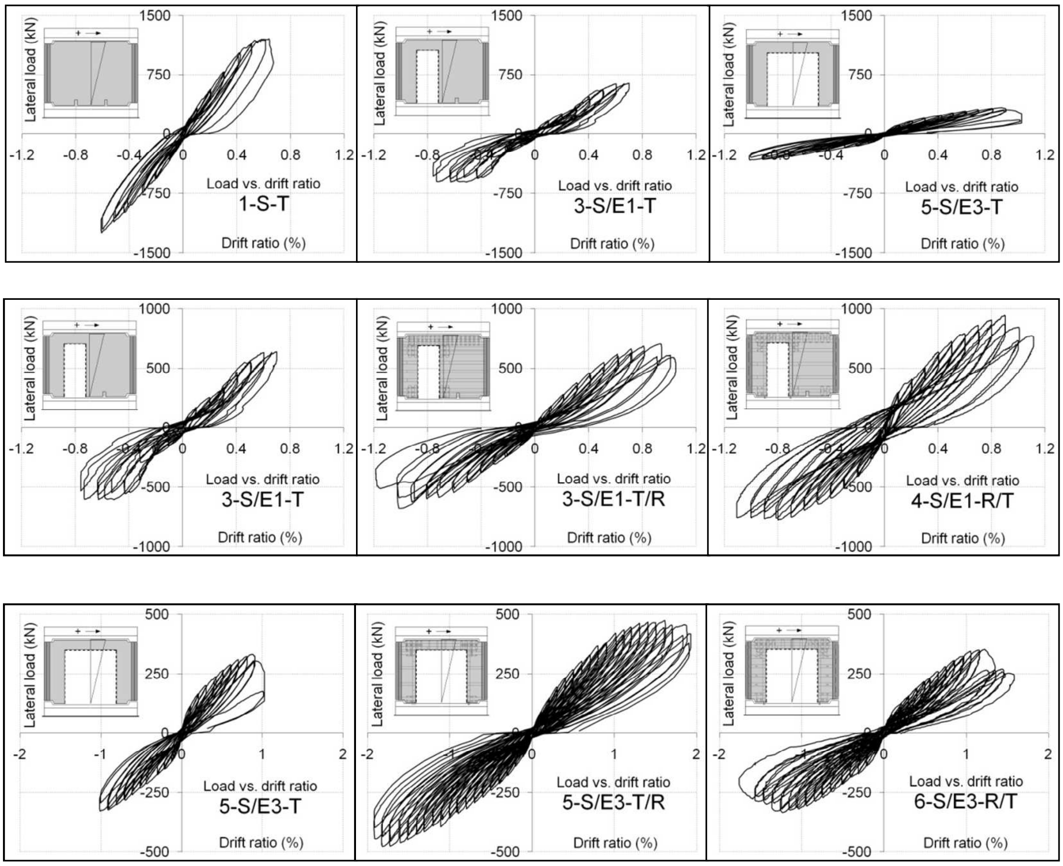

Figure 5: The load-displacement responses arranged along the comparison lines

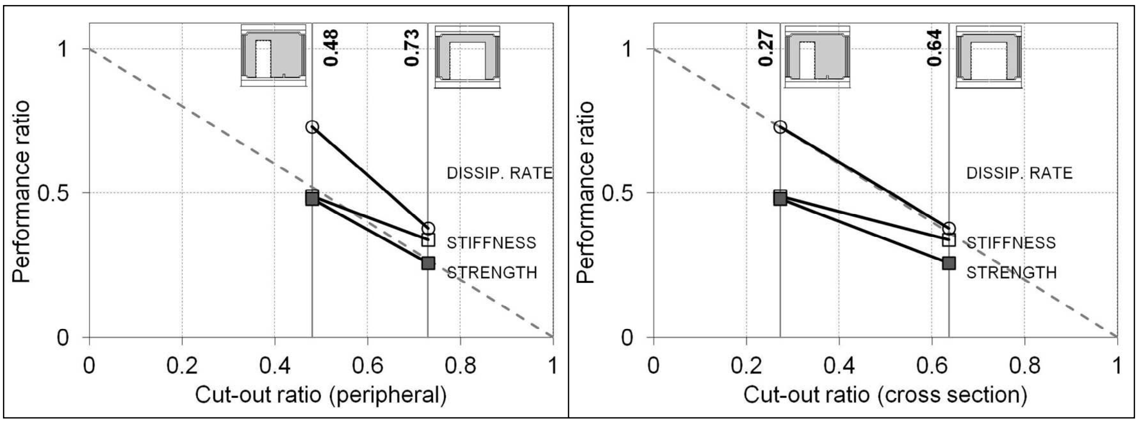

Figure 6: Weakening effect of the cut-out openings.

As regards the contribution of the three components (flexural, shear and confinement) of the FRP strengthening to the above performance, it can be concluded that the confinement FRP strips show the most stable response; the shear FRP strips debond in the vicinity of the inclined cracks; and the flexural CFRP-strips subjected to alternating tension-compression reversals parallel to fibre direction are likely to fail prematurely. In order to assess more clearly the components' contribution further subject-oriented investigations are necessary.

Practicing engineers can use the experimental results to evaluate the seismic response modifications which can be expected by CFRP-EBR retrofitting of the cut-out weakened precast concrete wall panels. CFRP layouts similar to the ones presented would yield the following results: the shear strength increases in average by 25%; the peak drift increases by 50%; the initial stiffness and the energy dissipation rate remain roughly the same; and the cumulative energy dissipation at ultimate increases by 2÷4 times. One should bear in mind that in reversed cyclic applications the flexural CFRP-EBR is susceptible to premature failure; thus, the authors recommends a safety factor of 3 for the flexural FRPs.

To quickly approximate the response characteristics of the precast RC walls weakened by doorway cut-outs according to the following equations can be used:

$$\mathbf{R_{weak}} = \mathbf{R_{sound}} \cdot \boldsymbol{\alpha}_\mathbf{p} \tag{1}$$

where

$\mathbf{R_{weak}}$ is the response characteristic of the weakened member in terms of shear resistance, initial stiffness or energy dissipation rate;

$\mathbf{R_{sound}}$ is the response characteristic of the sound (solid, as-built) member in terms of shear resistance, initial stiffness or energy dissipation rate;

$\boldsymbol{\alpha}_\mathbf{p}$ is the performance ratio, given by

$$\boldsymbol{\alpha}_\mathbf{p} = \mathbf{1} - \boldsymbol{\eta} \tag{2}$$

and

$$\boldsymbol{\eta} = \begin{cases} \sqrt{\mathbf{A_0/A_w}} \\ \mathbf{l_0/l_w} \end{cases} \tag{3}$$

where

$\mathbf{A_0}$ is the in-plane area of the opening;

$\mathbf{A_w}$ is the in-plane area of the wall;

$\mathbf{l_0}$ is the length of the opening;

$\mathbf{l_w}$ is the length of the wall.

Note that expression (1), (2) and (3) was derived from the AIJ recommendation[4]; however, the AIJ equation is reportedly[5] applicable only for peripheral opening ratios less than 0.4 and it refers only to the shear strength and stiffness. In the present research the above equation was experimentally verified for two opening ratios (0.48 and 0.73); in-between these values one can assume linear performance ratio-to-peripheral ratio relationship. Moreover, it is important to bear in mind that the relationship given in equation (1) was validated for the specific loading and boundary conditions applied in the present experimental program (outrigger effect by additional axial loads); further investigations are required to widen the loading and boundary conditions range.

5 CONCLUSIONS

Within this study it was shown that in given circumstances the response of the reinforced concrete large wall panels is characterized by very high shear resistance and about 10% energy dissipation ratio. The weakening effect of the cut-out opening was found to be in agreement with the predictions provided by the AIJ equation (Warashina et al., 2008. The relationship given in (1) was experimentally validated for the specific loading and boundary conditions applied in the present program; further investigations are required in order to widen the loading and boundary conditions range. Regarding the CFRP-EBR strengthening, the experimental results indicated that the energy dissipation capacity of the walls retrofitted by this technique increased significantly, whereas the other response characteristics were influenced in a smaller degree. This improvement of the seismic performance should be attributed primarily to the confinement and shear components of the strengthening system. The flexural FRPs were found to be susceptible to premature failure; however, it is not clear whether this type of failure is triggered by concrete substrate deterioration, i.e. local spalling and crushing, or directly by the adverse loading conditions (tension-compression reversals).

ACKNOWLEDGEMENTS

This research received financial support from the Romanian National University Research Council (CNCSIS) through a number of research grants and contracts: grant No. 355/2006, CNCSIS, type A, grant No. 1436/2006, CNCSIS, CEEX, type ET and grant No. 2/2007, PNII-RU-TD8.

REFERENCES

[1] National Institute of Statistics (2002). *Census of population and dwellings 2002*, Vol. 5, B-D-H, [online], available from: <http://www.insse.ro/cms/files/RPL2002INS/vol5/tablesdwellings.htm >, [accessed October, 2011].

[2] I. Demeter, *Seismic retrofit of precast RC walls by externally bonded CFRP composites*, PhD Thesis, Politehnica Publishing House, Timișoara, Romania (2011).

[3] I. Demeter, T. Nagy-György, V. Stoian, A.C. Dăescu and D. Dan, *Seismic performance of precast RC wall panels with cut-out openings*, 14th European Conf. on Earthquake Engineering. Paper No. 1004, (2010).

[4] M. Warashina, S. Kono, M. Sakashita and H. Tanaka, *Shear behavior of multi-story RC structural walls with eccentric openings*, The 14th World Conf. on Earthquake Engineering, S15-029, (2008).

[5] R. Taleb and S. Kono, *Shear behavior of multi-story reinforced concrete walls with openings,* Bulletin of IISEE. 45, 55-60, (2010).

OBJECT-ORIENTED PROGRAMMING FOR TOPOLOGY OPTIMIZATION OF STEEL TRUSS STRUCTURES BY MULTI-POPULATION PARTICLE SWARM OPTIMIZATION

Pruettha Nanakorn*, Wasuwat Petprakob† and Venkata C K Naga†

*Sirindhorn International Institute of Technology, Thammasat University
PO Box 22, Thammasat-Rangsit Post Office, Pathumthani 12121, Thailand
e-mail: nanakorn@siit.tu.ac.th, webpage: http://www.siit.tu.ac.th

Keywords: Particle swarm optimization, multiple populations, object-oriented programming, topology optimization, steel truss.

Abstract. *This paper demonstrates how object-oriented programming (OOP) can be used to create a program for topology optimization of steel trusses that employs multi-population particle swarm optimization (PSO). The OOP technique considers programs as communications and actions between entities called objects. Each object is a collection of data and their behavior. PSO mimics the swarm behavior of real animals. Each particle represents an animal and a population of particles therefore represents a population of animals. If OOP is used to implement PSO, each entity in PSO can be implemented as an object without any alteration to its physical meaning. In this study, OOP is used to develop a program for multi-population PSO for topology optimization of steel trusses. The development is natural and simple. The treatment of multiple populations of particles and the interaction between the populations can be done by simply creating objects, with appropriate data and behavior, to represent these populations. The OOP technique allows the extension of the ordinary PSO with one population to PSO with multiple populations to be done effortlessly.*

1 INTRODUCTION

Topology optimization of steel trusses is a challenging field of research in that real-life problems usually require consideration of large search spaces. In part, this results from the utilization of ground structures in forming optimization problems and also from a large number of steel sections available for selection. Truss topology optimization is a challenging problem also because, in topology optimization of a truss, there usually exist several local optimal solutions where the optimization can easily be trapped. Having several local optimal solutions can be expected since topology optimization allows the presence of truss members to be switched on and off, thus creating a kind of discontinuity in the evaluation of stress-constraint violation[1,2]. For this type of large optimization problem, the conventional optimization techniques are usually too rigid and cannot be used. On the contrary, evolutionary and swarm optimization techniques have shown promising performance[3-7]. These evolutionary and swarm optimization techniques consider many search points at the same time. Thus, the chance of being trapped in local optimal regions is reduced. In order to reduce the chance of being trapped even further, multiple populations of search points can also be used[8-10]. Being able to create programs that can support different designs of optimization algorithms well is desirable.

†Sirindhorn International Institute of Technology, Thammasat University, Thailand

Particle swarm optimization (PSO) is a popular swarm optimization technique that is based on the flocking behavior of animals[11-14]. Besides the method's good performance, its popularity is probably due to its simplicity. The performance of PSO is found to improve when multiple populations are used[15,16]. In multi-population PSO, several populations of particles are used to perform the search for the optimal solution. Information is exchanged from time to time between these populations, resulting in greater exploration of the search space. Different multi-population PSO algorithms are different in the way that information exchanges between populations are done. Since multi-population PSO employs more than one population of particles, it may be assumed that this type of algorithm requires significantly large computational resources and computational time. This is only true to a certain degree because the concept of using multiple populations works perfectly with the concept of parallel computing. Populations can be allowed to progress independently except during the times that information is exchanged between them. During their independent progressions, parallel computing can be used. PSO has been used to solve truss topology optimization problems with comparable levels of success[7,17].

The object-oriented programming (OOP) technique is a programming paradigm that treats programs as communications and actions between objects. The technique is quite appealing to engineers and scientists probably because its concept is natural to humans. By using OOP, programming becomes a kind of action planning for different scenarios and different participating agents. OOP enhances the reusability, maintainability, and expendability of programs. In the field of structural engineering, OOP has been used extensively in finite element (FE) programming[18-22]. The entities in the finite element method (FEM) can be treated quite naturally as objects in OOP. These entities are, for example, nodes, elements, materials, geometry sets, and boundary conditions. Similar to FEM, there are also distinct entities in PSO, such as particles and populations, which can be treated as objects. If OOP is used to implement PSO, the entities in PSO can be implemented as objects without any alteration to their physical meanings. In addition, when PSO is used in truss topology optimization, FEM is always a required tool that PSO uses to analyze truss structures. A program for truss topology optimization using PSO must be able to communicate well with the employed FE program. Programming PSO and FEM using the OOP technique allows the implementation of communications between PSO and FEM to be done efficiently.

In this paper, designs of object models for multi-population PSO for truss topology optimization are proposed. In order to create efficient designs of object models for multi-population PSO, object models of some relevant entities will also be designed and shown. These relevant models include the models for basic objects required in PSO, such as search points, as well as the models for some other evolutionary and swarm optimization algorithms. Implementation examples of the proposed designs are shown using the C++ programming language.

2 MULTI-POPULATION PSO

As aforementioned, multi-population PSO utilizes more than one population of particles to search the search space and enhances the degree of exploration by allowing information exchanges between the populations. The most important aspect of multi-population PSO is in fact how information is exchanged between the populations. Each population in multi-population PSO can be the simple PSO algorithm without any sophisticated modifications. Clearly, if no information exchange is allowed between the populations, using multiple populations will be the same as running single-population PSO many times.

When PSO is used for design optimization, each particle represents a design solution, and a population of particles, therefore, represents many design solutions. These particles move around the search space, searching for the global optimal solution. A particle in the population moves in a direction somewhere between the direction toward the best solution it has ever experienced and the direction toward the best solution the whole population has ever experienced.

Consider an optimization problem in a *D*-dimensional space. The movement of the particles in PSO during an iteration step is governed by the following expressions, i.e.

$$V_i^d = WV_i^d + C_1 r_{1i}^d \left(pBest_i^d - X_i^d \right) + C_2 r_{2i}^d \left(gBest^d - X_i^d \right), \tag{1}$$

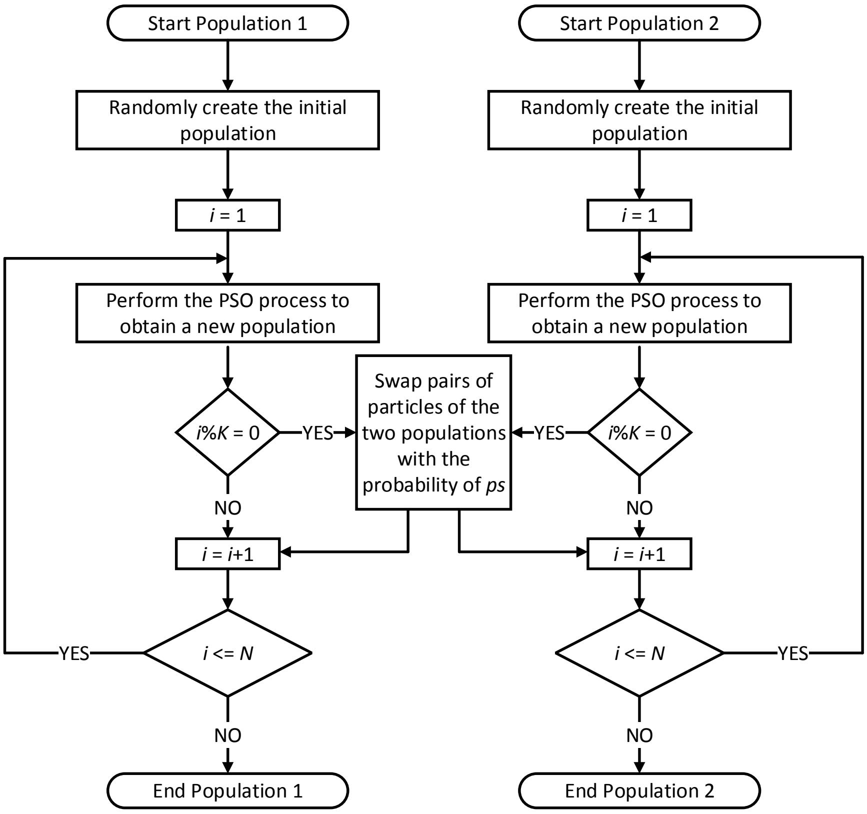

Figure 1: Two-Population PSO

$$X_i^d = X_i^d + V_i^d . \tag{2}$$

Here, V_i^d and X_i^d represent, respectively, the velocity and position of particle *i* in dimension *d*. In addition, W, C_1, and C_2 are user-defined constants while r_{1i}^d and r_{2i}^d are uniformly distributed random numbers on [0,1]. Moreover, $pBest_i^d$ represents the position in dimension *d* of the best solution that particle *i* has ever experienced, and $gBest^d$ represents the position in dimension *d* of the best solution that the whole population has ever experienced. The best solution that particle *i* has ever experienced is called the particle best of particle *i* while the best solution that the whole population has ever experienced is called the global best. It can be seen from Eq. (2) that, during each iteration step, the position X_i^d is modified by the velocity V_i^d. The velocity V_i^d is modified, in Eq. (1), from the current velocity in a direction somewhere between the directions toward $pBest_i^d$ and $gBest^d$. In Eq. (1), W, C_1, and C_2 are used to adjust the relative importance between the current velocity, the position of the particle best, and the position of the global best. The simple PSO is governed by Eqs. (1) and (2).

The simplest form of multi-population PSO algorithms may have only two simple-PSO populations, whose members are swapped from time to time. Multi-population PSO algorithms that are more complex can have more populations and use information exchange algorithms that are more sophisticated. Figure 1 shows an example flowchart for two-population PSO, where pairs of particles of the two populations are swapped with the probability equal to *ps* at every *K* iterations. Besides the time where their particles are swapped, the two populations are completely independent; thus, they can be executed in parallel.

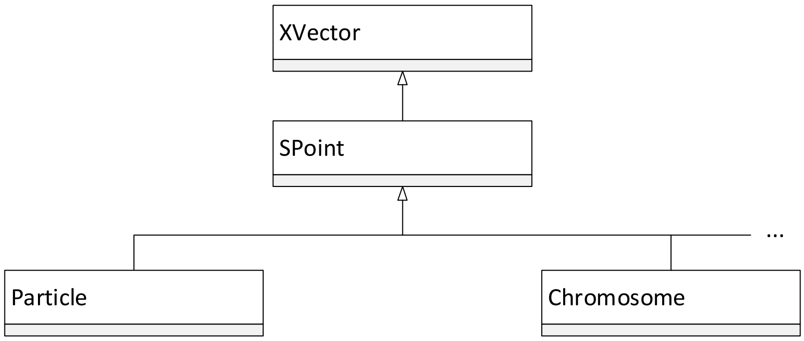

Figure 2: Classes for Search Points

3 CLASSES FOR MULTI-POPULATION PSO

Here, classes for multi-population PSO and some related classes are shown. When designing an object-oriented program for multi-population PSO, it is useful to keep in mind that all evolutionary and swarm optimization algorithms have virtually the same structure. They employ several search points and only differ in the way of how these search points move from iteration to iteration. It is therefore possible to create a system of object-oriented programs that can accommodate several types of evolutionary and swarm optimization algorithm. In OOP languages, an object is created by using the definition defined in a class. One of the best strategies that can be used to design classes for evolutionary and swarm optimization algorithms is to separate classes for optimization algorithms from classes that are used to examine solutions. In this study, objects that are used to examine solutions are called examiners. Different classes can be created for examiners of different optimization problems. For example, there can be an examiner constructed from finite element classes that performs finite element analysis of trusses for truss topology optimization. If classes for optimization algorithms are separated from classes for examiners that examine solutions, different combinations of optimization methods and optimization problems can be easily created. This actually demonstrates the reusability of the OOP technique.

The designs of several classes for evolutionary and swarm optimization algorithms are discussed below. Although the designs can be generally used with any OOP languages, their code is shown here in C++. Note that `XVector` is a vector template class derived from the standard `vector` class in C++.

3.1 Classes for search points

The first group of classes to be discussed is the group of classes for search points. Figure 2 shows the class diagram for these classes.

`SPoint`

As all optimization methods employ search points, having a base class for different types of search point can be useful. Here, `SPoint` is the base class for all classes of search points. The class is derived from `XVector` and, therefore, is also a vector. Each `SPoint` represents a point in the search space. The number of its vector elements is equal to the number of the dimensions of the search space, and each vector element stores a design variable. The C++ code for the class is shown below.

```
template <class T> class SPoint: public XVector<T>
{
protected:
	int ID;                          // ID number
	XVector<double> obj;             // Objective functions
	XVector<double> err;             // Degrees of constraint violation
	XVector<double> data;            // Storage for any necessary data
```

```
	...

public:
	SPoint(void);
	SPoint(const SPoint<T> &A);          // Copy constructor
	SPoint(const XVector<T> &A);         // Copy constructor
	virtual ~SPoint(void);               // Destructor

	// Overloaded operators
	const SPoint<T> &operator =(const SPoint<T> &A);
	const SPoint<T> &operator =(const XVector<T> &A);
	...
};
```

The template parameter `T` is the type of the design variables to be stored. The type `T` can be a simple type, such as double, or a complicated type defined as a class. An `SPoint` object also stores the values of objective functions and degrees of constraint violation. Moreover, a storage vector, `data`, is also available for any additional data that may be required.

Particle

`Particle` is a class for particles in PSO. It is derived from the base class `SPoint`. Additional data for PSO that are not available in `SPoint` are added to this derived class. The C++ code for the class is shown below.

```
template <class T> class Particle: public SPoint<T>
{
protected:
	XVector<double> velocity;                  // Particle's velocity
	Particle<T> pBest;                         // pBest
	...
public:
	Particle(void);                            // Constructor
	Particle(const Particle<T> &A);            // Copy constructor
	Particle(const XVector<T> &A);             // Copy constructor
	virtual ~Particle(void);                   // Destructor

	// Overloaded operators
	const Particle<T> &operator =(const Particle<T> &A);
	const Particle<T> &operator =(const XVector<T> &A);
	...
};
```

The type parameter `T` is kept as a parameter in order to allow both real and binary versions of particles to be created. A `Particle` object stores the particle's velocity in `velocity` and its particle best in `pBest`.

Chromosome

`Chromosome` is a class for chromosomes in genetic algorithms (GAs). It is also derived from the base class `SPoint`. The class is given here as an example of how inheritance in OOP can help increase the reusability of the code. The C++ code for the class is shown below.

```
class Chromosome: public SPoint<Gene>
{
protected:
	XVector<int> str;                          // Chromosome string
	...
public:
	Chromosome(void);
	Chromosome(const Chromosome &A);           // Copy constructor
```

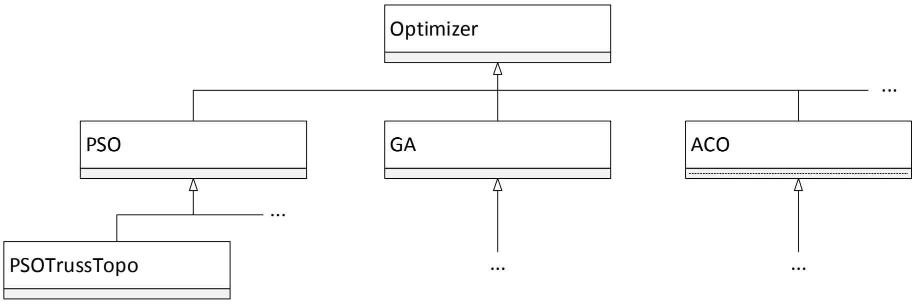

Figure 3: Classes for Optimization Algorithms

```
        Chromosome(const XVector<Gene> &A);          // Copy constructor
        virtual ~Chromosome(void);

        // Overloaded operators
        const Chromosome &operator =(const Chromosome &A);
        const Chromosome &operator =(const XVector<Gene> &A);
        ...
};
```

It can be seen that `Chromosome` is not a template class. The template parameter `T` of `SPoint` is set to `Gene`. Here, `Gene` is a class that represents genes in GAs. Each gene is a binary string that represents a design variable. `Chromosome` is simply a vector of genes. Using this structure of `Chromosome` allows binary strings of different lengths to be used for different design variables. In `Chromosome`, `str` is a vector that keeps the whole chromosome string, obtained by concatenating all bit strings from all genes.

3.2 Classes for optimization algorithms

The second group of classes is the group of classes for evolutionary and swarm optimization algorithms, including those for PSO. Figure 3 shows the class diagram for these classes.

`Optimizer`

This is the base class for all evolutionary and swarm optimization algorithms. The class contains data and methods that are common to most evolutionary and swarm optimization algorithms. It is convenient to create this `Optimizer` class as a template class in order that different types of search point and different types of examiner can be used. The C++ code for the class is shown below.

```
template <class Pnt,class Ex> class Optimizer
{
protected:
        XVector<Pnt> point;                          // Array of search points
        bool bBinary;                                // Binary problem or not
        Pnt currentBest;                             // Current best solution
        Pnt currentWorst;                            // Current worst solution
        XVector<Pnt> elite;                          // Elitist solutions
        XVector<Ex> examiner;                        // Examiners
        ...
public:
        Optimizer(void);
        virtual ~Optimizer(void);
        ...
};
```

In the code, `Pnt` is a template parameter that represents the type of search point. For example, for PSO, `Pnt` is the `Particle` type. On the contrary, for GAs, `Pnt` is the `Chromosome` type. Also in the code, `Ex` is the type of examiner. `Optimizer` contains the variables that are common among most evolutionary and swarm optimization algorithms. The most important one is `point`, which is an array of search points and is used to keep all search points in the algorithm. Another important variable is `examiner`, which is an array of examiners used in the optimization. As mentioned earlier, examiners examine design solutions for their merit. An optimization problem will have its own examiner class. One examiner can be used to examine all search points kept in `point`. If this is the case, the length of `examiner`, which is an array, can be set to one. However, when parallel computing is used, it is efficient to have one examiner for each search point so that the evaluations of all search points can be done independently. In that case, the length of `examiner` must be the same as the number of search points in the population.

In summary, an `Optimizer` object is a population of search points without the knowledge of how these search points should move. The knowledge of how the search points should exactly move will be defined by its derived classes.

<u>`PSO`</u>

`PSO` is simply a class for PSO. It is derived from the base class `Optimizer`. The class in C++ is shown below.

```
template <class T,class Ex> class PSO: public Optimizer<Particle<T>,Ex>
{
protected:
      Particle<T> gBest;                           // gBest
      double W,C1,C2;                              // Weights
      XVector<double> Vmax;                        // Maximum velocities
      ...
public:
      PSO(void);                                   // Constructor
      virtual ~PSO(void);                          // Destructor
      virtual void initialize();                   // Initializes the algorithm
      void randomParticle();                       // Creates particles randomly
      void moveParticle();                         // Moves particles
      void exchange(PSO<T,Ex> &another,double ps); // Exchanges particles
      ...
};
```

In the class, the way of how search points or particles move is defined in `moveParticle()`. Thus, it can be said that a `PSO` object is a population of particles equipped with the knowledge of how the particles should move according to the concept of PSO. The class also stores the global best of the algorithm in `gBest`. In addition, it also stores the user-defined constants in `W, C1,` and `C2`. The function `exchange` in a `PSO` object is used to exchange particles between the `PSO` object and another `PSO` object.

<u>`PSOTrussTopo`</u>

Since the `PSO` class contains only general data and behavior of PSO, it is usually helpful to derive a class from the `PSO` class that is tailored to truss topology optimization. In Figure 3, `PSOTrussTopo` is such a class and is shown in C++ below.

```
template <class Ex> class PSOTrussTopo: public PSO<double,Ex>
{
public:
      PSOTrussTopo(void);                   // Constructor
      ~PSOTrussTopo(void);                  // Destructor
      void initialize();                    // Initializes the algorithm
      void calcObjectiveAndErr();           // Calculates objectives and errors
      ...
};
```

From the code, it can be seen that `PSOTrussTopo` is derived from `PSO<double,Ex>`. This means that the type of variable in the optimization process is set to `double`. However, the type of the examiner is still kept as a template parameter of the `PSOTrussTopo` class. In this way, the type of the examiner can be defined when the class is used. The function `calcObjectiveAndErr()` in `PSOTrussTopo` is a function that requests the examiner to analyze all trusses and subsequently calculates the values of the objective function and the degrees of constraint violation to be used in the PSO process.

4 EXAMPLE IMPLEMENTATION

In this section, implementation of a two-population PSO is used as example implementation of the proposed OOP for multi-population PSO. The implementation is shown only in part. The `PSOTrussTopo` class is used for the demonstration. Since there are two populations of particles, two `PSOTrussTopo` objects are created and used. It is convenient to put the two objects in a vector as shown below.

```
XVector<PSOTrussTopo<TrussTopoExaminer>> myPSO;
myPSO.resize(2);
```

In the above code, `myPSO` is a vector of `PSOTrussTopo` objects. The examiners in `PSOTrussTopo` objects are from an examiner class called `TrussTopoExaminer`, whose details will be omitted here. The length of `myPSO` is set to two, meaning that there are two `PSOTrussTopo` objects, `myPSO(0)` and `myPSO(1)`, in the array. The two `PSOTrussTopo` objects are to be used to perform the PSO process. For example, the code shown below demonstrates how the two objects can be used to perform the PSO process in parallel.

```
parallel_for(0,(int) myPSO.size(),[&](int j){
      for(int i=1; i<=M; i++){
            myPSO(j).moveParticle();
            myPSO(j).calcObjectiveAndErr();
            myPSO(j).update_pBest();
            myPSO(j).update_gBest();
      }
});
```

Here, `M` is the number of iterations, during which there is no exchange of particles and the process can be performed in parallel.

The exchange of particles between the two populations can be performed using the following code.

```
myPSO(0).exchange(myPSO(1),ps);
```

Here, the whole population represented by `myPSO(1)` is sent by reference into the `exchange` function of `myPSO(0)`. `myPSO(0)` then pairs up particles from the two populations and performs the exchange with the probability equal to `ps`. Because `myPSO(1)` is sent into `myPSO(0)` via its reference, the algorithm performance is not compromised. Any sophisticated information exchange algorithms can be, in theory, created in a similar way.

5 CONCLUSIONS

In this paper, OOP for topology optimization of steel trusses by multi-population PSO is presented. The OOP technique is selected because it increases the reusability, maintainability, and expendability of the code. OOP treats programs as communications and actions between objects. Since, in OOP, entities found in evolutionary and swarm optimization algorithms can be treated as objects without any alteration to their physical meanings, programming these algorithms using OOP is natural and simple.

In order to design object models for multi-population PSO efficiently, object models of some relevant entities are also designed and discussed. These relevant entities include basic entities, such as search points, and some other evolutionary and swarm optimization algorithms. The most important classes for multi-population PSO are those that represent PSO algorithms. Each of the classes that represent PSO algorithms is in fact a population of particles with the knowledge of how the particles should move. In this paper, the `PSOTrussTopo` class is an example of this type of class. Since a population of particles is kept in an object, multiple populations can be created simply by creating many objects to represent these populations. The way of how information is exchanged between different populations can be added into the class that defines these population objects. Example implementation based on two-population PSO is shown in this paper. It can be seen from the example implementation that the required code can be very short and simple, which demonstrates well the usefulness of the OOP technique.

6 ACKNOWLEDGEMENTS

Wasuwat Petprakob and Venkata C K Naga receive graduate scholarships from Sirindhorn International Institute of Technology, Thammasat University, Thailand.

REFERENCES

[1] G.I.N. Rozvany, *On design-dependent constraints and singular topologies*, *Structural and Multidisciplinary Optimization* (2001);21:164-72.

[2] G.D. Cheng, and X. Guo, *E-relaxed approach in structural topology optimization*, *Structural Optimization* (1997);13:258-66.

[3] P. Hajela, and E. Lee, *Genetic algorithms in truss topological optimization*, *International Journal of Solids and Structures* (1995);32:3341-57.

[4] S.D. Rajan, *Sizing, shape, and topology design optimization of trusses using genetic algorithm*, *Journal of structural engineering New York, NY* (1995);121:1480-7.

[5] K. Deb, and S. Gulati, *Design of truss-structures for minimum weight using genetic algorithms*, *Finite Elements in Analysis and Design* (2001);37:447-65.

[6] P. Nanakorn, and K. Meesomklin, *An adaptive penalty function in genetic algorithms for structural design optimization*, *Computers and Structures* (2001);79:2527-39.

[7] G.C. Luh, and C.Y. Lin, *Optimal design of truss-structures using particle swarm optimization*, *Computers and Structures* (2011);89:2221-32.

[8] C.Y. Wu, and K.Y. Tseng, *Truss structure optimization using adaptive multi-population differential evolution*, *Structural and Multidisciplinary Optimization* (2010);42:575-90.

[9] D.S. Knysh, and V.M. Kureichik, *Parallel genetic algorithms: A survey and problem state of the art*, *Journal of Computer and Systems Sciences International* (2010);49:579-89.

[10] T. Park, and K.R. Ryu. A dual population genetic algorithm with evolving diversity. 2007. p. 3516-22.

[11] J. Kennedy, and R. Eberhart. Particle swarm optimization. Perth, Aust: IEEE; 1995. p. 1942-8.

[12] R.C. Eberhart, and Y. Shi. Comparing inertia weights and constriction factors in particle swarm optimization. California, CA, USA: IEEE; 2000. p. 84-8.

[13] M. Clerc, and J. Kennedy, *The particle swarm-explosion, stability, and convergence in a multidimensional complex space*, *IEEE Transactions on Evolutionary Computation* (2002);6:58-73.

[14] I.C. Trelea, *The particle swarm optimization algorithm: Convergence analysis and parameter selection*, *Information Processing Letters* (2003);85:317-25.

[15] Y. Jiang, T. Hu, C. Huang, and X. Wu, *An improved particle swarm optimization algorithm*, *Applied Mathematics and Computation* (2007);193:231-9.

[16] B. Niu, Y. Zhu, X. He, and H. Shen, *A multi-swarm optimizer based fuzzy modeling approach for dynamic systems processing*, *Neurocomputing* (2008);71:1436-48.

[17] B. Yang, and Q. Zhang. Applying a modified particle swarm optimizer to discrete truss topology optimization. 2010.

[18] G.C. Archer, G. Fenves, and C. Thewalt, *A new object-oriented finite element analysis program architecture*, *Computers and Structures* (1999);70:63-75.

[19] B.W.R. Forde, R.O. Foschi, and S.F. Stiemer, *Object-oriented finite element analysis*, *Computers and Structures* (1990);34:355-74.

[20] B. Patzák, and Z. Bittnar, *Design of object oriented finite element code*, *Advances in Engineering Software* (2001);32:759-67.

[21] B.C.P. Heng, and R.I. Mackie, *Using design patterns in object-oriented finite element programming*, *Computers & Structures* (2009);87:952-61.

[22] J. Besson, and R. Foerch, *Large scale object-oriented finite element code design*, *Computer Methods in Applied Mechanics and Engineering* (1997);142:165-87.

12th International Conference on
Steel, Space and Composite Structures
28-30 May 2014, Prague, Czech Republic

PUSH-OUT TESTS WITH MODERN DECK SHEETING AND REALISTIC TRANSVERSE LOADING

Sebastian Nellinger*, Christoph Odenbreit† and Robert M. Lawson‡

*University of Luxembourg
6 rue Coudenhove-Kalergi, L-1359 Luxembourg-Kirchberg
e-mail: sebastian.nellinger@uni.lu, webpage: http://www.uni.lu

Keywords: Push-out test, transverse loading, headed stud shear connector, profiled decking, composite beam, composite slab

Abstract. *The push-out test as proposed in EN 1994-1-1 originally was developed for solid slabs and not for composite slabs with additional steel sheeting. It leads to a load-slip behaviour of headed shear stud connectors which differs from the behaviour in the real beam. In particular, the vertical forces and negative bending moments of the composite slab at its support are ignored by this setup. Within the European research project "Development of improved shear connection rules in composite beams (DISCCO)" a total of 70 push-out tests was performed to investigate a more realistic push-out test setup. The influence of the transverse loading was investigated to develop a standard push-out test when additional steel sheeting is used. The test regime used to apply transverse loads in this investigation is described and the results of 10 push-out tests with 80 mm deep steel sheeting with pairs of 19 mm diameter headed shear stud connectors are presented. The observed bearing capacities of the shear connectors were over-predicted by the empirical reduction factor given in EN 1994-1-1 and the 6 mm criterion was not always satisfied, especially when no or only low transverse loads were applied. The application of transverse loads improved the ductility of headed shear stud connectors and the bearing capacity increased by up to 41%.*

1 INTRODUCTION

The use of composite beams with composite slabs in modern building applications has many advantages. They represent an economic way of building modern multi-storey offices, schools and hospitals. However, the existing rules in EN 1994-1-1[1] for the minimum degree of shear connection, in some cases, make the design of composite beams uneconomic or even impossible. This is especially valid for the use of modern deep deck profiles with widely spaced deck ribs and shear connectors.

The original calibration studies to obtain the bearing capacity of headed shear stud connectors were carried out in the early 1990s and focused on the influence of the deck profile shape on the resistance of through deck welded studs with a diameter of 19 mm. Modern deeper deck profiles with more widely spaced ribs have been developed over recent years and are threated in an undifferentiated way by the empirical reduction factor given in EN 1994-1-1[1].

In addition, the currently used push-out test setup according to EN 1994-1-1 Annex B2[1] originally was developed for solid slabs and not for composite slabs with additional steel

† University of Luxembourg, 6 rue Coudenhove-Kalergi, L-1359 Luxembourg-Kirchberg
‡ Steel Construction Institute, Silwood Park, Ascot, Berkshire, UK. SL5 7QN

sheeting. It is known that the load-slip behaviour of headed shear stud connectors in push-out tests differs from the results in real beams[2]. The reason for this lies in the loading and restraint conditions of the push-out test, which does not reflect sufficiently the real conditions of the composite beam. In particular, the effects of the vertical forces and negative bending moments of the composite slab at the line of the shear connectors are currently not taken into consideration.

2 PUSH-OUT TEST SETUP

2.1 Background

The push-put test setup proposed in EN 1994-1-1 Annex B2[1] originally was developed for solid slabs. The dimensions of the test specimen and the distribution of forces are shown in Figure 1. Compared to a composite beam, the shown setup considers well the distribution of the shear forces for the case of solid slabs. However, the recess which is used to ensure the spreading of the compression struts (c.f. Figure 1) is only “optional” in EN 1994-1-1[1] and it is typically not applied in push-out tests conducted in UK. If the dimensions of the slab and the recess as well as the position of the studs are not in the correct relation to each other, the compression struts might develop in unrealistic angels and consequently unrealistic forces. In particular, this is a problem when additional steel sheeting is used, as the spacing of the ribs dictates the placement of the shear connectors.

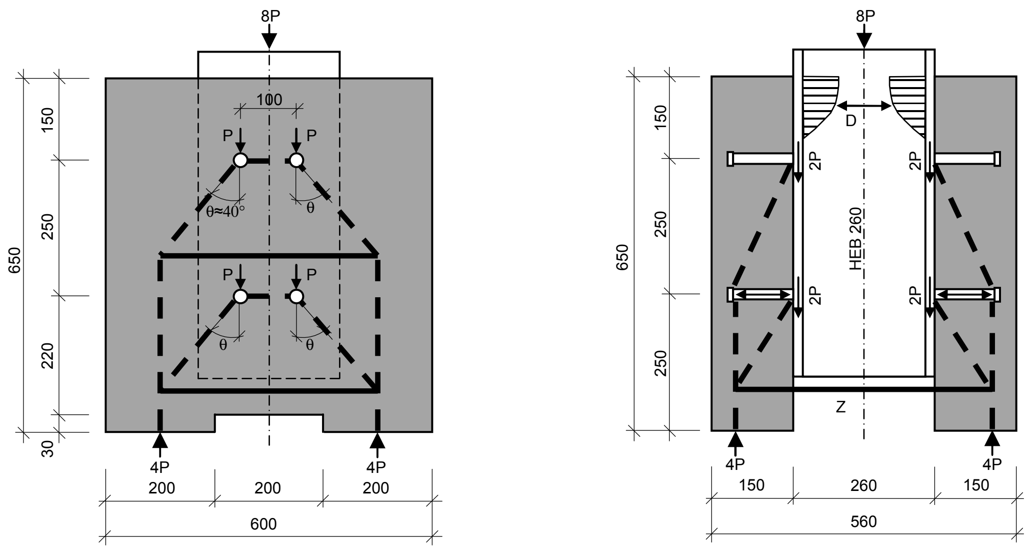

Figure 1: Dimensions of push-out test specimen according to EN 1994-1-1 Annex B2[1] and force distribution according to Roik et. al.[3].

The shown setup assumes tension bars to be used as a lateral restraint (c.f. Figure 1). The application of lateral restraints to the test specimen is controversy. Depending on the pre-stressing of the bars and the development of the tension force in the bars during the test, it leads to the development of compression between the concrete slab and the lowest row of studs. This leads to an unrealistic prediction of the bearing capacity. Vice versa, push-out tests can be placed on a sliding bearing, which could allow an undesired lift of the slab as a failure mechanism.

Besides the boundary conditions, discussions on the loading conditions arose[4], as the vertical forces and negative bending moments of the slab are ignored in the push-out test setup proposed in EN 1994-1-1[1]. Hence, the three-dimensional stress conditions around the shear connectors are not reproduced correctly and the development of cracks due to the negative bending moments of the slab is ignored. Both effects influence the load-slip behaviour, which is the reason why headed stud shear connectors in push-out tests behave different than in the real beam.

To reproduce the real loading conditions, push-out tests need to be loaded with additional eccentric transverse loads as shown in Figure 2. The transverse load was chosen to reflect the ratio of the vertical force of the slab to the shear force in the shear connectors of the composite beam. In addition, the influence of eccentric transverse loading (c.f. Figure 2b) and concentric transverse loading (c.f. Figure 2c) was investigated.

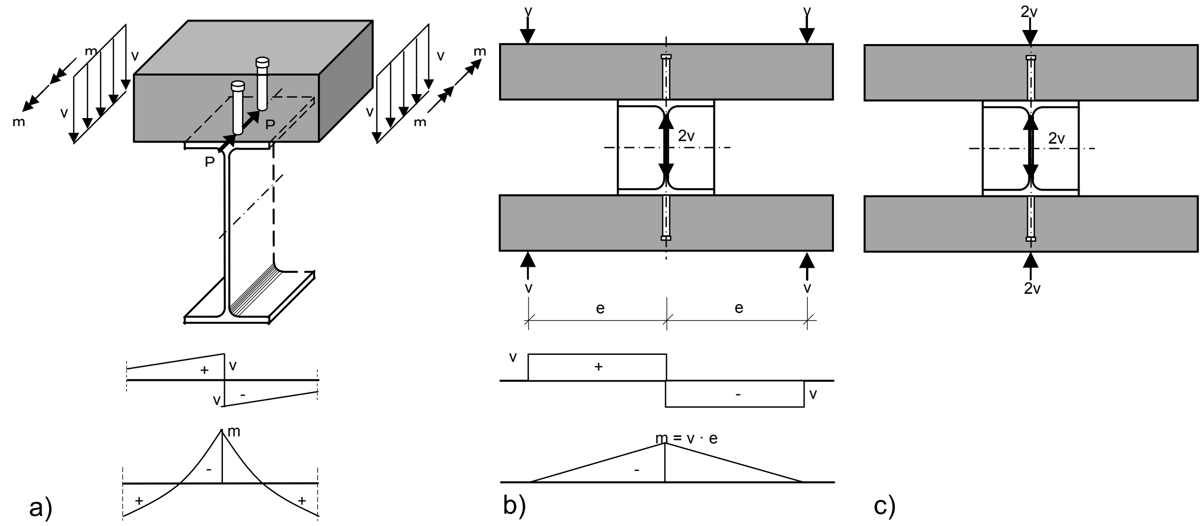

Figure 2: a) Internal forces and moments at the line of the shear connectors in a composite beam, b) their reproduction in push-out tests and c) push-out tests with concentric transverse loading.

2.2 Degree of transverse loading

To determine realistic values for the transverse load in the push-out tests, a parametric study was conducted. The study investigated single span composite beams with two types of additional steel sheeting – Cofraplus 60 and Ribdeck 80. The study considered the length of span of the slab between 3.00 m and 6.00 and for the composite beam between 8.00 m and 16.00 m. The concrete strength was taken as C30/37 and the steel grade was S355. The structure was exposed to a service load of 3.5 kN/m². With the design approach of EN 1994-1-1[1] the ratio between the slabs vertical force v and the beams shear force v_L was calculated at ultimate limit state.

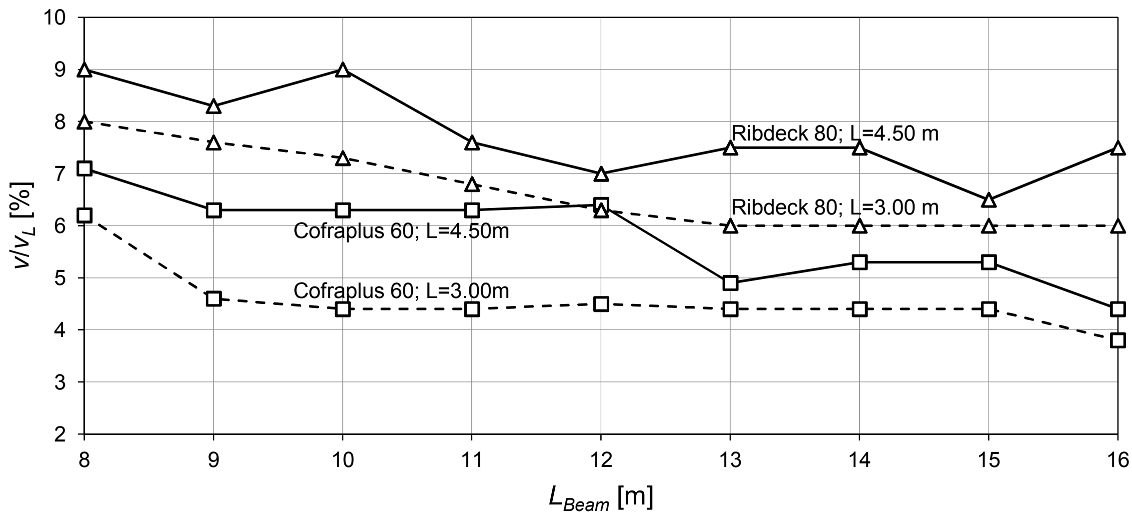

Figure 3: Ratio of the slabs vertical force v to the longitudinal shear force v_L vs. beam span at ultimate limit state.

Figure 3 shows exemplarily the results for composite slaps with a span of 3.00 m and 4.50 m, which are typical for modern deck profiles in un-propped constructions. It is shown, that the slabs vertical force v is about 4 to 10 % of the longitudinal shear force v_L which is introduced to the slab by the studs. The total load of the beam – $2v$ – lies between 8 and 18% of the longitudinal shear force.

For the presented push-out tests conservative transverse loads between 5% and 10% of the shear force per slab were applied.

2.3 Push-out test rig with transverse loading

The transverse loads were applied to the specimen by a hydraulic actuator using the test framing shown in Figure 4 and Figure 5. The framing consist of 3 elements. The actuator is fixed to element “2” and pushes element “1” against the concrete slab. Simultaneously the actuator pushes element “2” outwards and draws the tension bars. Thus, the transverse load is transferred to element “3” and loads the right slab of the specimen.

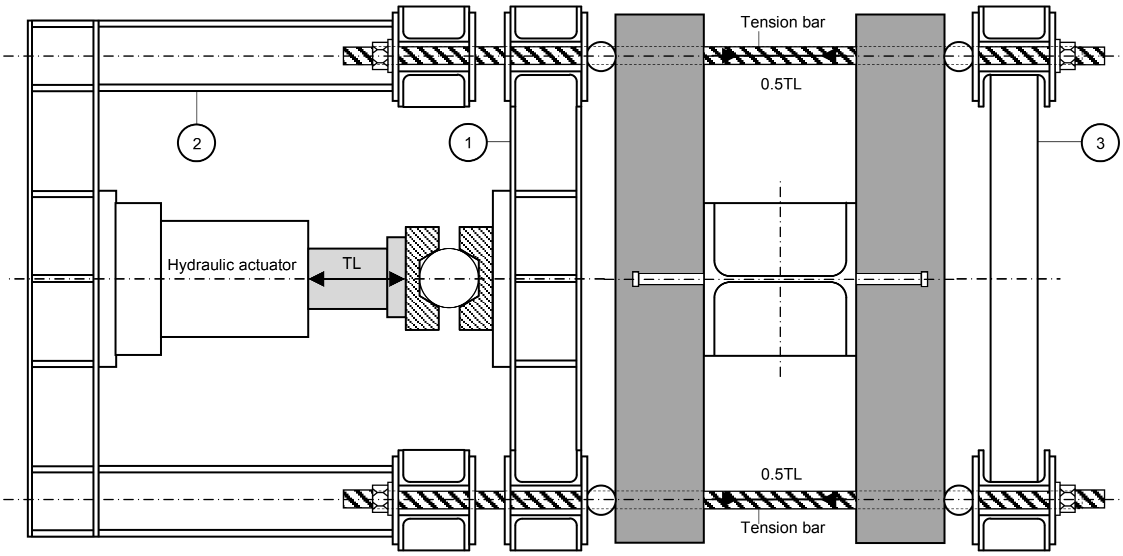

Figure 4: Functional principle of test rig for eccentric transverse loading

Figure 5: Test rig used for the application of transverse loads.

To use this setup also for the application of concentric transverse loads, beams were added to the elements “1” and “3” to push at the centreline of the slabs. The beam elements are attached with bolted connections to provide modularity of the test rig.

It is of crucial importance to ensure a sufficient spacing between the elements “1” and “2”. This space has to compensate all transverse displacements of the specimen, like the lift of the slabs. The compensation is achieved as the actuator is run force controlled and automatically adjusts to the displacement of the specimen.

3 TEST PROGRAMME

3.1 Specimen geometry and material properties

Within the research project DISCCO a total of 70 push-out tests was conducted investigating the influence of different composite deck shapes, the reinforcement pattern, the stud diameter, the number of studs per deck rib, the concrete strength and transverse loading.

The results of 10 push-out tests, using 80 mm deep steel sheeting (ComFlor 80) are presented, which have been focused on the influence of transverse loading. The dimensions of the composite slabs were 900x900x160 mm. A single layer of reinforcement was placed 30 mm above the top of the ribs. The concrete grade was C30/37 and was cast in horizontal position. The two halves of a specimen were welded together prior to testing. All specimens had pairs of headed stud shear connectors Ø19x125 mm, which were welded through the composite deck in mid position. A typical specimen is shown in Figure 6.

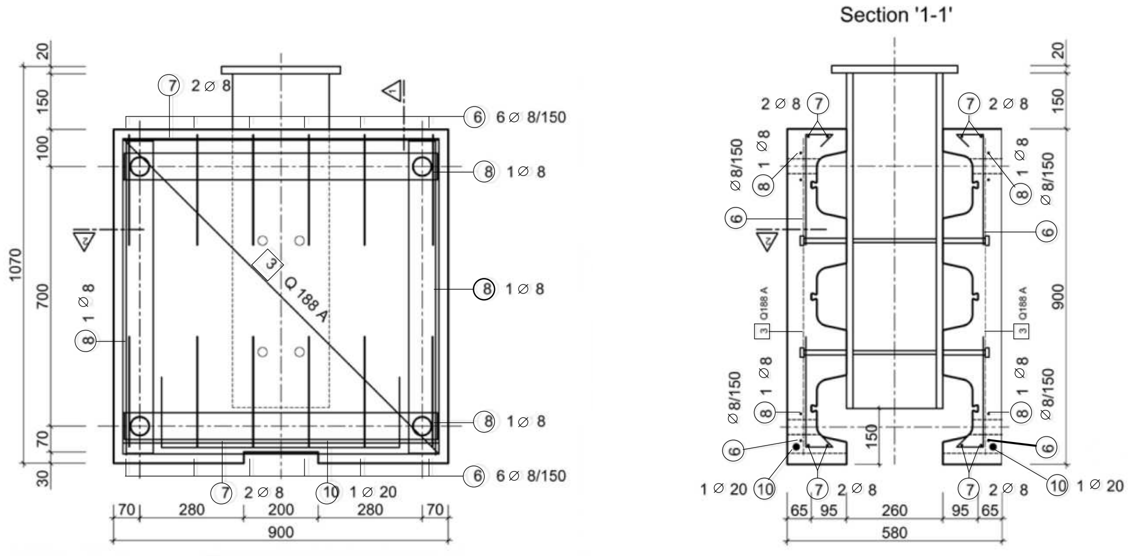

Figure 6: Typical push-out test specimen.

3.2 Investigated parameters

The influence of concentric and eccentric transverse loading as well as the influence of lateral restraints have been investigated. An overview of the loading and boundary conditions is given in Table 1.

Series	1-08			1-09	1-10			1-11		
Test	1	2	3	1	1	2	3	1	2	3
TL [kN]	Weak restraint		Strong restraint	8.8	17.5	13.2	0	17.5	17.5	17.5
Application				C	C	C	0	V	C	C
e [mm]	250	250	250	0	0	0	0	380	380	380

TL: Transverse load C: Constant with given values V: Variable, increasing with shear force

Table 1: Transverse loads and lateral restraints applied in push-out tests.

The tests 1-09-1 to 1-10-3 investigated the sensitivity for concentric transverse loading by applying transvers loads between 0 and 17.5 kN to the specimens. The values of the transverse loads were fixed according to the outcomes of the prior tests.

All tests in series 1-11 had eccentric transverse loads of 17.5 kN applied. As negative bending moments are present in all composite beams (but edge beams) more realistic results have been expected for this series.

In addition, series 1-08 investigated the influence of lateral restraints by fixing the tension bars directly to the slabs. The tests 1-08-1 and 1-08-2 used washers as fixation (c.f. Figure 7a), while test 1-08-3 used additional steel plates (c.f. Figure 7b).

a)  b) 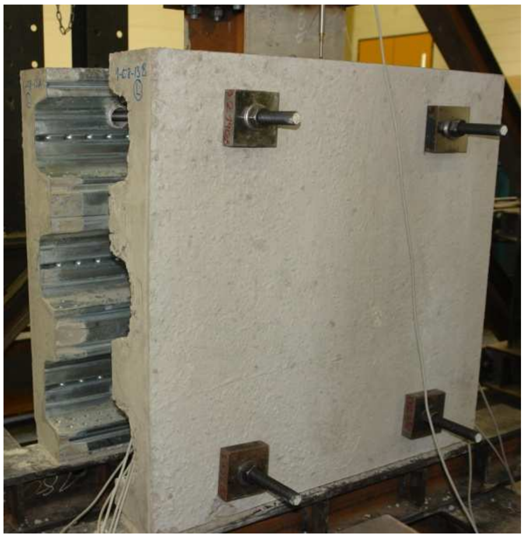

Figure 7: a) Weak lateral restraints with washers and b) strong lateral restraints with additional steel plates

4 TEST RESULTS

4.1 Failure mechanism

Independently from the boundary conditions and the transverse loading, all 10 push-out tests exhibited the same failure mechanism, subsequently referred to as rib pry-out (c.f. Figure 8). During the tests, this failure mode could be identified by visible cracks on the outside of the ribs at a slip of about 1.0 to 4.5 mm.

a)  b) 

Figure 8: a) Rip pry-out failure and b) stud deformation after testing.

When no (or only low) transverse loads were applied, the broken concrete block moved with the beam during subsequent loading. Thereby the rib rotated and pushed the slab outwards. Thus the studs exhibited plastic deformations above the weld collar, whilst the rest of the shank remained nearly straight. Only with higher transverse loading the ribs rotation was restrained and lead to plastic deformations of the upper part of the stud shank in combination with crushing of the concrete in front of the stud (c.f. Figure 8b). This is a load-displacement behaviour, significantly different to the commonly known concrete pull-out failure as the typical second peak load is not developing.

4.2 Test results

The load-slip curves of the push-out tests with concentric transverse loading are given in Figure 9. When no transverse loading was applied, rib pry-out was observed at a load of about 31 kN per shear connector. The failure load increased by about 28% to 39 to 41 kN (avg. 39.7 kN) per shear connector when transverse loads were applied. Only with high transverse loads of 17.5 kN – about

10% of the test load per slab – the test load increased during subsequent loading to about 49 kN per shear connector. The other tests remained at an almost constant load, whereby only the test with 8.8 kN transverse loading exhibited a drop of the test load of about 5 kN per shear connector after rib pry-out failure was observed. Due to this load drop, the 6 mm criterion of EN 1994-1-1[1] is not satisfied.

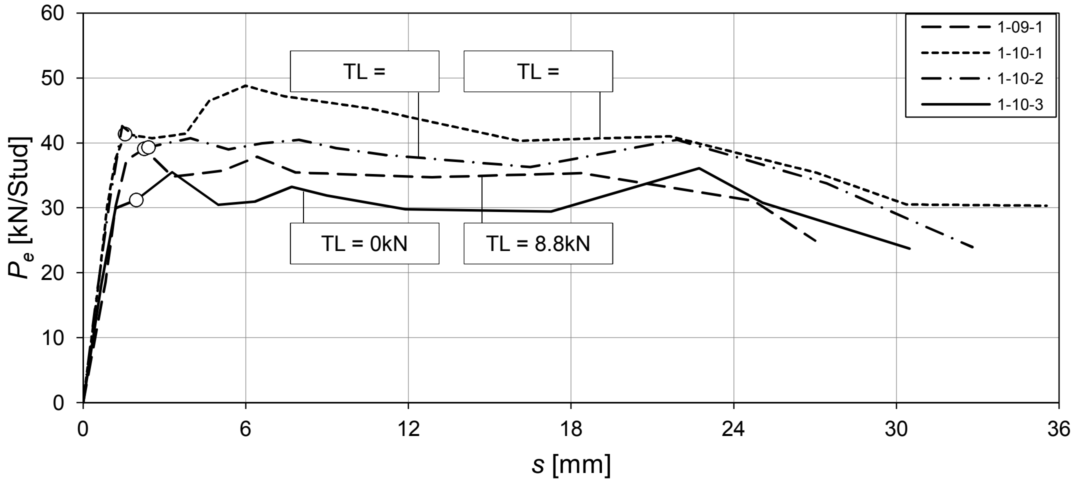

Figure 9: Load-slip curves of push-out tests with different degrees of concentric transverse loading.

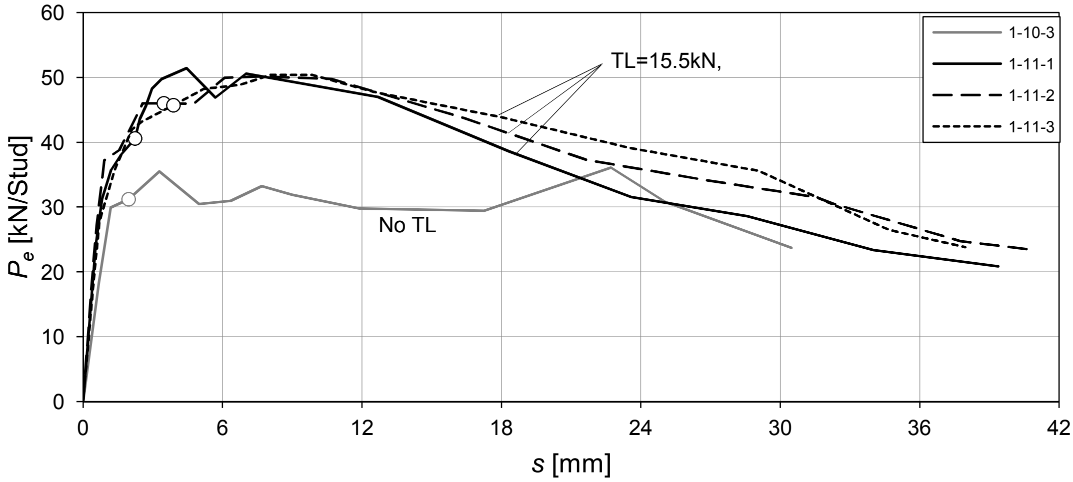

Figure 10: Load-slip curves of push-out tests with 17.5 kN eccentric transverse loading.

When the eccentric transverse load of 17.5 kN for series 1-11 was applied, the failure load increased to a value of about 40 to 46 kN (avg. 44.1 kN) per shear connector. This is about 11% higher than for the concentric loaded test 1-10-1 with a value of 40.75 kN per stud. The slip after the observation of rib pry-out failure is about 2 mm higher (compare Figure 9 with Figure 10). During subsequent loading the test load increased to about 50 kN per shear connector and showed afterwards an almost linear decrease of the shear force, see Figure 10.

The tests which used tension bars with washers as a lateral restraint (see Figure 7a) showed, that the diameter of the washers was too small compared to the diameter of the hole in the concrete. Therefore, the fixations slipped into the holes and the bars were not fully activated. This leads to lower but hardly reproducible tension forces in the bars. That means, the washers can be classified as “weak” restraints, nearly like without any tension bars. The replacement of the washers with steel plates (see Figure 7b) improved that behaviour, but constituted a fully rigid restraint. The adjacent forces in the tension bars have been unrealistic high.

Figure 11 shows the static load-slip curves of push-out tests with tension bars as a lateral restraint. The failure load of the tests is about 43 to 46 kN per shear connector. The two tests with weak restraints (c.f. Figure 7a) exhibited a drop of the test load to about 37 kN after the observation of rib pry-out failure, which has to be judged against the 6 mm criterion. During subsequent loading, the test load remained above this value until a slip of at least 18 mm was reached.

The third test of this series had strong restraints (c.f. Figure 7b) and the test load increased to about 60 kN after rib pry-out was observed. Measurements of the forces in the tension bars resulted in values of up to about 80 kN in each bottom bar and up to about 35 kN in each top bar.

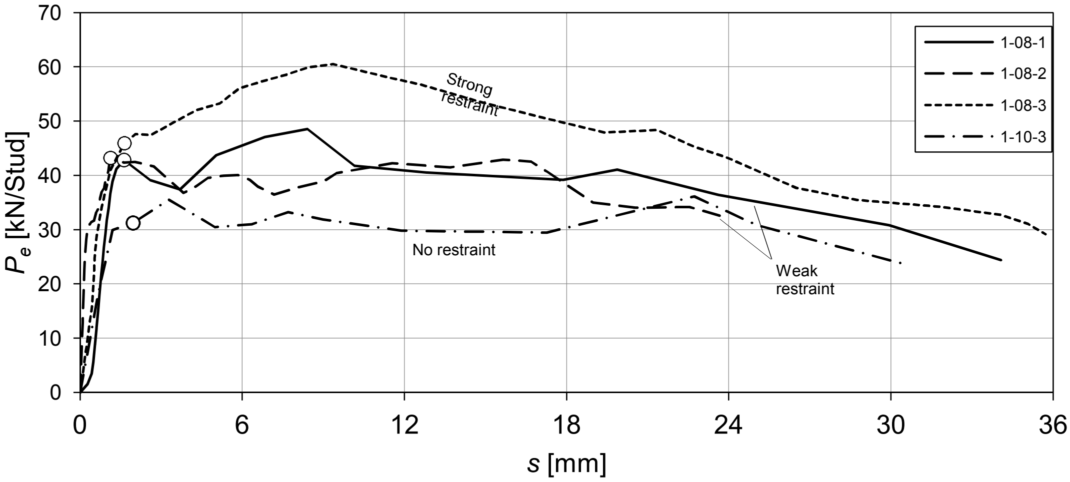

Figure 11: Static load-slip curves of push-out tests with lateral restraints.

4.3 Discussion of the test results

Figure 9 shows a comparison between static load-slip curves for tests with different concentric transverse loads between 0 kN and 17.5 kN. Depending on the transverse load, the bearing capacity after rib pry-out increases from 31.2 kN to about 39.7 kN (+27%) per shear connector. The actual value of the transverse load seems to have only a small influence on the failure load (c.f. Figure 12a), while at higher slips the bearing capacity increases proportionally to the applied transverse load (c.f. Figure 12b).

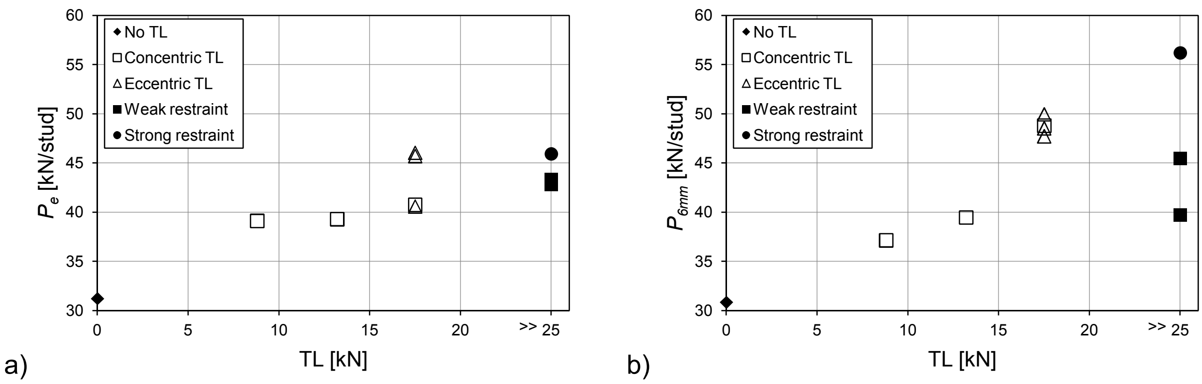

Figure 12: a) Load for rib pry-out failure and b) load at a slip of 6 mm vs. applied transverse loads.

For the eccentric transverse loaded tests, the average load after the observation of rib pry-out is 44.1 kN per stud. This is about 41% higher than without transverse loading (c.f. Figure 10). The eccentric transverse loaded tests have a higher bearing capacity than the concentric loaded test (c.f. Figure 13a). All four tests show a very similar load slip behaviour without significant differences.

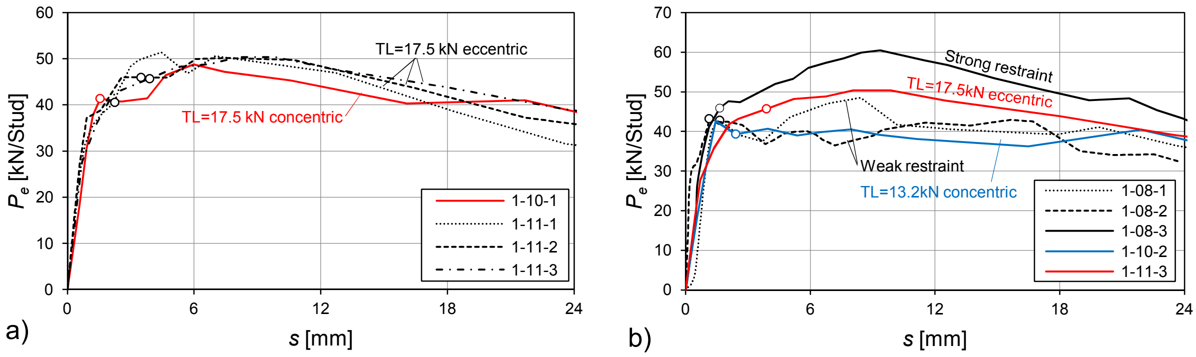

Figure 13: Comparison of a) tests with eccentric and concentric transverse loads and b) lateral restraints and transverse loads

The application of tension bars as a weak lateral restraint resulted in an average bearing capacity of 43 kN per stud which is 38% higher than without lateral restraint (c.f. Figure 11). The load slip curves of these tests lie between 13.2 kN and 17.5 kN transverse loading (c.f. Figure 13b).

The addition of steel plates as strong restraints leads to a load slip behaviour which is similar to other tests with high transverse loads. The resistance of a stud with strong lateral restraints is 45.9 kN, which is 47% higher than without restraints. Compared to eccentric transverse loads, the strong restraints lead to an about 4% higher resistance per stud. The maximum transverse compression in this test was about 230 kN, which is unrealistic high. However, it gives evidence that there is an upper limit for the increase of the test loads with increasing transverse loads (c.f. Figure 12b). Amongst others, this limit is related to crushing of the concrete at the contact surface of slab and the rib pry-out block.

4.4 Comparison between push-out test results and predictions according to EN 1994-1-1

The results of the push-out tests are compared to the empirical reduction factor formulae given in EN 1994-1-1[1], whereat the resistance of a headed stud shear connector in a solid slab is reduced by the factor k_t.

$$P_{t1} = 1.00 \cdot f_u \cdot \pi \cdot d^2/4 \tag{1}$$

$$P_{t2} = 0.374 \cdot \alpha \cdot d^2 \cdot \sqrt{f_{cm} \cdot E_{cm}} \tag{2}$$

$$k_t = \frac{0.7}{\sqrt{n_r}} \cdot \frac{b_0}{h_p} \cdot \left(\frac{h_{sc}}{h_p} - 1 \right) \tag{3}$$

The average resistance of a headed stud shear connector in a solid slab is given according to Roik et. al.[5] in equations (1) and (2). The resistance of a headed stud shear connector in the rib of a composite slab is calculated by multiplication of the reduction factor k_t (c.f. equation (3)) with the minimum of the values of equations (1) and (2). As shown in Table 2, all test results are over-predicted by EN 1994-1-1[1,5].

Without transverse loading or lateral restraints, only 49% of the predicted bearing capacity per shear connector are reached. Even with high transverse loading – which increased the bearing capacity by up to 41% - no more than 72% of the predicted bearing capacity are reached.

In average, the presented push-out tests reached only 68% of their predicted resistance according to EN 1994-1-1[1,5]. The observed failure mechanism is not covered accurately by the current standard.

Test	Experimantal resistance	EN 1994-1-1		Ratio
	P_e	k_t	P_t	P_e/P_t
	[kN]	[-]	[kN]	[-]
1-08-1	42.80	0.40	62.44	0.69
1-08-2	43.33	0.40	62.73	0.69
1-08-3	45.92	0.40	63.41	0.72
1-09-1	39.11	0.41	65.09	0.60
1-10-1	40.75	0.41	64.90	0.63
1-10-2	39.29	0.41	63.88	0.62
1-10-3	31.22	0.41	64.16	0.49
1-11-1	40.57	0.42	65.97	0.61
1-11-2	46.04	0.41	64.87	0.71
1-11-3	45.71	0.41	64.58	0.71

Table 2: Push-out test results and comparison to EN 1994-1-1[1,5]

5 SUMMARY AND CONCLUSIONS

The push-out test setup proposed in EN 1994-1-1 Annex B2[1] was developed for solid slabs and not for composite slabs with additional steel sheeting. It leads to a load-slip behaviour of the shear connectors that differs from the behaviour in the real beam as – amongst others – the vertical forces and negative bending moments of the composite slab at the line of the shear connectors are ignored.

A test procedure was developed on the basis of EN 1994-1-1[1] to investigate the influence of transverse loading onto the load-displacement behaviour of the shear connection when composite slabs with additional deep steel decking are used. Different degrees of transverse loading have been investigated as well as the influence of concentric and eccentric loading positions. The results of the tests show that the load bearing capacity of the studs increased by up to 41% by the application of realistic – but still relative low – transverse loads.

None of the 10 push-out tests presented in this article – as well as most of the other tests on open deck profiles conducted within the research project[6] – did reach its predicted resistance according to EN 1994-1-1[1,5].

The knowledge gained from these tests and the results of further numerical parametric studies will contribute to complement current calculation methods and develop new and more appropriate equations for the bearing capacity.

6 ACKNOWLEGEMENT

The research leading to these results is part of a common project of Steel Construction Institute, University of Stuttgart, University of Luxembourg, University of Bradford and ArcelorMittal and has received funding from European Community's Research Fund for Coal and Steel (RFCS) under grant agreement no [RFCS-CT-2012-00030].

REFERENCES

[1] EN 1994-1-1. Eurocode 4: Design of composite steel and concrete structures – Part 1-1: General rules and rules for buildings; German version EN 1994-1-1: 2004 + AC:2009

[2] Rambo-Roddenberry, M. D.: Behaviour and strength of welded shear stud conncetors. Virginia, Virginia Polytechnic Institute and State University, PhD-Thesis, 2002

[3] Roik, K.; Hanswille, G.: Zur Dauerfestigkeit von Kopfbolzendübeln bei Verbundträgern. Bauingenieur 62 (1987), pages 273-285

[4] Ernst, S.: Factors Affecting the Behaviour of the Shear Connection of Steel-Concrete Composite Beams. University of Western Sydney, Phd-Thesis, 2006

[5] Roik, K.; Hanswille, G.; Cunze, A.; Lanna, O.: Report on Eurocode 4 – Clause 6.6.2 Stud connectors, Report EC4/8/88. Ruhr-Universität Bochum, 1988

[6] Eggert, F.; Nellinger, S.; Kuhlmann, U.; Odenbreit, C.: Push-out tests with modern deck sheeting to evaluate shear connector resistances. Conference paper, EUROSTEEL 2014, September 10-12, 2014, Naples, Italy, to be published

PRE-STRESSED SINGLE LAYERED MEMBRANE STRUCTURES FOR SMALL AND MEDIUM SPANS

Michal Netušil

*Czech Technical University in Prague
Faculty of Civil Engineering, Department of Steel and Timber Structures
Thákurova 7, 166 29 Praha 6
e-mail: michal.netusil@fsv.cvut.cz, webpage: http://www.k134.fsv.cvut.cz

Keywords: Pre-stress, membrane, load transfer, steel substructure

Abstract. *Pre-stressed membrane structures are becoming more and more popular in modern architecture mainly because of their unique design, low self-weight and overall appearance. Membrane itself has to be taken into account as a fully load bearing element, which sufficiently caries the load due to the double-curved shape and activation by pre-stress. This contribution deals with the basic introduction of membrane architecture, designing of the shape, load transfer from membrane to its substructure, static evaluation and detailing of connections. Some case studies of textile membrane structures, performed in Czech Republic and other countries are presented.*

1 INTRODUCTION

Pre-stressed textile membrane or stainless steel net can play real load bearing role in overall structure and carry the load from very long spans without any additional load-bearing elements like rods, cables or secondary structures. Due to the intensive progress of IT and FE software in the last decades, non-linear 3D solution of the structures is still more and more available for civil engineers. There are even some specialized programs on the market, focused directly on membrane architecture. This kind of software can be used during whole design stage of membrane structure since the design of the shape, geometry, static evaluation of the stress states and internal forces in steel supporting structures and also for drawing of the cut pattern, useful for fabrication of the membrane in desired shape, which is usually very complex and “hand” transfer of the cut pattern to 2D drawings would be nearly impossible.

2 MEMBRANE SHAPING

Basic shape of each specific membrane has to reflect the state of stress under expected load, different camber of the structure will be used in a place, where high lever of snow is expected and on the other hand, more flat membranes can be used in a countries or areas without significant design snow load. The same attention has to be taken into account in case of wind load, which has the same importance like snow, but acts on the membrane mainly opposite way, it means causes a suction. Every load bearing membrane shape has to be designed including 2 countervailing curves (lines) which can carry both ways of loading – positive (snow) and negative (wind). Every membrane can carry only tension forces (or stresses), there is no effective bending stiffness of the element and all pertinent compression in the main membrane structure has to be avoided by properly designed shape and level of pre-stress.

2.1 4-point supported membranes

Basic and very frequently used shape of membrane canopies with smaller spans about approx. 15m is hyperbolic-parabolic, see Figure 1. Where two main tension fields are presented by lines connecting opposite corners.

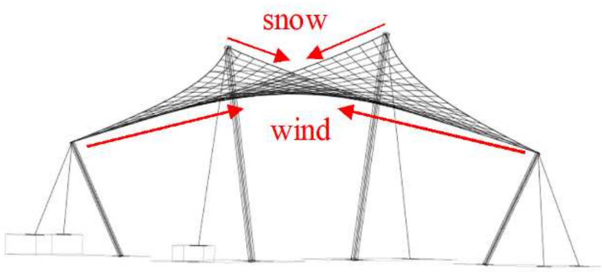

Figure 1: Hyperbolic-parabolic shape, on the left: main tension fields

2.2 Cones

Double-curved shape can be reached by conic arrangement, see Figure 2, where cones with positive and negative orientation are presented.

Figure 2: Cones, orientated in positive or negative shape

2.3 Arches

Arches serve as a stiff elements carrying load from membrane to substructure and define also one of desired countervailing curves, see Figure 3.

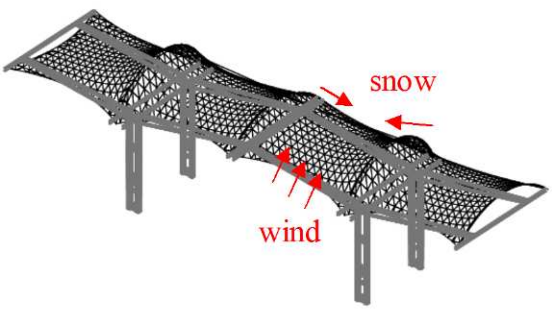

Figure 3: Arches

2.4 Waves, gables

Countervailing curves simply changing the curvature from positive to negative are presented by Waves, see Figure 4. These elements works as 2 lines curved against each other and must be pre-stressed enough to stay tensioned in both cases (wind, snow) because one type of load increases the force in one of the lines and decreasing the pre-tension in the other one.

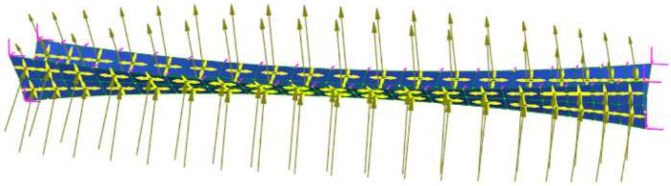

Figure 4: Waves, gables

Any other textile membrane roofing is more or less combination of these 4 types of shapes presented above.

3 MATERIALS OF SINGLE LAYERED MEMBRANES

Textile membrane is usually performed by high-tenacity polyester micro-yarn base cloth, coating under warp and weft tension throughout the manufacturing cycle and high-performance polymer surface layer, see Figure 5 on the left. Usual thickness of the textile for middle span structures is about 0,8-1,2mm and strength about 80-150MPa. Steel cable net strength differs from used cables (wires) and level of pre-stress. Action of the overall structure performed by stainless steel nets is nearly the same as membrane action, see Figure 5 on the right, but the main tension fields depends on the construction of the net and works mainly diagonally thru the eyes of the net.

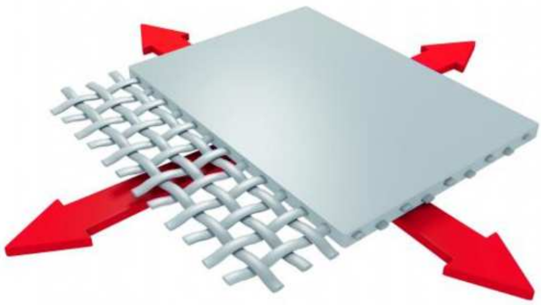

Figure 5: On the left: textile, on the right: stainless steel net

4 PRE-STRESS AND LOAD TRANSFER

Every part of the load carrying membrane has to be pre-tensioned, it means, appropriate level of tension stress has to be reached in whole area of the membrane by tightening of the edge cables or movement of the point or linear supports. All supports have to be designed and evaluated to carry the reaction from the membrane to its substructure. Linear support is often performed by “keder” profile, which is usually made of stiff polymer and membrane is doubled along it. Keder bar is inserted into the connecting profile, which can be assembled to the substructure by common connections (bolts, rivets, welding etc.), see Figure 6. This kind of connections takes place especially there, where supporting structure is stiff element like wall or continuous arch, beam or main ring of conic membranes.

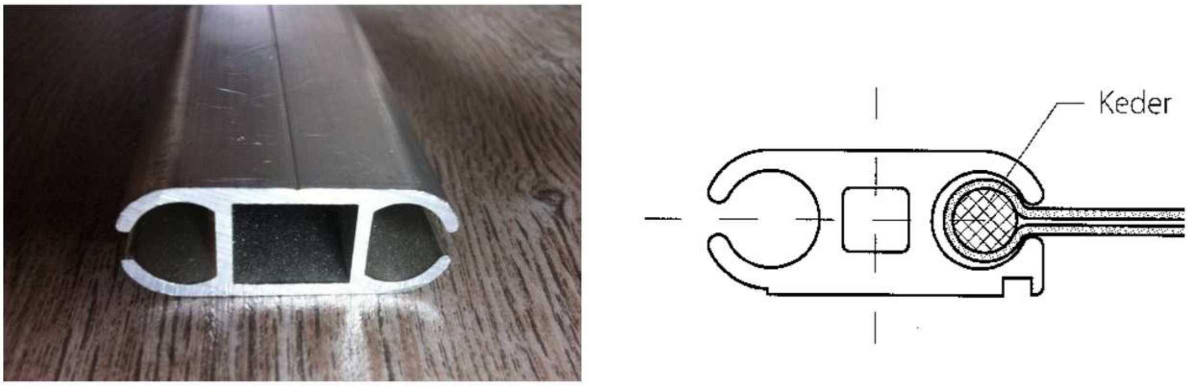

Figure 6: Keder bar in aluminum assembling profile, [1]

Similar principle is used in point supports, where the membrane is gripped between steel joining plates and keder bar serves as a stopper, see Figure 7.

Figure 7: Point support at the corner of the membrane

Part of the corner detail arrangement is also detailing of the edge rope connections. These ropes are placed in the pouches on the edges of the membrane and fitted into the corner profiles due to the threaded terminal via tube and tightened by nut. This detail serves to reach optimal pre-stress level and also for fine tuning to reach the smooth shape of the canopy and therefore has to allow rectification during the life-time of the structure. Radius (camber) of the edge rope plays significant role on the value of the corner reaction, because horizontal force in the rope is proportional to the radius of curvature in the same (desired) level of pre-stress in whole area of the membrane, see Figure 8, [1].

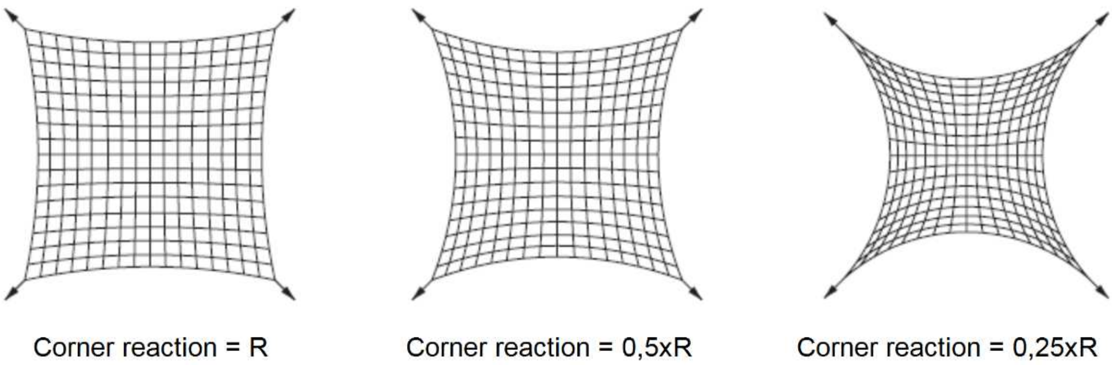

Figure 8: Influence of the edge rope radius on corner reaction

5 STEEL SUBSTRUCTURE

Steel supporting substructure has to carry the forces caused by external loads and pre-stress from membrane to ground base and also provides a spatial stability to overall structure, because membrane itself has no bending stiffness and neither bracing function. Horizontal stability of the structure is usually provided by 2-directional tendons or frame corners, see Figure 9.

Figure 9: Horizontal stability provided by 2-directional ropes or frame corners

Steel structure should be apart of complex numerical model together with the membrane to include the stiffness (compliancy) of the connection points into the calculation and determine the real interaction of the membrane and substructure. This is more important especially when membrane is linearly connected into the beam element (or arch), where compliancy of the structure near its support is significantly different form the middle of the span. Another possible solution is separate solving of membrane and substructure with using iterative process of tuning support stiffness according to the real stiffness of the steel structure at the connection points of the membrane, see Figure 10.

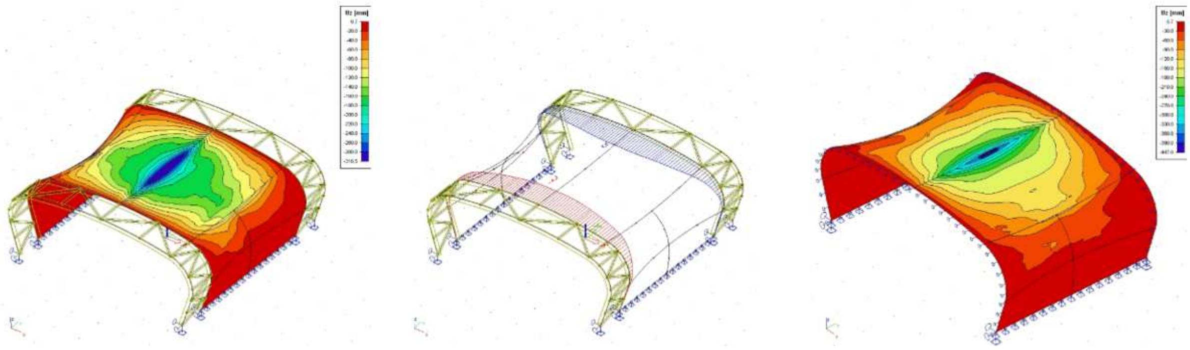

Figure 10: On the left: complex model, center and right: separate solution with stiffness tuning

Figure 11: End details of the columns – cable fitting, hinged base

In case of small or middle span canopies, steel columns are commonly designed from ordinary steel grade S355 with built-in details for assembling of the cables and hinged base, see Figure 11. Bottom hinges allows the column to rotate in the plane of the magnitude of the corner reaction from the membrane. This action is necessary for erection of the structure as well as for prestressing, see Figure 12.

Figure 12: Erection of the structure due to pivoting of the column

Main stabilizing cables of the columns must allow rectification as well, because they also serve for pre-tensioning and getting the membrane into desired shape by pivoting of the tips of the columns (due to rotation around hinges in the bottom). Therefore, turnbuckles have to be installed directly on the ropes, see Figure 13 on the left and center, or another solution with the same function has to be used, see Figure 13 on the right. Assembling of the base plates of the cables and columns to the base grounds are often made by chemical anchors. Gravitation bases are the most frequently used in case of small and middle spans canopies.

Figure 13: Rectifying members on the ropes

ACKNOWLEDGEMENT

This contribution was supported by the grant SGS14/038/OHK1/1T/11

REFERENCES

[1] Dipl.-Ing. Dr. Michael Seidel, *Tensile Surface Structures*, A Practical Guide to Cable and Membrane Construction, ISBN 978-3-433-02922-0, Ernst & Sohn, Berlin, Germany (2009).
[2] Pictures of the membrane architecture of the company Archtex were used in the contribution with permission, www.archtex.cz

NUMERICAL STUDIES OF TUBULAR T-JOINT SUBJECTED TO IMPACT LOADING

Hui Qu[a], Anling Li[a] and Jingsi Huo[b]

[a]School of Civil Engineering, Yantai University, Yantai, 264005, China
Tel: 86 535 6902606, Fax: 86 535 6902606
e-mail: quhuiytu@gmail.com

Keywords: tubular T-joint, impact loading, numerical analysis, energy dissipation mechanism, equivalent impact force estimation method

Abstract. *Joints play an important role in resisting impact loading in Tubular structures. In this paper, a finite element model is established to numerically study the failure modes and energy dissipation mechanism of tubular T-joint impacted by a drop hammer with the initial velocity of 7-10 m/s. The resistant mechanism is investigated based on the dynamic responses of the joints under impact loading. Strain, displacement and the failure modes of the T-joints are also predicted. Global and local deformations of the tubular joints are distinguished using an equal area axis method, which helps to discover the failure mechanism of the joints.*

1. INTRODUCTION

Tubular structure is the primary load bearing structural system in offshore jacket platform or breakwater due to its excellent axial loads resistance, lower resistance to fluid flow and fast track construction, transportation and erection. During its service period, it may be subjected to impact loads, e.g. the ship collision, floating iceberg collision, or explosion and fire resulted from leaking oil and gas. The pioneer research work on the impact behaviors of tubular structure can be traced back to Spares and Soreide [1]. The tubular joints are the critical structural components which play an important role in transferring load in the tubular structure. However, few tests and numerical studies had been reported to analyze the dynamic behaviors of tubular joints or tubular structures under impact loading. Jin et al. [2] presented a non-linear dynamic analysis procedure for simulating the dynamic responses of a tubular platform structure under impact action based on the forensic evidence from the damaged components, and then evaluating the global damage effects on the platform structure. Wang et al. [3] compared the impact resistance of reinforced and unreinforced tubular K-joints. Yu et al. [4] performed experimental study on mechanical behavior of steel tubular T-joint in fire and impact loading. Qu et al. ([5]-[7]) carried out a series of numerical

----

[a]School of Civil Engineering, Yantai University
[b]China Ministry of Education Key Laboratory of Building Safety and Energy Efficiency, College of Civil Engineering, Hunan University

studies on the dynamic behaviors of tubular T-joint under different impact loading conditions, which were aimed to discover the failure modes and impact resistant mechanism of tubular T-joints.

The impact tests and numerical analysis described in the above literatures generally focus on the failure modes and load-bearing capacity of steel tubes and tubular joints. Due to the instantaneous characteristic of the impact loading, the dynamic response of structure under impact loading is evidently different from that under static loading and is difficult to be recorded completely during the tests. This paper aims to develop a finite element model to unveil dynamic behavior of tubular T-joint under impact loading basing on the experimental results in reference [8]. The local buckling deformations of the chord are distinguished from the global deformations of the T-joints through an equal area axial method and the yield line theory.

2. FINITE ELEMENT MODELING

A finite element model is developed here to simulate the dynamic behavior of steel tubular T-joint under impact loading using the general purpose program ABAQUS [9]. Figure 1 shows the three dimensional finite element model of the tubular T-joint. It replicates the full scale tests which are to be described in Section 3. The drop hammer, brace, chord and rigid plates are simulated using 8-node 3D reduced-integration solid element (C3D8R). The meshes of the chord in the brace-chord connecting zone are refined to improve the accuracy of the FE analysis. The drop hammer is modeled as a rigid cylinder with the height of 400 mm and the diameter of 180 mm. Different impact energies (as shown in Table 1) are applied by changing the weight of the hammer. The center line of rigid plate at both ends of chord is simply supported and the top end of brace is free. An initial velocity, ranging from 7 to10 m/s, is applied to the drop hammer.

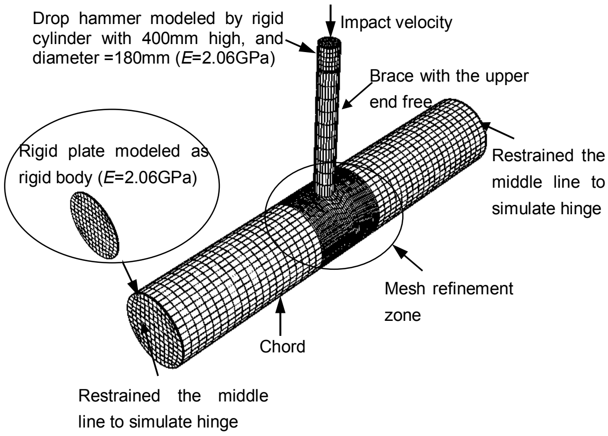

Figure 1 FEA model of T-joint under impact loading

A “Tie Contact” from ABAQUS is used to simulate the connection between the brace and the chord. “Self Contact” from ABAQUS is used to simulate the contact behavior between the hammer and the top cover plate of the brace during impact loading.

Under static load, the idealized uniaxial stress-strain relationship of mild steel is used to represent the elastic-perfectly plastic behavior of steel. As the yield stress of steel under dynamic loading is sensitive to strain rate[10], the dynamic flow stress of steel increases with an increase of strain rate. The Cowper-Symonds constitutive equation is used here to simulate the strain-rate sensitive behavior of steel under impact loading. The Cowper-Symonds constitutive equation is expressed as follow:

$$\sigma_{\mathrm{dy}} = \sigma_{\mathrm{y}}(1 + (\frac{\dot{\varepsilon}}{D})^{\frac{1}{n}}) \qquad (1)$$

where σ_{dy} is the dynamic yield stress at a uniaxial plastic strain rate, σ_{y} is the associated static yield stress, and $\dot{\varepsilon}$ is strain rate for steel, D is a rate-dependent constant and n is a positive dimensionless parameter. According to the literature (Abramowicz and Jones [10]), D=40 $s^{-1}$and n=5 for mild steel.

3. EXPERIMENTAL PROGRAMME

A series of tests on tubular T-joint under impact loading has been conducted by Qu and Huo [8], and some of the test results are used herein to validate the FE model proposed in this paper.

3.1 Specimen material and fabrication

Four tubular T-joints are tested using the drop hammer test machine at the Center for Integrated Protection Research of Engineering Structures (CIPRES), Hunan University. The test parameters were impact energy (E), length-radius ratio of chord (α) and diameter of chord (D). The details of each specimen is listed in Table 1, where D, T, L are the diameter, thickness and effective length of the chord, respectively; d, t, l are the diameter, thickness and length of the brace, respectively. m and v represent the weight and impact velocity of drop hammer.

Table 1 Summary of Test Information (adopted from reference [19])

Specimen number	Dimension of chord $D \times T \times L$ (mm)	Dimension of brace $d \times t \times l$ (mm)	α	Hammer weight m（kg）	Impact velocity v（m/s）	Impact energy E（kJ）	Impact capacity （kN）	Mid-span deflection （mm）
J14a	180×6×1890	89×4×600	21	460	7	11.27	289	45
J15a	180×6×1890	89×4×600	21	590	7	14.5	238	67
J14b	180×6×1890	89×4×600	21	460	10	23	-	110
J35b	325×7×1890	89×4×600	5.8	590	10	29.5	300	51

The chords and braces of four specimens are made from a 6-7m long cold-formed seamless steel tube and fully welded together. Three 6mm thick steel cover plates are welded to both the ends of the chord and the top end of the brace respectively. Strips of the steel tubes were made into tensile coupons and tested in tension. The yield strength (f_y) of 4mm, 6mm, and 7mm thick steel plates are 492MPa, 499MPa and 445MPa respectively, and the ultimate strength are 553MPa, 596MPa and 525MPa respectively.

4. ENERGY DISSIPATION MECHANISM OF TUBULAR JOINT UNDER IMPACT LOADING

The FE model was used to simulate the failure modes, dynamic responses of impact loads, lateral displacements and to predict the dissipated energy of the tubular T-joint. It is validated against the test in section 3. The comparisons of the numerical results with the experimental results and energy dissipation mechanism are shown as follows.

4.1 Failure modes

Figure 2 shows the comparisons between the numerical modeling and experimental results in the terms of failure modes of tubular joints under different impact energies. It can be seen that the numerical results agree well with the experimental results. No evident deformation in the brace, or crack and rupture in the weld toes of the T-joints are observed for both impact tests and numerical simulations. The failure modes indicate that all the specimens fail due to the remarkable local indentation of the chord at the position close to the joints and also due to the subsequent global bending of the chord.

(1) experiment

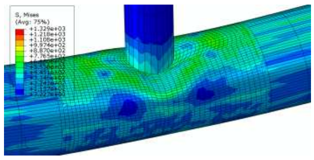

(2) simulation

(a) J14a

(1) experiment

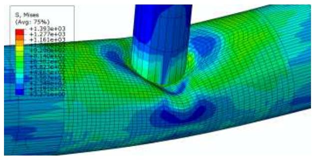

(2) simulation

(b) J15a

(a) experiment

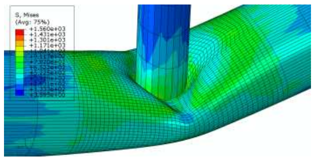

(b) simulation

(c) J14b

(a) experiment

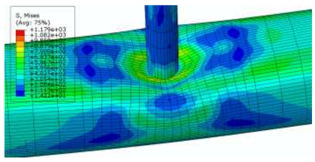

(b) simulation

(d) J35b

Figure 2 Comparisons of failure modes of tested specimens with numerical results

From the comparisons shown in Table 1 and Figure 2, it can be seen that Specimens J14a (E_k =11.2kJ, Figure 2-a(2)), J15a (E_k=14.5kJ, Figure 2-b(2)) and J14b (E_k =23kJ, Figure 2-c(2)) experienced different failure modes due to different impact energies. With the increase of impact energies, the failure modes of the three joints change from light local dent on the top surface of chord into severe local dent coupled with evident flexural buckling at the middle span of the chord. Although Specimen J35b (E_k =29.5kJ, Figure 2-d(2)) is loaded to failure under a larger impact energy, the failure mode is local indentation of the top surface of chord and slight global buckling, which is similar to that of Specimen J14a. The locally buckled zone is in an elliptical shape.

4.2 Impact load

Due to accident of the data logger system during the tests, the test results of Specimen J14b were not captured. After the drop hammer hit the top end of brace, the stress wave travels in the joint. As the transverse stiffness of chord is much less smaller than the axial stiffness of brace, the impact wave makes the top surface of chord near the intersection between chord and brace dent firstly, then the steel around the intersection between chord and brace start to yield progressively. The phenomena above make the signals recorded by the load cell embodied in the hammer, displacement transducer and strain gauges to fluctuate evidently at the beginning of impact.

The time history responses of impact load of Specimens J14a, J15a and J35b from numerical simulation (shown in Figure 3) agree well with the experimental results. The time history responses from both the simulation and the experimental results can be used to reveal the impact load resistance mechanism and deformational behavior. By analyzing the time history curves obtained from numerical analysis and experimental tests, it can be seen that it can be divided into three stages. Firstly, the impact force goes up to the maximum value sharply in a very short period of time. After being loaded to the peak load, the impact load decreases with sharp fluctuation during the second stage. Hereafter, the fluctuation gradually diminishes, therefore, the impact load versus time history curve tends to be flat and smooth. Finally, the impact load decreases to zero. The predicted impact forces and impact duration time from the numerical analysis are slightly less than those of experimental results. In order to further analyse the failure mechanism, seven typical time points are selected to highlight the deformational development of the tubular T-joint.

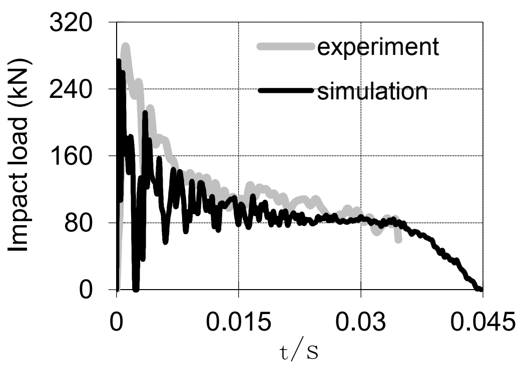

(a) J14a

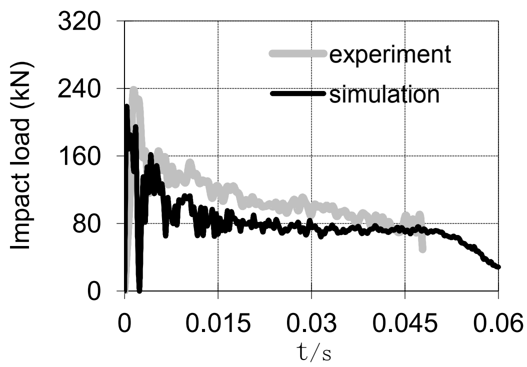

(b)J15a

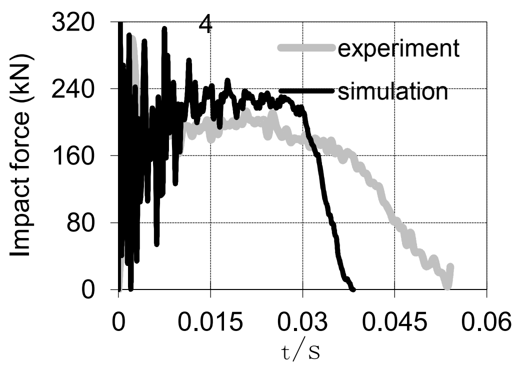

(c) J35b

Figure 3 Comparisons of measured impact load versus time history relations with numerical results

4.3 Impact displacement

Figure 4 shows the comparisons between the test results and numerical simulation of vertical displacement at the top end of the brace in Specimens J14a and J15a. As the displacement transducer failed to record the signals, the displacement of specimen J15a before 20ms is effective. It can be seen that the numerical results agrees with tested results in general. The predicted ultimate displacements are slightly higher than the test results.

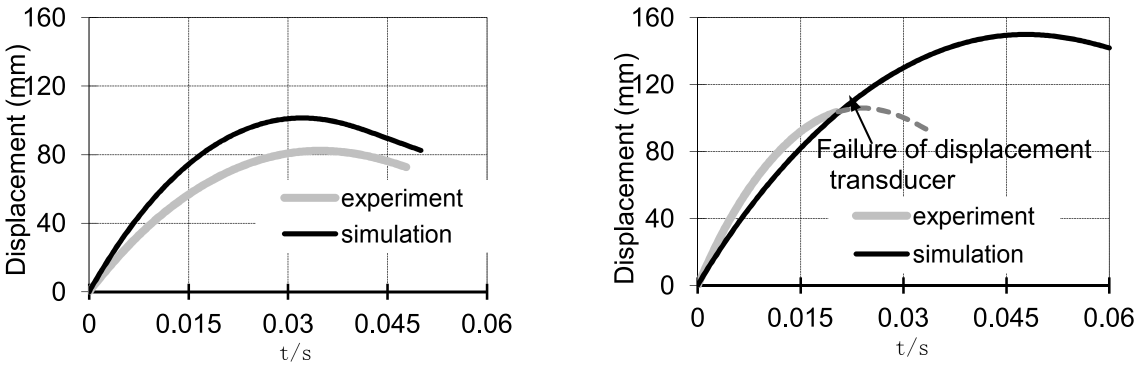

(a) J14a (b)J15a

Figure 4 Comparisons of measured vertical displacement versus time history relations with numerical results

4.4 Impact load versus displacement curves

Figure 5 shows the comparisons between the test results and numerical simulation in impact force versus displacement curves of Specimens J14a, J15a and J35b. The simulated peak impact forces of the three specimens are in good agreement with the test results while the deformation and initial impact resistance stiffness are slightly larger than those of experimental results.

All the discrepancy between the numerical simulation and test results can be attributed to that (1) the hammer and end-plate of brace in the FE model are simplified as rigid body and it would lead to a shorter contact duration time between the hammer and brace. (2) In the tests, the ends of chord are connected to a rigid base frame with two steel rollers. The imperfection of the specimens and base supports would lead to some rotational restraint at the end connections of the T-joints. It is difficult to accurately evaluate the rotational restraint in the simulation, therefore an idealized frictionless pin restrain is used in the FE model to represent the actual supports. Therefore, the test results would lead to a larger global bending stiffness of the specimens and smaller ultimate lateral displacement and larger impact force than the corresponding simulation results. Meanwhile, during the tests, the rotational restraint developed by the supports also dissipates some impact energy and it results smaller measured dissipated energy of the joint compared with the simulated results.

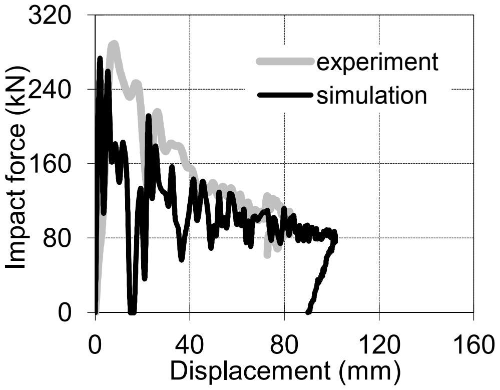

(a) J14a

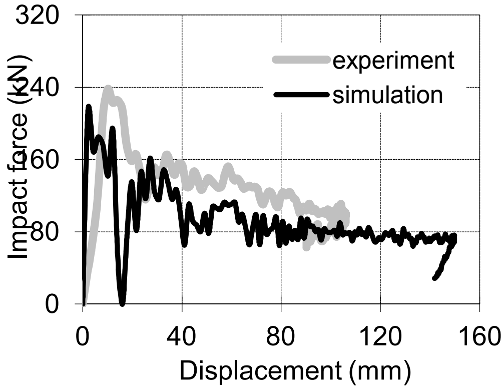

(b) J15a

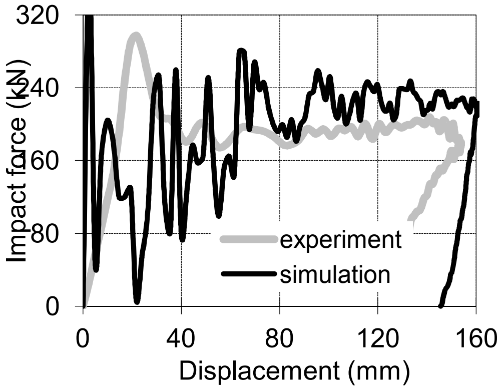

(c) J35b

Figure 5 Comparisons of numerical impact force versus displacement curves with tested results

4.5 Energy transformation

In the tests, the steel tubular T-joints are loaded with impact loading and significant plastic deformation is observed which is locally confined to the connection zone between brace and chord. Figure 2 demonstrates the local indentation mode and global buckling mode under impact loading. The impact energies are mainly dissipated by plastic deformation of steel tube. The dissipated energies can be determined by calculating the area between the impact force versus displacement curve (as shown in Figure 5) along the horizontal coordinate. Moreover, the plastically dissipated energy can obtained directly from the FE modeling. The measured and simulated dissipated energy and the ratio of dissipated energy to applied impact energy are shown in Figure 6. Figure 6-(a) shows the plastic dissipation energies calculated from FE model which are in good agreement with that from the test results. Figure 6-(b) shows the ratios of the dissipated energy to the applied impact energy, which are almost constant within the experimental parameters.

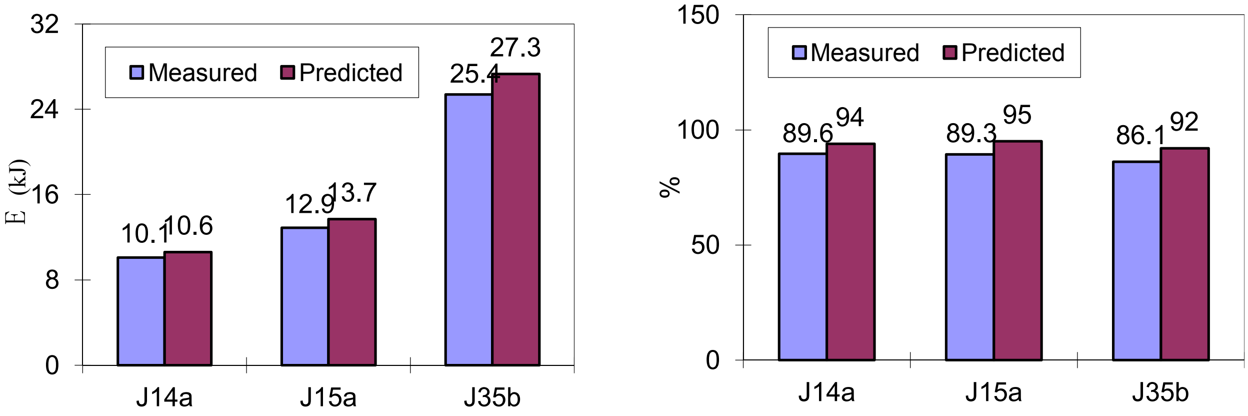

(a) Dissipated energy (b) Ratio of dissipated energy to applied impact energy

Figure 6 Comparisons of measured energy dissipation with predicted results

5. CONCLUSIONS

A finite element model to analyze the dynamic behavior of tubular T-joints subjected to lateral impact loading was developed in this paper. A series of tests conducted by the authors are presented to provide information for validation of the FE model and to investigate the failure and energy dissipation mechanism of tubular T-joints under impact loading.

From the results of this paper, the following conclusions may be drawn:

(1). The FEM model can be used to simulate the failure mode and dynamic responses of tubular T-joints subjected to lateral impact loading with good precision. The FE analysis indicates that the tubular joint experiences the coupled local and global deformations during the impact loading.

(2). The process of impact can be divided into three stages：loading on the brace, local buckling on the top surface of chord and global bending deformation of chord.

(3). The failure mechanism of tubular T-joints is dominantly controlled by the progressive local indentation of steel tube close to the brace-chord connection zone. Accordingly, the steel tubular T-joint under impact loading is vulnerable to local indentation.

(4). The impact energies are mainly dissipated by plastic deformation of steel tube. The ratios of the dissipated energy to the applied impact energy are almost constant within the experimental parameters.

ACKNOWLEDGEMENT

The work was funded by National Natural Science Foundation project (51108399, 51078139), Shandong Science Fund (ZR2011EL046) and the Program for New Century Excellent Talents in University (NCET-11-0123).

REFERENCES

[1] C.G. Spares and T.H. Soreide. *Plastic analysis of laterally loaded circular tubes*. Journal of Structural Engineering, 1983, 109(2): 451-467.

[2] W.L. Jin, J. Song, S.F. Gong and Y. Lu. *Evaluation of damage to offshore platform structures due to collision of large barge*. Engineering structures, 2005, 27(9): 1317-1326.

[3] X.L. Wang, Y.C. Zhang and Z.L. Wang. *Study on collision behavior of K-joint in offshore jacket platform*. Journal of Jiangsu University of Science and Technology (Natural Science Edition), 2007,21(4): 1-6. [in Chinese]

[4] W.J. Yu, J.C. Zhao, H.X. Luo, J.Y. Shi and D.X. Zhang. *Experimental study on mechanical behavior of an impacted steel tubular T-joint in fire*. Journal of Constructional Steel Research, 2011, 67(9): 1376-1385.

[5] H. Qu and Y. Zhang. *Mechanism analysis of impact performance for tubular T-joint*. In: 12th international conference on Inspection, Appraisal Repairs & Maintenance of Structures 2010, Yantai, China.Vol:1, 159-162.

[6] H. Qu and F. Chu. *Impact Performance Studies of T-tubular Joint impacted on the Chord*. Journal of Ship Mechanics, 2011,15(11):1306-1314. [in Chinese]

[7] H. Qu, Y. Zhang and Y.B. Shao. *Study of impact performance of tubular T-joint.* Journal of Ship Mechanics, 2012,16(1-2):156-164. [in Chinese]

[8] H. Qu, J.S. Huo and C. Xu. *Experimental study on tubular T-joints under drop hammer impact loads*. Journal of Building Structures, 2013, 34(4): 65-73 [in Chinese]

[9] ABAQUS. *ABAQUS 6.10, Theory manual and users Manual.* Pawtucket USA: HKSHibbitt, Karlsson & Sorensen Inc.. 2010.

[10] W. Abramowicz and N. Jones. *Dynamic axial crushing of square tubes*. International Journal of Impact Engineering, 1984, 2(2): 179-208.

LATERAL BUCKLING OF CONTINUOUS COMPOSITE BRIDGE GIRDER

Filip Rehor[*] and Jiri Studnicka[*]

[*]CTU in Prague, Faculty of Civil Engineering, Dep. of Steel and Timber Structures
Thákurova 7/2077, 166 29 Praha 6, Czech Republic
e-mail: <filip.rehor@fsv.cvut.cz> webpage: http://www.ocel-drevo.fsv.cvut.cz/ODK/en

Keywords: lateral buckling, distortion, bridge, composite, U-frame, FEM

Abstract. *Composite bridges consisting of several parallel bridge plate girders connected to a concrete deck are favourably used for middle spans. If the structure is continuous over several supports one of the main design tasks is to ensure stability. Lateral buckling may occur in the regions close to internal support where the compressed lower flange does not get any continuous lateral restraint. The tensile upper flange is restrained continuously in lateral displacement (rigidly) and rotation (flexibly). The steel part of deep bridge girders usually distorts while buckling and so called lateral distortional buckling (LDB) appears. The theory for lateral buckling of thin-walled cross-sections cannot be applied in case of LDB because of the cross-sectional distortion. In common practice the problem is solved by the method of inverted continuous U-frame. Recently the more precise solutions have been searched by using finite elements and finite strip methods.*

At the moment a parametrical study is being developed by the first author of this paper. A model of two parallel steel I-beams connected to a concrete deck corresponding to the U-frame model supported over three spans will be submitted for finite element analysis. Lateral bracings between two beams and web stiffeners are provided in specific distances. The parameters are: spacing of the beams, distance and stiffness of the bracings and depth of the steel section. The model will be verified according to other studies and then the critical moment and the ultimate moment will be observed according to the parameters. The aim of the study is to introduce a specific way for design of composite beams exposed to lateral distortional buckling. The preliminary model of one continuous composite girder was made in Abaqus software and structural behaviour was observed concerning eigenmodes and failure modes.

1 INTRODUCTION

The steel-concrete composite bridges are frequently used for road and railway bridges. The most common type for middle span is a structure consisting of two or more parallel I-beams connected to a concrete deck. The most benefit can be reached in case of simply supported single span bridge. The concrete deck is in compression while the most of the steel part of the section is in tension, that means the cross-section is in the 1st or 2nd class, and so plastic resistance can be reached in ultimate limit state even for deep sections.

In case of continuous multi-span bridge the situation becomes more complicated in hogging bending regions, where the concrete in tension must be neglected and only the reinforcement and the steel section usually of 4^{th} class transmit the bending moment. More over the steel parts in compression tend to buckling. Over the support local buckling of web and lateral buckling of the lower flange can likely occur. To avoid web buckling web stiffeners and to avoid lateral buckling lateral bracing are used both in various shapes and distances.

2 LATERAL BUCKLING

Many procedures has been developed how to deal with lateral buckling. The base for those procedures was developed by Vlasov[1] in 1960's as a part of his theory of thin-walled sections. The beam under bending loses its stability and buckles in lateral direction and in the same time torsion appears, the phenomenon was therefore called lateral torsional buckling (LTB). When some restrains of discrete or continuous bracing are present, this theory is still usable when the section stays rigid after buckling. This phenomenon can be called restrained torsional buckling. When distortion of the web appears the theory is then not absolutely correct and the lateral distortional buckling (LDB) arises. The special case when the restrains are present is sometimes called restrained distortional buckling. The difference between LTB of rigid section and LDB of composite section is depicted in Figure 1.

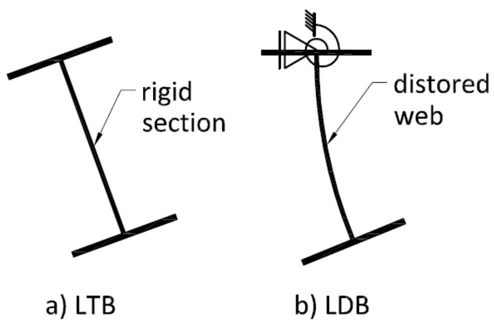

Figure 1: The cross-section after lateral torsional and distortional buckling

In case of the continuous composite girder the situation corresponds mostly to the last case, although the problem has been sometimes simplified to the restrained torsional buckling. The steel section is supported laterally by the concrete deck in displacement (rigidly) and in rotation (flexibly). While the compression parts buckles, the mode of buckling will be therefore distortional.

It should be also mentioned that the loss of stability over the internal support is usually combination of web buckling and LDB and it is hard to evaluate the participation of each.

2.1 Lateral distortional buckling

There has been no general analytical solution found for LDB. The most common way is to consider the compressed part of the section to be a continuously supported column and solve column buckling instead of distortional buckling using the beam-on-elastic-foundation method. This is usually called the method of continuous inverted U-frame and it will be described later.

LDB can appear in elastic or plastic state of the section. Elastic LDB precedes the yielding and affects the elastic bending capacity of the section, while inelastic LDB arises on the partially yielded section and affects its plastic bending capacity and rotational capacity. Plastic bending capacity cannot be employed in case of deep bridge girder sections in hogging bending regions, so the inelastic LDB is considered neither.

2.2 General approach

The computation of lateral buckling effects is in general similar to evaluating the effect of column buckling or local buckling. First the ideal beam is considered and the critical moment corresponding to the point of bifurcation is determined. Certain approaches can be used that are to be discussed later, or nowadays finite element method is often used for this purpose. Then the real structure with geometrical and material imperfection has to be taken into account and buckling resistance is determined using buckling factor χ_{LT} to reduce bending resistance. For this purpose buckling curves for column buckling are usually used.

3 DETERMINATION OF THE CRITICAL MOMENT

There has been remarkable research for determining the critical moment for continuous composite girders using either LTB or LDB approach. In general the critical moment is a function of geometrical properties of the steel section and the concrete deck, span of the girder and moment gradient and stiffness and positioning of the braces and stiffeners if present. In this chapter different procedures are described from simple U-frame to more complicated models including stiffeners and distortion.

3.1 Continuous inverted U-frame

As mentioned above the U-frame method solves generally column buckling of the compressive part of the section (mostly just compressive flange) instead of lateral buckling of the whole section. This 'column' is continuously supported by the web. The total stiffness of the support α_t is a combination of stiffness of the web, the web-flange joint, the flange-deck connection and the concrete deck.

The easiest but most inaccurate way to compute the critical moment is to determine critical force for compressed 'column' according to Bradford[2] from the equation

$$N_{cr} = \frac{\pi^2 E_a I_f}{L^2} + \frac{\alpha_t L^2}{\pi^2} \tag{1}$$

where E_a is the modulus of elasticity,
I_f is the second moment of area of the compressive flange,
L is span and
α_t is stiffness of continuous support.

The minimum of the critical force is found by putting $dN_{cr}/dL = 0$:

$$(N_{cr})_{\min} = 2\sqrt{E_a I_f \alpha_t} \tag{2}$$

and the critical moment is found from the section equilibrium conditions.

The expression more preferred and directly giving critical moment is according to Johnson[3]

$$M_{cr} = \frac{k_c C_4}{L}\sqrt{\left(GI_{at} + \frac{k_s L^2}{\pi^2}\right)E_a I_{fz}} \tag{3}$$

where k_c is the factor of geometry of the composite section,
C_4 is the constant depending on the moment diagram,
GI_{at} is Saint-Venant torsional stiffness
k_s is the rotational stiffness of the composite deck and steel web and
E_aI_{fz} is the bending stiffness of the compressive flange to the vertical axis.

This formula is a modification of that for LTB critical moment and is based on the U-frame model too though not so obviously. But the benefit of Saint-Venant torsional stiffness is included.

3.2 Consideration of stiffeners and braces

Web stiffeners and transversal braces are always used in the case of bridge girder, therefore they are important to be included in calculations. The main criteria concerning lateral buckling is their stiffness that can be expressed for instance as dimensionless stiffness α

$$\alpha = \frac{K_b L_u}{N_{cr,u}} \tag{4}$$

where K_b is stiffness of single stiffener,
L_u is their distance and
$N_{cr,u}$ is the critical load for a 'column' of the cross-section identical with the compressive flange and the critical length equal to L_u.

According to Johnson and Caffola[4] stiffeners with $\alpha \leq 2$ are flexible, and their stiffness should be 'smeared' over the length. The stiffeners with $\alpha > 2$ are rigid, and they should be treated as rigid supports. To the first group mostly web stiffeners are counted, to the second group lateral restrains such as H-frames, trusses and diaphragms.

Considering this division the early mentioned formulae for the U-frame can be modified and used. But the complex procedure according to Collin, Möller and Johansson[5] based on U-frame model and stiffeners study is more likely to use for this purpose. This method is specially developed for continuous composite bridge girders and it gives quite precise results. The 'column' section constitutes of compressive flange and adjacent 1/3 of the compressive part of the web and is simply supported over a span equal to the distance of transversal braces. The column is continuously supported by the stiffness of the web and the web stiffeners if present (Figure 3).

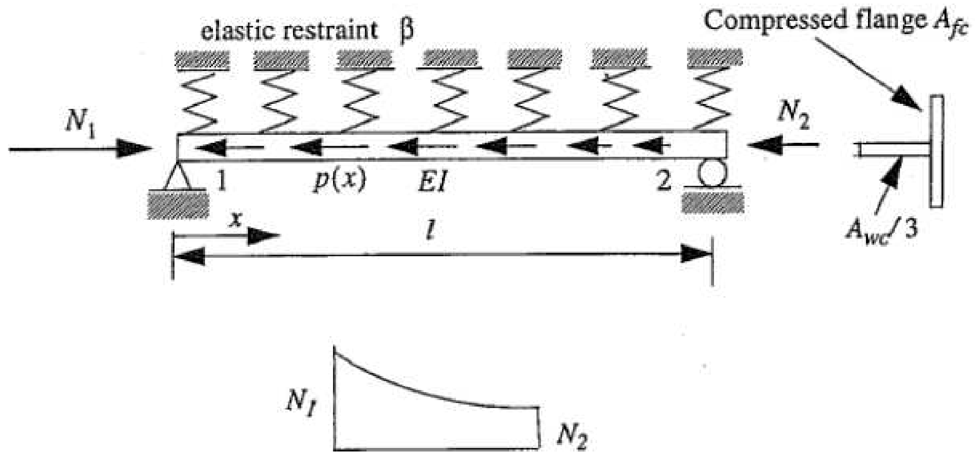

Figure 3: Scheme of analyzed segment according to Collin et. al.[5]

The formula for 'column' critical force is following

$$N_{1,cr} = \frac{\overline{m}_{cr} \pi^2 EI}{l^2} \tag{5}$$

where EI is the bending stiffness of the 'column'.

$\overline{m}_{cr}$ is a modifying factor including influence of continuous support and moment gradient and converting the problem to simply supported column buckling with the length

$$l_c = \frac{l}{\sqrt{\overline{m}_{cr}}} \tag{6}$$

Buckling in one or two half-waves on the length l_c is considered with two different formulae to calculate $\overline{m}_{cr}$. $\overline{m}_{cr}$ is a function of three parameters dependent on the stiffness of continuous support and moment and shear force gradients. The buckling slenderness λ is then ordinary expressed as

$$\lambda = \sqrt{\frac{N_{pl}}{N_{1,cr}}} = 1{,}1 \frac{l}{b_f \sqrt{\overline{m}_{cr}}} \sqrt{\frac{f_y}{E}} \sqrt{1 + \frac{A_{wc}}{3A_{fc}}} \tag{7}$$

where A_{fc}+$A_{wc}/3$ is the area of 'column' and b_f is the width of the flange.

3.3 Consideration of distortion

As was shown all practical procedures for calculation of lateral buckling critical moment for continuous composite girders are based on the column and lateral torsional buckling. However a few studies have appeared recently to deal with distortion. Vrcelj and Bradford[6] showed that LDB of composite girders depends besides the moment gradient on three parameters; torsional support α, beam parameter K and distortional parameter γ (introduced by them):

$$\alpha = \frac{k_z}{\pi^2 GI_t / L^2} \tag{8}$$

$$K = \sqrt{\frac{\pi^2 EI_w}{GI_t L^2}} \tag{9}$$

$$\gamma = \frac{t_w^3 L^2}{6(1-\nu)I_t h_w} \tag{10}$$

where k_z is torsional stiffness (corresponding k_s in Eq. 3),
L is span,
G is the shear modulus
I_t is torsional moment of area,
EI_w is warping stiffness of the steel part of the beam
t_w, h_w are geometrical characteristics of the web and
ν is the Poisson's constant for steel.

Most recently analytical formulae for LDB of non-composite doubly symmetric I-girders loaded by constant bending moment were founded by Kalkan and Buyukkaragoz[7]. In this case distortional buckling appears due to the remarkable slenderness of the web, and the expression for critical moment is similar to those for LTB (compare with Eq. 3):

$$M_{cr,LDB} = \frac{C\pi}{L}\sqrt{EI_z GI_{te}(1+W^2)}\text{, where } W = \frac{\pi}{L}\sqrt{\frac{EI_{we}}{GI_{te}}} \tag{11}$$

where C is a constant depending on the moment diagram,
EI_z is bending stiffness to the weaker section axis,
GI_{te} is effective torsional stiffness and
EI_{we} is effective warping stiffness.

The effective characteristics were observed for doubly symmetric I-section as

$$GI_{te} = \frac{t_f^4}{\frac{3}{4}\frac{1}{(b_f/2t_f)} + \frac{\pi^2(1-\nu^2)}{E}\left(\frac{d}{t_w}\right)\left(\frac{t_f}{t_w}\right)^2 \frac{1}{(L/t_f)^2}} \tag{12}$$

$$EI_{we} = \frac{EI_w}{1+\frac{1}{12}\left(\frac{d}{t_w}\right)\frac{1}{(L/t_w)}\left[\left(\frac{t_f}{t_w}\right)^3 + \frac{GI_{tf}}{GI_{tw}}\right]} \tag{13}$$

where b_f, t_f are dimensions of the flanges,
d, t_w are dimensions of the web,
E, ν are well known material characteristics for steel,
GI_{tf}, GI_{tw} are torsional stiffnesses of flange and web respectively and
EI_w is standard warping stiffness of the section.

The torsional and warping stiffness reduces more with increasing slenderness of web, increasing ratio between thickness of flange and web (t_f/t_w) and increasing ratio of torsional stiffness of flange and web. That means in general non-composite I-girders tend more likely to distortion when they have stockier flanges and slender webs. Whereas composite girders distort necessarily while buckling and extremely slender webs tend in this case more likely to local buckling. The future usage of these expressions for composite girders is therefore still questionable.

4 DETERMINATION OF THE BUCKLING MOMENT

The beam is suffering buckling moment when the load reaches its maximum in term of stability. This moment corresponds to ultimate bending capacity. Buckling moment is determined from ultimate bending capacity (plastic or elastic) using buckling factor χ_{LT}:

$$M_{b,Rk} = \chi_{LT} M_{Rk} \tag{14}$$

For slender bridge I-girders M_{Rk} is almost always elastic ($M_{el,Rk}$). The buckling factor is usually determined with respect to buckling curves and the value of slenderness $\bar{\lambda}_{LT}$. These buckling curves were based on experimental research (mostly on column buckling) and they are supposed to cover possible geometrical and material imperfections of section. The procedure is similar to calculating column buckling for simplification, but on the other hand it is very conservative.

Possible solution was suggested by Greiner and Taras[8] in 2010. They started from formulae in Eurocode[9] for computation of χ_{LT}

$$\chi_{LT} = \frac{1}{\phi + \sqrt{\phi^2 - \beta\lambda_{LT}^2}} \leq 1, \text{ where } \phi = \frac{1}{2}\left(1 + \alpha\left(\bar{\lambda}_{LT} - \bar{\lambda}_0\right) + \beta\bar{\lambda}_{LT}^2\right) \tag{15}$$

where $\beta = 1{,}0$ while $\bar{\lambda}_0 = 0{,}2$; or $\beta = 0{,}75$ while $\bar{\lambda}_0 = 0{,}4$. With these two cases corresponds different values for α too. Both possibilities are according to their FE analysis conservative. Based on that analysis more accurate procedure was developed respecting the fact buckling curves correspond to column buckling. The imperfections (middle part of the formula for ϕ) are related to the slenderness for weak axis bending λ_z. That corresponds to the assumption for column buckling. To get the consistence for lateral buckling, the multiplication by $(\lambda_{LT}/\lambda_z)^2$ is introduced. The final formula for welded I section exposed to LTB was derived as

$$\chi_{LT} = \frac{1}{\phi + \sqrt{\phi^2 - \lambda_{LT}^2}} \leq 1, \text{ where } \phi = \frac{1}{2}\left(1 + \left(\frac{\bar{\lambda}_{LT}}{\bar{\lambda}_z}\right)^2 \alpha_{LT}\left(\bar{\lambda}_z - 0{,}2\right) + \bar{\lambda}_{LT}^2\right) \tag{16}$$

where $\alpha_{LT} = 0{,}21\beta_{LT} \leq 0{,}64$ and $\beta_{LT} = \sqrt{W_{y,el} / W_{z,el}}$. This procedure was developed for LTB, but it might be used after little changes even for LDB of composite girders.

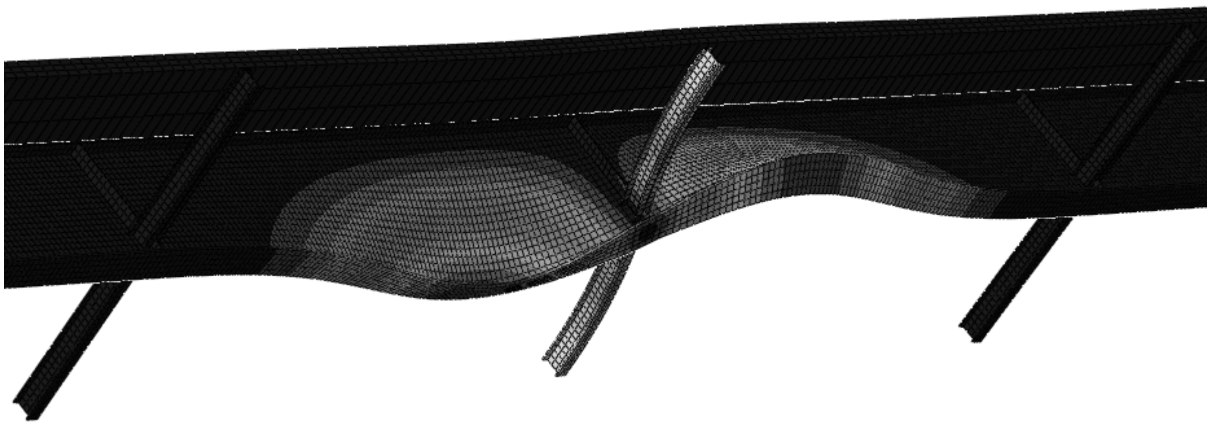

Figure 5: The first lateral buckling eigenmode

The other matter is to find the place, where lateral buckling is most likely to happen. Because there is the support exactly in the point of the maximal hogging bending moment buckling in this place is ruled out. According to Collin et. al.[5] the buckling of the lower flange takes place most likely between 0,2 to 0,3 of the distance between the support and first cross beam and they present a solution how to find it. It is based on equation for buckling of a column with unequal end forces:

$$\frac{N_R(\zeta)}{A} + \frac{N_{1R}}{W}\left(1 - \frac{N_{0R}}{N_p}\right)\left(1 - \frac{N_{0R}}{N_{0,cr}}\right)\frac{Wf_y}{N_{0R}}\frac{\sin\left(\frac{\pi x}{l_c}\right)}{\left(1 - \frac{N_{1R}}{N_{1,cr}}\right)} = f_y \tag{17}$$

where $N_{0,R}$, $N_{0,cr}$ are the buckling and critical force respectively for uniform axial force loading

A, W	are area and section modulus for the 'column' (see chap. 3.2)
$N_{1,R}$, $N_{1,cr}$	are the buckling and critical force respectively for non-uniform axial force loading, where $N_{1,R} = \chi_1 N_p$ and for $N_{1,cr}$ see Eq. 5,
$\zeta = x/l$	is observed from the Fig. 3,
l_c	is span of the 'column' (Eq. 6)
N_p	is the axial resistance of the section and
$N_R(\zeta)$	is the force in particular distance from the support when buckling load is applied.

Using this method buckling factor and buckling moment in several distances from the support can be calculated and minimal value of χ_1 can be found. The buckling moment is then compared with the moment acting in that particular section.

5 FINTE ELEMENT PARAMETRICAL STUDY

At the moment parametrical study is being developed by the first author of this paper for lateral buckling investigation of continuous composite bridge girder. The task is to model the behavior of inverted U-frame loaded uniformly and to evaluate thus the possibility of U-frame formation in the real structure.

5.1 The preliminary study

The research started with simpler model in Abaqus of one I beam connected to a concrete deck. The girder is continuous over three spans 40+60+40 m. Lateral braces are provided in 10 m distances. Web stiffeners are provided in variable distances and in some variants even not present. The depth of the web is mainly 2000 mm, and width of the flanges is mainly 500 mm, other dimensions are generally variable.

The models are submitted for buckling analysis. Eigenvalues and eigenmodes are obtained and critical moment is evaluated from the eigenvalue corresponding to the first lateral buckling eigenmode. Found eigenmodes are rescaled and used as imperfections for Riks analysis where the buckling moment is observed corresponding to the structural collapse.

While using uniformly distributed load difficulties for buckling analysis appears because of stress concentration over the support. The first several eigenmodes correspond usually to the web buckling, even though the web stiffeners are designed precisely according to Höglund[10]. The eigenmodes for lateral buckling are then again disturbed by web buckling. Undisturbed eigenmodes were so far obtained for the web thickness of 100 mm (Figure 5).

The representative values from the preliminary study are not yet available and they will be presented at the conference.

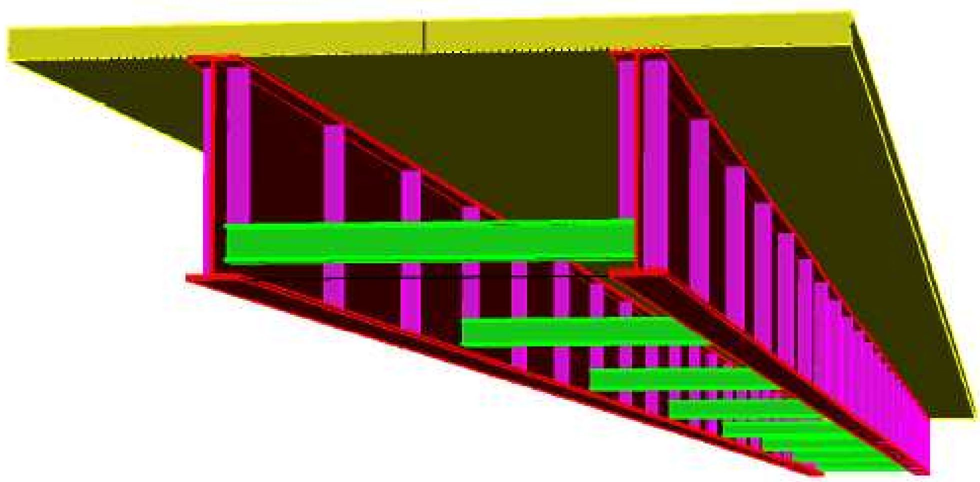

Figure 6: The finite element model scheme

5.2 The parametrical study

Based on results of the preliminary study a complex model of two I beams connected to a concrete deck (Figure 6) equipped with lateral braces and web stiffeners will be developed to observe behavior of the inverted U-frame and its components. The three-span bridge (with longer middle span) will suffer uniformly distributed load again and critical and buckling moment of the system will be observed.

The study will be performed with parameters:

- span of the girder
- depth of the I-section
- thickness of the concrete deck
- stiffness of stiffeners and braces and their distance

The critical moment and buckling moment values will be verified according to other studies and calculations according to early mentioned procedures.

6 CONCLUSIONS

The lateral buckling of continuous composite bridge girders is a field, where a lot of research is still required. The nowadays common used procedures have their certain limitations and in general are too conservative. The standard calculations for LTB cannot be used, because the section distorts during buckling. The inverted U-frame model is most commonly used to solve this phenomenon. Column buckling of continuously supported compressive part of the steel section is solved instead of lateral distortional buckling. There are more or less efficient ways to deal with the moment gradient but there are no practical procedures to deal with the distortion of the section.

The other tasks concerning lateral buckling of the web were mentioned. First the particular distance from the support where the buckling takes place has to be found. That was successfully solved for the U-frame method. Second the improvement using buckling curves developed for column buckling in case of lateral buckling has been recently achieved.

The finite element parametrical study for lateral buckling of continuous composite bridge girders is being developed started with the preliminary study. A model of two parallel I-beams connected to a concrete deck loaded uniformly will be subject for the study with earlier mentioned parameters. The transversal braces and web stiffeners will be present according to conventions in bridge design. On the base of this study the design procedure for lateral buckling will be improved. The results from the preliminary study will be presented at the conference.

REFERENCES

[1] Z.A. Vlasov, *Thin-walled elastic beams*, Gos. Izdat. Fiz.-Mat. Liter., Moscow, USSR (1959) (in Czech translation).

[2] D.J. Ohlers, M.A. Bradford, *Elementary behaviour of composite steel & concrete structural members*, Butterworth-Heinemann, Oxford, UK (1999).

[3] R.P. Johnson, *Composite Structures of Steel and Concrete*, Blackwell Publishing, Oxford, UK (2004).

[4] R.P. Johnson, J. Cafolla, *Stiffness and strength of lateral restraints of compressed flanges*, J. Constr. Steel Research,Vol. 42, No.23, pp. 73-93 (1997)

[5] P. Collin, M. Möller, B. Johansson, *Lateral-torsional buckling of continuous bridge girders*, J. Constr. Steel Research, Vol. 45, No. 2, pp. 217-235 (1998).

[6] Z. Vrcelj, M.A. Bradford, *Elastic distortional buckling of continuously restrained I-section beam-columns*, J. Constr. Steel Research, Vol. 62 No. 3, pp. 223-230 (2006).

[7] I. Kalkan, A. Buyukkaragoz, *A numerical and analytical study on distortional buckling of doubly-symmetric steel I-beams*, J. Constr. Steel Research, Vol. 70, No. 1, pp. 289-297 (2012).

[8] R. Greiner, A. Taras, *New design curves for LT- and TF-buckling consistent derivation and code-formulation*, Proceedings of International Symposium “Steel Structures:Culture & Sustainability 2010”, Paper No. 102, Istanbul, Turkey (2010).

[9] *EN 1993-1-1 Eurocode 3:Design of steel structures – Part 1-1: General rules and rules for buildings,* CEN, Brussels, Belgium (2005).

[10] T. Höglund, *Shear buckling resistance of steel and aluminium plate girders*, Thin-Walled Structures, Vol. 29, No. 1-4, pp. 13-30 (1997).

APPLICATION OF FRP COMPOSITES FOR DECKS OF TEMPORARY BRIDGES

Pavel Ryjáček* **and Martin Vovesný†**

*CTU in Prague, Faculty of Civil Engineering,
Thákurova 7, 166 29 Praha 6
e-mail: pavel.ryjacek@fsv.cvut.cz

Keywords: FRP, glass fibers, bridge deck, retrofitting

Abstract. *The FRP (Fibre Reinforced Polymers) are modern materials that have a number of advantages for the application for bridge structures, such as durability, low weight and high strength. The low weight leads to the significant increase of the load capacity of the existing bridges, where the FRP is applied. FRP materials consist of the matrix (epoxy or polyester resin) and fibres (usually glass, aramid or carbon). The FRP materials made from glass fibres and polyester resin (GFRP) were recently used in Czech Republic for bridge deck in different structural forms. These applications and related research will be described in the paper.*

1 INTRODUCTION

The common bridge decks for standard bridge engineering applications are made from steel or concrete. FRP is a still very rare solution, limited to the specific cases and research activities. The reason can be found in the financial costs and the lack of practical design advices and codes. This paper describes two cases, where the FRP bridge deck was applied and found to be a suitable and progressive solution. In both cases, the extensive research is hidden behind these applications.

2 RETROFFITTING AN OLD WWII BAILEY BRIDGE

After the World War II, the US army has built many temporary bridges in Czech Republic. In many cases, these structures remained in service until today. Unfortunately, the corrosion and the low durability of the timber deck lead to the need of their constant refurbishment.

The small village of Čtyřkoly, located south from Prague, has to take care of an old bailey bridge, which was built after the WWII, see Fig. 1. The costs for permanent repair of timber deck were a significant problem for the municipal budget. Finally, the deterioration of the deck led to the bridge closure in 2012. This caused the need of searching a new, long lasting bridge deck system with minimal needs for maintenance. The bridge including the deck had to carry the load up to 3,5t.

The three possibilities were analyzed during the design process. The oak deep impregnated timber deck, steel gratings deck and GFRP gratings deck. The costs for all three solutions were quite comparable in the range 42 – 73,- Euro/m2, see Table 1. Comparing the initial costs, the GFRP deck was slightly more expensive than other two systems. However, considering the long term costs, the GFRP panels were the most suitable solution, with the excellent durability, almost

† CTU in Prague, Faculty of Civil Engineering

no maintenance and a low noise impact on the inhabitants. Although the design load on the bridge is relatively small (traffic allowed for vehicles up to 3,5 t weight), the load capacity of the GFRP is much higher and does not limit the capacity of the structure.

Type of deck	Material	Cost per m2 (Euro)
Steel gratings, mesh size 33x33, bearing rod 40/3	Steel	42,-
GFRP gratings, mesh size 30x30, height 38mm	GFRP	73,-
Oak timber impregnated deck	Timber, D30	62,-

Table 1: Cost comparison of different solutions

Together with the deck refurbishment, the new painting was done on the steel cross beams and stringers. Unfortunately, budget did not allowed to repair painting on the main superstructure.

Figure 1: The heavily damaged timber deck on the closed bridge

Figure 2: The retrofitted bridge deck after completing – September 2012

The behavior of the deck is being watched during the service in periodic intervals. The current state of GFRP is very good, no damages and no impacts of the environment were observed, see fig. 2. It can be concluded, that GFRP can be cost effective solution not only for big projects, but also for small villages with very limited budget.

3 THE GFRP BRIDGE DECK PANEL FOR TEMPORARY BRIDGE

3.1 The initial phase

The temporary bridges in Czech Republic mainly consist of the TMS system, which is similar to the Bailey bridge. The strategic resources of Czech Republic store approximately 4 km of these bridge structures and serve during floods, natural disasters and bridge reconstructions. Unfortunately, the existing timber deck is not a suitable and durable solution and suffers from fast deterioration process. Therefore, the new concept of GFRP panel was proposed and is today in the final stage of the development.

Bridge deck panel was designed and fabricated by the manual joining of I-beams with top and bottom hand laminated plates. The design axle load is 300 kN. The cross section of deck panel and its dimensions are show on figure 3. The panel is made from polyester resin and e-glass fibres.

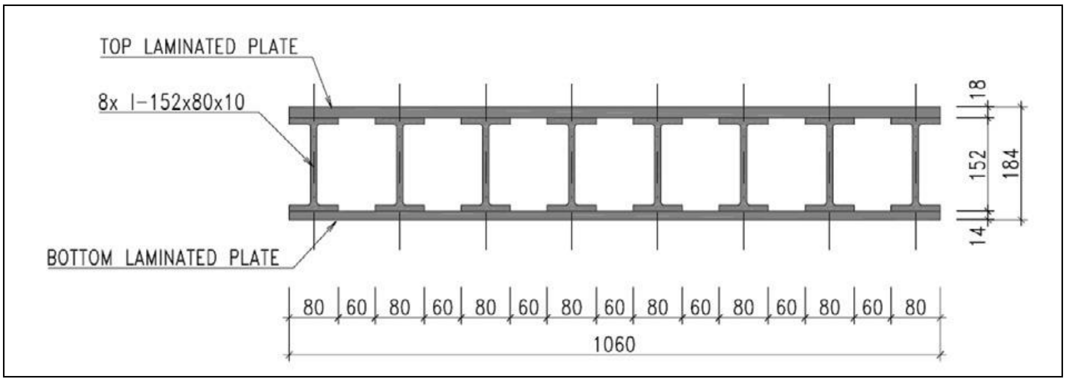

Figure 3: The cross section of the GFRP initial panel

The initial phase consisted in the development, numerical analysis and verification of the main load-bearing system. The experimental verification was done to evaluate the material parameters in orthogonal system directions and materials, bending test of the panel, load test in pure compression (simulation of the wheel over the support) and basic fatigue testing. The bending tests from this phase are shown on figure 4. Main results are given in the paper[1].

Figure 4: The load tests in the initial phase, different load positions

3.2 The prototype development

The initial phase was followed by the finalization of the panel for the real application. That included the system of fastening, drainage and inspection openings, horizontal restrain system to transfer brake forces and protection of the panel against water and dirt accumulation.

Based on the experimental results, the panel was optimized in order to minimize the financial cost. That was done by reduction of the upper (18 to 14 mm) and bottom (14 to 10 mm) laminated layer. The cross section of final prototype is shown on figure 5.

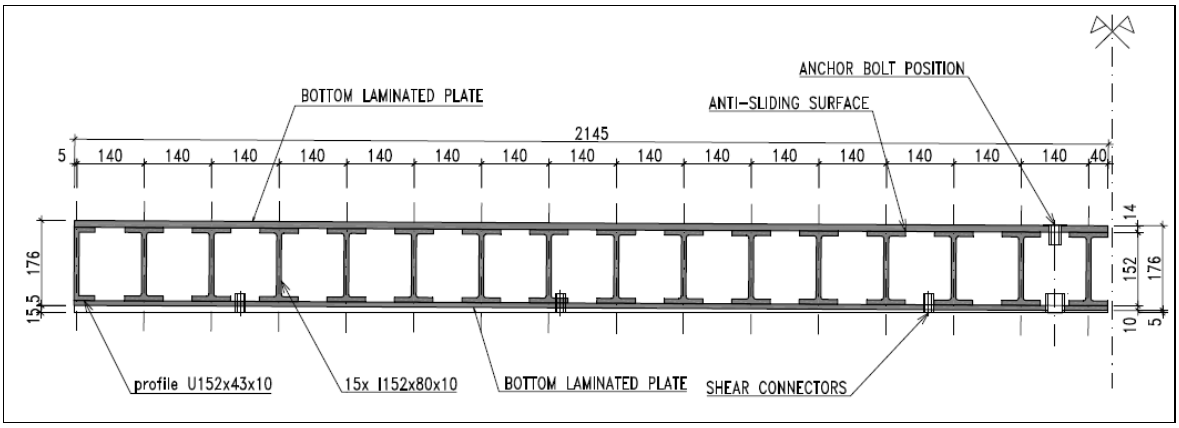

Figure 5: The cross section of the GFRP panel prototype

The prototype was fabricated and tested in the laboratory. Three different load cases were used for the verification. Their position and meaning is described in table 2.

Load case	Load position	Test load (kN)
Case 1	Mid-span, at the panel edge	283
Case 2	At the support – maximal shear effect	283
Case 3	Mid-span, inside of the panel, tested till the complete failure	283 - 400

Table 2: Experiment load cases

Totally 10 strain gauges LY41 20/120 were used to measure the strain on the top (2) and bottom (8) surface, see Fig. 6. The deflection was measured with inductive displacement transducer HBM WA 50 mm, see Fig. 7 is the panel mid-span and in the corners. The load was applied through the steel plate with dimensions 400 x 400 mm with hydraulic jack of the capacity 500 kN. The applied load was measured with force gauge CSP–M–60t–C3. Data were collected in HBM Spider 8 and HBM Quantum data acquisition system on 5Hz frequency.

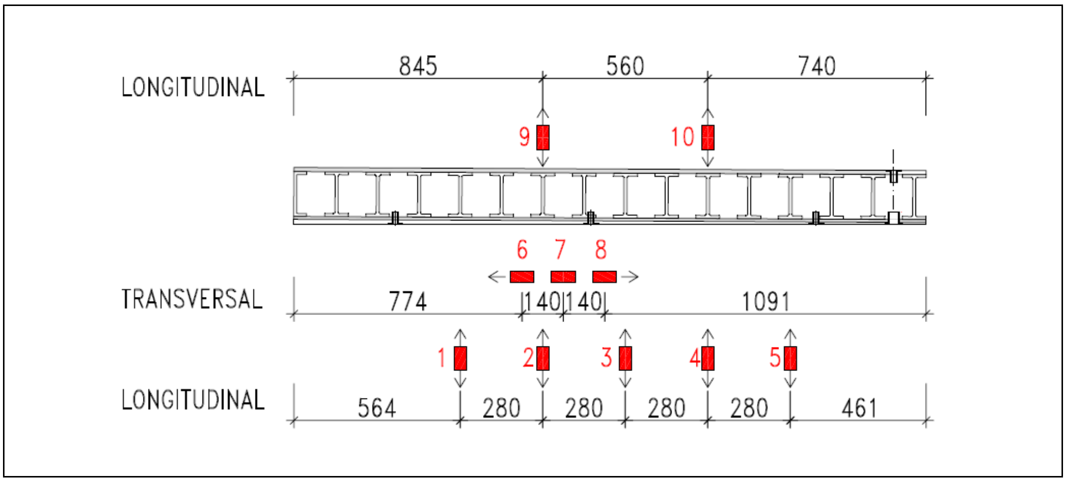

Figure 6: The position of strain gauges on the top and bottom side

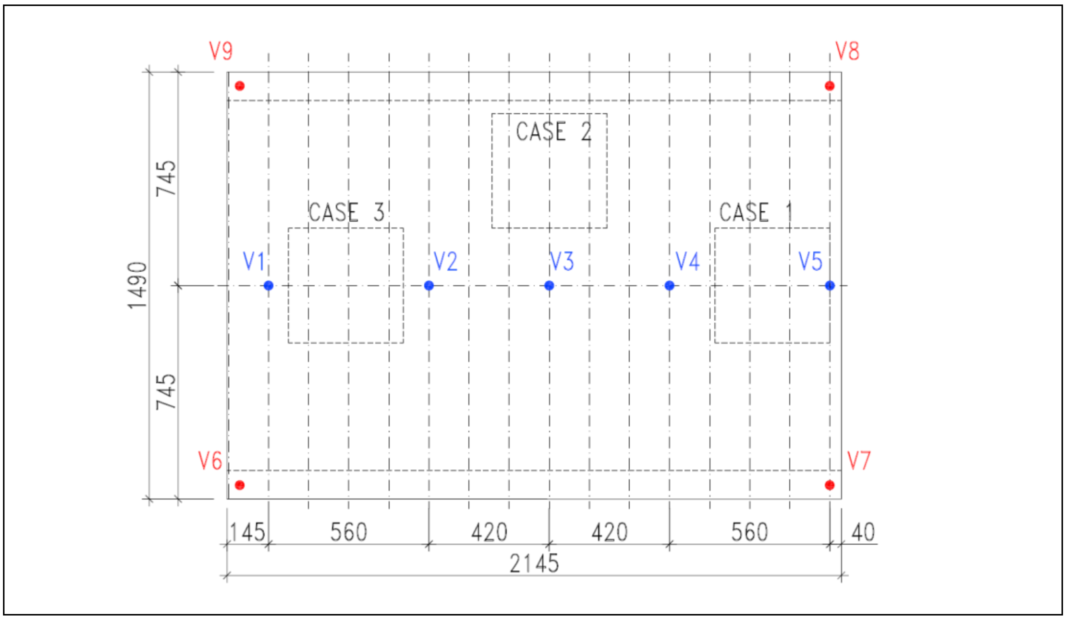

Figure 7: The position of deflection meters and load cases

Figure 8: The GFRP panel prototype during the load test – case 1 (left) and case 3 (right)

The load test is shown on figure 8. Panel was placed on the rubber strips to achieve the uniform support system.

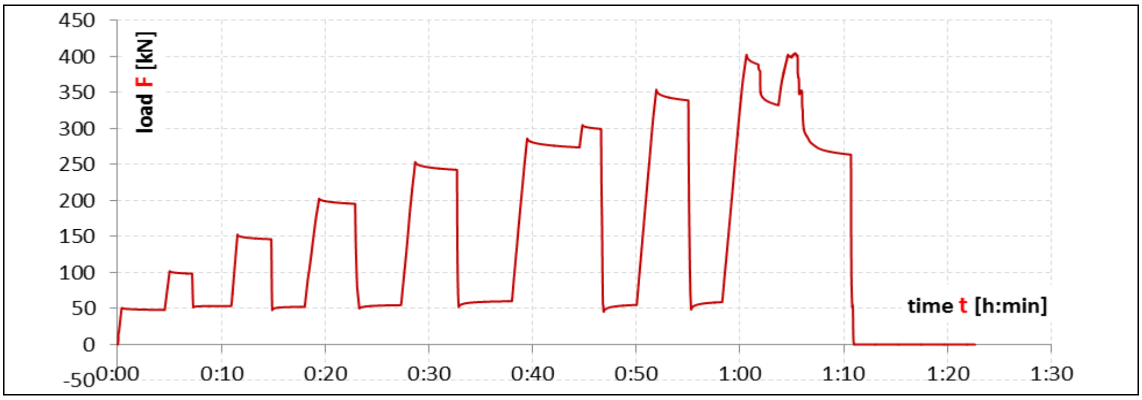

Figure 9: The system of the load application – case 3

The panel was loaded with the initial force of 50 kN. Then the load was periodically applied steps of 100, 150, 200, 250 and 283 kN. The case 3 was the loaded till the global failure, see Fig. 11. The main results are shown on Fig. 10 and 11. The figures show, that the behavior in the loading phase is mostly linear, until the limiting load was achieved. Then the permanent deflection persists. An interesting fact is that the unloading phase is not the same as the loading phase; the material memory effect can be observed. However, after unloading the strain is returned to the initial state.

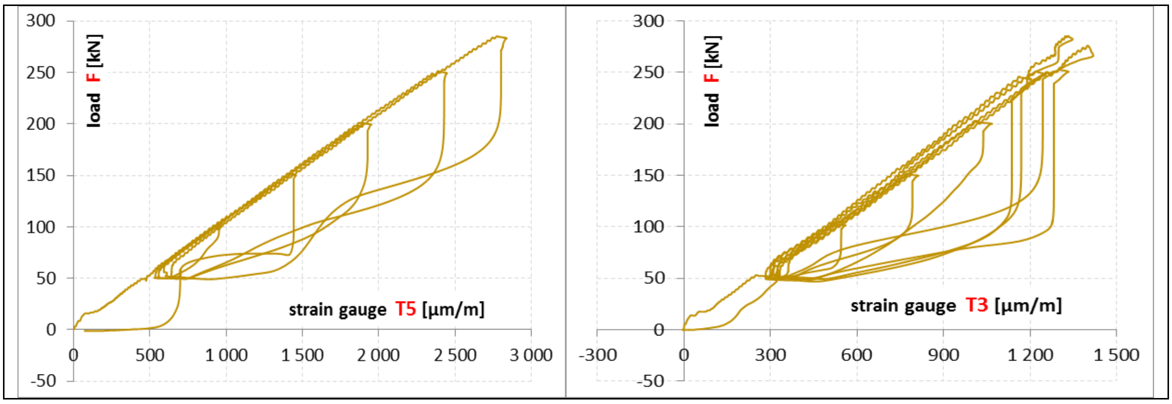

Figure 10: The relation between the load and the strain in most loaded strain gauge for case 1 (left) and case 2 (right)

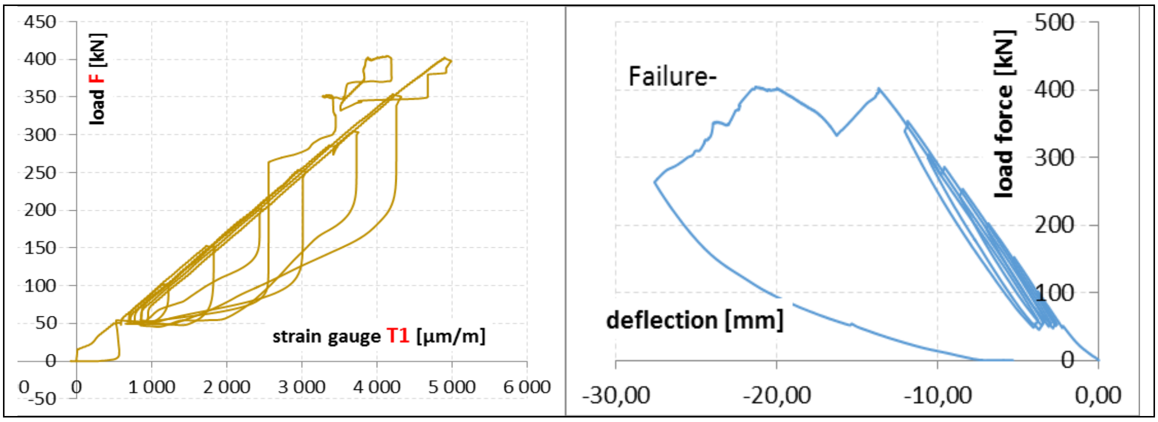

Figure 11: The relation between the load and the strain (left) or deflection (right) till the failure – case 3

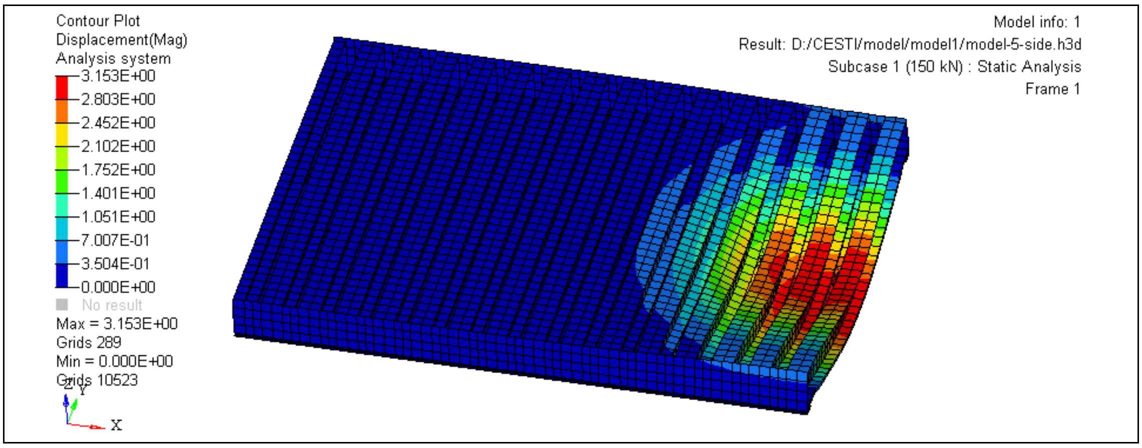

Figure 12: The numerical analysis of the GFRP panel, vertical displacement

The test load at the failure moment is much higher than the expected load (generally 12t for the axle). The load test will be followed by the comparison of the numerical models and fabrication of the testing series that will be applied on the real bridge structure and tested during the real traffic load.

4 CONCLUSIONS

Above mentioned applications show that there is an interesting and important potential in GFRP materials, especially if used on older bridges, where the higher cost of GFRP is balanced by their low weight, which leads to the significant increase in the load capacity and extending their life time. As the deck is the most extremely loaded bridge element, which is exposed to the environmental impact, the great care should be taken to the GFRP long-term behavior.

Research reported in this paper was supported by Competence Centres program of Technology Agency of the Czech Republic (TA CR), project Centre for Effective and Sustainable Transport Infrastructure (no. TE01020168)

REFERENCES

[1] Vovesný, M., Rotter, T.: *GFRP Bridge Deck Panel, Procedia Engineering*, Vol. 40, 2012, Pages 492-497, ISSN 1877-7058

12th International Conference on
Steel, Space and Composite Structures
28-30 May 2014, Prague, Czech Republic

IN-SITU TESTING OF RAILWAY BRIDGE INTERACTION WITH CONTINUOUSLY WELDED RAIL

Pavel Ryjáček[*], Vojtěch Stančík[*], Miroslav Vokáč[†] and Pavel Očadlík[‡]

[*]CTU in Prague, Faculty of Civil Engineering,
Thákurova 7, 166 29 Praha 6
e-mail: <pavel.ryjacek@fsv.cvut.cz>

Keywords: CWR, rail-bridge interaction

Abstract. *The continuous welded rail (CWR) is standardly used on almost all modern railway bridges. However, it's placement results in the interaction between CWR and the structure. That brings not only the longitudinal forces on the substructure, but also a significant additional stresses in the rail. These stresses can result either to the rail break, or track buckling. Unfortunately, the input parameters for performing numerical analysis are hardly accessible and they vary significantly in different sources. This paper describes the experimental verification of commonly used design parameters involving the R/B interaction. The main goal of this paper is to offer results of the extensive measurement that was carried out on the bridge near the city Děčín, which should contribute to a better understanding of this problem and of its numerical modelling.*

1 INTRODUCTION

The continuously welded rail (CWR) is nowadays generally used on almost all modern railway tracks and bridges. This type of rail replaced the formerly used jointed rail, which contributed to greater passenger comfort during the travels, clearing the permanent train bumping. The CWR also significantly decreased the dynamic influences on both the bridge structure and the vehicle due to removing the vibrations coming from crossing the rail joints. It empowered the possibility to design and build high speed railway tracks as well. However the CWR interacts with the bridge structure, which may result in remarkable stress increase in the rail. This fact means that the bridge-track interaction shouldn't be by the structural analysis neglected.

The forementioned additional stress is caused by the temperature change of the bridge and the rail, by the bending of the structure and by longitudinal forces coming from braking and acceleration. Especially the temperature change is very important for the examination of the rail mechanical behavior. Drop of temperature means increase of tensile stress in the rail, rise of temperature on the other hand increases the compressive stress in the rail. When the limit state is achieved, these loadings may result either in the rail break or in its buckling.

The track-bridge interaction also brings additional horizontal forces that negatively influence the substructure or the bearing dimensions. Designing the substructure members, especially the piers, is often very economically inconvenient, considering the values of horizontal forces according to valid codes. Simultaneously the bridge designers hardly obtain other scientific data that would be sufficient for the economical and reliable design. The input parameters needed for

† Czech Technical University in Prague, Klokner Institute
‡ VPÚ DECO PRAHA, a.s.

performing proper numerical analysis of the interaction also vary significantly. There are therefore many reasons to perform further research in this area of interest.

1.1 Track – bridge interaction

Small recapitulation of the bridge – rail interaction problem is offered in this subchapter. The longitudinal forces in the rail rise due to the rail-bridge coupling. This effect can be described with the longitudinal restoring force, which is defined as the ratio of longitudinal normal force change in the rail, compared with the distance change, in which this force change occurs. The amplitude of the longitudinal restoring force depends on the track – bridge relative displacement, on whether the track is loaded or unloaded, or on the bridge deck type.

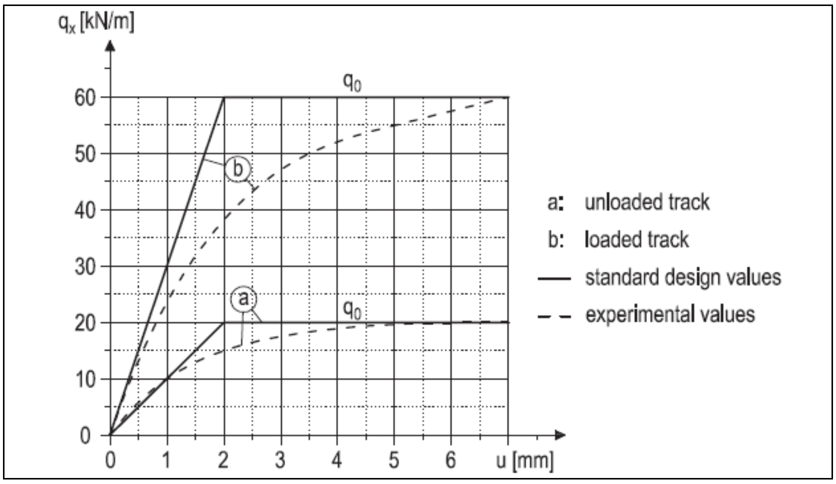

Figure 1: The nonlinear stiffness law[1]

The nonlinear stiffness law is shown in Figure 1, where the vertical axis describes the amplitude of the longitudinal resistance *q* [kN/m] and the horizontal axis describes the relative displacement *u* [mm]. The coupling deformation is limited to critical value of u_0, that means the linear elastic relation between the longitudinal resistance and the relative displacement lies below this limit value. The angle of the curve indicates the bond distributed stiffness *c* [kN/m2]. When the relative displacement reaches the limit value u_0, it means the longitudinal restoring force doesn't grow anymore, however it remains constant with the value of q_0. The graph on Fig.1 also displays how the ballasted track reacts to the loading, for the sudden change of ballast stiffness contributes to significant growth of longitudinal resistance. This fact is valid with small differences for rigid tracks too. The track resistance to longitudinal force is therefore affected by both the stiffness of the ballast and the fastening rigidity. However there are some other attributes, that have impact on the interaction, like the ballast vertical stiffness, the loading resulting from horizontally curved tracks, the additional force in bearing reducing the thermal expansion coefficient of the bridge to an effective value, the temperature variability due to the non-uniform temperature change and thermal permanency, the substructure rigidity or the placing of expansion devices and expansion joints. The interaction analysis that is currently performed by the European codes[2] consists of linear summation of the particular load cases including effects of the temperature, bridge bending, braking and nosing and comes from older UIC 774-3 code[3]. The analysis should respect the load history, for the conservative summation gives reliable results, which may be on the other hand much greater than the true results coming from proper nonlinear analysis[4].

This paper however concentrates on experimental verification of commonly used design parameters involving the R/B interaction. The main goal of this paper is to offer results of the extensive measurement that was carried out on the bridge near the city Děčín, which should contribute to a better understanding of this problem and of its modeling.

2 BRIDGE PARAMETERS

For the intention of developing the maximal loading in the rail it was chosen the available bridge of maximal span with lowest possible bending stiffness and without any rail expansion devices. As said before, the testing proceeded on the single-line railway bridge that is located on the track Děčín – Jedlová near the city of Děčín. This steel truss bridge of total length 151 m consists of three simple spans supported by massive stone piers and on either side of the last pier is being followed by the stone arch viaducts. The bridge deck is steel orthotropic and it transfers the ballasted track with clearance of 5 m across the river. The supporting structure of the tested bridge varies in each span. The outer spans 10 and 12 are Warren truss bridges with no vertical members, except in the portal, and no upper bracing. The middle span is a trussed arch with upper crossbracing. The bridge parameters are presented in Figure 2.

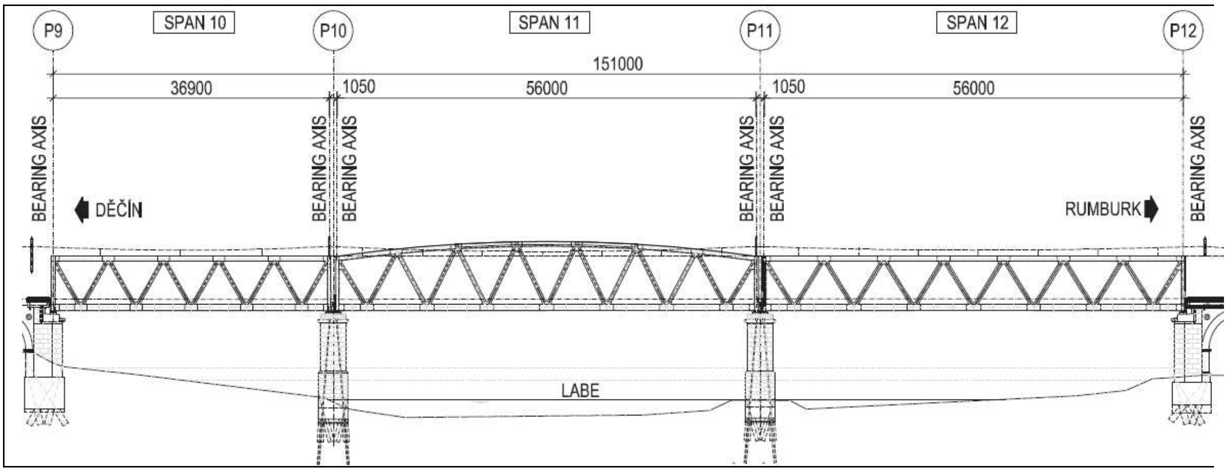

Figure 2: Bridge elevation

The main supporting structure of each span is placed on spherical bearings. The bridges and its sliding bearings are orientated identically accordingly to the thermal expansion movement. This layout is presented in Figure 3.

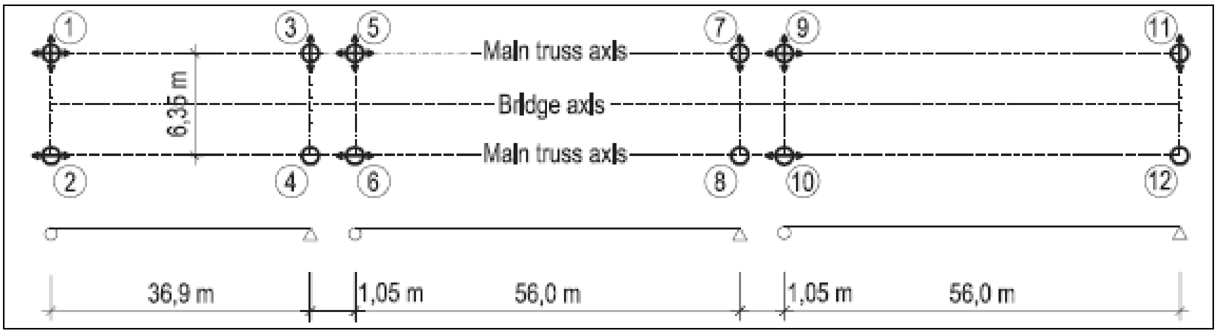

Figure 3: Bearings layout

3 EXPERIMENT

The testing of the track-bridge interaction was performed during the common static load test. Advantage of this procedure rests in lowering costs related with operating and renting the vehicles that were used as loading burdens. The main objectives of the experiment were the examination of the track resistance to longitudinal forces, the determination of maximal stress amplitudes during the loading in selected sections of the bridge and the longitudinal stress progression. Further analysis also presumes determination of the vertical stiffness from the measured experimental data. In ideal case the experiment should have registered the influence of the temperature change on the preceding parameters. For getting experimental data sufficient for the consequent evaluation was first necessary to specify the loading burdens and load cases, which would lead to the maximal rail strain.

3.1 Loading description

The loading burdens with enough electivity for the static load test were determined to be two heavy cranes EDK 750. For the following test of the track/bridge interaction was needed one more burden, which was determined to be the locomotive HV 749 The longitudinal location of the vehicles during the particular load cases was established on a preliminary 2D FEM model using the nonlinear analysis. This model also assumed various recommended values of longitudinal restoring force and limit relative displacement applied to different locations of the burdens on the bridge, which gave results helpful for the subsequent model equivalency verification.

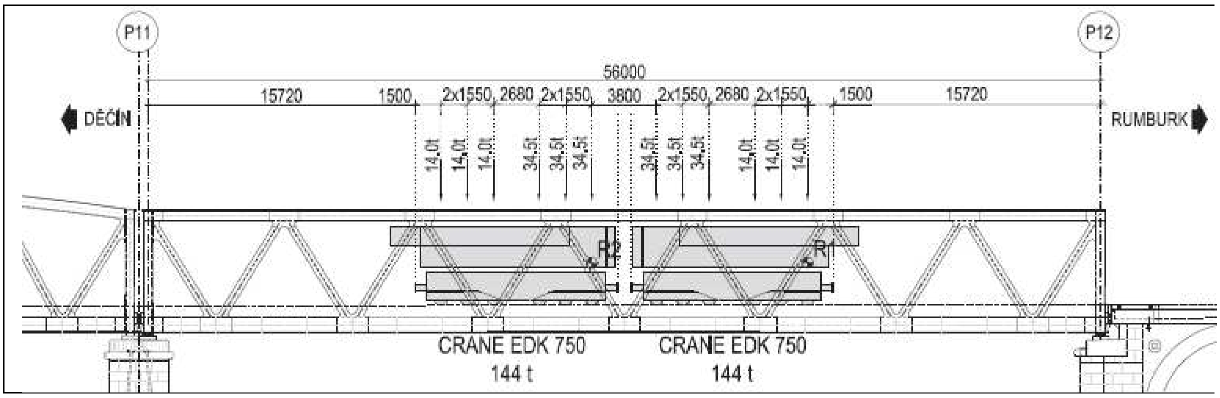

Figure 4: Load case 1

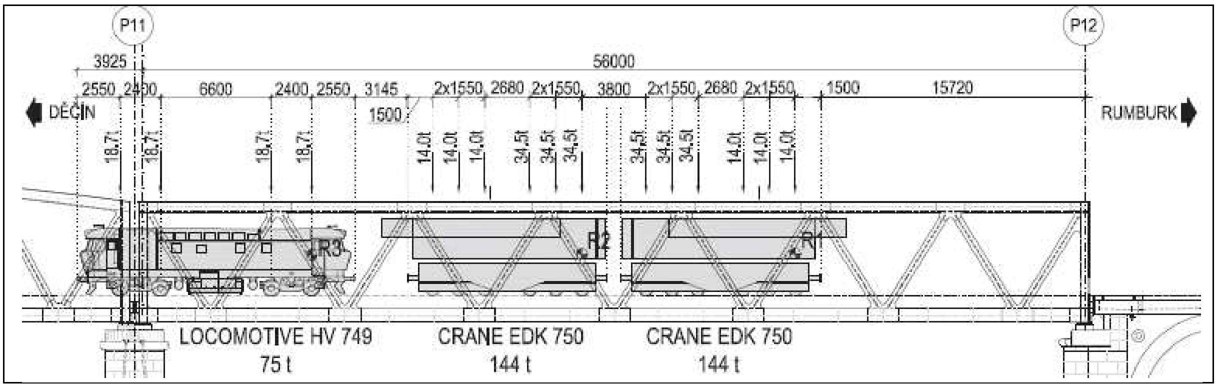

Figure 5: Load case 2

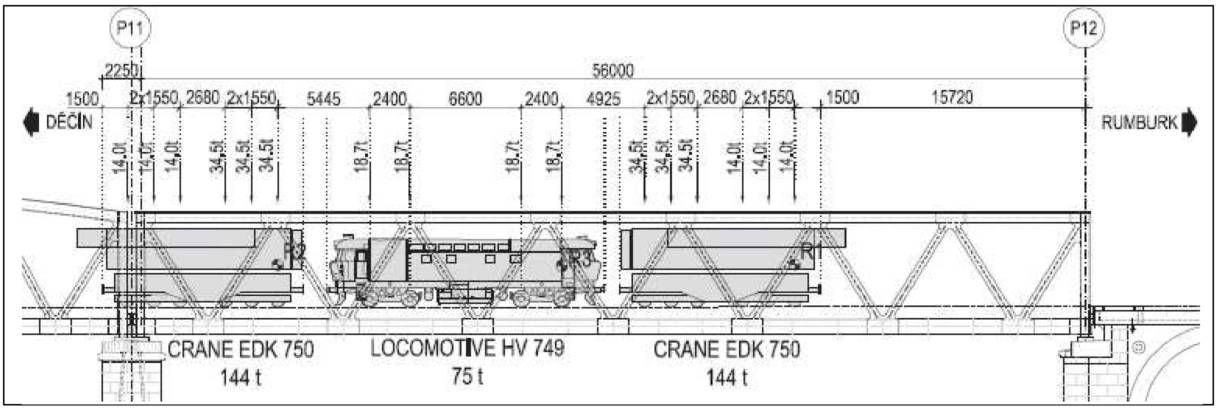

Figure 6: Load case 3

The load cases on the other hand proposed different goals. The load case 1 was designed to determine the coupling interface parameters while unloaded track. Remaining two load cases were meant to observe the change of these parameters using different levels of loaded track. The burdens and their location in particular load cases are presented in Figure 4, 5 and 6.

3.2 Measurement

Most of the measurements were carried out in the span 12 or on the involved piers, only some supplemental measurements took place in span 11 or behind the pier 12, see Figure 7. The experiment was carried out by the employees of CTU in Prague, Klokner Institute. During the testing there were observed the undermentioned parameters:

1. The rail and the bridge temperature
2. Rail straining
3. Bridge/rail relative displacement
4. Bearing displacement and rotation

The rail stress level was measured using the strain gauges 1-LY11-10/120 from the manufacturer HBM. They were placed in the rail gravity centre in order to eliminate the effects of its vertical bending. In the necessary bridge sections there were employed on both rails. The strain gauges connected in the half-bridge circuit allowed to measure strain change by the lengthwise located gauge and the lateral compensative gauge, which guaranteed the ability to obtain the stress change data coming from uniform temperature change, for the rail expands by the uniform temperature change in both directions, which is therefore registered by both the active and the compensative gauge and it results in the zero signal according to null stress level in the rail. In case of the CWR the longitudinal deformation is not allowed, that's why the longitudinal strain can't be measured. Still the rail stress can be observed, for the compensative gauge registers the vertical deformation, which leads to determination of the longitudinal mechanical stress change. However this procedure has to consider the generalized Hooke's law which brings the Poisson's ratio into count. By the conversion of the electrical signal to the mechanical it has been respected the gauges' constants, set by the manufacturer and the influence of the resistance grow in the long line wires.

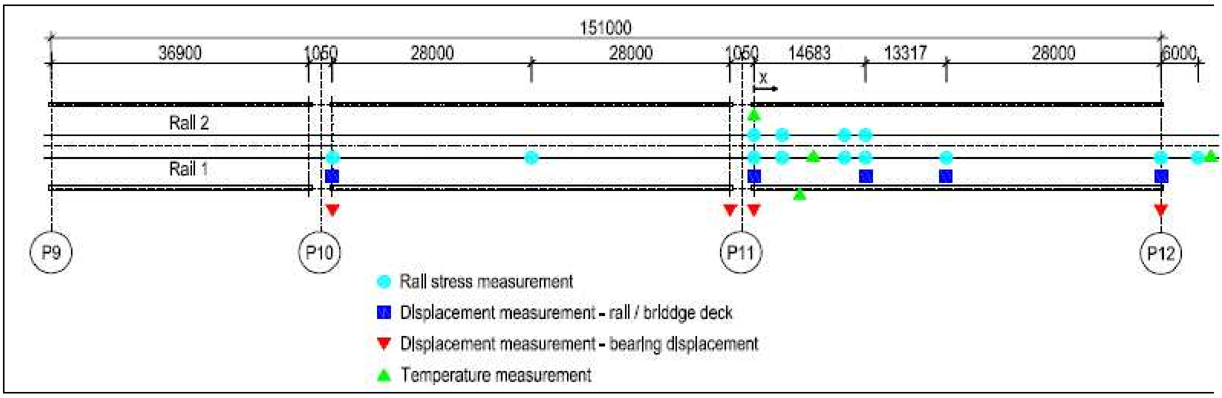

Figure 7: Gauge placement scheme

The temperatures were measured on the selected spots in the structure using the resistance thermometers Ni1000. Temperature change on the deck was measured with the gauge fastened to the bottom side of the orthotropic slab. Other thermometer was situated on the main truss diagonal near the pier P11 and another two were measuring the rail temperature fastened to the rail base. One was used for the rail on the bridge and the second one for the rail behind pier P12. The bearing displacement and the R/B relative displacement were measured with the potentiometric gauges. Bearing rotation was measured by the inclinometers. All the data were gathered by the 4 data loggers that saved the results every 2 minutes. The gauge arrangement scheme displays Fig.5. The longitudinal situation of any gauge in the following graphs in chapter 4 are described with the local coordinate x related to the sliding bearing on pier P11.

So as to be taken care of the correct understanding of the sequential results the time schedule of the whole experiment is shown in Table 1.

Time	Description
03:30 – 03:50	Static load test – span 10
04:15 – 04:45	Static load test – span 11
05:00 – 05:25	Static load test – span 12 – simultaneously LC1 for R/B interaction test
07:05 – 08:50	LC2 for R/B interaction test
09:25 – 09:34	LC3 for R/B interaction test
09:34 – 09:48	LC3 for R/B interaction test – EDK 750 departure
10:00	End of experiment

Table 1: Time schedule of the R/B interaction test

The experiment has meant to observe the influence of the temperature change on the R/B interaction attributes as well. It was expected a temperature rise on the dawn of the day but unfortunately it didn't reach the values of sufficient significance.

4 RESULTS

Gathered experimental data are related to the zero values, which were established when the test started. This means the obtained strain values cannot be considered as total values appearing in the rails, for there isn't known the temperature change contribution to rail straining state. This can only be discovered with the strain gauges being placed before the CWR anchoring or with the additional calculation knowing the exact CWR installation temperature. However the total stress isn't needed for purposes of this experiment, for the studied attributes can be derived from stress amplitudes, which are gained during the load cases. Knowing the longitudinal stress progression and the stress amplitude it can be easily determined the stress longitudinal progression related just with the partial load cases, so as to be confronted with the numerically obtained data. First goal of the evaluation is therefore determination of the stress amplitudes and stress longitudinal progression.

4.1 Rail stress in particular load cases

The stress is evaluated directly from each strain gauge with simple multiplication with the Young modulus. The undermentioned graphs in Figures 8, 9 and 10 showing stress amplitudes refer to the most compressive strained gauge, which location is described with the earlier defined local coordinate x. The graph referring to LC3 includes the tensile strained gauge too. The other graphs present the longitudinal stress progression in the time of reaching the stress amplitude because of its importance for validating the numerical data.

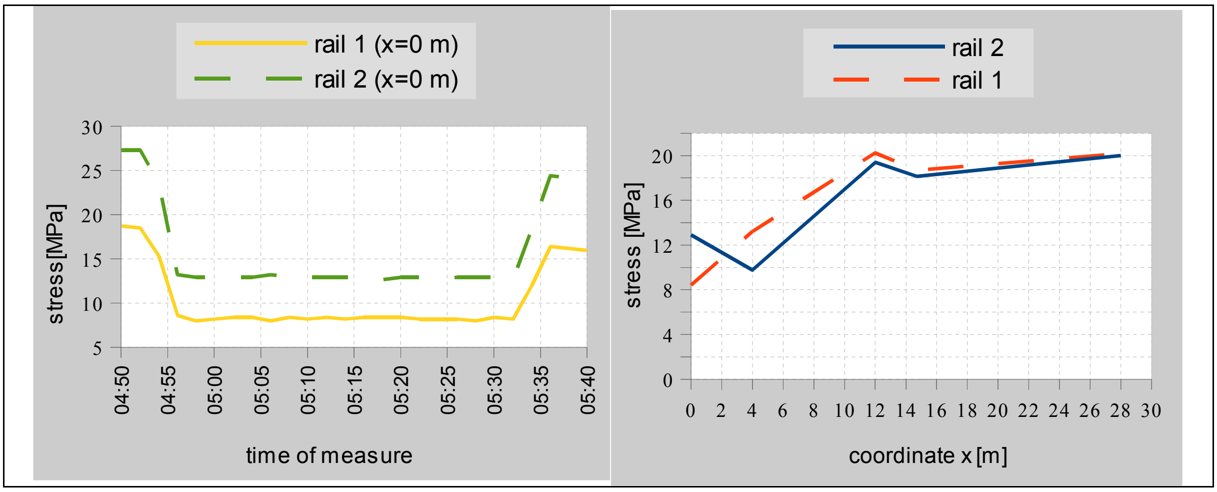

Figure 8: Load case 1 - amplitude of stress (left) and stress progression (right)

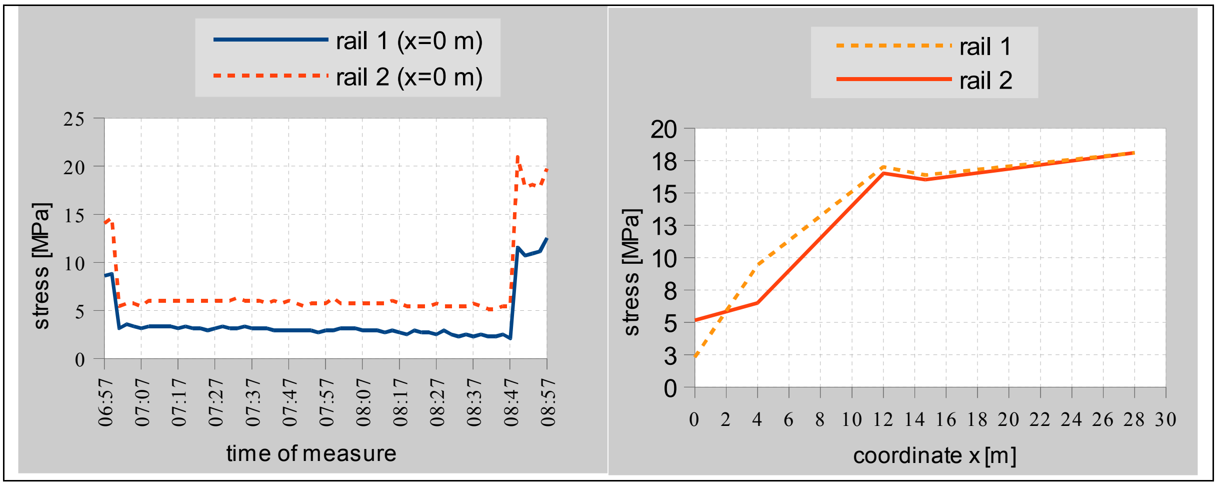

Figure 9: Load case 2 - amplitude of stress (left) and stress progression (right)

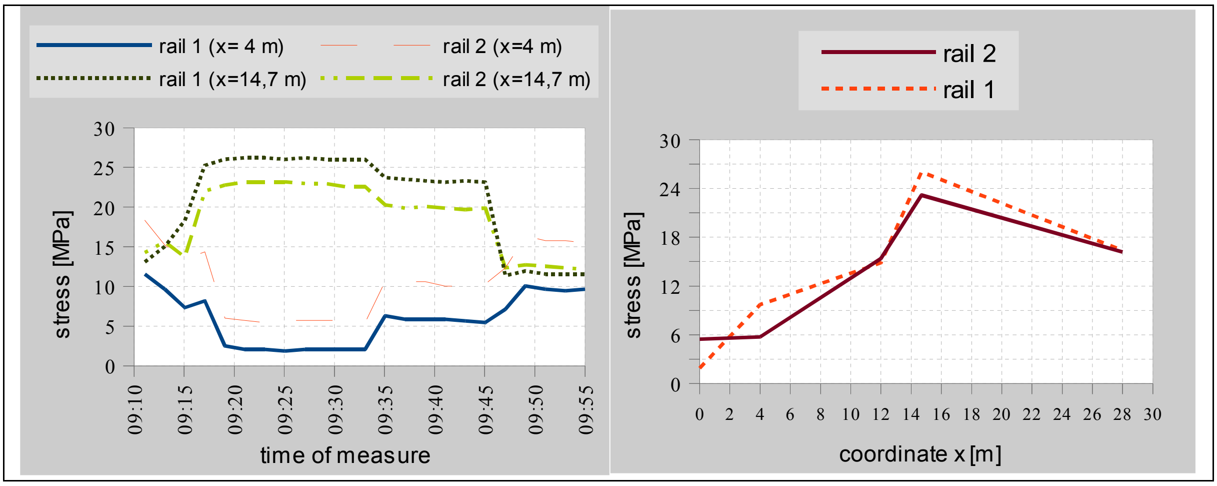

Figure 10: Load case 2 - amplitude of stress (left) and stress progression (right)

In LC1 the stress amplitudes in both rails are 13 MPa (rail 1) respectively 10 MPa (rail 2) which gives a total amplitude 23 MPa of compressive stress. The same way we can obtain values of total amplitudes in LC2 and LC3, which are determined to be 20 MPa for LC2 and 17 MPa for LC3. All these mentioned numbers refer to the strain gauge situated above the sliding bearing located on pier P11. One interesting finding from the longitudinal stress progression is the fact that there is some difference between the stresses appearing in both the rails. This stress difference will be therefore studied later in following subchapter. After evaluating the stress data from the gauges the evaluation can continue with the determination of the longitudinal restoring force.

4.2 Rail stress in particular load cases

The longitudinal restoring force is calculated as the ratio of normal force change and the related distance, where these two forces are determined. This force reaches different values for the loaded and unloaded track, as has been cleared in previous chapters and its values differs lengthwise the bridge accordingly to the reached R/B relative displacement. This means that the maximal obtained values of the longitudinal track to bridge resistance are referring to certain intervals on in the tested span. Though these intervals can be easily presumed thanks to the graphs of longitudinal stress progression in chapter 4.2, for the highest level of longitudinal resistance refers to the steepest interval that can be found in the mentioned particular graphs. The obtained maximal values of the longitudinal restoring force related to the testing time are presented on the graph below. Limit values were reached above the pier 11 for the LC1 and LC2 x=(0;4) m. In case of LC3 the limit value is being reached in the interval x=(12;14,67) m.

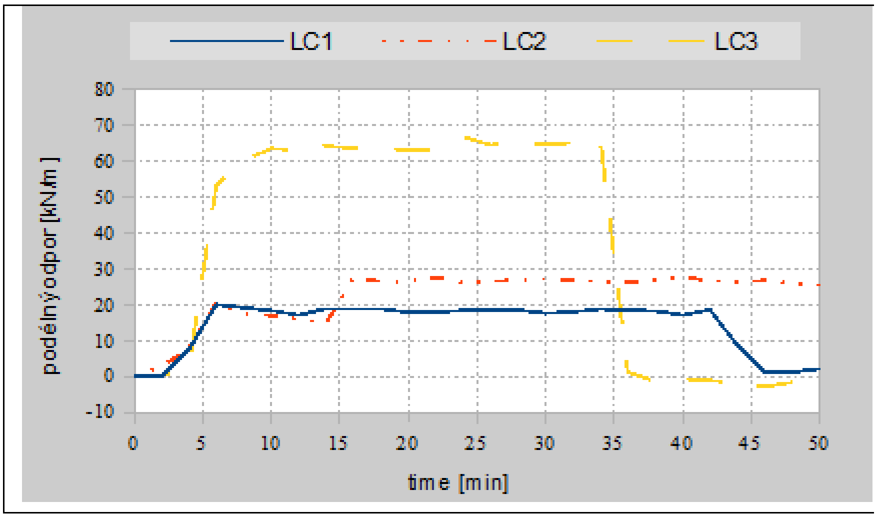

Figure 11: Longitudinal restoring force

4.3 Stress difference in both rails

For there has been indicated an evident difference in the straining of both rails, this problem was verified using the frequency of occurrence analysis. The graph shows the frequency of occurrence of stress difference amplitudes and in what gauges are these amplitudes reached. It has to be mentioned that the frequencies of occurrence were observed for the whole time of testing and it therefore fits the total time in which the related stress amplitudes are reached.

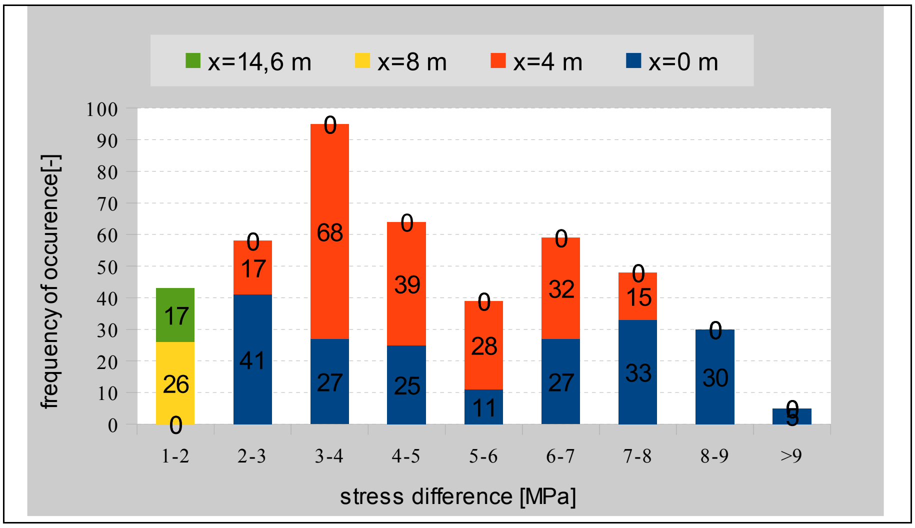

Figure 12: Stress difference between both rails

The graphs indicate that there is a significant difference in the stress state of both rails during the testing. The difference commonly reaches the values between 6 and 10 MPa, however these corresponds with the unloaded track. For the loaded track the stress difference is lowering as can be seen on previous graphs in chapter 4.1, which means this phenomenon is probably related with the non-uniform ballast stiffness that is equalizing under load.

4.4 Stress in time

The graph of stress progression in time is included for information only. It shows the local stress amplitudes depending on time and the influence of temperature change, which is almost constant and wasn't of any significance for this experiment. For better understanding of the progression see the experiment time schedule introduced in chapter 3.2. There are shown the three most strained gauges during the testing.

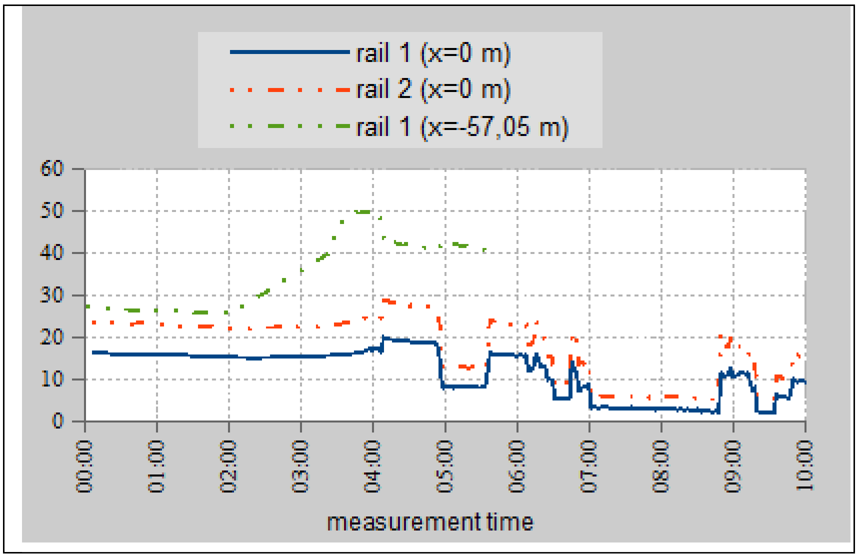

Figure 13: Stress progression [MPa] in time

5 CONCLUSIONS

The undermentioned conclusions are based on the results gained from the performed experiment and its confrontation with the preliminary 2D numerical model:

- The maximal stress amplitudes are situated above the sliding bearing (pier 12) in LC1, LC2 respectively in the distance of 14 m from the sliding bearing referring to LC3.
- During the evaluation there was indicated a stress level difference between both rails, which has normally reached values between 6 and 10 MPa in case of unloaded rail. However the difference in case of loaded track decreased significantly.

Research reported in this paper was supported by Competence Centres program of Technology Agency of the Czech Republic (TA CR), project Centre for Effective and Sustainable Transport Infrastructure (no. TE01020168)

REFERENCES

[1] Freystein, H., Geißler, K.: Interaktion Gleis/Brücke bei Stahlbrücken mit Beispielen. Stahlbau 82, Heft 2, 2013, Ernst & Sohn. p. 78 – 86.
[2] ČSN EN 1991-2 (73 6203) Eurokód 1: Zatížení konstrukcí - Část 2: Zatížení mostu dopravou. Praha: Český normalizační institut, 2005. 152 s
[3] UIC code 774-3 R, 2nd edition, 11/2001, Track/bridge interaction. Recomendations for calculations. UIC, 2001
[4] Ruge, P., Birk, C.: *Longitudinal forces in continuously welded rails on bridgedecks due to nonlinear track–bridge interaction*. Computers and Structures 85, p. 458–475, 2007

12th International Conference on
Steel, Space and Composite Structures
28-30 May 2014, Prague, Czech Republic

COMPONENT BASED FINITE ELEMENT MODEL OF STRUCTURAL CONNECTIONS

Lubomír Šabatka*, František Wald, Jaromír Kabeláč***, Lukáš Gödrich** and Jaroslav Navrátil***

*IDEA RS s.r.o.
U Vodárny 3032/2a, 616 00 Brno, Czech Republic
e-mail: sabatka@idea-rs.com, webpage: www.idea-rs.com

Keywords: Steel structures, structural connections, finite element model, component model, analytical model, design model

Abstract. *This paper refers to component based finite element model (CBFEM). Design focussed component model (CM) is compared to design finite element (DFEM) and research finite elements models (RSFEM). Procedure for composition of a model based on usual production process is used in CBFEM. Method is demonstrated on two types of connections. CBFEM results are compared to results obtained by component method for portal frame eaves moment connection. Design of moment resistant column base is demonstrated for a case loaded by two directional bending moments and normal force.*

1 COMPONENT AND FINITE ELEMENT MODELS OF CONNECTIONS

Component model of connections builds up on standard procedures of evaluation of internal forces in connections and their checking. Zoetemeijer [1] was the first who equipped this model with prediction of stiffness and deformation capacity. The elastic stiffness was improved in the work of Steenhius, see [2]. Basic description of components behaviour in major structural steel connections was used by Jaspart for beam to column connections [3] and by Wald for column bases [4]. The model was generalised by da Silva [5]. Method implemented in the current European structural standard for steel and composite connections, see [6] and [7], can be applied in majority of software for structural steel used in Europe. Procedure starts with decomposition of a joint to components, see Fig. 1, followed by their description in terms of normal/shear force deformation behaviour. After that, components are grouped to examine joint moment-rotational behaviour and classification/ representation in a spring/shear model and application in global analyses. The components in Fig. 1 represent: 1 – column web in shear, 2 – column web in compression, 3 – beam flange and web in compression, 4 - column flange in bending, 5 – bolts in tension, 6 – end plate in bending and 7 – column web in tension. Advantage of the component model is integration of current experimental and analytical knowledge of connections components behaviour (bolts, welds and plates). This provides very accurate prediction of behaviour in elastic and ultimate level of loading. Verification of the model is possible using simplified calculation. Disadvantage of component model is that experimental evaluation of internal forces distribution can be done only for limited number of joint configurations. In In temporary scientific papers, description of atypical components is either not present or has low validity and description of background materials. Models of hollow section connections are described

**Czech Technical University in Prague

***Hypatia Solutions s.r.o

in Ch. 7 of EN1993-1-8 [6] by curve fitting procedures; their compatibility with component model is unreliable. The CM´s are rather complex for hand calculation, resulting in a need to use of tools/design tables.

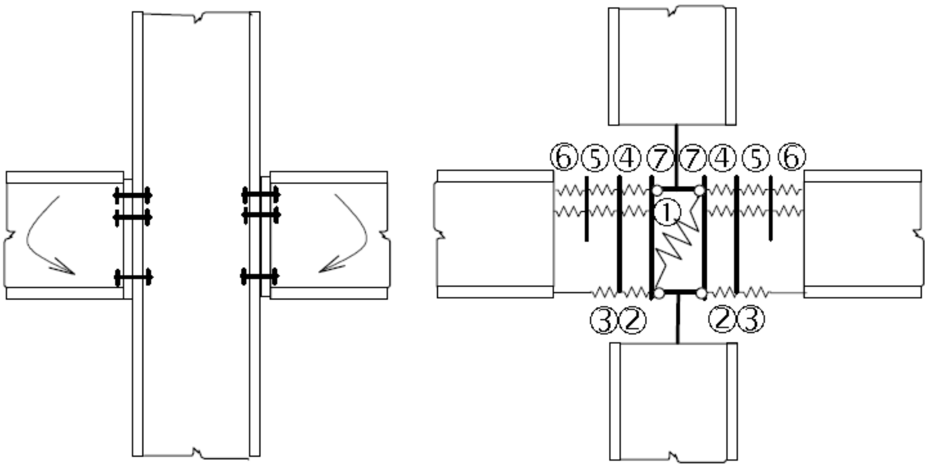

Figure 1: Component model of symmetrical beam to column connection with end plates

Finite element models (FEM) for connections are used from 70s of last century and they are research-oriented. Their ability to express real behavior of connections is making them a valid alternative to testing – standard and expensive source of knowledge of connection’s behavior. Native process of computer based design is validation and verification (VaV) of models, see [8]. Application of VaV to steel connections design is limited to a few published benchmark studies, see [9]. Comparison of VaV to different engineering application is still to be done [10]. Material model for RSFEM uses true strain stress-strain diagram, see Fig. 2. Design models DFEM uses design values of material properties. Strain is recommended to be limited to 5%, see cl. C.8(1) EN1993-1-5, [11]. Implementation of safety into advanced design models under ultimate limit state design is summarised in cl. C.9(2) EN1993-1-5 [11]. Standard procedure with partial safety factors for material/connections may be applied. More advanced and accurate solution, which takes into consideration the accuracy of model and material separately, gives more accurate and economical solution of structural connections.

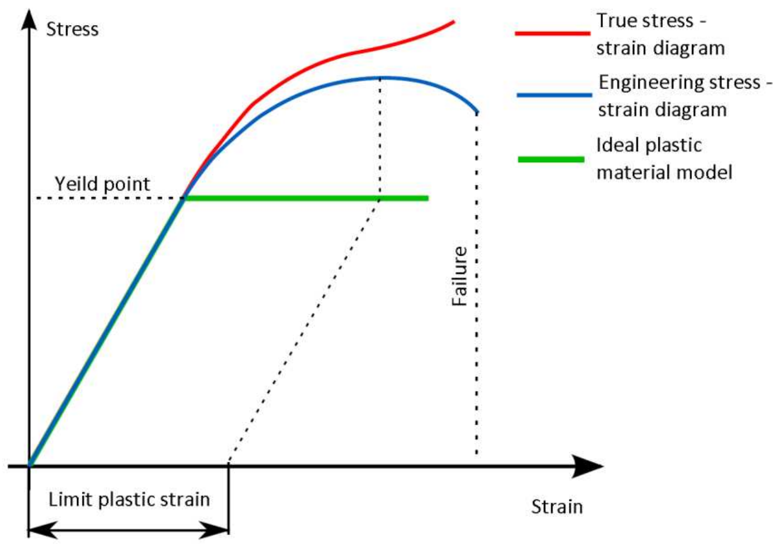

Figure 2: Material models of steel for research and design oriented methods

2 COMPOSITION OF CBFEM MODEL

First step in creating of the model is preparation of its geometry. Tailor made components were selected for CBFEM model, e.g. plate, bolt, weld, and stub of hot/cold formed cross section. Structural engineer creates the structural joint by applying manufacturing operations using these components, see Fig. 3. Meshing of the components is automatically done by software.

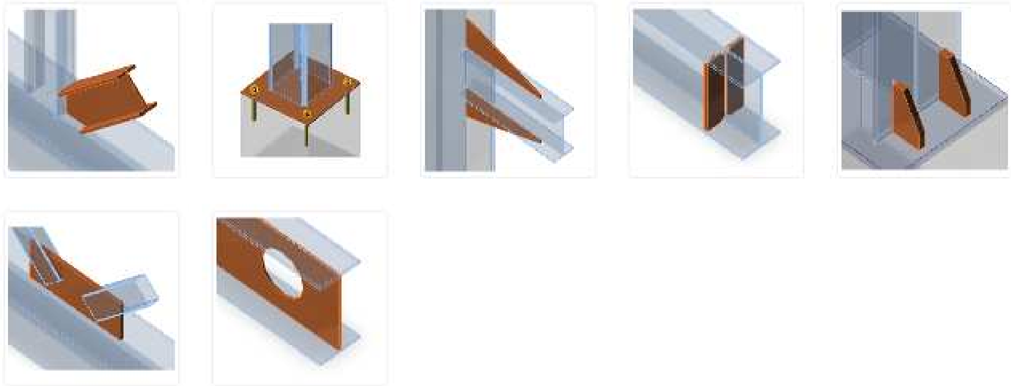

Figure 3: Manufacturing operations applicable to the structural joint

The plates connected by filled welds are modelled separately. They are connected by weld component only, which is characterised by weld in plane and out of plane tensile stiffness and resistance. The bolts are modelled as two fans of interpolation links with its tensile and shear trilinear stiffness and adequate resistance. Slender compressed plates are checked for local buckling. Possible post buckling behaviour of class 4 sections is introduced by effective stress of each compressed plate.

3 CASE STUDIES

3.1 Welded portal frame eaves moment connection

The CBFEM model of the portal frame eaves moment connection with parallel stiffeners was verified by the CM. Results show a good agreement between two models. After that, sensitivity study was performed. Beam IPE cross-section size is variable parameter shown on horizontal axis in the first case, see Fig. 4, and column HEA cross-section size is variable parameter in the second case, see Fig. 5. Column HEB 260 was considered in the first case and beam IPE 330 was considered in the second case. The resistance shown on vertical axis represents force couple of bending moment in plane M_y and vertical shear force V_z for which the ultimate limit state was reached. It is assumed, that bending moment and shear force values are equal. Resistance of the connection was governed by two components, column panel in shear and beam flange in compression. Comparison of critical component for both CBFEM and CM models was made. The same component was critical in both models for all parameters. Results of both models are very similar, differences in resistance are up to 7% and only in uncommon cases, e.g. column HEB 260, beam IPE 500. To cover the CBFEM model uncertainty, factor α_1 will be determined according to sensitivity studies [11].

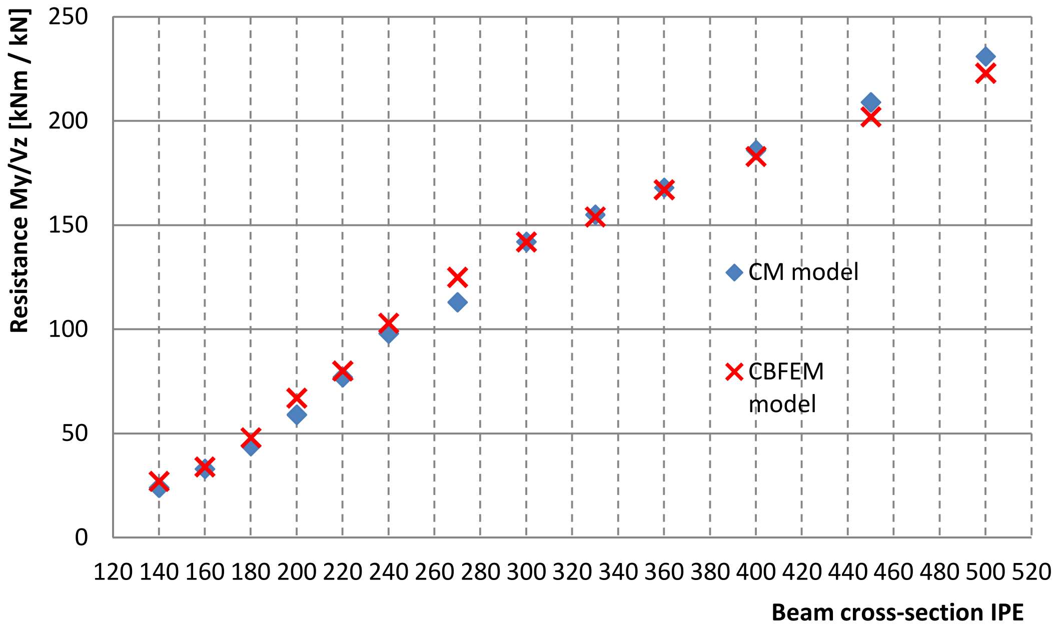

Figure 4: Sensitivity study, Column HEB 260, variable parameter is beam cross-section size

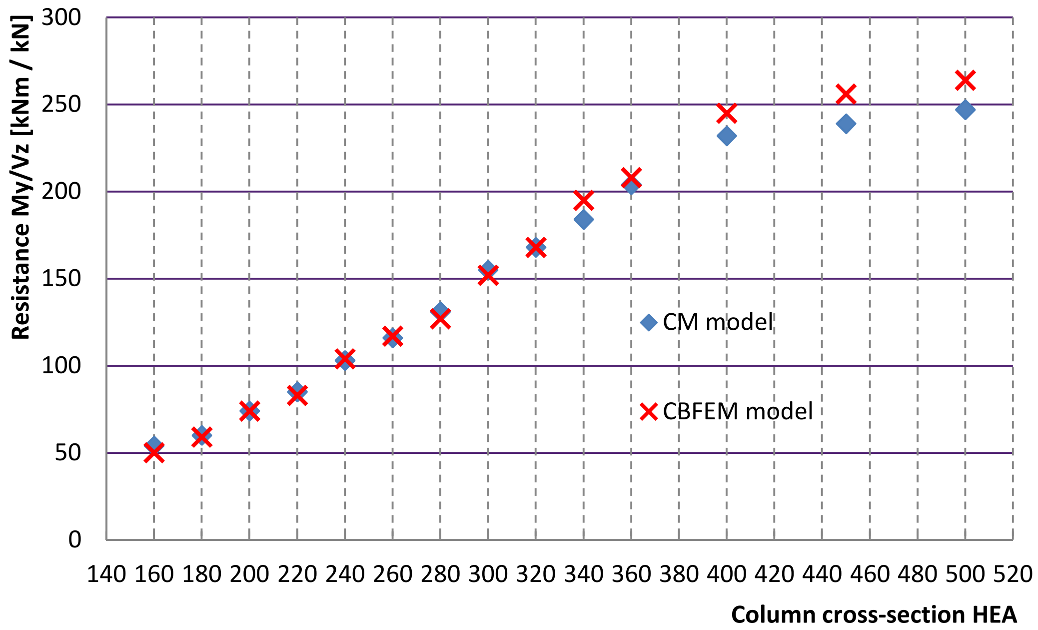

Figure 5: Sensitivity study, beam IPE 330, variable parameter is column cross-section size

Study of the moment connection in the corner of portal frame is visualised on Fig. 6. Design resistance and distribution of internal stresses are shown for three types of a joint - with unstiffened beam web, parallel stiffeners and inclined stiffener in compressed part of column web. These models were verified against CM with good accuracy. However, reaching this results using CM to the joint with inclined stiffener is very time consuming and with limited optimisation features.

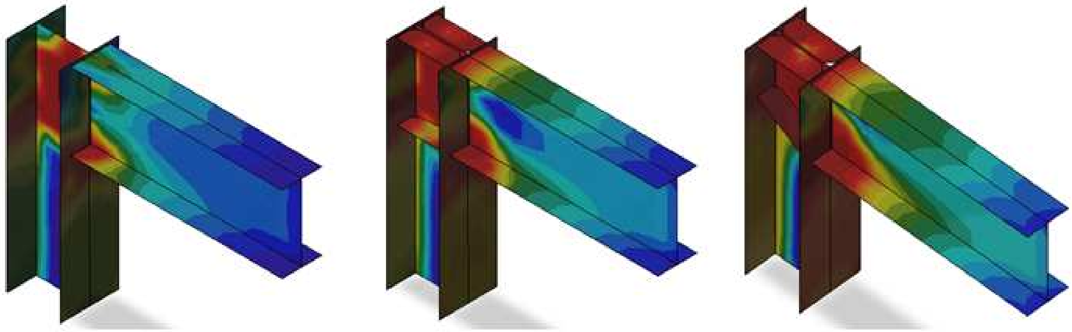

Figure 6: Influence of the shear stiffener to eaves moment connection;
from left 46,5 KNm; 61,3 kNm; and 73,0 kNm

3.2 Column base with base plate

Nowadays, tools using CM supports column base with base plate design with or without stiffeners. The example is calculated with loading in two perpendicular principal directions; in case of loading by bending moments in general plane the result is obtained by interaction, see cl. EN 1993-1-8. The accuracy of interaction is limited to linear behaviour and may result in 30 % overestimation. The CBFEM model was validated with good accuracy against experiments both from literature and carried out specifically for this purpose by authors. The verification of cases loaded by moment in major/minor axes performed against CM gives good results. The CBFEM model, directly performing calculation under general loading, allows engineers to optimise stiffeners and plate.

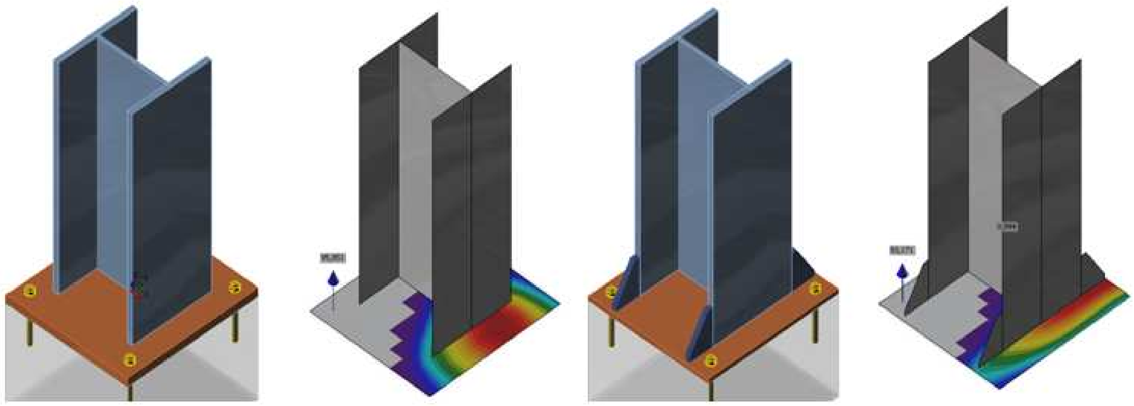

Figure 7: Stress in concrete under unstiffened base plate 35 mm (left)
and stiffened base plate 22 mm loaded by general moment (right)

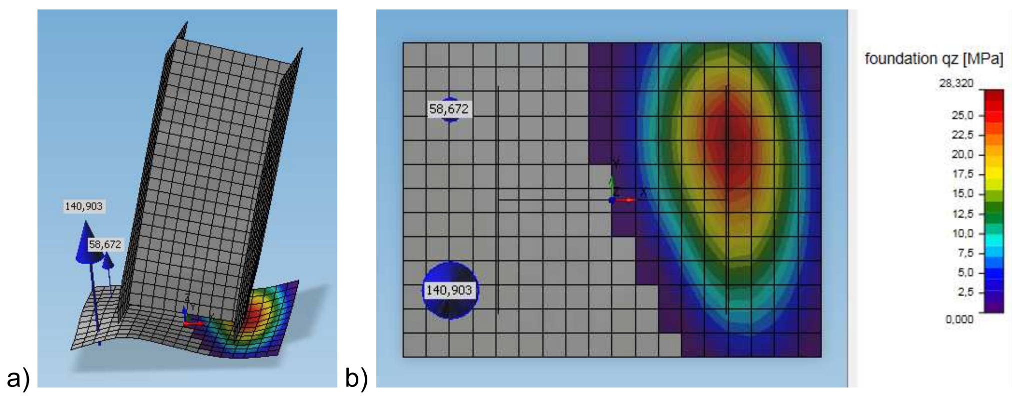

Figure 8: Base plate loaded by general moment
a) deformed shape, b) stress in contact area

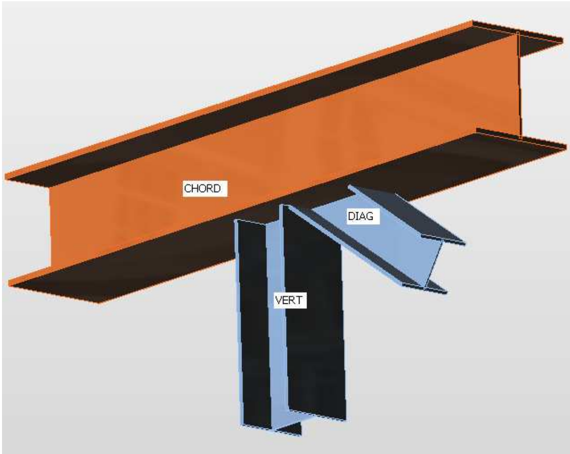

Figure 9: Geometry of joint with open cross-sections

3.3 Position of stiffeners

This example shows advantages of discrete analyses of stiffeners during the design. In case of slender compressed plates its eigenvalue and the stresses are limited by local buckling based on the plate geometry, relative slenderness, loading and boundary conditions.
Compressed upper chord of a truss of open sections HEA280 in the joint is exposed to normal force 1 336 kN, shear force 147 kN and bending moment 70 kNm, the compressed vertical cross section HEA180 is carrying 683 kN and in the diagonal HEA140 tensile force 611 kN, see Fig. 9. The strain in chord, see Fig. 10, reaches unacceptable 30 %, with limit value of 5% given by EN 1993-1-5. If two vertical stiffeners are designed, see Fig. 11, the strain decreases to 5,7 %. Three vertical stiffeners in Fig. 12 limit the strain to 3 % only. Two inclined stiffeners are close to optimum. Instead of plates 10 x 80 mm the plates 6 x 40 are designed.

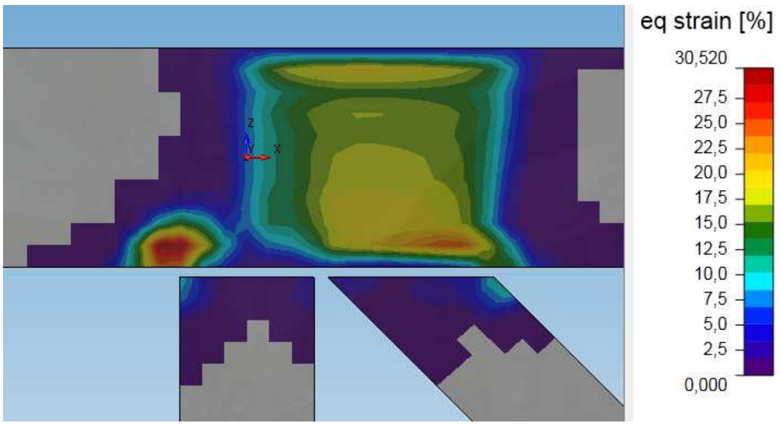

Figure 10: Strain in joint without stiffener

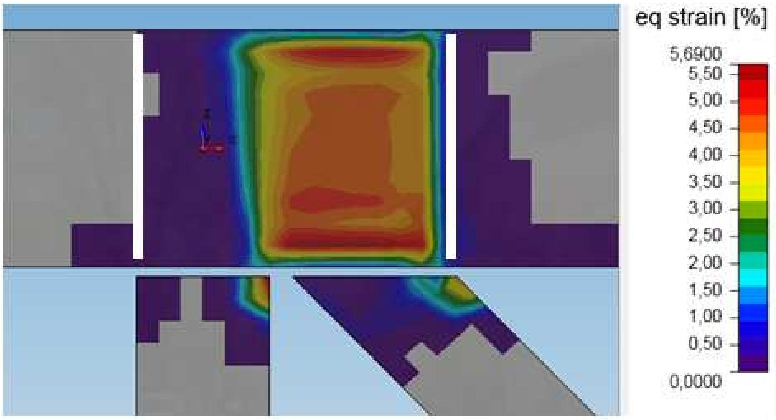

Figure 11: Strain in joint with two vertical parallel stiffeners

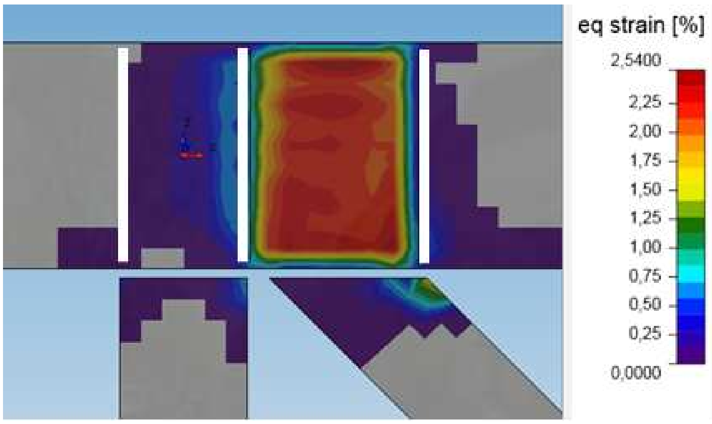

Figure 12: Strain in joint with three vertical parallel stiffeners

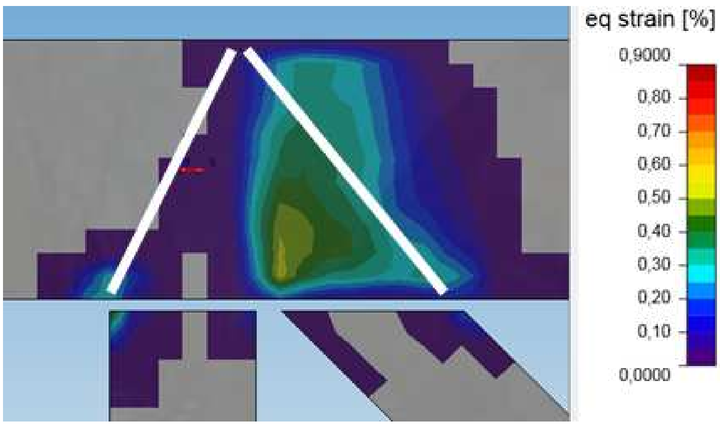

Figure 13: Strain in joint with two inclined stiffeners

4 CONCLUSIONS

Commonly used Component Method (CM) is laborious for hand calculation and its application by design tools in practice is limited to certain types of connections and their loading. Use of computer based design of structural connections by RSFEM is limited to proper validation and verification procedures.

Component Based Finite Element Model (CBFEM) was developed. Its validation using both published and undisclosed experiments with open and hollow section connections and column bases is under progress. Based on configurations verified by published results, CBFEM provides more variability in geometry and loading than simplified procedures in current CM.

ANNOUNCEMENT

This method was created under project MERLION supported by Technology Agency of the Czech Republic, project No. TA02010159.

REFERENCES

[1] Zoetemeijer, P.: *Summary of the Researches on Bolted Beam-to-Column Connections*. Report 6-85-7, University of Technology, Delft 1985.

[2] Steenhuis M., Gresnigt N., Weynand K.,*Pre-Design of Semi-Rigid Joints Ii Steel Frames*, Proceedings of the Second State of the Art Workshop on Semi-Rigid Behaviour of Civil Engineering Structural Connections, COST C1, Prague, 1994, 131-140.

[3] Jaspart J.P., Design of structural joints in building frames, *Prog. Struct. Engng Mater.*, 4 (2002) 18–34.

[4] Wald F., Sokol Z., Steenhouis M. and Jaspart, J.P., Component Method for Steel Column Bases, *Heron* 53 (2008) 3-20.

[5] Da Silva Simoes L., Towards a consistent design approach for steel joints under generalized loading, *Journal of Constructional Steel Research*, 64, 1059-1075, 2008.

[6] EN1993-1-8, Eurocode 3, Design of steel structures, Part 1-8, *Design of joints*, CEN, Brussels, 2006.

[7] EN1994-1-1, Eurocode 4, Design of composite steel and concrete structures, Part 1-1, *General rules and rules for buildings*, CEN, 2010.

[8] František Wald F., Kwasniewski L., Gödrichn L., Kurejková M., V*alidation and Verification Procedures for Connection Design in Steel Structures*, Proceedings Steel, Space and Composite Structures, in printing, Prague, 2014.

[9] Bursi O. S., Jaspart J. P., Benchmarks for Finite Element Modelling of Bolted Steel Connections*, Journal of Constructional Steel Research,* 43 (1-3), 1997, 17-42.

[10] Virdi K. S. et al, *Numerigal Simulation of Semi.Rigid Connections by the Finite Element Method*, Report of Working Group 6 Numerical, Simulation COST C1, Brussels Luxembourg, 1999.

[11] EN 1993-1-5, Eurocode 3: Design of steel structures - Part 1-5: *Plated Structural Elements,* CEN, Brussels, 2007.

12th International Conference on
Steel, Space and Composite Structures
28-30 May 2014, Prague, Czech Republic

EFFECT OF CHORD STRESS ON FIRE RESISTANCE OF TUBULAR JOINTS SUBJECTED TO AXIAL LOADING AT BRACE END

Yongbo Shao* and Yijie Zheng†

School of Civil Engineering, Yantai University, PR China, 264005
email: cybshao@ytu.edu.cn

Keywords: tubular joints, fire resistance, chord stress, critical temperature, ultimate strength

Abstract. *This paper presents experimental study on fire resistance of welded circular tubular T-joints subjected to axial loadings at the end of both brace and chord. In the investigation, three identical specimens in geometry are tested. These specimens are subjected to constant brace axial loading, but with different chord axial loadings. The different values of axial loading at the chord end are used to study the effect of initial chord stress on the overall behavior of tubular joints at elevated temperature. From experimental results, it is found that the magnitude of the initial chord stress has a remarkable effect on the fire endurance time and the critical temperature at failure.*

1 INTRODUCTION

Based on plentiful advantages of light weight, high strength, low drag coefficient and easy fabrication, circular tubular structures are of wide application in the tubular space structures, such as stadium, airport terminals, railway station and ocean platforms. Circular tubular joint has the most adoption in tubular structures due to its straightforward constructures, needless connectors, material saving and high bearing capacity. For the tubular T-joints, the chord is not only subjected to loading transferred from brace, but also subjected to axial loading at its both ends. For tubular structures used in ocean platforms, they face fire hazard because drilled oil or gas is combustible, and the burning velocity is very quick. Due to a severe deterioration of steel materials at elevated temperature, steel tubular structures may fail quickly in fire condition. Therefore, it is very meaningful to investigate the performance of steel tubular structures at elevated temperature.

Currently, the researches on fire resistance of tubular joints subjected to axial loading at brace end have been carried out. Nguyen et al.[1, 2] conducted both experiments and numerical analyses on the performance of tubular T-joints subjected to brace axial compression. Tan et al.[3] investigated the ultimate strength and failure modes of CHS T-joints subjected to brace axial loading at elevated temperature. Jin et al.[4] carried out both experimental and parametrical study on the post-fire behavior of tubular T-joints subjected to axial brace loading. Liu et al.[5] and Jin et al.[6] conducted experimental study and parametrical analysis on mechanical behavior of steel planar tubular truss under fire. Chen et al.[7] and He et al.[8] carried out experiments on the fire resistant behaviors of tubular T- and K-joints. Ozyurt et al.[9] carried out extensive numerical fire resistant simulations and analysis on the ultimate strength of tubular joints under brace axial compression. Gao et al.[10] carried out finite element analysis on fire resistance of tubular Y-joints.

However, all of these researches do not consider the effect of chord stress on the behavior of tubular joints at elevated temperature. Hence, to study the effect of chord stress on fire resistance of tubular joints subjected to axial loading at brace end is in of great need.

2 EXPERIMENTAL TEST

2.1 Specimen descriptions

Three identical specimens in geometry are manufactured for the experiments. The specimens are designed on basis of the actual operating condition of the laboratory. The length of the loading frame is 3 meters. To assemble the specimen and install the heating furnace, the length of the chord is designed to be 2.28 meters. The detailed sizes of the specimen are shown in Figure 1. A series of the geometrical parameters are also provided in Figure 1.

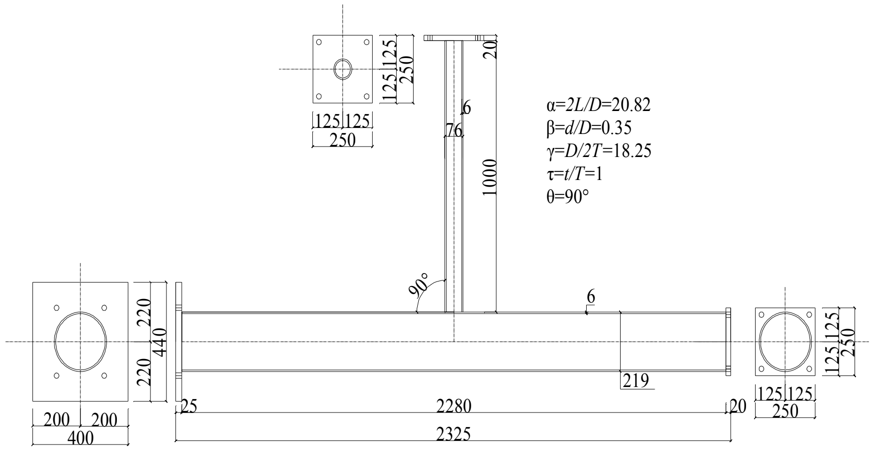

Figure 1: Geometrical dimension of the specimen

2.2 Test rig

A 3-m long loading frame is set up for conducting the experiments. A hydraulic jack is installed at the bottom of the top horizontal beam to apply compressive force at the end of brace. Another hydraulic jack is fixed at side wall of one column to exert a compressive force at one end of the chord. The strokes of the two hydraulic jacks are 300kN and 500kN respectively. The mid-segment of the specimen is placed in the heating furnace, and the furnace can provide heating process in accordance with ISO 834 heating curve. For the specimen, one end of the chord is fixed to the loading frame, and the other end of the chord is manufactured as a roller support. With regard to the end of brace, the boundary condition allows the horizontal and vertical displacements. The experimental devices are shown in Figure 2.

Figure 2: Overall view of test setup

2.3 Material properties

The mechanical properties of the steel materials used in the specimens are obtained through uni-axial tensile coupon tests, some important material properties are listed in Table 1, in which E is elastic modulus, f_y and f_u are yield stress and tensile stress of the steel materials respectively.

Tube diameter (mm)	E (GPa)	f_y (MPa)	f_u (MPa)
219	203	345	510
76	199	390	509.6

Table 1: Material properties of the specimens

3 MEASUREMENT

3.1 Temperature measurement

The specimens are heated up according to the ISO 834 heating curve set before the experiment. Based on the procedure debugged by the electric heater control system, the heating furnace works and the specimen can be heated up in accordance with ISO834 heating curve after 200℃(as shown in Figure 3).

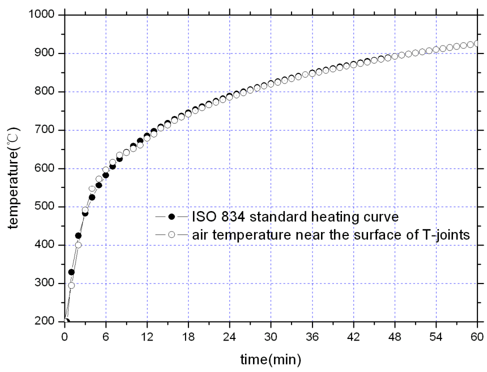

Figure 3: Comparison between ISO834 standard heating curve and test temperature

The temperature of the air in furnace and the temperature of heating wires are tested by using thermal couples to monitor the heating process. In addition, four points on the chord surface and on the brace surface are selected to meansure the temperature development during heating process. Three points are located insider the furnace and two of them are set on the chord surface and one point is located on brace surface. The fourth point is selected on the chord surface near one of the chord end, and this point is outside the furnace. The temperature of three measurement points inside heating furnace can represent the temperature of the joint region. The temperature of the forth measurement point can reflect the temperature variation of the region outside the heating furnace (as shown in Figure 4).

Figure 4: The temperature measurement points

3.2 Displacement measurement

Four Linear Variable Displacement Transducers (LVDT) are used to measure the displacements at some critical positions. The vertical displacement of the brace end can be measured straightway because it is outside the heating furnace. The displacements of the remaining three positions should be surveyed using the special measuring method indirectly. One is situated at the saddle of the specimen, and another is at the position of the crown, the last one is located at the middle of the chord (as shown in Figure 5).

Figure 5: Displacement measurement points

3.3 The measurement of forces

The loads applied at the brace end and at one chord end are recorded respectively by two load cells installed at the jacks. The readings can be fetched through the data acquisitions automatically.

4 TEST PROCEDURE

The experiment includes three stages. At the beginning, a load value with its magnitude of 50% of the ultimate strength is applied at the brace end. The ultimate strength of the T-joint under brace compression F_{ub} is calculated by using the FE software ABAQUS (as listed in Table 2). In the second stage, when the chord is under compression, the ultimate strength F_{cu} can be determined according to the yield stress f_y and the cross section area S of the chord. The formula is listed as follow:

$$F_{cu} = f_y \times S \tag{1}$$

The applied load on the chord end is calculated and listed in Table 3. The mechanical properties of the steel materials of the specimens are obtained through uni-axial tensile coupon tests.

Specimen	F_{ub} (kN)	Loading ratio (n_b)	Applied load P_b (kN)
SP-T1	132	0.5	66
SP-T2	132	0.5	66
SP-T3	132	0.5	66

Table 2: Values of applied forces on brace end

Specimen	S(mm^2)	F_{uc} (kN)	Loading ratio(n_c)	Applied load P_c (kN)
SP-T1	4012.92	1381.22	0	0
SP-T2	4012.92	1381.22	0.2	276.24
SP-T3	4012.92	1381.22	0.3	414.37

Table 3: Values of applied forces on chord end

5 EXPERIMENTAL RESULTS AND ANALYSIS

5.1 Experimental results

The failure modes of all three specimens subjected to elevated temperature are all plastic failure of chord face around brace/chord intersection area, as shown in Figure 6. In the course of experiment, along with the increase of the temperature, the material of the steel deteriorates gradually. Failure initiates firstly at the brace/chord intersection region which has high stress concentration and lower bearing capacity.

a) SP-T1 b) SP-T2 c) SP-T3

Figure 6: Failure modes of the specimens

5.2 Displacement-temperature curves

The displacement-temperature curves can be obtained from the experiments for each specimen. As shown in Figure 7, some conclusions can be summarized according to the differences of the displacement-temperature curves at saddle position. Before the elevated temperature reaches 200^{o}C, the expansion of the steel results in the upward movement of the brace end. After the temperature exceeds 200 ^{o}C, the effect of the material deterioration is greater than the heat expansion, and so the brace end begins to move down and the displacement increases gradually. After the temperature reaches a critical value, collapse occurs and the displacement increases rapidly.

The displacement-temperature curves are used to compare the fire endurance time and critical temperature of the three specimens. As seen in Figure 7, with the increase of the loading applied at the chord end, the fire endurance time decreases and the critical temperature reduces in turn.

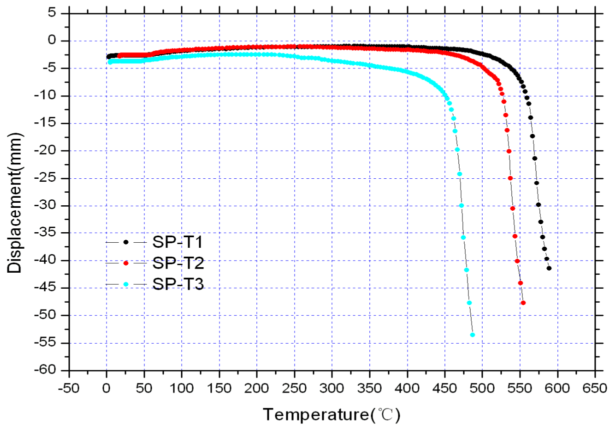

Figure 7: Displacement-temperature curves of specimens

6 CONCLUSIONS

According to the experimental results, the following conclusions can be summarized:

(1) Whether applying loading at chord end or not, the failure modes of tubular T-joints under brace axial compression at elevated temperature are all the plastic failure of chord face around brace/chord intersection area.

(2) The magnitude of the initial chord stress has a remarkable effect on the fire endurance time and on the critical temperature at failure. With the increase of the loading applied at the chord end, the fire endurance time decreases and the critical temperature reduces in turn.

REFERENCES

[1] M.P. Nguyen, T.C. Fung and K.H. Tan, *An experimental study of structural behaviors of CHS T-joints subjected to brace axial compression in fire condition*, Tubular structures ⅩⅢ, Hong Kong, 2010: 725-732.

[2] M.P. Nguyen, K.H. Tan and T.C. Fung, *Numerical models and parametric study on ultimate strength of CHS T-joints subjected to brace axial compression under fire condition*, Tubular structures ⅩⅢ, Hong Kong, 2010: 733-740.

[3] K.H. Tan, T.C. Fung and M.P. Nguyen, *Structural behavior of CHS T-joint subjected to brace axial compression in fire condition [J]*, Journal of Structural Engineering, ASCE, 2013, 139: 73-84.

[4] M. Jin, J.C. Zhao and J. Chang, *Experimental and parametric study on the post-fire behavior of tubular T-joint [J]*, Journal of Constructional Steel Research, 2010, 67(1): 75-83.

[5] M.L. Liu, J.C. Zhao and M. Jin, *An experimental study of the mechanical behavior of steel planar trusses in a fire*, Journal of Constructional Steel Research, 2010, 66: 504-511.

[6] M. Jin, J.C. Zhao and M.L. Liu, *Parametric analysis of mechanical behavior of steel planar tubular truss under fire*, Journal of Constructional Steel Research, 2010, 67: 75-83.

[7] C. Chen, Y.B. Shao and J. Yang, *Experimental and numerical study on fire resistance of circular tubular T-joints*, Journal of Constructional Steel Research, 2013, 85(1): 24-39.

[8] S.B. He, Y.B. Shao and H.Y. Zhang, *Experimental study on circular hollow section (CHS) tubular K-joints at elevated temperature*, Engineering Failure Analysis, 2013, 34: 204-216.

[9] E. Ozyurt, Y.C. Wang and K.H. Tan, *Elevated temperature resistance of welded tubular joints under axial load in the brace member*, Engineering Structures, 2014, 59: 574-586.

[10] F. Gao, X.Q. Guan and Z.G. Wu, *Finite element analysis on fire resistance of circular tube Y-joints*, Journal of Civil Engineering and Management, 2012, 29(1), 10-14.

12th International Conference on
Steel, Space and Composite Structures
28-30 May 2014, Prague, Czech Republic

NUMERICAL STUDY OF ALUMINIUM ALLOY CONTINUOUS BEAMS

Mei-Ni Su*, Ben Young† and Leroy Gardner‡

* PhD Candidate, Dept. of Civil Engineering, The Univ. of Hong Kong, Pokfulam Road, Hong Kong / Dept. of Civil and Environmental Engineering, Imperial College London, London SW7 2AZ, United Kingdom
e-mail: sumeinimay@hotmail.com

Keywords: Aluminium alloys; Continuous beams; Continuous strength method; Indeterminate structures; Numerical model; Parametric study; Plastic design; Structural design; Tubular sections.

Abstract. *The aims of this study are to investigate the behaviour of aluminium alloy continuous beams using finite element (FE) analysis and to underpin the development of revised design methods for indeterminate structures. FE analyses of two-span continuous beams (i.e. five-point bending) of square and rectangular hollow sections (SHS and RHS) are presented. The FE model was developed using ABAQUS 6.10-1, and the ultimate loads were determined when either a plastic collapse mechanism was formed or the material fracture strain was reached on the tension flange. Upon validation of the model against available experimental results, an extensive parametric study was performed to assess the effect of key parameters such as the cross-section aspect ratio, cross-section slenderness and the moment gradient on the strength, strain hardening behaviour and moment redistribution characteristics of aluminium alloy continuous beams. A total of 40 numerical results were generated and reported in this paper. The simulated ultimate loads were found to be beyond the theoretical loads that cause the first hinge to form, as well as the theoretical loads that cause the collapse mechanism to occur. A key characteristic of aluminium alloy, namely strain hardening, receives particular attention in the numerical investigation. In addition, the numerical results were also compared to design predictions from the American, Australian/New Zealand and European design standards and the continuous strength method for indeterminate structures. The design strengths predicted by the three specifications are found to be rather conservative, while the predications of the continuous strength method are more precise and consistent. The results reveal that strain hardening at the cross-sectional level and moment redistribution at the global system level have significant influence on the performance of stocky (plastic and compact sections) aluminium alloy structures, and should therefore be accounted for in efficient design.*

† Professor, Dept. of Civil Engineering, The Univ. of Hong Kong, Pokfulam, Hong Kong. E-mail: young@hku.hk
‡ Professor, Dept. of Civil and Environmental Engineering, Imperial College London, London SW7 2AZ, UK. E-mail: leroy.gardner@imperial.ac.uk

1 INTRODUCTION

Aluminium alloys are non-linear materials, and despite the fact that they are typically less ductile than structural steel and stainless steel, aluminium alloy structural sections may still have sufficient rotation capacity to allow moment redistribution and to enable the application of plastic design methods. The use of continuity in a structural system brings about several benefits, such as increased load-carrying capacity and reduced deflections. That is to say, for given loads and deflection limits, a more economical cross-section may be used[1]. Although aluminium alloys have been used in a range of structural engineering applications, underpinned by many international design standards, plastic design methods are not currently applicable in most of these standards. Thus, the structural behaviour of indeterminate aluminium alloy structures requires investigation.

Early studies into the inelastic behaviour of aluminium alloy structures were carried out at the end of the 1970s and in the early 1980s[2,3]. Strain hardening is one of the characteristics of aluminium alloys, which might affect the capacities of indeterminate structures. The ultimate strength of aluminium alloy materials can be as much as 30% higher than the yield strength, as shown in recent tensile coupon tests[4]. In 1986, Kemp[5] reviewed previous studies and concluded that strain hardening behaviour can influence the capacity of steel beams considerably. Byfield and Nethercot[6] and Kemp et al.[7] assessed experimentally the benefits of strain hardening in stocky (plastic and compact) steel sections and found that substantial increases in bending resistance beyond the fully plastic moment capacity can be achieved. In recent years, more studies[4, 8-12] recognized the influence of strain hardening on the ultimate strength of metallic materials. Another influential factor, moment redistribution, might also have a significant effect on the capacity of continuous beams. To examine the required ductility for moment redistribution, Manganiello et al.[13] investigated the inelastic flexural strength of indeterminate aluminium alloy structures by numerical means and verified the rotation capacity requirement in EC9[14]. Theofanous and Gardner[15] reported that when considering moment redistribution in stainless steel continuous beams, the accuracy of the predicted failure load can often be improved by more than 10% by considering strain hardening.

In terms of numerical simulations, there have been a great number of numerical studies on determinate aluminium alloy members, but simulations on indeterminate aluminium alloy structures are far fewer. Manganiello et al.[13] developed FE models on indeterminate aluminium alloy structures and validated the models against five-point bending tests conducted by Welo[16], after which the models were used to generate numerical results on fixed ended beams, continuous beams and portal frames.

In designing of aluminium alloy structural members, there are a number of established international design specifications, including the Aluminium Design Manual (AA)[17], the Australian/New Zealand Standards (AS/NZS)[18] and Eurocode 9 (EC9)[14]. EC9 provides the plastic hinge method for continuous beams as an alternative design approach in Annex H for Class 1 sections, to account for strain hardening behaviour in the inelastic range. De Matteis et al.[19] highlighted that EC9 was the first code to allow full inelastic analysis of aluminium alloy structures. However, plastic design is currently not available in the American and Australian/New Zealand Standards. A number of previous studies on aluminium alloy flexural members[12, 20-23] reported that although the existing design specifications are widely used by structural engineers, they are not fully efficient without considering strain hardening. Most recently, a deformation-based design approach, the continuous strength method (CSM) for indeterminate aluminium alloy structures, was proposed[23]. The CSM allows for moment redistribution as well as strain hardening in stocky (plastic and compact) sections that can sustain large plastic strains.

The aims of this study are to develop finite element (FE) models and generate numerical results for indeterminate aluminium alloy structures, as well as to form the foundation for design method development. In this study, the authors employ a numerical technique as an efficient tool to replicate the structural responses of five-point bending beams. The developed FE model was initially validated against tests on 10 continuous beams[23]. An extensive parametric study was then carried out based on the validated FE model. The most widely used design approaches for indeterminate structures including the American, Australian/New Zealand and European specifications together with the traditional plastic design, the plastic hinge method and the continuous strength method (CSM) for indeterminate aluminium alloy structures are, later, evaluated against 40 newly generated numerical results and 10 existing test results.

2 NUMERICAL MODEL

A series of five-point bending tests was initially replicated numerically by means of the non-linear finite element (FE) analysis package ABAQUS 6.10-1[24]. The measured stress–strain curves from tensile coupon tests on material cut from the flat portions of the test specimens were used in the analyses. The material nonlinearity was included in the FE models by specifying set of values of true stress and plastic strain to define a piecewise linear response. The relationship between true stress σ_{true} and engineering stress σ, as well as true plastic strain ε_{true} and engineering strain ε are given by Equations (1) and (2), respectively.

$$\sigma_{true} = \sigma(1+\varepsilon) \tag{1}$$

$$\varepsilon_{true} = \ln(1+\varepsilon) - \sigma_{true} / E \tag{2}$$

where E is the Young's modulus.

The reduced integration four-noded doubly curved shell element S4R was employed in the present study to model the continuous beams. The S4R general purpose shell element has six degrees of freedom per node and provides an accurate solution to problems of the nature addressed in this study[25]. The steel loading plates utilised in the tests were modelled using 10 mm thick solid elements that were free to rotate in-plane. A uniform mesh size of 10 mm × 10 mm was chosen for all specimens and bearing plates. These element types and size have been shown to perform well for the modelling of aluminium alloy structural members[12, 26-27].

Residual stresses in the test specimens were not measured and not explicitly modelled in the FE analysis for two reasons: (1) the presence of bending residual stress in extruded aluminium alloy sections is, to a significant extent, implicitly reflected in the material properties obtained from tensile coupon tests; (2) residual stresses have only a very small effect on the load-bearing capacity of aluminium alloy extruded members[28]. Initial local geometric imperfections were incorporated in the FE models in the form of the lowest regular elastic buckling mode shape. A linear eigenvalue buckling analysis was therefore initially performed. The initial local geometric imperfection amplitude was defined as 0.2 mm, which represented the average local imperfection amplitudes measured in the test specimens[4]. It was found that sensitivity of the simulated results to imperfections was generally relatively low.

Even though specimens displayed symmetry in geometry and loading configurations, modelling of the full specimen length (1690 mm) and cross-sections was performed. This was done to ensure that possible anti-symmetric local buckling modes were not suppressed, which, in some cases, had marginally lower corresponding eigenvalues than their symmetric counterparts[15]. The boundary conditions were generally modelled in accordance with the tests conducted in the laboratory. Line loads were applied at the bearing plates above the specimens, to avoid high load concentrations. Appropriate degrees of freedom were restrained at the bottom flange of the specimens to simulate simple supports. The beams were restrained longitudinally at mid-span only. Cross-sections at the loading points and supports were constrained to in-plane rotation only.

The interfaces between the steel bearing plates and the aluminium specimens were modelled using a contact pair. Hard contact in the normal direction and friction penalty contact (with the friction coefficient = 0.1) in the tangential direction were adopted between the solid plate (master surface) and the beam surface (slave surface). Penetration of the contact pairs was prevented. The loading control used in the FE analysis was similar to that used in the tests, where the load was applied by imposing vertical displacement to the solid bearing plates. The Riks procedure with automatic increment sizing, as described in ABAQUS 6.10-1[24] was used to allow the post-ultimate path of the modelled specimens to be captured.

3 MODEL VALIDATION

In this section, the FE models are validated by the comparison against 10 physical test results. Comparisons are made between failure modes, load-deformation behaviour and collapse loads, and failure criteria are defined for the FE model.

3.1 Failure Modes

Observed failure modes included inelastic local buckling, material yielding and the formation of a collapse mechanism, and tensile material fracture. Local buckling was most prominent in the compression flanges of the relatively slender sections, whereas the formation of a collapse mechanism comprising three plastic hinges was clearly observed in all simulated specimens. A comparison of the typical failure modes between tested and simulated specimens is depicted in Figure 1.

It should be noted that in the experimental program, some specimens failed by material fracture at the tension flanges, due to exceedance of the material fracture strain ε_f. This failure mode was accounted for by monitoring the tensile strains and identifying when the tensile fracture strain ε_f, as obtained from tensile coupon tests, was reached. This is shown in Figure 2, where a typical load-deformation response is given. In the graph, the solid dot signifies the point where the strain at the tension flange of the simulated specimen reaches the material fracture strain ε_f, hence signifying tensile failure

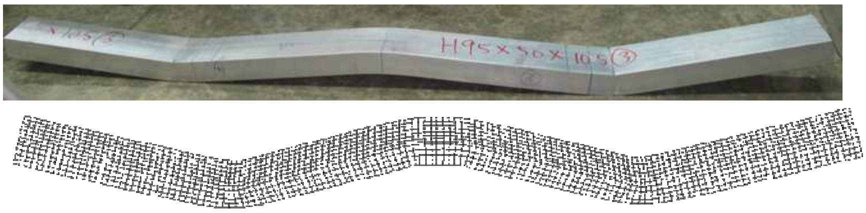

Figure 1: Experimental and numerical failure modes for specimen H95×50×10.5B5I

3.2 Load-Displacement Behaviour

The full load-deflection responses from all tests and simulations were compared; a typical example is shown in Figure 2. In general, the initial stiffness and the shape of the numerical load-deflection curves closely matched those obtained from the experiments. Overall, good agreement between the experimental and numerical results was observed, though for some cases, the predicted load-bearing capacity deviated to some extent from the test results. On average, ultimate loads F_{FE} were predicted to within 2% of the test results F_{exp} and with a low coefficient of variation (COV = 0.063), as shown in Table 1. However, the end rotations at ultimate loads (θ_{exp} and θ_{exp}) were less accurately captured, but predicted, in most cases within 10% of the experimental measurements, as shown in Table 1. Therefore, it can be concluded that the FE model developed herein is able to simulate accurately the behaviour of the tested members and to capture the strain hardening and the spread of plasticity in the aluminium alloy continuous beams.

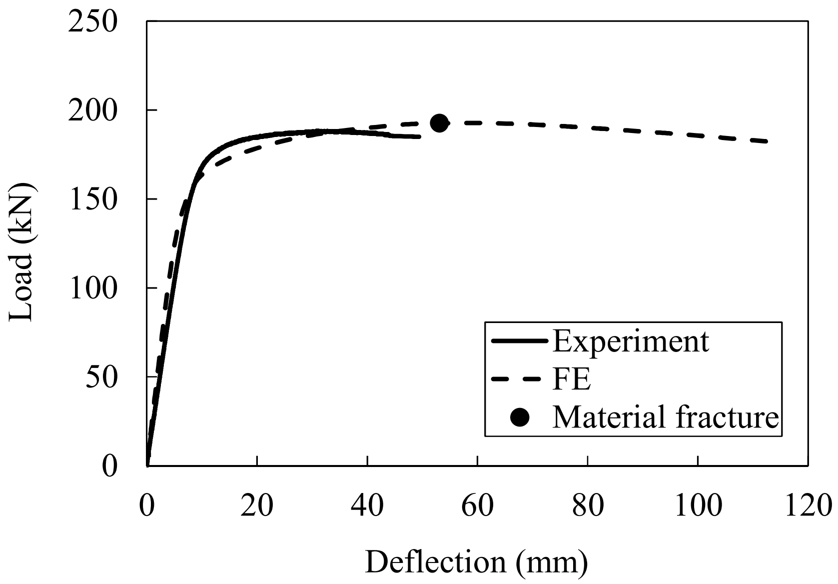

Figure 2: Experimental and numerical load-deflection curves for specimen H95×50×10.5B5I

Table 1. Comparison of ultimate loads and corresponding rotations between experimental and numerical results

Specimen	F_{exp} (kN)	F_{FE} (kN)	$\frac{F_{exp}}{F_{FE}}$	θ_{exp} (rad)	θ_{FE} (rad)	$\frac{\theta_{exp}}{\theta_{FE}}$
H55×70×4.2B5I	114.1	115.2	0.99	0.072	0.069	1.04
H55×70´4.2B5I-R	112.3	120.5	0.93	0.098	0.097	1.01
H70×55×4.2B5I	84.9	77.3	1.10	0.092	0.101	0.91
H50×95×10.5B5I	329.9	358.0	0.92	0.133	0.134	0.99
H95×50×10.5B5I	188.2	192.5	0.98	0.144	0.164	0.88
H64×64×3.0B5I	65.3	68.5	0.95	0.037	0.039	0.95
N50×95×10.5B5I	306.7	332.1	0.92	0.177	0.123	1.44
N70×120×10.5B5I	532.9	506.5	1.05	0.121	0.118	1.03
N120×70×10.5B5I	362.0	401.5	0.90	0.070	0.074	0.95
N120×120×9.0B5I	655.2	665.0	0.99	0.102	0.096	1.06
Mean			0.98			1.02
COV			0.063			0.156

4 PARAMETRIC STUDY

In this section, the validated FE model is used to conduct a parametric study aiming to develop a better understanding on the inelastic behaviour of indeterminate aluminium alloy structures. The parametric study was performed to expand the available data over a wider cross-section slenderness range and investigate the effect of key factors, such as the cross-section aspect ratios and the moment gradient, on the performance of aluminium alloy continuous beams. Cross-sections with outer wall dimensions up to 180 mm and the thickness varying between 3.5 mm and 12.0 mm were modelled. Thus, aspect ratios from 0.33 to 3.40 and a wide range of plate slenderness (*b/t* ratios: 4.25-55.14), covering the four cross-section classes, were considered. The overall beam lengths were 1690 mm, 2490 mm and 3690 mm for small (width 50 mm × height 130 mm, width 130 mm × height 50 mm), medium (width 140 mm × height 100 mm) and large (width 180 mm × height 180 mm, width 160 mm × height 200 mm) cross-sections, respectively. A total of 20 different cross-section dimensions were considered, together with two grades of aluminium alloy. The stress-strain material curves obtained from the tensile coupon tests of tube H64×64×3.0 (f_y = 233.8 MPa and f_u= 248.4 MPa) and +N95×50×10.5 (a tube reported in Su et al.[4], with f_y = 109.5 MPa and f_u= 177.4 MPa) were used to define material properties for high strength and normal strength aluminium alloys in the parametric study, respectively. The local geometric imperfections are assumed to be of the form of the lowest appropriate elastic buckling mode shape with an amplitude of 0.2 mm as measured in the experimental program.

In order to build up a large database of indeterminate aluminium alloy structures and thereafter to assess the different design approaches, a total of 40 numerical results have been generated herein. The FE model also allows for examining the load redistribution level and inelastic performance of continuous beams. The newly generated numerical results are presented in Table 2, with the same labelling system as described in Su et al.[23]. In the numerical model, the ultimate loads are determined when either the plastic collapse mechanism is formed or the material fracture strain ε_f is reached in the tension flange, whichever occurred on aluminium alloy continuous beams first

Table 2. Ultimate loads from FE parametric study

Specimen	F_{FE} (kN)	Specimen	F_{FE} (kN)
H180×180×12.0B5I	946	N180×180×12.0B5I	561
H180×180×9.0B5I	690	N180×180×9.0B5I	381
H180×180×6.0B5I	428	N180×180×6.0B5I	222
H180×180×3.5B5I	182	N180×180×3.5B5I	105
H160×200×12.0B5I	1006	N160×200×12.0B5I	596
H160×200×9.0B5I	718	N160×200×9.0B5I	392
H160×200×6.0B5I	432	N160×200×6.0B5I	221
H160×200×3.5B5I	183	N160×200×3.5B5I	99
H140×100×8.0B5I	378	N140×100×8.0B5I	252
H140×100×6.5B5I	306	N140×100×6.5B5I	199
H140×100×5.0B5I	232	N140×100×5.0B5I	142
H140×100×3.5B5I	151	N140×100×3.5B5I	86
H130×50×8.0B5I	221	N130×50×8.0B5I	138
H130×50×6.5B5I	183	N130×50×6.5B5I	111
H130×50×5.0B5I	143	N130×50×5.0B5I	83
H130×50×3.5B5I	99	N130×50×3.5B5I	55
H50×130×8.0B5I	521	N50×130×8.0B5I	327
H50×130×6.5B5I	420	N50×130×6.5B5I	244
H50×130×5.0B5I	317	N50×130×5.0B5I	166
H50×130×3.5B5I	208	N50×130×3.5B5I	97

5 COMPARISON OF TEST AND NUMERICAL STRENGTHS WITH DESIGN STRENGTHS

In this section, the experimental and numerical ultimate loads F_u are compared with the design strengths predicted by the American[17] (F_{AA}), Australian/New Zealand[18] ($F_{AS/NZS}$) and European[14] (F_{EC9}) specifications for aluminium alloy structures, as well as the capacities calculated based on the traditional plastic design method (F_{pl}), the plastic hinge method[14] ($F_{EC9\text{-}H}$) and the CSM for indeterminate aluminium alloy structures[23] (F_{csm}). Calculation concepts and design treatments of the aforementioned methods are explained in this section. The comparison between design values and numerical (and test) results are tabulated in Table 3 and plotted in Figure 3, where the conservatism of the current international design specifications is highlighted. Only specimens within the CSM applicability limit ($\overline{\lambda}_p \leq 0.68$) are discussed in this section.

5.1 International design specifications

The AA, AS/NZS and EC9 specifications have similar approaches for indeterminate structures, i.e. the global elastic design. The design collapse load is determined when the first hinge forms. However, these three specifications have different approaches and parameters to calculate the cross-sectional flexural resistance, finally leading to different design capacities for continuous beams. The mean values of the load ratios F_u/F_{AA}, $F_u/F_{AS/NZS}$ and F_u/F_{EC9} are 1.78, 1.98 and 1.67, with the corresponding coefficients of variation (COV) of 0.200, 0.213 and 0.164, respectively. Among them, the AS/NZS provides the most conservative predictions. Overall, the predictions of all three specifications may all be seen rather conservative, particularly for stocky sections, as indicated in Figure 3.

5.2 Plastic hinge method (EC9)

The plastic hinge method is included in Annex H of EC9 as an alternative plastic design method for indeterminate structures, which is mainly applied to plastic (Class 1) sections but can also be used for compact (Class 2) and semi-compact (Class 3) sections, provided specific accounts is taken of local buckling. The plastic hinge method ($F_{EC9\text{-}H}$) is applied to Class 1 sections herein; that is to say, predictions of F_{EC9} and $F_{EC9\text{-}H}$ only differ for Class 1 sections and are the same for Classes 2, 3 and 4 sections. The cross-sectional ultimate moment capacity M_u for the plastic hinge method is defined by Equation (3), where η is a correction factor to the conventional yield stress to take into consideration the available hardening behaviour of the material, α_ξ is the shape factor depending on the alloy ductility features as required in Annex G of EC9, and W_{el} is the elastic section modulus. The cross-sectional ultimate bending moment is calculated as a fully plastic moment with allowance for strain hardening. The plastic hinge method also takes benefits from global plastic analysis at the system level.

$$M_u = \eta\alpha_\xi f_y W_{el} \tag{3}$$

The predictions from the plastic hinge method are much more accurate compared to the existing international specifications. The ratio of experimental to predicted ultimate loads $F_u/F_{EC9\text{-}H}$ is 1.44, with a coefficient of variation (COV) of 0.183, as shown in Table 3.

5.3 Traditional plastic design method

Traditional plastic design is conventionally applied to continuous beams with Class 1 sections. The collapse load F_{pl} is the theoretical load causing a collapse mechanism based on the formation of plastic hinges at their full plastic moment capacities. It is determined by means of a global plastic design with the plastic moment capacity $W_{pl}f_y$ at each hinge, and therefore takes consideration of moment redistribution for continuous beams of Class 1 sections. Continuous beams of Classes 2, 3 and 4 sections are designed excluding redistribution, and the capacity is determined when the capacity of the most heavily loaded cross-section is reached, i.e. using elastic global analysis with cross-section capacities $W_{pl}f_y$, $W_{el}f_y$ and $W_{eff}f_y$ for Classes 2, 3 and 4 sections, respectively, where W_{pl}, W_{el} and W_{eff} are the plastic section modulus, elastic section modulus and elastic modulus of effective sections, respectively.

The mean ratio of experimental and numerical results to predicted values F_u/F_{pl} is 1.54, on average, with a COV of 0.143, using the traditional plastic design method, as shown in Table 3. This indicates that the capacity of non-slender sections can continue to rise significantly after the plastic hinge attains the prescribed moment capacity. The key diversion between the traditional plastic analysis and the plastic hinge method in EC9-H is the calculation of the capacity of Class 1 sections, with the latter allowing for strain hardening.

5.4 Continuous strength method (CSM) for indeterminate aluminium alloy structures

The comparison of the CSM with the test and numerical results gives a mean value of 1.32 and a corresponding COV of 0.137, as shown in Table 3. The CSM for indeterminate structures provides the most precise predictions of the test and numerical results, with predicted mean value being closest to unity and the COV being the lowest. The improved predictions are related to the deformation-based design approach, the allowance for moment redistribution and consideration of strain hardening. \Moreover, since the cross-section deformation capacity can be explicitly determined by the CSM according to the continuous relationship with the cross-section slenderness $\overline{\lambda}_p$, it is not necessary to classify the cross-sections into the discrete classes, and thus the CSM avoids the limitations of the conventional classification system.

Table 3. Summary of comparisons between experimental and numerical results and design strengths

	$\frac{F_u}{F_{AA}}$	$\frac{F_u}{F_{AS/NZS}}$	$\frac{F_u}{F_{EC9}}$	$\frac{F_u}{F_{EC9-H}}$	$\frac{F_u}{F_{pl}}$	$\frac{F_u}{F_{csm}}$
Mean,	1.78 (1.69)	1.98(1.85)	1.67(1.61)	1.44(1.42)	1.54(1.48)	1.32
COV	0.200(0.225)	0.213(0.249)	0.164(0.175)	0.183(0.173)	0.143(0.171)	0.137

Note that only 40 specimens are within the limits of applicability of the CSM ($\overline{\lambda}_p \leq 0.68$), while a total of 50 test and numerical results are covered by the other design methods. Values in brackets refer to the full database of 50 data.

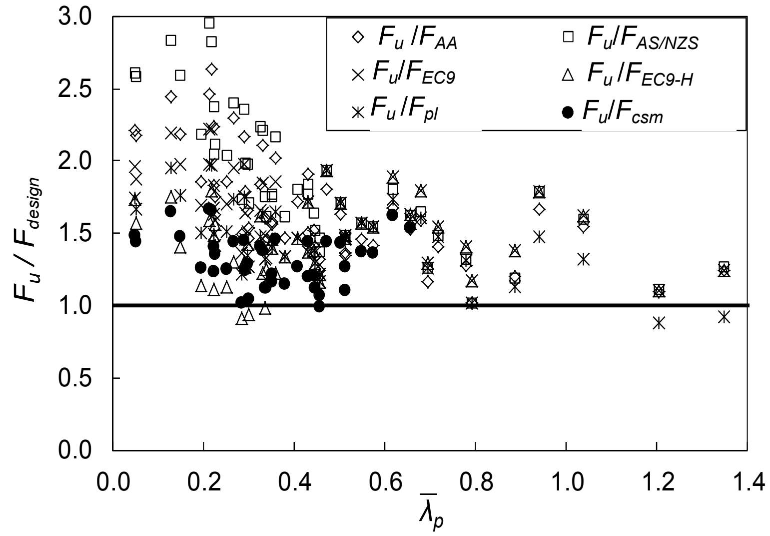

Figure 3: Comparison between test and numerical results with design strengths

6 CONCLUSIONS

Finite element models of continuous aluminium alloy beams have been developed and validated against test results. Upon validation, a parametric study was performed to generate 40 numerical results on aluminium alloy continuous beams. The combined experimental and numerical data set included a wide range of cross-sectional slenderness and aspect ratios on SHS and RHS members. These data were then used to investigate the design efficiency of American, Australian/New Zealand and European provisions, as well as the traditional plastic design analysis method, the plastic hinge method given in Annex H of EC9 and the continuous strength method for indeterminate aluminium alloy structures. The three specifications were found to be overly conservative in predicting the capacity of aluminium alloy continuous beams, especially for stocky (plastic and compact) sections. The other three design methods - the traditional plastic design analysis, the plastic hinge method and the continuous strength method - were found to estimate the ultimate loads more accurately, due to the adoption of global plastic analysis for stocky sections. In the comparison made herein, the continuous strength method was shown to provide the most accurate and consistent predictions. Besides the employment of global plastic design, the explanation for the good predictions relate to the system exploitation of strain hardening at the cross-sectional level and deformation-based design.

ACKNOWLEDGEMENT

The research work in this paper was supported by a grant from The University of Hong Kong under the seed funding program for basic research.

REFERENCES

[1] Nethercot, D. A., Li T. Q. and Choo, B. S. (1995) "Required rotations and moment redistribution for composite frames and continuous beams", *Journal of Constructional Steel Research*, 35(2): 121-163.

[2] De Martino A. and Faella C. (1978) "Plastic design of aluminum structures", *Costruzioni Metalliche*, (2). [in Italian].

[3] De Luca A. (1982) "Inelastic behavior of aluminum alloy continuous beams". *report. No. 506*. Napoli (Italy).

[4] Su, M., Young, B. and Gardner, L. (2013), "Testing and design of aluminium alloy cross-sections in compression" *Journal of Structural Engineering, ASCE*, accepted

[5] Kemp, A. A. (1986) "Factors affecting the rotation capacity of plastically designed members", *The Structural Engineer*, 64B(2): 28–35.

[6] Byfield, M. P. and Nethercot, D. A. (1998) "An analysis of the true bending strength of steel beams", *Proceedings of the ICE - Structures and Buildings*, 128(2), 188–197.

[7] Kemp, A. R., Byfield M. P. and Nethercot D. A. (2002) "Effect of strain hardening on flexural properties of steel beams", *The Structural Engineer*, 80(8): 29–35.

[8] Byfield, M.P., Davies, J. M. and Dhanalakshmi, M. (2005). "Calculation of the strain hardening behaviour of steel structures based on mill tests." *Journal of Constructional Steel Research*, 61 (2005): 133–150.

[9] Gardner, L. (2008). "The continuous strength method." *Proceedings of the Institution of Civil Engineers, Structures and Buildings* 161(3):127-133.

[10] Gardner, L., Wang, F. and Liew, A. (2011). "Influence of strain hardening on the behavior and design of steel structures." *International Journal of Structural Stability and Dynamics* 11(5): 855-875.

[11] Afshan, S. and Gardner, L. (2013) "The continuous strength method for structural stainless steel design" *Thin-Walled Structures*, 68(2013): 42-49.

[12] Su, M., Young, B. and Gardner, L. (2013), "Deformation-based design of aluminium alloy beams" *Engineering Structures*, submitted

[13] Manganiello M, De Matteis G, Landolfo R. (2006) "Inelastic flexural strength of aluminium alloys structures", *Engineering Structures*, 28(4):593-608

[14] European Committee for Standardization (EC9). (2007). "Eurocode 9: Design of aluminum structures—Part 1-1: General rules—General rules and rules for buildings." *BS EN 1999-1-1:2007*, CEN.

[15] Theofanous, M. and Gardner, L. (2010). "Experimental and numerical studies of lean duplex stainless steel beams" *Journal of Constructional Steel Research*, 66 (6): 816-825

[16] Welo T. *Inelastic deformation capacity of flexurally-loaded aluminium alloy structures*. Ph.D. thesis. Trondheim (Norway): Division of Structural Engineering, The Norwegian Institute of Technology; 1991.

[17] Aluminum Association (AA). (2010). *Aluminum design manual.* Washington, D.C.

[18] Australian/New Zealand Standard (AS/NZS). (1997). "Aluminum structures part 1: Limit state design." *AS/NZS 1664.1:1997*, Standards Australia, Sydney, Australia

[19] De Matteis, G., Moen, L. A., Langseth, M., Landolfo, R., Hopperstad, O.S. and F. M. Mazzolani (2001), "Cross-sectional classification for aluminum beams—parametric study", *Journal of Structural Engineering*, 127(3): 271-279

[20] Moen L.A., De Matteis, G., Hopperstad O.S., Langseth M., Landolfo, R. and Mazzolani, M. (1999) "Rotational capacity of aluminium beams under moment gradient II: numerical simulations." *Journal of Structural Engineering, ASCE*, 125(8): 921-929

[21] Zhu, J.H. and Young, B. (2009). "Design of aluminum alloy flexural members using direct strength method." *Journal of Structural Engineering, ASCE* 135(5): 558-566

[22] Kim, Y. and Peköz, P. (2010). "Ultimate flexural strength of aluminum sections" *Thin-walled structures*, 48(10-11): 857-865

[23] Su, M., Young, B. and Gardner, L. (2012), "Continuous beams tests on aluminium alloy hollow sections" *Proceeding of the Sixth International Conference on Coupled Instabilities in Metal Structures*, pp119-126 (2012, Glasgow)

[24] ABAQUS analysis user's manual (2010) version 6.10-1. ABAQUS Inc.
[25] Ellobody, E. and Young, B. (2005) "Structural performance of cold-formed high strength stainless steel columns", *Journal of Constructional Steel Research* 61 (12): 1631–1649
[26] Zhou, F. and Young, B. (2008) "Aluminum tubular sections subjected to web crippling—Part I: Tests and finite element analysis" *Thin-Walled Structures* 46 (4): 339–351
[27] Zhu, J.H. and Young, B. (2008a). "Numerical investigation and design of aluminum alloy circular hollow section columns", *Thin-Walled Structures* 46 (2008) 1437– 1449
[28] Mazzolani, F.M. (1994), *Aluminium alloy structures* 2nd. E&FN Spon Press

STABILIZATION EFFECT OF A TEXTILE MEMBRANE ON STEEL TUBE SUPPORTING ARCH

Ondrej Svoboda* and Josef Machacek*

*Czech Technical University in Prague, Faculty of Civil Engineering
Thakurova 7, 166 29 Prague, Czech Republic
e-mail: ondrej.svoboda.4@fsv.cvut.cz, webpage: http://people.fsv.cvut.cz/~machacek/

Keywords: Experimental verification, textile membrane, steel arch, stability, prestressing

Abstract. *Experimental investigation of a steel tube arch acting as a supporting internal element of textile membrane roofing together with preliminary numerical analysis is presented. Stabilizing effect of the membrane on load carrying capacity of the supporting structure is of the primary interest. While such structures are becoming frequent, complex analysis of membrane structures in interaction with steel structure (carbon/stainless steel perimeter or supporting elements) is rather demanding. To compare theoretical assumptions and results with reality, the model of a concert stage covered by fabric membrane and supported by arches was tested in laboratory and verified by numerical analysis. The model of reasonable size was created and tested to clarify the effect of the membrane on arch stability/deflection. Form of the structure was developed with help of form-finding software based on force-density method while prestressing and membrane stresses were received using SOFiSTiK software. Arrangement, membrane prestressing, loading steps and test evaluation is described in a detail. Finally preliminary theoretical arch assessment and test results are presented.*

1 INTRODUCTION

In last decades an enormous growth of textile membranes and plastic foils used for both permanent and temporary structures is apparent. New sophisticated materials were developed which enable light, esthetical, transparent or colorful covering of various surfaces exposed to weather and miscellaneous loadings.

The principal properties of these materials are published by relevant manufacturers, nevertheless the detailed anisotropic non-homogeneous structural behavior is still under investigation[1,2,3]. For common use the PVC coated polyester seems to be appropriate as inexpensive variant, giving up to 20 years lifetime (e.g. Précontraint FERRARI®), joined by welding or sewing. More expensive but longer lifetime provides glass fabric coated by PTFE (Teflon), possibly by silicon rubber or titanium dioxide, joined by bonding. Rather expensive but excellent material is expanded PTFE coated 2 sides by fluoropolymer film (TENARA®), joint by welding. The membranes may also be thermally insulated using Nanogel Aerogel™ and 2 sides coated with PTFE (in result translucent, with total thickness 9 mm, CABOT Cor.). High density polyethylene fabrics (HDPE, coated with LDPE) joined by sewing may also be used however, with short lifespan up to 10 years. Plastic foils of low thickness 50÷500 μm are used mainly as inflatable cushions, nowadays predominantly from ETFE (TEXLON®) or THV materials. Detailing of membrane structures and erection methods are well described by Seidel[4] and design in European Design Guide[5].

This paper describes experimental investigation of a membrane stabilizing effect to supporting steel arch. The interaction of textile membranes with supporting steelwork is demanding task and requires specialized software as EASY[6], FORTEN[7], SOFiSTiK[8], Rhino Membrane[9], NDN[10] or general sophisticated FEM software packages[11]. Possibility of simplified separate analysis of membranes and steel structure is limited by geometry due to non-linearity and inevitable prestressing[12]. Nevertheless, the supporting steel structure undergoes various assembly and definitive structural phases in which stabilizing effect of membranes on behavior of supporting steelwork is substantial.

During the tests the behavior of inner supporting steel arch loaded both alone and subsequently stabilized by a membrane was investigated and the results compared with preliminary non-linear analysis.

2 TEST MODEL DESIGN

The model represents an outdoor covered stage and its form was found using formfinder software[13]. The software enables intuitive manipulation with membrane shapes under required stress level in interactive way and export/import to other programs through DXF/DWG files. Constantly improved versions upgrade the software even for design of supporting elements. Theoretical background for finding membrane forms is well published[14, 15]. Supporting steelwork involves two supporting arches (outer and inner CHS tubes), bottom edge steel wire ropes and membrane plates, see Figure 1.

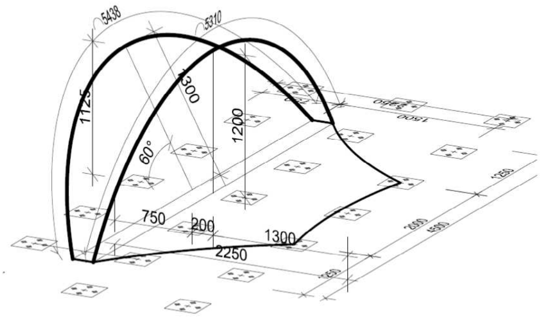

Figure 1: Geometry and View of the Model at Laboratory

The main dimensions of the model *LxBxH* are 4500x2250x1200 [mm], with height of the inner arch 1200 mm and inclination of the outer arch 60° in respect to horizontal. The membrane is PVC coated polyester fabric Ferrari® Précontraint 702S with opaque surface (weight 830 g/m^2).

The fabric is made of polyester scrim coated both sides with liquid PVC and PVDF topcoat, weldable for joining. The fabric developed and patented by the French manufacturing group Serge Ferrari is unique due to prestressing the base fabric before and during the coating operations. The operation ensures in both warp and fill directions similar elongation behavior and minimum creep. The thick coating supplies the membrane also with longevity and extraordinary resistance against soiling. Concerning material characteristics the biaxial test performed by Lab BLUM Stuttgart[16] is available. Both warp and fill braking strength was considered as $\sigma_{ult} \approx 56$ kN/m, while working stress $\sigma_{max} = \sigma_{ult}/5 \approx 11.2$ kN/m to exclude tearing and prestressing around $\sigma_p \approx 0.5$ kN/m. However, the material is due to its structure non-homogeneous, orthotropic (warp and fill directions) and non-linear. In accord with recommendation by Tensinet Analysis & Materials working Group[1] a simplified elastic approach may be employed using plane stress theory. The supplied test data give elastic moduli for warp and fill directions $E \approx 592.0$ and 342.9 kN/m respectively and Poisson's ratios $\nu \approx 1.01$ and 0.35 respectively (note the strange $\nu > 0.5$ necessary for modeling high level of warp-fill interaction and large negative strains occurring in fabrics under biaxial loading). For more demanding analyses Gosling[1] suggests strain-strain-stress approach using response surfaces linking strains to stresses through three dimensional representations for FE analysis.

New investigation by Galliot and Luchsinger[2,3] emerging from experimental results recommends for such textile membranes non-linear material model which depends on load ratios in warp and fill directions. Resulting model supposes orthotropic linear elastic behaviour for a given load ratio and is described by five parameters: warp and fill Young's moduli for 1:1 load ratio, the change in warp and fill Young's moduli and the Poisson's ratio. These values for FERRARI® 702 were established as 635.3 kN/m, 661.9 kN/m, 295.0 kN/m 168.5 kN/m and 0.196 respectively. Nevertheless, for preliminary numerical analyses a simplified isotropic approach with E = 660 kN/m and ν = 0.23 was used in this study.

The tubes from steel S355J0 were hot-formed in workshop. The investigated inner tube of ø 26.9x3.2 [mm] and outer one of ø 88.9x3.2 [mm] were welded to steel blocks to form frame acc. to Figure 1. Coupon tests of the inner steel tube resulted into average yield strength f_y = 475 MPa, ultimate strength f_u = 595 MPa and elongation 27.1 %. Modulus of elasticity was considered in accord with Eurocode 3 as E = 210 GPa.

Membrane was joined to the outer arch using riveted aluminium keder profile while to inner tube via alternating pockets. Common 7x7 wire peripheral rope from CarlStahl company with diameter of 6mm in curved cuff fastened the membrane to corner plates and anchors. The investigated inner arch was fitted with transducers (electrical potentiometers) in vertical (V), transverse (H) and longitudinal (L) directions to measure deflections. Their positions and loading points (P) are shown in Figure 2. In supports and middle of the arch strain gauges were placed always in four mutually perpendicular positions for later comparison with analysis.

The prestressing of the membrane resulted from the membrane cut as prepared by appropriate software[6] considering uniform prestressing of roughly P = 0.5 kN/m. During assembly the peripheral ropes were tightened and the membrane checked against wrinkling. Eight strain gages were placed at various locations within the membrane just for rough information on prestressing values. The measuring before and after prestressing resulted into average prestrain value of ε_y = 140 μm/m (i.e. $P \approx 0.09$ kN/m) in perpendicular direction to supporting arches and value of ε_x = 450 μm/m (i.e. $P \approx 0.30$ kN/m) in parallel direction to the arches.

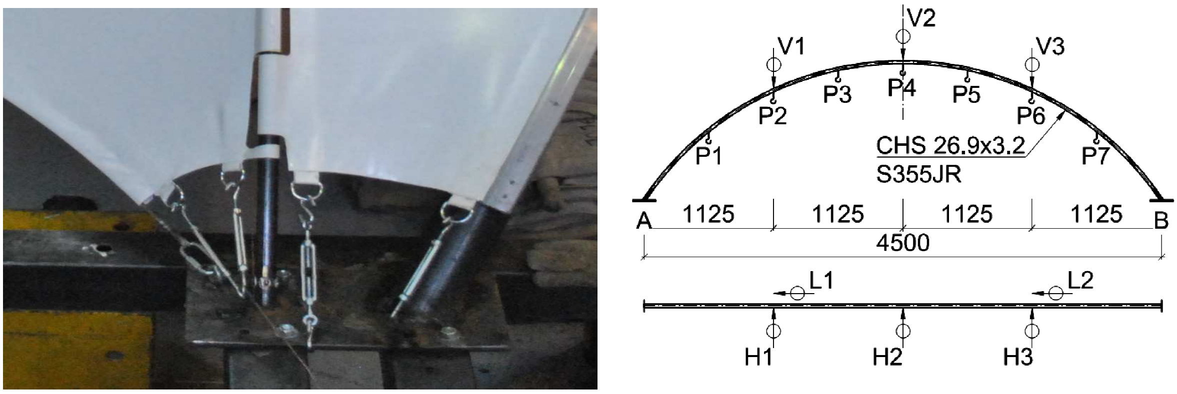

Figure 2: Anchoring of the Membrane (left), Position of Transducers and Loading (right)

3 TEST LOADING AND RESULTS

Two phases of each loading configuration were performed to investigate the stabilizing effect of the membrane. First the inner arch alone was loaded and seconds, after membrane assembly, the complete membrane structure in the same way. For loading calibrated pouches with steel pellets were used and suspended from seven given points P at the arch. The loadings were carefully arranged to simulate uniform symmetrical loading and asymmetrical loading corresponding to the first in-plane buckling mode. Loadings for arch alone are in Figure 3, for complete membrane structure in Figure 4.

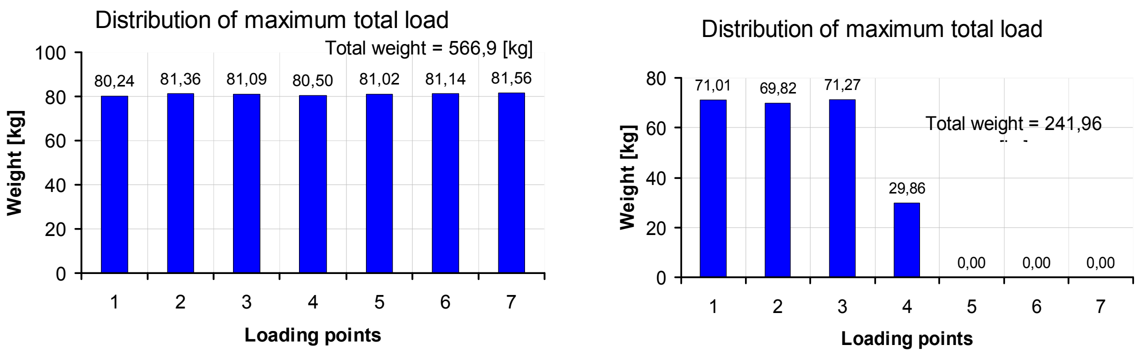

Figure 3: Maximum Symmetrical and Asymmetrical Loading for Arch Alone

Loading steps were roughly 1/10 of maximum loading, each followed by unloading. The tests were terminated when abnormal deflections out-of-arch plane or in-arch-plane were reached.

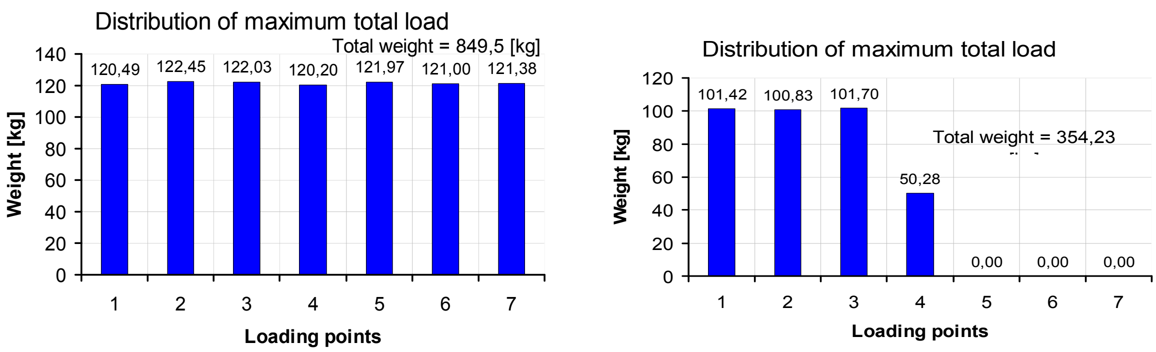

Figure 4: Maximum Symmetrical and Asymmetrical Loading for Complete Membrane Structure

3.1 Symmetrical loadings

Deflections of the inner arch under increasing loading in vertical and horizontal directions are shown in Figure 5 (unloading is not included and generally was fully elastic). The arch without membrane buckled out-of-plane at total loading approaching F_0 = 5.5 kN, with associated vertical deflection along all span down. On the other side the test with arch stabilized by the membrane was terminated under total load of F_M = 8.3 kN, showing very small and nearly linear increase of the mid span deflection. Stabilizing effect of the membrane is therefore enormous.

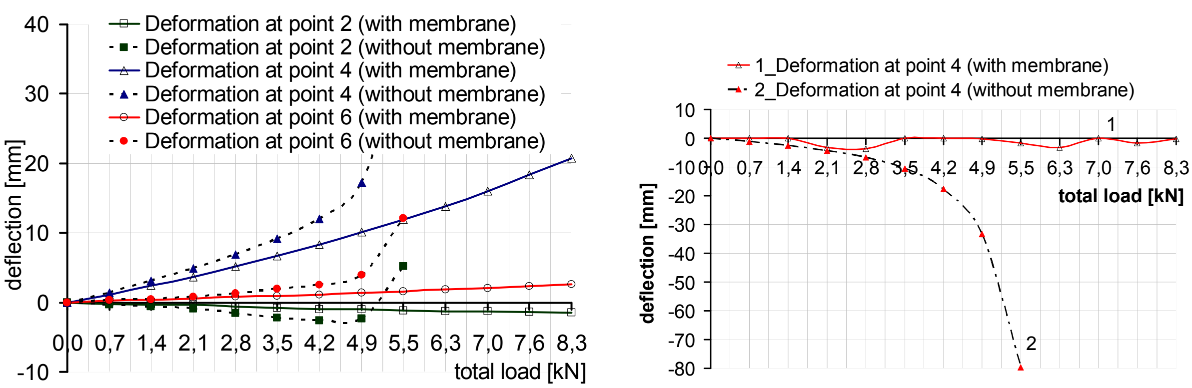

Figure 5: Vertical Displacement, Positive Down (left), Transverse Displacement (right)

3.2 Asymmetrical loadings

Vertical and transverse horizontal deflections under increasing loading are shown in Figure 6. Testing of the arch without membrane ("0") terminated under total loading $F_0 = 2.37$ kN, giving maximal vertical deflection δ_0 = 41.3 mm and horizontal one η_0 = 3.5 mm. The arch stabilized by membrane ("M") deflected much less, giving for the same loading $F_M = F_0 =$ 2.37 kN values δ_M = 18.5 mm and η_M = 0.5 mm. The stabilizing effect of the membrane concerning vertical deflection resulted into reduction of 45 %.

Difference comparing vertical deflections in positions V1 and V3 (according to Figure 2) gives $\Delta\delta_0$ = 68.3 mm and $\Delta\delta_M$ = 32.9 mm.

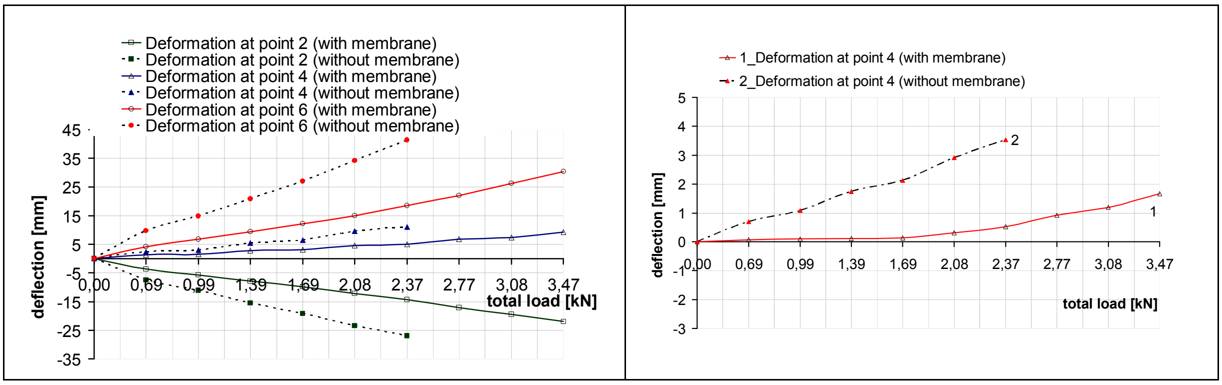

Figure 6: Vertical Displacement (left), Transverse Displacement (right)

Measured displacements and stresses (not presented) prove expected enormous effect of the membrane on buckling load and strength of inner supporting arch, particularly in asymmetrical loadings. Tests can be used for validation of corresponding numerical analyses.

4 NUMERICAL ANALYSIS

Preliminary GNIA (geometrically non-linear analysis with imperfections) using SOFiSTiK software was performed both for the inner arch alone and the complete membrane structure.

Arch alone analysis: The investigated inner tube was introduced as ø 26.9x3.2 [mm] with built-in supports, material S355J0 and Young's modulus E = 210 GPa. Measured shape of the inner arch tube was introduced into analysis (theoretical radius R = 2709 mm, support inclination 55.941°) with out-of-plane (transverse) deflection at the crown (w_0 = 17 mm). For the first information an elastic buckling analysis of the perfect arch under symmetrical loading in accordance with Figure 3 resulted into total critical loads $TL_{cr,1}$ = 6.7 kN (out-of-plane single wave buckling), $TL_{cr,2}$ = 15.4 kN (out-of-plane two waves buckling), $TL_{cr,3}$ = 18.7 kN (in-plane two waves buckling), etc.

GNIA transverse deflection curves for symmetrical loading are shown in Figure 7, indicating the first out-of-plane bifurcation earlier but in accordance with test, at roughly 4.9 kN. Similarly the vertical deflections for asymmetrical loading correspond well to test results, Figure 7 (right).

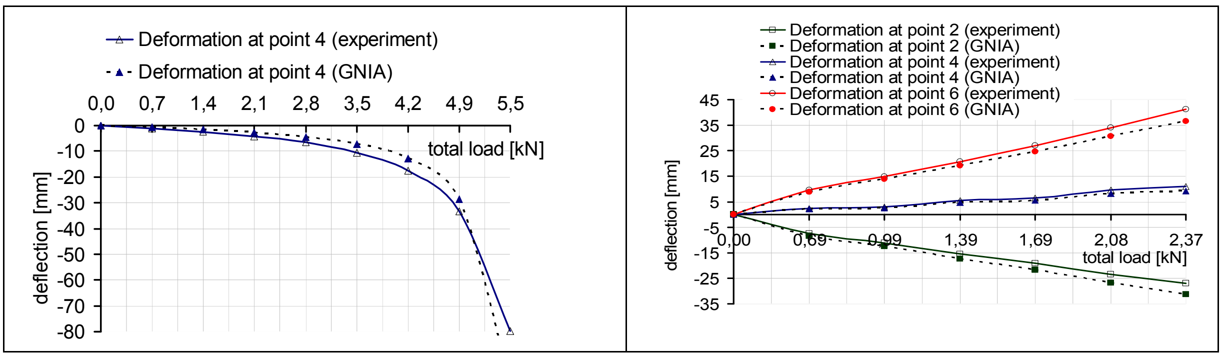

Figure 7: Comparison of the Test and GNIA Deflections of the Arch Alone (Transverse Deflection for Symmetrical Loading left, Vertical Deflection for Asymmetrical Loading right)

Membrane structure analysis: The membrane FERRARI® 702 was considered in a simplified way as an isotropic material. Due to uncertain thickness instead of stresses in MPa unit membrane forces in kN/m (N/mm) were introduced with Young's modulus E = 660 kN/m and Poisson's ratio $\nu = 0.23^2$. The uniform plane membrane prestressing in the analysis were considered in several variants (from P = 0.1 to 0.5 kN/m) due to uncertainty in measuring giving $P \approx 0.09$ up to 0.30 kN/m. Comparison of the test vertical deflection curves for the inner tube of the complete membrane structure and those resulting from GNIA analyses are shown in Figure 8.

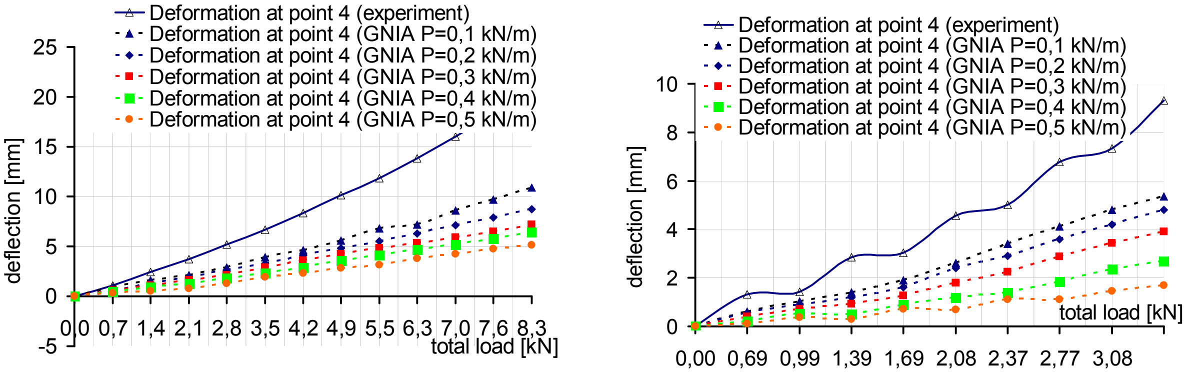

Figure 8: Comparison of the Test and GNIA Vertical Deflections of the Arch Stabilized by the Membrane (Symmetrical Loading left, Asymmetrical Loading right)

5 CONCLUSIONS

The paper describes an experimental investigation of the structural model of possible outdoor covered stage consisting from membrane of polyester fabric Ferrari® Précontraint 702S and supporting steel arches. The primary interest of the investigation concerned the stabilizing effect of the textile membrane on supporting inner steel arch behaviour serving as validation data for subsequent numerical geometrically non-linear analysis.

Experimental values illustrate expected substantial decrease of deflections/stresses and elimination of instability/ breakthrough of the supporting arch due to the membrane. Preliminary GNIA of the whole structure using SOFiSTiK software package proved to correspond well with the measured values for the arch alone (provided the measured imperfections of the arch were introduced). However, deflections of the whole membrane assembly depend considerably on the membrane prestressing which needs to be determined in a high quality to cover properly the behavior. Pockets used for fastening the membrane to the inner tested arch seem to be slightly slack and clear up the differences between GNIA and test in Figure 8.

Parametric studies on the instability phenomenon and its elimination for various membrane/arch material/geometrical data are under progress.

6 ACKNOWLEDGEMENT

All laboratory works were performed at the Central laboratory of Faculty of Civil Engineering of CTU in Prague. Thanks are due to relevant technicians and technical managers.

Supply of fully formed steel tubes by company EXCON a.s. Prague including delivery to laboratory is highly appreciated.

Thanks are due to company Archtex s.r.o. Prague for help with preparation and assembly of the textile membrane.

Financial support of the CTU in Prague grant SGS14/038/OHK1/1T/11 and grant of the Czech Grant Agency GACR No. 105/13/25781S is gratefully acknowledged.

REFERENCES

[1] P. Gosling, *Basic philosophy and calling notice, Tensinet analysis & Material working group*, Tensinews No. 13 (www.tensinet.com), pp. 12-15, (2007).

[2] C. Galliot, R. H. Luchsinger, *A simple model describing the non/linear biaxial tensile behaviour of PVC/coated polyester fabrics for use in finite element analysis*“, Composite Structures, Vol. 90, No 4, pp. 438-447 (2009).
[3] C. Galliot, R. H. Luchsinger, *Non-linear properties of PVC-coated fabrics used in tensairity structures*“, ICCM17, 27-31 July 2009, Edinburgh, UK, 10 p. (2009).
[4] M. Seidel, *Tensile Surface Structures - A practical guide to cable and membrane construction*, John Wiley & Sons, 240 p. (2009).
[5] B. Foster, M. Mollaert, *European design guide for tensile surface structures*, Tensinet, 354 p. (2004).
[6] technet gmbh Berlin-Stuttgart, http://www.technet-gmbh.com.
[7] ixForten 4000, http://www.ixforten.com/.
[8] SOFiSTiK 2014, http://www.sofistik.de/.
[9] Rhino Membrane, http://www.membranes24.com/rhino-membrane.html.
[10] membrane NDN software, http://www.ndnsoftware.com/.
[11] D. S. Wakefield, *Engineering analysis of tension structures: Theory and practice*, Engineering Structures, Vol. 21, No 8, pp. 680-690 (1999).
[12] D. Jermoljev, J. Machacek, *Interaction of non-metallic membranes with supporting steel structure,* METNET 2012 in Izmir, HAMK, October 10-11, Turkey, pp. 42-53 (2012).
[13] Formfinder Software GmbH, Wien. http://www.formfinder.at/main/software/.
[14] K. Linkwitz, *About formfinding of double-curved structures*, Engineering Structures, Vol. 21, No 8, pp. 709-718 (1999).
[15] L. Gründig, E. Moncrieff, P. Singer, D. Ströbel, *A history of the principal developments and application of the force density method in Germany*, Proc. IASS-IACM 2000, June 4-7, Greece, 13 p., (2000).
[16] Laboratorium BLUM Stuttgart, *Report on biaxial tests Précontraint 702*. Web pages of http://arc-ae.net/ARC1010-Pisco/, (2005).

12th International Conference on
Steel, Space and Composite Structures
28-30 May 2014, Prague, Czech Republic

NONLINEAR INELASTIC ANALYSIS OF SEMI-RIGID STEEL FRAMES

Tai H. Thai* and Brian Uy†

Centre for Infrastructure Engineering and Safety, The University of New South Wales
Sydney, NSW 2052, Australia
e-mail: t.thai@unsw.edu.au

Keywords: Advanced analysis, semi-rigid connection, steel frame, force-based method

Abstract. *In this paper, a reliable numerical procedure accounting for all sources of nonlinearities is presented for the nonlinear inelastic static analysis of space steel frames with semi-rigid connections. The material nonlinearities due to the residual stresses and material yielding are considered using a force-based fibre beam-column element. In this element, the spread of plasticity over the cross section and along the member length is captured by tracing the uniaxial stress-strain relations of each fibre on the cross sections located at the integration points along the member length. The geometric nonlinearities are included using geometric stiffness matrix and updating node coordinates. The nonlinear semi-rigid behaviour of beam-to-column connections is simulated using a zero-length connection element comprising of six translational and rotational springs. These elements are then implemented in a computer programme to study the ultimate strengths and responses of semi-rigid steel frames. The validity of the proposed programme is verified by comparing the obtained results with those available in the literature.*

1 INTRODUCTION

Since steel structures usually exhibit significantly nonlinear behaviour prior to achieving their ultimate load-carrying capacity, a second-order inelastic analysis or advanced analysis is the most rational mean for assessment of the performance of a whole structural system instead of using a conventional analysis/design approach. The advanced analysis of semi-rigid steel frames can be carried out using beam-column elements with either lumped-plasticity (plastic-hinge) model[1] or distributed-plasticity model[2]. Although the plastic-hinge model is simpler and more computationally efficient than the distributed-plasticity one, its accuracy depends heavily on the yield surface which is not always available and accurate for every section. Whereas the distributed-plasticity model can accurately capture the spread of plasticity over the cross section and along the member length by tracing the uniaxial stress-strain relation of each fibre on the cross sections located at the integration points along the member length. This model is adopted herein to study the inelastic behaviour of semi-rigid steel frames.

In general, a fibre beam-column element can be developed using either displacement-based method or force-based method. The displacement-based formulation which is commonly used in a standard finite element program is based on the assumptions of linear curvature and constant axial strain along the element, and consequently, requires many elements per member in the

* Postdoctoral Fellow
† Professor

modelling. The force-based formulation, on the other hand, is based on the assumptions of linear bending moments and constant axial force which strictly satisfy the equilibrium of the element in absence of element loads. As a result, only one element per member is required in the modelling. It is worth of noting that the implementation of the force-based formulation in a standard finite element program requires an iteration during the element state determination to satisfy the element equilibrium and compatibility[3]. However, this iteration can be eliminated by using the procedure proposed by Neuenhofer and Filippou[4] where both residual element displacements and unbalanced section forces are accepted in calculating element resisting forces, and thus further expanding the benefits of force-based models.

Although the force-based fibre models have been developed and well discussed in the above mentioned studies, no literature has been reported for the use of the force-based models for the advanced analysis of steel frames with semi-rigid connections. In this paper, the force-based fibre element is employed to predict the ultimate strength and behaviour of semi-rigid steel frames. The semi-rigid behaviour of beam-to-column connections is simulated using a zero-length connection element with six translational and rotational springs. Both force-based fibre beam-column and connection elements are then implemented in a computer programme written by the authors[5-6] for advanced analysis of steel frameworks. Numerical examples are presented to verify the validity of the present program.

2 ELEMENT FORMULATION

2.1 Force-based fibre beam column element

The displacements of a beam-column element can be decomposed into two parts as the rigid displacements and natural deformations. Since the rigid displacements do not introduce any strain on the element, the element stiffness matrix is derived only from the natural deformations. The natural deformations and forces of a beam-column element AB at the element and section level as shown in Figure 1 are grouped in the following vectors

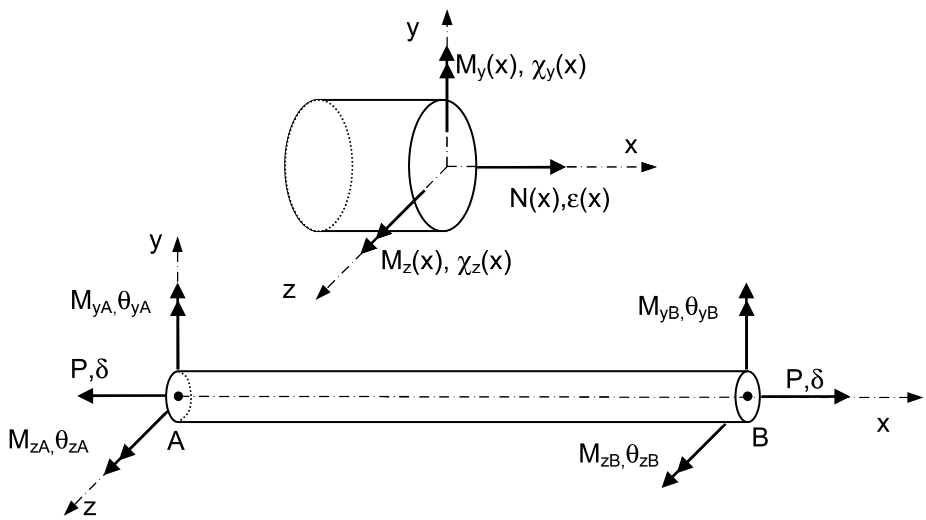

Figure 1: Natural Deformations and Forces at Element and Section Level

Element deformation vector

$$\{q\} = \{\delta \quad \theta_{yA} \quad \theta_{yB} \quad \theta_{zA} \quad \theta_{zB}\}^T \tag{1}$$

Element force vector

$$\{Q\} = \{P \quad M_{yA} \quad M_{yB} \quad M_{zA} \quad M_{zB}\}^T \tag{2}$$

Section deformation vector

$$\{d(x)\} = \{\varepsilon(x) \quad \chi_y(x) \quad \chi_z(x)\}^T \tag{3}$$

Section force vector

$$\{D(x)\} = \{N(x) \quad M_y(x) \quad M_z(x)\}^T \tag{4}$$

In the fibre model the whole element is divided into a number of cross sections located at the integration points along the member length, and each section is further divided into many fibres as shown in Figure 2. Thus, the spread of plasticity over the cross section and along the member length is easily captured by tracing the uniaxial stress-strain relations of each fibre on the cross sections.

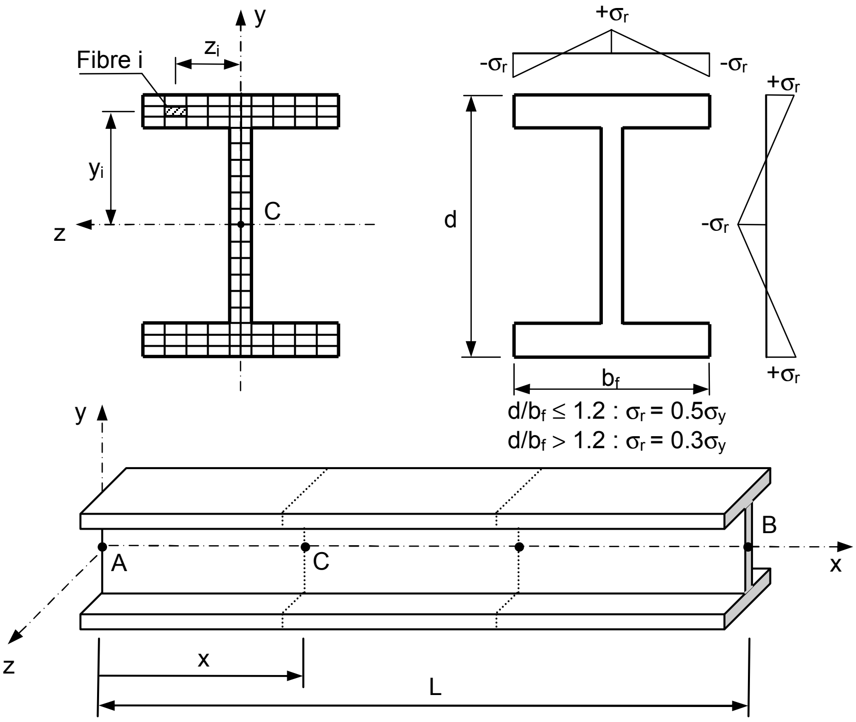

Figure 2: Fibre Model and ESSC Residual Stress Pattern for I-Section

By using the fibre concept, the residual stress can be easily included as the initial stress of a fibre. Based on the element equilibrium, the resisting forces at each section are derived from the fibre stress σ_i as

$$\{D(x)\} = \sum_{i=1}^{nfib} \sigma_i A_i \{1 \quad z_i \quad -y_i\}^T \tag{5}$$

From the Euler-Bernoulli assumption, the fibre strains are related to the section deformation through the compatibility condition

$$\varepsilon_i(x,y,z) = \varepsilon(x) + z_i \chi_y(x) - y_i \chi_y(x) \tag{6}$$

The fibre stresses are computed from the fibre strains using the constitutive equations

$$\sigma_i = E_i \varepsilon_i \tag{7}$$

where E_i is the tangent modulus of the fibre i. By substituting Eqs. (6) and (7) into Eq. (5), the section forces is derived from the section deformation as

$$\{D(x)\} = [k(x)]\{d(x)\} \tag{8}$$

where $[k(x)]$ is the section stiffness given by

$$\left[k(x)\right]=\sum_{i=1}^{nfib}E_iA_i\begin{bmatrix}1 & z_i & -y_i\\ z_i & z_i^2 & -z_iy_i\\ -y_i & -z_iy_i & y_i^2\end{bmatrix} \tag{9}$$

In the force-based method, the section forces are related to the element forces by

$$\left\{D(x)\right\}=\left[b(x)\right]\{Q\} \tag{10}$$

where $\left[b(x)\right]$ is a force interpolation matrix expressed in the absence of element loads as

$$\left[b(x)\right]=\begin{bmatrix}1 & 0 & 0 & 0 & 0\\ 0 & x/L-1 & x/L & 0 & 0\\ 0 & 0 & 0 & x/L-1 & x/L\end{bmatrix} \tag{11}$$

Adopting the small strain assumption, the principle of virtual work leads to the compatibility condition

$$\{q\}=\int_0^L\left[b(x)\right]^T\left\{d(x)\right\}dx \tag{12}$$

Using Eqs. (8) and (10), Eq. (12) can be rewritten as

$$\{q\}=\int_0^L\left[b(x)\right]^T\left[k(x)\right]^{-1}\left[b(x)\right]^T\{Q\}dx \tag{13}$$

The element flexibility matrix can be obtained from Eq. (13) as

$$[F]=\frac{\partial\{q\}}{\partial\{Q\}}=\int_0^L\left[b(x)\right]^T\left[k(x)\right]^{-1}\left[b(x)\right]^T dx \tag{14}$$

and the element stiffness matrix is obtained by inverting the element flexibility matrix

$$[K]=[F]^{-1} \tag{15}$$

Equations (12) and (14) imply that numerical integration is required. In this work, the Gauss-Lobatto quadrature scheme is adopted since it has integration points at each end of the element, where the plastic deformation is important, and hence performs better in detecting yielding. This integration scheme requires at least three integration points for a linear curvature distribution. Alternatively a Gauss quadrature requiring only two sections can also be used. However, this scheme is not efficient because the location of the integration points does not include the beam ends. Once the element stiffness in Eq. (15) is obtained, it is augmented with the GJ/L term to introduce the torsion term in the stiffness matrix. It should be noted that the element stiffness matrix given in Eq. (15) is only derived for the beam-column element without rigid body modes. To include the rigid body modes, the element stiffness matrix is modified as

$$[K_e]=[T]^T[K][T] \tag{16}$$

where the transformation matrix $[T]$ is given by

$$[T]_{6\times12}=\begin{bmatrix}-1 & 0 & 0 & 0 & 0 & 0 & 1 & 0 & 0 & 0 & 0 & 0\\ 0 & 0 & -1/L & 0 & 1 & 0 & 0 & 0 & 1/L & 0 & 0 & 0\\ 0 & 0 & -1/L & 0 & 0 & 0 & 0 & 0 & 1/L & 0 & 1 & 0\\ 0 & 1/L & 0 & 0 & 0 & 1 & 0 & -1/L & 0 & 0 & 0 & 0\\ 0 & 1/L & 0 & 0 & 0 & 0 & 0 & -1/L & 0 & 0 & 0 & 1\\ 0 & 0 & 0 & 1 & 0 & 0 & 0 & 0 & 0 & -1 & 0 & 0\end{bmatrix} \tag{17}$$

The following is a step-by-step summary of how to derive the element resisting forces from the known element displacement increments $\left\{\Delta U^i\right\}$ for the current iteration i in a nonlinear solution strategy.

Step 1: Extract the natural element deformation increments from $\{\Delta U^i\}$

$$\{\Delta q^i\} = [T]\{\Delta U^i\} \tag{18}$$

Step 2: Compute the element force increments

$$\{\Delta Q^i\} = \left[K^{i-1}\right]\{\Delta q^i\} \tag{19}$$

Step 3: Compute the section force increments

$$\{\Delta D^i(x)\} = \left[b(x)\right]\{\Delta Q^i\} + \{D_{unb}^{i-1}(x)\} \tag{20}$$

with $\{D_{unb}^{i-1}(x)\}$ being the unbalanced section force from the previous step according to Step 12.

Step 4: Compute the section deformation increments

$$\{\Delta d^i(x)\} = \left[k^{i-1}(x)\right]^{-1}\{\Delta D^i(x)\} \tag{21}$$

Step 5: Compute the fibre strain increments according to the incremental form of Eq. (6), and update the fibre strain $\varepsilon_i(x,y,z)$, fibre stress $\sigma_i(x,y,z)$ and fibre tangent modulus $E_i(x,y,z)$

Step 6: Compute the section resisting forces $\{D^i(x)\}$ according to Eq. (5)

Step 7: Update section stiffness $\left[k^i(x)\right]$ according to Eq. (9)

Step 8: Compute the unbalanced section deformation

$$\{d_{unb}^i(x)\} = \left[k^i(x)\right]^{-1}\left[\{D^{i-1}(x)\} + \{\Delta D^i(x)\} - \{D^i(x)\}\right] \tag{22}$$

Step 9: Compute the unbalanced element deformation

$$\{q_{unb}^i\} = \int_0^L \left[b(x)\right]^T \{d_{unb}^i(x)\}dx \tag{23}$$

Step 10: Update the element stiffness matrix $\left[K^i\right]$ according to Eq. (15)

Step 11: Compute the element resisting forces

$$\{Q^i\} = \{Q^{i-1}\} + \{\Delta Q^i\} - \left[K^i\right]\{q_{unb}^i\} \tag{24}$$

Step 12: Update the unbalanced section forces used in Step 3 for the next iteration $i+1$

$$\{D_{unb}^i(x)\} = \left[b(x)\right]\{Q^i\} - \{D^i(x)\} \tag{25}$$

By modifying the element resisting forces for the current iteration i with the term $\left[K^i\right]\{q_{unb}^i\}$, the compatibility is re-established and an iterative element state determination is unnecessary[4].

2.2 Zero-length connection element

To simulate the nonlinear semi-rigid behaviour of the beam-to-column connection, a zero-length connection element with three translational and three rotational springs is developed. This multi-spring element connects two nodes having identical coordinates. The spring element can also be used to simulate the rigid or hinge connection by assigning a very large or small stiffness value. The incremental form of the natural force-deformation relation of the connection element in which the coupling effects between springs are ignored is given by

$$\begin{Bmatrix} \Delta N_x \\ \Delta N_y \\ \Delta N_z \\ \Delta M_x \\ \Delta M_y \\ \Delta M_z \end{Bmatrix} = \begin{bmatrix} R_x^\delta & 0 & 0 & 0 & 0 & 0 \\ 0 & R_y^\delta & 0 & 0 & 0 & 0 \\ 0 & 0 & R_z^\delta & 0 & 0 & 0 \\ 0 & 0 & 0 & R_x^\theta & 0 & 0 \\ 0 & 0 & 0 & 0 & R_y^\theta & 0 \\ 0 & 0 & 0 & 0 & 0 & R_z^\theta \end{bmatrix} \begin{Bmatrix} \Delta \delta_x \\ \Delta \delta_y \\ \Delta \delta_z \\ \Delta \theta_x \\ \Delta \theta_y \\ \Delta \theta_z \end{Bmatrix} \tag{26}$$

where R_n^δ and R_n^θ are respectively the stiffness components of the translational and rotational springs with respect to the n axis ($n = x, y, z$). In this study, the translational springs R_n^δ and torsional spring R_x^θ are modelled by rigid springs, whilst the bending springs (R_y^θ and R_z^θ) are modelled by the nonlinear springs using the three-parameter model proposed by Kishi and Chen[7]. The Kishi-Chen model contains three parameters: (1) initial connection stiffness R_{ki}, (2) ultimate connection moment capacity M_u and (3) shape parameter n as shown in Figure 3. The moment-rotation relation of the Kishi-Chen model is expressed as

$$M = \frac{R_{ki}\theta}{\left[1 + \left(|\theta|/\theta_0\right)^n\right]^{1/n}} \;,\quad \theta_0 = \frac{M_u}{R_{ki}} \tag{27}$$

The tangent stiffness R_{kt} at an arbitrary rotation θ can be derived by differentiating Eq. (27)

$$R_{kt} = \frac{R_{ki}}{\left[1 + \left(|\theta|/\theta_0\right)^n\right]^{1+1/n}} \tag{28}$$

The force-deformation relation of the connection element with 12 degree-of-freedom can be obtained from Eq. (26) using the following transformation matrix

$$[T]_{6\times12} = \begin{bmatrix} -1 & 0 & 0 & 0 & 0 & 0 & 1 & 0 & 0 & 0 & 0 & 0 \\ 0 & -1 & 0 & 0 & 0 & 0 & 0 & 1 & 0 & 0 & 0 & 0 \\ 0 & 0 & -1 & 0 & 0 & 0 & 0 & 0 & 1 & 0 & 0 & 0 \\ 0 & 0 & 0 & -1 & 0 & 0 & 0 & 0 & 0 & 1 & 0 & 0 \\ 0 & 0 & 0 & 0 & -1 & 0 & 0 & 0 & 0 & 0 & 1 & 0 \\ 0 & 0 & 0 & 0 & 0 & -1 & 0 & 0 & 0 & 0 & 0 & 1 \end{bmatrix} \tag{29}$$

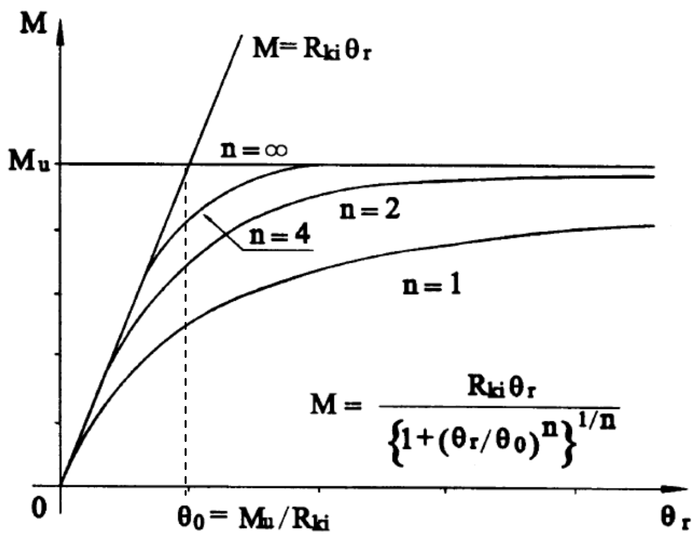

Figure 3: Moment-Rotation Behaviour of Three-Parameter Model [7]

3 VERIFICATION

The above force-based fibre beam-column element and zero-length connection element are implemented in a computer code[5-6] to study the second-order inelastic response of semi-rigid steel frames under static loads. The predictions obtained from the proposed program are compared with the results from existing studies through three numerical examples to verify for validity. In all numerical examples, each frame member is modelled by a single element with five integration points along the length and 80 fibres (40 at two flanges and 40 at the web) on each section. The residual stresses are also included using the ESSC residual stress pattern shown in Figure 2.

3.1 Vogel portal frame

The geometric dimension, section and material properties and applied loading of the Vogel portal frame are shown in Figure 4(a). Vogel[8] first analysed this frame with rigid connections as the European calibration frame for static inelastic analysis. Ngo-Huu et al.[9] recently studied the semi-rigid behaviour of this frame by replacing the beam-to-column connections by semi-rigid ones with the following connection properties[9]: initial connection stiffness $R_{ki} = 31,640$ kNm/rad, ultimate connection moment capacity $M_u = 141.2$ kNm, and shape parameter $n = 0.98$. It is worth noting that Vogel[8] used the plastic zone method with 15 elements for the columns and 14 elements for the beam, whilst Ngo-Huu et al.[9] used the refined plastic-hinge method with only one element per member in the modelling as in this study. The initial geometrical imperfections of the frame have been modelled directly in the analysis.

The obtained load-displacement predictions for both rigid and semi-rigid frames are compared with those given by Vogel[8] for the rigid one and by Ngo-Huu et al.[9] for the semi-rigid one in Figure 4(b). It can be seen that the proposed analysis results are in close agreement with both the plastic zone and refined plastic-hinge analyses. As expected, the strength of the semi-rigid frame is smaller than that of the rigid one.

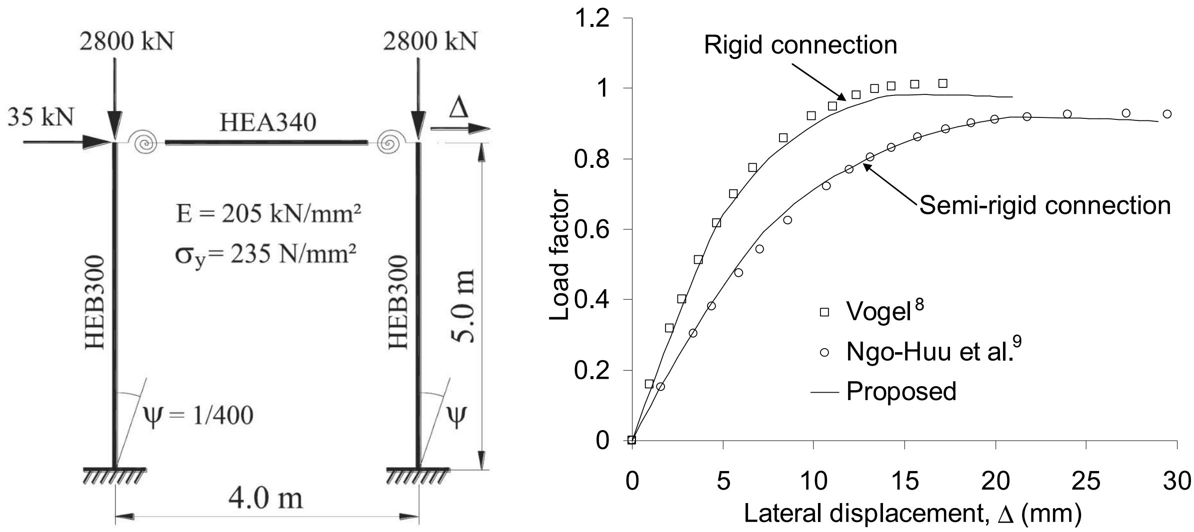

(a) Dimensions and properties (b) Load-displacement response

Figure 4: Vogel Portal Frame with Semi-Rigid Connection

3.2 Stelmack two-storey frame

The one-bay two-storey flexibly connected steel frame tested by Stelmack[10] is selected as a benchmark frame in the present study. The frame was fabricated from the same A36 W5×16 sections, and all columns are pinned supports as shown in Figure 5(a). The connections used in the frame were bolted top and seat angles connections of L4×4×1/2. Three parameters of the Kishi-Chen power model are determined by a curve fitting with the experimental moment-rotation curve as follows[1]: $R_{ki} = 4,520$ kNm/rad, $M_u = 24.9$ kNm, $n = 0.91$. In the analysis, gravity loading of 10.68 kN was first applied at third points of the beam of the first floor, and then lateral loads were applied as the second loading sequence.

The lateral load-displacement curves obtained by the present study are compared with both experimental results reported by Stelmack[10] and analytical results generated by Kim and Choi[1] using the refined plastic-hinge method in Figure 5(b). A good agreement between the results confirms the accuracy of the proposed program in predicting the ultimate strength and behaviour of semi-rigid frames.

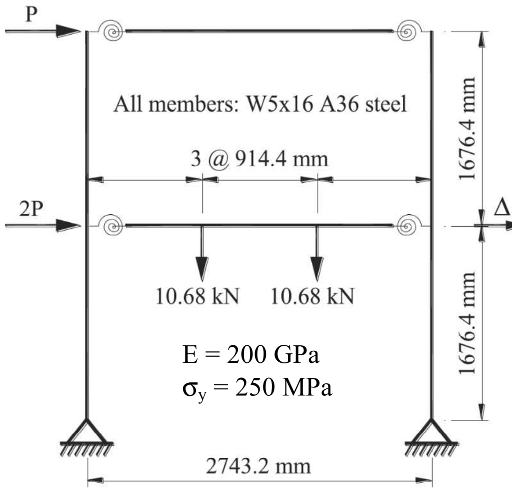

(a) Dimensions and properties

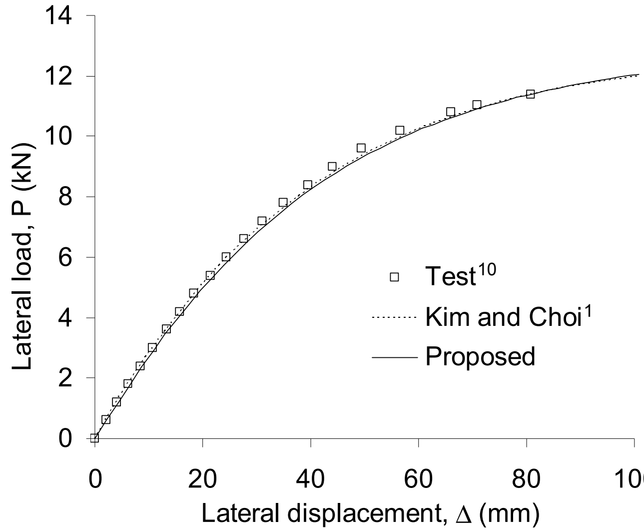

(b) Load-displacement response

Figure 5: Stelmack Two-Storey Frame

3.3 Orbison six-storey space frame

The last verification is carried out for a six-storey space frame. The geometric dimensions and section properties are shown in Figure 6(a). A36 steel with the yield stress of 250 MPa and Young's modulus of 206,850 MPa is used for all frame members. The frame is subjected to the combined action of gravity loads and lateral loads acting in the Y-direction. Uniform floor pressure of 9.6 kN/m^2 is converted to equivalent concentrated loads on the top of the columns, whilst wind loads are simulated by point loads of 53.376 kN in the Y-direction at every beam-column joints. The effect of rigid floor diaphragm action is neglected in this study.

The frame with the rigid joints was first analysed by Orbison et al.[11] using the plastic-hinge method. In order to assess the effects of the semi-rigid joints on the load-displacement response of the frame, Chiorean[2] modified the frame by replacing the rigid beam-to-column connections by the semi-rigid ones. The bolted top and seat angles connections were assumed for all beam-to-column connections of the frame and their characteristics are listed in Figure 6(b).

Figure 6(c) shows the load-displacement curves in the Y-direction at node A at the roof of the frame for both rigid and semi-rigid connections. The predictions obtained from the proposed program are compared with those generated by Chiorean[2] using the plastic zone approach. It can be observed that the obtained predictions are very close to the plastic zone solutions[2] especially for the ultimate load-carrying capacities. The slightly difference in the initial stiffness of the frame is due to the effects of shear deformations which is not considered in this study. It is indicated from Figure 6(c) that the effects of the semi-rigid connection is significant and should be considered in the advanced analysis of steel frameworks.

It should be noted that both present fibre analysis and plastic zone analysis by Chiorean[2] use the same number of element in the modelling of the frame. However, the plastic zone analysis by Chiorean[2] was based on a force-strain relationship which is not always available and accurate for every section. Meanwhile, the present analysis is based on the fibre model and thus can be used for any framed structures with arbitrary cross-sections.

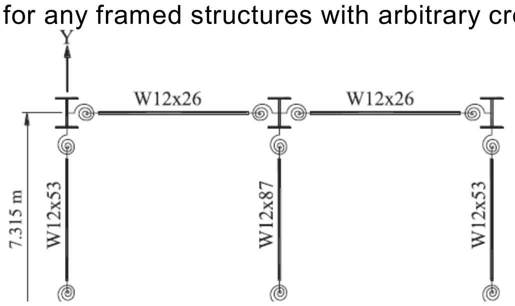

Beam section	Bending axis	M_u (kNm)	R_{ki} (kNm/rad)	n
W12x87	Strong	300	160,503.20	1.57
	Weak	300	52,267.75	1.57
W12x53	Strong	300	92,185.09	1.57
	Weak	300	20,776.82	1.58
W12x26	Strong	200	44,247.80	0.86
	Weak	200	3,752.54	0.86

(b) Connection properties[2]

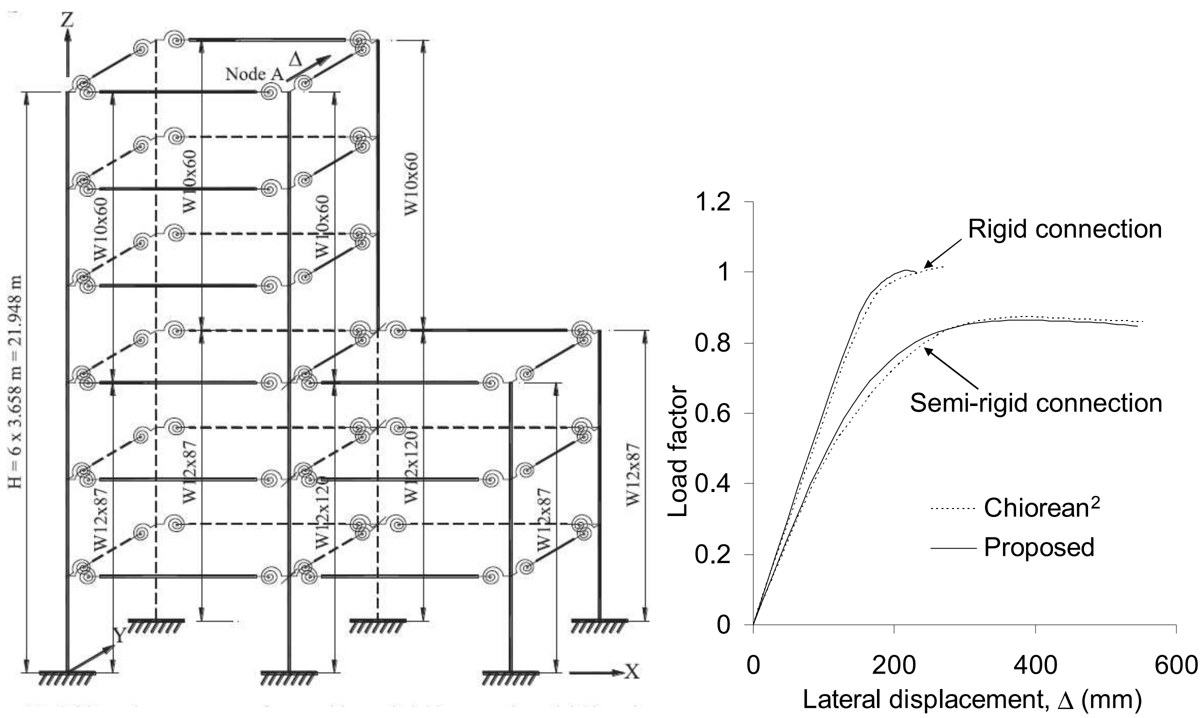

(a) Dimensions and properties (c) Load-displacement response

Figure 6: Orbison Six-Storey Space Frame

4 CONCLUSIONS

An accurate numerical procedure for nonlinear inelastic analysis of semi-rigid steel frames has been developed. The proposed analysis is based on the force-based beam-column fibre element which is capable of accurately capturing the spread of plasticity over the cross section and along the member length by using a single element per member. An independent zero-length connection element comprising of six translational and rotational springs is developed to simulate the rigidity of the beam-to-column connections. The validity of the proposed analysis has been verified by comparing the obtained predictions with the established results available from the literature. Through some numerical examples, it is verified that the proposed program can accurately predict the combined effects of geometric and material nonlinearities together with the connection rigidity for space steel frames.

5 ACKNOWLEDGEMENTS

This work was supported by the Australian Research Council (ARC) under its Discovery Early Career Researcher Award scheme (Project No: DECRA140100747). The financial support is gratefully acknowledged.

REFERENCES

[1] S. E. Kim and S. H. Choi, Practical advanced analysis for semi-rigid space frames, *International Journal of Solids and Structures* (2001), vol. 38, pp. 9111-9131.
[2] C. Chiorean, A computer method for nonlinear inelastic analysis of 3D semi-rigid steel frameworks, *Engineering Structures* (2009), vol. 31, pp. 3016-3033.
[3] E. Spacone, *et al.*, Mixed formulation of nonlinear beam finite element, *Computers & Structures* (1996), vol. 58, pp. 71-83.
[4] A. Neuenhofer and F. C. Filippou, Evaluation of nonlinear frame finite-element models, *Journal of Structural Engineering* (1997), vol. 123, pp. 958-966.

[5] H. T. Thai and S. E. Kim, Practical advanced analysis software for nonlinear inelastic analysis of space steel structures, *Advances in Engineering Software* (2009), vol. 40, pp. 786-797.
[6] H. T. Thai and S. E. Kim, Practical advanced analysis software for nonlinear inelastic dynamic analysis of steel structures, *Journal of Constructional Steel Research* (2011), vol. 67, pp. 453-461.
[7] N. Kishi and W. F. Chen, Moment-rotation relations of semirigid connections with angles, *Journal of Structural Engineering* (1990), vol. 116, pp. 1813-1834.
[8] U. Vogel, Calibrating frames, *Stahlbau* (1985), vol. 10, pp. 295-301.
[9] C. Ngo-Huu, *et al.*, Second-order plastic-hinge analysis of space semi-rigid steel frames, *Thin-Walled Structures* (2012), vol. 60, pp. 98-104.
[10] T. W. Stelmack, *Analytical and experimental response of flexibility connected steel frames*, University of Colorado, Boulder, USA (1982).
[11] J. G. Orbison, *et al.*, Yield surface applications in nonlinear steel frame analysis, *Computer Methods in Applied Mechanics and Engineering* (1982), vol. 33, pp. 557-573.

12th International Conference on
Steel, Space and Composite Structures
28-30 May 2014, Prague, Czech Republic

EXPERIMENTAL ASSESSMENT OF FRP STRENGTHENING STRATEGIES FOR PRECAST RC WALL PANELS

Carla Todut[1], Valeriu Stoian[2] and Daniel Dan[3]

[1]PhD Student, Civ. Eng.
2A, Traian Ialescu Street, Timisoara, Romania 300223
e-mail: carla.todut@student.upt.ro, webpage: http://www.ct.upt.ro

Keywords: experimental, FRP, strengthening, precast, RC, wall

Abstract. *The paper presents a part of an experimental program on precast reinforced concrete wall panels based on the analysis of their seismic performance, strengthening strategies and economic discussions. A number of two precast reinforced concrete wall panels were analyzed here, one having an initial narrow door opening and the other one having an initial wide door opening. Both specimens were post-damage strengthened using externally bonded carbon fiber reinforced polymer reinforcement. The main aspects related to the structural performance are presented and discussed for the post-damage strengthened specimens in comparison with the reference ones.*

1 INTRODUCTION

The evaluation of the seismic action for existing buildings requires appropriate tools in order to identify vulnerable structures and to provide rehabilitation resources where there is a need for intervention. An experimental program was developed at the Politehnica University of Timisoara, focused on precast reinforced concrete shear walls tested under earthquake conditons. Since the seismic behavior of lightly reinforced shear walls with different openings and cut-outs made in walls is not yet well understood, scientific research has to be carried out. Recent research on reinforced concrete walls strengthened with FRP composites were conducted by Li and Lim [1], Sánchez-Alejandre and Alcocer [2], Demeter [3], Mosoarca [4], Dan [5]. In this paper, two specimens with openings, called precast reinforced concrete wall panels, PRCWP (7÷8) are proposed and tested. Specimens PRCWP (7÷8) were first tested unstrengthened, then after they were repaired using high strength mortar, rehabilitated and tested again. The post-damage strengthening strategies presented in this paper implied externally bonded carbon fiber reinforced polymer reinforcement (EBR-CFRP). The seismic performance, lateral stiffness, horizontal displacement, ductility, energy dissipation capacity, failure modes and strain analysis are presented and discussed for the post-damage strengthened specimens in comparison with the reference elements.

2 EXPERIMANTAL PROGRAM

The part of the experimental program presented in this paper consists of two 1:1,2 scaled elements, namely PRCWP (7÷8) presented in detail in Todut et al. [6,7]. The specimens were first tested unstrengthened, then after they were repaired, rehabilitated and tested again. The specimens outlines and reinforcement details are presented in Figure 1. Specimen PRCWP (7-E1-T) has an initial narrow door opening, while PRCWP (8-E3-T) has an initial wide door opening (E3).

† Professor, PhD, Civ. Eng., Politehnica Univerisity of Timisoara, Romania
‡ Professor, PhD, Civ. Eng., Politehnica University of Timisoara, Romania

2.1 Material properties

Material tests were performed on both concrete and steel. Table 1 summarizes the results of the compression tests obtained on cube (150 mm edge) samples and Table 2 presents the steel reinforcement properties obtained experimentally. Unidirectional carbon fiber strips were used as EBR-CFRP for the post-damage rehabilitation of the specimens, and their geometrical and mechanical properties (based on manufacturer's data) are included in Table 3. The high strength mortar used to replace the heavily damaged concrete was Sika MonoTop 614, with a compressive strength at 28 days of 55 N/mm2 according to the product data sheet.

2.2 Behavior and results of reference elements

The behavior of the specimens during the experimental test showed a shear behavior in accordance with the testing process, exhibiting a significant number of cracks in all the regions of the panel, inclined cracks in the piers, concrete crushing and reinforcement yielding. Detailed data related to the test set-up, behavior and failure details of the elements are presented in Todut

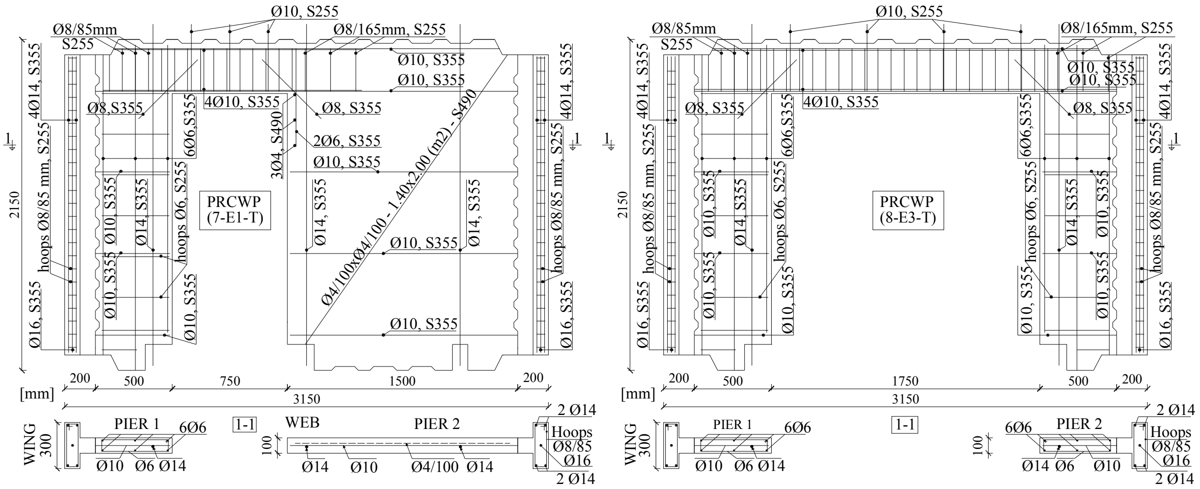

Figure 1 - The specimens' outlines and reinforcement details

Element	No. of samples	$f_{cm,cube}$ (N/mm^2)	f_{ck} (N/mm^2)	Class of concrete
PRCWP (7-E1-T)	3	45.48	30.17	C 30/37
PRCWP (8-E3-T)	3	17.48	12.28	C 12/15

Table 1- Properties of the concrete in the web panel specimen

Re-bar type	Grade	Φ (mm)	f_y (N/mm^2)	f_u (N/mm^2)	f_u / f_y	E_s (N/mm^2)
OB37	S255	6	400	550	1.38	207
		8	425	507	1.19	205
PC52	S355	8	424	553	1.30	208
		10	450	564	1.25	210
		14	395	584	1.48	206
		16	385	613	1.59	210
STPB	S490	4	618	667	1.08	208

Table 2 - Measured steel strengths

Component/system	Product name	Thickness [mm]	Areal weight [g/m^2]	Tensile strength [MPa]	Tensile modulus [GPa]	Elongation at break [%]
CF- fabric/strip	SikaWrap 230C	0.131	230	4300	238	1.8
Resin matrix	SikaDur 330	n/a	n/a	30	4.5	0.9

Table 3 - Geometrical and mechanical properties of the FRP system

et al. [8]. Failure details of the tested wall specimens are presented in Figure 2 [8,9]. During the experimental test of the PRCWP (7-E1-T) specimen, the first diagonal crack appeared in the right pier at 0.5% drift ratio, and G2 strain gauge recorded the yielding of reinforcement. Concrete crushing took place at the bottom right corner of the panel, top right corner of the door opening and cast in place mortar at the bottom right corner of the door opening. The vertical rebars of the welded wire mesh displaced, while the horizontal rebars of the welded wire mesh teared at 0.8% drift ratio. The failure of the specimen was brittle and occurred at 0.8% drift ratio. In the experimental test of PRCWP (8-E3-T), the first inclined crack appeared at 0.5% drift ratio in the right pier, while concrete crushing occurred at the top corners of the opening and the cast in place mortar. The failure of the specimen was recorded at 1.1% drift ratio.

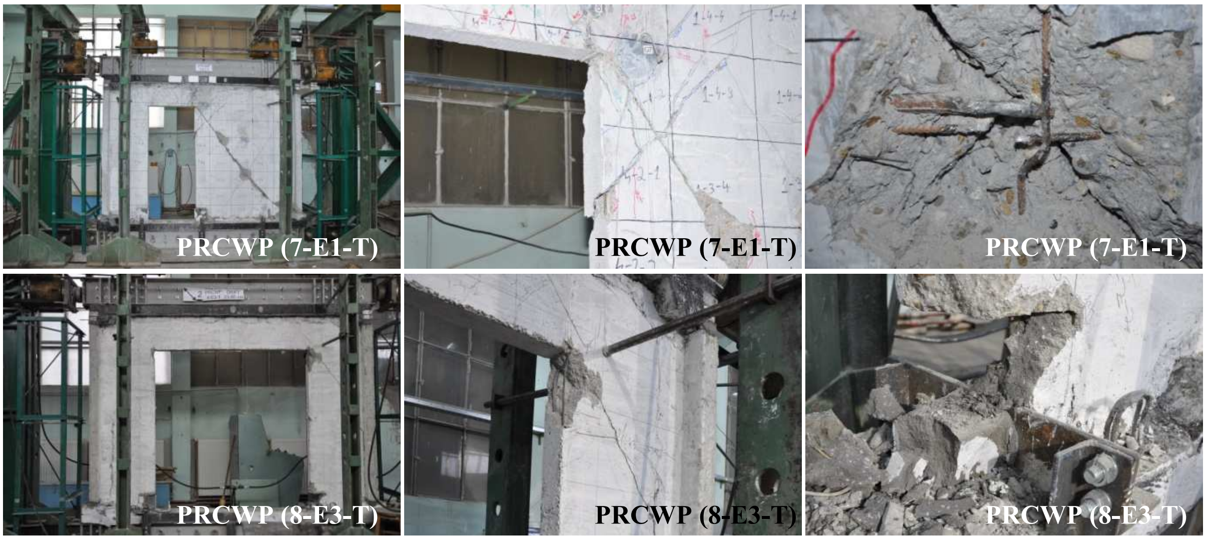

Figure 2 - Failure details of the reference specimens

2.3 Repair and strengthening of specimens

The strengthening strategies applied here intend to restore the initial load bearing capacity of the elements, the solution is qualitative, based on the behavior of the reference specimens.

2.3.1 Post-damage strengthening of specimens

The PRCWP (7-E1-T/R) and (8-E3-T/R) were repaired after the experimental test of the unstrengthened specimens using high strength mortar and then they were rehabilitated using EBR-CFRP (Figure 3) and tested again. The rehabilitation strategies presented here intended to increase the flexural, shear and confinement capacity of the specimens. Flexural strips were applied around the opening and along the upper edge of the spandrel. Short strips were placed horizontal until the top width of the opening and vertical at the top and bottom side of the opening.

Figure 3 - Rehabilitation strategies using EBR-CFRP

The bottom vertical strips were anchored to the foundation beam using CFRP tows. Shear horizontal strips were disposed on both piers anchored at their end by overlapping strips on the opening side and by short CFRP tows at the wing-side end. CFRP confinement was provided at the inside toe of both piers and the outer toe of pier 2, at the pier to spandrel connection regions and at the ends of the wing walls. Additional inclined strips were applied at the top corners of the opening for PRCWP (7-E1-T/R) specimen.

2.4 Testing methodology and test set-up

Detailed data related to the testing methodology and test set-up of the elements are presented in Demeter [3]. A general view of the test set-up is represented in Figure 4.The testing procedure consists in quasi-static reversed cyclic horizontal loads performed on 1:1.2 scaled precast RC wall panels. As the height of the wall is 2150 mm, 21.5 mm corresponds to 1% drift ratio. The displacement control was 0.1% drift ratio. Two cycles per drift were made. Constant axial loads were also applied in order to simulate the gravity loading condition at the base of the wall and alternating axial loads used for restraining the rocking rotation of the elements. During the experimental tests, the behavior of the specimens was monitored using pressure transducers (P), displacement transducers (D) and strain gauges placed on the FRP (G).

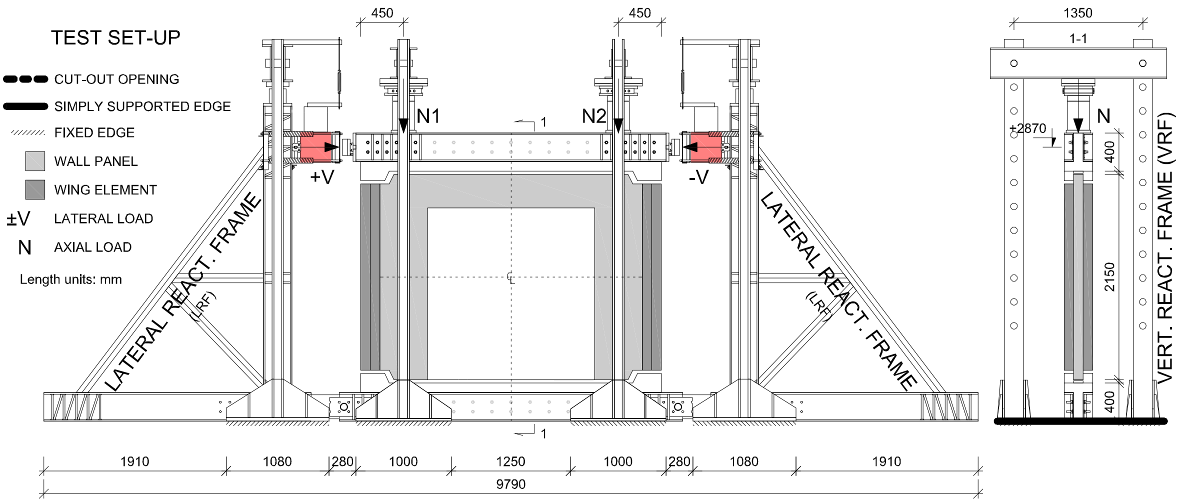

Figure 4 - Test set-up of the specimens

3 EXPERIMENTAL RESULTS AND COMPARATIVE STUDY

3.1 General behavior and failure modes of strengthened specimens

The behavior of the two post-damage strengthened specimens PRCWP (7-E1-T/R) and PRCWP (8-E3-T/R) revealed an expected behavior in accordance with the design strategies. During the experimental test, the specimens developed a significant number of cracks in the spandrel and piers. In the case of PRCWP (7-E1-T/R) the confinement strip at the bottom end of the wing wall fractured, while concrete crushing was taking place. Several shear strips and the confinement at the top right corner of the opening debonded with concrete surface in the right pier. In the case of PRCWP (8-E3-T/R), several shear strips debonded, the flexural strip from the top right corner of the opening expanded, while the shear strip in the same position teared. Failure details of the post-damage strengthened specimens are presented in Figure 5.

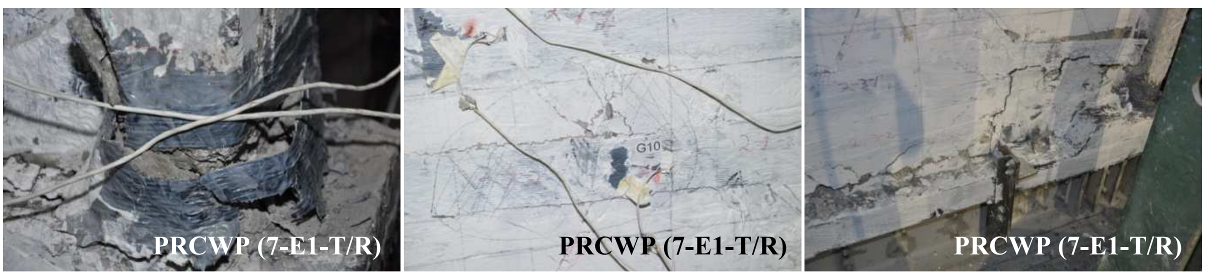

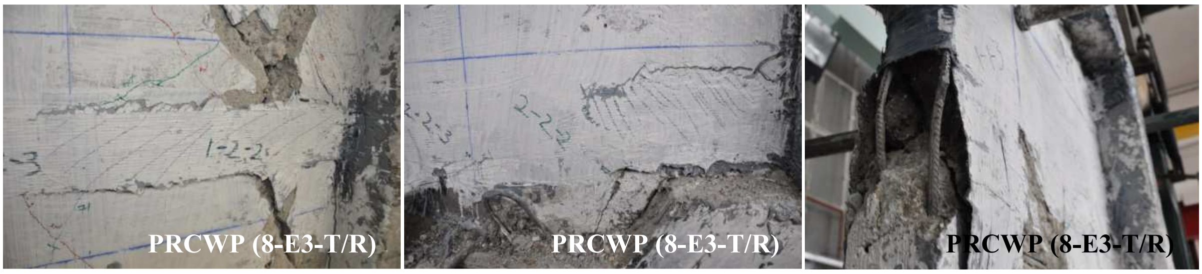

Figure 5 - Failure details of the post-damage strengthened specimens

3.2 Load-displacement response diagrams

For the two post-damage strengthened elements, the obtained lateral loads versus the lateral displacement response diagrams are presented in Figure 6, as a comparison with the same responses recorded on the reference elements. The hysteretic curves show that the post-damage strengthened PRCWP (7-E1-T/R) specimen almost recovered the initial strength, while the post-damage strengthened PRCWP (8-E3-T/R) specimen recovered the initial strength.

3.3 Energy dissipation

A comparison between the cumulative dissipated energy per half-cycle versus drift ratio within each experimental test performed is presented in Figure 7. It can be concluded that the lowest contribution in energy dissipation belongs to the specimen having wide door opening dimension, namely PRCWP (8-E3-T), with respect to the one with narrow door opening dimension, PRCWP (7-E1-T). Also in the case of the specimen with narrow door opening, the post-damage strengthened PRCWP (7-E1-T/R) specimen dissipated much more energy than the reference one (PRCWP (7-E1-T). For the post-damage strengthened PRCWP (8-E3-T/R), the dissipated energy was like in the case of the reference one.

3.4 Strain analysis

During the experimental tests, strain was measured on the vertical, horizontal and inclined reinforcing bars, and horizontal and vertical on the EBR-CFRP strips. In Figure 8 are presented the steel strain ε (‰) versus drift ratio for the current tested specimens. G7 strain gauge was applied on horizontal reinforcement near the top right corner of the narrow door opening (PRCWP 7-E-T), and G8 strain gauge was applied on horizontal shear strip near the top left corner of the wide door opening (PRCWP 8-E3-T/R).

3.5 Stiffness analysis

According to the stiffness versus drift ratio diagram represented in Figure 9, the wide door opening dimension (PRCWP 8-E3-T) induces higher reductions in the initial stiffness of the wall panel, compared to the wall with narrow door opening (PRCWP 7-E1-T). In the case of the post-damage strengthened PRCWP (7-E1-T/R), the initial stiffness resulted higher than for the reference element, while for the post-damage strengthened PRCWP (8-E3-T/R), the initial stiffness was like in the case of the reference one.

3.6 Ductility considerations

The ductility of the wall specimens was evaluated using the $\mu_{0.85}$ method. According to the method used, the ductility is defined as the ratio between the ultimate displacement to the displacement corresponding to 0.85 of the maximum load on the ascending branch of the monotonic envelope. The normalized ductility coefficient μ for the tested specimens is presented in Figure 10. It was concluded that the specimen having a wide door opening, PRCWP (8-E3-T) developed a higher ductility than the specimen having a narrow door opening, PRCWP (7-E1-T). The post-damage strengthened specimen PRCWP (7-E1-T/R) was much more ductile than the reference specimen, while the post-damage strengthened specimen PRCWP (8-E3-T/R) developed a smaller ductility compared to the reference specimen.

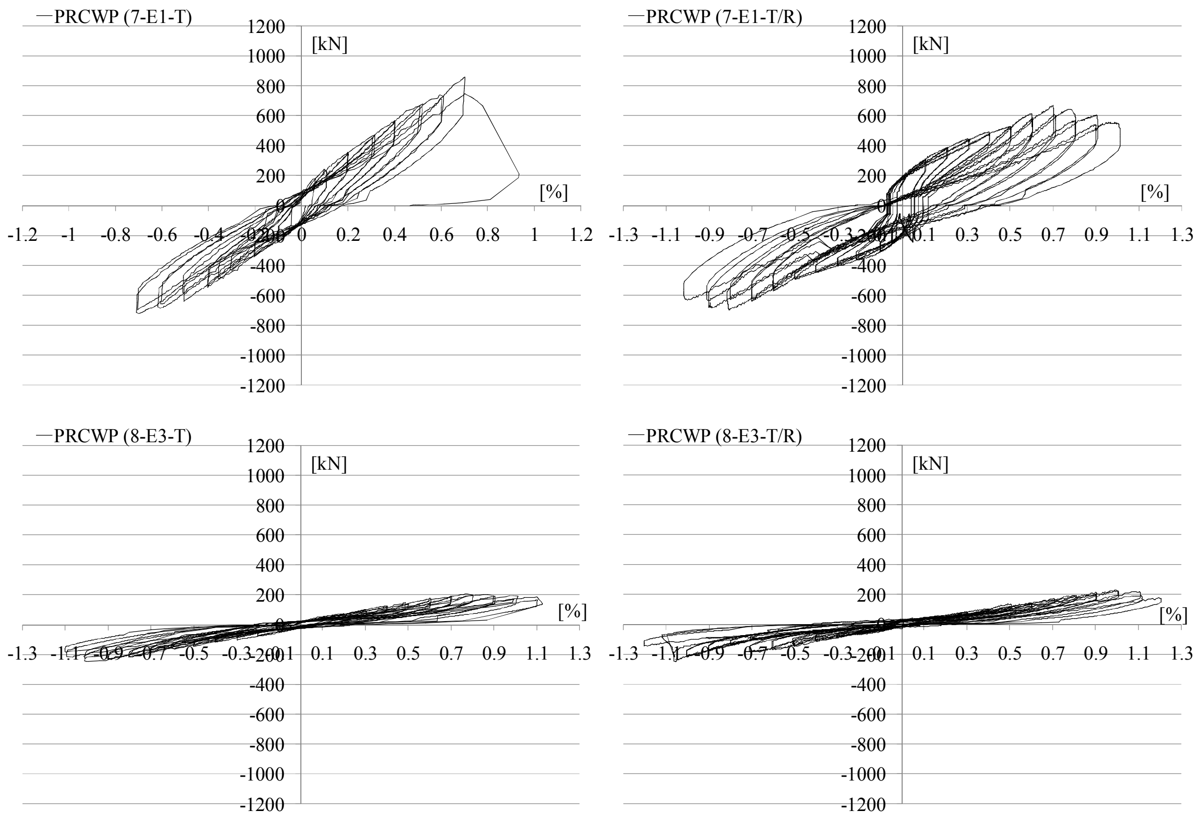

Figure 6 - Load-drift ratio hysteresis loops

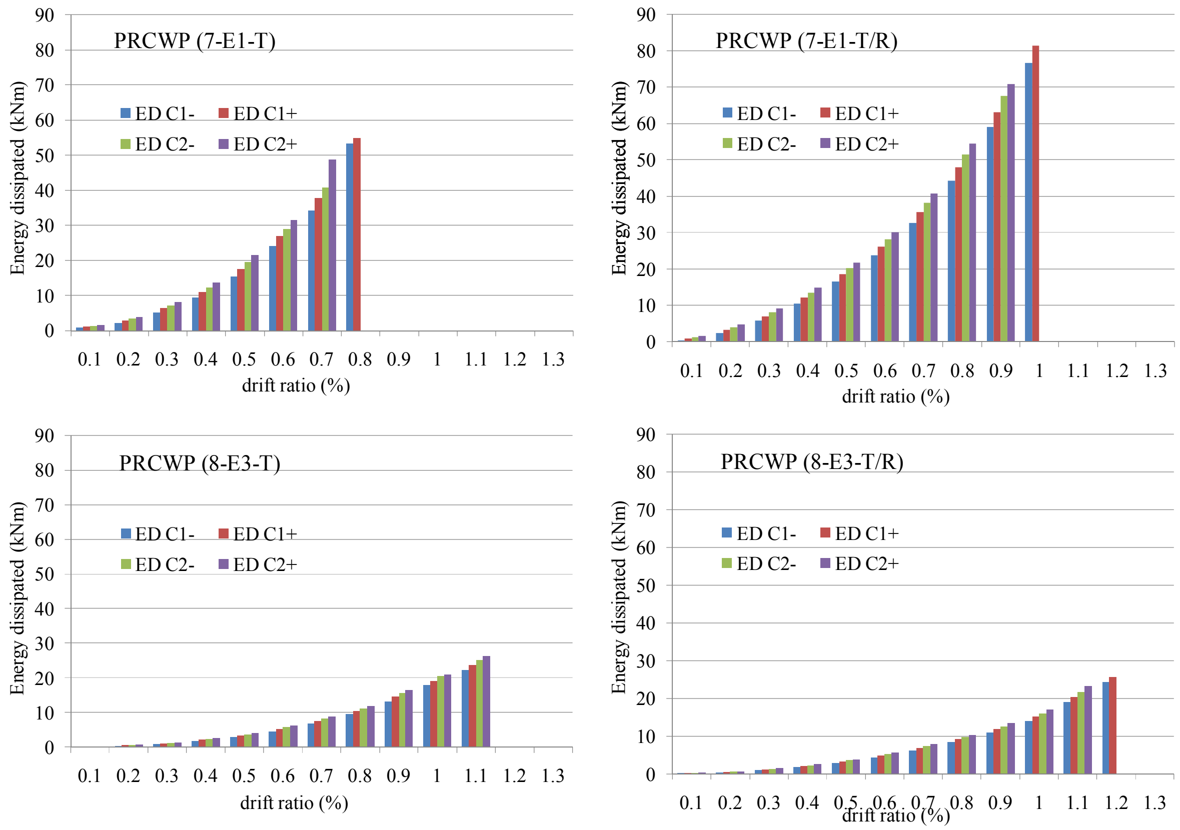

Figure 7 - The cumulative energy dissipation

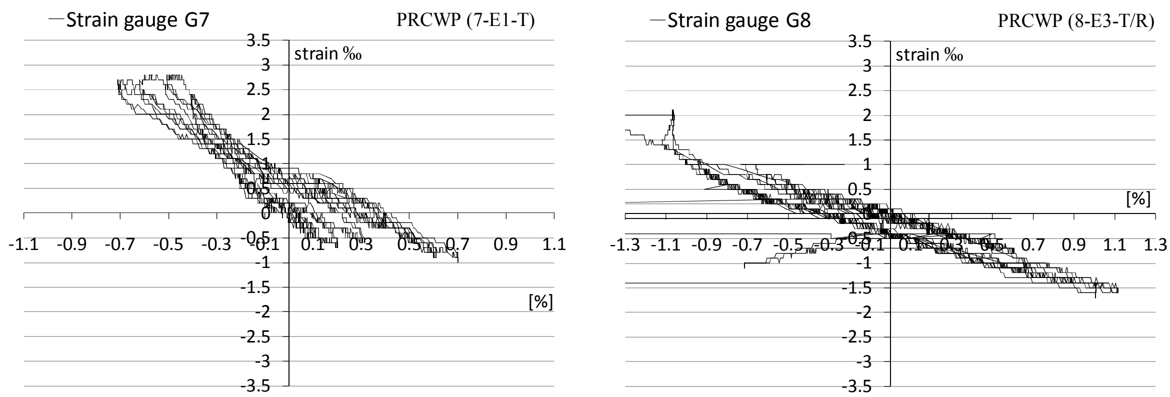

Figure 8 - Strain (ε) versus drift ratio

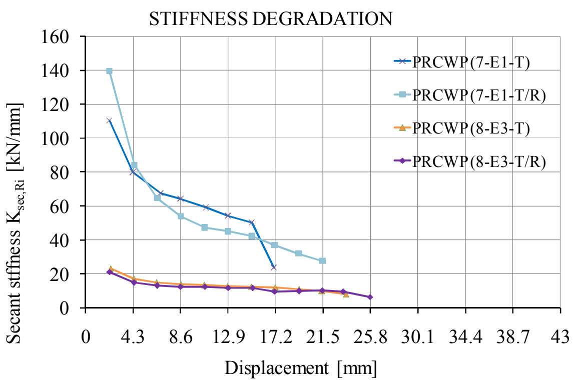

Figure 9 - Stiffness versus drift ratio diagram

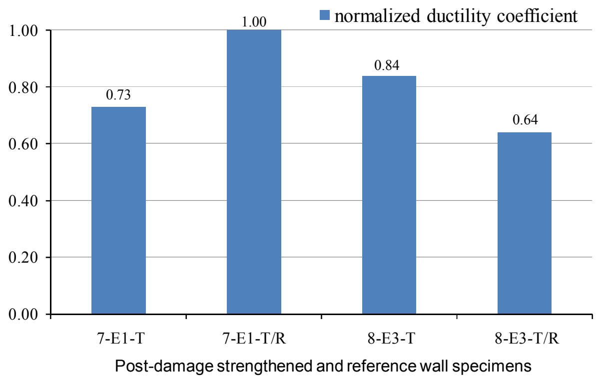

Figure 10 – Normalized ductility

4 CONCLUSIONS

The present paper describes the experimental aspects for a number of two precast reinforced concrete wall panels and presents the behavior for the strenghtened and reference elements. The following conclusions were made according to the current research:

-the behaviour of the specimens was in accordance with the testing methodology, developing a significant number of cracks, yielding of the reinforcement and concrete crushing;

-reinforced concrete wall panels with small openings, namely PRCWP (7-E1-T), dissipate more energy compared to the specimens with large opening dimensions, PRCWP (8-E3-T), where the deformation capacity is higher; only in one case here the strengthening, PRCWP (7-E1-T/R), served in a larger energy dissipation compared to the reference element;

-the ductility of the specimen having wide door opening, PRCWP (8-E3-T) was higher compared to the one having narrow door opening, PRCWP (7-E1-T); in the case of the post-damage strengthened PRCWP (7-E1-T/R) specimen, the ductility was significantly larger than for the reference specimen;

- horizontal reinforcement yielding was recorded near the top right corner of the narrow door opening, (PRCWP 7-E-T);

-large opening dimensions in the panels, PRCWP (8-E3-T) and (8-E3-T/R), induce significant reductions in the lateral resistance and stiffness towards the specimens having smaller opening dimensions, PRCWP (7-E1-T) and (7-E-T/R);

Further studies related to the numerical analysis for the strengthened and reference elements are in progress. The experimental work presented in this paper provides a basis for the development of an experimental program on precast RC panels externally strengthened with CFRP.

ACKNOWLEDGEMENT

Grant no. 3-002/2011, INSPIRE – Integrated Strategies and Policy Instruments for Retrofitting buildings to reduce primary energy use and GHG emissions, Project type PN II ERA NET, financed by the Executive Agency for Higher Education, Research, Development and Innovation Funding (UEFISCDI), Romania.

REFERENCES

[1] Bing Li and Chee Leong Lim, Tests on Seismically Damaged Reinforced Concrete Structural Walls Repaired Using Fiber-Reinforced Polymers, Journal of Composites for Construction © ASCE, September/October, pp 597-608, (2010).

[2] Alfredo Sánchez-Alejandre and Sergio M. Alcocer, Shear strength of squat reinforced concrete walls subjected to earthquake loading trends and models, Engineering Structures 32, pp 2466-2476, (2010).

[3] Demeter I., Seismic retrofit of precast RC walls by externally bonded CFRP composites. PhD Thesis, Politehnica University of Timisoara, (2011).

[4] Mosoarca, Seismic Behaviour of Reinforced Concrete Shear Walls with Regular and Staggered Openings After the Strong Earthquakes Between 2009 and 2011, Engineering Failure Analysis (2013).

[5] Dan D., Experimental tests on seismically damaged composite steel concrete walls retrofitted with CFRP composites, Engineering Structures 45, pp 338–348, (2012).

[6] Todut et al., Seismic performance of a precast RC wall panel retrofitted using CFRP composites, Proceedings of the 12th International Scientific Conference on Planning, design, construction and building renewal, Novi Sad, Serbia, (2012).

[7] Todut et al., Retrofitting Strategy for Earthquake Damaged Precast Concrete Wall Using FRP Composites, Fib Symposium "Engineering a Concrete Future: Technology, Modeling & Construction", Tel-Aviv, Israel, (2013).

[8] Todut C., Structural retrofit of precast reinforced concrete large wall panels affected by change of use, Inspire Report no.4, "Strategies for structural and thermal rehabilitation of buildings made of large precast reinforced concrete panels in order to reduce the primary energy consumption and the greenhouse gas emissions – InSPIRe", Timisoara, (2012).

[9] Todut, C., Stoian, V.; Demeter, I.; Nagy-György, T.; Ungureanu, V., Seismic performance of a precast RC wall panel retrofitted using CFRP composites - Proceedings of the 12th International Scientific Conference on Planning, design, construction and building renewal, Novi Sad, Serbia, (2012), pp 319-326.

12th International Conference on
Steel, Space and Composite Structures
28-30 May 2014, Prague, Czech Republic

NONLINEAR GEOMETRIC AND MATERIAL COMPUTATIONAL TECHNIQUE: HIGHER-ORDER ELEMENT WITH REFINED PLASTIC HINGE APPROACH

M. Trifunovic* and C.K. Iu†

*Faculty of Architecture, University of Belgrade, Belgrade 11000, Serbia

Keywords: Advanced analysis, steel structures, higher-order element formulation

Abstract. *This paper addresses of the advanced computational technique of steel structures for both simulation capacities simultaneously; specifically, they are the higher-order element formulation with element load effect (geometric nonlinearities) as well as the refined plastic hinge method (material nonlinearities). This advanced computational technique can capture the real behaviour of a whole second-order inelastic structure, which in turn ensures the structural safety and adequacy of the structure. Therefore, the emphasis of this paper is to advocate that the advanced computational technique can replace the traditional empirical design approach. In the meantime, the practitioner should be educated how to make use of the advanced computational technique on the second-order inelastic design of a structure, as this approach is the future structural engineering design. It means the future engineer should understand the computational technique clearly; realize the behaviour of a structure with respect to the numerical analysis thoroughly; justify the numerical result correctly; especially the fool-proof ultimate finite element is yet to come, of which is competent in modelling behaviour, user-friendly in numerical modelling and versatile for all structural forms and various materials. Hence the high-quality engineer is required, who can confidently manipulate the advanced computational technique for the design of a complex structure but not vice versa.*

1. INTRODUCTION

Recent advances in structural engineering incorporating second-order inelastic behaviour, together with sophisticated element formulation and numerical technique of a global system, into the models

† School of Civil Engineering and Built Environment, Queensland University of Technology, Australia

that permit realistic simulation and resolution of the global structural systems. This is particularly true and indispensable in large-scale structures where their weight effects must be minimized in the complicated form, such as aerospace structures, large span civil engineering constructions, and offshore structures, etc, which leads to enormous element number with intricate behaviour. Modern structural design is expected to overcome past challenges in efficient convergent rate, demanding lower amount of resources in terms of the element number and delivering better performance in terms of the degree of accurate behaviour to be captured through the second-order inelastic analysis. As a natural result, the second-order inelastic numerical technique for analysing the contemporary structures becomes a controversial and challenging research topic worldwide (Chan and Zhou ([1][2]); Iu and Bradford ([3][4][5])).

Izzuddin [6] developed the higher-order element formulation with the plasticity. Unfortunately, this approach is restrictive in the efficient convergence because of the plastic zone approach being adopted. On the other hand, the higher-order element formulation with the plastic hinge approach (one-element-per-member approach – Liew et al. [7]; Chan and Zhou ([8],[9])) was developed to replicate the second-order inelastic behaviour of a steel structure However, their approaches are also confined to the elasto-plastic material behaviour mainly.

To be competent in the geometric and particularly material modelling capacity, the present study addresses of an advanced computational technique (second-order inelastic analysis), which incorporates the refined plastic hinges (inelastic behaviour including gradual yielding, full plasticity and strain-hardening effect) into the higher-order element formulation (using least element number to simulate the second-order member bowing effect on a whole system and accurate element solutions under element loads). Eventually, the present advanced computational technique can well replicate the second-order inelastic bahaviour in the simple, efficient, versatile, reliable and accurate manner.

2. DISPLACEMENT FUNCTION OF HIGHER-ORDER ELEMENT

The deformations comprise the deformations u in the x direction, v in the y direction, w in the z direction and the twist ϕ about the x-axis. Based on the co-rotational coordinate system, the dependent variables of transverse deflections v and w are replaced by nodal rotations as θ_z and θ_y, about z- and y-axis, respectively, such as $\mathbf{u} = \{u, \theta_y, \theta_z, \phi\}^T$. These rotations are the dependent variables in turn which define the transverse deflections in the element stiffness formulation. The higher-order transverse displacement-based interpolation function of an element not only fulfils the essential boundary condition (compatibility condition), but also natural boundary condition (force equilibrium equation), in which equivalent mid-span moment M_0 and shear force S_0 measure additional deflection along an element due to element load effect as given from Eqs (1) – (4). Further, the elastic material law follows in the higher-order element function as written as

$$v = 0 \quad \text{and} \quad \frac{\partial v}{\partial x} = \theta_{z1} \quad \text{at } \zeta = 0 \tag{1}$$

$$v = 0 \quad \text{and} \quad \frac{\partial v}{\partial x} = \theta_{z2} \quad \text{at } \zeta = 1, \tag{2}$$

while the equilibrium equation of bending and shear force given by

$$EI_z \frac{\partial^2 v}{\partial x^2} = Pv - M_{z1}(1-\zeta) + M_{z2}\zeta + M_0 \tag{3}$$

$$EI_z \frac{\partial^3 v}{\partial x^3} = P\frac{\partial v}{\partial x} + \frac{M_{z1} + M_{z2}}{L} + S_0 \tag{4}$$

where $\zeta = x/L$. (5)

$$\begin{aligned} v = &\left\{\left[\zeta - \frac{\frac{1}{2}(48+5q)}{48+q}\zeta^2 + \frac{4q}{48+q}\zeta^3 - \frac{2q}{48+q}\zeta^4\right]\right.\\ &\left.+\left[-\frac{\frac{1}{2}(240+7q)}{80+q}\zeta^2 + \frac{80+9q}{80+q}\zeta^3 - \frac{10q}{80+q}\zeta^4 + \frac{4q}{80+q}\zeta^5\right]\right\}L\theta_{z1}\\ &+\left\{\left[\frac{\frac{1}{2}(48+5q)}{48+q}\zeta^2 - \frac{4q}{48+q}\zeta^3 + \frac{2q}{48+q}\zeta^4\right]\right.\\ &\left.+\left[-\frac{\frac{1}{2}(240+7q)}{80+q}\zeta^2 + \frac{80+9q}{80+q}\zeta^3 - \frac{10q}{80+q}\zeta^4 + \frac{4q}{80+q}\zeta^5\right]\right\}L\theta_{z2}\\ &-\frac{\overline{M}_0 L}{48+q}\left[\zeta^2 - 2\zeta^3 + \zeta^4\right] + \frac{\overline{S}_0 L^2}{80+q}\left[\zeta^2 - 4\zeta^3 + 5\zeta^4 - 2\zeta^5\right] \end{aligned} \tag{6}$$

$$\text{or} \quad v = N_1 L\theta_{z1} + N_2 L\theta_{z2} - N_m L\overline{M}_0 + N_s L^2 \overline{S}_0 \tag{7}$$

N_1, N_2, N_m and N_s are displacement functions with respect to rotations at first and second node, and element load contributed from moment and shear force components, respectively; the equivalent mid-span moment $\overline{M}_0$ and shear force $\overline{S}_0$ under the different sorts of element load are partially given in [10]; q is axial load parameter, in which positive sign means in tension, and vice versa.

3. ELASTIC HIGHER-ORDER ELEMENT FORMULATION

The element resistance or the secant stiffness formulation can be obtained from the first variation of the total potential energy equation Π.

$$\begin{aligned} M_{\alpha 1} = \frac{\partial U}{\partial \theta_{\alpha 1}} = &\frac{EI_\alpha}{L}\left[\frac{19200 + 800q + \frac{61}{7}q^2 + \frac{23}{1260}q^3}{(80+q)^2} + \frac{2304 + 288q + \frac{29}{5}q^2 + \frac{11}{420}q^3}{(48+q)^2}\right]\theta_{\alpha 1}\\ &+\frac{EI_\alpha}{L}\left[\frac{19200 + 800q + \frac{61}{7}q^2 + \frac{23}{1260}q^3}{(80+q)^2} - \frac{2304 + 288q + \frac{29}{5}q^2 + \frac{11}{420}q^3}{(48+q)^2}\right]\theta_{\alpha 2}\\ &+\frac{EI_\alpha}{L}\left[-\frac{q^2\overline{M}_0}{210(48+q)^2} - \frac{q^2\overline{S}_0 L}{630(80+q)^2}\right] \end{aligned} \tag{8}$$

or $M_{\alpha 1} = \frac{EI_\alpha}{L}\left(C_1\,\theta_{\alpha 1} + C_2\,\theta_{\alpha 2} - C_m \overline{M}_0 - C_s \overline{S}_0 L\right),$ (9)

$$M_{\alpha 2} = \frac{\partial U}{\partial \theta_{\alpha 2}} = \frac{EI_\alpha}{L}\left[\frac{19200 + 800q + \frac{61}{7}q^2 + \frac{23}{1260}q^3}{(80+q)^2} + \frac{2304 + 288q + \frac{29}{5}q^2 + \frac{11}{420}q^3}{(48+q)^2}\right]\theta_{\alpha 2}$$
$$+ \frac{EI_\alpha}{L}\left[\frac{19200 + 800q + \frac{61}{7}q^2 + \frac{23}{1260}q^3}{(80+q)^2} - \frac{2304 + 288q + \frac{29}{5}q^2 + \frac{11}{420}q^3}{(48+q)^2}\right]\theta_{\alpha 1} \quad (10)$$
$$+ \frac{EI_\alpha}{L}\left[\frac{q^2 \overline{M}_0}{210(48+q)^2} - \frac{q^2 \overline{S}_0 L}{630(80+q)^2}\right]$$

or $M_{\alpha 2} = \frac{EI_\alpha}{L}\left(C_1\,\theta_{\alpha 2} + C_2\,\theta_{\alpha 1} + C_m \overline{M}_0 - C_s \overline{S}_0 L\right)$ (11)

in which the subscript α denotes y or z, and

$$P = P_1 - P_2 = \frac{\partial U}{\partial e} + \frac{\partial U}{\partial q}\cdot\frac{\partial q}{\partial e}$$
$$= \frac{EAe}{L} + EA\sum_{\alpha = y,z}\Big[b_1(\theta_{\alpha 1} + \theta_{\alpha 2})^2 + b_2(\theta_{\alpha 1} - \theta_{\alpha 2})^2$$
$$+ b_{m1}(\theta_{\alpha 1} - \theta_{\alpha 2})\overline{M}_0 + b_{s1}(\theta_{\alpha 1} + \theta_{\alpha 2})\overline{S}_0 L + b_{m2}\overline{M}_0^2 + b_{s2}\overline{S}_0^2 L^2\Big] \quad (12)$$
$$= EA\left[\frac{e}{L} + \sum_{\alpha = y,z}\left(C_b + b_{m1}(\theta_{\alpha 1} - \theta_{\alpha 2})\overline{M}_0 + b_{s1}(\theta_{\alpha 1} + \theta_{\alpha 2})\overline{S}_0 L + b_{m2}\overline{M}_0^2 + b_{s2}\overline{S}_0^2 L^2\right)\right]$$

C_m and C_s provoke the second-order moment from the moment and shear force components respectively due to coupling effect of both axial loads and lateral element loads, whereas b_{m1}, b_{m2}, b_{s1} and b_{s2} exhibit axial force resistance subjected to the coupling effect between the axial loads and the lateral element loads as given in [10] basically.

The tangent stiffness of the present beam-column element can then be written in Eq. (13), which relates the incremental deformation to the corresponding external loads imposed on an element in the member coordinate.

$$\mathbf{K}_t = \frac{EI}{L}\begin{bmatrix} \frac{A}{I} + \frac{1}{L^2 H} & \frac{G_{y1}}{LH} & \frac{G_{z1}}{LH} & 0 & \frac{G_{y2}}{LH} & \frac{G_{z2}}{LH} \\ & \xi_y\left(C_1 + \frac{G_{y1}^2}{H}\right) & \frac{G_{y1}G_{z1}}{H} & 0 & \xi_y\left(C_2 + \frac{G_{y1}G_{y2}}{H}\right) & \frac{G_{y1}G_{z2}}{H} \\ & & \xi_z\left(C_1 + \frac{G_{z1}^2}{H}\right) & 0 & \frac{G_{z1}G_{y2}}{H} & \xi_z\left(C_2 + \frac{G_{z1}G_{z2}}{H}\right) \\ & & & \eta & 0 & 0 \\ & \mathit{symmetric} & & & \xi_y\left(C_1 + \frac{G_{y2}^2}{H}\right) & \frac{G_{y2}G_{z2}}{H} \\ & & & & & \xi_z\left(C_1 + \frac{G_{z2}^2}{H}\right) \end{bmatrix} \quad (13)$$

in which the coefficients G_n and H expressed in the tangent stiffness formulation in Eq. (13) are to measure the coupling effect between axial load and bending effect as listed in [10]. *I* is the second moment of inertia about the axis in which the buckling effect is considered. Also $\xi_z = I_z/I$ and $\xi_y = I_y/I$. The tangent stiffness matrix should assemble and transform into global coordinate as written in Eq. (14), as the incremental nodal displacements of a structure can then be obtained by tangent stiffness relationship.

$$\mathbf{K}_T = \sum_{\text{elements}} \mathbf{L}\,\mathbf{K}_e\,\mathbf{L}^{\mathrm{T}} = \sum_{\text{elements}} \mathbf{L}\left(\mathbf{T}^{\mathrm{T}}\,\mathbf{K}_t\,\mathbf{T} + \mathbf{N}\right)\mathbf{L}^{\mathrm{T}}, \tag{14}$$

in which **T** is transformation matrix relating the member forces to element force in local coordinate. **L** is the transformation matrix from local ordinate to global coordinate. And **N** is a stability matrix to allow for the work done of rigid body motion.

The moderate or large rotations at the end nodes of a higher-order element can be replicated by the co-rotational approach, when a joint orientation matrix Δ**L** of a higher-order element is attached at its end nodes as written in Eq. (15),

$$\Delta\mathbf{L} = \begin{bmatrix} \cos\Delta\Theta_n & \dfrac{-\cos\Delta\Theta_n \sin\Delta\Theta_y \cos\Delta\Theta_x - \sin\Delta\Theta_z \sin\Delta\Theta_x}{\cos\Delta\Theta_y} & \dfrac{\cos\Delta\Theta_n \sin\Delta\Theta_y \sin\Delta\Theta_x - \sin\Delta\Theta_z \cos\Delta\Theta_x}{\cos\Delta\Theta_y} \\ \sin\Delta\Theta_y & \cos\Delta\Theta_y \cos\Delta\Theta_x & -\cos\Delta\Theta_y \sin\Delta\Theta_x \\ \sin\Delta\Theta_z & \dfrac{-\sin\Delta\Theta_y \sin\Delta\Theta_z \cos\Delta\Theta_x + \sin\Delta\Theta_z \sin\Delta\Theta_x}{\cos\Delta\Theta_y} & \dfrac{\sin\Delta\Theta_y \sin\Delta\Theta_z \sin\Delta\Theta_x + \cos\Delta\Theta_n \cos\Delta\Theta_x}{\cos\Delta\Theta_y} \end{bmatrix}, \tag{15}$$

in which $\cos\Delta\Theta_n = \sqrt{1 - \sin\Delta\Theta_y \sin\Delta\Theta_y - \sin\Delta\Theta_z \sin\Delta\Theta_z}$ is unit directional cosine of an element; $\sin\Delta\Theta_z = \left(\Delta v_2 - \Delta v_1\right)/L$ is incremental rotations excluding rigid body motion in *z*-axis; $\sin\Delta\Theta_y = \left(\Delta w_2 - \Delta w_1\right)/L$ is incremental rotations excluding rigid body motion in *y*-axis; $\Delta\Theta_x = \left(\Delta\phi_1 + \Delta\phi_2\right)/2$ is incremental rotations excluding rigid body motion in *x*-axis, and then updated to be the latest transformation matrix $\mathbf{L}_{i+1}$ of a higher-order element through the incremental rotations in the incremental-iterative procedure as descripted as Eq. (16).

$$\mathbf{L}_{i+1} = \Delta\mathbf{L}_{i+1} \cdot \mathbf{L}_i, \tag{16}$$

It should be noted that all rotations in the transformation system is with respect to the incremental rotations of a higher-order element at the latest (*i*+1)-th iteration. And the incremental rigid body motion is assumed to be finite or linear characteristic.

4. REFINED PLASTIC HINGE FORMULATION

The Section 3 refers to the second-order elastic analysis of a higher-order element, whereas the nonlinear material constitutive law in terms of the refined plastic hinge stiffness approach is discussed in this Section. The incremental plastic hinge stiffness [11] is written,

$$\Delta S = \frac{EI}{L}\left(\frac{1 - \phi_f(\mathbf{f})}{\phi_i(\mathbf{f}) - 1} + \mu\right), \tag{17}$$

in which the incremental spring stiffness ΔS is such that $\infty > \Delta S > 0$, in which infinity and zero mean elastic and fully yielded, respectively; μ is strain-hardening parameters, of which the strain-hardening behaviour was first introduced by Iu and Chan [12] in the plastic hinge approach. The incremental spring stiffness is incorporated into the secant and tangent stiffness formulation as written in Eqs. (8) – (13), of which is described in [5] comprehensively.

The refined plastic hinge undergoes the partial or gradual yielding (incremental spring stiffness ΔS, i.e. $\infty > (1-\phi_f(\mathbf{f}))/(\phi_i(\mathbf{f})-1) > 0$), when the vector of actions at a node **f** are such that initial yielding function $\phi_i(\mathbf{f})$ exceeds unity but full yield function $\phi_f(\mathbf{f})$ is less than unity. The load vector **f** is such that full yield function $\phi_f(\mathbf{f})$ exceeds unity (i.e. ΔS=0) in full-plasticity. When the element experiences strain-hardening behaviour after full plasticity, μ is a certain value but greater than zero.

The material behaviour being formulated by the incremental plastic hinge spring stiffness includes gradual yielding, full plasticity and strain-hardening effect under both axial and bending effect, which is beneficial to study the inelastic buckling at the element level, and thereby superior over the conventional plastic hinge approach.

5. SYSTEM SOLUTION PROCEDURES

To evaluate the second-order inelastic behaviour of a whole structural system, the equilibrium solution at the nodes at global system level can be enforced through the incremental-iterative solution procedures with recourse to the incremental force equilibrium equation at *i*-th iteration at the *n*-th load increment, which is formulated by using the tangent stiffness $\mathbf{K}_T$, as given,

$$\Delta\mathbf{f}^n = \mathbf{f}^n - \mathbf{R}_i^n = \mathbf{f}^n - \mathbf{K}_s\mathbf{u}_i^n = \mathbf{K}_T\Delta\mathbf{u}_i^n \tag{18}$$

The unbalanced force $\Delta\mathbf{f}^n$ between external loads $\mathbf{f}^n$ acting at the nodes and nodal element resistance $\mathbf{R}_i^n$ at global system level is equivalent to the incremental nodal deformations $\Delta\mathbf{u}_i^n$ times the tangent stiffness of a structure $\mathbf{K}_T$. Thus, the incremental nodal deformations can be written as,

$$\Delta\mathbf{u}_i^n = \mathbf{K}_T^{-1}\Delta\mathbf{f}^n \tag{19}$$

The change of geometry of a whole structure can be measured by updating the global coordinate at the nodes of a structure, which is equivalent to the accumulation of total deformations at the nodes of a structure as given,

$$\mathbf{u}_{i+1}^n = \mathbf{u}_i^n + \Delta\mathbf{u}_i^n \tag{20}$$

At the meantime, the transformation system between global and local coordinates **L** is updated through the co-rotational approach as given in Eq. (16) to measure the latest change of geometry of a whole structural system at the co-rotational approach, which is used to evaluate the latest element resistance $\mathbf{R}_{i+1}^n$.

According to the incremental formulation in the element resistance evaluation (incremental secant stiffness formulation) which is compatible with the incremental spring stiffness formulation as described in Section 4, the element resistance $\mathbf{R}_{i+1}^n$ relying on accumulation of incremental element resistance $\Delta\mathbf{R}_i^n$ through the incremental deformations $\Delta\mathbf{u}_i^n$, as written,

$$\Delta\overline{\mathbf{u}}_i^n = \mathbf{L}^T\Delta\mathbf{u}_i^n;\ \overline{\mathbf{R}}_i^n = \mathbf{K}_s\Delta\overline{\mathbf{u}}_i^n;\ \mathbf{R}_{i+1}^n = \mathbf{R}_i^n + \mathbf{L}\Delta\overline{\mathbf{R}}_i^n \qquad (21);(22);(23)$$

in which $\overline{\mathbf{u}}_i^n$ and $\overline{\mathbf{R}}_i^n$ are respectively total deformations and nodal element resistance at element level. The unbalanced force at *n*-th load increment is therefore obtained as,

$$\Delta\mathbf{f}^n = \mathbf{f}^n - \mathbf{R}_{i+1}^n \qquad (24)$$

The above process is repeated until the unbalanced forces $\Delta\mathbf{f}^n$ at the nodes are eliminated, at which the equilibrium solutions at *n*-th load increment at the nodes can be attained, and the next (*n+1*)-th load increment $\mathbf{f}^{n+1}$ as given in Eq. (24) should begin until numerical instability.

6. NUMERICAL EXAMPLES

This section verifies the modelling capacity of the present advanced computational method in the context of the higher-order element formulation and the refined plastic hinge method; especially the geometric and material nonlinearities for the sake of design purpose of a structure. Apart from the competent modelling capacity, the present approach can simulate these nonlinearities with the least element number for an entire structure. Therefore, a few of examples are to verify the material and geometric nonlinear effects.

6.1 Fixed end beam with an asymmetric point load

This example exemplifies the material yielding due to bending only and load redistribution in the presence of plasticity of a fixed end beam. Liew et al. [13] studied this problem by both a refined plastic hinge method (elastic-gradual-plastic) and a hinge-by-hinge method (elastic-plastic), whereas Iu and Bradford [5]**Error! Reference source not found.** were through the refined plastic hinge method (elastic-gradual-plastic-strain hardening) as demonstrated in Fig. 1, but no strain-hardening behaviour is in effect in this modelling. The present method can replicate the inelastic behaviour of the fixed end beam very well with both approaches as shown in Fig. 1, at which the load factor PL/M_p is plotted against the normalised deflection $\Delta EI/M_pL^2$ as location 2. The refined plastic hinges are formed for gradual and full yielding in sequence (1→2→3) due to load redistribution as given in Fig. 1, of which indicates the load factor at various material yielding stages, such as gradual and full yielding.

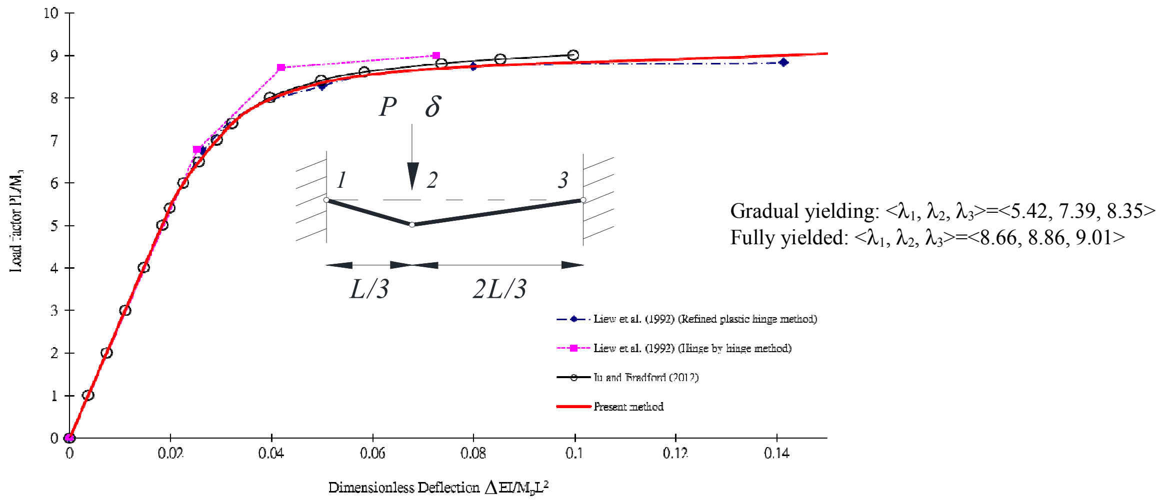

Figure 1: Normalized dimensionless load-deflection curve of a fixed end beam

6.2 Column buckling by the design code and present numerical technique

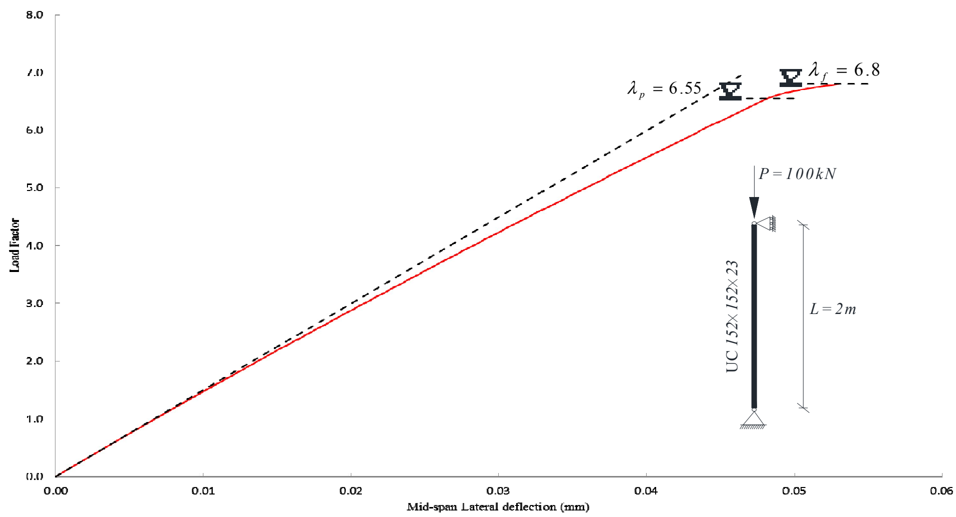

Figure 2: Load-deflection curve of a column is subjected to axial compression

This example studies the column buckling (i.e. P-δ effect) of a column, whose geometry and properties are given in Fig. 2. The behaviour of this column is studied by the design code [14], of which the ultimate load capacity is 6.85. When a mid-span plastic hinge is anticipated, the numerical modelling of this column is divided by 2 present higher-order elements. It is very close to those from present method as stated in Fig. 2. Hence the present advanced computational technique can capture the inelastic buckling, when the partial yielding at mid-span occurs at λ_p=6.55 and the mechanism is formed at λ_f=6.8. Therefore, the advanced computational technique can provide all range behaviour of a member as well as a whole structure instead of mere the ultimate load. As a result, this approach gives an overall picture for the structural engineers to make a holistic decision.

6.3 ECCS calibration frame for material behaviour

This frame in Fig. 3 is a benchmark solution by the ECCS for verifying the inelastic behaviour using the second-order inelastic analysis, at which includes gradual and full yielding, P-Δ and P-δ effect.

Vogel [15] studied this calibration frame by both plastic hinge and zone methods as depicted in Fig. 3. In this numerical model using the present advanced computational technique, only one higher-order element is required for each member. The present method can capture the inelastic behaviour of the ECCS calibration frame very well as seen in Fig. 3. The ultimate load level from the present method is 1.03, which are similar to 1.02 and 1.07 from plastic zone and plastic hinge method, respectively. The plastic hinges are formed at the top of the both columns, so the one element per member is justified. Therefore, this example can verify the second-order inelastic behaviour being captured by the present advanced computational technique. It means this approach can help safeguard the structure against the detrimental second-order inelastic effect for design purpose.

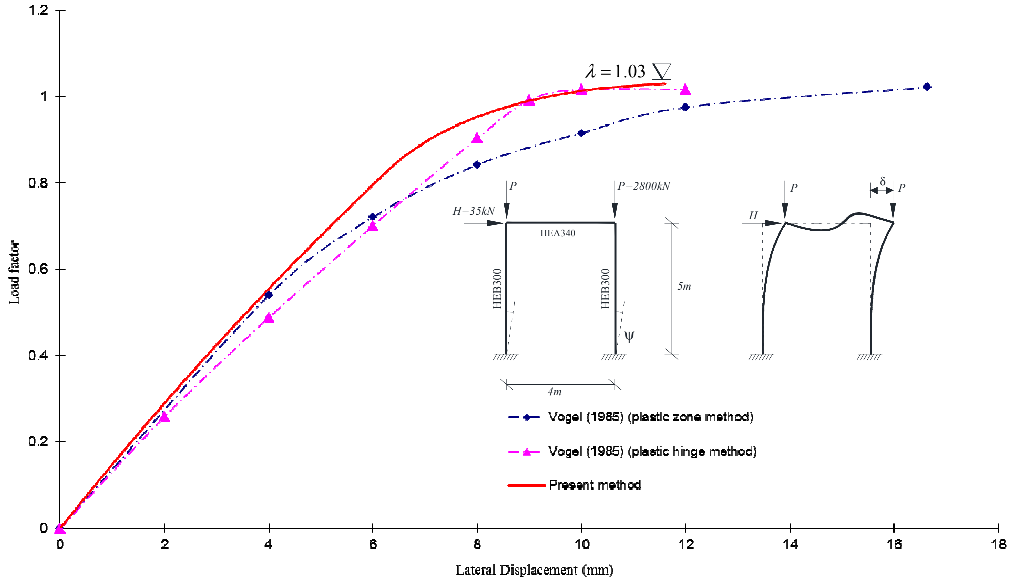

Figure 3: Load-deflection curve of the ECCS calibration frames for the inelastic analysis

7. CONCLUSIONS

This paper shows that the higher-order element stiffness formulation with the refined plastic hinge approach, at which using the least elements for a structure can replicate the material (including gradual, full yielding and strain-hardening effect) and geometric (including P-δ and P-Δ effect) nonlinearities in the effective, accurate and efficient manner. Unfortunately, the fool-proof ultimate element is yet to come. For example, the restrictions encountered includes,

1) The formulation of spring is always at the nodes, since it breaks the continuity assumption, while being formulated along an element.
2) It is hard to preserve competent material modelling and the modelling of second-order bowing using an element, because they are reliant on incremental and total equilibrium equation, respectively. Total plastic equilibrium equation is not straight forward to formulate.
3) For most of the finite element approach, they can hardly simulate the local effects, such as local buckling, fracture, etc., because 1D finite element formulation makes use of the governing equation of an overall element.

Therefore, it means the high-quality engineer must understand the capacity of the second-order inelastic analysis clearly whether or not the analysis can replicate the corresponding behaviour for the design of a structure, when different nonlinear analyses have their own restrictions so far; it is particular true when the fool-proof ultimate element is yet to come. At last, the great responsibility (for the engineer) comes from the great power (from the advanced computational technique).

REFERENCES

[1] Chan SL, Zhou ZH. Pointwise equilibrating polynomial element for nonlinear analysis of frames. Journal of Structural Engineering ASCE 1994; 120(6): 1703-1717.

[2] Chan SL, Zhou ZH. Second-order elastic analysis of frames using single imperfect element per member. Journal of Structural Engineering ASCE 1995; 121(6): 939-945.

[3] Iu CK, Bradford MA. Second-order elastic analysis of steel structures using a single element per member. Engineering Structures 2010; 32: 2606-2616.

[4] Iu CK, Bradford MA. Higher-order non-linear analysis of steel structures Part I: Elastic second-order formulation. International Journal of Advanced Steel Construction 2012; 8(2): 168-182.

[5] Iu CK, Bradford MA. Higher-order non-linear analysis of steel structures Part II: Refined plastic hinge formulation. International Journal of Advanced Steel Construction 2012; 8(2): 183-198

[6] Izzuddin BA. Quartic formulation for elastic beam-columns subject to thermal effects. Journal of Engineering Mechanics ASCE 1996; 122(9): 861-871.

[7] Liew JYR, Chen H, Shanmugam NE, Chen WF. Improved nonlinear plastic analysis of space frame structures. Engineering Structures 2000; 22: 1324-1338.

[8] Zhou ZH, Chan SL. Elastoplastic and large deflection analysis of steel frames by one element per member. I: One hinge along member. Journal of Structural Engineering 2004; 130(4): 538-544.

[9] Chan SL, Zhou ZH. Elastoplastic and large deflection analysis of steel frames by one element per member. II: Three hinges along member. Journal of Structural Engineering 2004; 130(4): 545-533.

[10] Iu CK, Bradford MA. Novel non-linear elastic structural analysis with generalized transverse element loads using a refined finite element. (submitted)

[11] Iu CK, Bradford MA, Chen WF. Second-order inelastic analysis of composite framed structures based on the refined plastic hinge method. Engineering Structures 2009; 31(9): 799-813.

[12] Iu CK, Chan SL. A simulation-based large deflection and inelastic analysis of steel frames under fire. Journal of Constructional Steel Research 2004; 60: 1495-1524.

[13] Liew JYR, White DW, Chen WF. Second-order refined plastic hinge analysis of frames. Structural Engineering Report CE-STR-92-12, 1992; Purdue University, West Lafayette, Indiana.

[14] AS4100 – 1988: Design of steel structures, Australian Standard.

[15] Vogel U. Calibrating frames. Der Stahlbau 1985; 10: 296-301.

12th International Conference on
Steel, Space and Composite Structures
28-30 May 2014, Prague, Czech Republic

POST-WELD HEAT TREATMENT OF HIGH STRENGTH S690 STEEL PLATE-TO-PLATE JOINTS - PART II: ULTIMATE STRENGTH

M.S. Zhao*, Y.F. Jin, C.K. Lee and S.P. Chiew

School of Civil and Environmental Engineering
Nanyang Technological University, Singapore
e-mail: *mzhao1@ntu.edu.sg

Keywords: post weld heat treatment, high strength steel, deformation capacity, ultimate strength

Abstract: *Literature shows that it is a big challenge for high strength heat treated steel to achieve sufficient deformation capacity to avoid brittle fracture under as weld conditions. This study experimentally investigated the potential improvement in the ductility of welded plate to plate joints by post weld heat treatment techniques. In total 15 plate-to-plate specimens in different shapes or thicknesses are heat treated and subsequently tested under uniaxial tension test. Test results in forms of global load-displacement curves at the brace end and strain-displacement curves at certain crucial locations show that post weld heat treatment is still effective to enhance the deformation capacity after welding without sacrificing the ultimate strength.*

1. INTRODUCTION

Welding is of great economic importance for steel structures, as one of most important tools available to the engineers in their efforts to reduce the production and fabrication costs. Greater freedom in design is also made possible by the use of welding. However, welding may cause a lot of troubles for the heat treated high strength steels, which was inherited from the heat-invulnerable microstructures[1]. Reports have shown that the amount of residual stress in welded quenched and tempered steel structures are high[2,3] and the deterioration of mechanical properties in the heat affected zone including strength, hardness and toughness is inevitable[4]. It would be such a loss for high strength steel structures if welding is not applicable.

In the part I of the twin papers, it was proven that the pre-mature failure is quite a problem for RQT-S690 plate-to-plate joints with thicknesses of 12 mm and 16mm. The failure appeared as brittle fracture at the weld toe instead of the more ductile fracture at the bolt area as the 8mm thick specimen. Further check of the fracture surface revealed that the heat affected zone (HAZ) was responsible for the fracture initiation. Therefore, a special coupon test was carried out to study the potential effects of post-weld heat treatment (PWHT) on the mechanical properties of the HAZ. The conclusion was that PWHT was effective in improving the properties of the HAZ under as weld (AW) condition.

Therefore, this study investigated the tensile behavior of the high strength steel plate-to-plate joints undergone post weld heat treatments. Joints in the same configuration as those in the Part-I were tested together with a new patch of specimens in 90° fabricated by double groove complete joint penetration method[5].

2. EXPERIMENTAL STUDY

2.1 Specimens

Two types of specimens were studied, i.e. RQT-S690 plate-to-plate joints in 45° and 90°, as shown in Figure 1. In fact, different expectations were given to these two types of joints: the 45° specimens would fail due to tension in the chord plate, while the chord plate of the 90° was actually taking bending loads. Nevertheless, both two types of loading were supposed to bring in the tensile failure at the weld toe or the bolt area.

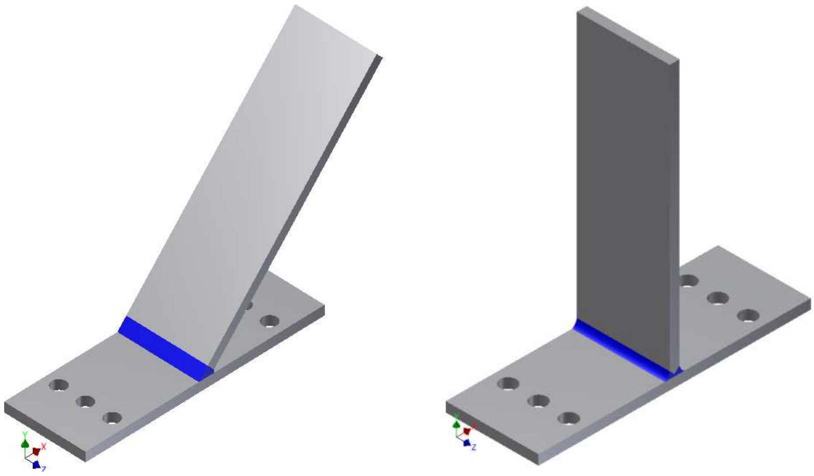

Figure 1: The Configuration of the Studied Specimens

2.2 Post weld heat treatment

PWHT for quenched and tempered steel as well as cold work hardened steel is not recommended by AWS (clue 3.14)[5], since PWHT may introduce unpredictable and extremely complicated changes into the microstructure of hardened steel weldments including RQT-S690. Based on the PWHT clues for normal strength steels by the AWS structural steel welding code, PWHT at 600°C and a sub-critical temperature 570°C were designed for RQT-S690. However, reduced maintaining time was used herein due to consideration of the fact that RQT-S690 was more vulnerable to heat compared to normal strength steels, as it was proven that maintain at 600°C for 10 minutes would be enough to induce noticeable changes to the mechanical properties of RQT-S690 base metal[6]. Basically, whichever smaller of the half of the required time for 8mm specimen and the minimum holding time was employed.

Specimen Thickness	Maintaining time (minutes)			
	600°C		570°C	
	AWS	Actual	AWS	Actual
8	20	15	38.4	20
12	30		57.6	
16	40		76.8	

Note: 15min is the minimum holding time required by AWS. 90° T specimens only went through the 570°C post weld heat treatment

Table 1: Parameters of Post Weld Heat Treatment

3. TENSILE TEST RESULT

3.1 Load-displacement curves

Again, the same set of equipments stated in the Part-I of the twin papers was used to conduct the tensile tests. The first patch of tests only included the 45° Y specimens in three different thicknesses. The employed PWHT methods were not able to change the failure type of those specimens, but did bring in certain changes to the load carrying capacity or the global ductility. All specimens except for those in 8mm showed failure mainly due to the brittle fracture at the weld toe. Generally, although PWHT at 600°C for 20 minutes (PWHT-600) improved the deformation ability, or the global ductility, of the specimens to some extent, the load carrying capacity at the same displacement level was compromised. However, an encouraging improvement at the maximum load could be seen for the 8mm and 16mm specimens, which motivated the further test for PWHT at a lower temperature (PWHT-570).

Compared to the effects of PWHT-600, the PWHT-570 seemed to be much gentler. For most of the loading time, the PWHT-570 just shared the same curve with the AW until the final stage. For the 8 mm specimens, only a small decrease in the final strength could be observed. The weld connection was proved to be stronger than the loading carrying capacity of the bolt area. Since the strength deterioration of the base material during PWHT was predicted according to the literature[6], the slight decrease of the global load carrying capacity was still acceptable. What is more, the PWHT-570 introduced something good to the 16 mm specimens as well. First, the LD curve of PWHT simply went much further than the AW. Second, the failure mode of the PWHT started to shift. For the AW specimen, a through thickness fracture (TTF) followed tightly to the first cracks in the weld toe. However, the first surface cracks appeared much later in the PWHT-570 specimen and the specimen was still able to carry more loads after that. Although the test ended about 850KN because the bolts failed, the displacement after the first cracks reached more than 15% of the total and the LD curve still had the potential to go higher. Since the designed shear load resistance of the bolts were supposed to be much higher than the weld connection, the PWHT for the 16mm was considered to be successful hence. However, every coin has two sides. The PWHT-570 still seemed to be too much for the 12mm specimens. Earlier failure was triggered by the fracture of the HAZ. The evidence is that the first cracks were followed by a long almost-horizontal stage in the LD curve until the final TTF. As for the reason, the notorious grain boundary grow in the microstructure by overheating[7] may be blamed for the embrittlement of the HAZ.

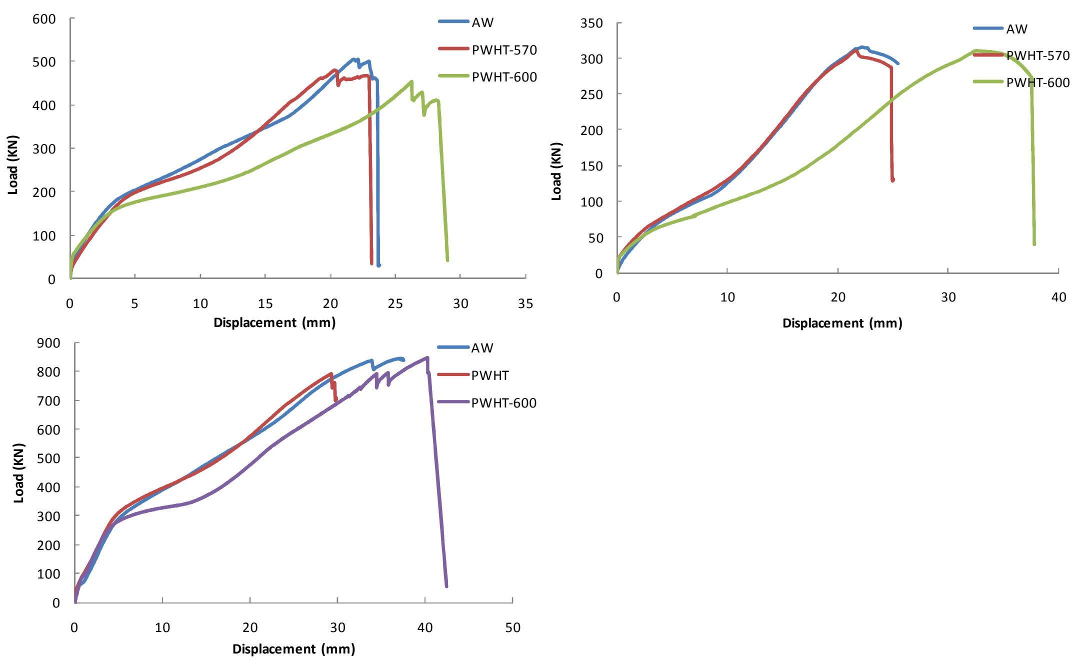

Figure 2： Load-Displacement Curves of the 45° Y Joints

Figure 3: Cracks in the HAZ (left) and Multiple Layer Fracture Surfaces (right)

As stated before, the loading types of the studied 45° Y and 90° T specimens were different. However, not much difference in the failure modes could be observed. The weld connection of the 8mm specimen was strong enough to bear loads until the bolt area failed. Therefore, it is reasonable that PWHT-570 only managed to lower down the ultimate strength in a negligible extent. The focus here was still give to the 16 mm specimen. It could be clearly seen that the specimens were still able to carry loads after the crack initiated in the HAZ for a long time. The test for PWHT-570 ended when the L-D curve reached 700KN again after cracking due to safety considerations. Checking after test revealed that the HAZ was only partially cracked at the middle of the weld toe, while necking was formed at the bolt area which was the sign of the failure type shifting, as shown in Figure 5. Accordingly, it could be confirmed that PWHT-570 was effective to improve the crack resistance in the HAZ and help avoiding brittle failure of the 90° T specimens in 16mm.

However, the embrittlement of overheating seemed to be exacerbated in the 12mm specimen. Different from the 45° Y specimens, the 12mm 90° T specimen failed in the way of TTF suddenly without any noticeable clue in the LD diagram.

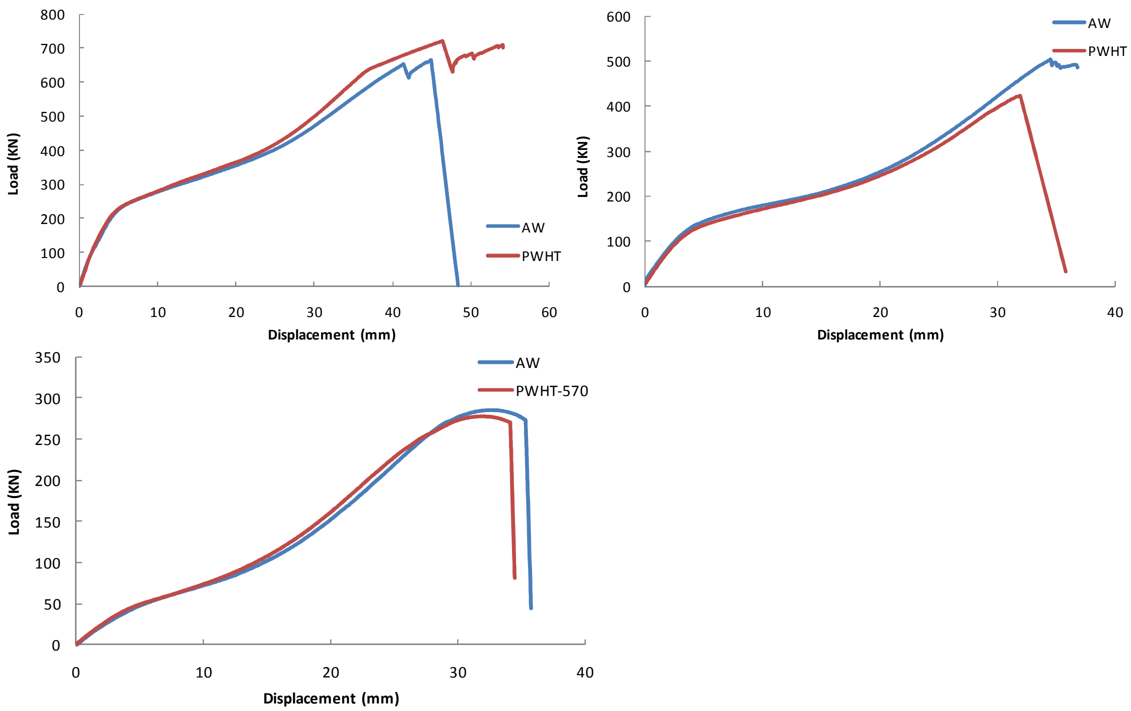

Figure 4: The Load-Displacement Curves of the 90° T Joints

Figure 5: Failure Modes of PWHT-570: Cracks in The HAZ (left) and Necking at The Bolt Area (right)

3.2 Strain Analysis

In order to study the strain of the HAZ – carried global load relationships, strain gauges were used to capture the strain developments in the HAZ. The load-strain curves of the measured point which was 0.4t (6.4 mm) away from the weld toe of the 16 mm 45° Y and 90° T specimens are shown in Figure 6. It was quite clear now that the PWHT strengthened the specimens by lower down the strains at the same load level so that the cracks in the HAZ were to be postponed.

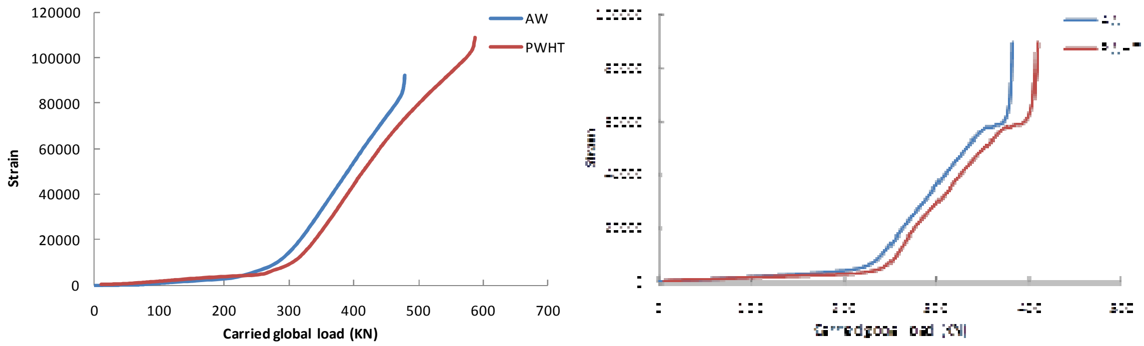

Figure 6: The Carried Global Load – HAZ Strain Curves of The 16mm 45° Y (left) and 90° T (right) Specimens

4. CONCLUSIONS

This study experimentally investigated the potential improvement in the ductility of welded plate to plate joints by post weld heat treatment techniques. In total 15 plate-to-plate specimens in different shapes or thicknesses are heat treated and subsequently tested under uniaxial tension test. Test results confirmed that PWHT could be useful to improve the load carrying capacity and deformation ability of the 16 mm plate-to-plate joints, and avoid the sudden brittle fracture. However, overheating could be detrimental to the joints as the 12mm specimens were weakened after the same PWHT procedures. Besides, PWHT showed almost no influence to the 8mm specimens, since they failed due to the insufficient load resistance of the cross section capacity at the bolt area rather than the weld connection.

REFERENCES

[1] H.K.D.H. Bhadeshia, R.W.K. Honeycombe, Steels: microstructure and properties, 3th ed., Elsevier Science & Technology, Oxford, United Kingdom, 2006.

[2] C.K. Lee, S.P. Chiew, J. Jiang, Residual stress study of welded high strength steel thin-walled plate-to-plate joints, Part 1: Experimental study, Thin-Walled Structures, 56 (2012) 103-112.

[3] Y.-B. Wang, G.-Q. Li, S.-W. Chen, The assessment of residual stresses in welded high strength steel box sections, Journal of Constructional Steel Research, 76 (2012) 93-99.

[4] T. Mohandas, G. Madhusudan Reddy, B. Satish Kumar, Heat-affected zone softening in high-strength low-alloy steels, Journal of Materials Processing Technology, 88 (1999) 284-294.
[5] AWS, Structural Welding Code, in: steel, American National Standards Institue, Miami, 2008.
[6] S.P. Chiew, M.S. Zhao, C.K. Lee, Mechanical properties of heat-treated high strength steel under fire/post-fire conditions, Journal of Constructional Steel Research, 98 (2014) 12-19.
[7] D. KAPLAN, G. MURRY, Thermal, Metallurgical and Mechanical Phenomena in the Heat Affected Zone, John Wiley & Sons, 2008.

12th International Conference on

STEEL, SPACE & COMPOSITE STRUCTURES

28-30 May 2014, Prague, Czech Republic

INDEX OF AUTHORS

N.B. Click on page number for authors with multiple papers

12th International Conference on

STEEL, SPACE & COMPOSITE STRUCTURES

28-30 May 2014, Prague, Czech Republic

INDEX OF AUTHORS

N.B. Click on page number for authors with multiple papers

International Conference on **STEEL STRUCTURES**
7-9 March 1984, Singapore

TABLE OF CONTENTS

2nd International Conference on **STEEL STRUCTURES**
18-19 September 1985, Jakarta, Indonesia

TABLE OF CONTENTS

3rd International Conference on **STEEL STRUCTURES**
17-18 March 1987, Singapore

TABLE OF CONTENTS

4th International Conference on **STEEL STRUCTURES**
18-19 September 1990, Jakarta, Indonesia

TABLE OF CONTENTS

5th International Conference on **STEEL STRUCTURES**
12-14 December 1994, Jakarta, Indonesia

TABLE OF CONTENTS

6th International Conference on **STEEL & SPACE STRUCTURES**
1 - 3 September 1999, Singapore

TABLE OF CONTENTS

BUILDING AND SPACE STRUCTURES

COMPOSITE STRUCTURES

BRIDGE STRUCTURES

FATIGUE AND FRACTURE

7th International Conference on **STEEL & SPACE STRUCTURES**
2 – 3 October 2002, Singapore

TABLE OF CONTENTS

COLD-FORMED STEEL STRUCTURES

BEAMS AND COLUMNS

CONNECTIONS

8th International Conference on

STEEL, SPACE & COMPOSITE STRUCTURES

15 – 17 May 2006, K. Lumpur, Malaysia

TABLE OF CONTENTS

TUBULAR STRUCTURES

FATIGUE AND FRACTURE

EARTHQUAKE AND DYNAMICS

COLD-FORMED STEEL STRUCTURES

FABRICATION AND CONSTRUCTION

INFORMATION TECHNOLOGY

COMPOSITE STRUCTURES

9th International Conference on

STEEL, SPACE & COMPOSITE STRUCTURES

10–15 October 2007, Yantai and Beijing, China

TABLE OF CONTENTS

BEAMS AND COLUMNS

CONNECTIONS

COMPOSITE STRUCTURES

CONCRETE-FILLED COLUMNS

MISCELLANEOUS – BEIJING

ISBN No. 978-981-05-7589-0

10th International Conference on
STEEL, SPACE & COMPOSITE STRUCTURES
18-20 May 2011, Gazimagusa, North Cyprus

TABLE OF CONTENTS

Technical Papers

Technical Papers

11th International Conference on

STEEL, SPACE & COMPOSITE STRUCTURES

12-14 December 2012, Qingdao, China

TABLE OF CONTENTS

Technical Papers

Technical Papers

ISBN No. 978-981-09-0077-9